

13th Workshop on Crystalline Silicon Solar Cell Materials and Processes

Extended Abstracts and Papers

Workshop Chairman/Editor: B.L. Sopori

Program Committee:

J. Rand, T. Saitoh, R. Sinton, M. Stavola,
D. Swanson, T. Tan, E. Weber, J. Werner,
B. Sopori, and M. Al-Jassim

Vail Marriott Mountain Resort
Vail, Colorado

August 10-13, 2003



NREL

National Renewable Energy Laboratory

1617 Cole Boulevard
Golden, Colorado 80401-3393

NREL is a U.S. Department of Energy Laboratory
Operated by Midwest Research Institute • Battelle • Bechtel

Contract No. DE-AC36-99-GO10337

13th Workshop on Crystalline Silicon Solar Cell Materials and Processes

Extended Abstracts and Papers

Workshop Chairman/Editor: B.L. Sopori

Program Committee:

J. Rand, T. Saitoh, R. Sinton, M. Stavola,
D. Swanson, T. Tan, E. Weber, J. Werner,
B. Sopori, and M. Al-Jassim

Vail Marriott Mountain Resort

Vail, Colorado

August 10-13, 2003

Prepared under Task No. WO97C100



NREL

National Renewable Energy Laboratory

1617 Cole Boulevard
Golden, Colorado 80401-3393

NREL is a U.S. Department of Energy Laboratory
Operated by Midwest Research Institute • Battelle • Bechtel

Contract No. DE-AC36-99-GO10337

NOTICE

This report was prepared as an account of work sponsored by an agency of the United States government. Neither the United States government nor any agency thereof, nor any of their employees, makes any warranty, express or implied, or assumes any legal liability or responsibility for the accuracy, completeness, or usefulness of any information, apparatus, product, or process disclosed, or represents that its use would not infringe privately owned rights. Reference herein to any specific commercial product, process, or service by trade name, trademark, manufacturer, or otherwise does not necessarily constitute or imply its endorsement, recommendation, or favoring by the United States government or any agency thereof. The views and opinions of authors expressed herein do not necessarily state or reflect those of the United States government or any agency thereof.

Available electronically at <http://www.osti.gov/bridge>

Available for a processing fee to U.S. Department of Energy and its contractors, in paper, from:

U.S. Department of Energy
Office of Scientific and Technical Information
P.O. Box 62
Oak Ridge, TN 37831-0062
phone: 865.576.8401
fax: 865.576.5728
email: reports@adonis.osti.gov

Available for sale to the public, in paper, from:

U.S. Department of Commerce
National Technical Information Service
5285 Port Royal Road
Springfield, VA 22161
phone: 800.553.6847
fax: 703.605.6900
email: orders@ntis.fedworld.gov
online ordering: <http://www.ntis.gov/ordering.htm>



Printed on paper containing at least 50% wastepaper, including 20% postconsumer waste



13th Workshop on Crystalline Silicon Solar Cell Materials and Processes

TABLE OF CONTENTS

Title/Author(s):	Page
<i>Meeting the Challenges of c-Si Photovoltaics: Workshop Theme</i> B. Sopori	1
<i>Sliver™ Solar Cells</i> A. Blakers, K. Weber, M. Stocks, J. Babaei, V. Everett, M. Kerr, and P. Verlinden	3
<i>Modeling of Industrial CZ and FZ Growth</i> T. Wetzel and W. Ammon	7
<i>Multiple Ribbon Growth Via String Ribbon Method</i> J. Hanoka	13
<i>Present Status and Prospects of Ga-Doped mc-Si Solar Cells</i> K. Fukui, S. Fujii, M. Tsuchida, S. Tanimoto, K. Sihirasawa, M. Dhamrin, and T. Saitoh	14
<i>Advanced Lifetime Spectroscopy</i> S. Rein and S. Glunz	18
<i>Progress in Manufacturable High-Efficiency Silicon Solar Cells Based on OECO Technology</i> R. Hezel	26
<i>High Efficiency, One-Sun Solar Cell Processing</i> W. Mulligan and R. Swanson	30
<i>Current Trends in Si Solar Cell Manufacturing</i> S. Shea	38
<i>Laser-Fired Contacts</i> R. Preu, E. Schneiderlöchner, A. Grohe, M. Hofmann, D. Kray, S. Glunz, and G. Willeke	39
<i>Dry Processing for Crystalline Silicon Solar Cells</i> G. Agostinelli, S. De Wolf, H. Dekkers, G. Beaucarne, Q. Le, H. Goldbach, R. Schropp, I. Pinter, G. Walther, K. Schade, P. Vitanov, M. Vukadinovic and M. Topic	47

<i>Advanced Wet Processing and Drying of c-Si Wafers Based on Diluted Chemistry and Ozone</i>	55
J. Osterkamp and J. Schreckendiek	
<i>Highly Efficient Multicrystalline Silicon Solar Cells</i>	62
P. Fath	
<i>SiN Coatings for Si Solar Cells: Understanding Their Multifunctional Role</i>	63
B. Sopori	
<i>Crack Formation and Propagation</i>	64
R. Ritchie	
<i>Properties of Si:H Mixed Amorphous Microcrystalline Phases</i>	65
C. Wronski and R. Collins	

Poster Papers

<i>A Study of Dendritic Web Silicon Growth</i>	73
X. Zhang, B. Raghathanachar, D. Meier, M. Dudley, and S. Mahajan	
<i>First-Principles Calculations of Nucleation Precursors in Nitrogen-doped Float Zone Silicon</i>	77
A. Karoui, F. Sahtout Karoui, and G. Rozgonyi	
<i>Modeling and Simulation of Dislocation Atmosphere Locking Effects in Silicon</i>	81
A. Karoui and G. Rozgonyi	
<i>Development of an Infrared Residual Stress Polariscopic for Solar Cell Inspection</i>	85
S. He, S. Danyluk, J. Tarasko, S. Lulu, A. Belyaev, and S. Ostapenko	
<i>Error Analysis of a Circularly Polarized Phase-Stepping Polariscopic</i>	88
S. He, T. Zheng, and S. Danyluk	
<i>PV Feedstock Costs – Five Year Outlook</i>	92
J. Maurits	
<i>Statistically Meaningful Data on the Chemical State of Iron Precipitates in Processed Multicrystalline Silicon Using Synchrotron-Based X-ray Absorption Spectroscopy</i>	96
T. Buonassisi, M. Heuer, A. Istraov, E. Weber, Z. Cai, B. Lai, M. Marcus, J. Lu, G. Rozgonyi, R. Schindler, R. Jonczyk, and J. Rand	
<i>Experimental Procedure for Determination of the Depth of Metal Clusters in XBIC/μ-XRF Mapping of Metal Clusters in Silicon Solar Cells</i>	102
O. Vyvenko, T. Buonassisi, A. Istratov, and E. Weber	
<i>Theory of Defects in Silicon Solar Cells at Finite Temperatures</i>	106
M. Sanati and S. Estreicher	
<i>Theoretical Predictions of Complex Formation Following Hydrogenation from a Nitride Layer</i>	110
J. McAfee and S. Estreicher	

<i>Characterization of H Introduced into Si By Hydrogenation from SiN_x Films</i>	114
M. Stavola, F. Jiang, A. Rohatgi, D. Kim, J. Holt, H. Atwater, and J. Kalejs	
<i>The Generation and Manipulation of Point Defects and Light Element Impurities in Silicon by Electron Irradiation</i>	118
N. Stoddard, G. Duscher, and G. Rozgonyi	
<i>Second-phase Particle Incorporation and the Occurrence of a Cellular Grain Size Distribution in Polycrystalline Sheet Silicon</i>	122
R. Zhang, G. Rozgonyi, J. Rand, and R. Jonczyk	
<i>Distribution of Oxynitride Particles and Oxygen Precipitates in Polycrystalline Sheet Silicon</i>	126
J. Lu, G. Rozgonyi, J. Rand, and R. Jonczyk	
<i>APIVT Epitaxial Growth on Zone-Melt Recrystallized Silicon</i>	130
T. Wang, P. Sims, M. Page, R. Bauer, M. Landry, R. Reedy, Y. Yan, and T. Ciszek	
<i>Solid-Source Doping of Float-Zoned Silicon with B, N, O, and C</i>	134
T. Ciszek	
<i>Ion Beam Mixing of Silicon-Germanium for Solar Cell Applications</i>	138
S. Abedrabbo, S. Salem, D. Arafah, A. Fiory, B. Sopori, and N. Ravindra	
<i>Stable Record Efficiencies for EFG and String Ribbon Solar Cells</i>	146
G. Hahn and P. Geiger	
<i>Predicting Multi-Crystalline Solar Cell Efficiency from Lifetime Measured in Silicon Blocks</i>	151
R. Sinton and T. Mankad	
<i>Dependence of Aluminum Alloying on Solar Cell Processing Conditions</i>	154
C. Honsberg, K. Anwar, H. Mehvarz, J. Cotter, and S. Wenham	
<i>Neutron Activation Analysis Study of Metal Content of Multicrystalline Silicon for Cost-Efficient Solar Cells</i>	158
A. Istratov, T. Buonassisi, R. McDonald, A. Smith, R. Schindler, J. Rand, J. Kalejs, and E. Weber	
<i>Characterization of Silver/Glass/Silicon Front Contact Interface In a Silicon Cell</i>	162
S. Sridharan, C. Khadilkar, T. Pham, and A. Shaikh	
<i>Metallic Precipitate Contribution To Generation and Recombination Currents in Electronic Devices Due to the Schottky Effect.....</i>	166
T. Tan and M. Negoita	
<i>Empirical Modeling of Ingot and Post Oxidation Level QSS Lifetime Measures in a Production Environment</i>	170
J. Coleman, J. Nickerson, and R. Sinton	

<i>Improvement of Electronic Quality in mc-Si Wafers with SiN_x:H Layer After Rapid Thermal Processing Accessed by Scanning Photoluminescence</i>	177
I. Tarasov, M. Dybiec, S. Ostapenko, A. Rohatgi, V. Yelundur, and A. Gabor	
<i>Light-Induced Lifetime Degradation in Multicrystalline Silicon</i>	182
D. Macdonald, L. Geerligs, and S. Riepe	
<i>Laser Doping for Crystalline Silicon Solar Cell Emitters</i>	186
A. Esturo-Bretón, T. Wagner, J. Köhler, and J. Werner	
<i>Double Sided Buried Contact Solar Cells on Czochralski Wafers</i>	190
P. Cousins, C. Honsberg, and J. Cotter	
<i>Silicon Surface and Heterojunction Interface Passivation Studies by Lifetime Measurement</i>	194
M. Page, Q. Wang, T. Wang, Y. Yan, S. Johnston, and T. Ciszek	
<i>Hydrogen Passivation of Iron in Multicrystalline Silicon</i>	199
L. Geerligs, A. Azzizi, D. Macdonald, and P. Manshanden	
<i>Superprism Reflector for Thin Crystalline Silicon Solar Cells</i>	203
T. Montalbo, K. Wada, and L. Kimerling	
<i>A Monte Carlo Approach for Assessing the Impact of Material and Process Variables on Solar Cell Performance and Manufacturing Cost</i>	207
A. Ristow and A. Rohatgi	
<i>Advances in Screen-Printed High-Sheet-Resistance Emitter Cells</i>	211
M. Hilali, V. Meemongkolkiat, and A. Rohatgi	
<i>Record High Efficiency Screen-Printed Belt Co-Fired Cells on EFG Si Ribbon (16.1%) and HEM mc-Si (16.9%)</i>	215
A. Upadhyaya, K. Nakayashiki, M. Hilali, A. Rohatgi, J. Kalejs, B. Bathey, and K. Matthei	
<i>Record High Efficiency Solar Cells on EFG (18.2%) and String Ribbon (17.8%) Silicon by Rapid Thermal Processing</i>	219
D. Kim, K. Nakayashiki, V. Yelundur, B. Rounsville, A. Rohatgi, A. Gabor, B. Bathey, and J. Kalejs	
<i>Hydrogen Enhanced Clusterization of Impurities Atoms in Crystalline Silicon</i>	224
B. Mukashev, Y. Gorelkinskii, and K. Abdullin	
<i>A Rapid, Non-Contact Method for Measurement of Si Wafer Thickness: Principles and Preliminary Results</i>	225
B. Sopori, C. Auriemma, C. Li, and J. Madjdpour	
<i>Detailed Study of Defects in Silicon Solar Cells by Cathodoluminescence Spectrum Imaging</i>	235
M. Romero, S. Ostapenko, M. Al-Jassim, I. Tarasov, and P. Sheldon	

Meeting the Challenges of c-Si Photovoltaics: Workshop Theme

Bhushan Sopori
National Renewable Energy Laboratory
1617 Cole Blvd.
Golden, CO 80401

The photovoltaic (PV) industry has been in a state of rapid growth for the last several years, leading to a production capacity that now exceeds 450 MW/yr. Even at this production rate, the size of the PV industry is only starting to have an impact on electric power production. The number of manufacturers continues to be quite small and is not likely to increase in the near future. Concomitantly, the growth is primarily through increased production at the existing facilities. Indeed, nearly all current manufacturers are expanding their production capacity. Thus, the current PV industry is facing a challenge of expansion and challenges to cope with “growing pains.” As the c-Si PV industry expands further, new challenges will emerge.

Increasing the production capacity is accompanied by multiple issues – higher throughput, faster processing, automation, implementation of cost-reduction approaches, and improving the process yields. Above all, these must be accompanied by the most important factor for cost reduction – increased efficiencies.

The c-Si PV industry has already embarked on several programs to reduce the PV energy costs. These include:

- Automation/wafer transport
- New equipment development
- Process development
- Process monitoring
- Use of thinner wafers
- New cell designs.

Although much of the work under these tasks is production-oriented engineering, a great deal of basic research must accompany them to develop appropriate solutions. For example, to handle wafer transport issues, a great deal of knowledge from the mechanisms of fracture, wafer damage, and wafer breakage mechanics is needed. Likewise, in the area of equipment development, the details of the processing must be determined. Indeed, each of the activities listed above has a broad spectrum of fundamental research to draw upon. The demand for high efficiency has resulted in acceleration of the time-to-market R&D results. The crystalline silicon R&D community has an immediate-term relevance and accountability as never before.

The theme of this workshop was chosen to highlight some of the challenges the c-Si community will most likely face. Accordingly, this workshop includes traditional sessions such as Crystal Growth, Impurities, Defects, and Gettering, along with sessions to specifically highlight these issues. These include:

- High-Efficiency Solar Cell Processing
- Advanced Processing Automation/Equipment
- What Will the Processing of Si Solar Cells Look Like in the Future?
- Commercial issues.

As usual, the workshop places a great deal of emphasis on the discussion and opinions of experts in the audience. For the first time, this workshop will include a rump session. This year's rump session will discuss R&D challenges in Si-PV. As expected, increase in production and reducing the cost of PV will require a well-concerted effort on commercial as well as laboratory fronts. Therefore, it is important to address both the near-term and the long-term R&D issues that can be supported by academic institutions through the DOE/NREL program.

This workshop is made possible by the devoted efforts and active participation of all attendees—speakers, discussion leaders, audience, workshop planners, and support from NREL/DOE. The format is rather heavy on discussion, allowing time to exchange the kind of information that is difficult to share in any other format. The poster sessions provide the latest research results, which at times may be only a few hours old. Participation of students is important, and the PV industry helps provide Graduate Student Awards. Together, we can help a smooth sailing as the Si-PV advances.

SLIVER™ SOLAR CELLS

A. Blakers¹, K. Weber¹, M. Stocks¹, J. Babaei¹, V. Everett¹, M.Kerr² and P.Verlinden²

1. Centre for Sustainable Energy Systems, ANU, Canberra, ACT 0200, Australia

2. Origin Energy Solar Pty. Ltd., GPO Box 1097, Adelaide, SA 5001, Australia

ABSTRACT

Thin (<70 micron) single crystal silicon cell solar cells have been manufactured through the use of a novel process involving selective etching. Narrow grooves are formed through the wafer. Cells are manufactured on the resulting silicon strips. These cells have a much greater surface area than the original wafer, leading to large decreases in processing effort and silicon usage. The size, thickness and bifacial nature of the cells create the opportunity for a wide variety of module architectures and applications.

INTRODUCTION

Crystalline silicon wafers remain the material of choice for photovoltaic modules, accounting for 90% of the photovoltaic (PV) market. However, the cost of the silicon remains a major barrier to reducing the cost of crystalline silicon photovoltaics.

Improvements in silicon usage in conventional ingot based technology have arisen through improved wafer sawing to reduce kerf losses and decrease wafer thickness. These changes are incremental and are limited by processing yield.

Substantial decreases in silicon usage requires a different approach. A variety of techniques for growing or harvesting thin layers of monocrystalline silicon have been developed [1,2]. Each has limitations in material quality or yield due to the silicon manufacturing technique.

A new technique for producing thin monocrystalline silicon solar cells has been developed at the Centre for Sustainable Energy Systems at the Australian National University, in conjunction with Origin

Energy. The new technology allows for large decreases in silicon usage by up to a factor of 12 (including kerf losses). In addition, it allows for a large reduction in the numbers of wafers processed per module by up to a factor of 35 compared to standard crystalline silicon technology. These factors allow the use of moderate to high quality silicon and more complicated wafer processing that enables high cell efficiencies while still obtaining significant \$/W_p cost savings.

THE SLIVER™ CELL CONCEPT

Solar cell texturing and micromachining technologies have used for many years the excellent selectivity of anisotropic etches for (111) surfaces. The new sliver cell process uses a micromachining technique to form deep narrow grooves in suitably masked wafers oriented such that the (111) plane is perpendicular to the wafer surface. Long narrow slots are opened perpendicular to the (111) plane in a masking layer on the wafer surface. Micromachining of the sliver cells commences at the surface of these narrow slots.

Trenches form vertically into the wafer. The base of the trench forms relatively rapidly compared to the (111) sidewalls. The micromachining continues until the trench extends the entire thickness of the wafer. The result is a large number of thin silicon strips in the centre of the wafer, held together by the unetched surrounds of the wafer (Figure 1). On 1mm thick 150mm wafers, these strips would typically be 100mm long, 1mm wide (wafer thickness) and 50-65 microns thick.

Cells are constructed on the narrow strips of silicon formed during the micromachining. Cell processing is completed while the

silicon strips are still supported by the silicon substrate at the edge of the wafer.

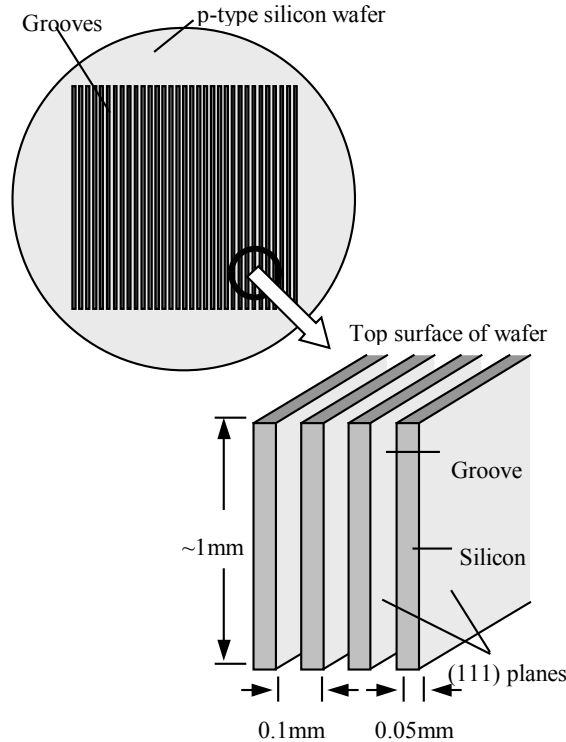


Figure 1: Selectively etched wafer. Long thin silicon slices are supported by the wafer frame.

The wafers are processed to produce solar cells (figure 2) using methods borrowed from the fabrication of high performance solar cells, such as heavy doping under the contacts, lightly doped emitter with good surface passivation and surface texturing. Heavy phosphorous and boron diffusions are applied to top and bottom surfaces of the wafer. These wafer surfaces become the long narrow edges of the silicon strips and therefore of the cells. The edges are subsequently metallised to form the p-type and n-type contacts. The sides of the grooves are textured using a novel texturing technique for (111) surfaces that offers near Lambertian light trapping properties. The grooves are then phosphorus diffused and passivated.

After processing, the cells are removed from the wafer frame. The resulting cells are long, narrow and thin. Typical Sliver™ cell dimensions are 50-100mm long, approximately 1-1.5mm wide and 50-

65microns thick. Since the cell processing is symmetric, the cells are perfectly bifacial.

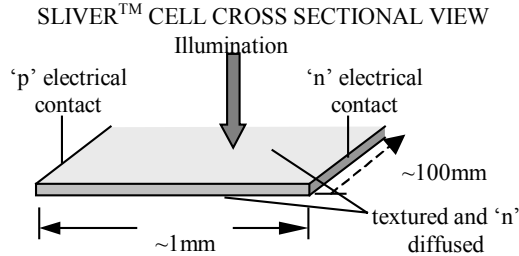


Figure 2: Schematic of the Sliver™ cell design.

The cell structure has the potential for excellent cell efficiencies. The cell is thin and there are collecting junctions on both sides of the cell. The emitter is lightly doped and the surface is well passivated. Therefore the cell has unity collection efficiency, even with low quality silicon.

The cell structure offers the opportunity for high cell voltages. The n and p contacts each cover only ~3% of the cell surface (at the edge) and can be independently doped for optimal passivation of the metal contacts.

The best cell result to date is from batch J50A. The cell has an open circuit voltage of 677mV, current of 19.6mA and fill factor of 76.0% with an efficiency of 18.6%. The cells from J50A are 960µm wide and 56 mm long. These cells are textured and have an oxide antireflection (AR) coating. The oxide AR coating limited cell efficiency due to reflection losses. Efficiencies exceeding 20% are expected with SiN AR coating and further technology optimisation. 19% test devices have been made with dicing saw cut cells that had random pyramid texturing.

SLIVER™ MODULES

Sliver™ cells differ radically from conventional cells in size and shape, being long, narrow, thin and flexible. Unlike conventional cells, Sliver™ cells have a width that is smaller than the thickness of the module. In addition, the cells are perfectly bifacial. This allows further silicon reductions by a factor of 2 to 3 through the use of a novel module design. A simple design approach is to introduce a

Lambertian reflector at the rear of a bi-glass module. The cells are positioned between the two layers of glass, spaced by a multiple of their width (typically from 1.5 to 3) (figure 3).

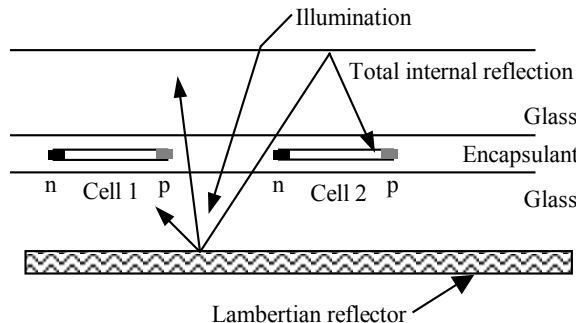


Figure 3: Lambertian reflector module design. The small width and bifacial nature of the Sliver™ cell enables the cells to be spaced out (in this case double cell width, halving silicon use).

Some of the light scattered from the rear reflector is directed onto the rear surface of the bifacial Sliver™ cell while another fraction of the light is reflected onto the glass where it is totally internally reflected back into the module. The remainder of the light is lost through the front glass. Conventional cells cannot have significant spacing (compared to the cell dimensions) without compromising greatly on efficiency due to their large size.

For cells spaced at double their width, about 84% of the light entering the module is captured in return for a 50% decrease in the silicon used per square metre. With 3-times spacing 74% of the light in the module is captured for a 67% reduction in silicon. Even better optical performance is possible with geometric designs. However, the cost of machining appropriate shapes and accurately aligning cells currently outweighs the performance benefits compared to the Lambertian reflector.

The small size of each cell means thousands of cells are required per square metre of module. These are assembled into modules at modest cost using high-speed assembling equipment similar to those developed for the microelectronics and opto-electronics industry. This automated cell placement

allows great flexibility in cell layout and interconnection.

By connecting cells in series, it is easier to build voltage than in conventional modules where the economies of scale favour large cells. Module output can be tuned from standard 12V applications to several hundred volts for grid-connected applications. Strings of Sliver™ cells with 200–400V output only require lengths of a few tens of centimetres. Series strings can be connected in parallel to increase current. These high voltage modules could allow for direct conversion from DC to AC without the requirement for voltage up-conversion.

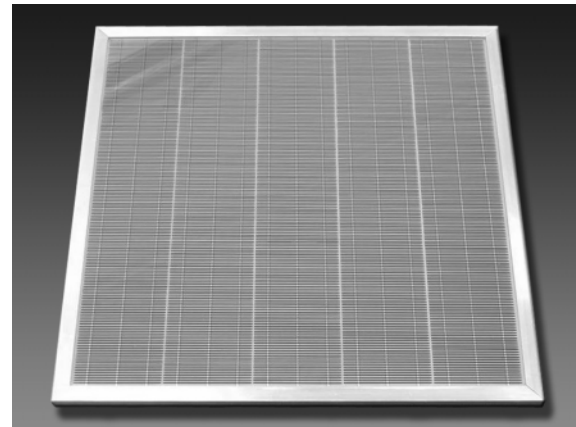


Figure 4: 1000cm² Sliver™ module. The cells are spaced at double their width and the module has a rear Lambertian reflector.

Since the cells are relatively small in area, so are the cell currents. This decreases the reverse current that any cell needs to tolerate during shading events. Cells can be designed which can reversibly breakdown to 100mA or more, alleviating the need for diode protection in the module. Modules containing strings of Sliver™ cells have passed hot spot tests without by-pass diodes.

A 580cm² prototype module was constructed with 500 0.56cm² Sliver™ solar cells. An efficiency of 12.3% was independently measured by Sandia National Laboratories. The cells were connected in four strings and were spaced with a gap between cells equal to their width. The cells were fabricated from 100mm wafers and had a SiN AR coat and no texturing. The voltage output of this module with the

strings in parallel was 80V. With the strings connected in series the V_{oc} was 320V.

Texturing offers large gains after encapsulation and should push this efficiency over 14%. An equivalent module with no gaps would have an efficiency of about 17%, but would cost more.

ADVANTAGES OF SLIVER™ CELLS

In addition to direct competition with conventional PV modules for power production, Sliver™ technology is well suited to other applications.

The high power-to-weight ratio is of interest for satellites and solar-powered aircraft, as is the bifacial response (to take advantage of the Earth's albedo). The cells are likely to be radiation tolerant because of their small thickness and the fact that there is a collecting junction on each surface. Building integrated Sliver™ modules take advantage of the fact that any degree of module transparency can be easily achieved by adjusting the Sliver™ spacing. Flexible modules can be created by suitable encapsulation of the Sliver™ cells (which are flexible due to their thinness). The ability to obtain high voltages in very small modules allows Sliver™ cells to be used to power small consumer items.

The combination of the novel cell processing and the module design flexibility provides Sliver™ cells with the potential for large savings in the amount of silicon required and the number of wafers used per MW of module production.

The gain in surface area from etching is determined by the pitch of the etching, the thickness of the wafer and the fraction of the wafer that can be etched to form silicon slices. Not all the wafer can be used due to the need for the edge of the wafer to form a frame to hold the cells. Additional area gains can be made by spacing the Sliver™ cells in the module. There is also a large reduction in the mass of silicon required per m^2 of module. In Table 1 a comparison is made with conventional pseudosquare Cz

wafers with thickness 320 μm , kerf 260 μm and module efficiency of 13.5% yielding around 13kg/kW_p. Per kW rating, there is a reduction in silicon usage of 8-12 times and a reduction in the number of wafers that need to be processed of 16-35 times.

Wafer thick. (mm)	Gap size in module	Silicon savings kg/kW	Processing reduction Wafers/kW	Module Effic. (%)
1.0	No gap	4 fold	10 fold	16.8
1.0	1x cell width	8 fold	16 fold	14.1
1.5	2x cell width	12 fold	35 fold	12.2

Table 1: Silicon mass and manufacturing savings possible with Sliver™ modules compared with conventional Cz modules.

Due to the silicon savings, better quality silicon can be used to maintain higher efficiency or lower quality material can be substituted to save costs. The saving in manufacturing is particular attractive as it allows for relatively expensive processing to be undertaken (e.g. photolithography, tube furnaces, evaporated and plated contacts) which help maintain high performance.

Sliver™ modules operate at slightly lower temperatures and have lower temperature coefficients than conventional modules. Temperature coefficients are reduced to 2.0mV because of the high V_{oc} .

Preliminary estimates show that the energy payback time of a Sliver™ module is only 1.7 years, two thirds of which is due to standard module components (glass, Al frame, encapsulant, etc).

CONCLUSIONS

Sliver™ PV technology offers large reductions in silicon consumption and wafer processing, together with other important advantages, while maintaining all of the advantages of single crystalline silicon.

REFERENCES

- [1] K.J. Weber, A.W. Blakers and K.R. Catchpole, Applied Physics A 69, 195 (1999)
- [2] Hiroshi Tayanaka, Kazushi Yamauchi, and Takeshi Matsushita, 2nd World Conference on PV Solar Energy Conversion, Vienna, 1998.

Modeling of Industrial CZ and FZ Growth

Th. Wetzel, W.v. Ammon

Wacker Siltronic AG, P.O. Box 11 40, D-84479 Burghausen, Germany
email: thomas.wetzel@wacker.com wilfried.ammon@wacker.com

Abstract

The present paper gives an overview on various aspects of numerical modeling of the industrial silicon crystal growth processes for both, the CZ and the FZ technology. For CZ growth it covers global thermal models, melt flow modeling and coupling of global thermal and melt flow modeling. In addition, there is a paragraph about the consideration of magnetic field influence in the melt flow models. For FZ growth there is a brief description of a complete model chain from the RF magnetic field through to the microscopic resistivity distribution in the final wafer.

The temperature fields in CZ crystals are used for defect modeling, which in turn allows a much more effective exploitation of the thermal modeling results. A brief introduction to the modeling capabilities for bulk defects is therefore given in the last chapter.

Introduction

The growth furnace design and growth process development remain to be extremely expensive steps of the technology development for silicon wafer manufacturing. That has been and is one of the main driving forces for the use of numerical modeling in the silicon wafer industry. The thermal simulation of the global heat transfer in crystal growth furnaces contributes substantially to keeping the development costs at an acceptable level. While the global thermal modeling with consideration of heat radiation and conduction has matured in the early and mid 90's, the explicit consideration of the melt flow influence on heat transfer has been focused on in recent years. The introduction of melt volumes of 250 kg and more in crucibles of 32" and more leads to turbulent features in the melt flow, which puts several challenges on modeling attempts. Both 2D axisymmetric and 3D models are used and various turbulence model types and modifications have been evaluated. Particularly the oxygen transport modeling remains a very challenging task, as an extremely precise description of all convection features is required for it.

In particular with the transition to 300 mm diameter CZ crystal growth, magnetic fields have become an important additional means to control heat and mass transfer in the large melt volumes. Numerical modeling facilitates the suitable design of inductor systems and helps to understand the effect of the magnetic fields on the melt flow.

However, the growth conditions do not only affect yield or pull rate, but also the quality of the crystals. Grown-in defects like voids, self-interstitial aggregates or oxygen precipitates can be detrimental or beneficial in subsequent wafer processing steps and for the performance of the

devices produced on the wafer. Therefore, defect engineering, i.e. the control of the formation of such defects, is an important part of the whole wafer production. Numerical modeling helps to predict the defect formation and behavior from crystal growth through to device manufacturing steps.

1. Crystal Growth

There are two major methods for producing silicon monocrystals from the melt. With the Czochralski (CZ) method, today crystals of up to 300 mm are grown. In the Floating Zone (FZ) technology, the development of a 200 mm industrial growth process has been accomplished just recently.

1.1 Czochralski Growth

Fig. 1 shows a longitudinal cut through a CZ growth furnace. The prediction of the temperature field in the whole furnace and in the crystal requires a global thermal simulation, taking into account the heat transfer by conduction, convection and radiation. Software tools for the conduction and radiation calculation along with the prediction of the melt-crystal interface are available from different institutes [1, 2, 3]. They are based on 2D axisymmetric models, employ view factor approaches for the heat radiation treatment and are based on the Finite Element Method (FEM) or the Finite Volume Method (FVM). Some of these codes allow the reproduction of transient growth processes or at least of transient parts of the growth process, like detachment and cooling down of the ingot [2].

With increasing melt volumes and crystal diameters, the consideration of the melt convection has become more important. The melt flow in large diameter CZ crucibles - today diameters of up to 32" with loads of up to 450 kg are used - is characterized by time dependent, three dimensional processes. The time needed for a fully transient, three-dimensional simulation of melt flow in a crucible of the mentioned size however, still prevents their application for industrial engineering purposes.

Therefore, 2D axisymmetric steady state models have been developed, that reproduce the most important features of the 3D flow, but do still provide reasonably short calculation time [4, 5]. One of the most critical parts in any CZ melt flow simulation, both 2D and 3D, is the consideration of turbulence.

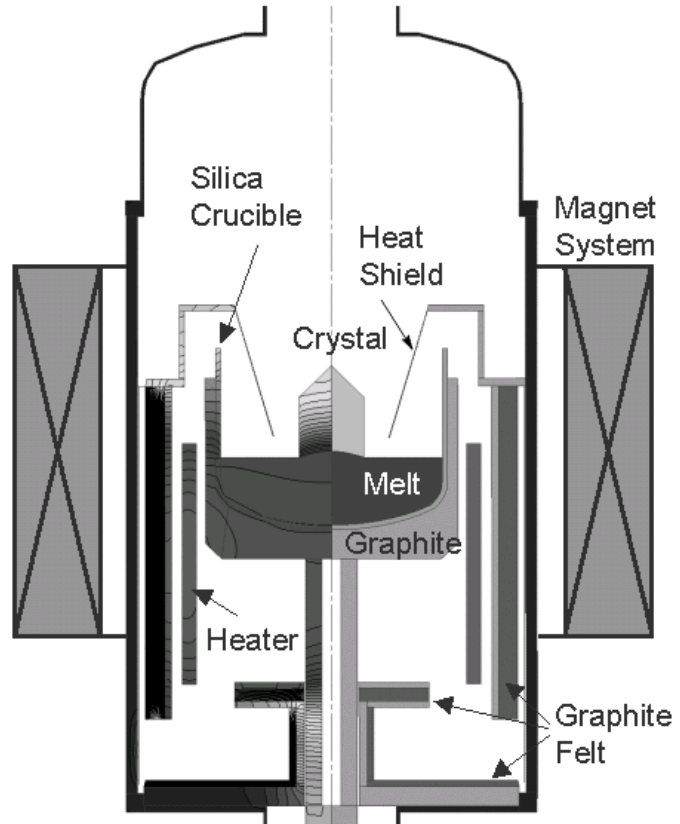


Fig. 1: Schematic layout of an industrial CZ puller and simulated temperature distribution (left)

The 2D simulation tools usually employ $k-\epsilon$ or LowRe $k-\epsilon$ or $k-\omega$ models. Such tools require careful experimental verification and modification based on comparisons with experiments [5, 6, 7]. A coupling of the global thermal and the local melt flow models facilitates to precisely reproduce the shape of the crystallization interface. The coupling usually employs an exchange of heat flux densities along the boundaries of the melt or the melt and crystal between the global and the local model. Then both, global and local model are solved iteratively or simultaneously. A conjugated solution of the heat and mass transfer in melt and crystal is also possible. A model proposed in [8] provided good agreement of the simulated melt-crystal interface shapes with measured ones for 200 mm crystals.

3D time dependent simulations with LES turbulence models [9] and simulations close to DNS [10, 11] are used to further develop the understanding of the flow behavior and to improve less time consuming simulation models. One goal of such attempts is the global modeling of oxygen transport in the CZ furnace, which is extremely sensitive towards any lack of precision in the turbulence modeling.

Another aspect, closely related to reliable melt flow prediction, is the modeling of magnetic field influence. In 300 mm CZ growth, different types of alternating (AC) magnetic fields as well as static (DC) magnetic fields are used. The incorporation of the melt flow models into the global heat transfer simulation tools facilitates direct consideration of the effect of such fields on the temperature distribution in the crystal and all coupled phenomena. A 2D axisymmetric model approach for the AC and DC magnetic field effect on the silicon melt is described in [5]. The model has been verified with experimental results from a CZ model setup with various magnetic fields [7, 12].

1.2 Floating Zone Growth

Fig. 2 shows a longitudinal cut through an FZ growth setup [13]. For the numerical simulation of Floating Zone growth there is a complete model chain necessary, starting with the prediction of the phase boundaries at feed rod, molten zone and crystal, based on RF field influence and heat transfer [14]. A second part of the model chain is covering the prediction of the transient melt flow and heat transfer based on 2D [15] and 3D [16] approaches. Based on the melt flow calculation results, the dopant transport can be simulated, yielding finally the macroscopic and microscopic resistivity distributions in the sliced wafers. The current development of 200 mm FZ crystal growth processes has been substantially supported by the use of such simulation models.

Beyond these applications, the influence of additional low frequency inductors has been modeled [14] and considerations

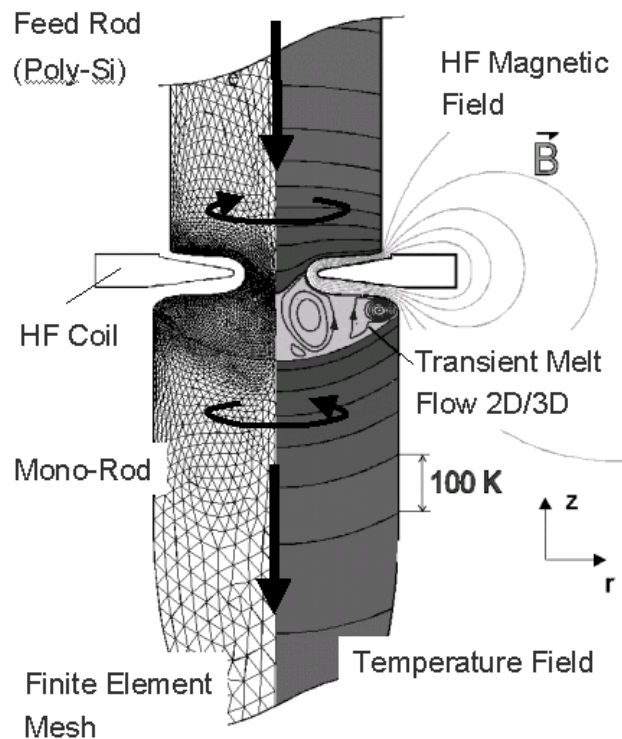


Fig. 2: Schematic layout of a Floating Zone setup with simulated features and FEM mesh

about the stress induced dislocation generation have been started [17]. A recently developed improved phase boundary simulation model is presented in [18].

3. Defect Modeling

There are different types of defects in silicon wafers, which are related to the crystal growth conditions and the thermal history of the crystal and wafer. During the solidification process, intrinsic point defects, namely vacancies and silicon self interstitials, are incorporated into the crystal. These intrinsic point defects form grown-in bulk defects during cooling down from melting to room temperature. Impurity atoms can also be incorporated into the growing crystal, later forming precipitates or other defects. The most common of these impurities is oxygen, which is dissolved from the silica crucible in CZ processes and transported through the melt to the crystallization front.

Three types of defects in CZ crystals will be mentioned here specifically: grown-in octahedral voids [19] formed by the aggregation of vacancies (Fig. 3), oxide precipitates [20] and the OSF ring [19].

Whether vacancy or self-interstitial related defects are found in a CZ crystal or crystal region, depends on the value v/G in that region at the crystallization interface during solidification (v being the pull rate, G the temperature gradient at the solid/liquid interface) [19, 21]. In addition to determining these quantities from the thermal simulation, models are used to directly describe the point defect dynamics, i.e. the diffusion and convection transport of these defects during crystal growth as well as their annihilation by recombination [22]. The combination of such simulation models with the thermal simulation results, in particular the transient temperature field in the crystal, allows to design the growth furnace and the growth process in such a way, that grown crystals show a desired defect species.

Furthermore, especially for fast grown, vacancy rich crystals, it is necessary to ensure a specific size and density of the grown-in voids. Simulation models have

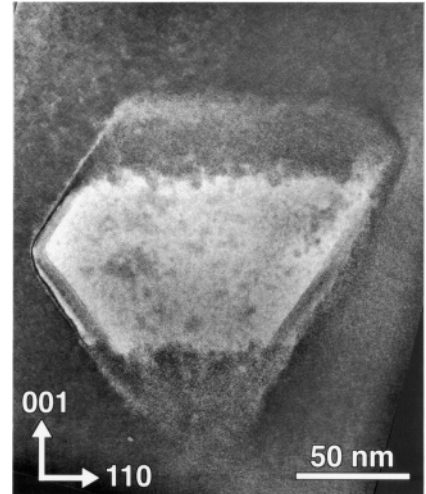


Fig.3: Octahedral void in an as-grown silicon crystal [19]

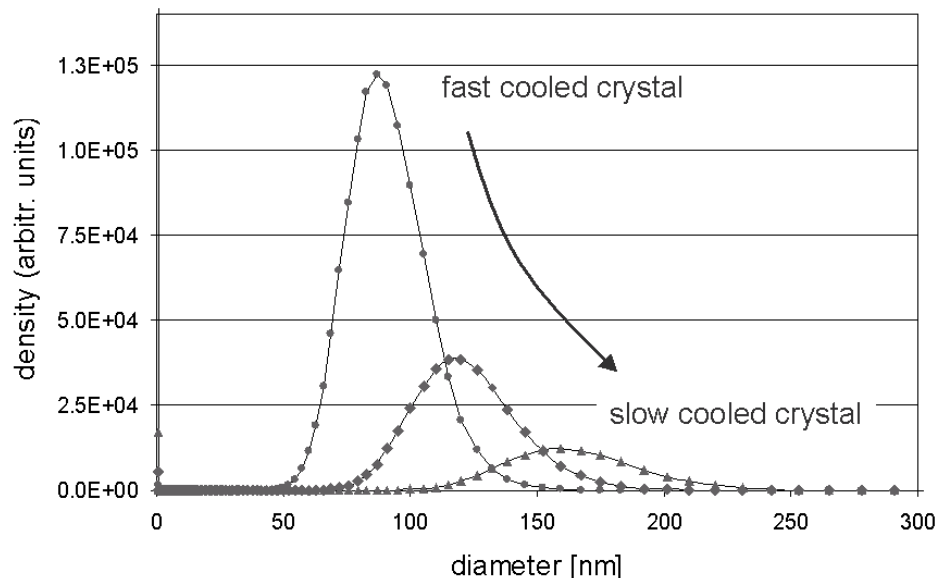


Fig. 4: Simulated size distributions of voids in crystals with different cooling rates

been developed, that describe the formation of such defects from vacancies [19]. The size of the grown in voids depends strongly on the cooling rate in a specific temperature interval during cooling down. Therefore, these models do also need the thermal history of the crystal as well as the results of the point defect models. More advanced models consider the point defect dynamics and the aggregation phenomena simultaneously. Fig. 4 shows simulated size distributions of voids in fast and slow cooled CZ crystals. The void formation models are also used to predict the impact of wafer heat treatment steps on size and density of the voids.

Much effort is put into the modeling of the behavior of oxygen in CZ silicon. As oxide precipitates are used as centers for internal gettering in microelectronic device manufacturing [20], models have been developed to predict the size and in particular the density of such defects in CZ crystals and wafers [23, 24]. At the same time it is known that such defects have an impact on the minority carrier lifetime, important e.g. for photovoltaic applications. While the modeling of the nucleation and growth of precipitates during the crystal growth, particularly in conjunction with other impurities like Nitrogen, is used for research and is still evolving, the growth and dissolution of BMD's in wafer processing steps is simulated on a day to day basis already.

Another well known defect phenomenon is the so called OSF ring, appearing on the wafer surface after wet oxidation. The nature and formation of the OSF ring has been studied by many authors (see [19] for further ref.). However, there is ongoing research activity in this field, as there are complex interactions of oxygen precipitation with other point defects or impurity atoms in the growing crystal, like Nitrogen, that affect e.g. the width of the OSF ring [25].

Summary

Numerical modeling is an integral part of today's industrial silicon crystal growth and wafer manufacturing R&D activities. In particular the crystal growth simulation with thermal and convection models, both for the CZ and the FZ method is a well established tool in the equipment and process development. With the explicit consideration of turbulent melt flow and the respective heat and mass transfer in the melt, the precision of the growth modeling, particularly the growth interface shape and temperature prediction for the crystal, has reached a remarkable level. Along with the progress in melt flow modeling, the modeling of electromagnetic field influence on melt flow has become an indispensable means for the puller design and the process development for both, the CZ and the FZ technology. Various model approaches for predicting crystal growth related defects, like grown-in voids or oxygen precipitates, have been developed and are successfully used in the industry.

References

- [1] Dornberger, E., Tomzig, E., Seidl, A., Schmitt, S., Leister, H.-J., Schmitt, Ch., Müller, G.: *Thermal Simulation of the Czochralski silicon growth process by three different models and comparison with experiment*. J. Cryst. Growth 181 (1997), 461 pp.
- [2] Van den Bogaert, N., Dupret, F.: *Dynamic global simulation of the Czochralski process I / II*. J. Cryst. Growth 171 (1997), pp. 65-93
- [3] Kurz, M., Puszta, A., Müller, G.: *Development of a new powerful computer code CrysVUN++ especially designed for fast simulation of bulk crystal growth processes*. J. Cryst. Growth (198/199) (1999), pp. 101-106
- [4] Lipchin, A., Brown, R.A.: *Hybrid finite-volume/finite element simulation of heat transfer and turbulence in Czochralski growth of silicon*. J. Cryst. Growth 216 (2000), pp. 192-203
- [5] Wetzel, Th., Muiznieks, A., Mühlbauer, A., Gelfgat, Y., Gorbunov, L., Virbulis, J., Tomzig, E., von Ammon, W.: *Numerical model of turbulent CZ melt flow in the presence of AC and CUSP magnetic fields and its verification in a laboratory facility*. J. Cryst. Growth 230 (2001) pp. 81-91

- [6] Lipchin, A., Brown, R.A.: *Comparison of three turbulence models for simulation of melt convection in Czochralski crystal growth of silicon*. J. Cryst. Growth 205 (1999) pp. 71-91
- [7] Krauze, A., Muiznieks, A., Mühlbauer, A., Wetzel, Th., Gorbunov, L., Pedchenko, A.: *Numerical 2D modeling of turbulent melt flow in CZ system with AC magnetic fields*. Proceedings of the Intl. Sc. Colloquium Modelling for Electromagnetic Processing, Hannover, 2003
- [8] Virbulis, J., Wetzel, Th., Muiznieks, A., Hanna, B., Dornberger, E., Tomzig, E., Mühlbauer, A., von Ammon, W.: *Numerical investigation of silicon melt flow in large diameter CZ-crystal growth under the influence of steady and dynamic magnetic fields*. J. Cryst. Growth 230 (2001) pp. 92-99
- [9] Evstratov, Y., Kalaev, V.V., Zhamakin, A.I., Makarov, Y. N., Abramov, A.G., Ivanov, N.G., Smirnov, E.M., Dornberger, E., Virbulis, J., Tomzig, E., von Ammon, W.: *Modeling analysis of unsteady three-dimensional turbulent melt flow during Czochralski growth of Si crystals*. J. Cryst. Growth 230 (2001) pp. 22-29
- [10] Vizman, D., Friedrich, J., Müller, G.: *Comparison of the predictions from 3D numerical simulation with temperature distributions measured in Si Czochralski melts under the influence of different magnetic fields*. J. Cryst. Growth 230 (2001) pp. 73-80
- [11] Enger, S., Gräßner, O., Müller, G., Breuer, M., Durst, F.: *Comparison of measurements and numerical simulations of melt convection in Czochralski crystal growth of silicon*. J. Cryst. Growth 230 (2001) pp. 135-142
- [12] Pedchenko, A., Gorbunov, L., Gelfgat, Y., et.al.: *Investigation of temperature field and melt flows in large-diameter CZ silicon modelling experiments with impact of magnetic fields*. Proceedings of the Intl. Sc. Colloquium Modelling for Electromagnetic Processing, Hannover, 2003
- [13] Virbulis, J.: *Numerische Simulation der Phasengrenzen und Schmelzenströmung bei der Züchtung von Siliziumeinkristallen mit dem Floating-Zone Verfahren*. Dissertation, Universität Lettlands in Riga 1997
- [14] Raming, G.: *Modellierung des industriellen FZ-Prozesses zur Züchtung von Silizium-Einkristallen*. Dissertation, Institut für Elektrowärme, Universität Hannover 2000
- [15] Mühlbauer, A., Muiznieks, A., Virbulis, A., Lüdge, A., Riemann, H.: *Interface shape, heat transfer and fluid flow in the floating zone growth of large silicon crystals with the needle-eye technique*. J. Cryst. Growth 151 (1995), pp. 66-79
- [16] Ratnieks, G., Muiznieks, A., Buligins, L., Raming, G., Mühlbauer, A., Lüdge, A., Riemann, H.: *Influence of the three dimensionality of the HF electromagnetic field on resistivity variations in Si single crystals during FZ growth*. J. Cryst. Growth 216 (2000), pp. 204-219
- [17] Muiznieks, A., Raming, G., Mühlbauer, A., Virbulis, J., Hanna, B., v. Ammon, W.: *Stress-induced dislocation generation in large FZ- and CZ-silicon single crystals—numerical model and qualitative considerations*. J. Cryst. Growth 230 (2001) pp. 305-313
- [18] Ratnieks, G., Muiznieks, A., Mühlbauer, A.: *Mathematical modelling of industrial FZ process for large (200mm) silicon crystal growth*. Proceedings of the Intl. Sc. Colloquium Modelling for Electromagnetic Processing, Hannover, 2003
- [19] Dornberger, E.: *Prediction of OSF Ring Dynamics and Grown-in Voids in Czochralski Silicon Growth*. Dissertation, Universite Catholique de Louvain 1997
- [20] Gilles, D., Ewe, H.: *Gettering phenomena in silicon*. Semiconductor Silicon 1994, Electrochemical Society Proceedings 94-10 (1994) pp. 772
- [21] Voronkov, V.V.: *The mechanism of swirl defects formation in silicon*. J. Cryst. Growth 59 (1982) pp. 625-643
- [22] Sinno, T., Brown, R.A., von Ammon, W., Dornberger, E.: *Point Defect Dynamics and the Oxidation-Induced Stacking Fault Ring in Czochralski-Grown Silicon Crystals*. J. Electrochem. Soc. 145 (1998) pp. 302
- [23] Esfandyari, J.: *Modellierung und Computersimulation der Sauerstoffpräzipitation in Silicium*. PhD Thesis, TU Wien 1995
- [24] Sueoka, K., Akatsuka, M., Okui, M., Katahama, H.: *Computer Simulation for Morphology, Size and Density of Oxide Precipitates in Czochralski Silicon*. Electrochemical Society Proceedings 25 (2002), pp. 40
- [25] von Ammon, W., Hözl, R., Wetzel, T., Zemke, D., Raming, G., Blötz, M.: *Formation of stacking faults in nitrogen doped silicon single crystals*. Microelectronic Engineering 66 (2003), pp. 234-246

MULTIPLE RIBBON GROWTH VIA THE STRING RIBBON METHOD

J.I. Hanoka
Evergreen Solar, Marlboro, MA, USA

String Ribbon is a method for producing polycrystalline silicon ribbon grown in a vertical configuration and in a continuous fashion. As such, it has been commercialized by Evergreen to where the present factory is at a 3-4MW/yr rate. This has been done with a technology that resulted in a single ribbon growing from a single crucible. Recent fundamental advances and innovative engineering developments have allowed for multiple ribbon growth from a single crucible. The engineering developments include the ability to measure temperatures in the neighborhood of molten silicon (1412°C) with an accuracy of 1°C , and a means of measuring silicon melt depth changes as little as 10 microns. More fundamental crystal growth discoveries have been in the areas of understanding and controlling molten silicon meniscus behavior, and in the control of the radiative environment near a growing ribbon.

In one case, termed Gemini, two ribbons are grown back to back out of a single crucible. Gemini is now in production in a limited scale and will be in full production with a total capacity of 10 –14 MW/yr by YE 2004. Present production Gemini ribbon is 8 cm wide, 300 microns thick, and doped p-type at 2-3 ohm-cm. Using some of the developments listed above, sustained growth as fast as 25 mm/minute and ribbon as thin as 125 microns have been grown in a Gemini configuration. Production efficiencies are continually improving. At present, the best batch (about 500 cells) average is 13.7% and the best Gemini cell made on our production line is 14.6%, with $\text{Voc} = 599 \text{ mv}$, $\text{Jsc} = 32.5 \text{ ma/cm}^2$, and fill factor = 0.75. Gemini allows for nearly halving some of the consumable costs for making ribbon substrates and so will be a major contributor towards the goal of lower cost silicon substrates.

An even further development in low cost silicon ribbon growth is that of the so-called Quad method. In this method, 4 ribbons will be grown out of a single crucible in a side to side orientation. The technique is still in the laboratory phase and the growth of 4 ribbons will first be done in about one month from the time of this workshop. The Quad technique employs an extremely narrow crucible, only about 2 cm. wide and is based on highly innovative concepts in silicon meniscus control. The concept has been validated on a single ribbon machine. Theoretical analysis of the Quad configuration has shown that there are forces at work that tend to promulgate flat ribbon. An example of the very flat ribbon grown in the single ribbon machine and possible with this concept will be shown. Given the very small crucible dimensions, the potential consumable cost reductions of such a set up are even lower than for the (already quite low) Gemini process.

Acknowledgements: The Gemini work has been funded under a PV Manufacturing R&D sub contract administered by NREL (Department of Energy, U.S.). The Quad work has been funded under a NIST ATP contract (Department of Commerce, U.S.).

Present Status and Prospect of Ga-doped mc-Si Solar Cells

K. Fukui¹, S. Fujii¹, M. Tsuchida¹, S. Tanimoto¹, K. Sihirasawa¹, M. Dhamrin² and T. Saitoh²

¹Kyocera Corporation, 1166-6, Nagatanino, Hebitimizo-cho, Yohkaichi, Shiga 527-8555 Japan

²Tokyo Univ. of Agr. & Tech., 2-24-16, Naka-cho, Koganei, Tokyo 184-8588 Japan

ABSTRACT

Recently, the mono- and the multicrystalline (mc) silicon wafer technology have dominated the photovoltaic market because of its advantage of conversion efficiency, reliability and cost in comparison with other technology. Especially the market share of mc-Si solar cell seems to be more than 50% in 2002. We have been investigating the mc-Si photovoltaic solar cells to reduce the cost for many years. The improvement of the solar cell efficiency has a drastic effect on the reduction of the solar cell cost. The improvement of mc-Si material especially boron related defects which decorate the band gap with various defects including well-known iron-boron pairs [1-2] is very important issue for the higher cell efficiency. In this paper, we have investigated an approach that leads to an efficiency improvement by the substitution of boron (B) by gallium (Ga) as the dopant material.

1. Characteristics of materials

About 30cm × 30cm Ga-doped mc-Si ingot was grown by conventional block casting technique. The resistivity profile in Ga-doped ingot shows a larger gradient than B-doped one as shown in Fig. 1 because Ga has a smaller distribution coefficient than B. This resistivity profile shows a correspondence with theoretical calculation using distribution coefficient and solidification ratio. Ga-doped mc-Si wafers and solar cells with different position of the ingot were used to evaluate the performance in comparison with B-doped mc-Si wafers.

Minority carrier diffusion length (Ld) of these materials was measured by Surface Photovoltage (SPV) technique. This technique is greatly influenced by surface recombination velocity when wafer thickness is below 4Ld. Diffusion length shown in Fig. 2 is relatively compared with each wafer at same surface condition. These data seem to be lower than that of values because the thickness is about 350 μm and is below 4Ld. Diffusion length of Ga-doped wafers shows a lower value than B-doped wafers especially in outer region of the ingot.

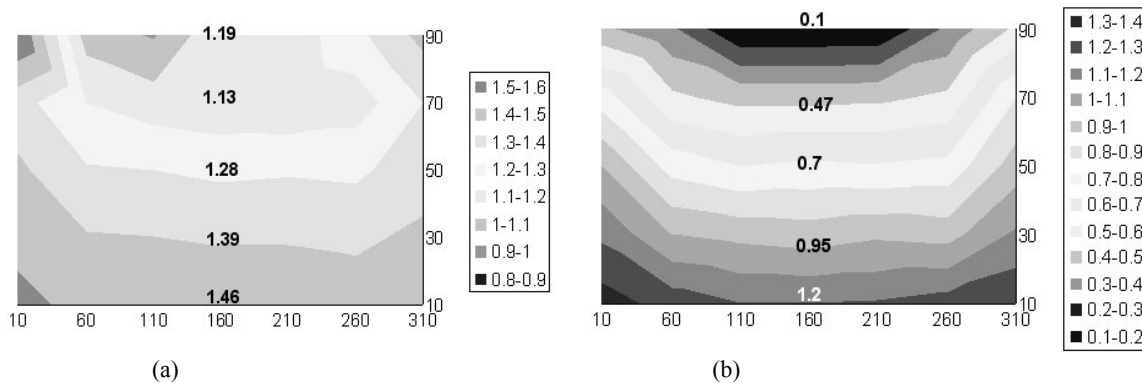


Fig. 1 Resistivity distribution of B-doped (a) and Ga-doped (b) Si ingots.

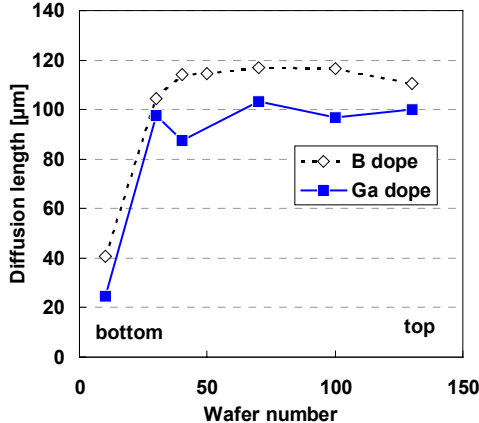


Fig. 2 Minority carrier diffusion length

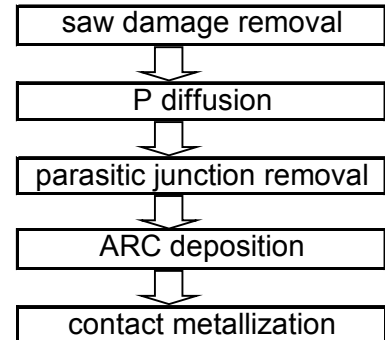


Fig. 3 Process sequence of 9 cm² sized mc-Si cell

2. Cell fabrication

2.1 Small size cells

For the first investigation 9 cm² (3cm × 3cm) sized solar cells from the Ga-doped and B-doped mc-Si materials were made in order to evaluate the difference and distribution of solar cell performance in the ingot. Fig. 3 shows a cell process sequence. The wafer surface was etched in alkaline solution to remove saw damage. P-diffusion was performed using POCl₃ liquid dopant source. Silicon nitride film was deposited on the cell using PECVD method as an ARC. Contact metallization was performed by screen printing and firing technique. The metal contacts include the front silver, rear silver aluminum and rear aluminum for BSF fired in a conveyor belt furnace. Finally, cells were cut into 3cm by 3cm size to evaluate the solar cell performance distribution in the wafer.

Fig. 4 shows a relation between the solar cell characteristics and the position in the ingot. The ratio of the cell characteristics is shown in this figure as relative cell performances to the cell from the bottom of B doped ingot. The short circuit current of Ga doped cell decreases from the bottom to the top of the ingot. The efficiency of the cells at the middle and the top of the Ga doped ingot is little lower than that of B doped cells, however

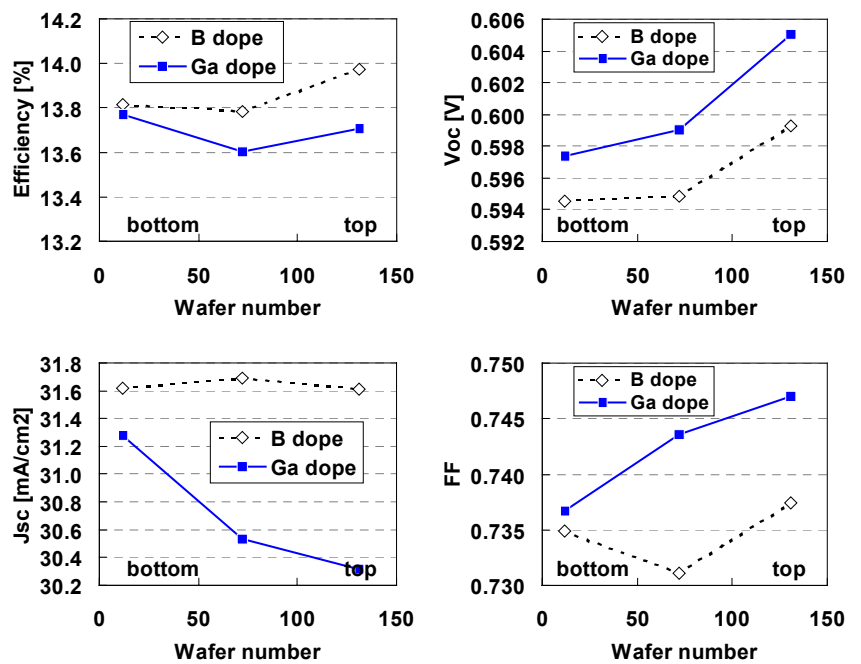


Fig. 4 Characteristics of 9 cm² sized mc-Si cells

similar cell efficiencies were obtained on both the materials from the bottom of ingot. Short circuit current of the solar cells on Ga doped material decreases from the bottom to the top of the ingot because the resistivity of Ga doped material shows larger distribution than B doped material as shown in Fig. 1. The efficiency of the cells from the bottom of both the ingots are not so bad as the Ld of the materials from the bottom of both the ingots is lower than another position of the ingot.

Fig. 5 shows the efficiency distribution of 3cm by 3cm sized solar cells in 15cm by 15cm wafers. Two sides of the square regions show lower performance than other regions on both the materials because these regions are near the mold when casting the ingot. The impurities from the mold and / or dislocation at these regions make cell efficiency decrease. These characteristics are in accord with the tendency of Ld as shown in figure 2. The efficiency of cells from Ga doped materials has large deviation compared with that from B doped materials.

2.2 High efficiency cells

Another investigations on 100 cm^2 ($10\text{cm} \times 10\text{cm}$) sized solar cells were performed using process sequence with highly refined texturing step as shown in Fig. 6 to investigate the potential of Ga doped mc-Si material. This texturing technique is now under working in Kyocera's standard cell process step which makes homogeneous and very fine texturing on mc silicon wafer. P diffusion process is modified because the surface morphology is quite different from the conventional surface treated cell. The hydrogen annealing after deposition of silicon nitride film on both the surfaces of the cells improves the bulk quality of the cell [3]. The both the contact metals were vacuum evaporated and front contact grid was formed using a photolithography lift off procedure. The MgF_2 film was vacuum deposited as a second layer of the dual layer AR coating. The solar cells from the B doped material were also fabricated.

The characteristics of the highest performance cells from Ga doped and B doped mc-Si ingots are shown in Table I respectively. I-V characteristics were measured under the global AM 1.5 condition at Kyocera using reference cell calibrated at JQA (Japan Quality Assurance Organization). The highest

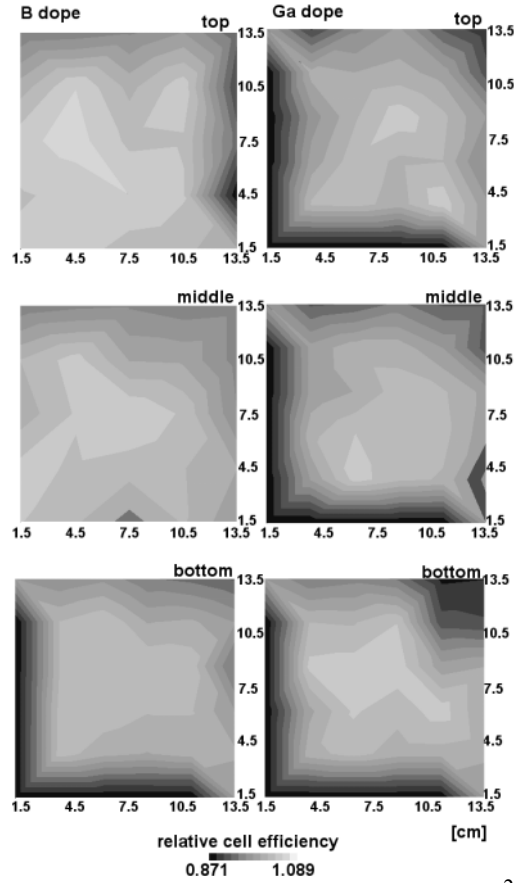


Fig. 5 Efficiency distribution of 9 cm^2 sized solar cells in 15cm by 15cm materials

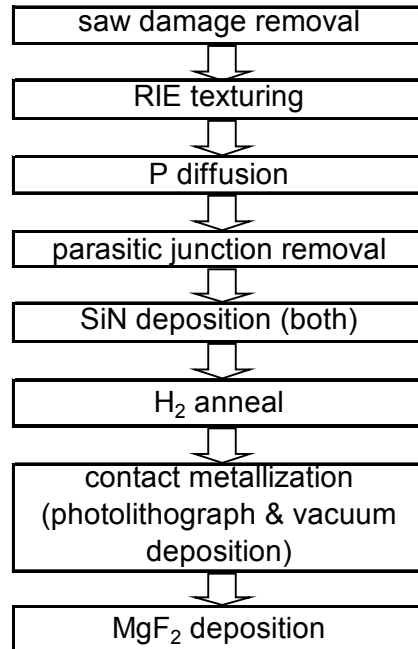


Fig. 6 Process sequence of $10 \text{ cm} \times 10\text{cm}$ sized mc-Si cell

efficiency of Ga doped cell was 16.6% and that of B doped cell was 17.2%. The dark I-V characteristics of these cells are shown in Fig. 7.

The diode parameters were estimated from the dark I-V characteristics. The ideal saturation current density I_{01} of these cells are also listed in Table I. I_{01} was calculated by

$$I = I_{01} \left(\exp\left(\frac{q(V - IR_s)}{kT}\right) - 1 \right) + I_{02} \left(\exp\left(\frac{q(V - IR_s)}{n_2 kT}\right) - 1 \right) + \frac{V - IR_s}{R_{sh}}$$

where I is the current, V is the applied voltage, q is the electron charge (1.602×10^{-19} [C]), k is the Boltzmann's constant (1.38×10^{-23} [J/K]), T is the temperature, I_{01} is the ideal diode saturation current, I_{02} is the non-ideal diode saturation current, n_2 is the diode ideality factor for non-ideal diode 2, R_s is the series resistance and the R_{sh} is the shunt resistance. The saturation current density and the open circuit voltage seem to be mutually related in these Ga doped cells.

Table I Characteristics of the highest performance cell from Ga doped and B-doped mc-Si ingots

Dopant Wafer No.	Jsc [mA/cm ²]	Voc [V]	FF	Effi. [%]	I_{01} [A/cm ²]
B-3	36.37	0.617	0.767	17.23	1.03E-12
Ga-260	36.33	0.608	0.751	16.60	1.56E-12
Ga-379	35.95	0.615	0.751	16.60	9.56E-13

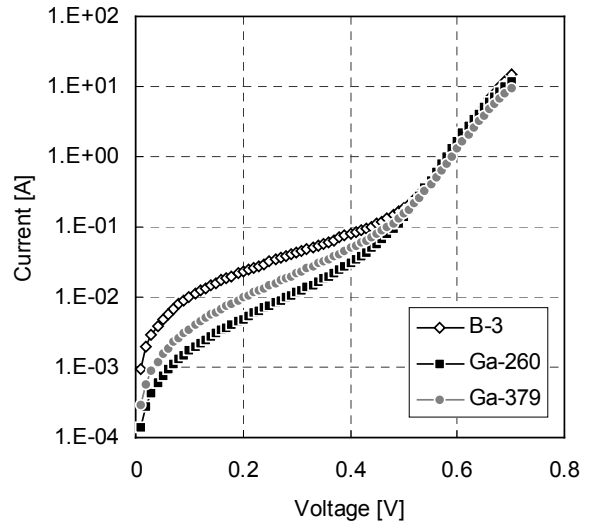


Fig. 8 Dark I-V characteristics of mc-Si cells

3. Discussions

The Ga doped mc Si materials were investigated to improve the solar cell efficiency by the substitution of boron (B) by gallium (Ga) as the dopant material. The highest efficiency of Ga doped mc-Si solar cell was 16.6% on 100cm² size cell, however the B doped cell was quite high efficiency of 17.23%. The efficiency of Ga doped mc Si solar cell was slightly lower than that of B doped cell. It seems that the bulk quality of Ga doped material is worse than that of B doped material. It is important issue to understand the Ga related defects and the other defect in Ga doped mc-Si material and to improve the resistivity distribution in the ingot by something new technique for industrial use.

The characteristics of Ga-doped mc-Si solar cell after light soaking has been investigated by M. Dhamrin et al.[4]. In their paper, Ga-doped mc-Si wafer was found to be very stable under illumination. Our future task will be focused on the development of higher efficiency Ga-doped mc-Si solar cell even after illumination.

REFERENCES

- [1] D. Macdonald, A. Cuevas, and J. Wong-Leung, *J. Appl. Phys.* **89**, 2001, p. 7932.
- [2] J. Schmidt, K. Bothe and R. Hezel, *29th IEEE Photovoltaic Specialists Conference*, 2002, p. 178
- [3] K. Shirasawa et al., *14th European Photovoltaic Solar Energy Conference*, 1997, p384
- [4] M. Dhamrin, *WCPEC-3*, “Fabrication and Evaluation of Ga-doped mc-Si Wafers and Solar Cells - A Promising Material for Future Photovoltaics-”, 2003.

ADVANCED LIFETIME SPECTROSCOPY

S. Rein and S.W. Glunz

Fraunhofer Institute for Solar Energy Systems (ISE), Heidenhofstr. 2, D-79110 Freiburg, Germany
Phone ++49 761-4588-5271; Fax ++49 761-4588-9000, e-mail: rein@ise.fhg.de

ABSTRACT: Lifetime spectroscopy (LS) always allows a complete defect characterization on one single sample if data from injection- and temperature-dependent LS (TDLS and IDLS) are combined. To allow an accurate modeling of entire TDLS curves, several physical extensions are introduced in the basic Shockley-Read-Hall (SRH) model. A new routine for data evaluation allows a transparent SRH analysis of IDLS and TDLS data and enables the accuracy and consistency of the determined defect parameters to be assessed. Applied to LS data from a molybdenum-contaminated silicon sample, the advanced LS enables the identification of a known molybdenum donor level at $E_t-E_F=0.317$ eV with an enhanced electron/hole capture cross section ratio $k:=\sigma_n/\sigma_p=13$. The good agreement with literature and the consistency of the LS results manifest the potential of the proposed advanced LS analysis. If the value for σ_p is taken from literature, the unknown electron capture cross section of the molybdenum donor level is determined as $\sigma_n=7.8\times10^{-15}$ cm⁻³.

1. INTRODUCTION

Although deep-level transient spectroscopy (DLTS) is accepted to be one of the most sensitive methods to detect and analyze small concentrations of electrically active defects, defect concentrations below the detection limit of DLTS can still significantly affect carrier recombination lifetime. Apart from detecting the presence of recombination-active defects, lifetime measurements allow a direct identification of defects if the injection and temperature dependence of carrier lifetime is analyzed [1, 2] using the standard Shockley-Read-Hall (SRH) theory [3, 4]. The basic suitability of temperature-dependent and injection-dependent lifetime spectroscopy (TDLS and IDLS) for defect characterization has already been demonstrated theoretically and experimentally: While standard TDLS [5-8] allows a direct determination of the energy depth E_t on a single sample, IDLS faces the problem that SRH parameterizations of a single IDLS curve is highly ambiguous. This ambiguity is overcome if a set of IDLS curves measured (i) on several samples with various doping concentrations (N_{dop} -IDLS) or (ii) on the same sample at various temperatures (T-IDLS) is subject to a simultaneous SRH fit [2]. While T-IDLS is subject of current investigations [9], N_{dop} -IDLS is already successfully established although being rarely applied [10, 11].

Recently, Rein et al. [12] have demonstrated that lifetime spectroscopy (LS) *always* allows a complete defect characterization on one single sample if TDLS and IDLS data are combined. Furthermore, it has been shown that *often* the modeling of the entire TDLS curve alone allows an unambiguous determination of both, the ratio $k:=\sigma_n/\sigma_p$ of the capture cross sections for electrons and holes and the exact energy position E_t within the band gap [12]. The recent successful decoding of the electronic structure of the well-known metastable defect in Czochralski silicon demonstrates the potential of this advanced LS [13].

In the present work further extensions of LS analysis are presented. On the one hand the basic SRH model is extended to allow an accurate simulation of TDLS curves in an extended temperature range. On the other hand a new routine for data evaluation is introduced: the determination of the ‘Defect-Parameter-Solution-Surface’ (DPSS). As discussed below, the newly developed DPSS diagram allows a transparent and comprehensive SRH analysis of IDLS and TDLS data and makes it possible to evaluate the accuracy and consistency of the defect parameters determined from lifetime spectroscopic curves which are dominated by the same defect center. In order to demonstrate the potential of this advanced LS for a detailed and complete defect characterization, we performed TDLS and IDLS measurements on an intentionally molybdenum-

contaminated p-type silicon sample. While the TDLS measurements are performed by means of the contactless microwave-detected photoconductance decay technique (MWPCD) (for details of the experimental setup see Ref. [7]), the IDLS measurements are accomplished by means of the quasi-steady-state photoconductance technique (QSSPC) [14].

2. ADVANCED TDLS ANALYSIS

Figure 1 shows the TDLS curve which has been measured by means of the MWPCD technique on the Mo-contaminated sample. The lifetime measurements were performed at the minimum bias light intensity excluding distortions of the mono-exponential photoconductance decay due to trapping effects (for details see Ref. [2]), which guarantees low-level-injection (LLI) conditions in the whole T -range. In order to minimize surface recombination, the samples were coated on both sides with silicon nitride, which leads to surface recombination velocities below 20 cm/s in the whole injection range [15].

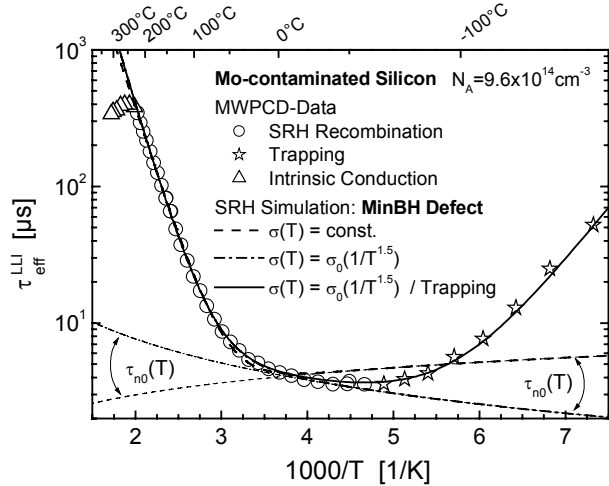


FIG. 1. TDLS curve measured by means of the MWPCD technique on an intentionally Mo-contaminated silicon sample ($[Mo] = 3.7 \times 10^{11} \text{ cm}^{-3}$, $N_A = 9.9 \times 10^{14} \text{ cm}^{-3}$). An accurate simulation of the *low temperature part* from 120 to 300 K is not achieved by the standard SRH model (dashed line) but requires the insertion of a temperature-dependent capture cross section (dash-dotted line). The lifetime increase below 200 K can be explained by superposed carrier trapping at an additional shallow level (solid line).

2.1. Superposed effects: Necessary extensions of standard SRH model

If advanced TDLS analysis is applied, the accuracy of defect parameter determination strongly depends on the accuracy of the SRH fit. To allow a comprehensive verification of the validity of the SRH theory, the investigated temperature range has been significantly increased from 200-500 K in all previous studies to 130-580 K in the present study, as shown in Fig. 1. The dashed line shows a least squares optimization of the basic SRH model whose temperature dependence arises from only three quantities: the SRH densities $n_I(T)$, $p_I(T)$, the densities of states $N_C(T)$, $N_V(T)$ and the thermal velocity $v_{th}(T)$. As can be seen, basic SRH theory fails to describe the observed temperature dependence in the whole T -range. While an adequate description is achieved under medium temperatures from 250-500 K, strong deviations are observed above 500 K and

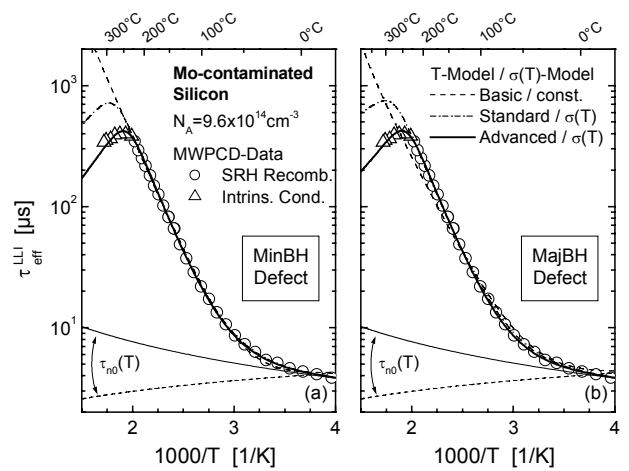


FIG. 2. SRH modeling of the *high temperature part* of the TDLS curve from Fig. 1 (a) for a MinBH defect and (b) for a MajBH defect. An accurate simulation of the Arrhenius increase for MajBH defects requires the $\sigma(T)$ -model while for MinBH defects $\sigma = \text{const.}$ suffices. For an accurate modeling of the lifetime decrease above 500 K, which is induced by the onset of intrinsic conduction, not only the temperature dependence of the majority carrier concentration (dash-dotted line) has to be considered but as well that of the band gap $E_{gap}(T)$ (solid line).

below 250 K. The physical origin of these deviations and the necessary extensions of the SRH theory to allow a quantitatively correct simulation of these superposed effects will be discussed in the following.

We first focus on the correct modeling of the low-temperature part of the TDLS curve. For temperatures below the onset of the Arrhenius increase (here: $T < 250$ K), SRH lifetime under low-level injection equals the minority capture time constant $\tau_{n0} := [N_i \sigma_n(T) v_{th}(T)]^{-1}$. Since a T -dependence of the defect concentration N_i is most unlikely, all deviations of the known T -dependence of v_{th} , which is displayed in Fig. 1 by the thin dashed line, have to be attributed to a T -dependence of the minority carrier capture cross section. If this temperature dependence is ignored, the spectroscopic result of the advanced TDLS analysis significantly depends on the choice of the lower bound of the fitted T -range.

Among the different models for carrier capture reported in literature the observed decrease of the capture cross section with increasing temperature is found particularly for attractive Coulomb centers and can be described in terms of $\sigma(T) = \sigma_0 T^\alpha$ with $\alpha < 0$ [16]. Since two different Mo-contaminated samples showed exactly the same temperature dependence in the low-temperature region with exponents $\alpha = -1.5$, the recombination-active molybdenum level most likely acts as an attractive Coulomb center. Thus modeling the low-temperature part of the TDLS curve elucidates the physical mechanism of recombination and provides an additional fingerprint of the defect which is unknown for most impurities. Unfortunately, the introduction of this $\sigma(T)$ -model with $\alpha = -1.5$ only improves the SRH fit in the T -range from 250-200 K, while below 200 K the discrepancy between fit and data is strong.

The strong increase of effective carrier lifetime below 200 K most likely originates from superposed carrier trapping at an additional shallow trap center. As derived in Ref. [17], bulk recombination in a system of two levels, one of which plays the role of a recombination center while the other acts as trapping center, is described by an asymptotic lifetime $\tau_a = \alpha \times \tau_r$ which is proportional to the actual recombination lifetime τ_r . The proportionality factor α is the higher the higher the trap concentration and the deeper the trap level and increases with decreasing temperature which leads to an increase of the asymptotic lifetime τ_a . Actually, it is τ_a that is determined from the mono-exponential photoconductance decay. As shown by the solid line in Fig. 1, an accurate modeling of the measured temperature dependence down to 130 K is achieved if an additional shallow trap level at $E_C - E_t = 0.15$ eV with a trap density of $N_{trap} = 6 \times 10^{14}$ cm⁻³ is assumed. Such trapping effects are often observed under low temperatures and have to be identified to avoid distortions of the extracted $\sigma(T)$ -model which may significantly affect the modeling of the Arrhenius increase and thus the accuracy of the spectroscopic result. Since the trapping effect screens pure recombination lifetime, the TDLS curve below 200 K is ignored in all the following SRH fits.

The details of the individual fits of the TDLS curve using different modifications of the SRH model are summarized in Tab. 1. In particular these are the T -boundaries of the fitting region, the quality of the fit and the extracted defect parameters.

Whether the underlying $\sigma(T)$ -model is considered or not leads to a fundamental difference in fitting the linear Arrhenius increase. As shown by the dashed lines in Fig. 2 the basic SRH model with temperature-independent capture cross sections only allows a correct modeling of the Arrhenius increase for a MinBH defect while that for a MajBH defect fails. The fact that the Arrhenius slope of the least squares optimized MajBH fit significantly deviates from the measured Arrhenius slope is reflected in a Chi^2 -value of the MajBH fit which is increased by more than an order of magnitude compared to that of the MinBH-fit (see first row in Tab. 1). From this observation we concluded in a previous work [12] that the relevant defect level of molybdenum is located in the upper half of the band gap. Nevertheless, if the $\sigma(T)$ -model extracted from the low-temperature part of the TDLS curve is introduced into the SRH analysis, the electron capture time constant $\tau_{n0}(T)$, which is a simple scaling factor of SRH lifetime, no longer decreases with increasing temperature (dashed line in Fig. 1) but exhibits a slight increase (dash-dotted line). As can be seen from the

dash-dotted lines in Fig. 2 this additional temperature dependence enables an accurate modeling of the linear Arrhenius increase for a MinBH *and* a MajBH defect with an energy depth of 0.31 eV. Since the fit quality is more or less the same, an unambiguous identification of the band gap half is no longer possible (second row in Tab. 1).

T-Model	$\sigma(T)$	Fit T-range	MinBH-defect			Quality			MajBH-defect			Quality		
			E_c-E_t	K	Chi^2	L	M	H	E_r-E_V	K	Chi^2	L	M	H
Basic	Const.	260..500 K	0.34 eV	5.1	0.05 (26.2)	X	+	X	0.28 eV	Arb.	0.73 (5.65)	X	-	X
Standard	$\propto 1/T^{1.5}$	200..500 K	0.31 eV	1.2	0.05 (6.57)	+	+	X	0.31 eV	Arb.	0.05 (7.47)	+	+	X
Advanced	$\propto 1/T^{1.5}$	200..580 K	0.32 eV	1.4	0.06	+	+	+	0.32 eV	~8	0.05	+	+	+

TAB. 1 Extracted defect parameters if the modeling of the TDLS curve in Fig. 1 is performed for different modifications of the SRH model assuming a MinBH and a MajBH defect, respectively. The quality of the SRH fits is classified in the low (L: $T < 260$ K), medium (M: $T = 260..500$ K) and high (H: $T > 500$ K) -temperature region as good (+) or bad (-). An 'X' indicates that the respective T -region was not considered for the least squares optimization. For each model those T -regions were ignored in which the model does not even allow a qualitatively correct fit. Since the given Chi^2 -values are thus artificially reduced for fits on a reduced T -range, the numbers in brackets give the Chi^2 -values which were post-calculated for the whole T -range from 200-580 K.

Further extensions of the SRH model arise from the attempt to model the high-temperature part of the TDLS curve. The observed lifetime decrease above 500 K originates from the abrupt onset of intrinsic conduction which leads to an exponential increase of the majority carrier concentration p_0 and thus to a strong decrease of the ratios n_i/p_0 and p_i/p_0 , which stipulate SRH lifetime under low-level injection in that T -region. This explains that the SRH modeling using the 'basic' T -model with T -independent equilibrium carrier concentrations $p_0=N_A$ and $n_0=n_i^2/N_A$, where n_i is the intrinsic carrier concentration at 300 K, does not even allow a qualitatively correct description in that T -region, as shown by the dashed lines in Fig. 2. Analytically the temperature dependence of the equilibrium majority carrier concentrations is given by $p_0(T) = 1/2 [N_A + \{N_A + 4 n_i(T)^2\}^{1/2}]$ (see Ref. [18]). As can be seen from the dashed-dotted lines in Fig. 2, the introduction of this standard T -model enables a modeling of the $n_i(T)$ -induced bent of the TDLS curve which is qualitatively correct though not quantitatively. The fact that the experimentally observed onset of intrinsic conduction is shifted to lower temperatures, implies a stronger T -dependence of $p_0(T)$ than assumed in the 'standard' T -model.

This observation can be explained by a well-known effect: the temperature-induced narrowing of the silicon band gap. The reduction of $E_{gap}(T)$ with increasing temperature leads to an enhanced increase of $n_i(T)$ and $p_0(T)$, respectively, and thus induces an onset of the TDLS bent at lower temperatures. A well established model for the temperature dependence of E_{gap} is found in Ref. [18]: $E_{gap}(T)=E_{gap}(0)-[\alpha T^2/(T+\beta)]$ with $E_{gap}(0)=1.170$ eV, $\alpha=4.73\times 10^{-4}$ eV/K and $\beta=636$ K. The implementation of $E_{gap}(T)$ in the T -model is subject to a fundamental restriction: While the band gap narrowing is fully considered in the calculations of the equilibrium carrier concentrations $p_0(T)$ and $n_0(T)$ to allow an accurate modeling of the intrinsic conduction, it is ignored in the calculation of the SRH densities $p_i(T)$ and $n_i(T)$. The reason for this simplification is the lack of a widely accepted model for the shift of defect levels in a flexible band gap and the level pinning, respectively. Thus, the temperature dependence of $p_i(T)$ and $n_i(T)$ is calculated for a constant energy distance of the defect level from both band edges which are determined for $E_{gap}(300$ K). The extraordinary performance of the SRH model being based on this 'advanced' T -model is demonstrated by the solid lines in Fig. 2. As can be seen, both, the bent due to intrinsic conduction and the Arrhenius increase, are perfectly modeled as well for a MinBH as for a MajBH defect with an energy depth of 0.32 eV. The detailed fit results are displayed in the third row of Tab. 1. Note, that the 'advanced' T -model has been further extended by an

improved model for the effective densities of states which is based on effective mass theory of electrons and holes [19]. A detailed analysis shows that the improved N_C - N_V -model slightly influences the position of the Arrhenius increase while it does not affect the low- and high-temperature parts of the TDLS curve.

2.2. Transparent SRH analysis: Defect parameter solution surface of TDLS curves

In order to quantify the accuracy of the defect parameters determined for the MinBH and the MajBH solution, the tolerance of the fitting model towards slight fluctuations of the fitting parameters has to be investigated. This investigation is performed with maximum transparency if the 'Defect Parameter Solution Surface' (DPSS) of the TDLS curve is determined. This new modeling procedure, in the following referred to as DPSS analysis, has recently been introduced in Ref. [13].

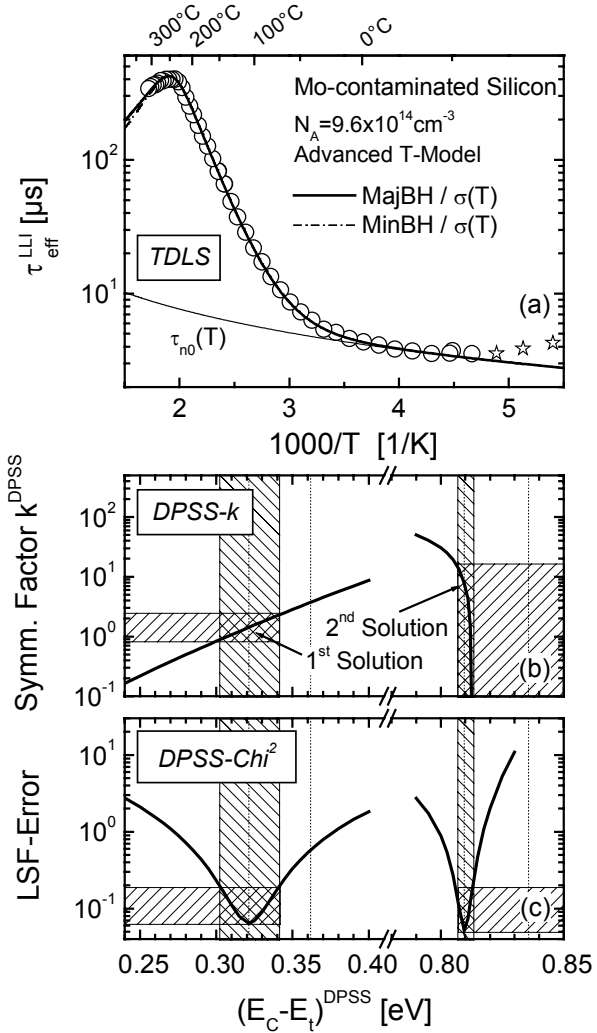


FIG. 3. Advanced SRH analysis of the TDLS data from Fig. 1 by means of the 'defect parameter solution surface' (DPSS) associated with the optimum SRH model. While a comparison of the minimum values of the displayed DPSS- χ^2 curves in general allows the identification of the true band gap half of the defect center, the width of each DPSS- χ^2 curve makes an error estimation for the extracted defect parameters possible.

Using the SRH model which has been identified as optimum in the previous section, the DPSS diagram is determined from least squares fits of the measured TDLS curve for specified but gradually varied energy levels E_C-E_t of the defect center. The resulting symmetry factors k and the corresponding χ^2 -errors of the least squares fit are displayed in Fig. 3b and c as a function of the energy level E_C-E_t (solid lines). Both curves together represent the DPSS of the TDLS curve and are referred to as DPSS- k and DPSS- χ^2 curve.

The practical value of the DPSS diagram consists in the fact that in general a comparison of the minimum values of the DPSS- χ^2 curves allows the identification of the true band gap half of the defect center, while the width of each DPSS- χ^2 curve makes an error estimation for the extracted defect parameters possible.

In the case of molybdenum the DPSS analysis shows that the solutions in the upper and the lower half of the band gap are identical in quality, which impedes the identification of the true band gap half and thus the identification of the k -factor. If a least squares error which is increased by a factor of 3 above its optimal value of 5.5×10^{-2} is defined as 'tolerable', the following ranges of acceptable values for the defect parameters can be deduced from the DPSS diagram as shown by the shaded areas in Fig. 3b and c. For the MinBH solution $E_C-E_t=0.30..0.34 \text{ eV}$ and $k=0.9..2.3$ and for the MajBH solution $E_C-E_t=0.312..0.318 \text{ eV}$ and $k=0.07..15$. The qualitative shape of the DPSS curves directly reflects the fundamental difference between MinBH and MajBH defects discussed in Ref. [12]. The steep DPSS- k and the narrow DPSS- χ^2 curve observed for the MajBH solution directly

arise from the fact that the onset temperature of the Arrhenius increase is independent of k for a MajBH defect. Analogous the existing k -dependence for a MinBH defect leads to a moderate slope of the DPSS- k curve and to a broader DPSS- χ^2 curve. Thus, concerning accuracy the defect parameters extracted from TDLS alone follow a pattern: For MinBH defects both defect parameters can be extracted with sufficient accuracy. MajBH defects on the contrary only allow an accurate E_f -determination while the k -determination in general fails, the extracted k -range being several orders of magnitude wide.

3. ADVANCED IDLS ANALYSIS

In order to reveal which of the two solutions obtained from the DPSS analysis of the TDLS curve provides the true defect parameters, the Mo-contaminated sample used for the TDLS investigation has been subject to an IDLS experiment. Figure 4 displays the IDLS curves measured by means of the QSSPC method. Since surface recombination is effectively suppressed in the whole Δn -range by means of a high quality SiN surface passivation, the measured effective carrier lifetime (open symbols) directly reflects bulk recombination. In order to extract the pure SRH lifetime related to the molybdenum centers in the bulk (closed symbols) in a maximum Δn range, the measured lifetime curve has to be corrected under low level injection ($\Delta n < 10^{13} \text{ cm}^{-3}$) for trapping effects by means of a bias correction proposed in Ref. [20]. Due to the low lifetime level, intrinsic Auger recombination has no effect on the measured IDLS curve under high-level injection (HLI).

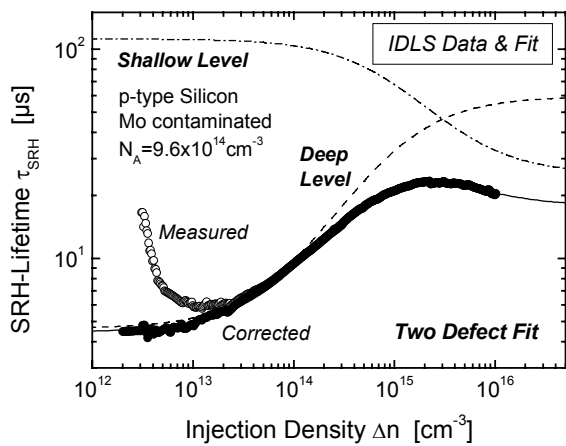


FIG. 4. IDLS curve measured by means of the QSSPC technique on the same Mo-contaminated sample as investigated in Fig. 1. The accurate SRH modeling of the measured injection dependence in the whole Δn -range requires two independent SRH centers whose impact is displayed separately.

parameterization of an IDLS curve is not unambiguous [2]. Thus, a detailed analysis of the IDLS data requires determining the ‘Defect Parameter Solution Surface’ which is associated with the defect center dominating the LLI part of the IDLS curve (see above). Within the DPSS-modeling procedure for the LLI-dominating defect center, the HLI-dominating defect center was taken into account in that its defect parameters were optimized once for a fixed shallow level. The resulting DPSS- k and DPSS- χ^2 curve of the LLI-dominating defect center are displayed in Fig. 5 (dashed lines) together with the corresponding curves for the TDLS data (solid lines). A fundamental difference between the DPSS curves determined from the TDLS and IDLS data can be observed: While the DPSS- χ^2 curves of the TDLS fits (solid line) show a

As can be seen from Fig. 4, the accurate SRH modeling of the measured injection dependence in the whole injection range requires two independent SRH centers whose impact is displayed separately. While the increase of SRH lifetime up to $\Delta n = 2 \times 10^{14} \text{ cm}^{-3}$ is well described by only the deep defect level (dashed line) and is hardly affected by the shallow center (dash-dotted line), the successful modeling of the observed slight decrease of SRH lifetime under HLI conditions (above $\Delta n = 10^{15} \text{ cm}^{-3}$) strongly depends on the shallow defect level. Such a coexistence of a deep (LLI-dominating) and a shallow (HLI-dominating) defect level is reported in literature for different impurities in silicon [9, 13]. Nevertheless, since TDLS is performed under LLI conditions, only the LLI-domination center is relevant for the comparison of IDLS and TDLS.

Concerning its applicability for defect characterization, IDLS faces the problem that the SRH

pronounced minimum which indicates the best TDLS parameterization (EC-Et, k), the DPSS-Chi² curve of the IDLS curve (dashed line) is totally constant over a broad range of energy levels, which nicely shows that the defect parameters cannot be determined from only one IDLS curve.

4. COMBINED DPSS ANALYSIS

Beyond the instructive illustration of the SRH simulation, the combined DPSS diagram in Fig. 5, which contains the DPSS curves of the IDLS *and* TDLS measurement on the Mo-contaminated sample, allows an accurate determination of the defect parameters of molybdenum from the intersection points of the DPSS-*k* curves obtained for the IDLS and TDLS measurement. Since the DPSS-*k* curve associated with the TDLS curve contains solutions of varying accuracy, the quality of both DPSS-*k* intersection points significantly depends on their energy distance from the corresponding minimum of the DPSS-Chi² curve related to TDLS. Since the DPSS-*k* intersection point in the upper half of the band gap strongly deviates from the corresponding DPSS-Chi² minimum in terms of the energy position, the TDLS solution in the upper half of the band gap has to be rejected for reasons of inconsistency. In the lower half of the band gap on the contrary, the energy positions of both, the DPSS-*k* intersection point and the minimum of the DPSS-Chi² curve, perfectly coincide. It can be concluded that the relevant molybdenum level is definitely located in the lower half of the band gap at $E_t - E_V = 0.317 \pm 0.005$ eV showing an electron/hole capture cross section ratio $k = 13 \pm 3$. The quality of this finding is manifested in the high accuracy observed for the coincidence of the DPSS-*k* intersection point and the DPSS-Chi² minimum. The error of the combined result, which is indicated by the shaded areas in Fig. 5, is thus estimated by the small E_t -error of the TDLS analysis deduced in Sec. 2.2 and a moderate k -error of 20% around the optimum k -value at the DPSS-*k* intersection point.

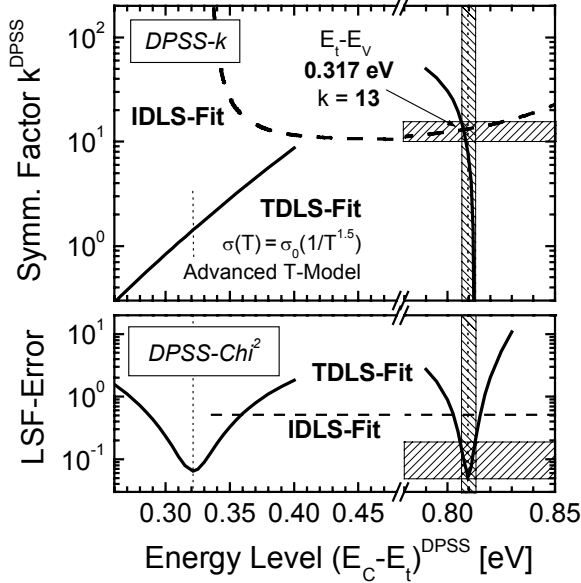


FIG. 5. Superposition of the DPSS diagrams associated with the IDLS and TDLS curve of the Mo-contaminated sample displayed in Fig. 1 and 4, respectively. Unambiguous determination of both molybdenum defect parameters from the intersection point of the DPSS-*k* curves in the MajBH. The coincidence of this intersection point with the minimum of the DPSS-Chi² curve manifests the accuracy of the determination and the necessity of the proposed extensions of the SRH model for the TDLS analysis.

5. CONCLUSION

In the present work it is demonstrated that a complete defect characterization is always achieved on a single sample if TDLS and IDLS are combined. It is shown that an accurate modeling of the entire TDLS curve in an extended temperature range from 130 to 580 K requires several physical extensions of the basic

SRH model which have a significant impact on the spectroscopic result. Under low temperatures the accurate modeling in general requires a $\sigma(T)$ -model which can directly be determined from the low-temperature part of the TDLS curve and thus represents an additional finger print of the defect. Under high temperatures an accurate modeling of the TDLS bent due to intrinsic conduction is only achieved if the temperature dependence of both, the equilibrium carrier concentrations $p_0(T)$, $n_0(T)$ and the band gap $E_{gap}(T)$, are considered.

In addition to these physical extensions of LS analysis a new modeling procedure for lifetime spectroscopic data is introduced which allows a transparent and comprehensive SRH analysis of IDLS and TDLS data by determining the associated ‘Defect-Parameter-Solution-Surface’ (DPSS). The newly developed DPSS diagram perfectly visualizes the ambiguity of IDLS fit results and makes it possible to assess the accuracy and consistency of the defect parameters determined from different lifetime spectroscopic curves which are dominated by the same defect center.

The application of this advanced LS analysis on a pair of TDLS and IDLS curves measured on an intentionally Mo-contaminated silicon sample demonstrates the excellent performance of lifetime spectroscopy. In good agreement with DLTS results from literature, two independent LS methods identified consistently a known molybdenum donor level at $E_t-E_V=0.317$ eV as center with highest recombination activity. Furthermore, the study reveals an enhanced electron capture cross section ($k=13$) which is determined at $\sigma_n=7.8\times10^{-15}$ cm⁻³. Allowing the exact determination of E_t and k , advanced lifetime spectroscopy presented in the current work provides a full picture of how such impurities affect cell performance.

ACKNOWLEDGEMENTS

The authors would like to thank P. Lichtner and E. Tavaszi for lifetime measurements. The authors would further like to acknowledge the funding by the German Ministry of Education and Research BMBF (contract number 01SF0010).

REFERENCES

- [1] W.M. Bullis and H.R. Huff, J. Electrochem. Soc. **143** (4), 1399-405 (1996).
- [2] S. Rein, T. Rehrl, W. Warta, and S.W. Glunz, J. Appl. Phys. **91** (3), 2059-2070 (2002).
- [3] W. Shockley and W.T.J. Read, Phys. Rev. **87** (5), 835-42+ (1952).
- [4] R.N. Hall, Phys. Rev. **87**, 387 (1952).
- [5] F. Shimura, T. Okui, and T. Kusama, J. Appl. Phys. **67** (11), 7168-71 (1990).
- [6] Y. Kirino, A. Buczkowski, Z.J. Radzimski, G.A. Rozgonyi, et al., Appl. Phys. Lett. **57** (26), 2832-4 (1990).
- [7] S. Rein, T. Rehrl, J. Isenberg, W. Warta, et al., Proc. 16th EPVSEC (Glasgow, UK, 2000), p. 1476-81.
- [8] S. Rein, T. Rehrl, W. Warta, and S.W. Glunz, Proc. 17th EPVSEC (Munich, Germany, 2001), p. 1561-6.
- [9] J. Schmidt, Applied Physic Letters (2003).
- [10] J. Schmidt, C. Berge, and A.G. Aberle, Appl. Phys. Lett. **73** (15), 2167-9 (1998).
- [11] D. Macdonald, A. Cuevas, and J. Wong-Leung, J. Appl. Phys. **89** (12), 7932-7939 (2001).
- [12] S. Rein, P. Lichtner, W. Warta, and S.W. Glunz, Proc. 29th IEEE PVSC (New Orleans, Louisiana, 2002), p.
- [13] S. Rein and S.W. Glunz, Appl. Phys. Lett. **82** (7), 1-3 (2003).
- [14] R.A. Sinton, A. Cuevas, and M. Stuckings, Proc. 25th IEEE PVSC (Washington DC, USA, 1996), p. 457-60.
- [15] H. Maeckel and R. Luedemann, (unpublished).
- [16] J. Bourgoin and M. Lannoo, *Point defects in semiconductors II. Experimental aspects* (Springer-Verlag, Berlin, West Germany, 1983).
- [17] E. Gaubas, J. Vanhellemont, E. Simoen, C. Claeys, et al., Proc. 7th International Autumn Meeting on Gettering and Defect Engineering in Semiconductor Technology (GADEST'97) (Spa, Belgium, 1997), p. 155-60.
- [18] S.M. Sze, *Physics of Semiconductor Devices*, 2nd Edition (John Wiley & Sons, New York, 1981).
- [19] M.A. Green, J. Appl. Phys. **67** (6), 2944-2954 (1990).
- [20] D. Macdonald, R.A. Sinton, and A. Cuevas, J. Appl. Phys. **89** (5), 2772-8 (2001).
- [21] L. Börnstein, *Semiconductors* (Springer-Verlag, Berlin, 1984).

Progress in Manufacturable High-Efficiency Silicon Solar Cells Based on OECO Technology

Rudolf Hezel

Institut für Solarenergieforschung Hameln/Emmerthal (ISFH), D-31860 Emmerthal, Germany

ABSTRACT

It is demonstrated that by the novel self-aligning OECO (Obliquely Evaporated Contacts) technology crystalline silicon solar cells with efficiencies exceeding 21% can be fabricated without masks and photolithography. For the standard OECO-MIS-n⁺p cell the suitability for mass production is currently tested using novel custom made high-throughput equipment. Results of lab- and industrial size devices are presented. Another high efficiency OECO type silicon solar cell with both contacts on the rear side and bifacial sensitivity is introduced. For this BACK OECO cell an almost symmetrical behaviour for front and rear side efficiency (18.1/17.4) could be achieved. The potential for very high efficiencies is outlined.

INTRODUCTION

Record laboratory efficiencies close to 25% have been reported for highly sophisticated crystalline silicon solar cells, applying numerous aligned photolithography as well as several high temperature steps. / 1 / However, only the combination of very high solar cell efficiencies with simple, time and energy saving processing including cost-effective materials is a promising way to make PV solar electricity more competitive. For this purpose a new generation of easy-to-fabricate high-efficiency crystalline solar cells based on the Obliquely Evaporated Contact (OECO) technology was recently introduced (2,3,4). Metal-insulator-silicon (MIS) contacts with low cost Al as metallization in conjunction with a shallow emitter (MIS-n⁺p) are used.

In the present paper basic features and recent results of the front-contacted standard OECO MIS-n⁺p solar cell are reported. This cell is currently in a pilot line test.

Furthermore, a novel high efficiency OECO type solar cell with both contacts on the rear side is introduced, which is able to convert sunlight incident onto the front and the rear side of the cell into electric power (BACK OECO CELL)

1.The Standard OECO Solar Cell

A schematic representation of the Standard OECO MIS-n⁺p solar cell is shown in Fig. 1. The main feature of the cell is the corrugated surface consisting of a set of parallel rectangular grooves. A shallow diffused n⁺ emitter is located at the silicon surface. The metal for the front grid fingers is obliquely evaporated upon an ultrathin low-temperature tunnel oxide on the upper part of the vertical flanks forming MIS contacts. On steep flanks high metal cross sections can easily be achieved without increasing the shadowing losses. The front surface of the cell is covered with PECVD silicon nitride acting both as passivation and antireflection coating.

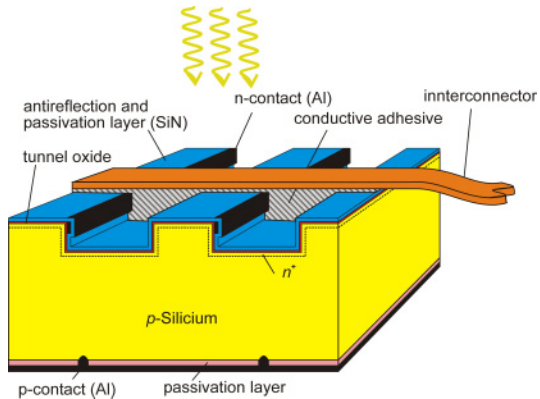


Figure 1: Schematic of the standard OECO cell structure. Busbar formation and tabbing are simultaneously performed using conductive adhesives.

A well passivated rear contact scheme based on local contact areas is formed by laser opening of the passivation layer and subsequent deposition of a continuous Al layer. The detailed processing sequence is described elsewhere /2,3,4/

1.1 Cell Manufacturing Technology

The three novel fabrication steps for OECO solar cells are: i) mechanical surface grooving to provide steep flanks for the front grid fingers, (ii) oblique evaporation of metal contacts and (iii) surface passivation by PECVD silicon nitride.

For surface grooving a special grinding system was constructed with an extended structured spindle arranged in a horizontal position. The tool is designed to groove Si wafers up to 150x150 mm² in one fast cut. For the oblique metal evaporation in a vacuum the self shading effect of the ridges is utilized, so that no masks or photolithography are required. /3,4/. High throughput is achieved since the wafers can be arranged closely spaced on a rotating cylinder /2,4/. Our custom-made evaporation equipment with a throughput of 700 wafers per hour requires a floor space of only 2.5 m². For passivation and AR coating of the OECO solar cells by plasma silicon nitride a remote plasma technique was used, achieving record low surface recombination velocities /5/.

1.2 Busbar formation and Cell Interconnection using electrically conductive adhesive technology

The OECO technology does not provide busbars which collect the current from the fingers and serve as solder areas for cell interconnection in module fabrication. Therefore this new cell type requires an alternative interconnection technology. By electrically conductive adhesives as widely used for chip mounting a metallic tab was attached to the cells simultaneously interconnecting the parallel grid fingers and the cells. The novel interconnection technology has several advantages compared to soldering: i) low process temperature (<200°C), ii) low mechanical stress and iii) lead-free.

In order to investigate the long-term stability of adhesive joints temperature cycles (-40°C to +85°C) under relative humidity up to 85 % were performed and the joint resistance of the interconnection from cell to tab was measured using different conductive adhesives. Also the UV radiation hardness of the interconnection was tested. The experiments confirmed excellent long term stability for special adhesives.

1.3 Results

In Table 1 the efficiencies after 24 h illumination of 4 cm^2 and 100 cm^2 OECO MIS- n^+ p solar cells using different silicon materials are summarized.

Area (cm^2)	Fz-Si		Cz-Si (Ga)		Cz-Si (B)	
	4	100	4	100	4	100
eta (%)	21.1*	20.0*	21	19.4*	18.3	17.9

Table 1. One sun efficiencies (after 24h illumination AM 1.5 G, 100 mW/cm^2 , 25°C) of 4 cm^2 and 100 cm^2 standard OECO MIS- n^+ p solar cells using different silicon materials. (*confirmed by FhG-ISE)

As can be seen, values even beyond 21% could be achieved for the small area cells. For $10 \times 10 \text{ cm}^2$ OECO solar cells record efficiencies up to 20% were resulting using FZ-Si as well as Ga-doped Cz-Si. In contrast to boron doped Cz-Si, the Ga-Cz-Si does not show any light induced degradation.

2. The back contacted and bifacially sensitive OECO solar cell (BACK OECO cell)

Placing both electrodes on the rear side of a solar cell is advantageous due to (i) improvement of efficiency since shading losses by the front grid are avoided, (ii) reduction of module fabrication costs since high throughput surface mount automated assembly can be used and (iii) better visual appearance of the PV modules.

The oblique-evaporation-of-contact (OECO) technology is particularly suitable for this kind of solar cells, since the separation of the n-and p-contact lines in order to avoid shunting is ingeniously simple and reliably accomplished without any masks or alignment /6/.

The structure of the novel back contact device, designated by us as BACK OECO solar cell, is schematically shown in Fig. 2.

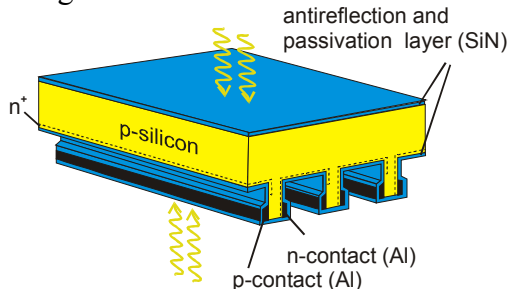


Fig. 2: Structure of the BACK OECO solar cell. Both contacts are on the back. Also the light reflected onto the rear side can be utilized

The characteristic features include: (i) A well passivated front surface by PECVD Si nitride, optionally with a floating junction (ii) A corrugated back surface with n-contact lines on one flank and p-contact lines on the opposite flank of the elevations. (iii) A n^+ emitter at the back surface except in the vicinity of the p-contacts, where a local back surface field can be introduced. (iv) The whole back surface is covered by a low temperature passivation layer (PECVD SiN). The high efficiency features and the low cost production features together with the detailed processing sequence using only industrially feasible self aligning steps are outlined elsewhere /7,8/. As an outstanding feature, bifacial sensitivity of the cell is included without extra processing.

2.1 Results

$2 \times 2 \text{ cm}^2$ cells were processed using $0.5 \Omega \text{ cm}$ FZ silicon wafers. By rear side grooving, the effective thickness was adjusted to $130 \mu\text{m}$. Only the front side was textured and both sides were coated with a simple AR layer of SiN. Preliminary results are presented in Fig. 3. As can be seen

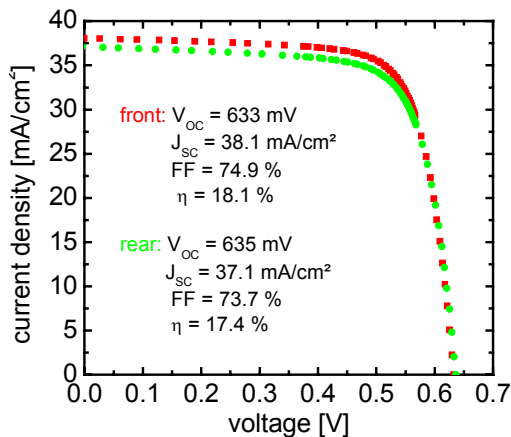


Figure 3: J-V curves of a BACK-OECO cell under front and rear side illumination, respectively (AM1.5G, 100 mW/cm², 25°C, aperture area 3,93cm²)

from the illuminated I-V curves, an almost symmetrical behaviour with efficiencies of 18.1% and 17.4% could be achieved for front and rear side illumination, respectively. Neither the non-textured rear side structure nor the diffusion profile are optimized. Simulations reveal that efficiencies of 22% are attainable for high quality FZ-Si or Ga-doped Cz-Si with a diffusion length of about 800 μm and a thickness between 200 μm and 300 μm . / 6,7 /With thinner wafers efficiencies above 20% can be obtained for lower quality material such as boron doped Cz-Si. Even for multicrystalline Si efficiencies up to 19% are feasible if the base width is reduced to 50 μm . As a further advantage of the OECO technology, the optimum base thickness can automatically be adjusted by the grooving process even below 50 μm .

Conclusion

Both the standard OECO solar cell and the BACK OECO cell described in this work have the potential to reach efficiencies well beyond 20% using Cz-Si in an industrial environment. The simplicity of the novel processing sequence, particularly excluding complex masking or aligned photolithography, in combination with the outstanding cell results make these cells to promising candidates for a significant cost reduction of solar electricity. Utilizing the bifacial sensitivity of the BACK OECO solar cells in the novel multifunctional bifacial module arrangements recently introduced by us, additional power gains of more than 50% are resulting compared to monofacial use /9/

References

- /1/ J. Zhao, A. Wang and M. A. Green, Prog. Photovolt. 7,411 (1999)
- /2/ R. Hezel, Ch. Schmiga and A. Metz, Proc. 28th IEEE Photov. Spec. Conf. Anchorage (1999) p. 184) (2000)
- /3/ A. Metz and R. Hezel, Solar Energy Mater. Sol. Cells 65, 325 (2001)
- /4/ R. Hezel, Sol. Energy Mater. Sol. Cells 74, 25 (2002)
- /5/ T. Lauinger, J. Schmidt, A. Aberle and R. Hezel, Appl. Phys. Letter 68, 1232 (1996)
- /6/ R. Hezel, Proc. 29th IEEE Photov. Spec. Conf., New Orleans, 114 (2002)
- /7/ J. W. Mueller, A. Merkle and R. Hezel, Proc. PV in Europe, Conf. And Exhibition, Rome, 48, (2002)
- /8/ J. W. Mueller, A. Merkle and R. Hezel, Proc. 3rd World Conf. On Photovolt. Energy Conversion Osaka, 2003 (inpress)
- /9/ R. Hezel, paper submitted to Progr. Photovolt.

HIGH EFFICIENCY, ONE-SUN SOLAR CELL PROCESSING

William P. Mulligan and Richard M. Swanson
SunPower Corporation, 430 Indio Way, Sunnyvale, CA 94085, U.S.A.

ABSTRACT

Higher cell efficiency is critical to the continued cost reduction for crystalline silicon solar modules and systems. Efficiency loss mechanisms in conventional and high-efficiency solar cells are reviewed. Performance enhancing process options are described for both front contact and rear contact cell designs. Realization of very high cell efficiencies depends on an integrated approach process improvement – no single process step can deliver high efficiency on its own. The advantages of rear contact cell design for high efficiency processing are described. SunPower has achieved 21.1% efficiency on a 149cm² cell made by low-cost production processes.

INTRODUCTION

Recently there has been renewed industrial interest in high efficiency silicon solar cells [1]. This interest is motivated by the large leveraging effect that higher cell efficiency has in reducing overall photovoltaic module and system costs. Figure 1 depicts the major cost components of a typical crystalline silicon module. Wafered silicon represents fully 50% of the finish module cost. Because higher cell efficiency means more power from same piece of silicon, efficiency improvement results in a directly proportional savings in crystal growth and wafering costs on a dollars per watt basis. Similarly, many cell processing costs are lower with higher efficiency. For example, the cell power output per operator move and per capital equipment dollar are both improved with higher cell efficiency. In module assembly, less glass, EVA, and Tedlar are used to make a module with the same output power. Finally, because installation and BOS component costs are somewhat dependent on module area, higher module efficiency leads to lower system costs. SunPower has estimated the typical system integration and installation savings are about \$0.05 per watt per absolute point of increased module efficiency, depending on the application.

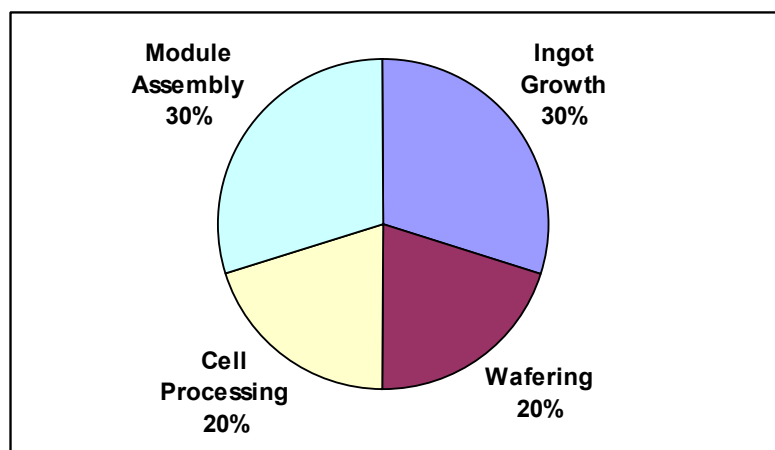
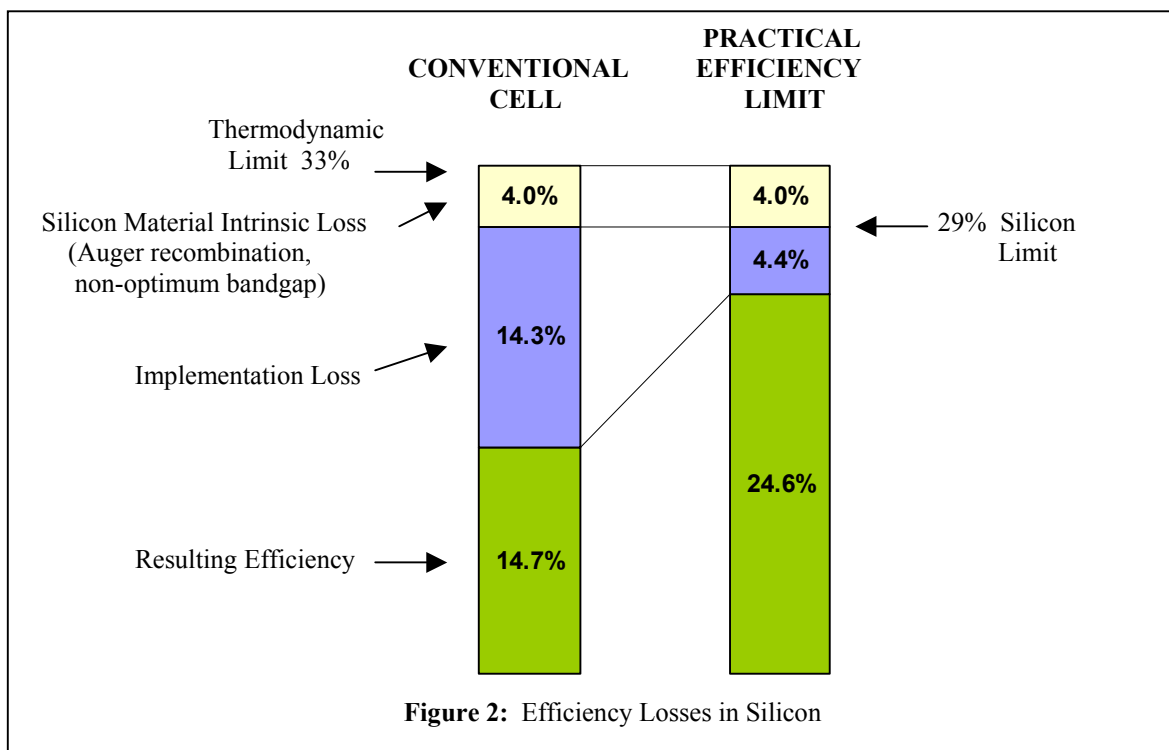


Figure 1: Major cost components of a typical crystalline silicon module.

Solar cell processing represents only about 20% of the total module cost. Improved solar cell processing that leads to higher efficiency, however, can leverage tremendous savings in wafer, cell processing, module, and system costs. Investments in improved cell processing that result in higher efficiency can therefore make excellent economic sense.

HIGH EFFICIENCY SILICON – HOW FAR CAN WE GO?

The thermodynamic limit to efficiency for a single junction solar cell under one-sun illumination (figure 2) is about 33%. For silicon, its non-optimal bandgap and Auger recombination reduce this limit to 29%. Implementation losses, including bulk, surface, and junction recombination, optical losses, and series resistance limit practical efficiencies to well below 29%. For conventional crystalline silicon solar cells, the implementation losses are typically 14 to 15%. The practical limit to silicon solar cell efficiency is about 24 to 25%, with implementation losses of only 4 to 5%. Small area laboratory cells from several groups have approached this limit [2, 3]. Top performing production cells include Sanyo's HIT cell at 21.2% for a 100cm² cell [4] and SunPower's 21.1% 149 cm² cell, described below.



Typical loss mechanisms and their approximate magnitudes for a conventional crystalline silicon solar cell are depicted schematically in figure 3a. The most important loss mechanisms include junction recombination, rear surface recombination, bulk recombination, and reflection from the front grids.

Projected efficiency losses for a high-efficiency, rear-contact solar cell near the practical efficiency limit are shown in figure 3b. In this case, the dominant loss mechanisms are rear surface recombination, front surface recombination, and escape reflectance from the front. High efficiency front contact designs would have similar losses, with slightly lower front recombination loss but with additional loss from front grid reflectance.

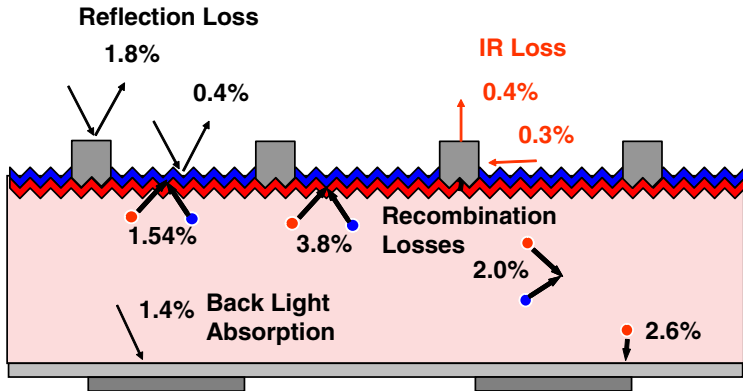


Figure 3a: Efficiency losses for a conventional silicon solar cell ($\eta=14.7\%$)

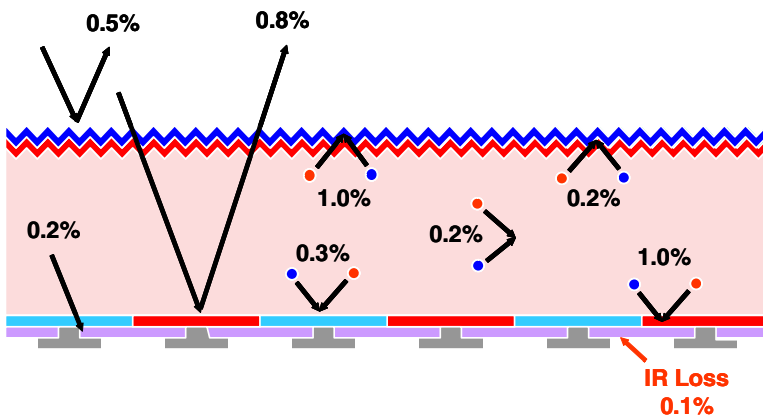


Figure 3b: Efficiency losses for a rear-contact solar cell near the practical efficiency limit ($\eta=24.6\%$).

HIGH EFFICIENCY PROCESS DESIGN

In order to improve cell efficiency, the loss mechanisms must be reduced. Strategies generally are focused on reducing carrier recombination processes. Popular efficiency enhancing process improvements include:

- Aluminium or boron back-surface field (BSF), to reduce back surface recombination
- Selective emitter, to reduce front junction recombination
- Silicon nitride anti-reflection coating to reduce bulk and front surface recombination through a combination of hydrogen passivation and fixed charge effects.
- Laser buried groove metallization to reduce grid reflectance, as well as providing a selective emitter.
- Oxide passivation with restricted metal contact openings to reduce back and/or front surface recombination.
- Rear surface reflector to improve light trapping.
- Higher lifetime silicon wafer to reduce bulk recombination.

IMPLEMENTATION OF HIGH EFFICIENCY FEATURES

Simply adding individual process features is no guarantee of significant and cost-effective efficiency improvement. Figure 4 shows the PC-1D modeled impact of step-wise addition of common high-efficiency process improvements for a conventional crystalline silicon solar cell, with front n⁺ diffusion, screen-printed front and back metal grids, anti-reflection coating and texture.

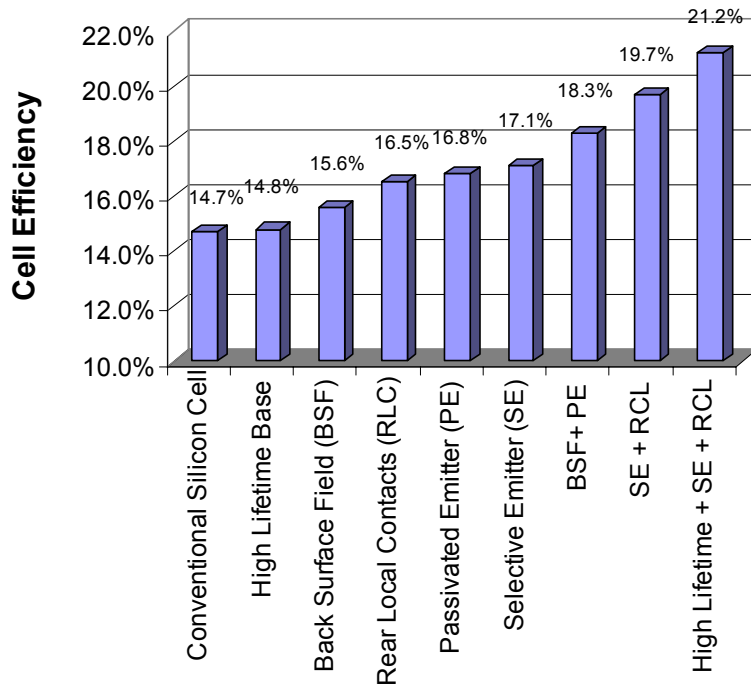


Figure 4: Efficiency Impact of High-Efficiency Process Features

As seen in the figure, simply using quality high-lifetime wafers, such as float-zone, leads to very little efficiency improvement in a convention cell. This is because bulk recombination is not the dominant loss mechanism at these relatively low efficiencies – for higher efficiency designs this changes. Adding a back-surface field, the most widely implemented efficiency enhancement, also returns only a modest efficiency improvement. This may explain why BSF is not yet universally adopted although it is relatively easy to implement. More complex efficiency enhancing process features, including rear local contacts, passivated and selective emitters provide somewhat more improvement, but perhaps not enough to justify their increased cost of processing.

If you fix only one major recombination mechanism, the efficiency impact of this fix is tempered by the fact that the remaining recombination mechanisms become increasing important. Bigger efficiency gains are available when you combine more than one efficiency enhancing feature—the combined effect of several process enhancements is more than the sum of the individual components. For example, adding a BSF gives 0.9 percentage point improvement, whereas adding a passivated emitter gives 1.1 percentage points. Adding both together gives 3.6 percentage points, nearly twice the sum of the individual contributions. We

see that there is a multiplicative performance effect, whereas the cost of adding the two features is closer to additive. Very high efficiency cells are possible only when you combine all of the important high efficiency process features. This conclusion also applies to high-efficiency rear-contact solar cell designs.

ADVANTAGES OF REAR CONTACT CELL DESIGN

SunPower manufactures high-efficiency rear-contact solar cells, depicted schematically in Figure 5. Interdigitated n+ and p+ diffusions and grid lines are used to collect photogenerated carriers entirely from the back of the cell. There are no front gridlines so metal reflection loss is entirely eliminated. The design trade-off encountered in conventional cells, where there is a compromise between grid resistance and grid reflection, disappears. The back grid can cover the entire back surface, greatly reducing resistance loss.

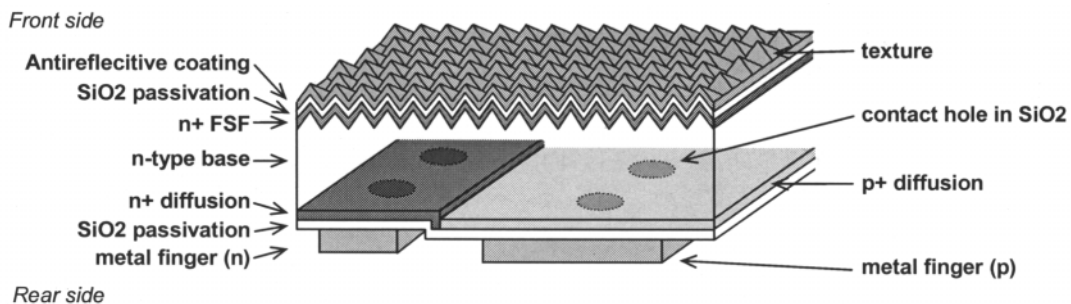


Figure 5: Schematic diagram of SunPower's rear-contact solar cell (not to scale).

Unlike front contact cells, the front junction is not used for lateral current conduction, nor does it need to make good ohmic contact to the top grid. Therefore, the front junction is lightly doped which contributes to a significant reduction in junction recombination current. Design features include silicon dioxide passivation and dopant diffusions on both the front and back surfaces that are designed to reduce surface recombination losses. The cell uses localized point contacts to reduce metal-semiconductor contact area and thus reduce rear surface recombination loss. An important feature is that the back surface naturally has quite high reflectance due to the SiO₂ passivation layer. This promotes efficient light trapping. High minority carrier lifetime is required for any high efficiency cell. This cell design, however, is particularly sensitive to bulk lifetime as most carriers are generated near the front surface and must diffuse through the entire wafer thickness to reach the collecting junctions at the rear. The only p-type doping in SunPower's cell is confined to the back diffusion. This eliminates conventional light induced degradation seen in cells made of p-type Czochralski, and also cells in n-type silicon with boron front junctions.

In many respects, a backside contact cell is simpler to manufacture than a high efficiency two sided design. This is because metallization and contact openings are confined to one side of the wafer, so only one contact opening and metal deposition required.

SUNPOWER'S LOW-COST REAR-CONTACT SOLAR CELL

Historically, SunPower's high-efficiency rear-contact solar cells have been fabricated with conventional semiconductor processing technology, including photolithography. Using such

processing, SunPower produces cells with one-sun efficiencies approaching 23% but at costs affordable to just a few niche applications, such as solar airplanes [2] and solar cars [5].

To reduce fabrication costs, SunPower has developed low cost screen-printing technology to fabricate the rear devices features. SunPower is also using low-cost photovoltaic float-zone silicon starting material (PV-FZ), recently available from Topsil [6], that has very high minority carrier lifetime.

While high minority-carrier lifetime is a critical for all high-efficiency solar cell designs, this is particularly true for rear-contact solar cells where most carriers must traverse the full thickness of the solar cell to be collected. If a rear-contact solar cell has a low lifetime—and therefore a short diffusion length—carriers will recombine in the bulk before they are collected. In SunPower’s new low-cost cell designs, the dependence of efficiency on lifetime is even greater, because some minority carriers must travel significant lateral distance in addition to traversing the thickness of the cell in order to reach the collecting junction.

Figure 5 shows how cell efficiency depends on lifetime for a low-cost rear-contact solar cell. The line shows the results of 2D ATLAS simulation and the symbols show the experient results from cells made from 0.7 ms wafers and from 3 ms wafers. Experimental details and test methods were reported previously [7]. It is concluded that the low-cost, rear-contact solar



Figure 5: Cell efficiency vs minority-carrier lifetime for a low-cost, rear-contact solar cell. The line shows the results of 2D ATLAS simulation and the symbols show experiental results for cells made from 0.7 ms and 3 ms wafers, where all cells were fabricated in a single production lot.

cell should be fabricated from wafers with lifetime > 1 ms. Topsil’s new PV-FZ product meets these specifications.

One key aspect to high-efficiency processing is maintaining high lifetime throughout cell processing. Good analytical tools are required to diagnose problems and control the cell process. Figure 6 is an example lifetime map of a wafer that has been degraded during processing:

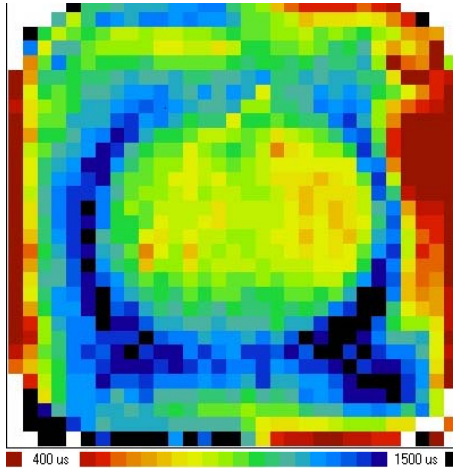


Figure 6: Lifetime map of a wafer degraded during cell processing.
(Semilab Wt-85 lifetime mapping tool)

The thickness of a rear-contact solar cell affects its efficiency in a number of ways. Decreasing the thickness increases the collection efficiency of minority carriers because, on average, the carriers have a shorter distance to travel before being collected at the rear $p-n$ junction. Reducing cell thickness also decreases the dark recombination current because there is less bulk for recombination to occur and reduces the influence of edge recombination [8]. Similar effects occurring in front contact cells have been sometime used to predict large increases in cell efficiency as cell thickness is reduced.

Decreasing cell thickness, however, also decreases the number of electron–hole pairs generated by illumination because there is less silicon to absorb photons. Improving light trapping can help mitigate this effect, but practically we have found that the increased collection efficiencies described above are approximately offset by the decreased generation. Figure 7 shows how cell efficiency depends on wafer thickness for SunPower low-cost, rear-contact cell design. The line shows the results of ATLAS 2D simulation and the symbols show the median experimentally measured values. Both the simulation and the expeirment indicate that the efficiency plateaus over the range 160–280 μm .

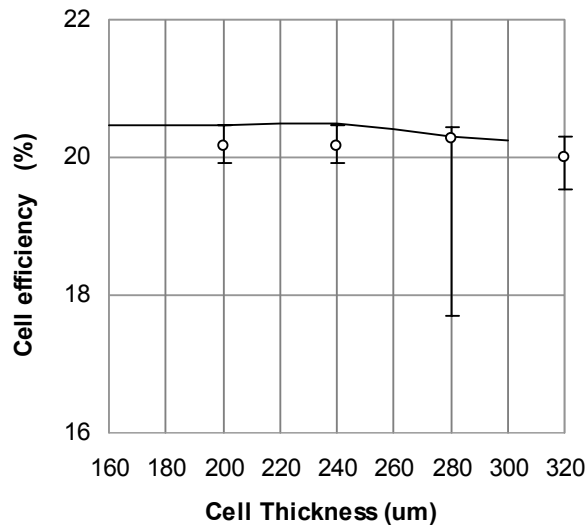


Figure 7: Cell efficiency vs thickness for a low-cost, rear-contact solar cell. The line shows the 2D simulation and the symbols show the median efficiency of experimental cells with thickness: 200 μm , 240 μm , 280 μm , and 320 μm .

Recently, SunPower has fabricated rear-contact solar cells from entirely low-cost processing (no photo-lithography). This cell was fabricated in SunPower's new Austin, TX pilot line and was fabricated by production operators. Reported below are test results as measured by the National Renewable Energy Laboratory (NREL).

Area (cm²)	Silicon	Voc (mV)	Jsc (mA/cm²)	FF	Eff (%)
148.6	PV-FZ	676	39.0	0.800	21.1

Table I: Output parameters of low-cost rear-contact solar cells at 100 mW/cm², AM1.5g 25 °C.

CONCLUSIONS

Silicon solar cell efficiency improvements can result in big savings in solar module and system costs. The practical efficiency limit for silicon and the strategies for implementing efficiency enhancing process improvements were described. Effectively minimizing carrier recombination mechanisms requires implementing several high-efficiency process features simultaneously. High efficiency back-contact solar cells have all of these features and are relatively simple to fabricate. Low-cost, large solar cells are being fabricated in a production setting and conversion efficiencies have reached 21.1%.

REFERENCES

- [1] J. Bernreuter, "High, higher, the highest", *PHOTON International*, May, 2003.
- [2] J. Zhao, A. Wang, and M.A. Green., "24.5% Efficiency Silicon PERT Cells on MCZ Substrates and 24.7% Efficiency PERL Cells on FZ Substrates", *Progress in Photovoltaics*, 7, p471, 1999
- [3] C.Z. Zhou, P.J. Verlinden, R.A. Crane, R.M. Swanson, "21.9% Efficient Silicon Bifacial Solar Cells," Proceedings of the 26th IEEE Photovoltaic Specialists Conference, Anaheim, September 29 - October 3, 1997, pp. 287-290
- [4] M. Tanaka, S. Okamoto, S. Tsuge, and S. Kiyama, "Development of HIT Solar Cells with more than 21% Conversion Efficiency and Commercialization of Highest Performance HIT Modules," *Proc. WCPEC-3, Osaka Japan, May 11-18, 2003, to be published*.
- [5] P.J. Verlinden et al., "7000 high efficiency cells for a dream", *Progress in Photovoltaics*, 2, p. 143, 1994.
- [6] J. Vedde, L. Jensen, and T. Claussen, "Float-Zone Silicon for High Volume Production of Solar Cells," *Proc. WCPEC-3, Osaka Japan, May 11-18, 2003, to be published*.
- [7] K.R. McIntosh, M.J. Cudzinovic. D.D. Smith, W.P. Mulligan, and R.M. Swanson, "The Choice of Silicon Wafer for the Production of Low-Cost Rear Contact Solar Cells," *Proc. WCPEC-3, Osaka Japan, May 11-18, 2003, to be published*.
- [8] R.A. Sinton *et al.*, *Proc. 13th EC PVSEC*, p. 1586, 1995.

Current Trends in Si Solar Cell Manufacturing

Steve Shea, BP Solar

Manuscript not available at the time of printing.

Laser-Fired Contacts

R. Preu, E. Schneiderlöchner, A. Grohe, M. Hofmann, D. Kray, S. Glunz, G. Willeke

Fraunhofer Institut für Solare Energiesysteme, Heidenhofstr. 2, D-79110 Freiburg

Phone: +49-761-4588-5260, Fax: +49-761-4588-9250, E-mail: Ralf.Preu@ise.fhg.de

1 DIELECTRICALLY PASSIVATED SOLAR CELLS

In the 1980s the deposition of passivating dielectric coatings on weakly doped silicon surfaces has been implemented in high-efficiency solar cell technology. Further progress has been made by the introduction of highly doped regions below the contacts, enabling low contact resistance and further reduction of the average surface recombination velocity of contacted surfaces. Both proposed routes to high efficiency, the point contact solar cell by Swanson [1] as well as the passivated emitter and rear locally diffused cell by Green and co-workers rely on this approach [2]. Up to now these two solar cell designs have proven to be the most powerful designs to reach high efficiencies on crystalline silicon solar cells [3,4].

The use of dielectrically passivated rear surfaces is encouraged by the trend to higher efficiencies and thinner wafers in order to reduce the price per power unit. Nevertheless, the realization of this approach in industrial production has progressed slowly. BP's laser grooved buried contact cell had been the only commercial solar cell produced in large quantity [5], making use of the high carrier collection properties of a selective emitter and a dielectrically passivated front surface. Just recently Sun Power announced the fabrication of large area rear contact solar cells on a pilot line scale in Texas. These cells are processed on thin float zone silicon wafers and yield efficiencies of more than 20% [6].

The laser-fired contact process (LFC) scheme was proposed three years ago as a simple route to an industrial feasible passivated solar cell rear [7,8]. This paper reviews the current status of the progress in understanding and processing LFC.

2 BASIC PRINCIPLE OF THE LASER FIRED CONTACT APPROACH

The LFC process mainly comprises four individual steps (Fig. 1): (i) the preconditioning of the surface in order to prepare it for (ii) the subsequent deposition of a dielectric and (iii) an aluminum layer and finally (iv) the local alloying of the point contact using a focussed laser pulse, which potentially can form a local back surface field (BSF). LFC significantly reduces the number and costs of process steps when compared to the photo-lithographic processing of solar cells [9].

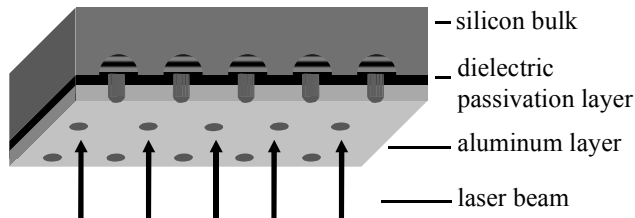


Fig. 1: Scheme for a LFC rear.

3 STRUCTURAL PROPERTIES OF LASER FIRED CONTACTS

3.1 Laser-ionised secondary neutral mass spectroscopy

Laser-ionised secondary neutral mass spectroscopy (L-SNMS) has been performed in order to investigate on the depth profile of the atomic compositions within a LFC [10]. The visual characterization of a LFC typically yields two distinct regions: an inner circle with a rough surface and a surrounding circle with a rather smooth surface (compare area 2 and 1 in Fig. 2a respectively). Profiles for the detection rate of aluminum and silicon of these two areas have been taken and are shown in Fig. 2b. Obviously for the inner circle aluminum is found in much deeper regions as well as more silicon closer to the surface when compared to the outer circle. From these results it can be concluded that an alloy is formed at least in the inner circle of the LFC.

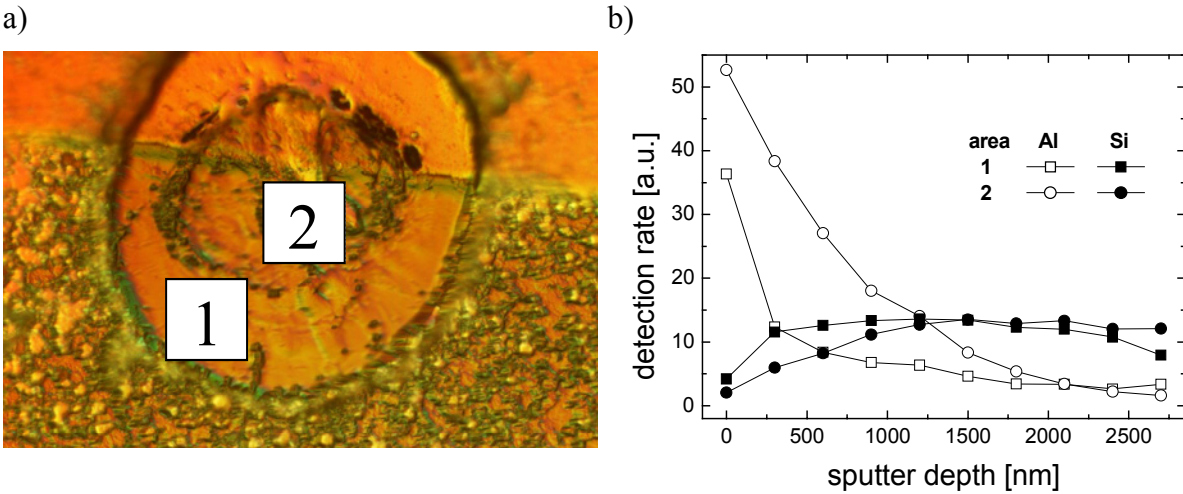


Fig. 2: L-SNMS characterization of a LFC. a) LFC Image taken by light-optical microscope. In the lower part the sputter crater from the L-SNMS can be seen. b) Detection rates in arbitrary units of Al_2 and Si_2 of two areas in the LFC contact.

3.2 Electron beam induced current measurements

Electron beam induced current (EBIC) measurements have been used to characterize LFC on n-type wafers [11]. Fig. 3 shows EBIC and SEM images of a LFC. In the superposition of the two pictures it becomes obvious, that a high current is detected beneath the contact, clearly implying that a junction is formed. The border is not defined sharply since the diffusion length of the electron created carriers is non-zero. The geometry of the crater and the alloyed regions depend on the laser parameters chosen. It can be seen that the area showing a junction-like behavior is limited to a certain range around the center of the LFC. This range coincides with the range of high aluminium detection using the L-SNMS characterization. The spatial laser power density profile in the used ground mode corresponds to a Gaussian distribution. Obviously the pulse energy is sufficient for the formation of a p^+ -zone only in the center of the LFC.

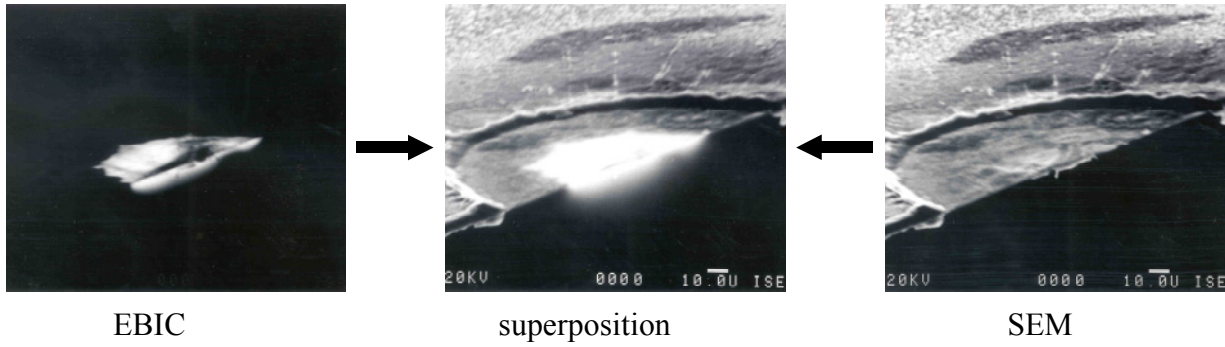


Fig. 3: Superposition of an EBIC and a SEM image for an oblique view on a cleaved wafer with the cleaving edge running through the middle of a LFC point on n-type silicon.

4 ELECTRICAL PROPERTIES

A simple test structure process sequence has been developed for the optimization and characterization of the electrical properties of the contact and the surface passivation. The test structure features three different devices. The starting material is a high lifetime float-zone (FZ) monocrystalline silicon wafer. The wafer surface is chemically cleaned and dielectrically passivated using the designated material layer on both sides (device 1). Then 2 μm aluminum is deposited by means of physical vapor deposition on one side and subsequently locally laser-fired (device 2, see Fig. 4). This structure can be characterized by minority carrier lifetime measurements in order to find the average surface recombination velocity of the contacted surface. After these measurements a further aluminum layer is deposited on the non-aluminum side and subsequently laser-fired (device 3, see Fig. 4). Finally by contacting both sides of the device a dark IV-curve is taken in order to determine the resistance, which leads to an upper limit of the average contact resistance.

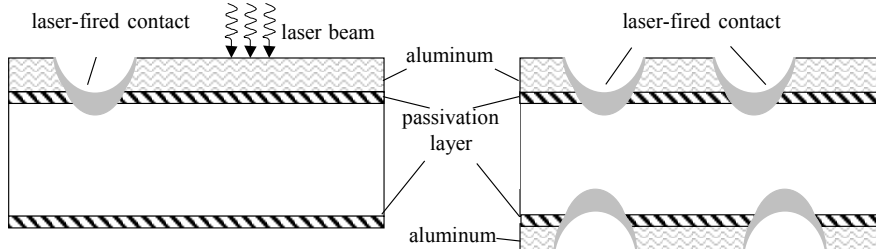


Fig. 4: Cross view sketch of the LFC test structure (left: determination of the mean surface recombination velocity, device 2; right: determination of the contact resistance, device 3).

The test structure is used to optimize the parameters of the passivating layers as well as the parameters of the laser process. Highly passivating layers are generally sensitive to thermal post-deposition treatments. Fig. 5a shows lifetime measurements of four silicon nitrides being deposited on 1 Ωcm FZ-silicon using the process sequence described above. The high initial lifetimes of four silicon nitride layers (#7,8,11 and 12) are in the range of 600 cm/s to 1800 cm/s and show that they could be attractive candidates for a passivated rear cell. After the aluminum deposition all lifetimes are reduced, but most pronounced for nitride #7. The measured lifetimes are further decreased after the LFC process as can be expected due to the increased recombination below the contacts, but the

effect is very pronounced for #7 and #12. The silicon nitrides #8 and #11 yield a lifetime of approximately 200 μ s, sufficient for a highly efficient rear passivated solar cell. Considering only these results, it is not clear whether the lower reduction is due to a higher stability against the impact of the thermal laser treatment or if the different behavior of the silicon nitrides for the LFC process could be attributed to a non-sufficient firing through which would result in an inferior contact behavior. Therefore, the IV-curve measurements for the respective devices 3 are performed. The IV-curve measurements show an ohmic behavior in the range from -0.7 to +0.7 V and, as can be taken from Tab. 1, the normalized resistance derived lies in a range around 1 $\Omega \text{ cm}^2$ clearly showing that a good contact is formed.

Using a PECVD-silicon oxide layer on top of the silicon nitride does reduce the degradation of the surface passivation quality due to the aluminum deposition and the LFC process and furthermore increases the internal reflectance of the rear structure as will be published elsewhere.

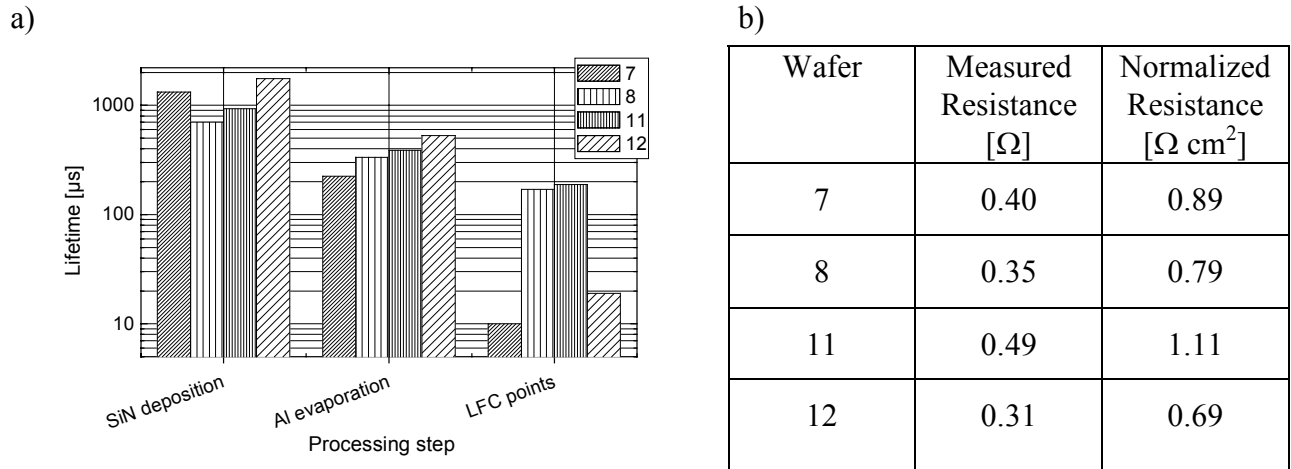


Fig. 4 and Tab. 1: Determination of the electrical properties of LFC test devices using four different PECVD-silicon nitride layers. a) development of the carrier lifetime at different stages of device processing. b) resistances for device 3, yielding upper limits of the contact resistance.

5 SOLAR CELLS

5.1 Processing of solar cells

For cell preparation we used our random or inverted pyramid passivated emitter and rear (PERC) solar cell process on high lifetime mono-crystalline silicon wafers (Fig. 5) [12]. On the front side the structure comprises a homogeneous emitter diffusion ($\rho_{\text{sheet}} = 120 \Omega/\text{sq.}$), a 105 nm thick thermal oxide and photolithographically defined evaporated contacts. The low saturation current and the low series resistance are beneficial in order to determine exactly the electrical properties of the rear side of a solar cell. The local rear point contact formation was performed either by laser-firing or by the standard photolithographic masking and subsequent etching of the dielectric layer. In both case 2 μ m of aluminum have been deposited on the rear, either after or before the local treatment. In general the distance between contact points is 1 mm. Thermally processed silicon oxide as well as PECVD silicon nitride are used as the dielectric passivation layers on the rear side.

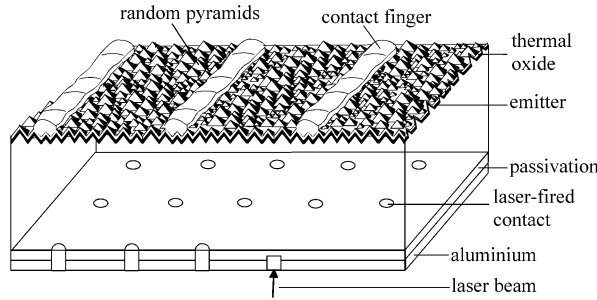


Fig. 5: Scheme for a high-efficiency cell with laser-fired contacts.

5.2 Results on p-type silicon with varying resistivity

The high performance of the classical PERC-rear contact is limited to a base resistivity of approximately $1 \Omega \text{ cm}$ or less, due to the increasing contact resistance as well as the increased influence of the high surface recombination velocity for the local metal-semiconductor contact. If the LFC process forms a local back surface field the performance for lowly doped material should be much better. Thus, the different cell processes have been applied to wafers in a range from 0.5 to $10 \Omega \text{ cm}$. Plotting the open circuit voltage of the cells versus the doping concentration on a logarithmic scale yields a linear behavior for both rear contact processes. The decrease of V_{oc} for small doping concentrations is much more pronounced for the PERC than for the LFC process. This is an indication for a lower surface recombination velocity in the case of LFC. The same trend of higher performance is obtained for the fill factor of the cells yielding a pronounced efficiency advantage of 19.8% compared to 15.3% on $10 \Omega \text{ cm}$ material for the LFC and the reference cells, respectively. A maximum efficiency of 21.4% has been achieved for a LFC cell on $1 \Omega \text{ cm}$ FZ silicon. Thorough investigations for cells on p-type silicon wafers with varying resistivity show, that LFC can be well described by a p^+ -zone surrounded by a shallow zone of low lifetime [10,11]. The performed calculations result in an effective rear surface recombination velocity of just around 35 cm/s on $10 \Omega \text{ cm}$ and just around 100 cm/s on $1 \Omega \text{ cm}$.

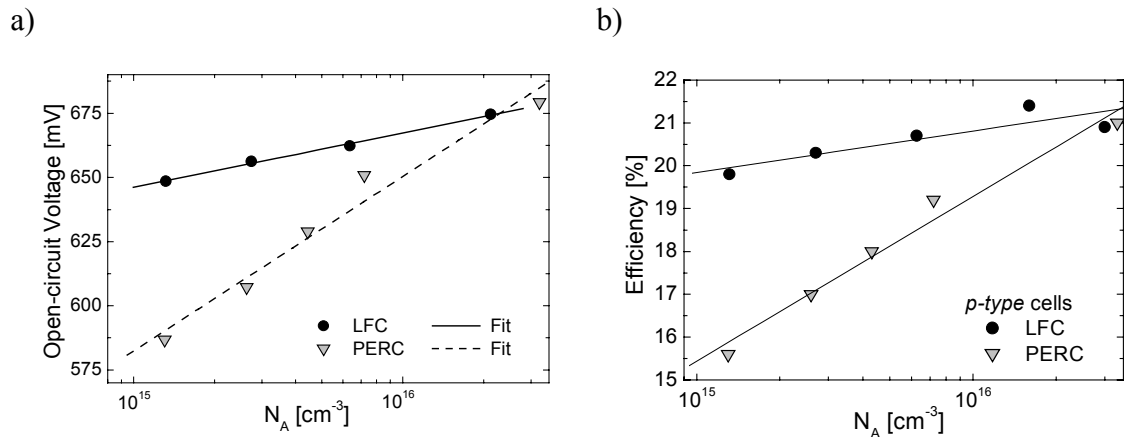


Fig. 6: Solar cell results on $0.5 \Omega \text{ cm}$ to $10 \Omega \text{ cm}$ FZ silicon wafers. a) V_{oc} versus N_A linearly fitted with the dark saturation current J_0 times a constant. b) Measured efficiencies for LFC and PERC cells on p-type silicon. The lines are guides-to-the-eye.

5.3 Results on n-type solar cells

Usually the above cell process is used for p-type silicon only. Nevertheless LFC on n-type wafers should form a junction [11]. In Fig. 7 two different structures (n^+np^+ and the usual n^+pp^+) are shown. Obviously the structure of the n^+np^+ is not well suited in order to reach high current efficiencies, since the majority of minority carriers have to travel a long way to the junction on the rear, while at the same time the design of the front side is not adequate for a rear contact cell. Thus the distance of the contact points have to be reduced in order to match the limited diffusion length of the material.

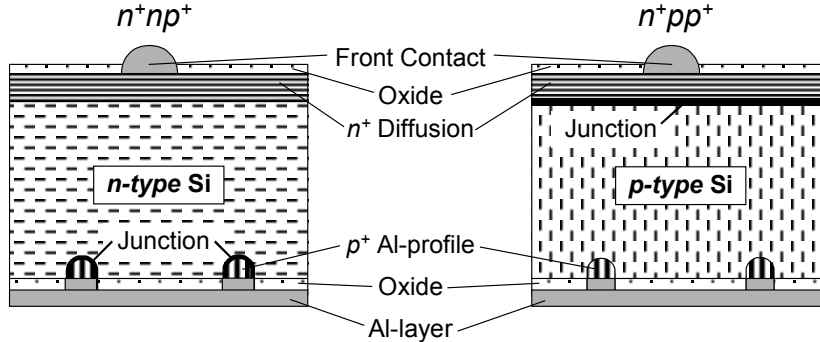


Fig. 7: LFC cell with n^+np^+ structure (left) and n^+pp^+ structure (right). The front texturization is not shown.

LFC solar cells have been fabricated on monocrystalline n-type silicon with a resistivity of $1 \Omega \text{ cm}$. The results of efficiencies of up to 13.5% and V_{oc} s of up to 634 mV are clearly showing that the LFC process creates a working junction beneath the contacts (Tab. 2) by means of aluminum diffusion and/or alloying. The open-circuit voltage of the junction-like LFC is much more sensitive to the laser processing compared to the BSF-like LFC on p-type silicon as can be seen from the open circuit voltage measured on n^+pp and n^+np solar cells using different laser parameters (Tab. 3). The n^+np cell structure proves to be a very sensitive tool for laser parameter optimization.

Table 2: Solar cell results for the n^+np^+ structure using a LFC aluminum junction.

Cell	Pitch [μm]	V_{oc} [mV]	J_{sc} [mA/cm^2]	FF	η [%]
NRP4_25.3	500	634.4	28.16	0.703	12.6
NRP4_23.5	100	616.7	30.16	0.729	13.5

Table 3: Open circuit voltage for LFC cells on n- and p- type using two different laser processes.

Laser parameters	$0.5 \Omega \text{ cm } n^+pp^+ \text{ cell}$	$1 \Omega \text{ cm } n^+np^+ \text{ cell}$
A	677 mV	592 mV
B	664 mV	252 mV

5.4 Thin solar cells on medium quality material

The passivated rear approach with local contacts is especially beneficial for the processing of thin solar cells, since the bowing implied by the alloying of a homogeneous aluminum BSF is omitted and the surface recombination properties of the rear surface become more important. Line shaped LFC have been used to contact the rear side of very thin high-efficiency solar cells on $0.8 \Omega \text{ cm}$ boron doped Cz-silicon down to a thickness of $63 \mu\text{m}$ [13]. There is a significant gain in J_{sc} and V_{oc} when moving from $243 \mu\text{m}$ thick to the thin wafers which can be clearly attributed to the low carrier lifetime of boron doped silicon. An efficiency of 18.7 % has been reached on a $63 \mu\text{m}$ wafer, to our knowledge the highest efficiency on a Cz-silicon solar cell of this thickness.

Tab. 4: IP-PERC on annealed $0.8 \Omega \text{ cm}$ with line shaped LFC rear side ($2 \mu\text{m}$ Al).

W [μm]	Mat.	V_{oc} [mV]	J_{sc} [mA/cm 2]	FF [%]	η [%]	Pitch [μm]
63		645	37.3	77.8	18.7	2000
133	Cz (B)	626	36.7	79.0	18.1	1000
243		603	34.0	79.2	16.2	1500

6 TRANSFER TO INDUSTRIAL PRODUCTION

The transfer of LFC to industrial solar cell production depends mainly on two achievements: the development of suitable cost-efficient equipment and the implementation into an economical cell process, while keeping the high efficiency potential, have to be demonstrated. The upcoming transfer steps and the performance of LFC in comparison to the standard screen-printed Al-BSF have been thoroughly discussed in [14] and [15]. A break through with respect to the throughput of the laser process has been achieved with the transfer of the LFC process from a system with fixed laser beam to a new automated system with a scanning head (Fig. 8). Using this system the process time to process an area of 100 cm^2 was reduced from several minutes to just one second [16]. All results presented in this paper have already been obtained with this system.

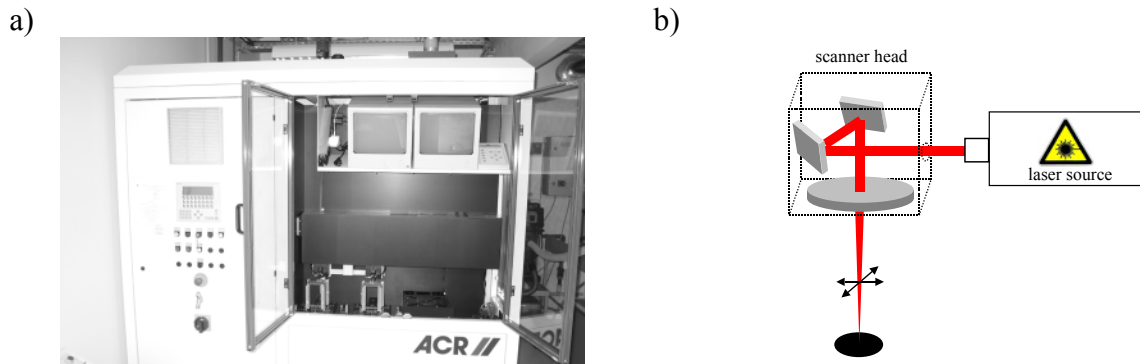


Fig. 8 Automated Nd:YAG laser system. a) front view with automated handling. b) scanning head set-up. The laser beam is moved using two rotating mirrors.

7 CONCLUSIONS

After the first three years of development we have found that the LFC process can

- form a p⁺-region beneath a significant part of the contact area,
- be optimized for given boundary conditions using a simple test devices,
- be used for highly efficient solar cells (max. efficiency 21.4 % on a 250 µm, 1 Ω cm FZ silicon wafer) on a wide range of wafer resistivity (0.5-10 Ω cm) and thickness (63 µm).
- be processed in just one second on 100 cm² cell area with a single scanning laser system.

As a consequence the industrial transfer of the LFC approach is currently under way.

ACKNOWLEDGEMENT

The authors gratefully acknowledge the assistance of T. Leimenstoll, E. Schäffer, D. Osswald, R. Wassie, H. Lautenschlager and G. Emanuel. Parts of this work were supported by the DAAD under contract number D0205411. Special thank is dedicated to A. Cuevas from the Australian National University for initiating the LFC work on n-type silicon wafers.

REFERENCES

- [1] R. M. Swanson, Sol. Cells **17** (1986) 85-118.
- [2] M. A. Green, A. W. Blakers, J. Zhao, A. M. Milne, A. Wang, and X. Dai, IEEE Trans. Electron Devices **37** (1990) 331-336.
- [3] P. J. Verlinden, R. A. Sinton, K. Wickham, R. A. Crane, and R. M. Swanson, Proc. 14th EU-PVSEC, Barcelona, Spain (1996) 96-99.
- [4] M. A. Green, J. Zhao, and A. Wang, Proc. 2nd WCPEC, Vienna, Austria (1998) 1187-1192.
- [5] T. M. Bruton, K. C. Heasman, J. P. Nagle, D. W. Cunningham, N. B. Mason, R. Russel, and M. A. Balbuena, Proc. 12th EU-PVSEC, Amsterdam, The Netherlands (1994) 761-762.
- [6] K. R. McIntosh, M. J. Cudzinovic, D. D. Smith, W. P. Mulligan, and R. M. Swanson, Proc. 3rd WCPEC, Osaka, Japan (2003) in print.
- [7] R. Preu, E. Schneiderlöchner, R. Lüdemann, and S. W. Glunz, Patent WO 02/25742, DE 100 46 170 (2000).
- [8] R. Preu, PhD Thesis Thesis, Fernuniversität - Gesamthochschule Hagen, 2000.
- [9] E. Schneiderlöchner, R. Preu, R. Lüdemann, S. W. Glunz, and G. Willeke, Proc. 17th EU-PVSEC, Munich, Germany (2001) 1303-1306.
- [10] A. Grohe, E. Schneiderlöchner, M. Hermle, R. Preu, S. W. Glunz, G. Willeke, and S. Walz, Proc. 3rd WCPEC, Osaka, Japan (2003) in print.
- [11] S. W. Glunz, A. Grohe, M. Hermle, E. Schneiderlöchner, J. Dicker, R. Preu, H. Mäckel, D. Macdonald, and A. Cuevas, Proc. 3rd WCPEC, Osaka, Japan (2003) in print.
- [12] S. W. Glunz, J. Knobloch, C. Hebling, and W. Wetting, Conference Record 26th IEEE PVSC, Anaheim (1997) 231-234.
- [13] D. Kray, H. Kampwerth, A. Leimenstoll, S. W. Glunz, and G. P. Willeke, Proc. 3rd WCPEC, Osaka, Japan (2003) in print.
- [14] R. Preu, E. Schneiderlöchner, A. Grohe, S. W. Glunz, and G. Willeke, Proc. 29th IEEE PVSC, New Orleans, Louisiana, USA (2002) 130-133.
- [15] R. Preu, D. Biro, G. Emanuel, A. Grohe, M. Hofmann, D. M. Huljic, I. E. Reis, J. Rentsch, E. Schneiderlöchner, W. Sparber, W. Wolke, and G. Willeke, Proc. 3rd WCPEC, Osaka, Japan (2003) in print.
- [16] E. Schneiderlöchner, A. Grohe, S. W. Glunz, R. Preu, and G. Willeke, Proc. 3rd WCPEC, Osaka, Japan (2003) in print.

Dry Processing for Crystalline Silicon Solar Cells

G. Agostinelli¹, S. De Wolf¹, H.F.W. Dekkers¹, G. Beaucarne¹, Q.N. Le², H.D. Goldbach³, R.E.I. Schropp³, I. Pinter⁴, G. Walther⁵, K. Schade⁶, P. Vitanov⁷, M. Vukadinovic⁸ and M. Topic⁸

¹IMEC vzw, Kapeldreef 75, B-3001 Leuven (Belgium) - ²Photowatt International (France) - ³Debye Institute, Utrecht University (The Nederlands) - ⁴MFA Research Institute for Technical Physics and Material Sciences (Hungary) - ⁵Secon Semiconductor Equipment Gesellschaft GmbH (Austria) - ⁶FAP Forschung und Applikationslabor Plasmatechnik GmbH (Germany) - ⁷Central Laboratory of Solar Energy and Renewable Energy Sources (Bulgaria) - ⁸Faculty of Electrical Engineering, University of Ljubljana (Slovenia)

In the period 1998-2002 the average yearly growth rate of Photovoltaics has been close to 35%. Such an aggressive trend is typical for renewable energy sources (the most impressive example being Wind Energy), but may not sound impressive enough as long as the worldwide production capacity of PV industry is close to ‘only’ 500 MWp/year, as today. If a growth rate above 25% were to be sustained, however, PV market would reach a size above 100 GWp/year between 2020 and 2030. If one tried to turn these digits into an equivalent number of solar cells, and then considered the material, water, chemicals, waste that need to be consumed, treated or produced with current solar cell process, then he or she would become immediately conscious of how the issue of sustainability of Photovoltaics can no longer be put off. By sustainability we mean both *industrial* and *environmental* sustainability, which unfortunately are two issues that can easily conflict with each other.

In this paper, we intend to discuss how and if dry processing of conventional Silicon Solar Cells can provide the synergy to meet the PV market growth challenge with a low environmental impact. Present day technology involves many high temperature processing steps, excessive use of wet chemical cleaning and water rinsing steps (more than 10 million liters of water per 1MWp cell production). Some of these steps produce undesirable effects, too. To name one example, acidic texturisation: it is a very aggressive treatment, which brings about nasty waste products and decreases the yield on very thin mc-Si wafers because etch pits weaken their mechanical properties. Substitution of the wet processing steps with a generic dry process, based on plasma, would present remarkable advantages. The environmental benefits of dry processing are rather evident; it would virtually get rid of the water and it would significantly reduce the chemical waste treatment. From an industrial point of view, it presents a strong potential for process cost reduction, is suitable for large area, high throughput manufacturing. Due to its novelty it presents some challenges, but at the same time it has several technological advantages, e.g. stress-free and low temperature processing. As technology is not yet mature, it can be foreseen that in the next 2-3 years there will be a transition to a hybrid process (wet/dry) and only later manufacturers will get the motivation and drive for developing a fully dry, in line process. A generic dry process would ideally remove all wet chemical and water rinsing processing steps, reduce the health risk in the production, and lead to higher cell efficiencies. For the front end, possible process innovation include:

- dry plasma etching process for saw damage removal, phosphorous silicate or emitter etch
- isotropic dry plasma texturing process applicable to all type of silicon substrates
- plasma immersion diffusion suitable for solar cell emitter formation
- application of amorphous-Si /crystalline-Si heterostructures for emitter formation
- PECVD silicon nitride deposition process with a high deposition rate

For the rear surface, given the drive towards thin, large area crystalline silicon substrates, it will be necessary to progressively abandon the Al-alloy BSF. ‘New generation’ screen printing pastes with low-bowing and improved BSF will make it for the short term, but in order to achieve the necessary low surface recombination velocities and light trapping schemes required for ultrathin (100-150µm) wafers, a leap to Local BSF structures with integrated cell or module backside reflector will be needed. Such structures could be based on different concepts, e.g.:

- Local Al-BSF contacts with PECVD silicon nitride or other dielectrics as a passivation layer
- application of amorphous-Si/crystalline-Si and/or µcrystalline-Si/crystalline-Si heterostructures

Current research activities of our consortium aim at developing and implementing an integrated cell process based on this vision. Proof of concepts for these processing steps have already been demonstrated and currently industrial type ‘dry’ cells on mc-Si substrates with efficiencies ranging from 14.5 to 16% can be manufactured on large (4 to 5”) multicrystalline silicon wafers of less than 200 μ m thickness. In the remainder of the paper we will discuss in detail each of these dry plasma processing steps.

Dry Etching/Texturing

Although plasma etching is a well established, commercial technology in microelectronics, it is not widely used in solar cell production, with the exception of junction edge isolation in barrel type reactors. Various plasma etching systems are available on the market, but their application to solar cells surface processing is faced with stringent requirements in terms of throughput, surface preparation and plasma-induced damage. What makes plasma etching so appealing is the prospect of avoiding wet chemical disposal and large use of water. However, to date, the only fully dry etching process that made its case up to solar cell level is the Cl-based Reactive Ion Etching (RIE) process of Kyocera [1].

Dry etching can serve -at least in theory- for multiple purposes in solar cell processing: saw damage removal, texturisation, phosphorous glass removal, edge or planar junction removal. Recent progresses in the field lead to think that some of these applications will soon make their way to pilot lines. Saw damage can be effectively removed, with very high etching rates (up to 20 μ m/minute) and low surface damage, by means of combined RIE/Chemical Downstream Etching (CDE); the same technique is suitable for one-sided emitter etch, hence backside processing and surface preparation. Surface texturing can also be achieved, but the mainstream approach of RIE based on SF₆ or SF₆/O₂ presents considerable technological issues, the main of which being ion damage, and so far has always led to poor results at cell level unless the surface be treated with wet chemical Damage Removal Etching (DRE) or even Forming Gas Anneal (FGA). Reconsidering this approach may turn into a winning choice. IMEC, too, has been following in the past a line of investigation on SF₆/O₂ RIE, but has recently opted for a dry texturing process based on chlorine chemistry. The use of Cl₂ leads to a better, crystallographic dependent etching (figure 1), that results in a pyramid-like structure. Reflectivity and emitter saturation currents in the same order of those obtained with wet isotexturing can be achieved. No DRE is needed. The etching rate is very high, uniform, and the process can be applied to as-cut wafers. Safety and environmental concerns play at a first sight against this choice, but a reasoned assessment, as we will point out later, reveals that with present technology its impact can be significantly smaller than that of fluorine chemistry, at a lower cost.

Phosphorous Silicate Glass (PSG) removal by plasma etching can be carried out with commercial systems, but it needs to be virtually damage-free, residual-free and furthermore requires a high selectivity between PSG and Silicon in order to avoid etching of the emitter. Rentsch et al [2] have shown that with perfluoro-compounds it is possible to achieve a selectivity PSG/Si above 10, with a rate of about 80nm/min but the process still leads to slightly lower cells’ efficiency in comparison to HF glass removal.

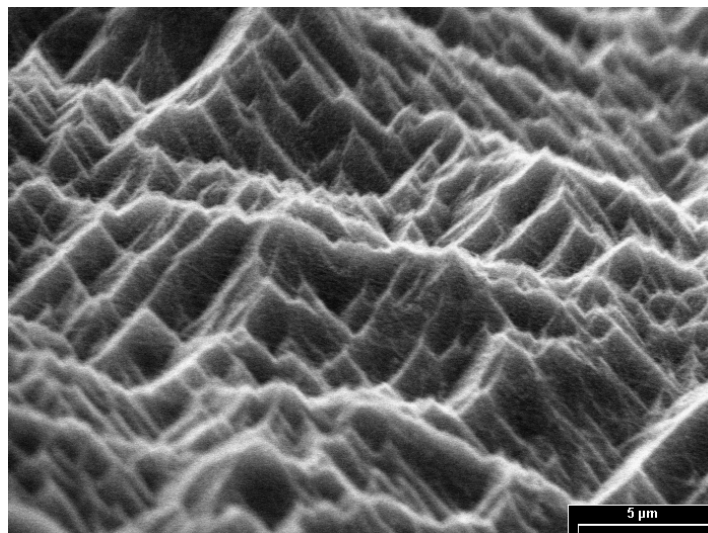


Figure 1. Chlorine based Plasma etching. Cl₂ leads to crystallographic dependent etching that results in a pyramid like structure.

Let us now come to the issue of the environmental impact of plasma etching. We do not have data on the solar cell industry, but we can at least look at the experience of semiconductor industry for an educated guess. In semiconductor industry, perfluoro-compounds (PFCs), hydro-fluoro-compounds (HFCs) and sulphur-hexafluoride (SF_6) are the used classes of materials in plasma technology as a source of fluorine for etching Si, SiO_2 and $SiNx$. Their use is considered to be very convenient in the PV community, in that most of these gases present no health hazard. The process residuals though are substances as SiF_4 , HF, SOF_2 , SO, CO and SOF, which are toxic and/or polluting agents. Therefore waste treatment of gas residues is needed and can be realized by dissolving the residue products in water. This makes the water acidic and requires subsequent neutralisation. The amount of waste disposal, anyway, is significantly lower than that of wet processing. The issue with PFCs, HFCs and SF_6 is their enormous Global Warming Potential (GWP). For example, the strong infrared absorption of SF_6 and its long lifetime in the environment makes its GWP to be 24000 times greater (per unit mass) than that of CO_2 , the predominant contributor to the greenhouse effect [3].

Compound	Compound	Atmospheric lifetime [years]	GWP
Carbon dioxide	CO_2	200	1
Methane	CH_4	12	21
Nitrous oxide	N_2O	120	310
HFC-23	CHF_3	264	11700
HFC-32	CH_2F_2	5.6	650
HFC-41	CH_3F	3.7	150
HFC-134	$C_2H_2F_4$	10.6	1000
HFC-134a	CH_2FCF_3	14.6	1300
Perfluoromethane	CF_4	50000	6500
Perfluoroethane	C_2F_6	10000	9200
Perfluorobutane	C_4F_8	3200	8700
Perfluoropropane	C_3F_8	2600	7000
Nitrogen triflouride	NF_3	180	9720
Sulphur hexaflouride	SF_6	3200	23900

Table 1 Global Warming Potential of various plasma etching gases compared with the major greenhouse gases

The cumulative effect of GHGs emission from semiconductor industry is smaller than that of other pollutants (CO_2 , CH_4 , NO_x), yet on a projected scale a business as usual scenario would lead to an emission level of high GWP gases in 2010 that is more than 3 times the 1990 levels. Programs for abatements in the semiconductor industry exist though they are voluntary (e.g. the US EPA PFC Emission Reduction Partnership, launched in 1996) and it will be so until the Kyoto Protocol will not enter in force and there will be no binding sanctions for violators.

For the PV industry, in the prospect of a large scale production, high GWP gases emissions are obviously no option, and further post process treatment is required. Etching emission reduction technologies are available and are based on point-of-use plasma abatement, thermal destruction, catalytic decomposition, capture/recovery and substitution, with abatement efficiencies between 90% and 97%. Currently their costs reduce the economical advantage of dry processing. The industrial implementation of a process based on Fluorine plasma chemistry, therefore, may turn out to be more problematic than it looks. Chlorine is an environmental *no-no* in as much as the same way as F-containing gases, although for different reasons. Cl_2 has no high GWP per se but it is toxic, its handling requires proper safeguards and it has a very high Ozone Depletion Potential (ODP). But Cl is relatively easy and cheap to process and neutralise. When analysing the full cycle (direct/indirect processing + waste treatment), Chlorine has a lower environmental impact with a lower cost. Environmental issues of plasma etching for application in PV industry need to be carefully assessed. The presence of gases with a very high GWP in the process may turn into a boomerang if this issue is not handled in time, hence the need for alternative routes to high GWP gases or a viable route for their abatement/recycling.

Fast deposition SiNx:H

Hydrogenated Silicon Nitride films deposited by low temperature Plasma-Enhanced Chemical Vapor Deposition (PECVD) have found a very wide application in solar cell processing as antireflection coating (ARC) or passivation layer. In multicrystalline Silicon Solar Cells, the unique possibility of making use of PECVD SiNx:H for simultaneous ARC, bulk and surface passivation, combined with low temperature of deposition and adjustable refractive index makes it a pivotal technology for conventional solar cell processing. Despite the absence of surface damage and the resulting excellent surface passivation properties of Remote PECVD SiNx, Low Frequency (LF, 10-500 KHz) Direct PECVD proved to be a valid alternative for manufacturing due to its better bulk passivation properties and the less stringent requirements for industrial solar cells' emitter surface passivation. Recently, it has been shown that opportune deposition parameters adjustment can lead to surface recombination velocities below 100 cm/s on p-type mc-Si material, making D-PECVD suitable for rear side passivation, too [4]. Direct PECVD has initially been developed because it can guarantee a higher throughput/system cost ratio. Still, the deposition rates of LF D-PECVD systems are in the order of a few angstroms per second, making it the process bottleneck in a high throughput environment. Industrially sustainable high production capacity passes necessarily through the development of a 'fast' PECVD SiNx system with deposition rates >1nm/s which *at the same time* preserves the optical, surface and bulk passivation qualities of 'slow' deposition PECVD SiNx. Increasing the Plasma frequency increases the deposition rate, but generally at the expenses of bulk passivation properties. Reasonable surface passivation and refractive index around 2.00 can be easily attained with deposition rates up to 2.9 nm/s in the VHF regime (40.68 and 81.36 MHz). Yet after thermal treatment processed solar cells do not show the same bulk improvement with HF SiNx passivation as they do with LF SiNx (figure 2).

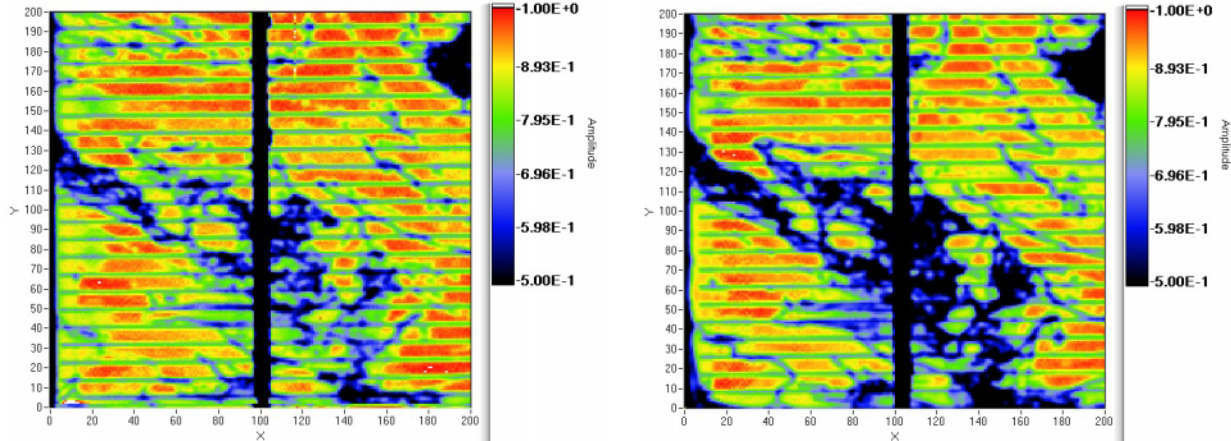


Figure 2. LBIC current maps (detail, signal in a.u.) indicating the Low Frequency (left) and High Frequency (right) Direct PECVD SiNx bulk passivation properties on two cells processed on neighboring mc-Si wafers. Despite the same optical characteristics (identical refraction index) the recombination activity of defects is sensibly higher when High Frequency SiNx is deposited over the surface.

In order to solve these issues a deeper understanding of the passivation mechanisms of Hydrogenated Silicon Nitride is necessary. In this process of investigation diverse experiments have brought about facts, which evidence the need revise or extend the models that have been proposed so far [5,6,7]. One current view is that bulk hydrogenation is strongly enhanced by Al-induced vacancies created during the co-firing step, and that this Al-SiNx synergy is the reason for significant improvement of the cell performance. It is very difficult however to come to a conclusive proof of this synergy, in that each step (thermal treatment of SiNx:H and Al-alloyed BSF formation) separately brings about an improvement of the cell performance (Al-BSF by segregation gettering [8,9]), but is not tolerant to a second, subsequent thermal treatment. This is a rather important issue, in view of the fact that the mid term goal in industrial solar cell

processing is to give up full coverage Al-BSF in order to improve surface passivation and reduce wafer bowing on very thin substrates. Another question is where the hydrogen is released from, and how. It has been suggested that the Si surface region may be hydrogenated during the plasma deposition and from there it would diffuse further into the bulk during the thermal treatment[7]. ERD measurements [10] have shown that no Hydrogen is present in the Si surface region after the deposition of nitride. The Si/SiNx interfacial region seems to play a stronger role. Surface pre-treatment and density of the layer appear to be key parameters for the bulk passivation process, and surface damage to enhance hydrogen dissociation. The next question is which types of defects are passivated by hydrogen, and how much Hydrogen goes effectively in the bulk. Very small quantity of Hydrogen appears to diffuse in the bulk [10], yet there is a remarkable improvement of the IQE. All these questions need to find an answer if the bulk passivation properties of silicon nitride are to be properly controlled.

'Dry' emitters

Junction diffusion in solar cells is a well-established process that leads to optimal results. The investigation of plasma-based alternative routes to conventional phosphorous diffusion is motivated by substantially two reasons: the possibility of an integral, fast, in-line process at low cost, and the prospect of attaining higher efficiencies. In a hypothetical production environment where all other front-end and back-end process are executed by plasma, it can be envisaged that wafers, always lying in a horizontal position, would be transported automatically without handling through the plasma line; conventional POCl_3 diffusion would be the interruption point in this process chain. Two alternatives have been considered for substitution of POCl_3 diffusion: Plasma Immersion Ion Implantation (PIII) and a-Si/c-Si heterostructures for emitter formation.

The PIII-Rapid Thermal Processing (RTP) technique is cost-effective and suitable for high throughput; it can lead to very shallow junctions with the highest P dopant concentration at the surface and it does not create diffusion glass and parasitic junction. A very good uniformity can be achieved in the chamber, which poses no problems for scalability to large area Silicon wafers. PIII emitters realised on 4" mc-Si wafers show an excellent response in the short wavelength range, and saturation currents in line with those of POCl_3 emitters. Cell level results are still slightly lower than those of conventional cells. The PIII process requires very high levels of safeguards, due to the use of Phosphine (PH_3), which is extremely toxic and flammable.



Figure 3. The PIII system (left) and a close up of the chamber with four 5" samples (right)

a-Si/c-Si and μ c-Si/c-Si heterostructures are investigated as a technologically feasible alternative to c-Si homojunctions. Their processing looks relatively simple and the heterojunction is formed by depositing the emitter in a PECVD chamber at temperatures of 200°C or below. The excellent results obtained by Sanyo with their HIT cell on n-type substrates (21.3% on a 100cm² cell [11]) worked as a drive for many

R&D groups who launched and still launch themselves into the development of this technology on p-type wafers, with the faith of developing an equally successful process suitable low-cost, p-type mc-Si substrates. The best results obtained on p-type wafers to date are 16.2 % on FZ silicon [12] and 14.6% on mc Si [13]. As long as the goal is that of a viable process for mc-Si wafers the ‘break-even’ efficiency would be in the order of 16% on 5” wafers (significantly below Sanyo’s record), provided the production costs and throughput are reduced or maintained. As interface recombination in these cells is not the limiting recombination mechanism, V_{oc} is limited by recombination in the c-Si quasi-neutral region, making the absorber material, its minority-carrier lifetime and doping density (and of course surface passivation) crucial in determining the final cell’s efficiency. The absence of gettering due to the elimination of the phosphorous diffusion step is a barrier to competitive cell’s efficiency in the industrial environment, until starting high quality material will be available at low cost. Despite $V_{oc}s$ in excess of 650 mV [14] that can be obtained on high quality p-type FZ material, the cell efficiency is still limited by its short circuit current, when not by its FF. The major issues with the development of this technology are surely related to the Transparent Conductive Oxide (TCO), which is deposited on top of the a-Si or μ c-Si emitter. With standard ITO, 4 to 6 mA/cm² of current are lost in reflection and absorption in the layer, which need to be traded off with its sheet resistance. Penetration of In/Sn atoms in the Si substrate can be detrimental for the cell operation, and it is known that the preparation conditions of ITO (temperature and rate of deposition, post deposition temperature treatments in different gas atmosphere) have a strong influence on the cell’s performance. Other issues are the preparation of an effective low resistance and low surface recombination velocity back contact, and the realisation of a fast and inexpensive metallisation process suitable for in line production (e.g. screen printing at low temperature).

Plasma-based Back Surface Processes

Conventional industrial solar cells make use of screen printed, Al-alloyed BSF as back contact. Al-alloyed BSF is relatively expensive (>10 €c/Wp), yet very functional. By mere screen printing and firing of Al paste, it is possible to ensure an ohmic contact with low resistance, type conversion of the rear junction, a back surface field and a certain extent of segregation gettering of metallic impurities. Unfortunately this process is not suitable for thin wafers, due to three major reasons: wafer bowing, insufficient effective surface recombination velocity and low reflectivity. It can be predicted that full coverage Al-alloyed BSF will progressively be phased out in favour of Local BSF structures with a passivating layer, ported from existing processes for high efficiency solar cells. The technology transfer from research labs to an industrial environment poses a few heavy constrains related to the technology, scalability and economical feasibility of the process. For example, for mc-Si material the possibility of using Conventional Thermal Oxide (CTO) is ruled out, because the process would lead to wafer poisoning.

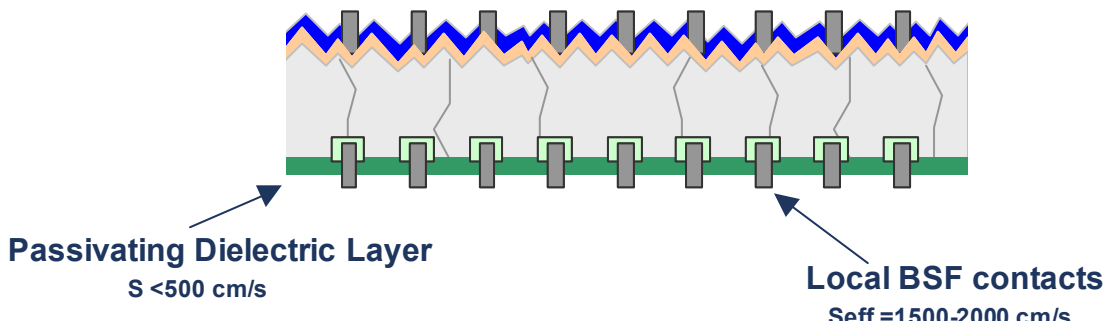


Figure 4. Generic Cell Structure

In order to be able to preserve or possibly increase current cell's efficiency the passivating layer should have a surface recombination velocity of less than 500 cm/s. It further requires to be sufficiently cheap and to have the possibility to be deposited with a high throughput. Plasma based processes are not a mandatory choice but they are convenient. They are suitable for high throughput, they can be cost effective and most of all there are already PECVD layers known for their excellent surface passivation qualities, which have been employed in high efficiency solar cells [Dauwe]. The two layers of choice are PECVD SiNx and a-Si. In both cases, it is known that very low surface recombination velocities (<200 cm/s) can be measured on bare wafers passivated with either of these layers, even on mc-Si material. Cell level results though are more difficult to attain with a simplified process sequence. In the case of SiNx, the problem resides in the parasitic shunting of the induced floating junction (IFJ), in that structuring of the backside metallisation pattern in order to provide separation between the electrode and the IFJ is impractical. Optimisation of the layer for low interface charge and better interface quality is therefore necessary, but this is not an easy task with D-PECVD SiNx, due to the surface damage. A source of other minor problems with SiNx is the non uniformity of its passivation properties according to grain orientation and surface treatment. Amorphous Si presents excellent surface passivation qualities (figure 5), does not require contact separation, but it requires careful surface cleaning and it needs a finishing process below 300 °C, which turns to be an issue if a local BSF contact is to be formed at the rear. These processes require therefore further optimisation in order to be suitable for upscaling in a commercial line, but they do have all the potential to become a viable substitute to full coverage Al-Alloy BSF.

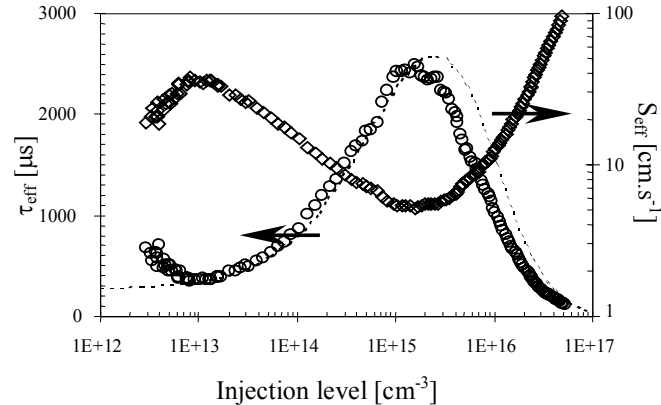


Figure 5. τ_{eff} and S_{eff} versus Δn for a p-type FZ $1\Omega\text{cm}$ substrate. The surface-passivation (both sides) was provided by direct PECVD intrinsic a-Si layers.

Amorphous Si presents excellent surface passivation qualities (figure 5), does not require contact separation, but it requires careful surface cleaning and it needs a finishing process below 300 °C, which turns to be an issue if a local BSF contact is to be formed at the rear. These processes require therefore further optimisation in order to be suitable for upscaling in a commercial line, but they do have all the potential to become a viable substitute to full coverage Al-Alloy BSF.

Conclusions

Dry processing is a topic that attracts considerable interest in the PV community. The motivations for this interest are diverse. The more pressing one is the need to find a short term solution to the increasing production costs of DI water and chemical waste treatment. Then, related to the rapid growth of PV market and the perspective of large production capacity, comes the generic vision of a fully in line, integral process for solar cells with a high throughput. And last, because it is not yet perceived as an imminent issue, the need for a more environmentally friendly production process. All these issues may be, but are not necessarily, solved with the introduction of an integral process based on plasma technology. The driving element for dry process -saving costs on water and waste disposal- does not find such a clear-cut answer in plasma processes. Plasma etching and texturing do get rid of the water, but introduce serious environmental issues, whose costs and effects risk to jeopardise the benefits. Until a cheap and effective solution to gas abatements is available, reducing or eliminating the consumption of GWP gases is essential.

PIII and a-Si/c-Si μ c-Si/c-Si heterostructures may become a cost effective way to produce emitters in an hypothetical, fully automated in-line plasma process for cheap substrates, but there is still way to go before seeing these processes implemented in a production line. In particular, heterostructures will only become advantageous when the starting bulk quality of the material will be high enough in comparison with the cell thickness, or alternative gettering processes make their case for production. Until then, phosphorous gettering will be essential to upgrade the initial bulk lifetime of the substrates [15].

For the backside, it will be necessary to progressively abandon the full coverage Al-Alloy BSF in favour of LBSF structures with a passivating dielectric. This will have the twofold effect of reducing the cell's production costs and increase cell's efficiency. Plasma technologies look like a natural candidate to deposit the passivating dielectric, but may be not be the only viable and cost effective solution.

It is reasonable to predict that dry processing will progressively make its way through the production lines as the PV market size grows bigger and bigger and that, as a side effect, this will contribute to provide momentum for PV thin film technologies, which are largely based on large-area PECVD processes, in that the larger market volume for deposition systems will reduce the initial investment costs. In this sense dry processing may not only provide the key to large capacity for Crystalline Silicon, but will also provide the synergy that is necessary for the transition from the first to the second generation of photovoltaic devices in the next decades.

ACKNOWLEDGEMENTS

This Work was partially funded By the European Commission under the FP5, project ADVOCATE, contract ENK6-CT-2001-00562

REFERENCES:

- [1] Y. Inomata, K. Fukui, and K. Shirasawa, *Sol. Ener. Mater. Sol Cells* 48 (1997) 237
- [2] J. Rentsch, G. Emanuel, C. Schetter, T. Aumann, D. Theirich, J. Gentischer, K. Roth, M. Fritzsche, K.H. Dittrich and R. Preu, "Plasma Etching for Industrial in-line Processing of c-Si Solar Cells", *Proc. 3rd World Conference on Photovoltaic Energy Conversion* (2003)
- [3] Intergovernmental Panel on Climate Change (IPCC), "Climate Change 1995" J.T. Houghton, L.G. Meira Filho, B.A. Callander, N. Harris, A. Kattenberg and K. Maskell (Eds.), Cambridge University Press, Cambridge, New York, p. 22, 1996
- [4] F.W. Dekkers, F. Duerinckx, S. De Wolf, G. Agostinelli, J. Szlufcik, "The influence on Surface Preparation on the Rear Surface Passivation of mc-Si by Thermally Treated Direct PECVD Silicon Nitride", *Proc. 3rd World Conference on Photovoltaic Energy Conversion. Osaka, Japan* (2003)
- [5] A. Rohatgi, V. Yelundur, J. Jeong, A. Ebong, D. Meier, A. M. Gabor and M.D. Rosenblum, *Proc. 16th Eu PVSEC, Glasgow, UK* (2000) pp 1120-1123
- [6] F. Duerinckx and J. Szlufcik, *Sol. Ener. Mater. Sol Cells* 72 (2002) 231
- [7] B.L. Sopori, Y. Zang and R. Reed, *Proc. 29th IEEE PVSC, New Orleans, USA*; 2002; pp. 222-226.
- [8] H. Hieslmair, S. Mc Hugo, E.R. Weber, *Proc 25th IEEE PVSC, Washington, USA*, 1996, pp 441-444
- [9] H. Porre, S. Martinuzzi, M. Pasquinelli, I. Perichaud and N. Gay, *Proc 25th IEEE PVSC, Washington, USA*, 1996, pp 629-632
- [10] H.F. Dekkers, S. De Wolf, G. Agostinelli, J. Szlufcik, T. Pernau, W.M. Arnoldbik, H.D. Godbach and R.E. Schropp, "Investigation on mc-Si Passivation using Deuterated Silicon Nitride", *Proc. 3rd World Conference on Photovoltaic Energy Conversion. Osaka, Japan* (2003)
- [11] M. Tanaka, S Okamoto, S Tsuge and S. Kiyama, "Development of HIT Solar Cells with more than 21% Conversion Efficiency and Commercialisation of Highest Performance HIT Modules", *Proc. 3rd World Conference on Photovoltaic Energy Conversion, Osaka, Japan* (2003)
- [12] M. Scherff, A. Froitzheim, A. Ulyashin, M. Schmidt, W Fahrner and W. Fuhs, *Proc. PV in Europe, Rome, Italy*, 2002, p.216
- [13] A. Ulyashin, M. Scherff W. Fahrner, R. Bilyalov and J. Poortmans *Proc. PV in Europe, Rome, Italy*, 2002
- [14] N. Jensen, R.M. Hausner, B. Bergmann, J.H. Werner and U. Rau, *Progr. Photovolt: Res. Appl.* 10 (2002) 1-13
- [15] S. De Wolf, G. Agostinelli, H.F.W. Dekkers and J. Szlufcik, *Acta Physica Slovaca*, vol.53 No.2, 135-142

Advanced Wet Processing and Drying of c-Si Wafers based on diluted Chemistry and Ozone

Juergen Osterkamp and Juergen Schreckendiek
ASTEC GmbH, Germany

Abstract

A wet cleaning and drying procedure characterized by simplified process steps is presented. The complete cleaning and drying procedure which is based on diluted hydrofluoric acid (dHF) and ozone needs only 2 process steps and one rinse step. Selected examples demonstrate that using this procedure meets the current requirement of low metal concentration on silicon wafers. Due to the short process sequence, low processing time and positive environmental aspects the cleaning and drying system based on this procedure is a space saver, cost efficient to run and suitable for high throughput. Still some work has to be done to fit, optimize and especially control the process window under mass production conditions for the different customer specific applications. Only when process and equipment are coordinated to the different cell structures and to customer's requirements the result will be satisfying and will meet the global challenge.

Introduction

To enable people all over the world using extensively photovoltaic electricity it is an absolute must that the use of PV modules becomes more cost effective. Therefore the generation of electrical energy produced by PV modules to a competitive price (< 1 US\$/Wp) is the big challenge by 2010.

It is assumed that worlds PV module production made of mono- or multi crystalline Silicon wafers will decline from 81% in 2001 to 60% in 2010, while the production of ribbon & sheet silicon will increase from 6,5% in 2001 to 15% in 2010.¹

That means that crystalline solar cells still keep the work horse during the next 7 years and most of the PV R&D is done in this field.

To achieve the cost target R&D groups and production engineers work hard all over the world. Their objectives in crystalline and ribbon & sheet silicon based cell production are in general:

- A significant reduction in consumed silicon material (3-6 gram Si/Wp)
- Development of innovative cell structures with high efficiency (>17% multi-Si, >22% mono-Si) and related fast low-stress manufacturing technologies suitable for mass production systems
- Development of necessary pastes, chemicals and needs required for these processes
- Design and development of fast mass production and handling equipment (> 0.01 m²/sec), with high yield for those thin and sensitive crystalline silicon cells
- A reduction of the costs of ownership by using less or cheaper consumables

With its process background and experiences with wet process equipment for semiconductor wafer manufacturing, three years ago ASTEC decided to face these challenges.

In the meantime ASTEC's patented HF/O₃ based process is successfully used for efficient metal removing and stress free drying as well as for cost saving phosphor glass etching and drying in single tank equipment. Finally some of the top ten solar cell manufacturers are producing their solar cells under mass production conditions with ASTEC equipment, which can have a throughput of up to 0.015 m²/sec. (depending on the kind of process).

Metal removal

It is obvious that solar cell manufacturer have to improve the metal concentration on the silicon surface if they like to achieve high quality solar cells. Metallic impurities and mobile ions are known to be responsible for the lifetime of the charge carriers in a solar wafer. The higher the metal or mobile ion level the shorter the lifetime and the lower the cell efficiency. Already a concentration of 1 ppb Fe in the silicon will lead to a significant deterioration of the solar cell and has to be strictly avoided.²

Especially critical is the metal removal from wafer surfaces before thermal processes like thermal processes like diffusion, annealing, CVD and oxidation.³ For higher efficient solar cells it becomes necessary to integrate such "critical cleaning" sequences before phosphorus diffusion and silicon nitride depositions and other high temperature steps like oxidation or CVD depending on the chosen cell structure.

The classical RCA cleaning

Developed since the middle of the 60th and published in 1970, the so called RCA clean with the standard cleaning recipes SC1 (ammonium hydroxide, hydrogen peroxide and water) and SC2 (hydrochloric acid, hydrogen peroxide and water) have evolved to a successful tool in the semiconductor industry.⁴ Depending on the detailed cleaning requirement, modifications were applied using H₂SO₄ (sometimes combined with H₂O₂) for removal of organic contamination or films. Further, HF was used to dissolve uncontrolled grown native oxide including inherent contaminations.

A typical RCA cleaning sequence is shown in figure 1.

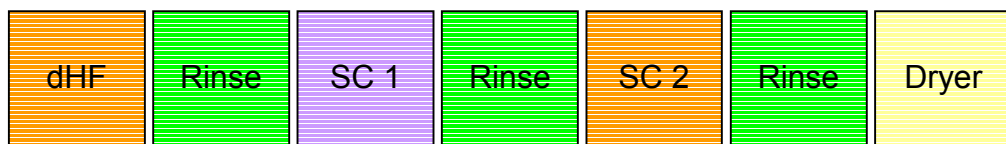


Figure 1: Typical RCA Clean

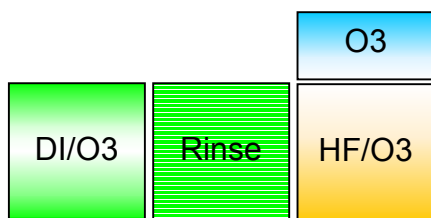


Figure 2: ACD Clean

When no organic layers hinder the access of HF to the Si surface, the cleaning sequence can start with a diluted HF step to remove silicon dioxide (SiO_2). Typically, the etching process is followed by a rinse bath and then by a SC1 step. SC1 has two purposes: lifting or loosening of particles or silicon deposits formed during the HF etching process and formation of a chemical oxide film. Exposure to SC1 results in a slow etching of the bulk silicon surface. The chemical oxide formed is low density and quite hydrated unlike thermal oxides. Typically a layer 10 to 20 Å thick is formed during the SC1 treatment. This chemical oxide has an unpredictable structure and typically has a lower breakdown voltage. Presumably, the newly formed layer is cleaner than the sacrificed oxide; however, this chemical oxide surface will contain metal and organic impurities that are present in the basic cleaning solution. SC1 supports further removal of organic compounds due to hydroxyl radical reactions. Although SC1 is extremely good at removing particles and also removing some metals by forming $\text{Me}(\text{NH}_3)_x$ complexes (e.g. Cu, Au) other metals contained in SC1 solution (e.g. Al, Fe, alkaline metals) are kept in the newly grown dioxide.

In order to remove these metals, SC2 is used as a next step. In SC2 solutions, many of the common metallic contaminants are removed from the wafer surface following cleaning with SC1. Finally the wafers have to be dried without watermarks. Many drying techniques have been attempted. Some of these include drying wafers in isopropanol (IPA) vapor rather than spin-drying, dipping wafers into liquid IPA before spinning or vapor drying and drying wafers slowly moving them from mixture of liquid IPA and hydrochloric acid.

Besides the number of process and rinsing steps, for a high throughput production, the decay of H_2O_2 and NH_4OH losses can be a challenge. Further, high metal loads due to the high throughput, can have an additional impact on the actual H_2O_2 concentration by catalyzed decay.

Alternative Cleaning and Drying process

Under the aspect of cost savings, usage of environment benign processes and development of cleaner chemicals, during the last years cleaning processes have evolved, which apply diluted chemicals. HF and ozone play an important role in these new cleaning procedures.

Ozonized DI water, when used in conjunction with HF and HCl,⁵ can provide a very effective and inexpensive critical cleaning sequence that removes rests of organic material as well as particulate and metallic contaminants.⁶ Furthermore it is shown that a very effective metal removing and stress-free drying process based on diluted HF with ozone can improve quality and can reduce costs.

Because HF has an incomparable effectiveness of removing silicon dioxide it is retained as a part of the HF/O₃ sequence. Since DI/O₃ is a very effective oxidizer, it will be readily form the chemical oxide as needed. Particle removal is accomplished by alternating HF and DI/O₃ dispenses to oxidize and then etch away particles. Finally the SC2 treatment, which is used to remove many of the common metallic contaminants, is easily replaced by the HF/O₃ process which also includes the stress-free drying step.

The result is that the four step RCA cleaning sequence (dHF – SC1 – SC2 – Drying) can be replaced by a process that only has two steps (DI/O₃ – HF/O₃ including drying). This process sequence eliminates two chemical steps from the RCA-Clean and has drastically reducing rinsing requirements. (See figure 2)

Combined with ASTEC's reclaim rinse tank system the rinse water consumption for such an optimized wet bench is only 24 l/m² processed surface (front and back).

This very low water consumption has a strong positive environmental advantage which helps to improve the “green” image of the PV industry. Furthermore it saves 400,000 Dollars for DI-water or 66,000 m³ per year.

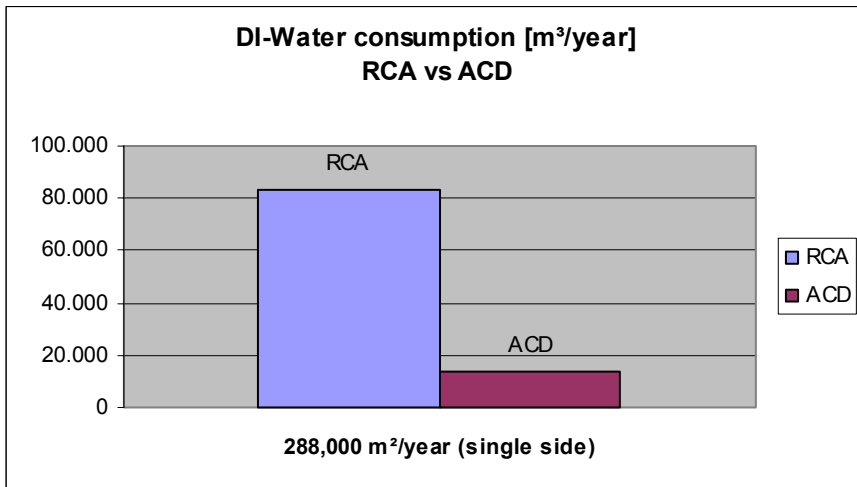


Figure 3: Comparison DI-water Consumption RCA vs ACD

Diluted HF with dissolved ozone is regarded as a high efficient means of removing certain metallic species while preventing plate back from solution. The hydrophobic, H-passivated surface, resulting from HF/O₃-last processing is desirable in terms of providing enhanced film adhesion and minimizing electrical contact resistance. Furthermore the hydrophobic surface helps to dry the wafers easily. When the wafers are lifted out of the diluted HF/O₃ they come out DRY without any other effort. Special designed carrier and integrated lift mechanism in the bath or the use of a carrierless handling system ensures, that no stains or watermarks remain on the wafer surface. A separate drying system is not necessary.

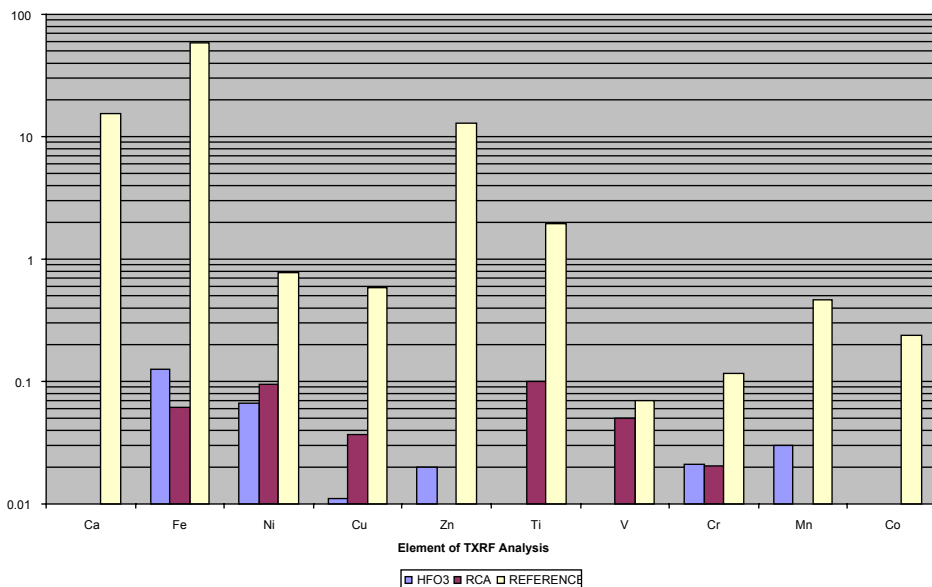


Figure 4: TXRF data comparing Metal Removal Performance between a modified RCA process vs. a HF/O₃ cleaning and drying process

Although chemically quite stable, the resulting surface is extremely susceptible to organic and particulate contamination. Therefore the hydrophobic and dry wafer surface can be re-oxidized exposing it to gaseous ozone directly above or behind the HF/O₃ bath. The surface becomes hydrophilic. The formation of stable native oxide proceeds spontaneously in only a couple of seconds. The process described here is known as the AD (ASTEC Drying) process which has been patented and is also known as “HF/O₃ Drying”. In combination with the preceding step of particle removal a complete cleaning and drying procedure is consisting of only 2 process steps. This shortened cycle yields the same results as a conventional RCA cycle.

In case that hydrophilic layer like Si₃N₄ or SiO₂ which has to be preserved on the wafer surface, either an extremely dilute HF concentration is used in the dryer or in combination with an HF/O₃ dip hot water drying is performed. The HF still allows a slight etch of the surface.

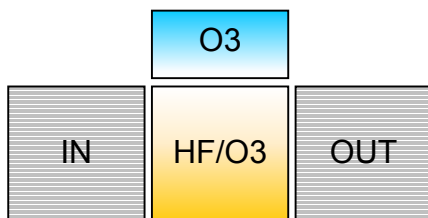
Phosphor Glass etching

Because of its effectiveness in removing phosphor glass, HF is used for this process. In the chapter before it was mentioned that pure bulk silicon etched by HF has an H-terminated surface which is hydrophobic. What suggests itself to use the HF/O₃ treatment for etching the phosphor glass, to remove metals and to dry the wafers in only one bath?

A typical layout of an automatic phosphor glass etch equipment can be seen in figure 5 where it is compared with a phosphor glass etch equipment based on HF/O₃.



Normal Phosphor Glass etch equipment



HF/O₃ Phosphor Glass etch equipment

Figure 5: Footprint Comparison of Phosphor Glass Etch Equipment

A footprint reduction of 50% and a cost reduction of DI water of more than **83.000 US\$/year** (288.000 m²/a single side, 13.824 m³ DI-water) is the result.

Beside these enormous benefits a further trial with 1,000 customer wafers showed another advantage of HF/O₃ treatment. The test wafers already saw phosphorus diffusion and then they were etched with HF/O₃ including the ozone gas hydrophilization. After that they were cleaned in a plasma clean before they were processed through a silicon nitride deposition. Finally they run through metallization.

Besides checking cell efficiency and cosmetic appearance it was of particular concern that the wafer surface after etching was sufficient clean so that the silicon nitride did not detach during the metallization firing step.

Process	Voc	Isc	Eff	FF	Popping [%]
HF/O3 incl. 90 sec Hydrophil.	100	101	100	99	5
Customer Standard	100	100	100	100	100

The result was that the HF/O3 treated wafers showed comparable results in efficiency and appearance but they showed 95% less detach of the silicon nitride during metallization firing.

Equipment

To support the mass production of solar cells with advanced cell structures and to achieve the goal of low cost of ownership ASTEC developed beside the mentioned processes reliable wet bench equipment for batch processing and handling features.

Some highlights can be seen in the following pictures.



Picture 6: HF/O3 system for metal removing and drying integrated in an automatic wet bench (capacity 200 w/batch)



Picture 7: ASTEC Diamond Carrier (ADC) optimized for wet processing and drying (wafers placed under 45° - diamond form)



Picture 8: ASTEC fork gripper for transfer of up to 100 wafers at one batch

Conclusion

The process of combined metal removal and drying of c-Si wafers presented here excels by small footprint, low chemical consumption, highly efficient removal of metals as well as stress free drying. Combined with a DI/O3 step for particle cleaning it is a cost reducing and very efficient critical cleaning sequence which becomes more and more important before diffusion, oxidation and other furnace processes. The process is proven for a specific requirement under mass production conditions.

Integrated in a wet bench with optimized process and rinse tanks as well as a handling system which guarantees quick transfer of thin wafers in special carriers, it helps solar cell manufacturer to produce solar cells according their targets. These targets often are different. Efficiency, lifetime, costs, weight and appearance are some of it. Processes and equipment have to be fitted to each customer's requirements. Only when cell structure, processes, supporting chemicals, equipment and handling logistics work together hand in hand the result will be satisfying.

References

-
- ¹ Bank Sarasin & Cie AG, Switzerland, „Sarasin Research, PV 2002 Markt, Akteure und Prognosen“
- ² Park, H. C. R. Helms, M. Tran and B.P. Tiptlett, „Effects of Surface Iron on Recombination Lifetime and its Removal From Silicon Wafers,” Proceedings of the Third International Symposium of Cleaning Technology in Semiconductor Device Manufacturing, 1993, V 94-7, The Electrochemical Society, p. 50-57
- ³ Eric J. Bergmann, Sebastian Lagrange, Martine Claes, Stefan De Gendt and Erika Röhr “Pre-Diffusion Cleaning Using Ozone and HF”, Proceedings of the fifth International Symposium on Ultra Clean Processing of Silicon Surfaces (UCPSS 2000) p. 85-88
- ⁴ Kern, W - Overview and Evolution of Semiconductor Wafer Contamination and Cleaning Technology – in: Handbook of semiconductor wafer cleaning technology – Science, Technology and Applications, ed. Werner Kern, Park Ridge, NJ 1993
- ⁵ T. Hattori, T. Osaka, A. Okamoto, K. Saga and H. Kuniyasu - Contamination removal by single-wafer spin cleaning with repetitive use of ozonized water and dilute HF, J. Electrochem. Soc., 9(1998) 3278-3284
- ⁶ M. Allessandri, E. Bellandi, F. Pipia, F. Cazzaniga, K. Wolke and M. Schenkl – Particle Removal Efficiency and Silicon Roughness in HF-DIW/O3/Megasonics Cleaning, Solid State Phenomena (1999) 65-66 pp 27-30

Highly Efficient Multicrystalline Silicon Solar Cells

Peter Fath

Manuscript not available at the time of printing.

SiN Coatings for Si Solar Cells: Understanding Their Multifunctional Role

Bhushan Sopori¹, Chuan Li¹, Ajeet Rohatgi², Vijay Yulander²

1. National Renewable Energy Laboratory, Golden, CO

2. Georgia Institute of Technology, Atlanta, GA

ABSTRACT

Hydrogenated silicon nitride ($\text{SiN}_x:\text{H}$) is now used by nearly all solar cell manufacturers as an antireflection coating on Si solar cells. This exclusive use of SiN is prompted by the fact that it can accomplish the following multiple functions: (i) act as an excellent antireflection (AR) coating whose refractive index can be tailored by controlling the deposition conditions, (ii) serve as a buffer through which a contact metallization can be fired to make reliable ohmic contacts, (iii) produce a passivation layer to reduce the surface recombination of the device, and (iv) allow diffusion of H into the device to passivate defects and impurities for improved device performance. Thus, it is expected that use of ($\text{SiN}_x:\text{H}$) can eliminate several process steps in the fabrication of high-efficiency solar cells, concomitantly lowering the solar cell fabrication cost. In a typical commercial solar cell processing sequence, a thin layer of silicon nitride is deposited by a plasma-enhanced chemical vapor deposition process on the front (facing the sun) side of an N/P junction to serve as an AR coating. Often, it is desirable to have a thin SiO_2 layer under the nitride layer. A nitridation process also produces an accumulation of positive charge at the ($\text{SiN}:\text{H}-\text{Si}$) interface that helps in surface passivation. Furthermore, because nitridation is performed in an atomic H ambient, it introduces H into a thin plasma-damaged surface layer. Following the nitride deposition, a Ag-based contact metallization is then screen printed and fired through the nitride. In this step, the metal penetrates through the nitride to form a low-resistance ohmic contact, while the H diffuses into the bulk of the cell to passivate impurities and defects. The multipurpose role of nitride demands that it be a low-absorption AR coating, serve as a barrier layer for control in metallization, and promote favorable electronic processes that can passivate the surface, as well as the bulk, of the device. It is imperative that ($\text{SiN}:\text{H}$) deposition and processing be designed carefully to optimize optical and electronic properties of the solar cell. The desirable features of a well-designed layer are the following: (i) the front surface of the cell should have very low reflectance within a broad band of wavelengths, (ii) it should yield low surface-recombination velocity on the N^+/P device, (iii) it should interact with Ag-based paste to form a uniformly wettable flux, and (iv) it should encapsulate H within the surface layer of Si and prevent its out-diffusion in subsequent processing.

An integration of these multiple functions demands a detailed knowledge of various mechanisms that influence optical parameters, interface charge, and transport of H in Si. This paper will review optical properties of ($\text{SiN}:\text{H}$) and its design as an optimum AR film, the role of ($\text{SiN}:\text{H}$) as a metallization buffer, process considerations for retention and subsequent diffusion of H to produce impurity defect passivation, and considerations for surface passivation by the nitride coating. We will review properties of nitride needed to accomplish these features for a high-efficiency Si solar cell on low-cost substrates.

Crack Formation and Propagation

Rob Ritchie

University of California, Berkeley

Manuscript not available at the time of printing.

Properties of Si:H Mixed Amorphous Microcrystalline Phases

C. R. Wronski and R. W. Collins

Center for Thin Film Devices, the Pennsylvania State University, University Park, PA 16802

Introduction

Researchers at The Pennsylvania State University have shown that the thin film Si:H prepared under moderate-to-high H₂-dilution conditions with low temperature rf plasma enhanced chemical vapor deposition (PECVD) evolves from the amorphous phase to a mixed amorphous + microcrystalline phase [(a+μc)-Si:H] with the accumulated thickness of the layer. The thin film material in the amorphous regime of growth has been called “*protocrystalline*” Si:H and exhibits a higher degree of ordering than materials deposited under similar conditions without H₂-dilution [1-3]. Furthermore they showed that the phase evolution of this material with thickness and, in particular, the transition to the mixed-phase (a+μc)-Si:H material, depends not only on hydrogen dilution ratios, $R=[H_2]/[SiH_4]$, but also on the substrate material. Consequently, without using real time spectroscopic ellipsometry (RTSE) or equally powerful techniques, it is not possible to control the growth of the protocrystalline Si:H materials and cell structures or to characterize their properties reliably. The insights into the growth process and microstructural evolution into the (a+μc) mixed Si:H phase obtained from RTSE have been extended to characterization of the optoelectronic properties of these phase and their effect on solar cell properties.

Growth and Microstructural Evolution of Protocrystalline Si:H

A key capability of RTSE is the ability to generate deposition phase diagrams for different R, different deposition conditions and different substrate materials. In such a diagram, the transition thicknesses are plotted as continuous functions of a key deposition parameter. In low temperature PECVD, R is used as the abscissa of the phase diagram since it exerts the greatest control over the phase of the film -- from a-Si:H at low R to μc-Si:H at high R. Over a wide range in R, however, Si microcrystallites have been observed to nucleate from within the growing a-Si:H phase after a critical phase-transition thickness that decreases with increasing R.

The phase diagrams have led to the concept of *protocrystalline* Si:H deposition. There are three important characteristics of this film growth regime. As its name implies, the protocrystalline growth regime is one in which a-Si:H is deposited initially, but given sufficient accumulated thickness, microcrystallites nucleate from the amorphous phase. Thus, the growing film will ultimately evolve first to mixed-phase (a+μc)-Si:H and finally to single-phase μc-Si:H. Once the a→(a+μc) transition is detected, however, the growing material is no longer considered protocrystalline. A second characteristic of the protocrystalline growth regime is the substrate dependence of the phase of the growing material. If the Si:H film grows in the protocrystalline regime on a freshly-deposited amorphous film substrate (such as R=0 a-Si:H), the same deposition conditions would lead to single-phase microcrystalline silicon growth on a freshly-

deposited μ c-Si:H substrate film. Thus, under protocrystalline growth conditions, local epitaxy is favored on a c-Si substrate; however, crystallite nucleation is suppressed on an amorphous substrate. A third characteristic of the protocrystalline growth regime is the observed enhanced degree of nuclei coalescence that yields the smoothest surfaces among a-Si:H films on an amorphous substrate.

At moderate to high values of R , however, a roughening transition is observed in which crystallites nucleate from the growing amorphous phase. Because the nucleation density is usually low and the crystallites grow preferentially, the crystalline protrusions generate a surface roughness layer that increases rapidly in thickness with the bulk thickness, d_b . Once the growing film crosses this transition and the crystallite volume fraction exceeds a critical value, the (a+ μ c) mixed phase material becomes unsuitable as an i-layer component of an a-Si:H-based solar cell. For thin films that have already undergone the a \rightarrow (a+ μ c) transition, a second transition is possible that occurs at even greater bulk layer thickness. In this transition, the crystalline protrusions that extend above the surface have become large enough to make contact, leading to

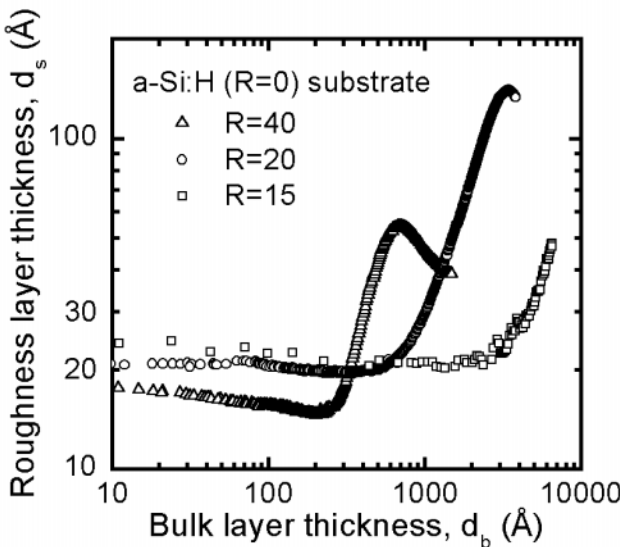


Figure 1. Surface roughness layer thickness (d_s) versus bulk layer thickness (d_b) extracted in analyses of RTSE data collected during the deposition of Si:H with $R=15$, 20, and 40, all on $R=0$ a-Si:H substrate films.

depends not only on the other fixed deposition conditions, temperature, and total gas pressure, but also on the influence over crystallite nucleation. Deposition phase diagrams are very convenient in the design of devices since they describe the regimes of layer thickness and deposition parameter space within which single-phase a-Si:H, (a+ μ c)-Si:H, and single-phase μ c-Si:H are obtained [4]. As a review of such phase diagrams, Figure 2 is presented which shows the proposed schematic structure of ~ 5000 Å thick Si:H films on $R=0$ a-Si:H substrate films, given as a continuous function of R along with the thicknesses of the a \rightarrow (a+ μ c) and (a+ μ c) \rightarrow μ c transition boundaries. There are several important features illustrated in Fig. 2 that should be pointed out. The first is

a crystallite coalescence process with continued film growth. This process is manifested in the data as a transition from surface roughening to smoothening during mixed-phase film growth. Once the crystallites have coalesced to cover the growing film surface completely, single-phase μ c-Si:H growth proceeds with a resumption of surface roughening. For optimum μ c-Si:H i-layers in solar cells, one generally seeks to deposit the film using the lowest R value possible while maintaining the film within the microcrystalline growth regime throughout the deposition. The evolution of the roughness layer thickness, d_s , as a function of bulk layer thickness, d_b , for three values of R are shown in Figure 1.

The a \rightarrow (a+ μ c) roughening transitions, and the (a+ μ c) \rightarrow μ c smoothening transitions can be incorporated readily into deposition phase diagrams. The phase diagram

the continuous decrease with R of the thickness at which the transition of protocrystalline a-Si:H into the $a+\mu c$ phase occurs. This characteristic has very important consequences in the design of protocrystalline solar cells with different thickness which until now have not been recognized [5]. Another feature is the increase with R in the nucleation density of μc -Si at the $a \rightarrow a+\mu c$ transition which are key to the subsequent growth of the $a+\mu c$ mixed phase. A third point that can be made is the decrease with R of the range of boundaries between which the $a+\mu c$ Si:H phase present before coalescing into the μc Si:H phase.

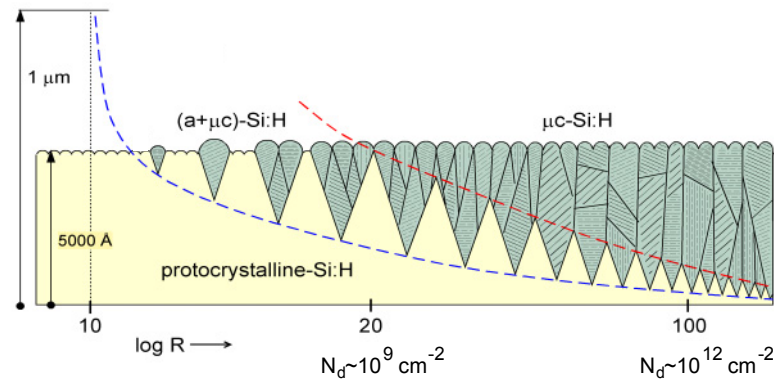


Figure 2. Schematic of the structure of Si:H films prepared as a function of R . The dashed and dotted lines identify the $a \rightarrow (a+\mu c)$, and $(a+\mu c) \rightarrow \mu c$ transitions, respectively. Also indicated are the corresponding densities of μc -Si:H nuclei present at the $a \rightarrow (a+\mu c)$ transition.

Correlations of the phase diagrams for intrinsic Si:H layers with the corresponding electronic properties and p-i-n device performance demonstrate that the optimum i-layers for a-Si:H p-i-n and n-i-p solar cells are obtained at the maximum possible R value for the desired thickness without crossing the $a \rightarrow (a+\mu c)$ boundary of the phase diagram into the mixed-phase growth regime [6]. It should be emphasized that because the R value at this phase boundary depends on both the nature of the substrate and the i-layer thickness, these aspects of the materials or device structure must be specified in order to identify the optimum conditions. The unique characteristic of protocrystalline Si:H is that not only is it a superior optoelectronic material but also its higher stability to light induced degradation as measured for both materials and devices.

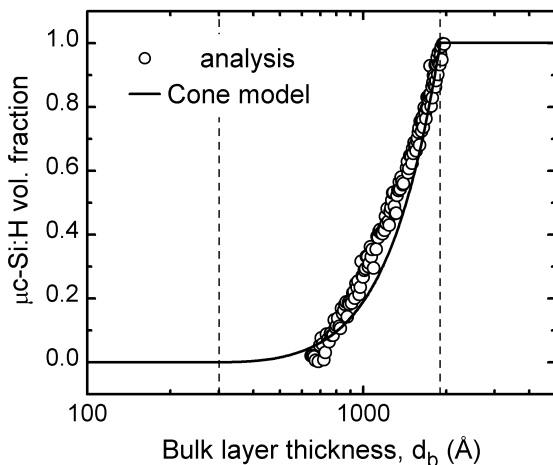


Figure 3. Depth profile in the volume fraction of the microcrystalline phase throughout the mixed-phase ($a+\mu c$) Si:H growth regime for the $R=20$ Si:H deposition on c-Si from Fig. 1 (points). Also shown as the solid line is the prediction of the microcrystallite cone growth model depicted in Figure 4.

respectively, and a surface roughness layer, modeled as a mixture of the outerlayer material and void with fixed volume fractions of $1-f_{sv}$ and f_{sv} , respectively. The solid line in Fig.3 is the result for $f_{\mu c}$ versus d_b , the thickness of the film, established using the cone model of microcrystallite evolution. Figure 4 identifies how this microcrystallite cone model is constructed. In this model, it is assumed that all microcrystalline nuclei originate at the $a \rightarrow (a+\mu c)$ transition layer thickness ($d_{b,trans}$). The area density of such nuclei is assumed to be N_d , and the nuclei are assumed to grow preferentially at the expense of the surrounding a-Si:H phase with a constant, thickness-independent cone angle, θ . For example, for the deposition of Fig. 3, values of $\theta=19^\circ$ and $N_d=1.1 \times 10^{10} \text{ cm}^{-2}$ are determined.

Figure 4 presents results for the cone angle θ and the nucleation density N_d plotted as a function of the $a \rightarrow (a+\mu c)$ transition thickness for a series of Si:H films prepared on both c-Si and R=0 a-Si:H substrates under different conditions of H₂-dilution, plasma power, and substrate temperature. Results deduced solely from RTSE using this approach have been compared and found to be completely consistent with those from cross-sectional transmission electron microscopy (XTEM) and from atomic force microscopy (AFM). It is found that the nucleation density decreases significantly with increasing $a \rightarrow (a+\mu c)$ transition thickness, yet the crystallite cone angle is nearly constant between 15° and 20°. The consistency between the indirect (but real time) optical measurements and the direct (but ex situ) structural measurements, provides strong support for the generality of the cone growth model for microcrystallinity as depicted in Fig. 4.

Optoelectronic and Solar Cell Properties of Mixed Amorphous Microcrystalline Phases

The systematic studies employing RTSE have described the transitions from the amorphous protocrystalline to the microcrystalline phase as well as the microstructure of the (a+ μc) phase as a function of the accumulated thickness for Si:H films prepared at moderate-to-high R ($10 \leq R \leq 100$). These studies suggest that the electronic transport properties in such materials are anisotropic as well as thickness-dependent, and as a result, it is problematic to characterize the electrical properties of the films assuming homogeneity versus thickness. Furthermore, difficulties are encountered when attempting to correlate basic material and device properties because of the differences in transport behavior arising from the inhomogeneity and anisotropy.

Detailed studies have been carried out on the optoelectronic and solar cell properties of protocrystalline Si:H which have been characterized in detail [6]. The optoelectronic and solar cell properties of the mixed-phase (a+ μc)-Si:H and single phase μc -Si:H layers have been investigated by incorporating them into the i-layers of p-i-n solar cell structures and interpreting their effects on device characteristics. The experimental approach was to assess the effects of these layers by comparing results for cell structures absent any $a \rightarrow \mu c$ transition layers with those

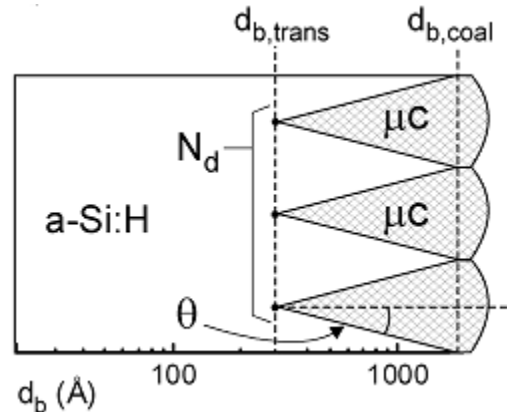


Figure 4. Schematic of the cone growth model used to estimate the microcrystallite nuclei density and cone angle.

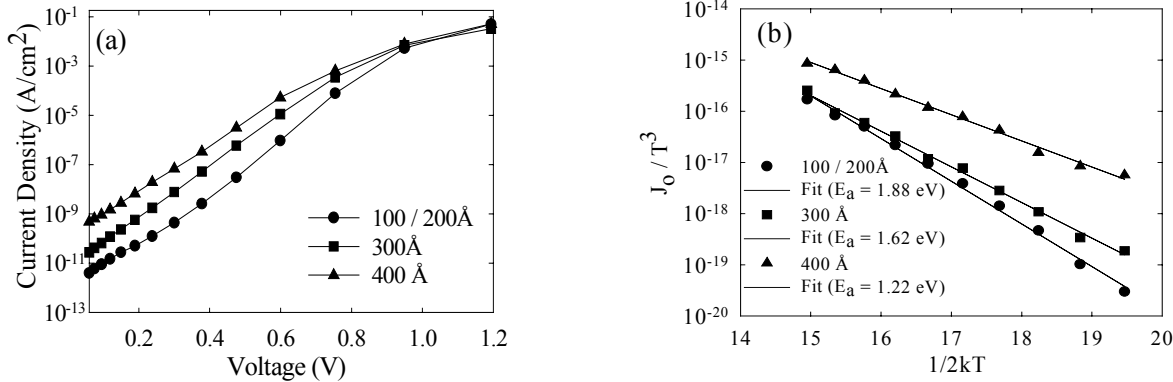


Figure 5. (a) Experimental dark J-V characteristics of 4000 Å p-i-n cells having R=10 bulk i-layers and different thickness R=40 p/i interface layers. (b) Thermal activation plots of J_0/T^3 for the cells shown in (a). The symbols are experimental results and the solid lines are exponential fits used to extract E_μ .

for structures incorporating such layers at different depths from the p/i interface. In such studies, information about the depth profile of the i-layer mobility gaps was obtained from the solar cell light and dark J-V characteristics and their temperature dependence, as well as from numerical modeling of these characteristics [9, 10].

It was found that for optimized p-i-n a-Si:H solar cells having high quality contact and interface regions, the dark currents at low forward bias voltages are determined by recombination rates in the bulk i-layer which are exponentially dependent on its mobility gap (E_μ) [10]. The E_μ value of the i-layer plays a key role in transport and collection of photo-generated carriers under illumination and in cells whose characteristics are dominated by the properties of the bulk i-layer [11]. With homogeneous i-layers the dark J-V characteristics exhibit the classical exponential diode behavior wherein J_0 can be obtained from the intercepts of the linear regions of the semi-log plots. It was found that reliable E_μ values can be obtained from the dependence of J_0 on temperature in such p-i-n cells when interface recombination is sufficiently low so that J_0 is primarily determined by recombination-generation in the bulk i-layer. The dependences of J_0/T^3 on temperature then yield well-defined slopes with values of E_μ that are in excellent agreement with the values measured with internal photoemission [12].

The correlations among carrier recombination kinetics in the bulk i-layer, J_0 , and E_μ established for p-i-n cells with homogeneous i-layers were then extended to include the more complicated cases of cells with evolving i-layers such as described here. This included a study carried out on a series of R=10 protocrystalline p-i-n cells each with a total i-layer thickness of 4000 Å, where a R=40 layer was incorporated at the p/i interface of each cell with the thicknesses ranging from 100 Å to 400 Å. Insights into the electronic properties of the transition material from amorphous to mixed-phase Si:H and then to single-phase μ c-Si:H that give rise to deleterious effects on cell performance could be obtained from the dark J-V characteristics of the cells as shown in Fig. 5a. The increase in carrier recombination-generation (R-G) in the vicinity of the phase transition region can be directly inferred from the systematic increase of the dark currents in the exponential region as the R=40 Si:H layer thickness increases from 100 to 400 Å and traverses the phase boundary as indicated in Fig. 2. The increase by two orders of magnitude in the room temperature value of J_0 clearly indicates a large increase in R-G currents

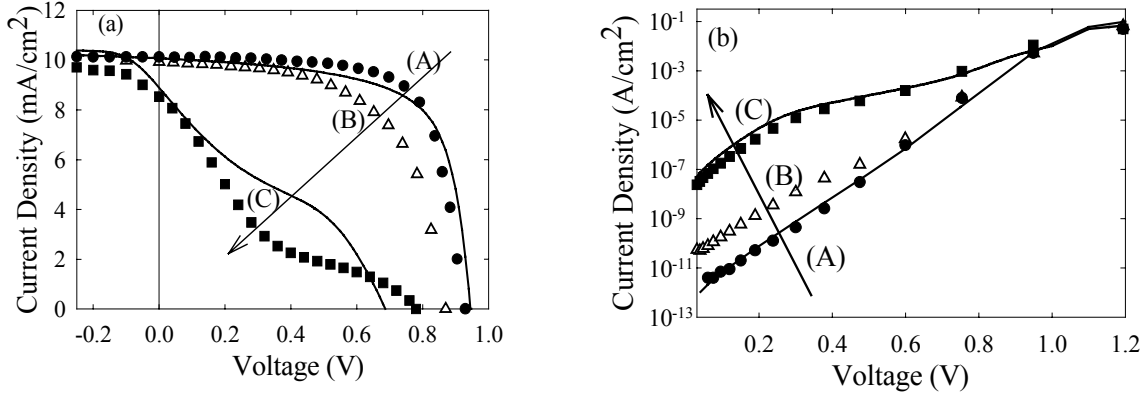


Figure 6. Experimental data (symbols) and simulations (solid lines) for the J-V characteristics of cells A, B, and C measured at room temperature (a) under 1 sun illumination and (b) in the dark. Direction of the arrows indicate decreasing distance between the $a \rightarrow (a+\mu c)$ transition and p-contact.

that can be attributed primarily to changes in the mobility gap. This is evident from Fig. 5b wherein plots of J_o/T^3 versus $(2kT)^{-1}$ are shown for the results in Fig. 5a. The decreases of E_μ to 1.66 eV for the 300 Å interface layer and to 1.22 eV for the 400 Å layer indicate that over a thickness of 200 Å there is a transition from the amorphous phase to a material having a mobility very close to that of bulk microcrystalline Si:H.

Additional insights into the transitions as well as their effect on cell characteristics of 4000 Å thick cell structures could be obtained from a study carried out on a cell in which a 400 Å R=40 p/i interface (similar to that described above) was followed by an R=20 bulk i-layer region (referred to here as cell C). The characteristics of this cell were then compared with those of the optimized structure described above having a 200 Å R=40 p/i interface and a homogeneous R=10 bulk region (referred to as cell A), as well as a cell deposited with a one-step R=20 i-layer (referred to as cell B). Ellipsometry studies show that the $a \rightarrow (a+\mu c)$ transition in the R=20 layer deposited on an amorphous film occurs after an accumulated film thickness of approximately 1000 Å, while on a R=40 layer that has traversed the phase boundary it proceeds in the microcrystalline phase so that the i-layer is fully microcrystalline. The experimental J-V results at room temperature for cells A, B, and C are shown in Figs. 6a and 6b under 1 sun illumination and in the dark, respectively. It can be seen in Fig. 6a that the FF and V_{oc} are the highest for cell A since the thickness and R values in the two step i-layer are chosen so that protocrystallinity is maintained. The cell performance becomes progressively worse for cells B and C as the position of the transition to mixed phase in the i-layer approaches the p-contact (indicated by the direction of the arrows).

This drop in cell performance is attributed to narrow gap material in the i-layer of cells B and C whose presence is reflected in the dark J-V characteristics as shown in Fig. 6b. The carrier recombination rates in a p-i-n cell can be explained by the large contribution of the narrow gap material to the recombination currents at low forward bias and the inflection points in the dark J-V characteristics observed in Fig. 6b. The simulation result shown in Fig. 6b (solid line) was carried out for cell C assuming a 400 Å wide gap Si:H layer with the remainder of the i-layer as a narrow gap μc -Si:H material having a mobility gap of 1.15 eV. The latter value was obtained

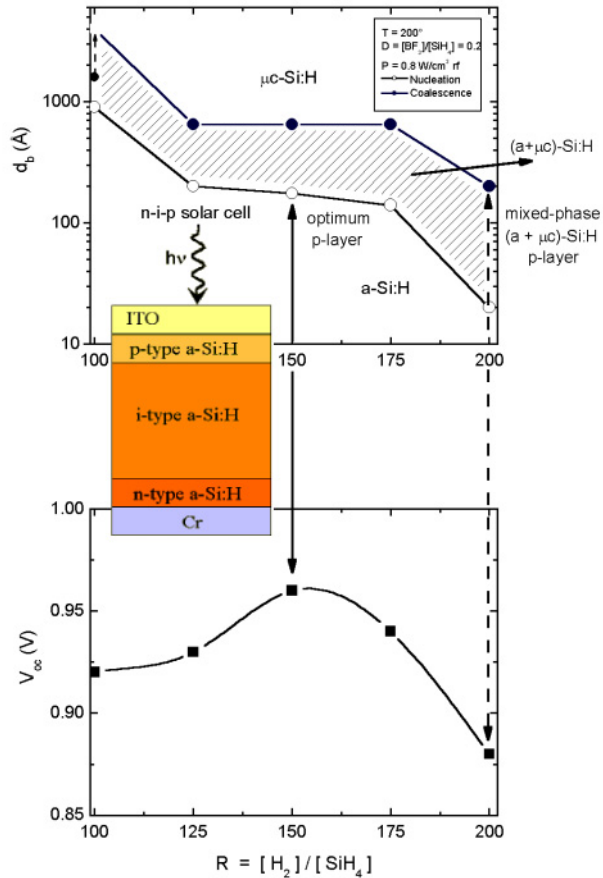


Figure 7. The extended phase diagram depicting the bulk thickness (\AA) as a function of R for p-type Si:H deposition with BF_3 doping $D=0.2$ on a-Si:H substrates; also shown is 1 sun V_{OC} as function of R for solar cells with the corresponding 200 \AA p-layers.

within the protocrystalline amorphous Si:H growth regime without crossing into the mixed ($a+\mu c$) phase. It is interesting to note here that for a long time it has been proposed that highly doped μc Si:H layers have been responsible for obtaining high V_{OC} . This is due to the erroneous conclusions drawn about the thin p-layers in cells from results obtained on much thicker films in which the ($a+\mu c$) mixed and μc phases were present.

Summary

A brief review was presented of the growth and microstructure of *protocrystalline* Si:H, deposited by low temperature PECVD. This material cannot be adequately described as “edge material” as is often done because of the thickness dependence of the phase transition. The development of deposition phase diagrams from RTSE measurements was presented which identify the transition from amorphous \rightarrow amorphous + microcrystalline to fully microcrystalline Si:H phases as function of different deposition parameters. Results were also presented on the

experimentally from plot of J_o/T^3 vs. $(2kT)^{-1}$ for cell C. Both results suggest that the transition from the amorphous phase to a fully coalesced microcrystalline phase in the $R=40$ film occurs over a thickness of only a few hundred angstroms. The large decreases of the FF in cells B and C are a direct consequence of the phase transitions. Such characteristics could only be modeled for i-layers consisting of two distinctly different layers—a wide gap amorphous layer and a narrow gap microcrystalline one [13]. The results of the simulation for cell C is shown as a solid line in Fig. 6a, where the less than perfect fit is probably due to the necessary oversimplification of the highly anisotropic microcrystalline material when a one-dimensional simulator such as AMPS is being used.

The concept of protocrystallinity and the changes in E_μ present in the ($a+\mu c$) mixed Si:H phase was also successful in explaining the nature of p-type Si:H films doped with BF_3 . Guided by the phase diagrams developed as function of R and doping concentrations it was possible to carry out a systematic development of high V_{OC} in n-i-p a-Si:H solar cells, such as illustrated in Figure 7 [14, 15]. The RTSE results, confirmed by TEM and AFM measurements, show that the optimum p-layers for obtaining high V_{OC} clearly lie

evolution of the microstructure in the (a+ μ c) Si:H mixed phase with thickness from the onset at the a \rightarrow (a+ μ c) phase to its transition to a fully μ c phase. Examples were then presented how RTSE was utilized in a *unique* approach for characterizing the optoelectronic properties of the (a+ μ c) mixed phase with highly anisotropic properties. Results were presented on p-i-n solar cells with controlled micro-structural composition in which the mobility gaps of the Si:H mixed amorphous microcrystalline phases were obtained. Meaningful correlations could be made between the materials and solar cell characteristics since in these studies the uncertainties associated with the initial nucleation and subsequent growth of Si:H films on different substrate materials were eliminated. The insights provided here into the transition from protocrystalline Si:H to mixed-phase Si:H and then to single-phase μ c-Si:H are of critical importance to the engineering of cell structures with high performance and improved stability.

References:

1. R.W. Collins, A.S. Ferlauto, G.M. Ferreira, C. Chen, J. Koh, R.J. Koval, Y. Lee, J.M. Pearce and C. R. Wronski, *Solar Energy Materials and Solar Cells*, **78**, 143 (2003).
2. Y. Lu, S. Kim, M. Gunes, Y. Lee, C.R. Wronski, and R.W. Collins, *Mater. Res. Soc. Symp. Proc.* **336**, 595 (1994).
3. J. Koh, A.S. Ferlauto, P.I. Rovira, C.R. Wronski, and R.W. Collins, *Appl. Phys. Lett.* **75**, 2286 (1999).
4. J. Koh, Y. Lee, H. Fujiwara, C.R. Wronski, and R.W. Collins, *Appl. Phys. Lett.* **73**, 1526 (1998).
5. R.J. Koval, J. Koh, Z. Lu, L. Jiao, C.R. Wronski, and R.W. Collins, *Appl. Phys. Lett.* **75**, 1553 (1999).
6. C.R. Wronski, R.W. Collins, J.M. Pearce, R.J. Koval, X. Niu, A.S. Ferlauto, and J. Koh, *Mater. Res. Soc. Symp. Proc.* **715**, A.13-4.1 (2002).
7. R.W. Collins, A.S. Ferlauto, G. M. Ferriera, C. Chen, R.J. Koval, J.M. Pearce, and C.R. Wronski, *Mater. Res. Soc. Symp. Proc.* **762**, A5.10.1 (2003).
8. H. Fujiwara, Y. Toyoshima, M. Kondo, and A. Matsuda, *Phys. Rev. B* **60**, 13598 (1999).
9. R.J. Koval, J.M. Pearce, A.S. Ferlauto, R.W. Collins, and C.R. Wronski, *Mater. Res. Soc. Symp. Proc.* **664**, A16.4 (2001).
10. R.J. Koval, A.S. Ferlauto, J.M. Pearce, R.W. Collins, and C.R. Wronski, *J. Non. Cryst. Solids*, **299-302**, 1136 (2002).
11. J. Deng, J.M. Pearce, R.J. Koval, V. Vlahos, R.W. Collins, and C.R. Wronski, *Appl. Phys. Lett.* **82**, 3023 (2003).
12. C.R. Wronski, S. Lee, M. Hicks, and S. Kumar, *Phys. Rev. Lett.* **63**, 1420 (1989).
13. R.J. Koval, “Microstructurally Engineered Improvements in he Performance and Stability of Si:H Based Thin Film Solar Cells”, PhD Thesis, The Pennsylvania State University, 2001.
14. R.J. Koval, C. Chen, GM. Ferreira, A.S. Ferlauto, J.M. Pearce, P.I. Rovira, C.R. Wronski, and R.W. Collins, *Appl. Phys. Lett.* **81**, 1258 (2002).
15. V. Vlahos, J. Deng, J.M. Pearce, R.J. Koval, R.W. Collins and C.R. Wronski, *Mat. Res. Soc. Proc.* **762**, A7.2 (2003).

A Study on Dendritic Web Silicon Growth

X. Zhang^a, B. Raghathamachar^b, D. L. Meier^c, M. Dudley^b, S. Mahajan^a

^a Department of Chemical and Materials Engineering, Arizona State University, Tempe, AZ 85287-6006, USA

^b Dept. of Materials Science & Engineering, State University of New York at Stony Brook Stony Brook, NY 11794, USA

^c EBARA Solar Inc., 1801 Route 51, Jefferson Hills, PA 15025, USA

Introduction

Dendritic web silicon is one of the promising large-scale territorial photovoltaic (PV) materials. As shown in Fig. 1, the as-grown web silicon has flat and mirror-like surfaces and small thickness ($\sim 100 \mu\text{m}$). These features help to reduce the work on cutting and polishing to the minimum. Web silicon contains low contamination at the level that rivals CZ wafer. The solar cells made on web silicon can provide high conversion efficiency of up to 17%.

The growth of web silicon is initiated by dipping a crystal seed [(111) silicon dendrite] into the supercooled silicon melt. By controlling the thermal profile, two dendrites grow downward from the ends of a thick button. As the seed, the button and the two dendrites are pulled up together, web silicon grows from the liquid film which is bounded by the two dendrites and pulled up by a small distance above the melt surface. Odd number of twin planes that are introduced by the seed are contained in the web silicon.

Currently, web silicon of 4 cm to 7 cm wide can be grown depending on the growth conditions and the silicon ribbon can be grown for longer than 10 meters. Growing longer and wider silicon ribbon is an essential for further lowering the cost for the fabrication of solar cells. However, polycrystalline structures are more likely to be developed in the wide ribbons and cause the cessation of growth. In this work, we studied the growth mechanism, formation of polycrystals and the termination of web silicon growth by the polycrystals.

Experimental Results and Discussions

The silicon ribbon consists of web, dendrite and fillet regions as shown in Fig. 2. The dendrites grow into the melt. The web region does not extend into the melt or below the solid/melt interface. The fillet regions are partially covered by the melt.

Web silicon samples were made by withdrawing them rapidly after they had grown stably for a few meters. In these samples, the web growth interface of normal growth conditions was frozen and the morphology of growth interfaces of these samples can be examined. AFM images of fillet region on the web silicon surface, web silicon growth

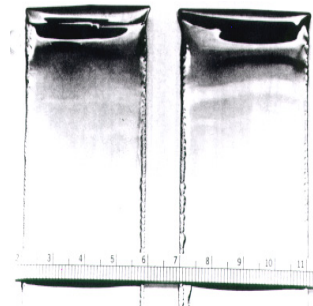


Fig. 1. Photo picture of dendritic web silicon

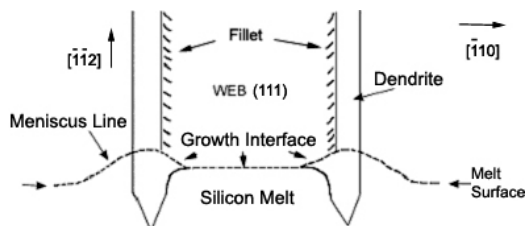


Fig. 2. Silicon ribbon crystal structure

interface region and growth interface between the web and the dendrite regions are shown in Figs.3, 4 and 5, respectively.

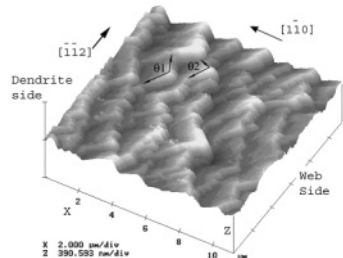


Fig. 3. AFM image of steps in the fillet region.

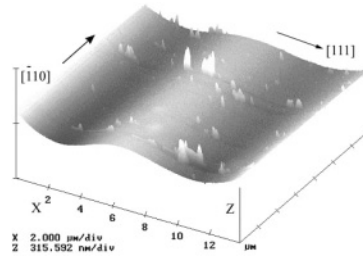


Fig. 4. AFM cross-section image of web growth interface.

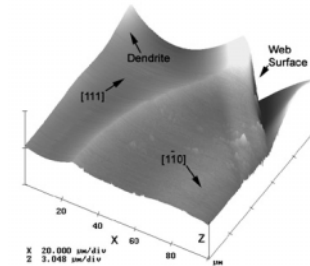


Fig. 5. AFM cross-section image of growth interface between web and dendrite.

The fillet surface was curved and was consisted of small steps that are stacked on (111) web surface. The tips of those steps were extended to the web center (in $\pm [\bar{1}10]$ direction). These steps were grown from the silicon liquid that partially covered the fillet region. For (111) silicon crystal growing in the liquid, $<\bar{1}10>$ directions are the fast growth directions^[1]. Under normal growth conditions, the web surface was totally above the solid/melt interface in the web region. Therefore, there was no liquid source for the step extending on the web surface and, the steps stopped extending when they reached the solid/liquid interface at the edge of fillet region.

The growth interface (cross-section) of the web region is in near $(11\bar{2})$ orientation and is mostly flat with only small surface undulations as shown in Fig. 4. This result confirms that the growth of web region is leaded by layer flow on the interface under small amount of suppercooling (the growth driving force) and along the near planer isothermals on the growth interface. The small surface undulation may be due to the thermal fluctuation during the fast pulling. The steps in the curved fillet growth interface (cross-section) are the sources for the layers flow in the $\pm[\bar{1}10]$ directions to the center of web growth interface. Due to the large surface energy of $\pm(\bar{1}10)$ planes, only large steps were observed in that curved region as shown in Fig. 5.

By observing large number of chemical etched web silicon samples, as shown in Fig. 6, it was found that twin planes may grow out of web crystal during different growth stages and the web without twin planes inside could also grow for a long distance (several meters). Twin planes in the web region were extended from the bounding dendrites and the twin planes position in those dendrites did not change during the growth.

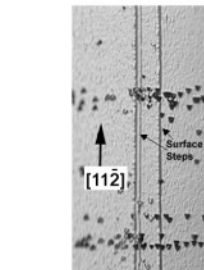
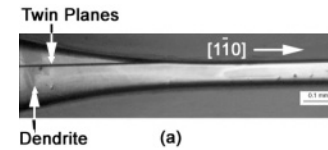
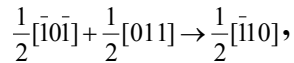


Fig. 6. Cross-section (a) and plan-view (b) images of chemical etched web silicon.

Initially, twin planes were at the same position with the center of thermal profile as shown in Fig. 7(a). When the thermal profile center was shifted toward one of the web surfaces, the meniscus which was determined by the thermal profile^[2] would tend to shift as shown by the dotted lines in Fig. 7(b). On the front side, a small portion of web surface would then be slightly covered by melt and the surface steps in fillet region might extend on the liquid covered web surface. That result in the increase of web thickness on that side and the creation of new growth interface. On the back side of web, growth was limited by the new meniscus shape. Finally, the web was totally shifted so that the new center of web matched the center of thermal profile and the meniscus could remain the shape for normal growth. However, the twin planes remained at the same position during the web position shift, and that results in the position of twin planes being closer to one of the web surfaces or, out of web region.

As the web silicon becomes thinner and thinner for the newly grown ribbons, it is hard to hold the twin planes in the web even under small amount of thermal profile shift. Therefore, it is common to observe twin free web silicon from the new ribbons.

Long edge dislocations with Burgers vector of $\pm 1/2[1\bar{1}0]$ lying in $[11\bar{2}]$ web growth direction are created in the web region that contains twin planes. They are created by the dislocations reaction^[3]:



which occurs on the twin plane or by directly nucleating dislocations on the web surface and then extending to the twin-matrix boundary where the stresses are highly concentrated.

The edge dislocations with same signs may align themselves in the $(1\bar{1}0)$ planes to form the sub-grain boundaries to lower the system energy. The sub-grain boundaries stop the slip dislocations. On the chemical etched web samples it was observed that the pits from those blocked dislocations are aligned along the ribbon growth direction on web surface and on the cross-section of those regions as shown in Fig. 8.

For the web region without twin planes, new edge dislocations would not be generated. The existent edge dislocations and sub-grain boundaries could grow with the web and became the highly strained regions because they blocked the slip dislocations. In

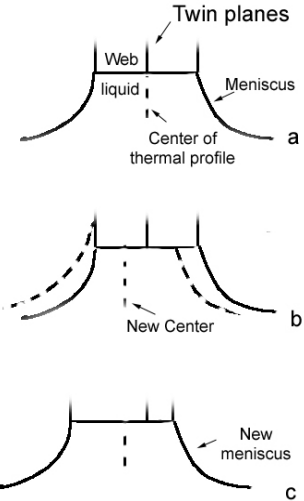


Fig. 7. Schematic side-view of web region shows the shift of web position during the growth

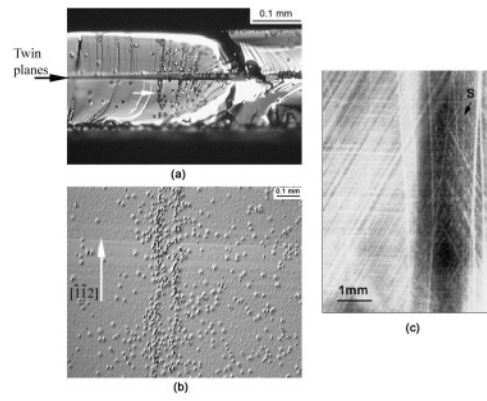


Fig. 8. Etch pits alignment on the cross-section (a) and the web surface (b). TXT image from $2\bar{2}0$ reflection for the edge dislocation (c).

Fig. 9(a), it shows that the high stresses were concentrated in the region with high density of edge dislocations. The grain boundary was initiated in that region and then penetrated to the other web surface as shown in Fig. 9(b). Due to the high local stresses, those grain boundaries became the origin sites for new structural defects such as dislocations, twin planes and new grain boundaries as shown in Fig. 10. The new grain boundaries could propagate to the growth interface and eventually, strong polycrystalline structures would be developed as shown in Fig. 11.

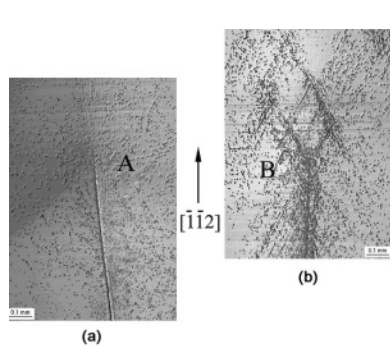


Fig. 9. Chemical etched web front (a), and back (b) surface in the region grain boundary started.

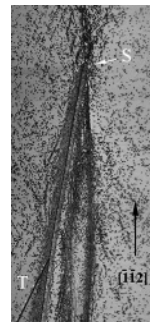


Fig. 10. Chemical etched web surface shows new defects created from grain boundary

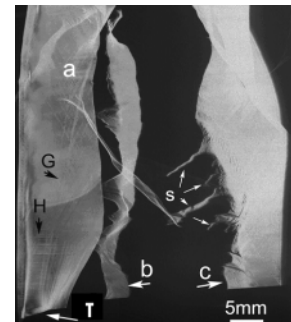


Fig. 11. TXT image of terminal region of a polycrystalline web

The web could keep growing with grain boundary but the growth conditions would be worse and in the grain boundary regions, the step flow on the growth interface from both dendrites could be interrupted. Due to the larger amount of supercooling, two-dimensional nucleation on the interface of the grains in the middle of web will occur. Under that growth conditions, small grains could start and spread over the whole solid/melt interface to form a polycrystalline layer that led to the unstable web growth and finally the termination of the growth.

Conclusions

The step flow on the web solid/melt interface results in the stable web growth. Step flowing on the web surface may result in the increasing of web thickness. Web growth does not depend on twin planes and web silicon may contain no twin due to thermal profile position shift. Polycrystalline structures interrupts the web growth from layer flow on the growth interface and results in the termination of web growth.

Acknowledgement

The authors would like to thank EBARA Solar, Inc. for providing the silicon ribbons for this study and for the financial support.

References

- [1] T. F. Ciszek, in: Solid/Melt Interface Studies of High-speed Silicon Sheet Growth, UC-63 DOE/JPL-W08746-83-2, 1985.
- [2] T. Surek, J. Appl. Phys. 47 (1976) 4384.
- [3] A. N. Westmeyer, S. Mahajan, B. B. Bathey, G. Neugabauer, J. Jessup, D. L. Meier, Material Sci. & Eng B65 (1999) 177.

First-Principles Calculations of Nucleation Precursors in
Nitrogen-doped Float Zone Silicon

A. Karoui,¹ F. Sahtout Karoui, G. A. Rozgonyi
North Carolina State University, Raleigh, NC 27695-7916, USA.

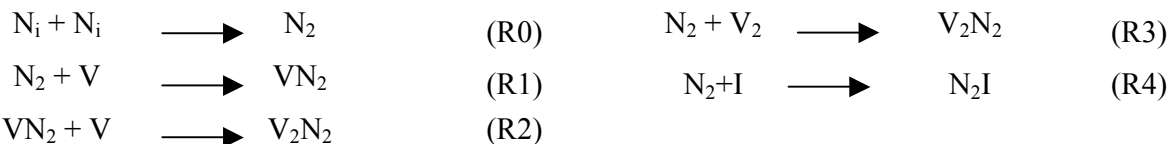
Abstract: Density functional theory calculations were done to investigate the atomic structure, energy of formation and stability of nitrogen-vacancy complexes in N doped FZ silicon. In addition we used molecular mechanics to calculate the potential wells/barriers for vacancy and oxygen trapping/repulsion by these complexes. We found that N₂ in a split interstitial position and V₂N₂ are very stable compared to VN₂. The latter can only be weakly coupled to oxygen atoms, whereas it reconstructs into stable V₂N₂ by trapping a vacancy. It is suggested that N₂ and V₂N₂ act as nucleation centers for oxygen precipitation rather than for void formation.

Introduction

Nitrogen doping of Float Zone silicon crystals (N-FZ Si) has attracted considerable attention for its ability to reduce self-interstitial related A-swirl defects and vacancy related D-defects, as well as to increase the mechanical strength of large diameter silicon wafers [1-3]. Even at low concentration, N appears to have a strong locking effect on dislocations, thus reducing the occurrence of warpage caused by thermal stresses during wafer processing [1]. Nitrogen in silicon is a highly reactive species and interacts strongly with point defects and impurities like oxygen and vacancies. In N-FZ Si co-doped with oxygen, if oxygen is present in concentrations typical of CZ crystals (0.8-1.0x10¹⁸ cm⁻³), N-O complexes will form [1,4-7]. Nitrogen has also a dramatic effect on the density and size of oxygen precipitates and vacancy aggregates i.e. COPs/voids and making them smaller and denser. The formation and dissolution mechanisms of extended defects in N doped Si are mainly driven by N-V-O complexes. [8, 9]. Most of nitrogen (80%) in silicon are paired [4] leaving all Si and N fully coordinated hence, removing any associated electrical activity. In this paper, we present results of Molecular Mechanics (MM) calculations on the ability of nitrogen-vacancy defects to trap oxygen, vacancies and self-interstitial silicon. The atomic structures, formation energies, and stability of nitrogen-vacancy complexes have also been investigated using ab-initio Density Functional Theory (DFT) calculations. Both analyses have been correlated in order to predict the most likely atomic structures for N-related defects in N-FZ Si.

Atomic Structure and Stability of N₂, VN₂, and V₂N₂ Defects

Infrared spectroscopic studies on laser annealed N-implanted high resistivity p-type FZ Si have shown that most of nitrogen atoms are incorporated in pair centers, which are bonded to silicon [10]. Direct evidences of V-N complexes in annealed N-FZ have been reported based on, platinum diffusion [11], positron annihilation of N₂⁺ implanted wafer [12], and DLTS measurement [13]. Vacancy concentrations in N-FZ Si can vary from 2.5x10¹³ cm⁻³ to 10¹⁵ cm⁻³ depending on the temperature [9, 11]. Nitrogen at concentration of 10¹⁵ cm⁻³ induces a downward shift in the critical v/G ratio enabling N to trap vacancies at high temperature [14]. The solid-state chemical reactions considered are:



¹ nas_karoui@ncsu.edu

The small covalent radius of N atom (i.e., 0.75 Å versus 1.11 Å for Si) and the large electronegativity of nitrogen, which pulls charges from its Si neighbors, makes the Si-N bond shorter and stronger as shown in Fig. 1.

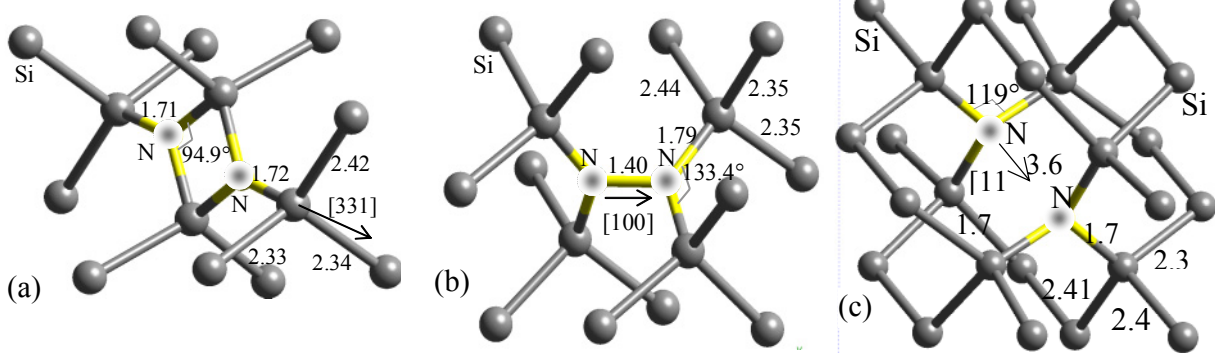


Fig. 1: Relaxed structures of (a) N_2 , (b) VN_2 , (c) V_2N_2

The calculated energies of formation in the ground state, -4.1 eV for N_2 , 2.0 eV for VN_2 , and -5.2 eV or -1.0 eV for V_2N_2 depending on the reaction path (R2 or R3), show that V_2N_2 when formed from VN_2 is the most stable, followed by N_2 and V_2N_2 formed from a divacancy. The reaction forming VN_2 is endothermic and hence not stable and necessitates some energy to form. On the other hand, VN_2 defect in Si is foreseen as an active complex at high temperature and contributes to the formation of very stable N_2 through the reaction $\text{VN}_2 + \text{I} \rightarrow \text{N}_2$, and V_2N_2 thru reaction R₂, which subsequently dominate the mechanisms of nucleation and growth of extended defects in Si crystals. We showed in previous ab-initio calculations, that at high temperature and at very low nitrogen concentrations, only about 10% of the vacancy concentration are coupled to N_2 , while for high nitrogen concentrations about 75% of vacancies are trapped by nitrogen pairs [15]. The small size and high density of voids observed in N-FZ Si could result from a lower mobility and concentration of vacancies due to the formation of V-N complexes. Therefore, the formation of V_2N_2 from VN_2 is favored during crystal growth, since the divacancy cannot form above 600K [16]. Nevertheless, based on DLTS and ESR measurements, Abe suggested recently [17] that di-vacancies, coupled with N pairs might exist in annealed wafers at a concentration as high as $3.5 \times 10^{15} \text{ cm}^{-3}$.

Interaction Potential of N_2 , VN_2 and V_2N_2 with Oxygen and Vacancies

N_2 and V_2N_2 are stable defects and may act as trapping centers for point defects like O, V and I. For this purpose, we have calculated the potential energy variation of the crystal during the diffusion of an O atom, a vacancy and a self-interstitial from infinity to the vicinity of N_2 , VN_2 , V_2N_2 complexes. From these calculations and as shown in Fig. 2 and 3, it appears that N_2 and V_2N_2 complexes have a strong capability for attracting O inducing a potential well of -2.8 and -2.4 eV respectively. The potential well full width is about 9 Å; if one neglects additional strain effects induced by accumulated oxygen, the V_2N_2 complex surrounded by trapped interstitial O atoms may result in a grown-in nucleus of roughly 2 nm in diameter. This supports the stable grown-in nuclei found in oxygen rich Si crystals. The potential energy during V migration towards N_2 and V_2N_2 defect is only about -0.1 and -0.3 eV respectively, see Fig. 3, which show that these defects are unable to firmly trap vacancies. The significant difference (about one order of magnitude) between the potential well depth for V and that for O interstitial indicates that N_2 and V_2N_2 attract preferentially oxygen. We found that N_2 has also some potentiality to attract self-interstitial silicon creating a potential well of about -0.65 eV when a self-interstitial in hexagonal site is located in its vicinity. This may explain the reduction of swirl defects in N-FZ Si.

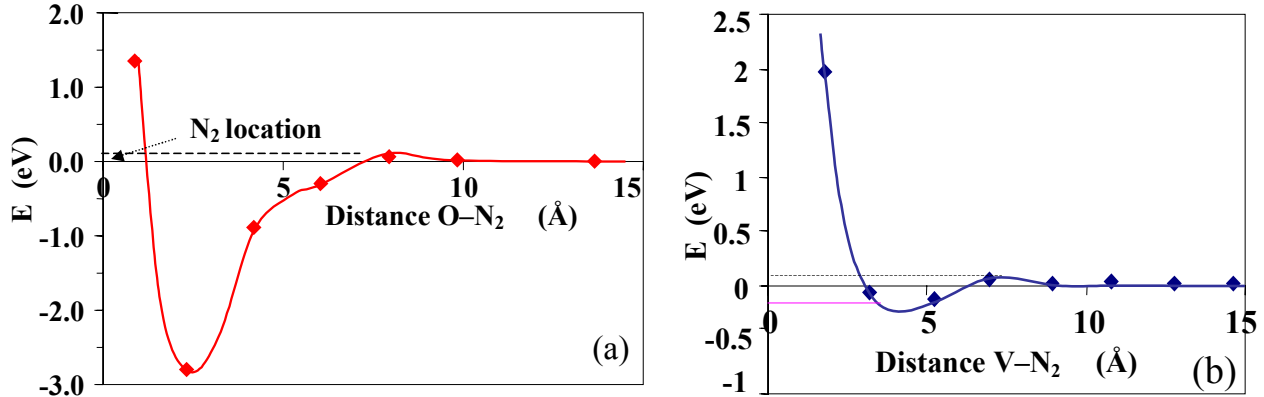


Fig. 2: Variation of the interaction potential energy of (a) O and N₂ (b) V and N₂, as a function of the separation distance point defect-complex.

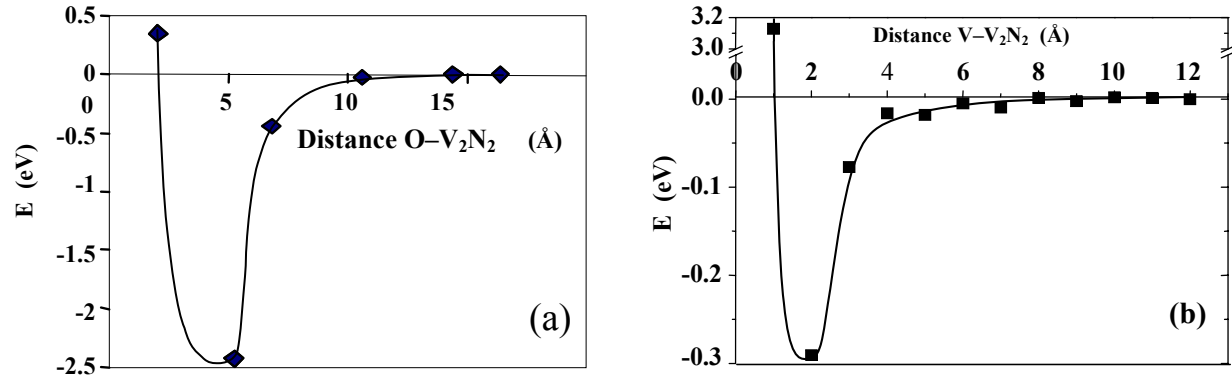


Fig. 3: Variation of the potential energy during (a) O, and (b) V migration towards a V₂N₂ defect.

We found that VN₂ complexes repulse oxygen atoms, see Fig 4; the potential energy reaches its maximum (+0.8 eV) when an O atom approaches the core defect, i.e. O sits on the Si-Si bond next to VN₂, which corresponds to that of oxygen in VN₂O. Therefore, the potential barrier of 0.8 eV for O adsorption by VN₂ is in agreement with the unstable character of VN₂O and VN₂O₂ obtained in the ground state by DFT calculations [18]. For the vacancy there is a very small potential of about -0.15 eV when the vacancy is located on the second neighboring lattice site to VN₂; however when the vacancy sits adjacent to VN₂ the potential well jumps to -7.3 eV inferring that V and VN₂ can reconstruct easily into the very stable and immobile V₂N₂ defect thus, effecting vacancy concentration. Further coupling with vacancies was found unlikely [19].

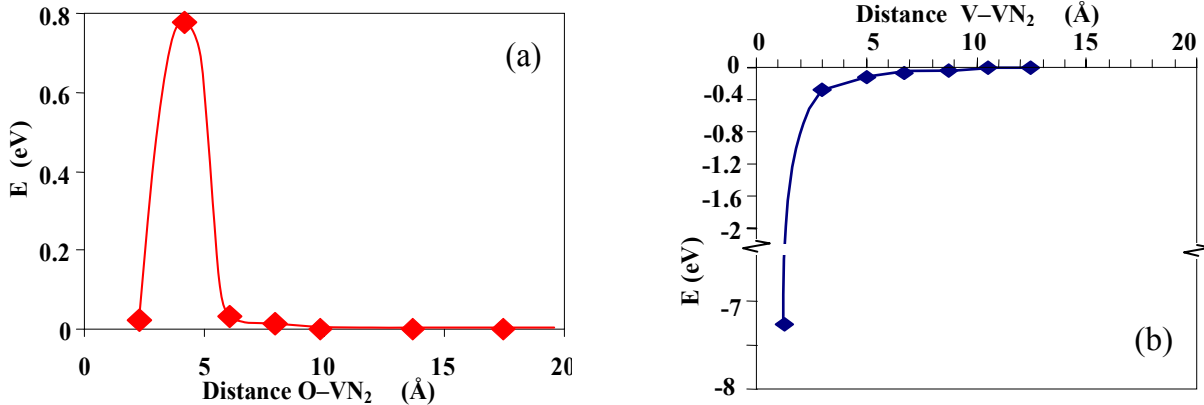


Fig. 4: Variation of the potential energy during (a) O and (b) V migration towards a VN₂ defect.

Conclusion

The calculated energies of formation of N-V complexes in the ground state show that V₂N₂ when formed from VN₂ is the most stable, followed by N₂ and V₂N₂ formed from a divacancy. VN₂ is less stable, but acts as an important intermediary species for the formation of the more stable N₂, V₂N₂ complexes, which subsequently dominate the nucleation and growth of extended defects. Our DFT and MM calculations showed that VN₂ would reconstruct easily to V₂N₂ when a vacancy is nearby. N₂ and V₂N₂ act as preferential nucleation centers for oxygen precipitation more than as an effective trapping center for vacancies explaining the dominance of SiO₂ precipitation over large void formation. It appears from our calculations that N₂ can also attract self-interstitial silicon thereby reducing A-defects in N-FZ Si.

References

- [1] T. Abe, T. Masui, H. Harada, J. Chikawa, Proc. of the Third International Symp. on Very Large Scale Integration Science and Technology, Eds., W.M.Bullis and S. Broydo, p. 543 (1985).
- [2] M. Tamatsuka, N. Kobayashi, S. Tobe; T. Masui, ECS PV. **99-1**, p. 456 (1999).
- [3] W. v. Ammon, P. Dreier, W. Hensel, U. Lambert, L. Koster, Mater. Sci. and Eng., **B36**, 33 (1996).
- [4] H. J. Stein, Mat. Res. Soc. Symp. Proc., Vol. **59**, p.523 (1986).
- [5] D. Yang, D. Que, K. Sumino, Stat. Sol. (B), **210**, 295 (1998).
- [6] P. Wagner, R. Oeder, W. Zulehner, Appl. Phys. A, **46**, 73-76 (1988).
- [7] A. Karoui, F. S. Karoui, A. Kvít, G.A. Rozgonyi, and D. Yang, Appl. Phys. Lett., **80**, 12, 2114(2002).
- [8] K. Nakamura , T. Saishoji, S. Togawa, J. Tomioka, Proceedings of Silicon Materials Science and Technology Forum '99, Kazusa Academia Park, p. 116 (1999).
- [9] W. v. Ammon et al., J. of Crystal Growth., **226**, 19, (2001).
- [10] H. J. Stein, J. Electrochem. Soc., **134**, 2592 (1987).
- [11] F. Quast, P. Pichler, H. Ryssel, R. Falster, ECS PV. **2000-17**, Eds., C. L. Claeys, P. Rai-Choudhury, M. Watnabe, P. Stallhofer, H. J. Dawson, p.156 (2000).
- [12] L. Shaik Adam et al., Appl. Phys. Lett., **79** (5), 623 (2001).
- [13] N. Fuma, K. Tashiro, K. Kakumoto and Y. Takano, Jpn. J. Appl. Phys., **35**, Pt. 1, 4A, 1993 (1996).
- [14] V. V. Voronkov and R. Falster, J. Electrochem. Soc., **149** (3), G167-G174 (2002).
- [15] A. Karoui, F. S. Karoui, G. A. Rozgonyi, M. Hourai, K. Sueoka, to appear in J. Electrochem. Soc.
- [16] A. Resende, ENDEASD report, 1 (1999).
- [17] T. Abe, Proc. of the Forum on the Science and Technology of Silicon Materials, Eds. H. Y. Kaneta, and K. Sumino, Shonan, Kanagawa, Japan 2001, p. 19 (2001).
- [18] F. Sahtout Karoui, A. Karoui, G. A. Rozgonyi, M. Hourai, K. Sueoka, to appear in Solid State Phenomena.
- [19] H.Kageshima and A.Taguchi, K.Wada, App. Phys. Lett., **76**, 25, 3718 (2000).

Modeling And Simulation of Dislocation Atmosphere Locking Effects in Silicon

A. Karoui,¹ G. A. Rozgonyi
Materials Science and Engineering Dept.
North Carolina State University, Raleigh, NC 27695-7916

Abstract

We present a theoretical study on edge dislocation locking by impurities in silicon. Three groups of impurities: (i) light atoms O, N, and C, (ii) large atoms Ga, Ge, and As, and (iii) small dopant atoms B, P, and Al are considered. Based on an impurity size effect model, these three groups will produce distinctively different dislocation locking effects. Atoms from the first group strongly bind with edge dislocations. In the second group, Ge can withstand only 1/3 of the separation stress that the first group can sustain. The third group has no shear stress resistance to dislocation separation. The dislocation atmosphere for O, N, and C are all similar with a slightly stronger occupancy probability for O and N in the vicinity of the dislocation core. Germanium has only a small chance to reach the dislocation core. Boron and P atoms can not be trapped at all by the dislocation. At a local atomic fraction of 10^{-4} , the impurity binding energy with an edge dislocation varies from 0.008 eV/Å for P to 1.7 eV/Å for N and 1.8 eV/Å for O. In addition, using molecular mechanics on system of 34552 atoms the self energy of an edge dislocation was calculated to be 156 meV/Å.

I. Introduction

Early work on the interaction of point defects with a stress field by Cottrell and Bilby¹ increased understanding phenomena such as material hardening,^{2,3} and subsequently gettering issues and electrical activities as explored by EBIC.⁴ We believe that for a clean dislocation fully reconstructed that the size-effect arising from volume mismatch due to impurity/host crystal atoms is the primary factor in the dislocation-impurity interactions. In this paper we are investigating the composition of edge dislocation atmosphere and the interaction energy due to the atomic size mismatch. We have varied the impurity type and the atomic fraction within the atmosphere. Large variations in the interactions of impurity-dislocations were observed and discussed.

II. Model Used for of Dislocation-Impurity interactions

In addition to the self-energy barrier for migration of a dislocation, the binding energy of foreign atoms (including dopants) to the dislocation must be considered when determining the activation energy for dislocation migration. The major part of this energy comes from the strain compensation by foreign atoms and includes "size interaction" and "shape deformation" terms. The size difference between silicon atoms and gettered atoms relieves stresses near the dislocations, thus reducing the overall energy of the system. The first order size effect elastic interaction between an edge dislocation and an impurity was first studied by Cottrell and Bilby¹ who considered that the point defect is a center of compression/dilatation in an isotropic continuum. The energy commonly referred to as the first order size effect elastic interaction was approximated by the expression¹ $E_{size} = \frac{\mu b(1+\nu)\Delta V \sin \theta}{3\pi(1-\nu)r}$, where ΔV is the change in the lattice volume caused by the

impurity, μ is the shear modulus of Si, ν the Poisson ratio, \mathbf{b} the dislocation Burger's vector (i.e, 3.84 Å for edge dislocation in silicon), and θ and \mathbf{r} the dopant coordinates in the dislocation referential.

Johnson⁵ in his analytical formalism described the interactions of defects with dislocations by decomposition of the defect displacement field in which one component bears the anisotropic elastic

¹ nas_karoui@ncsu.edu

deformation. For each displaced/deformed octahedral site, the interaction energy with the dislocation was reported in Ref.6. The probability of occupancy of individual sites was computed using Fermi-Dirac distribution.⁷ Occupancy for the i^{th} site is $R_i = \exp\left(-\frac{E_i}{kT}\right)$ where E_i is the interaction energy of that site with the dislocation.⁵ The probability of occupation of the i^{th} site by a given impurity atom is $P_i = \frac{R_i}{F + R_i}$. The parameter F is determined by the continuity equation given in Ref. 7. The sensitive issue related to the use of impurity Fermi-Dirac distribution, first introduced by Louat⁸ while arguing the Maxwell Botzmann distribution used by Cottrel et al.¹ The Fermi-Dirac distribution was debated by Besher⁹ and further clarified by Johnson.⁷

The occupation probability attached to the impurity distribution around dislocation depends on the concentration of dopants and the dislocation density. The range for fraction sites involved in making the atmosphere was chosen between 10^{-5} to 10^{-1} . Using the spatial distribution of the occupation probability, an atmosphere of dopant atoms near the dislocation line was constructed. Under stress the dislocation may migrate, if it can separate from the impurity atmosphere.

The major assumptions in the used model are (i) the atom added impurity occupies an interstitial position, i.e., the larger octahedral sites in FCC structure, and (ii) the atom shape deformation has a secondary effect. Concerning the dopant atoms, although they generally sit in substitutional positions in the defect free silicon crystal, this can not be assured within the dislocation atmosphere. Within the dislocation stress field the majority of impurities are also expected to occupy the larger octahedral sites (due to their high concentration), which is likely to justify the interstitial site assumption for dopants as well.

III. Results and Discussion:

1) Edge dislocation core

Molecular Dynamics is used to find the exact atomic structure of the core and to evaluate the self-energy of a clean dislocation at equilibrium. Two samples were constructed, with and without edge dislocation. The sample diameter is $\sim 144\text{\AA}$ and its thickness is $\sim 35\text{\AA}$. The atomic system comprises 29610 Si terminated with 4942 H atoms and a total of 56759 covalent single bonds. Figure1 shows the silicon sample with edge dislocation in its center; the crystal direction is $[110]$. Si atoms were left mobile and H atoms immobile during sample relaxation to better preserve the crystal symmetry. The numbers (5) and (7) point to the penta- and septa-rings, respectively. The difference in the total energy of the dislocated and the defect free samples provided a dislocation energy of formation of 156 meV/ \AA .

2) Impurity Distributions within the Dislocation Atmosphere

The used atomic sample is an atomic periodic structure; its unit cell contains 2961 Si atoms and has a cylindrical symmetry along the dislocation sense vector. The unit cell is made of two $(\bar{1}11)$ atomic planes. The sample radius, determined from the dislocation density, is half of the distance between two dislocations. For a density of $100 \text{ cm}/\text{cm}^3$ the unit cell radius is equal to 70\AA . In Fig.2 (a) nitrogen atoms appear to populate the dislocation core immediate surrounding with high probability of site occupation as compared to other elements (not shown). The penta-ring and one of the two upper hexa-rings, both in the compressive part of the dislocation domain, are the most likely zones for trapping light element atoms. The lower part of the septa-ring is unlikely to hold this type of atoms.

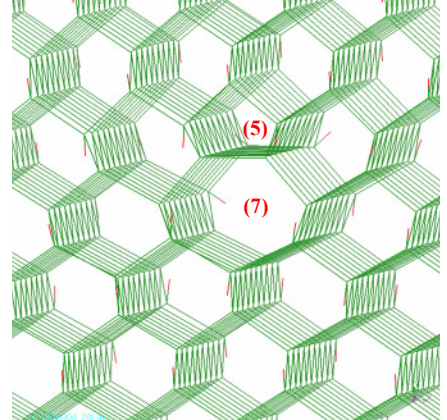


Fig. 1: Portion of the silicon sample used to determine the self-energy of an edge dislocated.

Oxygen, N and C locate themselves in tetrahedral positions in the top region (compressive side) of the dislocation. These two light elements have a preference for the penta-ring. Carbon was found to distributed in a more diffuse way than Nitrogen around the dislocation. Germanium has no preference for the penta-ring but a little for the septa-ring. Even though germanium locates itself preferentially in the dilated half space by the dislocation (bottom region), see Fig.2 (b), it does not populate the near field of the edge dislocation. This shows that Ge is way less effective in locking an edge dislocation than O, N, and C. It is important to note the differences in the trapping probability lead by O then N then C, while Ge is repelled. Oxygen is very likely to locate itself in the very core of the edge dislocation and its distribution spans over a cylinder of 7 neighbors radius. This behavior is slightly attenuated for N and little more attenuated for C. This leads to the conclusion that the three impurities play almost the same role for the atmosphere composition with slight reduction for N then C. In contrast, Ge totals only 1.1 site in the vicinity of the dislocation core and absent elsewhere.

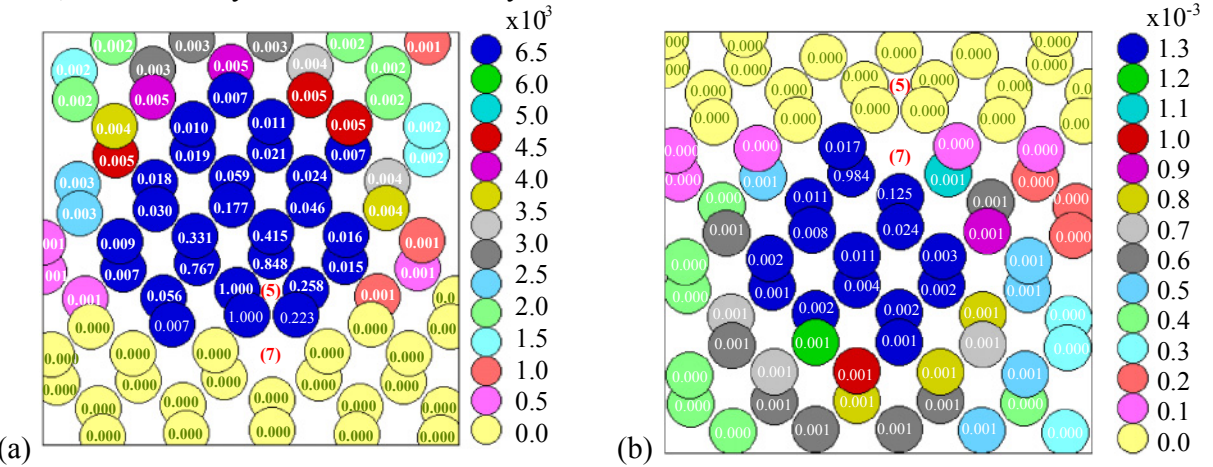


Fig.2: Impurity distribution at $x=10^{-4}$ and 300°K shown in $(\bar{1}\bar{1}0)$ plane of a 90° dislocation field for nitrogen (a), and germanium (b). Occupancy probability is written on the lattice sites. Note the large differences in the N and Ge occupancy probabilities and that N does not rest in the dilated region of the dislocation (bottom side) whereas Ge sits in that zone.

3) Impurity-dislocation binding energy and shear stress for dislocation separation

Impurity-dislocation interaction energies are given in Fig. 3 (a). The maximum magnitude represents the binding energy, given per dislocation unit length in Table I, for local impurity atomic fraction of 10^{-4} . Oxygen, nitrogen then Carbon appear to be distinctively well bound to dislocation, whereas for instance P and B and to lesser extent Ge do not attach themselves to the dislocation.

Table I: Dislocation-impurity binding energy of an edge dislocation with 10^{-4} nitrogen at $T=300\text{K}$.

	P	Ge	B	C	N	O
Binding Energy (eV/ \AA)	0.0077	0.338	1.19	1.54	1.66	1.80

The minimum shear stress required to separate the dislocation from its atmosphere is proportional to the maximum of the energy gradient given in¹⁰ as $\tau = \frac{1}{2\sqrt{2} b^2} \left(\frac{dE}{dx} \right)_{\max}$. The shear stress is proportional to the gradient of the impurity-dislocation interaction energy. It appears the highest for N then for O and C, see Fig. 3 (b), however no resistance to separation shear stress is shown by B and P impurities. Dislocation in presence of Ge can withstand only very small shear stress, since only 1.2 sites in the dislocation core vicinity can be occupied by Ge. Note the domain of 2.5 \AA in width around the dislocation equilibrium position, where no resistance to shear stress exists for dislocation movement. The domain width is smaller than the Burger's vector.

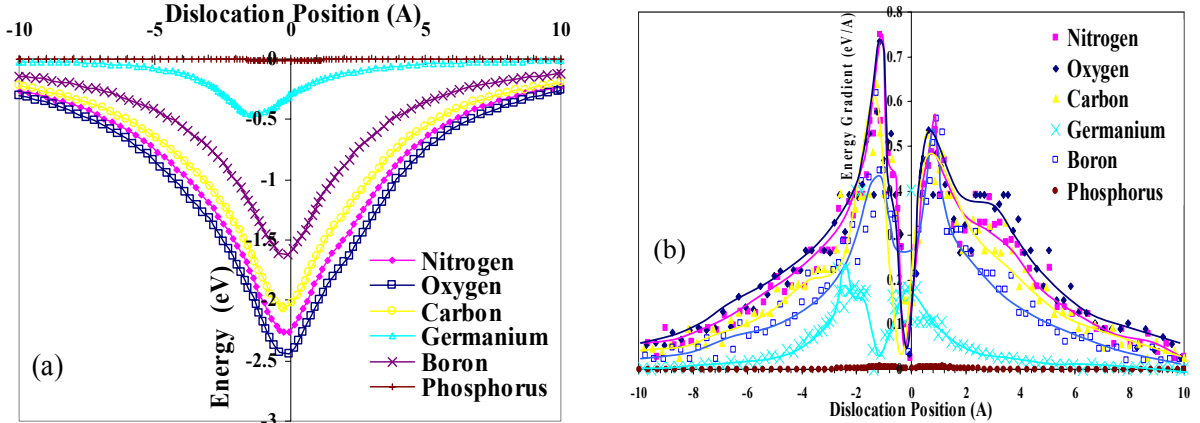


Fig. 3: (a) Impurity distributions in a 90° dislocation field at T=300°K (impurity content is 10^{-4}).
(b) Energy gradient (\sim shear stress) vs. separation distance dislocation-impurity atmosphere.

The relationship of impurity concentration and atmosphere formation was investigated for nitrogen only. The trend for the binding energy as a function of C_N , the N atomic fraction in the dislocation atmosphere, was found to be a power function that is: $E(\text{eV}) = 18.4 C_N^{0.22}$. This fitting does not account for the observed saturation beyond an atomic fraction of $x=10^{-2}$. We found for a nitrogen fraction of 10^{-3} , at 3.5 Å away from its equilibrium position, the dislocation must overcome a shear stress twice as high as for an atomic fraction of 10^{-5} , while it increases drastically (four times) for a concentration of 10^{-3} . The shear stress increases significantly and seems to have higher effects at concentrations between 0.1% and 1% in the vicinity of the dislocation, while it seems to saturate above 1%. This shows a limitation in the doping level for dislocation locking.

IV. Conclusion

Among the studied impurities O, N, and C, appear to locate themselves at the core of edge dislocations. These three impurities play slightly the same role for the atmosphere composition. They spread over a cylinder whose radius is about 7 neighbors (in the plane normal to the dislocation line). In contrast Ge is rarely gettered by edge dislocation since occupation of only 1.2 site is allowed. The penta-ring and the upper hexa-ring, both in the compressive part of the dislocation domain, are the most likely zones for oxygen atom localization; whereas the septa-ring which is in the dilation side of the dislocation (lower part) repels O atoms. Likewise N and C in tetrahedral interstitial positions locate themselves in the compressive side of the dislocation. It was found that carbon is distributed in a slightly more diffuse way than nitrogen and oxygen around the dislocation. The self-energy of a clean edge dislocation, calculated by molecular mechanics and found equal to 156 meV/Å, appeared one order smaller than the size effect of trapped N, O, and C impurities. Our calculations lead to an empirical relation of the binding energy of N with an edge dislocation as a function of the atomic fraction within the dislocation atmosphere.

References

- [1] A. H. Cottrel and B.A.Bilby Proc. Phys. Soc. A, **62**, 49 (1949).
- [2] A. w. Cochardt, Acta Metall. 3, (1955)
- [3] D. M. Barnett and W. D. Nix, Acta Metall. 2, (1955).
- [4] D. Cavalcoli, A. Cavallini, E. Gombia: Phys. Rev. B **56** (1997) 10208.
- [5] R. A. Johnson, J. Appl. Phys., **50**, 1263 (1979).
- [6] A. S. Nandedkar, and R.A.Johnson, Acta Metall. 30, 2055 (1982).
- [7] R. A. Johnson, Phys. Rev. B, **24** (12), 7383 (1981).
- [8] N. Louat, Proc. Phys. Soc. **50**, 1263 (1979).
- [9] D. N. Beshers, Acta Metall. **6**, 521 (1958).
- [10] A. S. Nandedkar and R. A. Johnson Acta Metall. **30**, 2055 (1982).

Development of an Infrared Residual Stress Polariscopic for Solar Cell Inspection

S. He and S. Danyluk

Georgia Institute of Technology

The George W. Woodruff School of Mechanical Engineering

Atlanta, Georgia 30332-0405

J. Tarasko, S. Lulu, A. Belyaev and S. Ostapenko

University of South Florida

Department of Mechanical Engineering

Tampa, Florida 33620

Abstract

Two complementary IR polariscope systems, full-field circularly polarized and scanning linearly polarized, have been developed, calibrated, compared and applied to CZ, cast, EFG and string ribbon sheet silicon in the as received, cleaned and phosphorous diffusion steps of PV cell processing. The techniques are non-contact and robust and correlate with surface photovoltaic and lifetime measurements.

Introduction

There are a number of ways to produce sheet silicon as a substrate for PV cells. Methods include the growth of boules and castings that are then wire sawn or wafered into sheet, and direct growth of sheet by the edge-defined film growth (EFG) or string processes. The boules, castings and sheet are believed to contain residual stresses because of the thermal gradients in the solidification process, and sawing, laser dicing and cell processing further cause the redistribution of the residual stresses. When the sheet is cut out of bulk material or when the sheet is prepared into blanks, warpage can occur as a result of out-of-plane residual stresses. However flat sheet can contain in-plane stresses which are not easily detected and which may contribute to fracture in subsequent processing of the ribbon into cells.

The perimeter of the sheet, and in some cases the front and back surfaces, may also contain micro-cracks which, because of the cutting and shaping operations, will eventually propagate and fracture the cell if they fall in the region of tensile residual stresses or if tensile stresses are created due to handling.

Besides fracture, residual stresses can also generate and propagate dislocations and it is believed that this will eventually impact electron-hole lifetimes and the efficiencies of PV cells. As sheet becomes thinner, the grown-in residual stresses, coupled with the stresses imposed during manufacturing, can become a significant problem in the yield of cells. There has been a significant effort in the past to develop non-contact techniques that expose the in-plane residual stresses[1] but none of this work is of sufficient robustness or sensitivity for implementation in the manufacturing of PV cells.

Our work is focused on developing a robust, non-contact (optical) method to determine the stress distribution in the sheet silicon, validate the technique in a statistically significant set of experiments and apply the techniques to PV sheets at various stages of cell processing so that the evolution of the stress distribution can be understood and perhaps optimized. This paper summarizes some of this work.

Experimental Methods

These are two optical methods that are being developed to measure the in-plane residual stresses in sheet silicon. Both methods use a white light source to generate near infrared (NIR) wavelengths and to examine the transmitted intensity of the NIR through the sheet silicon samples. Figure 1 shows a schematic diagram of a "full-field" infrared polariscope[2,3] where the silicon sample is irradiated with a collimated, circularly polarized light source. The quarter waveplate and the analyzer are used for phase stepping and the beam splitters are used to pass the light beams multiple times through the sample to increase the transmitted light intensity and the resolution (fringe multiplication). This technique requires approximately 30 seconds to image a sample, including image capturing and data processing. The sensitivity is approximately 1 MPa, and the spatial resolution is 1 mm. The details of the setup will not be discussed here but is available in other publications[4].

The second method involves the scanning of a focused light beam (60 μm in diameter) over a silicon sheet and the detection of the transmitted NIR radiation[5]. Figure 2 shows a schematic diagram of the experimental setup. The light source is collimated, polarized and focused, then the light "spot" scans the silicon sheet and the transmitted light is detected. The spatial resolution of this technique is determined by the dimension of the light spot, which is of the order of 60 μm . This technique has a substantially better spatial resolution than the full-field polariscope, but the scanning substantially increases the length of time to detect the transmitted light beam. It takes about 5 hours to image a sample with a dimension of 4 x 4 in.

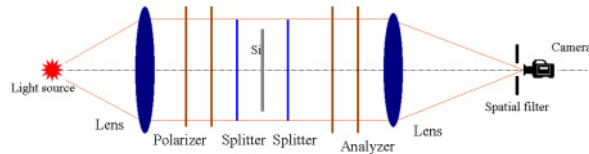


Figure 1. Schematic Diagram of the Circularly Polarizing Full Field Infrared Polariscope

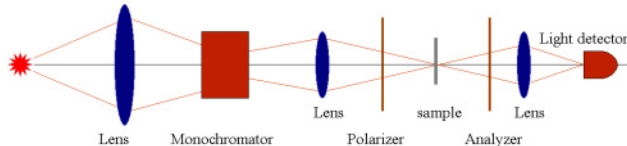


Figure 2. Schematic Diagram of a Scanning Linearly Polarizing Infrared Polariscope

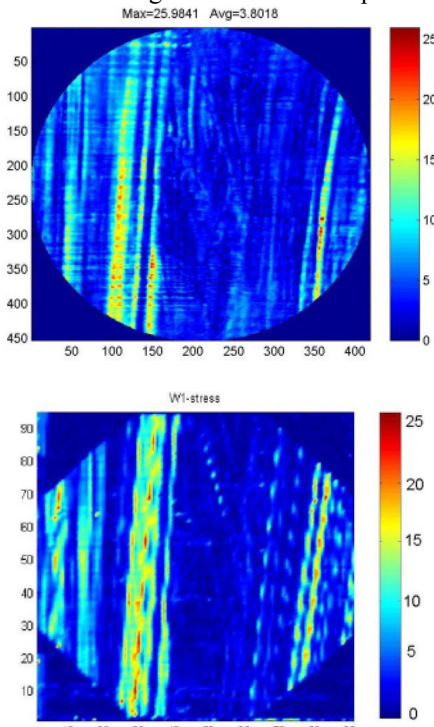


Figure 3. Residual stress distributions obtained by the full field (a) and scanning polariscope (b) in a typical EFG wafer.

Typical Residual Stress Distributions in EFG and Cast Sheet

Typical residual stress maps of EFG and cast sheet obtained by the two techniques are shown in Figure 3. This figure shows the stresses in the same central portion of a 4 x 4 EFG and cast “wafer”. The overall dimension of the images is approximately 80 mm in diameter but the edges of these images does not represent the actual edges of the wafers. The images show a good correspondence of stress magnitudes with a maximum of 26 MPa and an average of 3.8 MPa for the EFG wafers, and maximum of 15 MPa and an average of 3 MPa for the cast wafers.

Photoluminescence and Lifetime Measurements

Photoluminescence (PL) and Surface Photovoltage (SPV) measurements have also been used to examine the samples. Figure 4 shows an example of the PL and SPV results for the same wafers whose residual stress data is shown in Figure 3. The surface photovoltaic results are related to dislocations and the PL to minority carrier lifetimes, both impacting the efficiency of photovoltaic cells because of the recombination properties of these materials. It is seen that high lifetime regions generally correspond to high stress areas of the wafers.

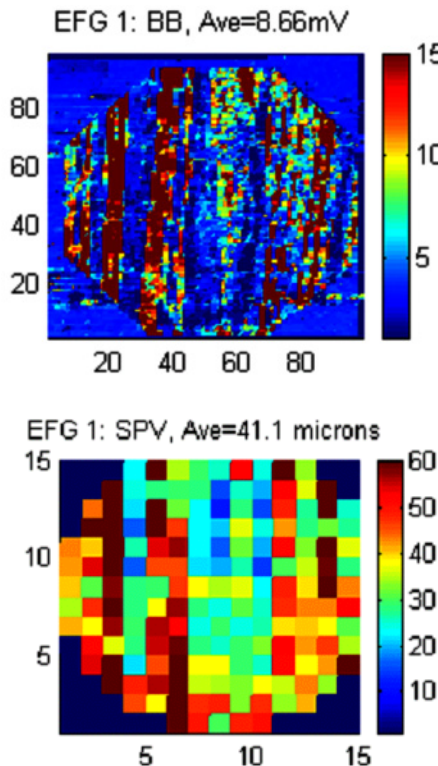


Figure 4. PL (a) and SPV (b) images of the same EFG wafer shown in Figure 3

In-Plane Residual Stresses, Measurements of Wafers at Various Stages of Processing

The two polariscope techniques are being applied to a series of wafers obtained from four industrial partners: RWE Schott, Evergreen Solar, BP Solar and EBARA Solar, and the wafers are being processed at the Georgia Tech University Center of Excellence for Photovoltaic Research (UCEP). Measurements are made on wafers which are then shipped between the two universities. The process steps are shown in Figure 5. Results to-date have been obtained for the bare wafers, after cleaning and etching and after phosphorus diffusion. The results are shown in Table I for cast, Cz, EFG and String Ribbon wafers. It should be noted that the thickness of the wafers varies as shown in the Table and the in-plane residual stresses are reported as the “Maximum” and “Average” for the field of view of the 80 mm diameter image shown in Figure 3.

As can be seen in Table 1, there is a significant difference in the residual stress for the cast, CZ and string ribbon samples in some cases varying a factor of two. The residual stresses of the EFG wafers do not seem to vary with these processing steps.

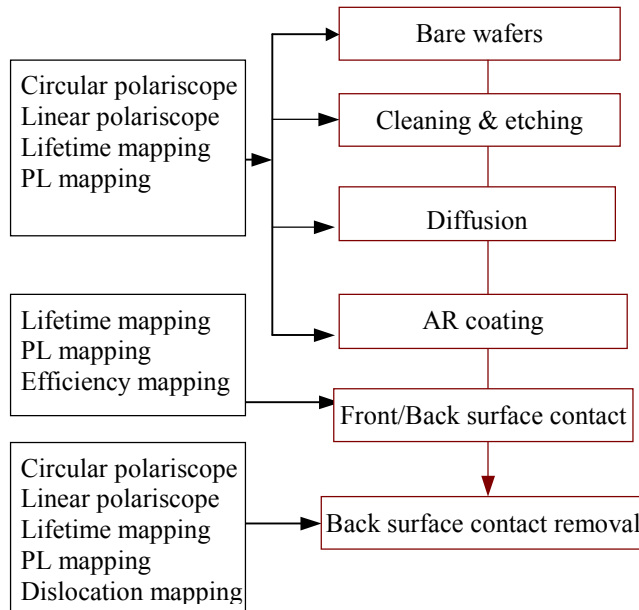


Figure 5. Process Steps for PV cell manufacturing done at UCEP.

Conclusions

There has been significant progress in the development of mechanical and optical design of the two polariscopes. The systems are robust and the results from the two correlate. The full-field polariscope has a spatial resolution of 1 mm and can produce images in less than 1 minute. The scanning system has spatial resolution of the order of 60 μm . Surface photovoltage and photoluminescence measurement appear to correlate to the residual stress measurements. The measurements of the etching and phosphorous diffusion show significant difference in the CZ, cast and string ribbon samples.

Acknowledgements

This project is supported by NREL under contract #AAT 2-3165-06. The authors would like to thank Dr. Bobby McConnell at NREL, and Drs. Rohatgi and Upadhyaya at Georgia Tech for their support of this work.

References

1. A. K. Dutta, P. K. Ajmera, "Simulation and observation of the images of dislocations in (100) silicon using infrared piezo-birefringence," *J. Appl. Phys.*, vol. 69, no. 11, Jun 1991
2. T. Zheng and S. Danyluk, "Nondestructive measurement of in plane residual stress in thin silicon substrates by infrared transmission", *Matl. Evaluation*, vol 50, no 10, Oct 2001, pp1227-1233.
3. T. Zheng and S. Danyluk, "Study of stresses in thin silicon wafers with near-infrared phase stepping

photoelasticity", *J. Mater. Res.*, vol 17, no. 1, Jan 2002, pp 36-42.

4. S. He and S. Danyluk, "Residual Stress Characterization for Solar Cells by Infrared Polariscopy", National Center for Photovoltaics and Solar Program Review Meeting, Denver Colorado, 2003.
5. S. Ostapenko, I. Tarasov, J. Kalejs, C. Heissler and E-U. Reisner, "Defect monitoring using scanning photoluminescence spectroscopy in multi-crystalline silicon wafers," *Semicond. Sci. Technol.*, 15 (2000) 840–848.

Table 1. Residual stress (full-field) in silicon sheet (MPa)

Thickness	Maximum		Average				
	Bare	Etched	Diffused	Bare	Etched	Diffused	
Cast wafers							
1	0.326	11.79	9.07	8.09	2.67	1.34	1.62
2	0.325	12.96	5.64	7.55	2.69	1.17	1.57
3	0.325	16.03	8.15	8.77	3.32	1.31	1.61
4	0.326	14.84	6.75	7.43	3.18	1.27	1.60
5	0.328	12.45	6.54	7.31	2.34	1.26	1.60
6	0.327	10.89	6.56	8.32	2.65	1.26	1.49
7	0.326	11.67	6.91	6.34	2.75	1.25	1.40
8	0.328	14.11	9.30	9.80	3.97	1.67	1.77
9	0.325	16.67	7.09	6.87	2.46	1.52	1.49
10	0.346	10.19	7.57	9.39	2.15	1.66	1.75
CZ wafers							
1	0.319	23.84	6.82	8.79	4.68	1.52	1.62
2	0.322	18.87	6.86	8.08	4.52	1.09	1.51
3	0.321	18.23	7.76	7.13	4.73	1.94	1.26
EFG wafers							
1	0.260	25.98	33.26	30.32	3.82	5.53	5.06
2	0.305	12.12	22.60	25.25	2.24	4.05	3.73
3	0.256	18.95	23.45	25.34	3.28	4.74	4.78
4	0.240	22.75	35.45	27.88	3.50	5.98	4.67
5	0.265	17.36	31.37	18.54	2.19	4.02	2.43
6	0.279	20.69	27.15	42.25	2.63	5.05	5.03
8	0.258	23.42	29.99	33.67	3.52	6.20	4.85
9	0.291	17.58	19.92	27.22	2.43	4.20	3.93
10	0.280	23.53	34.14	27.58	3.69	5.89	6.45
String Ribbon samples							
1	0.276	21.00	35.19	23.43	4.39	8.61	6.00
2	0.296	19.47	28.31	19.91	3.91	7.46	5.40
3	0.281	32.49	33.75	25.32	4.91	7.80	4.79
4	0.288	28.84	39.94	24.26	4.98	8.93	4.72
5	0.302	14.65	39.97	29.20	3.52	4.39	4.22
6	0.326	27.38	22.71	21.22	4.90	4.97	4.47
7	0.269	28.58	32.19	33.50	4.04	9.50	5.86
8	0.288	30.57	42.51	26.81	4.87	8.15	4.74
9	0.277	20.65	33.79	23.75	4.27	6.76	5.80
10	0.280	19.90	29.96	18.39	4.07	6.30	4.90

Error Analysis of a Circularly Polarized Phase-stepping Polariscope

Shijiang He, Tieyu Zheng, Steven Danyluk

The George W. Woodruff School of Mechanical Engineering

Georgia Institute of Technology

Abstract

This paper summarizes the analysis of the systematic and random errors in a circularly polarized phase-stepping polariscope. The sources of error considered in this paper consist of the misalignment of the optical elements and the image digitization. The results show that the error in the magnitude of stresses is around 1.0 MPa for a typical photovoltaic wafer with a thickness of 300 μm , and the error in the digitization can be ignored.

Key words: polarscope, phase-stepping, error analysis, digital

Introduction

A polarscope is used to obtain the stresses in a transparent solid by detecting fringes caused by the stress-induced birefringence[1]. Since silicon is transparent to infrared light with a wavelength above 1100nm, we have developed a polarscope that uses an IR light source[2,3,4]. The stress sensitivity of the polarscope has been enhanced by phase stepping, that boosts the accuracy by 0.01~0.05 fringe orders, and which is 10 times more accurate than the conventional fringe counting methods[5].

Traditionally, the polarscope is used for a specimen with a thickness of the order of millimeters, where multiple fringes are observed, and the phase is unwrapped to remove the phase discontinuity. The error, which is of the order of a fractional fringe, is negligible compared with multiple fringes. However, for a typical photovoltaic silicon wafer with a thickness of less than 300 μm , only a partial fringe can be observed, and the error analysis is therefore crucial to determining the system sensitivity and validating of measurement.

The errors associated with wavelength mismatch and nominal inclination have been analyzed by Patterson [6,7]. His results show that the maximum error is of the order of 0.012 fringe order. The wavelength mismatch is negligible for the infrared polarscope because a narrow bandwidth filter is used to obtain the monochromatic light with a bandwidth of 10nm. The wavelength mismatch is therefore not considered in this paper. The main sources considered in this paper are the angular misalignment of the two waveplates and the two polarizers, and the image digitization.

Theory of light propagation in Polariscope

As shown in Figure 1, the near infrared (NIR) polarscope consists of a narrow band filter, two polarizers, two waveplates, two lenses and a digital camera. The light propagation in a polarscope consisting of these components shown in Figure 1 can be described by the Stokes vector and Muller matrix[8]. For white light illumination with no polarization, the Stokes vector \mathbf{S} is given as,

$$\mathbf{S} = [1 \ 0 \ 0 \ 0]^T \quad (1)$$

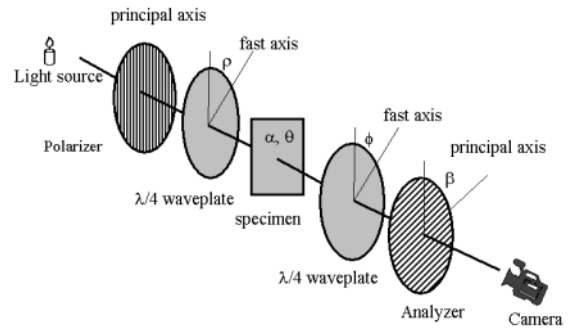


Figure 1. The experimental setup for testing the circular polarized light

where T represents the matrix transpose. An ideal linear polarizer is described by the matrix $\mathbf{P}(\beta)$, where β is the angle between the principal axis of the polarizer and the reference axis.

$$\mathbf{P}(\beta) = \begin{bmatrix} 1 & \cos 2\beta & \sin 2\beta & 0 \\ \cos 2\beta & \cos^2 2\beta & \sin 2\beta \cos 2\beta & 0 \\ \sin 2\beta & \sin 2\beta \cos 2\beta & \sin^2 2\beta & 0 \\ 0 & 0 & 0 & 0 \end{bmatrix} \quad (2)$$

The specimen and quarter waveplates can be considered as phase retarders, and described by a Muller matrix

$$\mathbf{M}(\theta, \alpha) = \begin{bmatrix} 1 & 0 & 0 & 0 \\ 0 & \cos^2 2\theta + \sin^2 2\theta \cos \alpha & (1 - \cos \alpha) \sin 2\theta \cos 2\theta & \sin 2\theta \sin \alpha \\ 0 & (1 - \cos \alpha) \sin 2\theta \cos 2\theta & \sin^2 2\theta + \cos^2 2\theta \cos \alpha & -\cos 2\theta \sin \alpha \\ 0 & -\sin 2\theta \sin \alpha & \cos 2\theta \sin \alpha & \cos \alpha \end{bmatrix} \quad (3)$$

where β is defined above, and α is the retardation. For an ideal quarter waveplate, $\alpha = \pi/2$. A circular polarscope can be analyzed by the concatenation of Muller matrices.

$$\mathbf{S} = \mathbf{S}_m + \mathbf{P}(\beta) \mathbf{M}\left(\phi, \frac{\pi}{2}\right) \mathbf{M}(\theta, \alpha) \mathbf{M}\left(\rho, \frac{\pi}{2}\right) \mathbf{P}(0) \mathbf{S}_0 \quad (4)$$

where $\mathbf{S}_m = [m, 0, 0, 0]^T$ accounts for the background light. $\mathbf{P}(0)$ and $\mathbf{P}(\beta)$ are the polarizer and analyzer respectively.

$\mathbf{M}(\rho, \pi/2)$, $\mathbf{M}(\theta, \alpha)$, $\mathbf{M}(\phi, \pi/2)$ are the Muller matrices of the three retarders, the first waveplate, the specimen and the second waveplate respectively. There are four unknowns in equation (4): the photoelastic parameters of the specimen α , θ and input light \mathbf{S}_0 and environmental light \mathbf{S}_m . So at least four equations are needed to solve for the photoelastic parameters. A commonly used technique is the six-step phase-stepping proposed by Peterson and Wang[4], which provides six independent equations. The orientations of the optical elements and the corresponding output light intensities are given in Table 1.

Table 1 Relation between the optical element angles and the transmitted intensities in phase-stepping

β	ϕ	Light intensity
$\pi/4$	0	$I_1 = I_m + I_a(1 + \cos \alpha)/2$
$-\pi/4$	0	$I_2 = I_m + I_a(1 - \cos \alpha)/2$
0	0	$I_3 = I_m + I_a(1 - \sin 2\theta \sin \alpha)/2$
$\pi/4$	$\pi/4$	$I_4 = I_m + I_a(1 + \cos 2\theta \sin \alpha)/2$
$\pi/2$	$\pi/2$	$I_5 = I_m + I_a(1 + \sin 2\theta \sin \alpha)/2$
$3\pi/4$	$3\pi/4$	$I_6 = I_m + I_a(1 - \cos 2\theta \sin \alpha)/2$

The sequence of simultaneous equations is solved for the relative retardation α and the isoclinic angle θ , where

$$\theta = a \tan 2(I_5 - I_3, I_4 - I_6)/2 \quad (5)$$

and

$$\alpha = a \tan^{-1} \left[\sqrt{(I_4 - I_6)^2 + (I_5 - I_3)^2} / (I_1 - I_2) \right] \quad (6)$$

It is worth pointing out that we use the function *atan2* instead of *atan* in Matlab because this function gives θ in the range of $-\pi/2$ to $\pi/2$, which means compressive and tensile stress can be distinguished.

Error Analysis

There are mainly two types of error in photo-stepping photoelasticity, namely those associated with the optical elements and those associated with the image process devices such as the camera, the CCD array and the image digitization.

Angular misalignment of the two waveplates and polarizers is the most dominant error associated with these optical elements. In the following analysis, both systematic and random errors will be analyzed. For the purposes of this paper, the angular misalignment is assumed to be one degree.

1. Error in the first waveplate

The first polarizer and waveplate pair is used to generate the circularly polarized light beam, and the misalignment of these two will generate elliptically polarized light. The setup shown in Figure 2 is used to check the quality of

the polarization. The setup can be described by the matrices.

$$\mathbf{I} = \mathbf{P}(\alpha) \mathbf{R}(\theta, \pi/2) \mathbf{P}(0) \mathbf{S}_0 \quad (7)$$

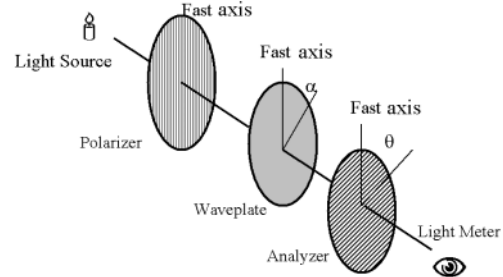


Figure 2. The experiment setup for test the quarter waveplate

where \mathbf{I} is the Stock vector of the transmitted light. Assuming that the angular misalignment is $\Delta\theta$, then $\theta = \pi/4 + \Delta\theta$, so that the light intensity detected is given by

$$I = 1 + \frac{1}{2} [\cos(2\theta) - \cos(2\theta + 4\Delta\theta)] \approx 1 + 2\Delta\theta \sin \theta \quad (8)$$

For a small misalignment, the transmitted light can be approximated by a Taylor expansion as shown in Equation 8. The light is circularly polarized or constant when $\Delta\theta = 0$. The circular polarization is totally destroyed if the misalignment reaches six degrees. This test can also be used to fix the systematic misalignment.

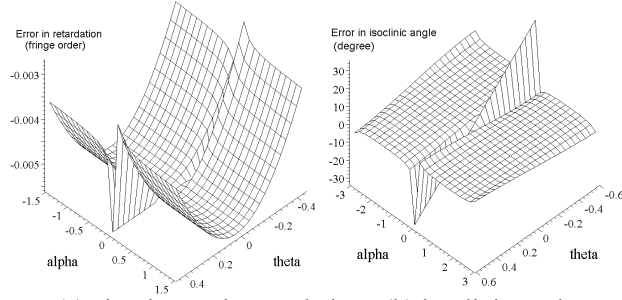
There is only one systematic error in the first quarter waveplate because it is fixed during phase stepping. The error of the misalignment can be analyzed by introducing a offset $\Delta\rho$, usually one degree, into the angular position ρ in Equation 4. The analysis is too complicated to be handled manually, and the software Maple is used to deal with the complexity. In this case the transmitted light is given by

$$\mathbf{S}_i = \mathbf{P}(\beta_i) \mathbf{M}\left(\phi_i, \frac{\pi}{2}\right) \mathbf{M}(\theta, \alpha) \mathbf{M}\left(\frac{\pi}{4} + \Delta\rho, \frac{\pi}{2}\right) \mathbf{P}(0) \mathbf{S}_0 \quad (9)$$

where ϕ_i, β_i ($i = 1..6$) are the six positions defined in Table 1. The above equations are substituted in Equations (5,6) and the photoelastic parameters are obtained. As shown in Figure 4, the error is a function of the photoelastic parameters. The isoclinic angle exhibits negligible error except in the undefined regions where the fringe order is integral. In these regions, the isoclinic angle will oscillate between $-\pi/2$ and $\pi/2$, which may introduce ambiguity in phase unwrapping. This is not a problem for the measurement of in-plane residual stress in silicon because of the low stress levels.

The maximum error in the isochromatic retardation is about 0.04 fringe/degree, or 0.4 MPa/degree for a typical wafer. This value reaches its maximum when $\theta = 0, \pi/2$,

and remains almost constant with the variance of real retardation. This misalignment will shift the stress vertically in the four-point bending experiment since it has a constant isoclinic angle.



(a) isochromatic retardation (b) isoclinic angle
Figure 3. Error in misalignment of the first quarter waveplate of 1 degree.

2. Error in the second waveplate

Unlike the first waveplate, both systematic and random errors are present in the misalignment of the second waveplate. The systematic error is derived in the same way as the first. The analytical expression can also be obtained by a Taylor expansion. The error in the retardation is given as

$$\Delta\alpha = 2\Delta \sin(2\theta) \sin^2 \alpha \quad (10)$$

The distribution is shown in Figure 4. The systematic error in the isoclinic angle of the second waveplate is constant and equals the amount of misalignment, $\Delta\theta$.

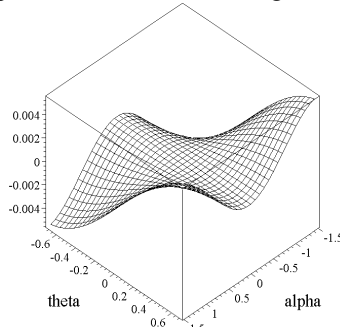


Figure 4. The systematic error in retardation due to the misalignment of the second quarter waveplate. The error in isoclinic angle is constant.

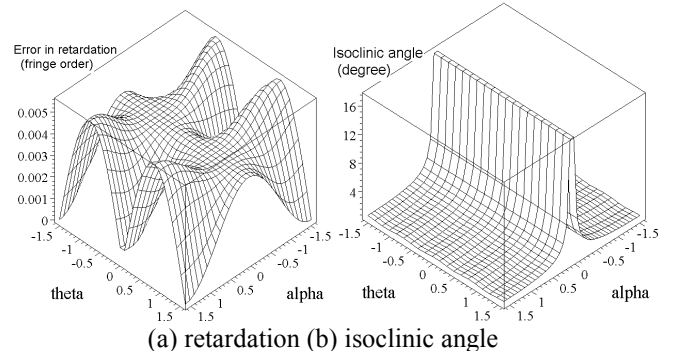
The random error can be analyzed in the same way. The difference is that the misalignments are different in each step of the phase stepping, so the light intensities of the six images are given by

$$\mathbf{S}_i = \mathbf{P}(\beta_i) \mathbf{M}\left(\phi_i + \Delta\phi_i, \frac{\pi}{2}\right) \mathbf{M}(\theta, \alpha) \mathbf{M}\left(\frac{\pi}{4}, \frac{\pi}{2}\right) \mathbf{P}(0) \mathbf{S}_0 \quad (11)$$

The errors of the isoclinic angle and the isochromatic retardation can be obtained through the theory of error propagation.

$$\Delta\alpha = \sqrt{\sum_{i=1}^6 \left(\frac{\partial\alpha}{\partial\phi_i} \Delta\phi_i \right)^2}, \quad \Delta\theta = \sqrt{\sum_{i=1}^6 \left(\frac{\partial\theta}{\partial\phi_i} \Delta\phi_i \right)^2} \quad (12)$$

The random error can be obtained by substituting Equation (11) into the Equation (12). For simplicity, the maximum uncertainty in the alignment is assumed to be one degree. It is worth pointing out that there are only three rotations of the second waveplate. Figure 4 and 5 show the distribution of the systematic and random errors respectively. Again, it is found that the error in the isoclinic angle is small except in the undefined regions which are an artifact of the software used in the calculation. On the other hand, the random error in the isochromatic retardation reaches its maximum in the undefined region, while the systematic error is zero.

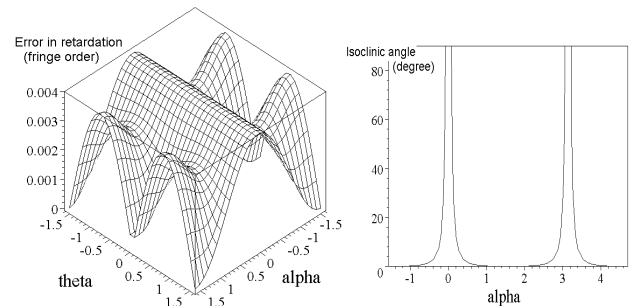


(a) retardation (b) isoclinic angle
Figure 5. The random error due to the misalignment of the analyzer.

3. Error in the analyzer

The error due to the analyzer also contains two parts: a systematic error and a random error. These are analyzed exactly in the same way as the second waveplate.

The systematic error in the retardation is the same as that of the second waveplate shown in Figure 4, but there is no systematic error in the isoclinic angle. As shown in Figure 6, the random error in the isochromatic parameter is close to that of the second waveplate, but it is not exactly the same. The maximum error is a little larger than that caused by the second waveplate.



(a) retardation (fringe) (b) isoclinic angle (degree)
Figure 6. The random error due to the misalignment of the analyzer.

4. Error in the image digitization

In phase-stepping, the images are captured by a CCD camera and then converted to digital signals. The main sources of error in the digital image are electronic noise and digitization error. The electronic noise can be reduced by averaging multiple images, our work normally averages over thirty images. The digitization error usually is considered to be one gray level. The error in the photoelastic parameters can be expressed as

$$\Delta\alpha = \sqrt{\sum_{j=1}^6 \left(\frac{\partial\alpha}{\partial I_j} dI_j \right)^2}, \quad \Delta\theta = \sqrt{\sum_{j=1}^6 \left(\frac{\partial\theta}{\partial I_j} dI_j \right)^2} \quad (13)$$

The intensities of phase-stepping are given in Table 1. By substituting the light intensities into Equation (13), the errors can be obtained as

$$\Delta\alpha = 1/\sqrt{2}I_a \quad \text{and} \quad \Delta\theta = 1/2\sqrt{2}I_a \sin\alpha \quad (14)$$

where $I_a = \sqrt{(I_1 - I_2)^2 + (I_4 - I_6)^2 + (I_5 - I_3)^2}/2$ is the effective contrast of the images. As shown in Equation 14, both errors are inversely proportional to the effective contrast. For a typical measurement, the range of I_a is between 20 to 35, which means the error of retardation is between 0.03 and 0.05 of a fringe order, or 0.3 MPa to 0.5 MPa. The error of the isoclinic parameter is still small except in the undefined regions.

In the six-step phase-stepping, the effective contrast is dominated by the first two images: the bright field and the dark field. A 8 bit digital camera has 255 gray levels. The background light I_m consumes the space of gray levels and does not leave enough space for image contrast. To reduce the error, the contamination of background light can be reduced and the bright field enhanced to some maximum limit set by the experimental conditions of the setup.

5. Combined error in the system

The sources of error considered here consist of: the angular misalignment of the two waveplates and the polarizer, the wavelength mismatch of the two waveplates, and the digitization error. The combined error is the sum of these errors as is known from the theory of error propagation. As shown in Figure 7(a), the maximum error in stress is approximately 1.0 MPa. The two peaks in this figure again show the location and instability in the undefined regions. The combined error in isoclinic angle shown in Figure 7(b) is negligible except in the undefined regions.

Conclusions

The systematic and random errors caused by the angular misalignment of the two waveplates, the analyzer and the image digitization in a phase-stepping polariscope are

analyzed. In all these cases, the error in the isoclinic angle can be ignored except in the undefined regions. The error in the phase retardation varies with the real photoelastic parameters, and the maximum error caused by all these sources combined is approximately 1 MPa.

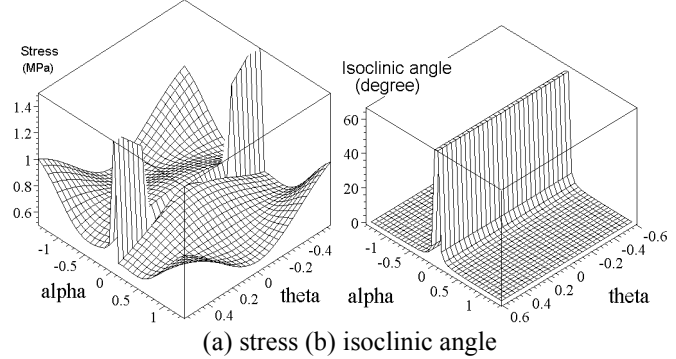


Figure 7. The combined error due to the misalignment of all optical elements

Acknowledgments

This research was partially supported with funds from the NREL; contract #AAT 2-3165-06. Thanks go to Robert McConnell for support of this work.

References

1. K. Ramesh, "Digital photoelasticity advanced techniques and applications", Springer-Verlag, New York, 2000.
2. S. He and S. Danyluk, "Residual Stress Characterization for Solar Cells by Infrared Polarimetry", National Center for Photovoltaics and Solar Program Review Meeting, Denver Colorado, 2003.
3. T. Zheng and S. Danyluk, "Nondestructive measurement of in plane residual stress in thin silicon substrates by infrared transmission", Matl. Evaluation, vol 50, no 10, Oct 2001, pp1227-1233.
4. T. Zheng and S. Danyluk, "Study of stresses in thin silicon wafers with near-infrared phase stepping photoelasticity", J. Mater. Res., vol 17, no. 1, Jan 2002, pp 36-42.
5. A. Ajovalasit, S. Barone, G. A. Petrucci, "A review of automated methods for the collection and analysis of photoelastic data", J. Strain Anal Eng Des. Vol 33, 1998, pp. 75-91.
6. W. Ji and E. A. Patterson, "Simulation of errors in automated photoelasticity", Exptl. Mech., vol. 38, no. 2. 1998, pp.132-139.
7. E. A. Patterson, W. Ji and Z. F. Wang, "On image analysis for birefringence measurements in photoelasticity", Optics and Lasers in Engineering, vol. 28, 1997, pp. 17-36.
8. P. S. Theocaris, "Matrix theory of photoelasticity", Springer-Verlag, New York, 1979.

PV Feedstock Costs—Five Year Outlook
Jan Maurits
Solar Grade Silicon, LLC

Polysilicon Supply and Demand

In 1998, the polysilicon industry was responding to rapidly increasing demand from the semiconductor industry, building new plants and expanding production facilities¹. This anticipated demand did not develop, with only 15,900 tons shipped in 1998 (Table 1). The downturn in the semiconductor industry continued through 2001 with slow recovery. In response, the poly suppliers cut back on expansion plans and operated at reduced volumes to match semiconductor demand. Installed capacity for the next five years, from 2003, is forecast in Table 1. Consensus of the semiconductor forecasting services is for semiconductor recovery in 2003-2004². Table 1 assumes an average growth in semiconductor-grade poly at 10% per year to 26,600 tons by 2008. The polysilicon suppliers will add capacity based only on semiconductor demand, since the \$40-\$60/ kg pricing allows construction of new capacity at capital costs up to \$100/kg. Solar grade silicon will be supplied from scrap, secondary material and a limited number of reactors modified for solar grade poly (SOG) production. The amount of polysilicon available to the PV industry is determined by installed capacity minus the volume required for the electronics industry. The seven major suppliers operate ten production facilities. Two of the suppliers in three of the facilities have decided not to deliberately produce SOG, but to market only secondary material and scrap to the PV market. One facility, ASiMI, Moses Lake, WA, has been converted to a dedicated SOG supplier, Solar Grade Silicon, LLC. Other suppliers have been willing to modify a limited number of reactors to produce a Direct SOG poly, some sold at or below full production cost in order to keep experienced people employed and equipment utilized during the semiconductor downturn. When semiconductor growth resumes, this material will not be available, or available only at higher prices, since new capacity must be funded by higher margins.

Table 1 charts the total PV demand for feedstock in metric tons, recording the historical 25-35% growth to 2003, but assuming a conservative 15% per year rate for the next five years^{3,4}. The values assume an improvement in conversion efficiency from 14 Mtons/MW to 12 Mtons/MW for Cz and multicrystalline technologies by 2005. A wafer thickness of 300 microns corresponds to about 12 Mtons/MW. It is unlikely that conversion will drop to 10 Mtons/MW over the next five years, as breakage rates increase with thinner wafers. The listed production capacity available for SOG production includes the total scrap, secondary material, and unused capacity (Capacity – IC Demand). Some suppliers have announced plans for new capacity for SOG at lower costs. This material is expected to be available starting in 2004 and is added to the available SOG volumes in Table 1. Solar Grade Silicon, LLC, Moses Lake, WA announced in March 2003 start of a R&D program to develop a commercial fluid bed reactor to produce silane-based granular polysilicon at about \$20/kg. Plans are to have production of 2000 Mtons in 2006. Wacker Chemie, Burghausen, Germany, reported in 2002 development of a trichlorosilane-based fluid bed reactor for granular SOG, starting in 2003 at a capacity of 200 Mtons/yr. A pilot plant at 500 Mtons/yr at \$25/kg is expected by 2006. Solar World and Degussa, Germany, announced in 2002 a JV to produce silane-

based SOG, developing a polysilicon tube CVD reactor and a fluid bed reactor process for granular polysilicon. They expect to produce 800 tons by 2005. There have been several R&D projects for purification of metallurgical grade silicon over the past twenty years and more continue to be studied⁴. It is unlikely that any of these will be in production in the next five years.

Table 1. Polysilicon supply, semiconductor and PV demand, and available SOG capacity in metric tons

Year	Poly Supply Prod. Capacity	IC Demand 10% Growth	PV Demand 15% Growth	Available SOG Cap.- IC Demand	Available SOG With New Cap.
1998	19,000	15,900	2300	3250	
1999	22,000	14,400	2900	7600	
2000	23,300	17,000	3500	6300	
2001	23,300	13,000	4700	10300	
2002	23,300	15,000	6400	8300	
2003	25,400	16,500	7300	8900	
2004	25,400	18,100	8100	7300	7750
2005	25,400	20,000	9000	5400	6900
2006	25,400	22,000	10500	3400	6700
2007	27,300	24,200	12000	3100	7700
2008	30,000	26,600	13500	3400	8500

SOG Sources and Cost Projections

Table 2 lists the projected feedstock costs and volumes in metric tons of scrap, directly produced SOG, new capacity of SOG, total PV feedstock demand, and the difference between capacity and demand (Balance) as shortfall to be purchased as semiconductor-grade poly. Scrap poly is from two sources: potscrap and rejects from semiconductor silicon crystal growth; and reject material from polysilicon production. Prior to 1995, the semiconductor silicon crystal growers would ship about 20-30% of production as tops and tails, reject crystals, and potscrap at prices ranging from \$5-20/kg. As shortages developed, this material was found to be more valuable when used internally for production of test wafers and some IC wafers. As a result, the available scrap for PV is now about 5% of crystal production. Scrap from polysilicon production consists of small diameter rods, filament pieces, rod ends with graphite, small chips/granules, chunks with surface powder, and other contaminated material rejected for semiconductor-grade poly. Some of this material is packaged as secondary-grade poly and shipped as SOG, so about 7% of polysilicon production is classified as scrap. Direct SOG represents the available polysilicon capacity (total capacity minus semiconductor demand) for production of SOG. Direct SOG will account for 63% of demand this year. By 2008, Direct SOG will account for only 10% of demand, as the available capacity is used for semiconductor-grade polysilicon. Some suppliers have decided not to produce Direct SOG. For forecasting purposes, the total capacity is considered to be available, since these suppliers may decide to produce SOG at higher prices. Source, shape, size, purity, and volume determine a price range from \$25-35/kg. New SOG represents new polysilicon production capacity added to address the PV market and requires new capital investments and technology development funds. Some of the suppliers have implemented their plans, but it is ambitious to assume these new technologies will be available in large volumes by

2008, when they are projected to account for 38% of demand. The difference between PV demand and capacity from Scrap, Direct SOG and New SOG is listed as Balance. For this year, capacity exceeds demand by 2500 tons, assuming all of the available capacity could be used for SOG. The situation will be marginal in 2004; a 25% PV growth rate would cause a 500 ton shortfall. By 2005, the shortfall starts to increase rapidly. The PV industry will have to compete with the IC industry for this polysilicon at higher prices, or restrict shipments

Table 2. Projected costs and volumes of PV feedstock in dollars per kilogram for metric tons.

Year	Scrap	Direct SOG	New SOG	Total Demand	Balance
Price	\$5-\$20/kg	\$25-\$35/kg	\$20-\$30/kg	Metric Tons	\$40-\$60kg
2003	2700	7100		7300	2500
2004	2700	5500	450	8100	500
2005	2800	3600	1500	9000	(1100)
2006	2900	1600	3300	10500	(2700)
2007	3000	1200	4600	12000	(3200)
2008	3300	1300	5100	13500	(3800)

Cost Reduction Opportunities

Table 3 lists the cost reduction opportunities for suppliers and users. The polysilicon suppliers have implemented some options to reduce costs: increasing deposition rate, reducing the number of rod processing steps (filament reactors), adopting a wide range of chunk sizes (filament reactors), reducing the analytical sampling plan, and using bulk packaging. The faster deposition rate reduces electricity costs and increases throughput; however, the faster rate increases dendritic growth, powder content, and structural voids. At this point, the suppliers have reduced production costs for SOG up to \$12/kg, as reflected in semiconductor-grade poly pricing at \$40-\$60/kg, and Direct SOG at \$25-\$35/kg. Granular form polysilicon can be produced at cheaper costs since the fluid bed reactor is more energy efficient and has greater throughput than the filament reactor. Specification issues affecting granular poly costs are size distribution, shape, powder content, hydrogen content, and surface impurity levels.

Reduced processing steps and more cost-efficient packaging may increase the levels of surface metals and carbon impurities. It is important that the impurity levels affecting ingot yields or cell efficiencies be identified. The often unknown and suspect levels of impurities in scrap make this a risky source of feedstock, increasing costs beyond the attractive initial price. As large quantities of Direct and New SOG become the major sources, data exchanges between suppliers and users will yield statistically significant data for the design of a comprehensive SOG specification.

The users have realized significant cost reductions from slicing yields, the opportunity now is for ingot growth cost reductions by cooperative efforts with the polysilicon supplier. For Cz and multicrystal growth methods, the optimal mixture of polysilicon rods, chunks and chips/granules will improve crucible packing, thus increasing crystal weight or volume per run. Poly granules have a packing density about 1.5 g/cc, chunks about 1.66 g/cc and rods about 2 g/cc. An optimal mix of rods, chunks, and

chips/granules for a 24 inch dia. Cz crucible can increase ingot weight by 40 kg, saving \$5/kg for a crucible load. Rods can be loaded faster than chunks, so load time can be reduced. Rods have a faster melt-in time than chunks or chips, so electricity use is reduced and throughput increased. Incoming material handling charges can be reduced by the use of bulk packaging. Just-in-time delivery reduces inventory charges. Larger bulk packages, over 1 metric ton, would further reduce packaging, inventory, and shipping costs. Purity has a major effect on costs if impurities reduce cell efficiency. Increasing the cell efficiency by 1% is equivalent to a \$10/kg feedstock cost for the total PV module cost. It is estimated that ingot growth costs could be reduced by at least \$18.50/kg ingot with initial cooperative efforts.

Table 3. Cost reduction opportunities for suppliers and users with cost savings estimates in dollars per kilogram.

Supplier Cost Reductions		Ingot Growth Cost Reductions	
Item	Cost Savings Est.	Item	Cost Savings Est.
Dendritic Structure		Crucible Loading	\$ 5/kg
Powder		Load Time	\$ 0.2/kg
Size Distribution		Melt Time	\$ 3/kg
Sample Plan		Packaging	\$ 0.1/kg
Bulk Packaging		Inventory	\$ 0.2/kg
Purity		1% Cell Efficiency	\$ 10/kg
Total	~ \$ 12/kg	Total	~ \$ 18.50/kg

In Cz furnaces, recharge systems allow the crucible to be reloaded with polysilicon after the first crystal pull. This extends the crucible life, with 3 to 6 pulls from one crucible. Hot zone life is increased and energy efficiency is increased. Shell Solar⁵ reported power consumption reduced by 51%, production increased 20-25%, and cell efficiency improved 5%. Recharge systems can use rods or granules. As the polysilicon supplier and ingot grower cooperate to design optimal delivery systems, further ingot growth cost reductions can be realized.

References

1. J. Maurits, "Polycrystalline Silicon-World Demand and Supply" 8th Workshop on Crystalline Silicon Solar Cell Materials and Processes, National Renewable Energy Laboratory, Publication CP-520-25232, August 17-19, 1998
2. In-Stat/MDR, "Cautious Optimism about Chip Market Growth", Semiconductor International, June, 2003
3. H. A. Aulich, F-W Schulze, "Silicon Supply for Solar PV", Renewable Energy World, November, 2002
4. A. Bjorseth, B. Ceccaroli, "Availability of Solar Grade Silicon-A Critical Issue for the Further Growth of the Photovoltaic Industry", presented at the ISES Solar World Congress 2003, Goteborg, Sweden, June 14-19, 2003
5. The Columbian, "Technology to Make Silicon Crystals Promises Energy, Environmental Savings" Knight Ridder/Tribune Business News, April 3, 2000

**Statistically meaningful data on the chemical state of iron precipitates
in processed multicrystalline silicon using synchrotron-based X-ray absorption
spectroscopy**

**T. Buonassisi¹, M. Heuer¹, A.A. Istratov¹, E.R. Weber¹, Z. Cai², B. Lai², M. Marcus³, J. Lu⁴,
G. Rozgonyi⁴, R. Schindler⁵, R. Jonczyk⁶, and J. Rand⁶**

¹University of California and Lawrence Berkeley National Lab., Berkeley, CA;

²Advanced Photon Source, Argonne Nat. Lab., Argonne, IL;

³Advanced Light Source, Lawrence Berkeley National Lab., Berkeley, CA;

⁴North Carolina State University, Raleigh, NC;

⁵Fraunhofer Institute for Solar Energy Systems, Freiburg, Germany;

⁶AstroPower Inc., Newark, DE.

X-ray fluorescence microscopy (μ -XRF), x-ray beam induced current (XBIC), and x-ray absorption spectromicroscopy (μ -XAS) were performed on fully-processed BaySix cast multicrystalline silicon and aluminum-gettered AstroPower Silicon-Film™ sheet material. Over ten iron precipitates – predominantly of iron silicide – were identified at low lifetime regions in both materials, both at grain boundaries and intragranular defects identified by XBIC. In addition, large (micron-sized) particles containing oxidized iron and other impurities (Ca, Cr, Mn) were found in BaySix material. The smaller iron silicide precipitates were more numerous and spatially distributed than their larger oxidized iron counterparts, and thus deemed more detrimental to minority carrier diffusion length.

Sample preparation.

Low-lifetime regions of as-grown AstroPower Silicon-Film™ and fully-processed Bay-Six cast multicrystalline material were identified with Electron Beam Induced Current (EBIC) and Laser/Light Beam Induced Current (LBIC), respectively, to determine regions of interest for this study. The AstroPower sample was aluminum gettered at 800°C for 4 hours to simulate actual solar cell gettering. The two materials were then chemically etched to remove the first few microns from the both surfaces, and in the case of the BaySix sample, to remove the anti-reflection coating and frontside metallization grid.

Experimental techniques.

X-ray fluorescence microscopy (μ -XRF) is a powerful technique for mapping the distribution of trace transition metal impurities in silicon.^{1,2} The physical principle of μ -XRF is similar to electron microscope-based energy dispersive spectroscopy (EDS), the only difference that synchrotron-based x-rays (and not electrons) are the excitation radiation. As a result, μ -XRF has a much lower Bremsstrahlung background, a larger probing depth that is limited only by the existing fluorescence attenuation length (36 microns for Fe, 70 microns for Cu), and an overall higher sensitivity compared to its electron counterpart. The only disadvantage is a much larger spot size (50-5000nm) compared with field emission transmission electron microscopes (~0.2nm). Nevertheless, because of the high flux (typically 10^9 - 10^{11} photons/s) of synchrotron-based XRF systems and a relatively weaker interaction between the excitation radiation and bound electrons, large volumes of material can be probed with high sensitivity, making this an ideal tool for detecting spatially inhomogeneous transition metal precipitates in PV-grade silicon.

In addition, the X-ray Beam Induced Current (XBIC) technique, an x-ray equivalent of Laser/Light Beam Induced Current (LBIC), can yield information about the recombination activity of defects. This powerful combination of XBIC and μ -XRF provides, simultaneously, information about the recombination activity and elemental nature of a transition metal precipitate.

Once an XBIC/ μ -XRF map is obtained over a certain area of interest, one can obtain information about the chemical nature of transition metal defects via X-ray Absorption Spectromicroscopy (μ -XAS). μ -XAS is an umbrella term including the X-ray Absorption Near-Edge Spectroscopy (XANES) and Extended X-ray Absorption Fine Structure (EXAFS) techniques. XANES yields information primarily on the oxidation state and immediate environment (first neighbors) of the atoms measured, whereas EXAFS yields information about the extended environment (second, third, etc. neighbors) and bonding configuration of the probed atoms.

For sample pre-characterization, XBIC/ μ -XRF were performed on Beamline 10.3.1 of the Advanced Light Source (ALS) of Lawrence Berkeley National Laboratory, with multilayer mirror focusing, optimal peak flux $\sim 10^{10}$ photons/s, and spot size $\sim 2 \times 2 \mu\text{m}^2$. To obtain chemical information from the extended fine structure of select precipitates, XBIC/ μ -XRF/ μ -XAS were performed on Beamline 10.3.2 of the ALS with multilayer mirror focusing, two-crystal Si (111) constant-exit monochromator, peak flux $\sim 10^{10}$ photons/s, and minimum spot size $\sim 5 \times 5 \mu\text{m}^2$. For detailed mapping and oxidation analysis of smaller precipitates, μ -XRF/XANES were performed at Beamline 2-ID-D of the Advanced Photon Source (APS) of Argonne National Laboratory with zone plate optics, Kohzu Si (111) monochromator, peak flux $\sim 10^{11}$ photons/s and spot size $\sim 200 \times 200 \text{ nm}^2$. Although reliable and reproducible XANES could be performed on precipitates equal to or smaller than the beam spot size by eliminating all translational motion of the monochromator crystals and employing a small correction factor for beam defocusing, EXAFS measurements were not possible at 2-ID-D because of current limitations in the focusing optics while scanning over wide energy ranges.

Iron was selected as the choice element of this study, given that it is a proven efficiency killer of silicon devices³ and is by an order of magnitude the most abundant impurity in mc-Si.⁴

AstroPower results.

The most striking feature of AstroPower material was the extended intragranular iron precipitates (Fig. 1). These precipitates were very noticeable in XBIC, easily located by their strong recombination activity. μ -XANES analyses on these precipitates revealed that iron is present in neutral oxidation state, most likely FeSi₂, by comparison with standard material (Fig. 2).

It is possible that these intragranular precipitates are associated with the void/dislocation complexes identified via TEM investigations of *Zhang et al.*⁵ The large free surface available at the voids and the strain fields at the associated dislocations offer an abundance of precipitation sites for Fe, and the fact that these complexes are distributed throughout the bulk means that Fe can more quickly diffuse to these structural defects than to other sinks, such as surfaces or grain boundaries.

In addition to these characteristic intragranular defects, a recombination-active grain boundary was scanned with μ -XRF (Fig. 3, scan area $5 \times 35 \mu\text{m}^2$) to reveal the fine structure of the Fe precipitates at this extended defect. The grain boundary, the electrical activity of which was characterized by XBIC at ALS Beamline 10.3.1, was located at APS 2-ID-D by the change of intensity of the monochromatic beam scattering peak from one grain to another. In the case of this sample, the variation was high, in the range of 25-27%. This large change in scattering intensities reveals that this is a high angle grain boundary, which previous studies⁶ have suggested

should be an efficient sink for metals. Indeed, the μ -XRF analysis revealed a multitude of very small precipitates evenly spaced at the grain boundary. A XANES analysis, shown in Fig. 2, on one such precipitate in Fig. 3 revealed that the precipitate most closely matches FeSi_2 . Horizontal and vertical μ -XRF scans revealed that the precipitate is smaller than or equal in diameter to the beam spot size of 200nm. By taking a 60 second XRF point scan on the point of maximum signal, and comparing the signal peak intensity with a standard NIST 1833 thin foil, it was possible to obtain a lower estimate the size of the precipitate assuming all Fe is contained in one single spherical FeSi_2 precipitate close to the surface by using the following formulae:

$$\text{Fe in Precipitate [atoms/cm}^{-2}\text{]} = \frac{\text{Counts}/60\text{s/Precipitate}}{\text{Counts}/60\text{s/Standard}} \cdot \text{Fe in NIST 1833 Calibration Standard [atoms/cm}^{-2}\text{]} \quad (1)$$

$$\text{Volume of Precipitate [cm}^3\text{]} = \frac{\text{Fe in precipitate [atoms/cm}^{-2}\text{]} \cdot \text{Spot Size [cm}^2\text{]}}{\text{Density of } \text{FeSi}_2 \text{ [atoms/cm}^3\text{]}} \quad (2)$$

Assuming a spherical geometry, the radius of this particular precipitate at the grain boundary was calculated to be 13.8 nm. Notice the denuded zone before the grain boundary contains no such Fe precipitates.

BaySix results.

A particularly recombination-active grain boundary from the bottom of the ingot was characterized by XBIC on ALS Beamline 10.3.1 which revealed a denuded zone. This same area was identified at APS Beamline 2-ID-D via a change in intensity of the elastic scattering peak. It was noted that the change of scattering intensity between grains, while a noticeable 11-12%, was smaller than what was observed in the AstroPower sample, an indication that this might be a smaller angle grain boundary. It is known that "clean" structural defects, especially "gentle" defects such as low-angle grain boundaries, do not tend to have noticeable recombination activity at room temperature.⁷ The high recombination activity of this structural defect and the presence of a denuded zone are good indications of the presence of impurities.

A μ -XRF scan located a series of iron-containing precipitates along the length of the grain boundary, as shown in Fig. 4, and summarized in Table 1. Note the step size of the scan shown in Fig. 4 is 3000 nm, while the beam spot size was a mere 200 nm, suggesting even more such precipitates could be present but may have been missed. These precipitates were substantially larger than those noted in AstroPower material (see Table 1). A small 16x16 μm^2 scan was performed along the grain boundary with 200 nm step size, but no precipitates with diameter equal to or less than the spot size were detected within 1s accumulation time, unlike the AstroPower material, indicating that the Fe distribution along the grain boundary of this sample is indeed different.

Table 1. Dimensions and chemical state of the precipitates (* - shown in Fig. 4)

Precipitate Label	X dimension (nm)	Y dimension (nm)	Chemical State
P1	≤ 200	570	FeSi_2
P2	~ 1500	~ 1200	Fe_2O_3
P3*	1250	892	Fe_2O_3
P4*	275	772	FeSi_2
P5*	≤ 200	710	FeSi_2
P6*	290	547	FeSi_2

XANES analyses (summarized in Table 1) on the precipitates revealed two general species of iron precipitate: (1) A number of small (\leq 200-770 nm diameter) precipitates identified as iron silicide (FeSi_2). As in the AstroPower sample, these FeSi_2 precipitates do not contain other metal impurities. However, the sizes of the precipitates are much larger, and they are distributed with greater distances in between. (2) A few large ($>$ 900 nm diameter) oxidized iron clusters, closely resembling the chemical form identified by McHugo et al.⁸ While these precipitates contain primarily iron, other impurities (e.g. Cr, Mn, Ca) are also present. It is possible that "large" (on the order of a micron in diameter) pieces of dirt or rusted stainless steel are incorporated into the melt, where at high temperatures, they secrete iron into the surrounding crystal. This iron then precipitates at nearby extended defects, forming FeSi_2 .

To test this hypothesis, a Czochralski silicon sample with a 1.3 μm polysilicon layer deposited with chemical vapor deposition was contaminated with iron by scratching the backside with a wire. The sample was heated at 1150°C for 2 hours to simulate a high temperature step. The iron gettered to the polysilicon layer was analyzed with μ -XAS at ALS Beamline 10.3.2, yielding an almost perfect match with a FeSi_2 standard. This is additional evidence that dissolved iron in multicrystalline silicon tends to precipitate to form iron silicide clusters, which are known to be recombination active lifetime killers.³ Further investigations must be performed to fully understand this precipitation phenomenon.

Conclusions.

For the first time, statistically meaningful data was acquired on the chemical state of iron precipitates in PV-grade mc-Si. The grand majority of intragranular iron precipitates in AstroPower and iron precipitates at grain boundaries in AstroPower and BaySix materials were identified as iron silicide (FeSi_2). Because of the low dissolution barrier of FeSi_2 and the numerical abundance of these precipitates, the rate of gettering of iron from these precipitates is thus most likely kinetically-limited as suggested by Plekhanov *et al.*⁹, and not dissolution-limited. Nevertheless, at least in BaySix material, a few large impurity precipitates containing primarily oxidized iron but also an abundance of other metals may take much longer to completely dissolve, thus complicating any model of gettering based on a distribution of tiny FeSi_2 precipitates.

Acknowledgements.

Special thanks to Elizabeth Schäffer for performing LBIC measurements on BaySix material. This work was funded by NREL subcontract AAT-2-31605-03, and the AG-Solar project of the government of Northrhein-Westfalia (NRW), funded through the Fraunhofer Institute for Solar Energy Systems (ISE) (Germany). The operations of the Advanced Light Source at Lawrence Berkeley National Laboratory are supported by the Director, Office of Science, Office of Basic Energy Sciences, Materials Sciences Division, of the U.S. Department of Energy under Contract No. DE-AC03-76SF00098. Use of the Advanced Photon Source was supported by the U.S. Department of Energy, Office of Science, Office of Basic Energy Sciences, under Contract No. W-31-109-ENG-38.

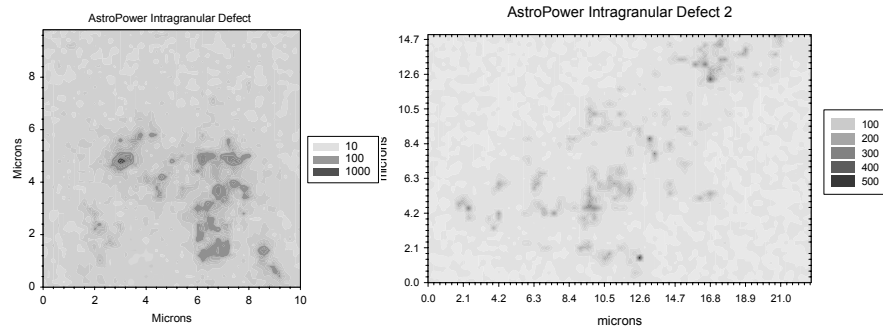


Fig. 1. μ -XRF image of two areas of Astropower material, containing clusters of iron.

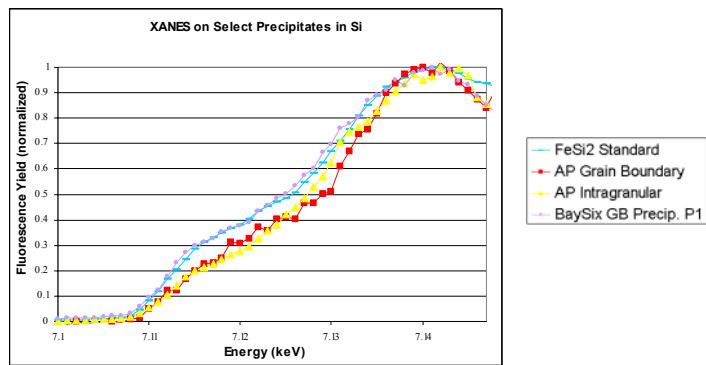


Fig. 2. Comparison of μ -XANES spectra of FeSi2 standard and three iron precipitates found in Astropower (AP) and BaySix materials.

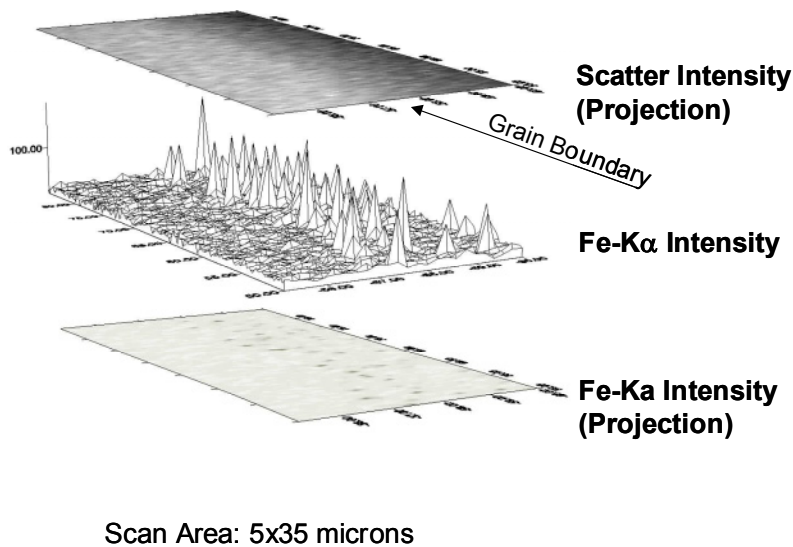


Fig. 3. μ -XRF scan of a grain boundary area of Astropower sample.

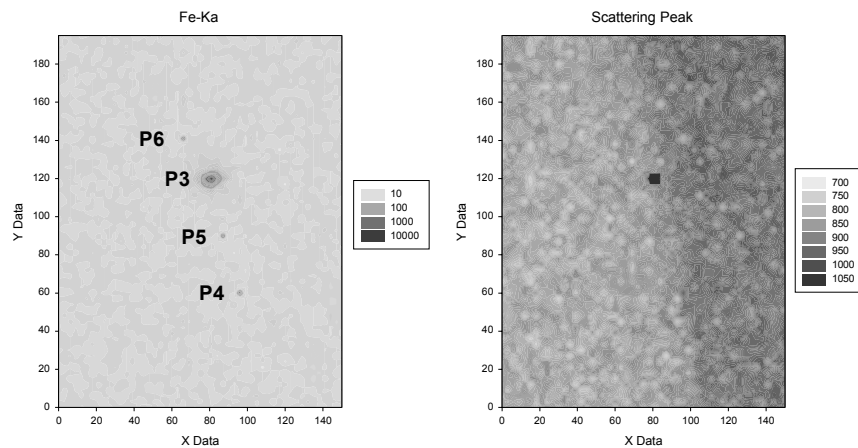


Fig. 4. μ -XRF scan (left) and scattering peak (right) of a grain boundary area of Baysix sample.

REFERENCES.

- ¹ S. A. McHugo, A. C. Thompson, A. Mohammed, G. Lamble, I. Périchaud, S. Martinuzzi, M. Werner, M. Rinio, W. Koch, H.-U. Höfs, and C. Häßler, Journal of Applied Physics **89**, 4282-4288 (2001).
- ² S. A. McHugo, A. C. Thompson, C. Flink, E. R. Weber, G. Lamble, B. Gunion, A. MacDowell, R. Celestre, H. A. Padmore, and Z. Hussain, Journal of Crystal Growth **210**, 395-400 (2000).
- ³ A. A. Istratov, H. Hieslmair, and E. R. Weber, Applied Physics A: Material Science & Processing **70**, 489-534 (2000).
- ⁴ A. A. Istratov, T. Buonassisi, E. R. Weber, R. J. McDonald, A. R. Smith, R. Schindler, J. A. Rand, J. Kalejs, *see this volume*.
- ⁵ R. Zhang, G. Duscher, J. Rand, and G. A. Rozgonyi, in *Nanoscale investigations of polycrystalline silicon for photovoltaic applications*, Breckenridge, CO, 2002, p. 206.
- ⁶ A. Ihlal, R. Rizk, and O. B. M. Hardouin Duparc, Journal of Applied Physics **80**, 2665-2670 (1996).
- ⁷ J. Bailey, and E. R. Weber, Phys. stat. sol. (a) **137**, 515 (1993).
- ⁸ S. A. McHugo, A. C. Thompson, G. Lamble, C. Flink, and E. R. Weber, Physica B **273-274**, 371-374 (1999).
- ⁹ P. S. Plekhanov, R. Gafiteanu, U. M. Gosele, and T. Y. Tan, Journal of Applied Physics **86**, 2453-2458 (1999).

Experimental procedure for determination of the depth of metal clusters in XBIC/ μ -XRF mapping of metal clusters in silicon solar cells

O.F. Vyvenko^(1,2), T.Buonassisi⁽¹⁾, A.A.Istratov⁽¹⁾, and E.R.Weber⁽¹⁾

⁽¹⁾ University of California and Lawrence Berkeley National Laboratory,
Berkeley, CA 94720, USA

⁽²⁾ St. Petersburg State University, 198504 St. Petersburg, Russia

Microprobe X-ray fluorescence (μ -XRF) in combination with X-ray beam induced current (XBIC) proved to be an efficient tool for characterization of solar cell materials, which allows one to map distribution of transition metal clusters with a micron scale resolution and simultaneously and in-situ assess their recombination activity [1-3]. These tools are similar to electron beam induced current (EBIC) or laser beam induced current (LBIC) techniques with the primary difference that a focused x-ray beam is utilized instead of an electron or laser beam. EBIC/LBIC techniques allow one to determine the depth of a defect by changing the penetration depth of the exiting beam, which is achieved by varying the accelerating voltage or wavelength of the exciting light beam. Unfortunately, this approach cannot be used to determine the depth of a defect with the XBIC/ μ -XRF technique since the Beamline 10.3.1 uses incoming x-rays with the energies determined by the parameters of the synchrotron and the mirrors used in the set-up. That is why we developed another approach to determine the depth of defects from the surface by taking advantage of the geometry of experimental set-up at the Beamline 10.3.1.

In order to understand the principle of the depth determination technique, it is important to have a basic understanding of the layout of the experimental setup at Beamline 10.3.1. A diagram of the XBIC/ μ -XRF experiment is shown in the Fig.1.

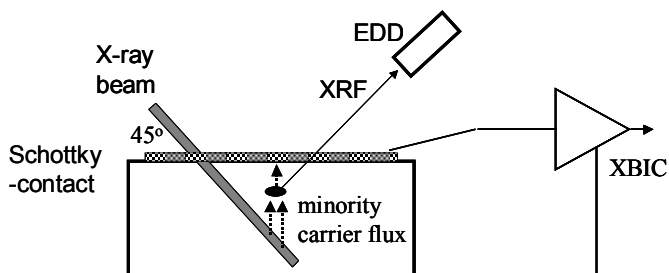


Fig. 1. A schematic diagram of the XBIC/XRF experiment.

An intense X-ray beam from the synchrotron with approximately 3×10^{10} photons/s is focused in a $(1-2) \times (1-2) \mu\text{m}^2$ spot using elliptically bent multilayer mirrors. The incident X-ray beam has a wide range of photon energies with a peak of intensity at 12.4 keV. The beam hits the sample surface at an angle of 45 degrees. The emanating X-ray fluorescence is detected by a Si:Li detector. Minority carriers induced due to absorption of X-ray photons are collected with a Schottky diode. A reduction of the minority carrier diode current due to enhanced recombination at a defect gives rise to the appearance of the XBIC-contrast.

A schematic diagram depicted in the Figure 2 explains the depth determination method of the defect by using two subsequent XBIC/μ-XRF mappings of the area of the sample with the defect of interest before and after 180° sample rotation around the axis perpendicular to the sample surface. In the coordinate system of the sample, the 180° rotation is equivalent to the change of the direction of the incident beam with respect to the sample, as shown by the dotted lines in the Figure 2. In this way, the apparent position of the image of a defect relative to the surface features of the sample on the XBIC or μ-XRF map will change as it is schematically depicted at the bottom of the Figure 2. The depth d of the object of interest in the bulk of the sample as well its true coordinate along the x -axis can be calculated as half-difference and half-sum of the x -distances of the object relative to the surface mark before and after rotation, respectively (see also the Figure 2 caption). In theory, one could perform full 3D imaging by taking a sequence of measurements at different sample rotation angles. However, to determine the depth of the defect it is sufficient to measure the changes of the position of the defect relatively to a surface feature (which, if necessary, can be prepared intentionally by evaporating a metal dot on the sample surface) before and after 180° sample rotation. The maximum depth that can be measured with this method is defined by the attenuation depth of the exciting X-ray beam (in our case, 180 μm), the minority carrier diffusion length in XBIC-mapping (typically 30-100 μm) and, in the μ-XRF-mapping, by the attenuation depth of the fluorescent radiation (typically 20-50 μm depending on the element). The accuracy of the method is determined by the spot size of the focused beam, by the scan step size, and by the sharpness of the surface reference and the defect image.

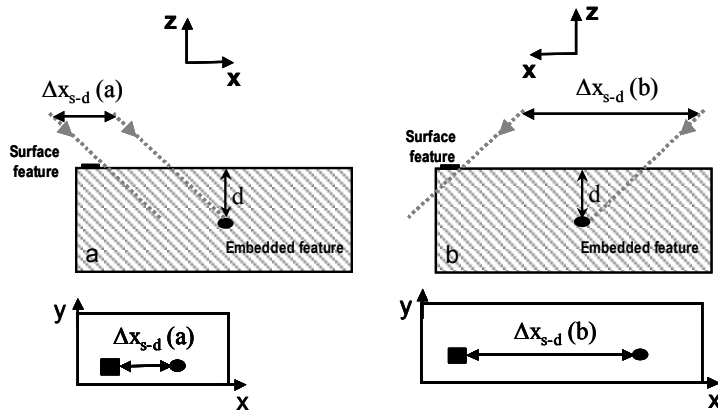


Fig.2. A schematic diagram explaining defect depth determination by using two subsequent XBIC/μ-XRF scans performed before (a) and after (b) 180° sample rotation around z-axis, perpendicular to the sample surface. The direction of X-ray beam with respect to the sample is depicted with dotted straight lines. The depth d of the object of interest (*embedded feature*) and its true distance Δx_{true} on x -scale with respect to a *surface feature* (reference) are calculated by the expressions: $d = (\Delta x_{s-d}(b) - \Delta x_{s-d}(a))/2$, $\Delta x_{\text{true}} = (\Delta x_{s-d}(b) + \Delta x_{s-d}(a))/2$, where $\Delta x_{s-d}(a)$, $\Delta x_{s-d}(b)$ are the apparent distances between the image of the object and the image of the *surface feature* (reference) obtained on the XBIC/μ-XRF maps of the scan a and b respectively.

Figure 3 presents an example of the depth determination experiment performed on a fully processed silicon solar cell made from prototype RGS material (Ribbon-Grown-on-Substrate). Under certain growth conditions in RGS material, oxygen is known to precipitate at extended crystallographic defects, causing the formation of channels of inverse conductivity type. These

channels may efficiently collect minority carriers from a greater depth of the substrate than the average minority carrier diffusion length when they extend from the emitter into the bulk. Current collecting channels can be identified in beveled EBIC maps as bright spots [5]. The existence of the collecting channels explains a relatively high current collection efficiency of this type of solar cell material despite a very low minority carrier diffusion length.

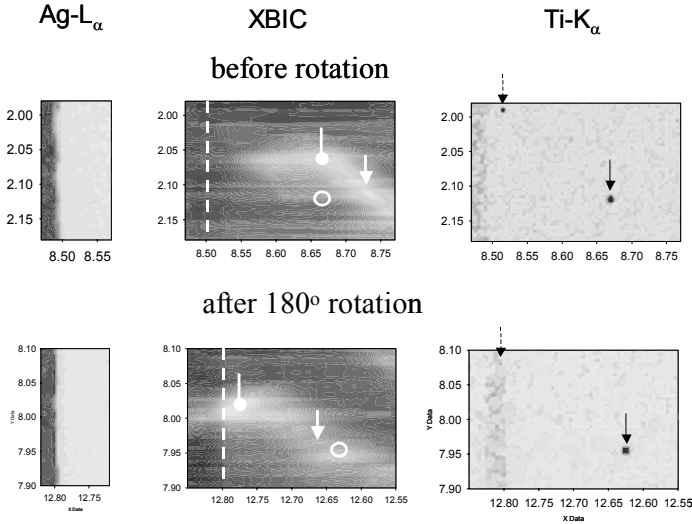


Fig.3. Determination of depth of current collecting channels in prototype RGS silicon by XBIC/μ-XRF 180 degrees rotation experiment. The upper and bottom row of images are taken before and after the rotation of the sample by 180° around the axis perpendicular to the sample surface. The bright XBIC-contrast which images the shape of the current collecting channels changes after sample rotation (middle image column). Left and right image columns are μ-XRF silver and titanium maps, respectively, which were used as surface reference features. All three maps in every row were measured in a single scan.

The left column in Fig. 3 represents XRF intensity maps of the silver L α_1 fluorescence peak (2.984 keV). Silver is the main component of the contact strips. The Ag-L α fluorescence has an extinction depth in silicon as small as 3 μm and therefore could be used as a surface mark. Two images in the middle column of Figure 3 represent the XBIC-contrasts of the collecting channels as appeared before and after a 180° rotation of the sample. The position of the contact strip edges are redrawn from the silver map on the XBIC maps as dashed lines. A shift of the current collecting channel to the right relatively to the strip position and noticeable changes of the collecting channel image shape after the rotation are obvious. An area marked with sharp arrows shifts to the right by approximately 80 μm , whereas the area marked with the round-end arrow shifts by approximately 150 μm . These values imply that the conducting channel goes down from the right to the left from the depth of 40 μm to the depth of 75 μm .

The right-hand-side column represents the XRF intensity map of the titanium K α line. Titanium is a minor component of the contact strips which can be recognized in the images. Additionally, two titanium dots marked with dark arrows are seen in the images. The position of the lower dot with respect to the contact strip does not change after the rotation of the sample suggesting that it is a titanium particle on the sample surface. The upper titanium dot image shifted after the rotation by 20 μm to the right and overlaps with the contact strip. Due to a strong absorption of the Ti-K α radiation (4.5 keV) by silver in the contact strip the XRF-contrast of the dot became weaker after the rotation. The shift corresponds to the defect depth of 10 μm and its

true position on the x-scale is just in the middle between the position seen in the upper map and the contact strip.

The funding for this research was provided by NREL, subcontract AAT-2-31605-03, and by the AG-Solar project of the government of Northrhein-Westfalia (NRW). The Advanced Light Source operations are funded by the Director, Office of Energy Research, Office of Basic Energy Sciences, Materials Sciences Division, of the US Department of Energy under Contract No. DE-AC03-76SF00098. The authors gratefully acknowledge fruitful discussions with M. Kittler, W.Seifert, A.Thompson, S.A.McHugo, H.Hieslmair, G.D. Ackermann, R. Ynzunza, and Z. Hussein, R.Schindler and G.Hahn.

7. References

1. O. F. Vyvenko, T. Buonassisi, A. A. Istratov, H. Hieslmair, A. C. Thompson, R. Schindler, and E. R. Weber, *J.Appl.Phys.* **91**, 3614 (2002).
2. O. F. Vyvenko, T. Buonassisi, A. A. Istratov, E. R. Weber, M. Kittler, and W. Seifert, *J. Phys.: Cond. Matter* **14**, 13079 (2002).
3. T. Buonassisi, O. F. Vyvenko, A. A. Istratov, E. R. Weber, and R. Schindler, in *Defects and impurity engineered semiconductors and devices III*, S. Ashok, J. Chevallier, N. M. Johnson, B. L. Sopori, and S. Okushi, Editors, p. 179, Mat. Res. Soc. (2002).
4. S. A. McHugo, A. C. Thompson, C. Flink, E. R. Weber, G. Lamble, B. Gunion, A. MacDowell, R. Celestre, H. A. Padmore, and Z. Hussain, *J. Cryst. Growth* **210**, 395 (2000).
5. O. Breitenstein, M. Langenkamp, and J. P. Rakotonaina, *Solid State Phenom.* **78-79**, 29 (2001).

Theory of defects in silicon solar cells at finite temperatures

Mahdi Sanati and Stefan K. Estreicher

Physics Department, Texas Tech University, Lubbock, TX 79409-1051
NREL contract AAT-1-31605-04

Polycrystalline Si solar cells contain defects, impurities, and complexes which limit carrier lifetimes. The identification of these defects, the role(s) they play, and their interactions with common impurities such as H, O, or C requires a combination of microscopic experimental and first-principles theoretical studies. Until now, theory has been restricted to T=0K, and the free energies of defects could not be calculated. However, defects form, diffuse, and/or dissociate at finite temperatures, and solar cells operate above room temperature. We present here the first systematic extension of first-principles theory to include the vibrational free energy, which is the most important of the missing contributions. The computational effort is substantial. However, this allows us to calculate the energetics of defects as a function of temperature. In this paper, we present evidence that our calculations are accurate up to at least 800-900K in the case of silicon. The temperature-dependence of the binding energy of copper pairs is given as one application to defect problems.

1. Goals

The improvement in the efficiency and reliability of poly-Si solar cells achieved in the past decade has been partly driven by a better understanding of defects and defect passivation. First-principles theory plays an important role in this understanding, as it provides a lot of microscopic information about structures, vibrational properties, formation and binding energies, and other defect properties. Yet, all the theoretical work done so far[1] (by us and all other groups) involves the total *electronic* energy, i.e. is done at T=0K. But all semiconductor devices undergo annealing steps at high temperatures. Further, solar cells function above room temperature (RT), and their efficiency sometimes diminishes over time. This suggests that some unwanted defects diffuse and precipitate (thus creating new recombination centers) or that some complexes dissociate (thus changing their electrical activity). Such processes slowly degrade the material. In order to predict the binding and formation energies of defects and complexes as a function of temperature, first-principles theory must be extended to include free energies.

Today's first-principles theory predicts quantitatively many properties of (simple) defects, and thus complements the experimental findings. Systematic geometry optimizations provide the structures and relative energies of native defects, impurities, pairs and larger complexes. The stability, configuration, and symmetry information confirm or rule out models based on experimental data. More importantly, the predictions of the vibrational spectra of the most stable defects allows a direct connection to infra-red (IR) absorption, Raman, and sometimes even photoluminescence (PL) data. Today, the predictions of local vibrational modes (LVMs) is much more quantitative than it was just a few years ago, with many frequencies predicted within 1-2% of the measured ones.

The total electronic energy obtained from density-functional (DF) theory[2] involves the electronic ground state. This is perfectly appropriate for semiconductors such as Si (unless it is heavily doped or during high-T anneals) because few electrons populate the excited (conduction band) states. Classical molecular-dynamics (MD) simulations[3] add a classical temperature via the kinetic energy of the nuclei. However, even in MD runs, only the (ground state) electronic energy and the nuclear repulsion + kinetic energies are included. We show here how first-principles calculations can be extended to include the vibrational free energy, thus allowing the calculation of total energies as a function of

temperature. The key points of the free energy calculations are described in section 2. The calculation of the specific heat, vibrational entropy, and zero-point energy in perfect (defect-free) Si cells are in Sec. 3. We apply the method to the calculation of the binding energy of copper pairs in section 4. Some consequences of these developments are discussed in section 5.

2. Theoretical background

The starting point of these calculations is first-principles DF theory coupled to MD simulations within the SIESTA[4,5] package. ‘First-principles’ means that no parameter in the calculation is fitted to an experimental database. The host crystal is represented with periodic 64-host atom supercells. The electronic problem is solved self-consistently within the local density approximation. The exchange-correlation potential is that of Ceperley-Alder[6] parameterized by Perdew-Zunger.[7] Ab-initio pseudopotentials in the Kleinman-Bylander[8] form are used. The basis sets consist of numerical linear combinations of atomic orbitals. In the present work, double-zeta basis sets are used with polarization functions on selected atoms. The k -point sampling is limited to $k=0$.

The vibrational frequency analysis, which is the key to the present developments, is carried out within linear response theory at $T=0K$.[9] This method allows the entire dynamical matrix to be calculated from derivatives of the density matrix relative to atomic coordinates. Extensive testing[9] of known local vibrational modes (LVMs) for light impurities in Si has shown that the LVMs calculated in this manner are typically within 2% of the observed ones. The method also accurately predicts ‘pseudo-LVMs’[10] as well as the Γ phonon, which is calculated[11] at 535cm^{-1} and measured[12] at 524cm^{-1} .

The experimental work is (almost) always done at constant pressure, and therefore the Gibbs free energy should be calculated. However, since our vibrational spectra are calculated at $T=0K$ and the temperature dependence of the lattice constant is ignored, we focus here on the Helmholtz free energy F (constant volume). Working at constant volume rather than constant pressure is appropriate up to several hundred degrees Celsius because the thermal expansion coefficient of Si is very small ($4.68\times 10^{-6}\text{K}^{-1}$ at RT). Further, in Si and at RT, the measured[13] difference C_p-C_v is 0.0165J/molK , a correction of only 0.08% to $C_p=20\text{J/mol K}$.

The (total) Helmholtz free energy $F=U-TS$ contains the internal energy U and the entropy S , which is the sum of the electronic, configurational, and vibrational entropies. In insulators and moderately-doped semiconductors, the electronic entropy can be ignored up to high temperatures since few electrons populate the excited states. The configurational entropy is proportional to the logarithm of the number of possible configurations and must be calculated for each defect separately. But the vibrational entropy is always present. Note that $F_{\text{vib}}(T=0K)$ is the total zero-point energy (ZPE). The vibrational part of the Helmholtz free energy (of the cell) is given by[14]

$$F_{\text{vib}} = k_B T \int_0^{\infty} \ln \{ \sinh x/2 \} g(\omega) d\omega \quad \text{with} \quad \int_0^{\infty} g(\omega) d\omega = 3N$$

where $g(\omega)$ is the phonon density of states and $x = \hbar\omega/k_B T$. In the perfect cell, the integral stops at the Γ phonon and $g(\omega > \omega_{\Gamma})=0$. If the cell contains a defect, $g'(\omega) + \sum_{\text{LVM}} \delta(\omega - \omega_{\text{LVM}})$ where the sum includes all the modes above the Γ phonon (LVMs and resonant modes). The perturbed quantities are primed. We obtain the phonon density of states from the calculated normal mode frequencies of the cell, with or without a defect. If the discrete set of frequencies is used, the results are within 5-6% of experiment. With a continuous $g(\omega)$ (obtained by averaging), the results are within 2% of experimental data.

3. Perfect cell results

Once F_{vib} is calculated, the vibrational entropy S_{vib} and the vibrational contribution to the specific heat C_V are obtained from standard thermodynamics relations. In the harmonic approximation, these are

$$S_{\text{vib}} = -(\partial F_{\text{vib}}/\partial T)_V \quad \text{and} \quad C_V = -T(\partial^2 F_{\text{vib}}/\partial T^2)_V$$

The calculated (measured) ZPE is 6.20 (6.01) kJ/mol, S_{vib} at 300 or 800K is 18.40 or 40.31 (18.82 or 41.57) J/mol K, and C_V at 300 or 800K is 19.52 or 24.03 (19.99 or 25.36) J/mol K. Figure 1 shows the specific heat (calculated in the Si_{64} cell: C_V , measured in ‘perfect’ Si: C_p). In the harmonic approximation, C_V converges toward $3k_B$ at high temperatures. The experimental data begin to diverge around 800-900K because of anharmonic (and maybe electronic entropy) contributions.

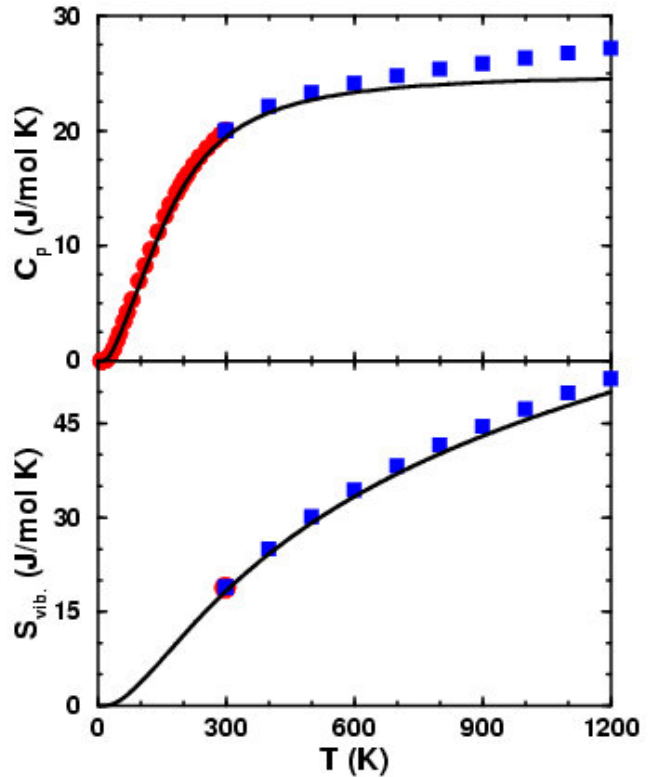
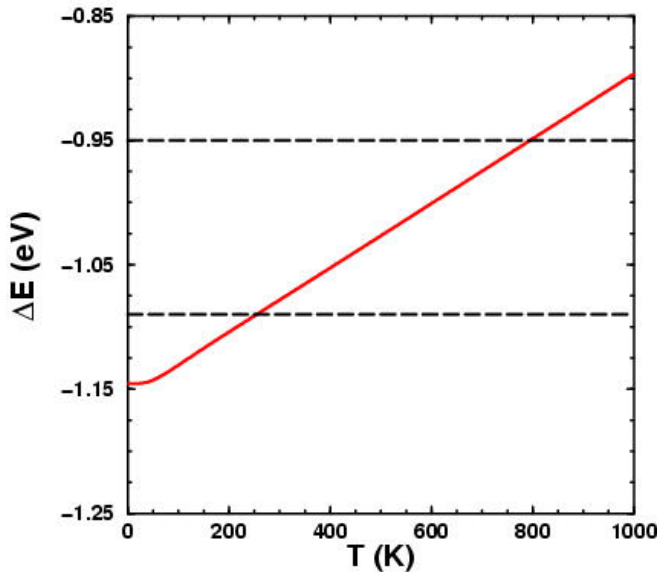


Fig. 1: Calculated (black line) and measured (blue squares: [15], red bullets: [13]) specific heat (top) and vibrational entropy (bottom) per atom vs. temperature.

4. Binding energy of the copper pair

We now apply the calculation of free energies to the substitutional-interstitial copper pair in Si, $\{\text{Cu}_s, \text{Cu}_i\}$. This pair has recently been identified[10] as the defect responsible for the 1014meV PL band. The phonon sidebands have been shown to be caused by a specific vibrational mode of the pair. Theory also predicts the observed symmetry of the defect, C_{3v} . However, the *binding* energy E_b calculated at $T=0\text{K}$ is 1.16eV, while the measured *dissociation* energy E_d is $1.02 \pm 0.07\text{eV}$. Since E_d should be equal E_b plus the migration energy $E_m = 0.18 \pm 0.02\text{eV}$ [16], the calculated E_b is much too large. Of course, in the experimental work, the dissociation actually occurs while the sample is being annealed at a few hundred degrees Celsius. We must therefore calculate the binding energy at $T>0$ temperatures rather than use the $T=0\text{K}$ value. Fig. 2 shows the calculated E_b vs. T . Clearly, under the experimental conditions, theory does predict that $E_d=E_b+E_m$.

Fig. 2: The calculated binding energy ($E_b = -\Delta E$) of the $\{Cu_s, Cu_i\}$ pair in Si decreases with temperature and its value above $\sim 600K$ is consistent with the measured dissociation energy (see text). Note that at $T=0K$, E_b converges toward 1.16eV *if* the total ZPE is ignored.



5. Discussion

The theory developments discussed here show that we can now calculate the total energy of defects as a function of temperature. Since these are the first such calculations, a lot of testing and further fine-tuning will be required. The dynamical matrix calculations require very large amounts of computer time, and are close to the limit of what can be calculated today. In our approach, the phonon density of states is obtained from the normal mode frequencies calculated in real space in the entire periodic supercell. The zero-point energy, vibrational entropy, and specific heat obtained in the defect-free cell are very close to the values measured in perfect Si, suggesting that the method we propose is very accurate. The examples discussed here and elsewhere[11] show that total energy differences vary by several tenths of an eV, much more than usually assumed. There are many applications directly relevant to photovoltaics, such as the calculation of the binding energies as a function of temperature, in order to identify which defect structures become less stable under operating conditions.

References

1. S.K. Estreicher, Materials Today **6** (6), 25 (2003)
- 2 W. Kohn W, Rev. Mod. Phys. **72**, 1253 (1999)
3. S.K. Estreicher and P.A. Fedders, in *Computational Studies of New Materials*, ed. D.A. Jelski and T.F. George (World Scientific, Singapore, 1999), p.27-73.
4. D. Sánchez-Portal, P. Ordejón, E. Artacho, and J.M. Soler, Int. J. Quant. Chem. **65**, 453 (1997)
5. E. Artacho, D. Sánchez-Portal, P. Ordejón, A. García, J.M. Soler, Phys. Stat. Sol. (b) **215**, 809 (1999)
6. D.M. Ceperley and B.J. Alder, Phys. Rev. Lett. **45**, 566 (1980)
7. S. Perdew and A. Zunger, Phys. Rev. B **32**, 5048 (1981)
8. L. Kleiman and D.M. Bylander, Phys. Rev. Lett. **48**, 1425 (1982)
9. J.M. Pruneda, S.K. Estreicher, J. Junquera, J. Ferrer, and P. Ordejón, Phys. Rev. B **65**, 075210 (2002)
10. S.K. Estreicher, D. West, J. Goss, S. Knack, and J. Weber, Phys. Rev. Lett. **90**, 035504 (2003)
11. M. Sanati and S.K. Estreicher, Phys. Rev. Lett. (submitted)
12. J. Menéndez and M. Cardona, Phys. Rev. B **29**, 2051 (1984)
13. P. Flubacher, A.J. Leadbetter, and J.A. Morrison, Phil. Mag. **4**, 273 (1959)
14. A.A. Maradudin, E.W. Montroll, G.H. Weiss, and I.P. Ipatova, *Theory of Lattice Dynamics in the Harmonic Approximation* (Academic, New York, 1971)
15. I. Barin, *Thermochemical data of pure substances* (VCH, Weinheim, 1995)
16. A.A. Istratov, H. Hieslmair, T. Heiser, C. Flink, and E.R. Weber, Appl. Phys. Lett. **72**, 474 (1998)

Theoretical predictions of complex formation following hydrogenation from a nitride layer

Jason L. McAfee and Stefan K. Estreicher

Physics Department, Texas Tech University, Lubbock, TX 79409-1051
NREL contract AAT-1-31605-04

The hydrogenation of poly-Si material from a nitride layer injects H into the material and produces substantial passivation of (yet unidentified) defects throughout the bulk. It is not known if the process involves some N injection as well. Hydrogen passivates defects and interacts with many impurities in the material. In this paper, we report on the theoretical identification of the most likely N, {N,H}, and {C,H} complexes that could appear in infra-red (IR) absorption spectra following the hydrogenation (the IR work, done by M. Stavola, is reported elsewhere). The (preliminary) carbon results are included in this work as C is the most common impurity in EFG material. Our first-principles calculations reveal the most stable structures, binding energies, and vibrational spectra of these defects.

1. Goals

The understanding of hydrogenation and passivation from a nitride layer has been lacking because of the absence of microscopic information. Many years after the process has been developed (mostly by trial-and error), there is still no knowledge of how hydrogen penetrates into the material, how much of it is present in the bulk, which defects and impurities it interacts with, and how passivation results. The present research involves systematic and microscopic experimental and theoretical studies aimed at quantifying the role(s) of hydrogen and identifying the key defects and complexes involved. The experimental work, done by the co-PI of the project, Mike Stavola at Lehigh University, consists of infrared (IR) absorption measurements of H-defect and H-impurity complexes. These results are presented in a separate paper. The research discussed here involves first-principles theoretical studies of the stability and properties of H-impurity complexes. The goals are to predict and characterize the H-related complexes that are the most likely to be observed in the experimental work, thus allowing the rapid identification of any new H-related IR lines following the hydrogenation.

Since the passivation process involves the hydrogenation from a nitride layer, we assume that not just H but also some N could be injected into the material during the high-temperature anneal. Therefore, we studied interstitial nitrogen (N_i) and its interactions with the vacancy, the self-interstitial, another N_i , and H. The complete results of these investigations have recently been submitted for publication.[1] Since the most common impurity in EFG material is C, we are also studying substitutional (C_s) and interstitial (C_i) carbon as well as the $\{C_s, C_i\}$ pair and two $\{C_s, H, H\}$ complexes. The latter defects have been detected following the hydrogenation of C-rich Si. The C-related work is still ongoing and the results reported here are preliminary. The calculations include the stable structures, the binding and formation energies, some chemical details, as well as the complete vibrational analysis for the most stable complexes. All the local vibrational modes (LVMs) associated with these complexes are predicted.

The present calculations are of the ‘first-principles’ type, which means that the theory contains no parameter fitted to an experimental database. The key details of the methodology are described in section 2. The configurations, symmetries, binding energies, and vibrational spectra of the defects associated with N are in section 3, and those for C in section 4. The paper concludes with a brief discussion in section 5.

2. Theoretical background

All the results presented below were obtained with first-principles density-functional theory[2] coupled to molecular-dynamics (MD) simulations.[3] The implementation is based on the SIESTA[4,5] package. The host crystal is represented by periodic 64-host atom supercells. The electronic problem is solved self-consistently within the local density approximation. The exchange-correlation potential is that of Ceperley-Alder,[6] parameterized by Perdew-Zunger.[7] Ab-initio pseudopotentials in the Kleinman-Bylander[8] form are used. The basis sets consist of numerical linear combinations of atomic orbitals. In the present work, double-zeta basis sets with polarization functions on selected atoms. The k -point sampling is a $2\times 2\times 2$ Monkhorst-Pack[9] mesh, except for constant-temperature MD runs and the calculations of vibrational spectra which require substantial computer resources and are limited to $k=0$.

The vibrational frequency analysis is carried out within linear response theory.[10] This method allows the entire dynamical matrix of the cell to be calculated from derivatives of the density matrix relative to atomic coordinates. Extensive testing[10] of known LVMs for light impurities in Si has shown that the frequencies calculated in this manner are typically within 2% of the observed ones. The method has also been shown to be very accurate for the calculation of ‘pseudo-LVMs’, which are localized impurity-related modes buried in the phonon bands.[11]

This combination of theoretical tools allows us to calculate the stable and metastable structures using simulated quenching and conjugate gradients, the relative energies of the various structures, the binding and formation energies of the complexes, as well as complete vibrational spectra. We also obtain a lot of chemical information about the bonding through Mulliken population analyses.

3. Nitrogen-related complexes

The nitrogen defects considered here are interstitial N_i , substitutional N_s , $N_i +$ the Si self-interstitial $\{N_i,I\}$, the interstitial-interstitial $\{N_i,N_i\}$, substitutional-interstitial $\{N_s,N_i\}$, and substitutional-substitutional $\{N_s,N_s\}$ pairs, and two nitrogen-hydrogen complexes, $\{N_i,H\}$ and $\{N_s,H\}$. They are all described in detail in Ref.[1] and we focus here on some key results. The defect with the lowest formation energy is $\{N_i,N_i\}$. Figure 1 shows this pair (left), as well as the $\{N_i,H\}$ and $\{N_s,H\}$ complexes (center and right, respectively). These are the three complexes most likely to appear in IR spectra following the hydrogenation, should N also diffuse into the sample during the process.

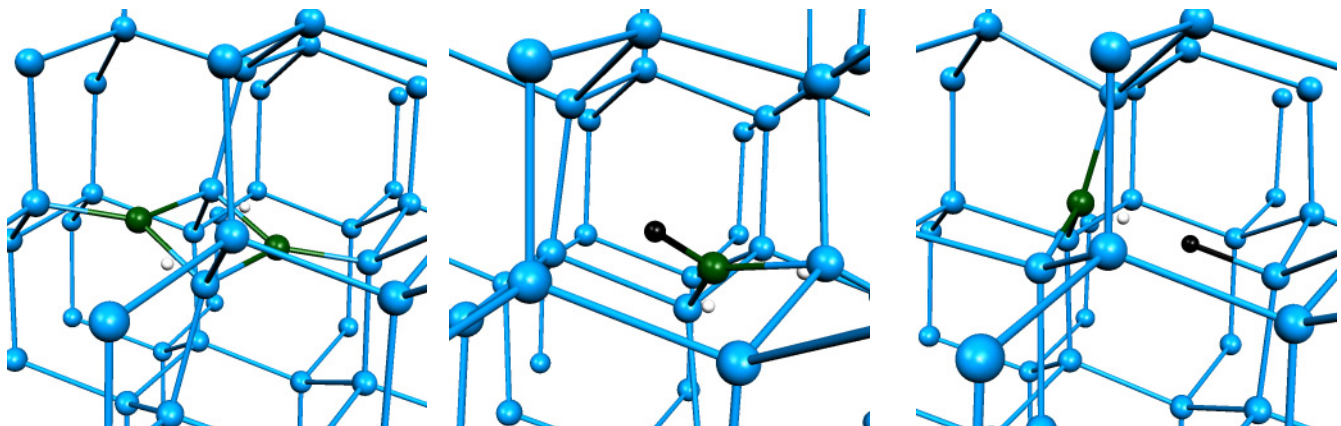


Fig. 1: The $\{N_i,N_i\}$ pair (left) and the $\{N_i,H\}$ and $\{N_s,H\}$ complexes (center and right, respectively). The light blue spheres are Si, the dark green spheres are N, and the small black spheres are H. The large white dots show the location of the perfect substitutional sites.

The vibrational spectrum of $\{N_i, N_i\}$ consists of six modes associated with the motion of the two N atoms. They occur at 1036, 934, 730, 705, 308, and 252cm^{-1} , respectively. Note that two frequencies (at 962.1 and 765.6cm^{-1}) associated with this complex have been observed.[12] They correspond to our 934 and 730cm^{-1} modes, respectively. Six additional modes are associated with the four Si nearest-neighbors to the N atoms (Fig.1, left), and are discussed elsewhere.[1] The LVMs associated with the $\{N_i, H\}$ complex are at 3065 (N-H stretch) and 1160cm^{-1} (H wag). Those associated with $\{N_s, H\}$ are at 2024 (Si-H stretch) and 569cm^{-1} (H wag). The binding energies of H to N_i and N_s were calculated relative to H_{BC} , neutral isolated bond-centered (BC) hydrogen. The reactions $N_i + H_{BC} \rightarrow \{N_i, H\}$ and $N_s + H_{BC} \rightarrow \{N_s, H\}$ release 2.07 and 1.87eV, respectively.

4. Carbon-related complexes

Following the hydrogenation, H has ample opportunity to interact not just with native defects but also with carbon, which is the most common impurity in EFG material. In fact, the presence of several $\{C, H\}$ complexes should be expected. We have studied interstitial C_i , substitutional C_s , the $\{C_s, C_i\}$ pair, and are studying a range of $\{C, H\}$ complexes. The complete results will be discussed elsewhere. We focus here on two $\{C_s, H, H\}$ complexes which have been observed[13,14] following the hydrogenation of C-rich Si. There are two distinct $\{C_s, H, H\}$ complexes, which we (and other authors[14]) find to be nearly degenerate in energy. Both have trigonal (C_{3v}) symmetry and involve a C-H and a Si-H bond, but at different near-BC and anti-bonding (AB) sites. The $C_sH_2^*A$ complex is $C_s - H_{BC} \dots Si - H_{AB}$ (Fig.2, left) and the $C_sH_2^*B$ complex is $Si - H_{BC} \dots C_s - H_{AB}$ (Fig.2, right).

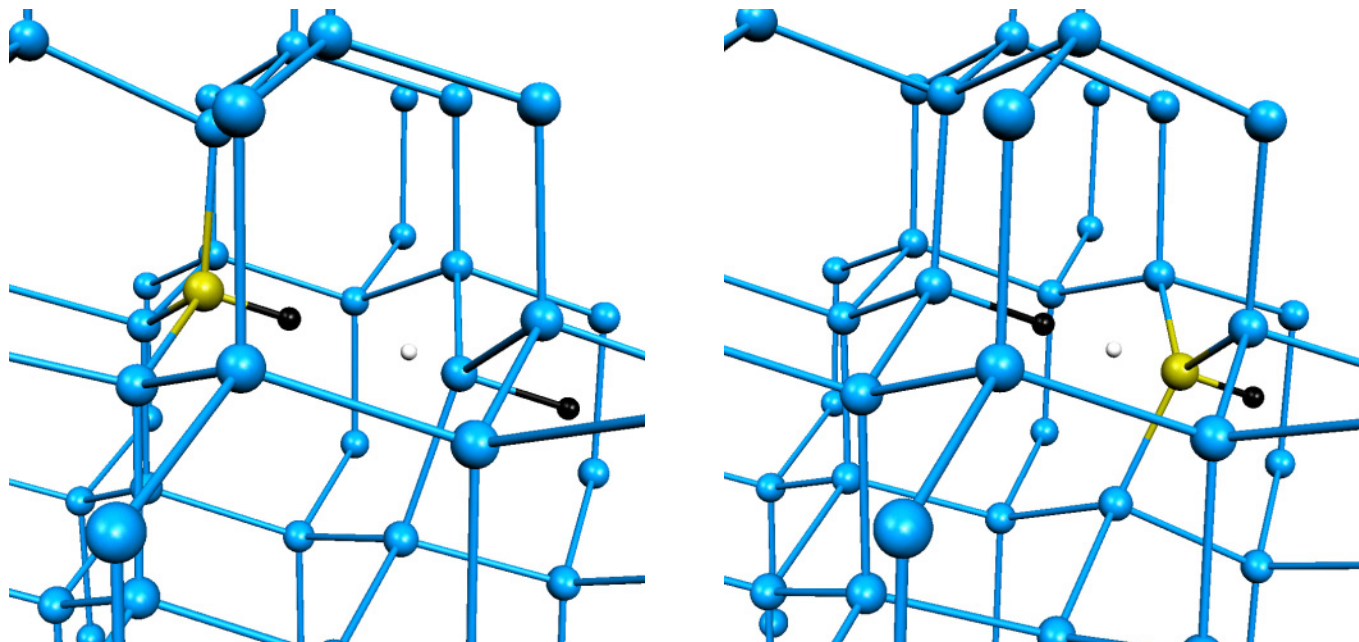


Fig. 2: The $C_sH_2^*A$ (left) and $C_sH_2^*B$ (right) complexes: The light blue spheres are Si, the yellow spheres are C, and the small black spheres are H. The large white dots show the location of the perfect substitutional sites.

In $C_sH_2^*A$, the C_s - H_{BC} and Si - H_{AB} stretch frequencies are measured at 2752 and 1921cm^{-1} , respectively.[13] Our calculated modes are at 2846 and 1857cm^{-1} , respectively. In $C_sH_2^*B$, the observed Si - H_{BC} stretch is at 2210cm^{-1} [14] and we calculate this mode to be at 2159cm^{-1} . No C - H_{AB} mode has been reported in the experimental studies, but we calculate it to be at 2674cm^{-1} . It is an IR-active mode and should be observable.

At T=0K, the total electronic energy difference between $C_sH_2^*A$ and $C_sH_2^*B$ is only 0.004 eV, suggesting that these two complexes should always coexist. Note that (i) this value does not include the difference in total zero-point energy, and (ii) the total (electronic plus free energy) difference between these two defects has yet to be calculated as a function of temperature. The binding energy of $C_sH_2^*(A)$ (or B) was obtained relative to the interstitial H_2 molecule in Si, i.e. from the reaction $C_s + 2H_{BC} \rightarrow C_sH_2^*$ which releases 1.06eV (slightly more than the 0.8eV reported in by other authors[14]).

5. Discussion

Systematic studies of nitrogen- and carbon-related defects in Si and their complexes with H are being carried out. The results are all obtained from first principles and a direct connection to experiment is provided by the vibrational spectra of the defects. The key results obtained so far are as follows.

(i) The most stable N-related defect is Si is the interstitial $\{N_i, N_i\}$ pair. It is characterized by four LVMs at 1036, 934, 730 and 705cm^{-1} and two pseudo-LVMs at 308 and 252cm^{-1} , respectively.

(ii) The $\{N_i, H\}$ and $\{N_s, H\}$ complexes have also been considered. Their binding energies of H (relative to H_{BC}) are of the order of 2eV, suggesting that they should form if enough N and H is present in the material. These complexes are characterized by H-related stretch and wag LVMs at 3065 and 1160cm^{-1} (for $\{N_i, H\}$), respectively, and 2024 and 569cm^{-1} (for $\{N_s, H\}$), respectively.

Until now, none of these the three complexes described in (i) and (ii) has been detected in the IR work (experimental part of this contract), which suggests that little or no N diffuses into the sample during the hydrogenation.

(iii) Hydrogen is known to interact with C in Si and forms two nearly energetically degenerate $\{C_s, H, H\}$ complexes which we label $C_sH_2^*A$ and $C_sH_2^*B$. The binding energies relative to the interstitial H_2 molecule is just above 1eV. Our calculated structures agree well with those of other authors[14] and our calculated LVMs are quite close to the measured ones. More studies of C in Si and its interactions with H are under way.

References

1. J.L. McAfee, He Ren, and S.K. Estreicher, Phys. Rev. B (submitted).
2. W. Kohn W, Rev. Mod. Phys. **72**, 1253 (1999).
3. S.K. Estreicher and P.A. Fedders, in *Computational Studies of New Materials*, ed. D.A. Jelski and T.F. George (World Scientific, Singapore, 1999), p.27-73.
4. D. Sánchez-Portal, P. Ordejón, E. Artacho, and J.M. Soler, Int. J. Quant. Chem. **65**, 453 (1997).
5. E. Artacho, D. Sánchez-Portal, P. Ordejón, A. García, J.M. Soler, Phys. Stat. Sol. (b) **215**, 809 (1999).
6. D.M. Ceperley and B.J. Alder, Phys. Rev. Lett. **45**, 566 (1980).
7. S. Perdew and A. Zunger, Phys. Rev. B **32**, 5048 (1981).
8. L. Kleiman and D.M. Bylander, Phys. Rev. Lett. **48**, 1425 (1982).
9. H.J. Monkhorst and J.D. Pack, Phys. Rev. B **13**, 5188 (1976).
10. J.M. Pruneda, S.K. Estreicher, J. Junquera, J. Ferrer, and P. Ordejón, Phys. Rev. B **65**, 075210 (2002).
11. S.K. Estreicher, D. West, J. Goss, S. Knack, and J. Weber, Phys. Rev. Lett. **90**, 035504 (2003).
12. R. Jones, S. Öberg, F. Berg Rasmussen, and B. Bech Nielsen, Phys. Rev. Lett. **72**, 1882 (1994).
13. V.P. Markevich, L.I. Murin, J. Hermansson, M. Kleverman, J.L. Lindström, N. Fukata, and M. Suezawa, Physica B **302-303**, 220 (2001).
14. B. Hourahine, R. Jones, S. Öberg, P.R. Briddon, V.P. Markevich, R.C. Newman, J. Hermansson, M. Kleverman, J.L. Lindström, L.I. Murin, N. Fukata, and M. Suezawa, Physica B **308-310**, 197 (2001).

Characterization of H introduced into Si by hydrogenation from SiN_x films

Michael Stavola¹, Fan Jiang¹, A. Rohatgi², D. Kim², J. Holt³, H. Atwater³, and J. Kalejs⁴

1. Department of Physics, Lehigh University, Bethlehem, Pennsylvania 18015

2. School of Electrical Engineering, Georgia Institute of Technology, Atlanta, Georgia 30332

3. Department of Applied Physics, California Institute of Technology, Pasadena, California 91125

4. RWE Schott Solar, Inc., Billerica, Massachusetts 01821

Abstract: A promising method to introduce H into multicrystalline Si solar cells in order to passivate bulk defects is by the post-deposition annealing of an H-rich, SiN_x surface layer. It previously has been difficult to characterize the small concentration of H that is introduced by this method. Infrared spectroscopy has been used together with marker impurities in the Si to determine the concentration and depth of H introduced into Si from an annealed SiN_x film.

Hydrogen is commonly introduced into multicrystalline Si solar cells to reduce the deleterious effects of defects and increase the minority carrier lifetime [1-8]. A promising method to introduce H is from a hydrogen-rich (~20 at.%) layer of SiN_x that is deposited onto the Si to act as an antireflection coating [4-8]. A post-deposition anneal is used to diffuse H from the SiN_x layer into the Si in order to hydrogenate defects in the bulk Si. Unfortunately, it has been difficult to detect directly the H that is introduced because of its small concentration. Therefore, the effectiveness of the hydrogenation that results from the post-deposition annealing of SiN_x layers has remained controversial [9,10]. Furthermore, the indiffusion of H into Si is often limited by trapping [11], making the appropriate effective diffusion constant to describe the penetration depth of H uncertain. In the present paper, a method that combines infrared (IR) spectroscopy with marker impurities that can trap H in Si is used to determine the concentration and depth of H that is introduced into Si from a SiN_x layer. Pt impurities are used as model traps for H because the Pt-H complexes in Si are thermally stable (up to 650°C) and their H vibrational absorption lines have been identified [12]. Furthermore, the intensities of the Pt-H IR lines have been calibrated so that the concentration of H in the Si sample can be estimated [13].

To increase the sensitivity of vibrational spectroscopy for the detection of small concentrations of H-containing defects, IR absorption measurements have been made for samples in a multiple-internal-reflection (MIR) geometry. Samples with dimensions 15 x 18 x 1.5 mm³ were made from lightly doped Si grown by the floating-zone method. The ends of the samples were beveled at 45°. The probing light was introduced through one of the beveled ends so as to be multiply reflected many times from the internal surfaces as it passes through the sample (Fig. 1). Pt impurities, to be used as traps for H, were diffused into the Si samples at a temperature of 1225°C. The resulting Pt concentration is estimated to be ~10¹⁷ cm⁻³ from solubility data in the literature [14]. SiN_x layers were deposited onto the Si samples either by plasma-enhanced chemical vapor deposition (PECVD) [7] or by hot-wire chemical vapor deposition (HWCVD) [15]. The substrate temperature for the depositions was ~300°C and the nitride layer thicknesses were ~80 to 100 nm. Samples were annealed in a tube furnace in an ambient of flowing N₂. IR absorption measurements were made with a Bomem DA3 FTIR spectrometer equipped with a KBr beamsplitter and an InSb detector. Samples were cooled for IR measurements to near 4.2K with a Helitran, continuous-flow cryostat.

IR spectra are shown in Fig. 2 for a Si:Pt sample onto which a SiN_x layer had been deposited by HWCVD. The broad band centered at 2160 cm⁻¹ is due to Si-H bonds in the H-rich SiN_x layer [16]. For anneals performed at successively higher temperatures, the Si-H band from the SiN_x decreases in intensity and an H vibrational line at 1880 cm⁻¹, assigned previously to the neutral charge state of the PtH complex in Si [13], grows in intensity. No other IR lines due to H-containing defects in the Si bulk were detected

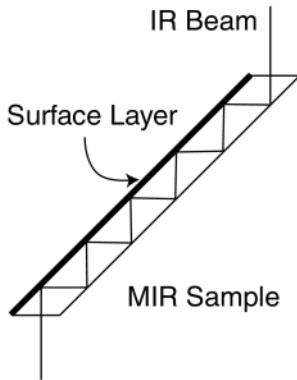


Fig. 1. Multiple-internal-reflection geometry used for IR measurements of Si samples hydrogenated from a SiN_x surface layer.

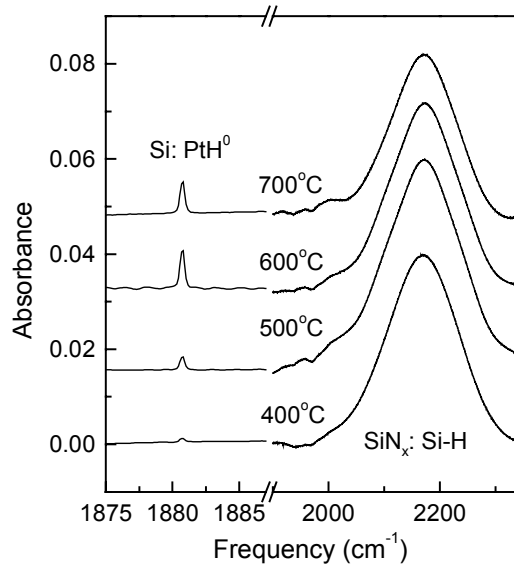


Fig. 2. IR spectra for a bulk Si:Pt sample with a SiN_x layer deposited on its surface by hot-wire CVD. The sample was annealed (10 min.) at the indicated temperatures to introduce H into the Si. Vibrational lines assigned to Si-H bonds in the SiN_x layer and to PtH complexes in the Si are shown.

in our experiments. These results show unambiguously that H from the SiN_x surface layer diffuses into the Si substrate during a post-deposition anneal and that this H forms complexes with defects in the bulk.

The intensity of the PtH IR line at 1880 cm^{-1} provides quantitative information about the concentration of H in the Si sample. From the calibration of the intensity of the PtH line reported in ref. (13), the concentration of PtH complexes is related to the area of the 1880 cm^{-1} absorbance line by,

$$[\text{PtH}] (\text{cm}^{-3}) = 2.6 \times 10^{16} \text{ cm}^{-1} \left(\int A d\bar{\nu} \right) / d_{\text{eff}}. \quad (1)$$

Here, $\bar{\nu}$ is the frequency of the light in wavenumbers, and A is the absorbance (which is related to the absorption coefficient by $A = \alpha d_{\text{eff}} \log_{10} e$). For the MIR geometry shown in Fig. 1, the optical path length, d_{eff} , is proportional to the thickness d of the hydrogenated layer and is given by,

$$d_{\text{eff}} = N d \sec \theta = (L \cot \theta / w) d \sec \theta. \quad (2)$$

Here, L is the length of the MIR sample, w is its thickness, θ is the bevel angle, and N is the number of passes the light makes through the absorbing layer. For our samples, with $L = 18 \text{ mm}$, $w = 1.5 \text{ mm}$, and $\theta = 45^\circ$, the MIR geometry, when compared with a single pass at normal incidence, typically increases the optical path length by a factor of $N \sec \theta \approx 17$. Initially, the thickness d of the absorbing layer is unknown. In this case, the product of the defect concentration times the layer thickness, or the areal density, can be determined from the area of the absorbance line [17].

Fig. 3(a) shows the PtH IR line for a sample that had been hydrogenated by a post-deposition anneal (5 min. at 600°C) of a SiN_x layer deposited by PECVD. To determine the depth of H penetration, hydrogenated samples were mechanically thinned in successive steps in which ~ 50 to $100 \mu\text{m}$ were removed from the surface onto which the SiN_x had been deposited. Figs. 3(a) and (b) show that the areal density of PtH centers is reduced as layers are removed successively from the sample. The linear

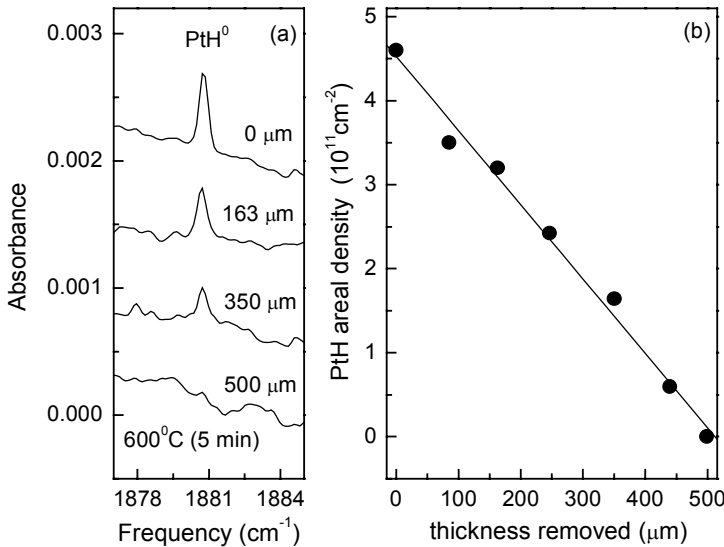


Fig. 3. (a) IR spectra showing the vibrational line of the PtH complex in a Si:Pt sample that was hydrogenated by the post-deposition annealing (5 min at 600°C) of a PECVD SiN_x film. Spectra were measured after a surface layer of the indicated thickness had been removed from the sample. (b) The areal density of PtH complexes remaining in the sample vs. the thickness of the layer removed from the surface, derived from the data shown in (a).

decrease of the IR intensity with the increasing thickness of the removed layer shows that the concentration of PtH centers for these annealing conditions is approximately constant up to a maximum penetration depth of 500 μm into the sample.

The concentration of PtH complexes can be determined from their areal density once the thickness of the hydrogenated layer has been determined. The concentration of PtH complexes for the sample whose spectra are shown in Fig. 3 is $1 \times 10^{13} \text{ cm}^{-3}$. The sample whose spectra are shown in Fig. 2 was thinned and studied similarly by IR spectroscopy (following the anneal at 700°C). In this case, the penetration depth of H was estimated to be $1 \times 10^3 \mu\text{m}$, and the concentration of PtH complexes was determined to be $5 \times 10^{13} \text{ cm}^{-3}$.

The concentration of H introduced into Si from a SiN_x layer has been found to be modest in the experiments performed here, i.e., from near 1 to $5 \times 10^{13} \text{ cm}^{-3}$. The H that diffuses into the Si bulk corresponds to the order of only ~ a tenth of a percent of the total H that is liberated from the SiN_x coating by an anneal at near 600°C. For example, for the data shown in Fig. 2, the 600°C anneal reduces the area of the 2160 cm^{-1} Si-H IR band by 5%. If we estimate that the 80 nm-thick SiN_x layer contains a H concentration of $\sim 1 \times 10^{22} \text{ cm}^{-3}$, this corresponds to an areal density of released H of $\sim 4 \times 10^{15} \text{ cm}^{-2}$. The intensity of the 1880 cm^{-1} PtH line following the anneal at 600°C leads to an areal density of PtH complexes in the Si of $6 \times 10^{12} \text{ cm}^{-2}$, or only 0.15% of the total H released from the SiN_x. While the concentration of H introduced into Si is small, it is, nonetheless, sufficient to affect the electrical activity of dislocations and impurities like the transition metals that are highly effective lifetime killers. Our experiments suggest that hydrogenation of Si from a SiN_x layer yields a H concentration that lies between optimistic estimates of the amount of H that can be introduced into the Si bulk [9] and the negative viewpoint taken by Boehme and Lucovsky that bulk hydrogenation does not occur [10].

The results presented here provide information about the diffusivity of H during hydrogenation from SiN_x. There has been considerable interest in the penetration depth of H into Si because of its importance in the design of processes that will optimize the hydrogen passivation of solar cells [3,18]. The diffusivity of H in Si was measured at high temperature in an early study by Van Wieringen and Warmoltz [19] and gives the diffusion constant,

$$D = 9.4 \times 10^{-3} \exp(-0.48 \text{ eV} / kT) \text{ cm}^2/\text{s}. \quad (3)$$

Subsequent studies have found that the D given by Eq. (3) is valid for the diffusion of H⁺, the dominant charge state of H in Si at elevated temperature [20], for situations where H does not interact with other

defects and where relatively immobile H₂ molecules are not formed [11]. In many experimental situations, the diffusion of H is limited by trapping, and an effective diffusion constant is found that is typically two to three orders of magnitude smaller than Eq. (3) would predict [11]. Therefore, it becomes important to obtain data on the indiffusion depth of H that are valid for specific hydrogenation conditions. The data in Fig. 3 show that for a 5 min. anneal at 600°C, the thickness of the hydrogenated layer that results is ~500 μm. Eq. (3) gives a diffusion constant of $D = 1.6 \times 10^{-5} \text{ cm}^2/\text{s}$ at 600°C; for a 5 min. anneal, this value would give a \sqrt{Dt} diffusion length of 690 μm. This comparison shows that the effective diffusion constant in our experiments is roughly within a factor of two of the value extrapolated from the results of Van Wieringen and Warmoltz [19]. (A similar conclusion is obtained from the H penetration depth determined for the sample annealed for 10 min. at 700°C.) This is a surprising result, given that one might expect the H penetration depth to be limited by trapping in our experiments and to be greatly reduced from the value predicted from Eq. (3). Nonetheless, the rapid indiffusion observed here is consistent with the effectiveness of typical annealing treatments of a few minutes near 750°C used to passivate Si solar cells and suggests that such anneals drive H deep into the Si bulk.

We thank Mark Rosenblum for his assistance with our experiments. Work performed at Lehigh University was supported by NREL Contract No. AAT-1-31606-04 and NSF Grant No. DMR-0108914.

References

1. C. H. Seager, D. S. Ginley, and J. D. Zook, *Appl. Phys. Lett.* **36**, 831 (1980).
2. J.I. Hanoka, C.H. Seager, D.J. Sharp, and J.K.G. Panitz, *Appl. Phys. Lett.* **42**, 618 (1983).
3. B.L. Sopori, X. Den, J.P. Benner, A. Rohatgi, P. Sana, S.K. Estreicher, Y.K. Park, and M.A. Roberson, *Solar Energy Materials and Solar Cells* **41/42**, 159 (1996).
4. R. Hezel and R. Schörner, *J. Appl. Phys.* **52**, 3076 (1981).
5. R. Lüdemann, *Mater. Sci. Eng. B* **58**, 86 (1999).
6. A. Rohatgi, P. Doshi, J. Moschner, T. Lauinger, A.G. Aberle, and D.S. Ruby, *IEEE Trans. Electron. Dev.* **47**, 987 (2000).
7. A. G. Aberle, *Sol. Energy Mater. Sol. Cells* **65**, 239 (2001) reviews the SiN_x passivation of c-Si solar cells and includes a historical overview.
8. F. Duerinckx and J. Szlufcik, *Sol. Energy Mater. Sol. Cells* **72**, 231 (2002).
9. B. L. Sopori, Y. Zhang, and R. Reedy, Proc. 29th IEEE-Photovoltaic Specialists Conference, New Orleans, May 2002, edited by R. D. McConnell (Report No. NREL/EL-590-32461).
10. C. Boehme and G. Lucovsky, *J. Appl. Phys.* **88**, 6055 (2000); *J. Vac. Sci. Technol. A* **19**, 2622 (2001).
11. M. Stavola, in *Properties of Crystalline Si*, edited by R. Hull (INSPEC, London, 1999), p. 511.
12. S.J. Uftring, M. Stavola, P.M. Williams, and G.D. Watkins, *Phys. Rev. B* **51**, 9612 (1995).
13. M.G. Weinstein, M. Stavola, K.L. Stavola, S.J. Uftring, J. Weber, J.-U. Sachse, and H. Lemke, *Phys. Rev. B* **65**, 035206 (2002).
14. *Impurities and Defects in Group IV Elements and III-V Compounds*, Vol. III/22b, in the Landolt-Bornstein, New Series, edited by O. Madelung and M. Schulz (Springer, Berlin, 1989).
15. J.K. Holt, D.G. Goodwin, A.M. Gabor, F. Jiang, M. Stavola, and H.A. Atwater, *Thin Solid Films*, to be published.
16. A. Fadini and F.-M. Schnepel, *Vibrational Spectroscopy* (Wiley, New York, 1989), p. 41.
17. The integrated absorption coefficient is proportional to the concentration of absorbing centers. However, the absorbance, A, determined by experiment, is proportional to the product of the absorption coefficient times the thickness of the absorbing layer. The integrated absorbance, therefore, is proportional to the concentration of centers times the thickness of the absorbing layer, that is, to the areal density.
18. J. P. Kalejs and S. Rajendran, *Appl. Phys. Lett.* **55**, 2763 (1989).
19. A. Van Wieringen, and N. Warmoltz, *Physica* **22**, 849 (1956).
20. C. Herring, N. M. Johnson and C. G. Van de Walle, *Phys. Rev. B* **64**, 125209 (2001).

The Generation and Manipulation of Point Defects and Light Element Impurities in Silicon by Electron Irradiation

*N. Stoddard, G. Duscher, and G. Rozgonyi
Materials Science and Engineering Department,
North Carolina State University, Raleigh, NC, 27695-7916*

Introduction

The use of nitrogen doping in high purity silicon has been a topic of much research in the last few years.¹ Both Czochralski and Float Zone single crystal silicon benefit from the introduction of low concentrations ($< 10^{15} \text{ cm}^{-3}$) of nitrogen. Specifically, nitrogen-doped Czochralski silicon (N-CZ Si) has increased denuded zone integrity and size², along with a higher density of smaller oxygen precipitates in the bulk which provides improved gettering ability compared to nitrogen free CZ Si.³ Although the oxygen precipitate growth rate and size are limited by oxygen diffusion, which requires high temperatures, the precipitate density is independent of annealing temperature since they grow from nuclei that exist in the as-grown N-CZ Si.³ Theoretical work⁴ suggests that the split-interstitial N₂ complex is quite stable and tends to form vacancy complexes, either as VN₂ or, more prevalently, V₂N₂. These complexes tie up vacancies at high temperature and reduce the formation of voids by delaying their onset temperature during cooling.⁵

Frenkel defect generation and interaction with impurities under a 200kV transmission electron microscope (TEM) beam have recently been observed in N-CZ Si.⁶ The Frenkel pairs do not all recombine due to the presence of nitrogen and its complexes, but can permanently separate. The interstitial atoms, stimulated by further electron collisions, diffuse away from the e-beam irradiated zone; leaving behind nitrogen related complexes that either accumulate vacancies to produce voids, or oxygen atoms to initiate SiO₂ nucleation. The benefit of this nanoscale TEM laboratory is that normally high temperature extended defect nucleation processes are observed at room temperature in an area of the TEM operator's choosing.

Materials and Methods

[100] oriented N-FZ and N-CZ plan-view samples were prepared by conventional TEM thinning methods, which include grinding, polishing, dimple grinding and ion milling. The irradiation was performed at 200 kV in JEOL 2010F and Topcon 002B electron microscopes, while high-resolution imaging, Electron Energy Loss Spectroscopy (EELS), and scanning TEM (STEM) in Z-Contrast and bright field modes were performed on the JEOL instrument.

Results and Discussion

Figure 1 depicts a N-CZ Si sample in both bright field and Z-Contrast modes of the STEM. The dark and light arcs visible in A) and B), respectively, delineate the boundary of the irradiated region, located near the edge of the TEM foil. In Z-Contrast images B), C) and D), the low signal dark areas correspond to a high concentration of vacancies, while the high signal bright areas are denser, being either rich in self-interstitials or composed of silicon dioxide. Z-Contrast image features are generally due to differing elemental distributions (based on atomic number Z), varying sample thickness or density fluctuations.⁷ Since this sample is pure CZ silicon, we can attribute the contrast to local Si density variations or the presence of oxide. In addition, EELS chemical analysis has shown that high oxygen concentrations exist both inside

the large irradiated region and in a speckled ring just outside of it, as can be seen in Figs. 1C and 1D. It is believed that the electron excitation greatly enhances oxygen diffusion, eventually leading to clustering and precipitation. Ripening of oxygen clusters inside the irradiated zone

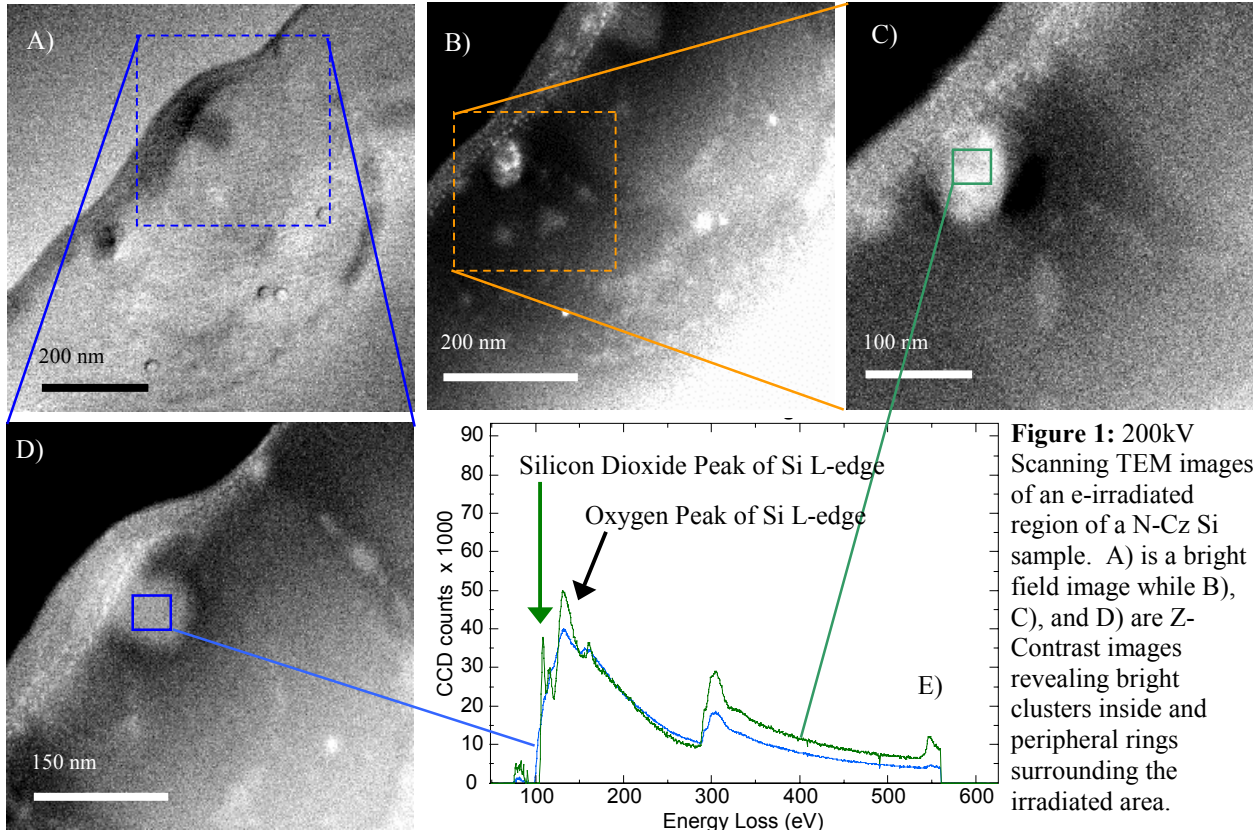


Figure 1: 200kV Scanning TEM images of an e-irradiated region of a N-Cz Si sample. A) is a bright field image while B), C), and D) are Z-Contrast images revealing bright clusters inside and peripheral rings surrounding the irradiated area.

has been observed as longer irradiation times are used, a process that competes with diffusion out of the beam volume. While nitrogen concentrations were too small for measurement by EELS, the oxygen is readily detected and has some dramatic effects. For example, of the two large bright spots in Figs. 1C and 1D, the sharply defined EELS spectra, see Fig. 1E, for the boxed area in Fig. 1C clearly indicates the presence of pure silicon dioxide. This particle has fairly distinct boundaries, while the bright area in 1D has softer edges and is a mix of silicon and silicon dioxide, as indicated by its EELS spectrum. No particle like either of these two was found elsewhere in the sample. From the point of view of diffusion and coarsening, the particle locations can be explained as schematically illustrated in Fig. 2. Since the irradiation consists of fairly random electron stimulated diffusion events within a finite beam area, as shown in Fig. 2A,

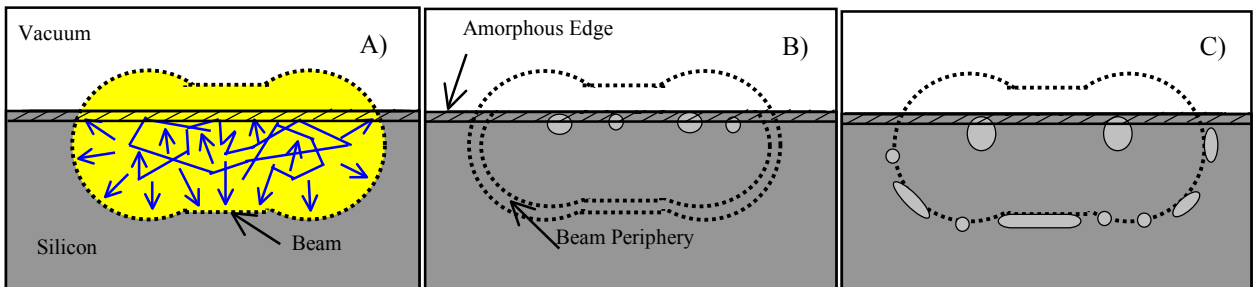


Figure 2: Illustration of diffusion, nucleation and coarsening effects during electron irradiation

some silicon and oxygen will leave the beam area near the periphery, while oxygen in the middle will tend to accumulate at nitrogen related complexes in the center and at favorable sites, such as the amorphous edge of the sample, as illustrated in Fig. 2B. The final picture, see Fig. 2C, has the central clusters consolidated and coarsened and a distinct ring of clusters around the edge of the beam. This matches the observations of Figs. 1A and 1B, which focus on an area that was irradiated for 30 minutes.

Nitrogen-doped FZ silicon exhibits the same separation of interstitials and vacancies described above for N-CZ samples, see the Z-Contrast micrograph in Fig. 3A. The irradiated area appears as a dark circle whose weaker contrast corresponds to a lower concentration of silicon atoms, i.e. a higher concentration of vacancies. A diffuse brighter halo of excess interstitials surrounds the dark circle. EELS spectra, see Fig. 3C, from the bright areas also revealed another interesting phenomenon: the front slope of the silicon L-edge has a distinctive step feature in the bright ring outside the beam area. This feature is quite pronounced compared to reference bulk measurements at the same thickness, and consistent with results from similar areas of the N-CZ Si sample. This step is indicative of excess plasmon scattering, an effect generally attributed to a high concentration of interstitial silicon, supporting the theory that self-interstitials diffuse out of the excited volume over time.

There are, however, important differences compared to the N-CZ Si due to the lack of oxygen. First, there is no atomic clustering or oxide formation, as is obvious from Fig. 3A. This

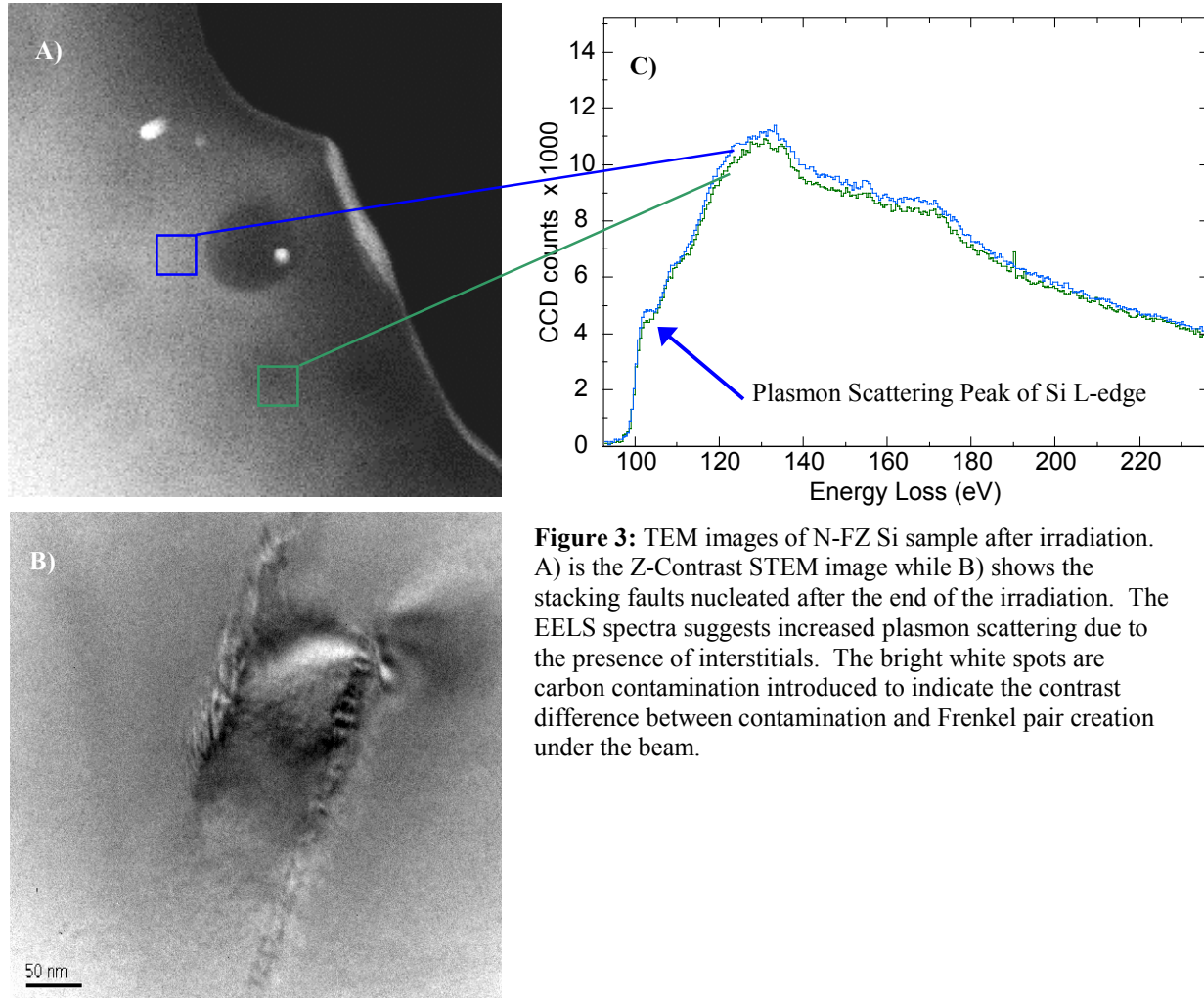


Figure 3: TEM images of N-FZ Si sample after irradiation. A) is the Z-Contrast STEM image while B) shows the stacking faults nucleated after the end of the irradiation. The EELS spectra suggests increased plasmon scattering due to the presence of interstitials. The bright white spots are carbon contamination introduced to indicate the contrast difference between contamination and Frenkel pair creation under the beam.

is more or less as expected, strongly supporting the role of oxygen in the growth of the atomic clusters. A second, more surprising difference is the presence of faint, brighter lines emanating from the halo. The most likely explanation is that the lines are directions of preferred interstitial silicon diffusion. In addition to having no detectable oxide formation, the FZ samples also respond differently to the stress from the point defect imbalance built up by the interstitial/vacancy segregation. Irradiated spots in CZ samples are stable over long times, but the FZ samples exhibit stress-induced extended defect formation fairly quickly after being irradiated. An example of this is shown in Fig. 3B. In areas close to the edge of the sample, the stress can be accommodated without nucleating faults, due to the extreme thinness of the sample. Thus, introducing low concentrations of oxygen to FZ crystals is likely to prevent the stress-induced defect formation.

Discussion and Conclusion

The formation of stress-induced defects in N-FZ Si via irradiation is an interesting phenomenon. The N-CZ lattice looks no different, even at high resolution, than the N-FZ lattice, yet it is evidently stronger. The strengthening is not coming from detectable particles, even of nanometer size, but must be the result of lattice changes due to the impurity concentrations. Irradiating samples with different oxygen concentrations leads us to propose the following quantitative experiment. First, to determine the level of stress introduced by irradiation, a quantitative value for the number of point defects separated during irradiation could be obtained from empirical estimates or simulation of the electron irradiation. From this, the stress on the surrounding lattice could be derived, which, coupled with information on strain from the analysis of the extended defects, could provide key information on the microscale and nanoscale mechanical properties of the material.

This is just one of many possibilities for studying nanoscale material properties using the room temperature electron irradiation technique. A unique aspect of using 200 keV TEMs is that the electrons are limited by momentum conservation to transferring at most 20 eV of energy to a silicon atom, providing just enough impulse to create knock-ons, and not so much that cascades of damage occur. Interstitial diffusion is also enhanced, but not unreasonably so, allowing nucleation and growth processes that usually occur only at high temperatures to be studied at room temperature and in an observation tool of the highest resolution with chemical analysis capability.

References

- ¹ Rozgonyi, GA, Semiconductor Silicon 2002, *Electrochemical Society PV 2002-1*, 149-162
- ² Tamatsuka M, Kobayashi N, Tobe S and Masui T, *Electrochemical Society PV 99-1*, 456-467
- ³ Nakai K, Inoue Y, Yokota H, Ikari A, Takahashi J, Tachikawa A, Kitahara K, Ohta Y and Ohashi W, *Journal of Applied Physics*. **89** (8), 4301-4309 (2001)
- ⁴ Karoui A, Karoui FS, Rozgonyi GA et al, *Electrochemical Society PV 2002-2*, 670-676
- ⁵ Kageshima H, Taguchi A, Wada K. *Applied Physics Letters* **76** (25), 3718 (2000)
- ⁶ N. Stoddard, A. Karoui, G. Duscher, A. Kvitt and G. Rozgonyi, *Electrochemical Society, High Purity Silicon VII PV 2003-*
- ⁷ S. J. Pennycook and L. A. Boatner, *Nature*, **366**, 565 (1988).

Second-phase Particle Incorporation and the Occurrence of a Cellular Grain Size Distribution in Polycrystalline Sheet Silicon

R. Zhang¹, G. A. Rozgonyi¹, J. Rand², and R. Jonczyk²

¹Department of Materials Science and Engineering, North Carolina State University, Raleigh, NC;

²AstroPower, Inc., Newark, DE

Abstract. This paper discusses the structural, electrical and chemical results obtained from polycrystalline sheet silicon used in solar cell production. The grain size distribution in a cellular pattern was identified, and correlated with minority carrier recombination lifetime value variations. Second-phase particles were directly observed through Infrared imaging. A mechanism wherein insoluble particles can be pushed, engulfed within a grain, or trapped at grain boundaries during crystallization was proposed to explain the aforementioned cellular grain size distribution.

1. Introduction

We present recent characterization results on 600 to 800 μm thick polycrystalline sheet silicon grown at rates greater than three meters per minute [1]. Due to the ample presence of both light element (O, N, C) and metallic (Fe, Cu, Ni, etc.) impurities, and a variety of extended structural defects, the interaction between impurities and defects is very complex, making the optimization of growth process difficult. However, using a complementary set of characterization techniques covering structural, electrical and chemical probes, we are able to establish a relationship between the incorporation of second-phase particles (oxide/nitride/carbide) and the cellular distribution of grain size, which significantly impacts the minority carrier recombination lifetime and the final device performance.

2. Experimental and Results

Polycrystalline Silicon-FilmTM sheet silicon produced by AstroPower was electrically and structurally characterized using laser-microwave photo conductance decay (μ -PCD) and an orientation dependent etching solution (NaOH), respectively. Infrared imaging was performed on double-sided polished samples to directly observe the distribution of second-phase particles within sheet silicon, which was then compared with grain structure revealed by preferential Secco etching/Nomarski imaging.

Initially, the μ -PCD technique was applied to obtain a map of the electrical activity, i.e., lifetime of minority carriers, across a wafer. A typical section of a lifetime map (8 cm x 8 cm) is shown in Fig. 1, along with a corresponding histogram. Note the pronounced cellular pattern, consisting of dark patches with low lifetime values ($\sim 0.5 \mu\text{s}$) interspersed periodically throughout the whole silicon sheet, surrounded by a network of regions with higher lifetime values ($3 \mu\text{s}$). This cellular pattern was consistently observed for a variety of thermal processing histories.

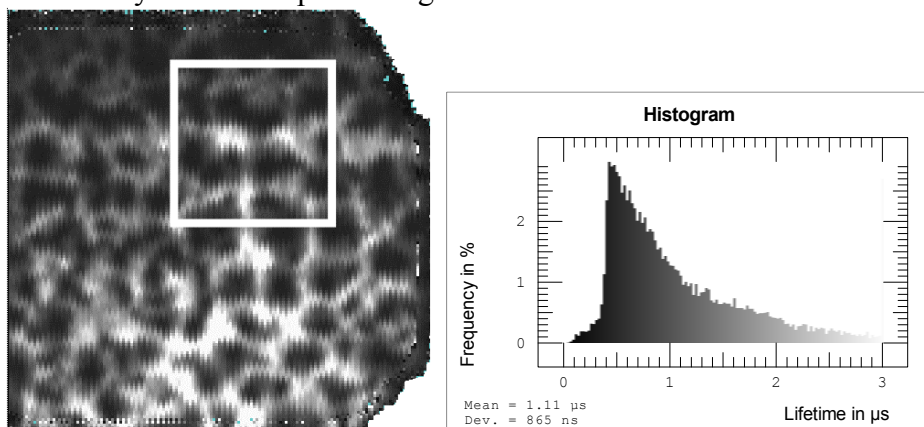


Figure 1: Minority carrier lifetime map of sheet silicon (8 cm x 8 cm), and corresponding histogram.

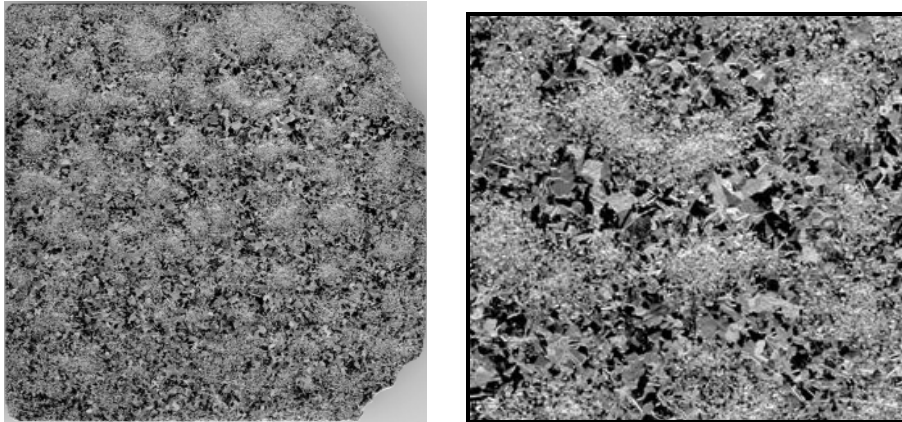


Figure 2: Optical images of the same sample as in Fig. 1, after 30 seconds NaOH etch, together with a blow-up of the region marked by a white rectangle in Fig. 1.

Figure 2 shows corresponding optical images of the same field as in Fig. 1, obtained with an office optical scanner, following 30 seconds etching with NaOH to delineate grain orientations and grain sizes. Note the confirmation of a cellular pattern illustrating that the low lifetimes correspond to fine grains, and higher lifetime values consist of large grains. This grain size dependence was also verified, data not shown here, by Electron Beam Induced Current (EBIC) imaging performed on regions with high or low lifetime values, respectively.

The question arises as to the origin of the grain size shrinkage and lifetime value degradation in the context of cellular pattern formation. Sheet silicon samples after double-sided polishing were further investigated using a QICAM Infrared Mono 8-bit camera, see Fig. 3 for a complete map of a 12 x 12mm sample, which reveals an in-depth cellular pattern of particles similar to that observed in Fig. 1. The dark contrast of particles is due to their absorption of infrared light, while the white spots are over-exposed areas that occurs at low magnification.

Although these particles vary in size and shape, they tend to assume a dendrite-like morphology, as shown in Fig. 4 (c). Curved bands of these particles generally surround large particle free regions which extend around 5 mm, comparable to those of large-grain cellular pattern regions in the lifetime map in Fig. 1. Thus, it is likely that the thermodynamic or kinetic driving force for the formation and distribution of dendrite-like particles is the actual cause of the lifetime map cellular pattern.

Nomarski and Infrared images on typical regions rich in or free of large particles, respectively, are shown in Fig. 4 following a 30 sec Secco etch. The images in Figs. 4 (a) and (b), where the average grain size can reach about 0.5 mm or even 1 mm, are free of large particles, although there is a uniform distribution of small particles of sizes of a few microns. Also, note the grain shrinkage around the large particles indicated by arrows

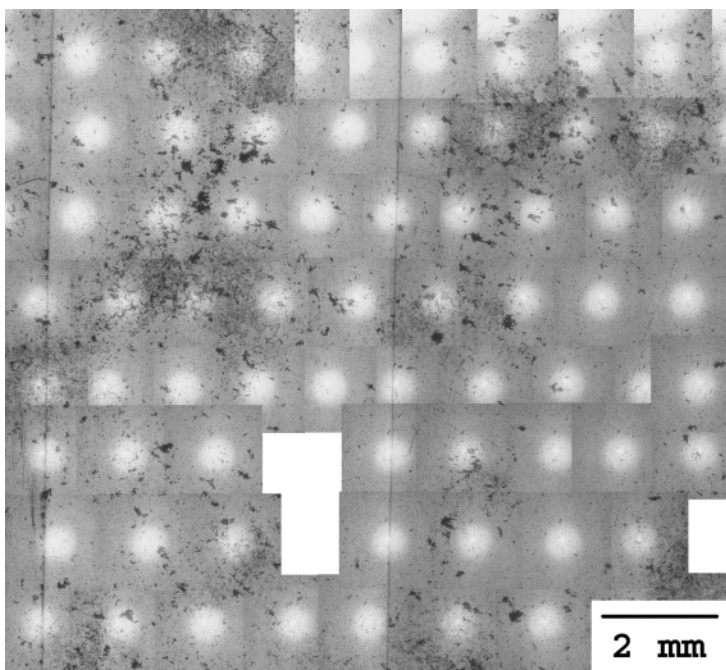


Figure 3: Multiple exposure composite infrared map across a double-side polished 12 x 12mm sample of sheet silicon. Note that those white dots in this figure are due to the non-uniform illumination from light source.

in Fig. 4 (b), and compare the Nomarski and Infrared images on the same region rich with large black absorption zones in Figs. 4 (c) and (d), which exhibit characteristic dendrite-like morphology, in spite of their differences in size and shape. Under close observation, the large black absorption zones are actually agglomerates of smaller dendrites of sizes of ~ 0.1 mm. In regions rich with dendrites, the grain size is greatly reduced to around 0.1 mm and the black Nomarski surface spots are, in fact, just the small tips of extended underlying dendrites.

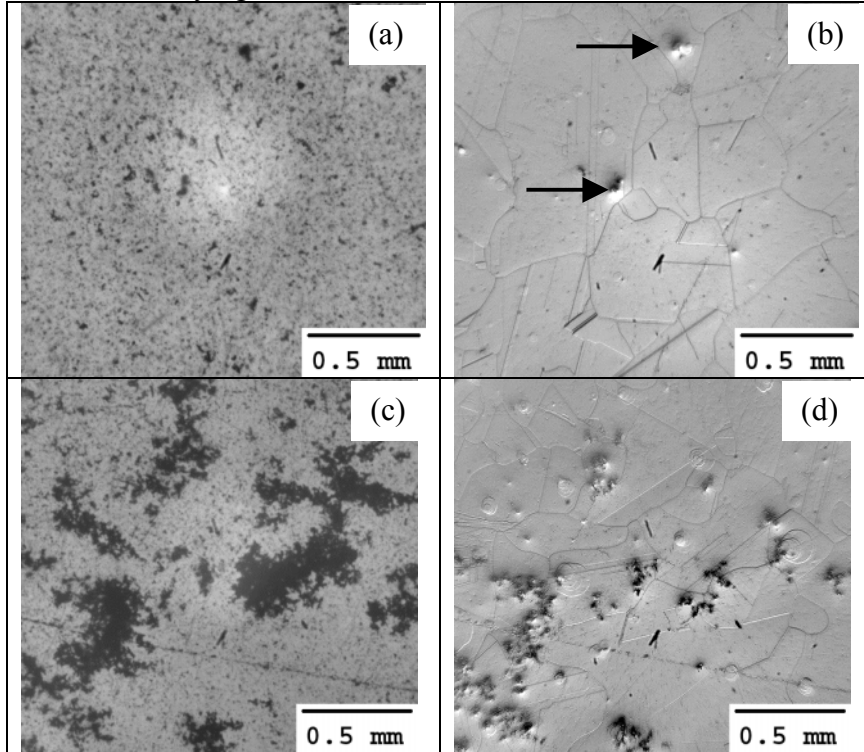


Figure 4: Infrared (a) and (c), and Nomarski, (b) and (d), images on typical regions rich and free of large particles.

The chemical identification of dendrite-like particles has been obtained from Scanning Electron Microscopy/Energy Dispersive Spectrum, in which elements of Si, N, O and/or C have been identified [2], as well as by Fourier Transform Infrared Spectroscopy, see poster by J. Lu [3]. The bulk phase diagram of the Si-N-O system [4] shows that SiN_2O , which is the only thermodynamically stable and crystalline form of silicon oxynitride, can solidify at a temperature higher than the melting point of Si. Then SiN_2O dendrites are incorporated into the sheet silicon during the subsequent solidification process.

3. Modeling of the Cellular Pattern

To interpret the above results, an established model [5] describing the behavior of insoluble particles during crystallization was adapted from the solidification theory of alloy casting for Al-Mg. In a multidirectional solidification process (which occurs in the present case), particles can be pushed, engulfed within a grain, or trapped at grain boundaries, depending on many factors, e.g., particle size and density, interface shape, solidification rate, etc. The presence of insoluble particles with different sizes complicates the solidification process, since particles exceeding a critical size are pushed by the crystallization front into the surrounding liquid regions, while those smaller are entrapped [5]. Thus, it is possible to obtain grains of 1 mm diameter without the structural disturbance of large particles, see Fig. 4 (b), corresponding to the case of R (particle diameter) $< R_C$ (critical particle diameter) in Fig. 5. In neighboring regions where rejected particles are pushed and accumulate, then during subsequent solidification the volume buildup of insoluble particles causes the solid/liquid interface to break down. The crystalline structure is then changed from a columnar grain structure to a smaller grain “equiaxed” structure. In the small grain regions, particles are entrapped at grain boundaries, see the case of $R > R_C$ Fig. 5, giving rise to the structure shown in Fig. 4

(d). This cycle is repeated throughout the whole sheet silicon growth process, resulting in the cellular structure observed in Figs. 1 and 2.

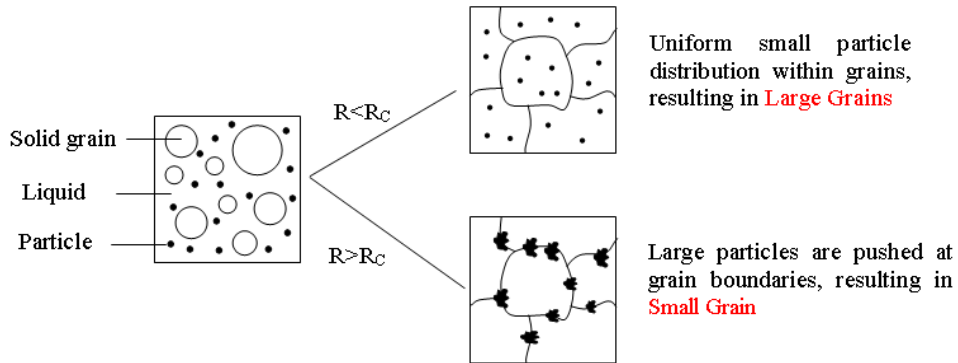


Figure 5: Possible structures in multidirectional solidification as a function of particle diameter.
Note that solidification rate and convection level will also be key issues [5].

4. Conclusions

This report is an initial attempt to describe the behavior of insoluble second phase particles in sheet silicon samples, and indicates that the growth mechanism responsible for those regions with low lifetime values is related to the incorporation of second-phase particles during the solidification process. Without the introduction of insoluble particles, uniform 1 mm grains should be generally feasible in sheet silicon, enabling an average lifetime increase to 2 or 3 μs after thermal treatments. More growth and diagnostic efforts are needed in order to understand the dendritic precipitation process of SiN_2O , as well as its relation the analysis of particle and cell formation.

Acknowledges

The authors are very grateful to Ernest Van Dyk of the University of Port Elizabeth for his help on Infrared imaging.

Reference:

1. J. S. Culik et al., “*Progress in 15-MW Single-Thread Silicon Film Solar Cell Manufacturing Systems*”, 17th ECPVSEC, Munich, October 2001.
2. R. Zhang, G. Duscher, J. Rand, and G.A. Rozgonyi, “*Nanoscale Investigation of Polycrystalline Silicon for Photovoltaic Applications*”, 12th Workshop on Crystalline Silicon Solar Cell Materials and Processes, Breckenridge, CO, 2002, P 206.
3. J. Lu, G.A. Rozgonyi, J. Rand, and R. Jonczyk, “*Distribution of Oxynitride Particles and oxygen Precipitates in Polycrystalline Sheet Silicon*”, 13th Workshop on Crystalline Silicon Solar Cell Materials and Processes, Vail, CO, 2003.
4. E. P. Gusev, H. C. Lu, E. L. Garfunkel, T. Gustafsson, and M. L. Green, “*Silicon Oxynitrides*”, pg. 8576 in **Encyclopedia of Materials: Science and Technology**, Vol 9, K. H. Buschow *et al.*, Ed., Elsevier, 2001.
5. D.M. Stefanescu and B.K. Dhindaw, “*Behavior of Insoluble Particles at the Solid/Liquid Interface*”, pg. 142 in **ASM Handbook: Casting**, Vol 15, D.M. Stefanescu *et al.*, Ed., American Society for Metals International, 1988.

Distribution of Oxynitride Particles and Oxygen Precipitates in Polycrystalline Sheet Silicon

Jinggang Lu and George Rozgonyi

*Materials Science and Engineering Department, North Carolina State University,
Raleigh, North Carolina 27695-7916*

James Rand and Ralf Jonczyk

Astropower Inc., Solar Park, Newark, Delaware 19711

ABSTRACT: The distribution of oxynitride particles and oxygen precipitates in polycrystalline sheet silicon was studied by preferential etching/Nomarski optical microscopy and microscopic Fourier transform infrared spectroscopy. It was found that more oxynitride particles are located in small grain regions, and in a middle of the wafer cross section. The inclusions deeper in the wafer contain more oxygen than those near the top-surface. Cross sectional FTIR indicates that a 200 μm wide interstitial oxygen denuded zone is present in the as-grown wafer, which is sustained as an oxygen precipitate/stacking fault free zone after solar cell processing. It was concluded that particle rejection and the build-up of impurities at the solidification front result in interface breakdown, which gives rise to the increased particle trapping in the middle of a wafer.

I. INTRODUCTION

The direct growth of silicon sheet has received increased attention [1] in recent years because it is highly suitable for low-cost terrestrial-based solar cells. Due to the relatively large contact area with refractory materials used as die or substrate, the impurity concentration in sheet silicon is usually high, and in some cases, foreign particles might be incorporated into the sheet. The low cost silicon feedstock used for the sheet growth also contains a high concentration of impurities. Although metallic impurities are generally considered to be the dominant lifetime killers, light elements O, N, and C can also degrade cell performance by forming detrimental complexes (oxygen thermal donor, boron-oxygen light degradation defect, etc). It is also known that dislocations and/or stacking faults can be generated during the light element precipitation, and precipitates in themselves are effective recombination sites. The presence of the precipitates also impact transition metal gettering. To take advantage of the high throughput production and low-cost feedstock of the sheet formation process, detailed knowledge regarding the impact of light elements on cell performance is required. This paper examines the dynamics of oxynitride particle and oxygen precipitate distribution in sheet silicon.

II. EXPERIMENT

Polycrystalline sheet silicon wafers about 800 μm thick were boron doped to a resistivity of 2 to 3 ohm·cm. The grain size ranged from 100 μm to 1mm. Samples were polished, Secco etched, and examined under a Nomarski optical microscope. Included particles of 1-3 μm diam were identified, which were usually associated with dislocation clusters. The chemical composition of the particle was analyzed by X-ray energy dispersive spectroscopy using a Hitachi 3-3200N scanning electron microscope, while the distribution of the oxynitride particles and interstitial oxygen was characterized by microscopic FTIR. The lateral distribution of the oxynitrides within large and small grain regions of a double-side polished wafer were examined by micro-FTIR with a 500 μm diam infrared beam, whereas depth profiles were obtained on polished cross-sections with a spectral resolution of 4 cm^{-1} and a step size of 40 μm . A 1.5 mm wide strip was cut from the wafer and double-side polished to ~350 μm thick in the cross section direction, i.e., perpendicular to the sample surface. A rectangular aperture was used with an infrared beam size of 500 x 50 μm^2 . The long edge parallel to the sample surface increased the beam intensity, while the short edge was kept

perpendicular to the sample surface to increase the spatial resolution. The interstitial oxygen profile across the sample thickness was determined from the intensity of the 1107cm^{-1} peak using a calibration factor of $3.14 \times 10^{17} \text{ cm}^{-2}$, and correlated with etching/Nomarski microscopy.

III. RESULT AND DISCUSSION

A. Distribution of oxynitride particles

Figure 1 is a Nomarski optical micrograph of an as-grown sample after a 15 sec Secco etch, which shows a number of second phase particles surrounded by dislocation clusters. Due to the short etching time, dislocations appeared as small dots instead of well resolved pits. Considering the silicon sheet was grown at 3 meters/min and the

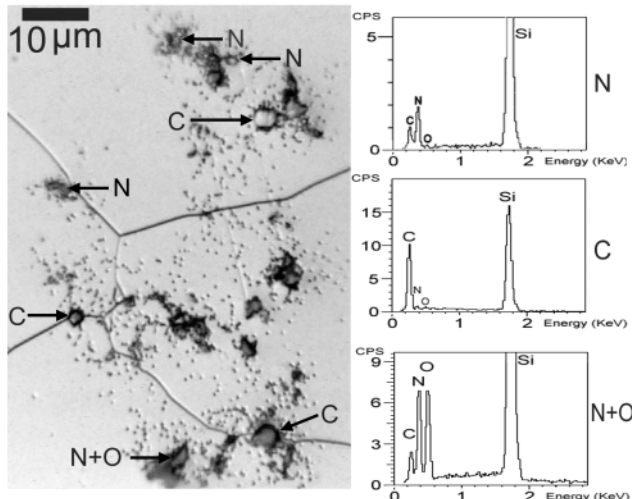


Fig. 1. Nomarski image of an as-grown sample after 15 sec Secco etching and the corresponding SEM-EDS spectra of the particles.

cooling rate following the solidification was very fast, these $1\text{-}3 \mu\text{m}$ large particles are believed to have been incorporated into the silicon matrix as inclusions rather than by precipitation during cooling. Note the included particles are usually associated with dislocation clusters resulting from thermal expansion/contraction stresses. The particles in Fig. 1 were further characterized by SEM, and EDS spectra, also shown in Fig. 1, were acquired from each of the particles. Note that there are basically two kinds of particles, which contain primarily carbon or nitrogen.

A comparison of large and small grain regions of an as-grown sample after a 60 sec Secco etch, see Fig. 2, show that more inclusions/ dislocation clusters exist in the smaller grain regions. Regions with different grain sizes were also examined by FTIR with an infrared beam size of $500 \mu\text{m}$ in diameter and the spectra are compared in Fig. 3. Consistent with the etching/Nomarski results, the amount of $\alpha\text{-Si}_3\text{N}_4$ and SiNO present in the small grain regions was twice that of large grains. A higher content of particles is usually accompanied

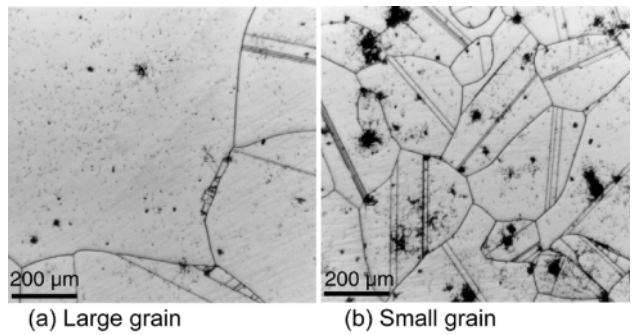


Fig. 2. Nomarski images of large and small grain regions after 60 sec Secco etching.

by a higher concentration of impurities. It is likely that the presence of the included particle and the high concentration impurities is the cause of the smaller grain size. Note that the position and shape of the absorption bands from the large and small grain regions in Fig. 3 are essentially the same, indicating all particles have similar compositions.

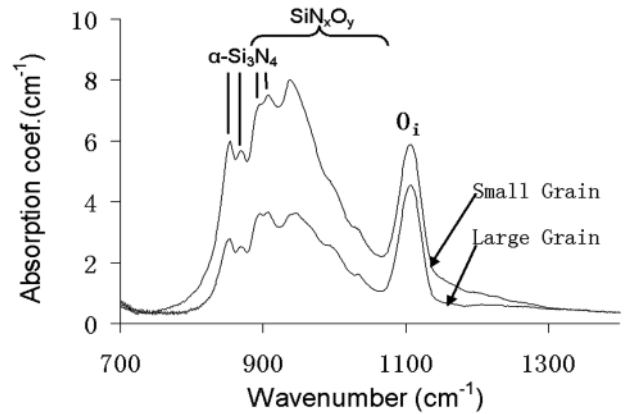


Fig. 3. FTIR spectra of large and small grain regions. The depth distributions of $\alpha\text{-Si}_3\text{N}_4$ and SiNO were characterized by cross-sectional micro-FTIR using a $500 \times 50 \mu\text{m}^2$ beam and $40 \mu\text{m}$ steps. The spectra in Fig. 4 are shifted relative to each other

for clarity. We can see that there are more oxynitrides ($800\text{-}1060\text{ cm}^{-1}$) appearing in the middle of the wafer than in the near surface regions. It is known that the segregation coefficients of transition metals, nitrogen, carbon and aluminum are all much smaller than unity, and also known that sufficient small particles can be pushed by the solidification front[2,3]. The build-up of impurities and particles at the solidification front due to segregation and particle pushing are likely causes of interface breakdown. Particle and impurity trapping will increase enormously when morphological breakdown occurs, as observed in previous silicon directional solidification studies [4].

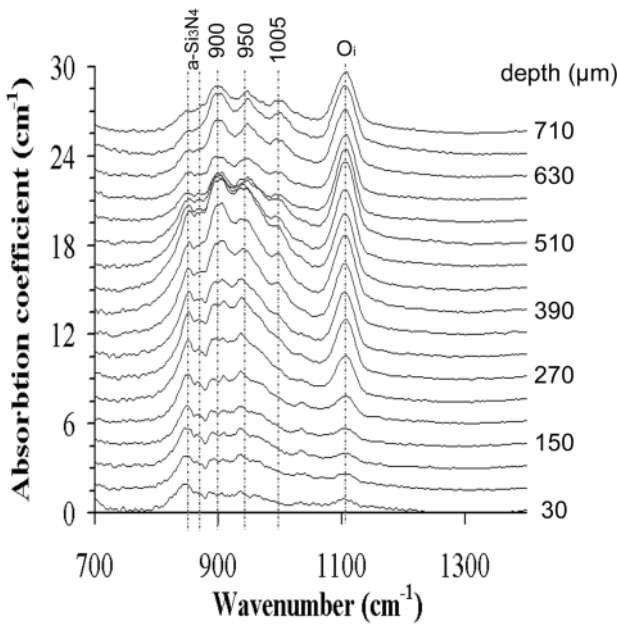


Fig. 4. Cross-sectional FTIR spectra from the as-grown sample with a step size of $40\mu\text{m}$ and an aperture size of $500\times 50\mu\text{m}^2$.

Note that in addition to the overall oxynitride band intensity changing with depth, the detailed structure also changes, see Fig. 4. We can see that the SiNO bands from the near top-surface region arise almost entirely from $\alpha\text{-Si}_3\text{N}_4$. With the increase of the depth, the absorptions at ~ 900 and 950 cm^{-1} become stronger relative to that at 850 cm^{-1} and some detail structure become less well defined. Considering that the oxynitride absorption will shift to higher wavenumber with increasing oxygen content[5,6], it appears that oxynitrides located at the deeper region contain more oxygen.

The oxygen content might vary with different inclusions, resulting in broader absorption bands. The composition variation is likely to be related to the $[\text{O}_i]$ distribution. In the deeper region where the oxygen concentration is high, $\alpha\text{-Si}_3\text{N}_4$ might react with oxygen by forming oxynitride $\text{Si}_2\text{N}_2\text{O}$; while there will be no oxynitride formation at the near top surface oxygen-depleted region. It has been shown[7] that the formation of oxynitride $\text{Si}_2\text{N}_2\text{O}$ is thermodynamically favorable only if the oxygen concentration is higher than $2.82\times 10^{17}\text{ cm}^{-3}$.

B. Oxygen denuded zone near the top surface

The $[\text{O}_i]$ depth profile was calculated from the cross sectional FTIR spectra in Fig. 4, and is shown in Fig. 5. Note an oxygen denuded zone, with a depth of $200\mu\text{m}$, formed near the top-surface. After solar cell processing, samples were cross sectional polished and examined under Nomarski

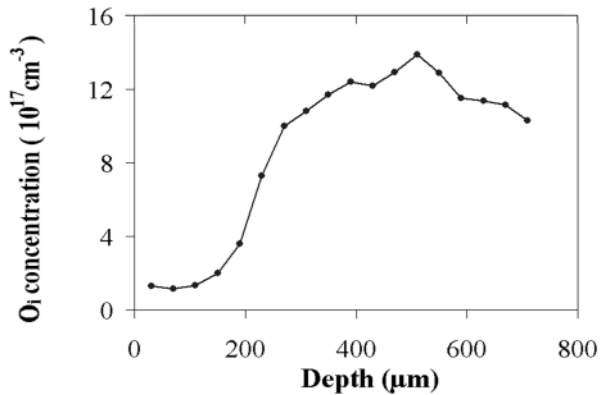


Fig. 5. $[\text{O}_i]$ and oxynitrides depth profiles from the cross-sectional FTIR measurements.

microscope after 30 sec Secco etch. Figure 6 (a) is a low magnification image of a near top-surface large grain region. We can see that a well defined, $\sim 250\mu\text{m}$ wide precipitate denuded zone formed near the top surface. Under higher magnification, see Fig. 6 (b), it is evident that the precipitates in the deeper region are either isolated oxygen precipitates or stacking faults. Unlike the large grain region, the precipitate denuded zone in the small grain region can only be resolved in the high magnification image, see Fig. 7. Note there are few stacking faults in Fig. 6 (b) and the defects in the deeper region are mainly isolated oxygen precipitates. The fact that stacking faults only formed in the large grain regions suggests that

grain boundaries are acting as an effective sink for self-interstitials. Due to the high diffusivity of self interstitials, stacking fault formation was greatly reduced throughout the whole small grain. In the large grain region, a 50-100 μm stacking fault denuded zone formed near grain boundaries, as observed in our previous studies [8].

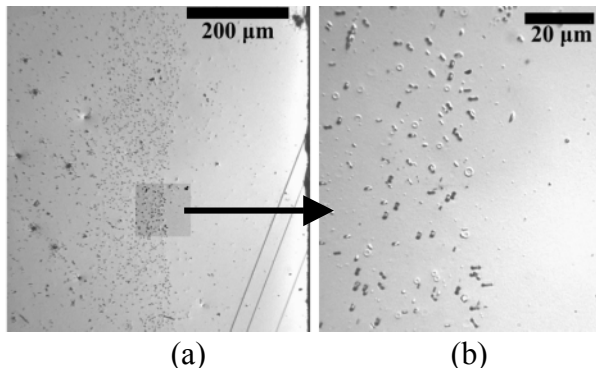


Fig. 6. Cross sectional Nomarski micrographs of a near top-surface large grain region of a processed sample after 30s Secco etching.

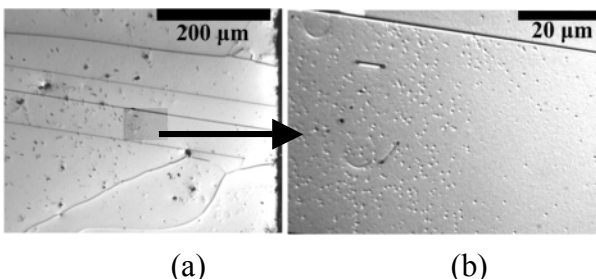


Fig. 7. Cross sectional Nomarski micrographs of a near top-surface small grain region of a processed sample after 30s Secco etching.

Considering that the diffusion length of finished sheet silicon cells is around 100 μm and the denuded zone can reach \sim 200-300 μm , clearly the high density of oxygen precipitates /stacking faults formed in the deeper region can be used to getter transition metals from the near surface region.

IV. CONCLUSIONS

Preferential etching/Nomarski microscopy and microscopic FTIR studies show that more oxynitride particles are located in small grain regions, and in a middle of the wafer cross section. The inclusions deeper in the wafer contain more oxygen than those near the top-surface. Cross sectional FTIR indicates that a 200 μm wide interstitial oxygen denuded zone is present in the as-grown wafer, which is sustained as an oxygen precipitate/stacking fault free zone after solar cell processing. It was concluded that particle rejection and the build-up of impurities at the solidification front result in interface breakdown, which gives rise to the increased particle trapping in the middle of a wafer.

ACKNOWLEDGMENTS

The authors would like to thank Simon Lappi and Dale Batchelor for their help on FTIR and SEM measurements, respectively.

REFERENCE:

- [1] J. P. Kalejs, Solar Energy Mater. & Solar Cells, **72**, 139 (2002).
- [2] G. F. Bolling and J. Cisse, J. Crystal Growth, **10**, 56 (1971).
- [3] W. Rempel and M. G. Worster, J. Crystal Growth, **223**, 420 (2001).
- [4] P. S. Ravishankar and J. P. Dismukes, J. Crystal Growth, **71**, 579 (1985).
- [5] T.S. Eriksson and C.G. Granqvist, J. Appl. Phys. **60** (6), 2081 (1986).
- [6] Prado, I. Martil, M. Fernandez, and G. Gonzalez-Diaz, Thin Solid Films **343-344**, 437 (1999).
- [7] J. Lu, G.A. Rozgonyi, J. Rand, and R. Jonczyk, "Included Particles in Polycrystalline Sheet Silicon", to be published.
- [8] J. Lu, M. Wagener, G. Rozgonyi, J. Rand, and R. Jonczyk, J. Appl. Phys. **94**, 140 (2003).

APIVT Epitaxial Growth on Zone-Melt Recrystallized Silicon

T.H. Wang,¹ P.E. Sims,² M.R. Page,¹ R.E. Bauer,¹ M.D. Landry¹
R. Reedy,¹ Y. Yan,¹ and T.F. Ciszek¹

¹National Renewable Energy Laboratory, Golden, CO 80401

²AstroPower, Inc., Newark, DE 19716

Introduction

Single-junction thin-film silicon solar cells require large grain sizes to ensure adequate photovoltaic performance. Using 2D silicon solar cell simulations on the quantitative effects of grain-boundary recombination on device performance [1], we have found that the acceptable value of effective grain boundary recombination velocity is almost inversely proportional to grain size. For example, in a polycrystalline silicon thin film with an intragrain bulk minority-carrier lifetime of 1 μ s, a recombination velocity of 10^4 cm/s is adequate if the grain is 20 μ m across, whereas a very low recombination velocity of 10^3 cm/s must be accomplished to achieve reasonable performance for a 2- μ m grain. For this reason, large grain size on the order of hundreds of μ m is currently a prerequisite for efficient solar cells, although a more effective grain-boundary passivation technique may be developed in the future.

One way to achieve such large-grained silicon layers is by zone-melt recrystallization (ZMR) to make a seed layer on an inexpensive high-temperature substrate, followed by device-quality epitaxial layer growth. The ZMR silicon seed layer is heavily contaminated due to the high-temperature melt process, even though its crystallinity may be excellent. Epitaxy preserves the crystallinity and maintains low impurity levels in the active absorber layer by a lower-temperature process. Even with the relatively high-temperature (1150°C) trichlorosilane atmospheric pressure chemical-vapor deposition (APCVD) technique, Sims et al. [2] demonstrated over 9%-efficient solar cells in an epitaxial layer on a ZMR seed layer using an AstroPower-developed ceramics substrate. An inexpensive and fast epitaxy process at a lower temperature (~900°C) may be able to further improve the material quality by reducing impurity contaminations. We report here on epitaxial silicon film growth on ZMR silicon seed layers by the atmospheric-pressure iodine vapor transport (APIVT) [3] with such desired characteristics.

Experimental

AstroPower, Inc. - A silicon layer was deposited onto a proprietary ceramics substrate by CVD. This special ceramics is high-temperature compatible, chemically stable, and closely matched to silicon in thermal-expansion coefficient. It is fabricated by a low-cost tape cast process with an estimated material cost of ~\$10/m². This silicon layer is then zone-melt recrystallized to make a large-grained 40- μ m-thick seed layer with the grains elongated along the scanning direction of the line heater/substrate transport. Typical grain width is about a few tenths of a mm. APCVD with trichlorosilane was used to grow 26- μ m-thick epitaxy films for comparison to APIVT growth.

NREL - The ceramics substrates with ZMR silicon seed layers were cut into 2.5-cm x 2.5-cm squares to fit our experimental APIVT reactor. The general APIVT deposition process has been described elsewhere [3]. However, maintaining a clean interface is critical to obtain epitaxial growth. In the current experimental system, this clean condition is accomplished by heating the substrate to the source temperature before actual growth starts, which avoids the build-up of silicon iodides at the film/substrate interface. An oxygen-free ambient in the reactor is also critical. Combining cycle-purging and continuous-purging is effective in removing oxygen from the reactor. We also used a resin-based gas purifier for the argon and hydrogen purge gases. During growth, the substrate temperature was lowered to 900°C to minimize impurity contamination and to still be able to maintain low defect density. Dopant boron is incorporated into the films from the pre-doped source silicon at a 1-to-1 ratio. Epitaxial film thickness ranges from 25 μm to 50 μm . Grown films are characterized by secondary-ion mass spectrometry (SIMS), transmission electron microscopy (TEM), scanning electron microscopy (SEM), and optical microscopy.

Surface morphology

Figures 1a, 1b, and 1c show different appearances of the epitaxial silicon film sur-

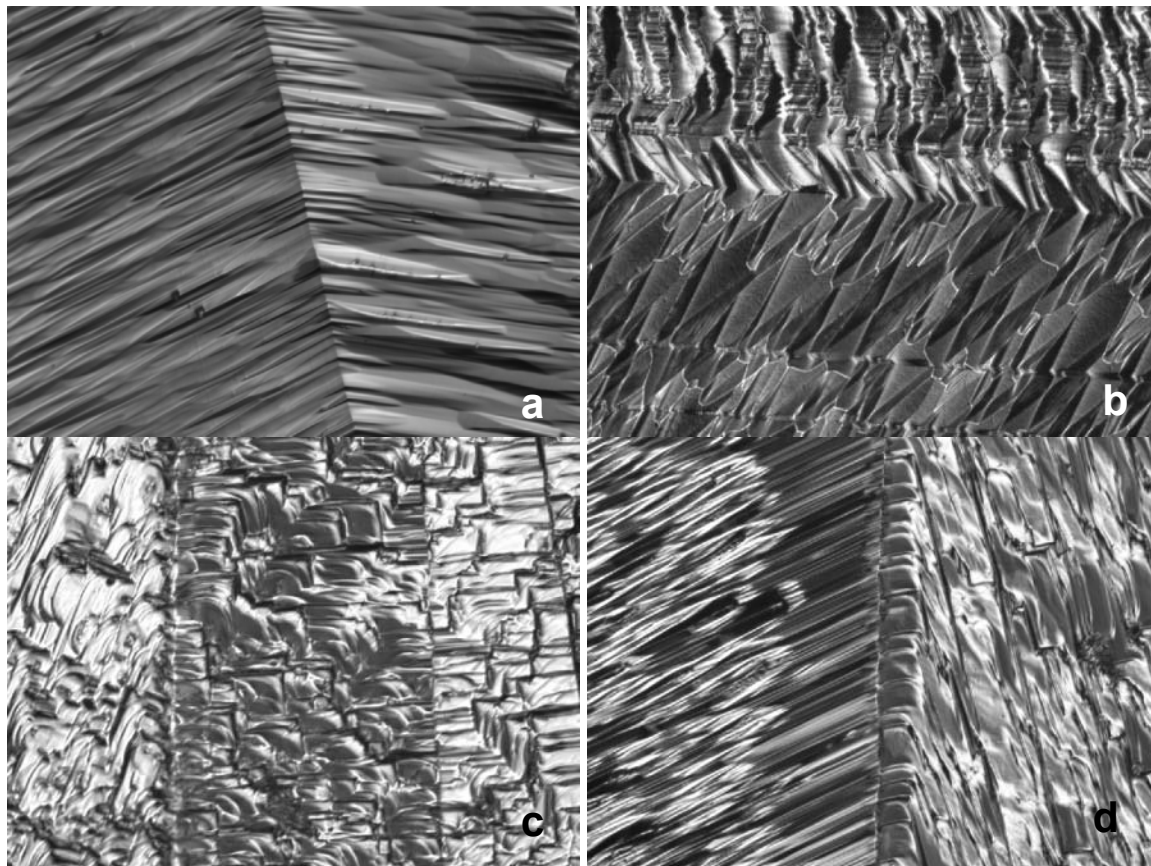


Fig. 1. Nomarski photomicrograph showing surface morphology of APIVT epitaxial silicon films grown at 900°C on a ZMR seed layer. Picture width = 350 μm .

faces. Depending on their orientations, some grains have smooth surfaces (only 1-2- μm variations); others have rough ripples or ridges as high as 10 μm in a 45- μm -thick film. Growth at grain boundaries appears to be very conformal; there are no apparent voids or holes at grain boundaries. At some large-angle grain boundaries (Fig. 1d), thicker growth was seen, probably due to locally higher free energy that leads to faster growth. These films were grown at 900°C with an average rate of 1 $\mu\text{m}/\text{min}$.

Comparison with high-temperature APCVD

Films grown by trichlorosilane APCVD at 1150°C at 4.3 $\mu\text{m}/\text{min}$ generally show macroscopically smoother surfaces (Figs. 2a and 2b). This is to be expected, as higher temperature tends to increase microscopic roughness and reduce macroscopic roughness. A thermal CVD process in principle also has a higher free-energy driving force than the near-equilibrium APIVT process.

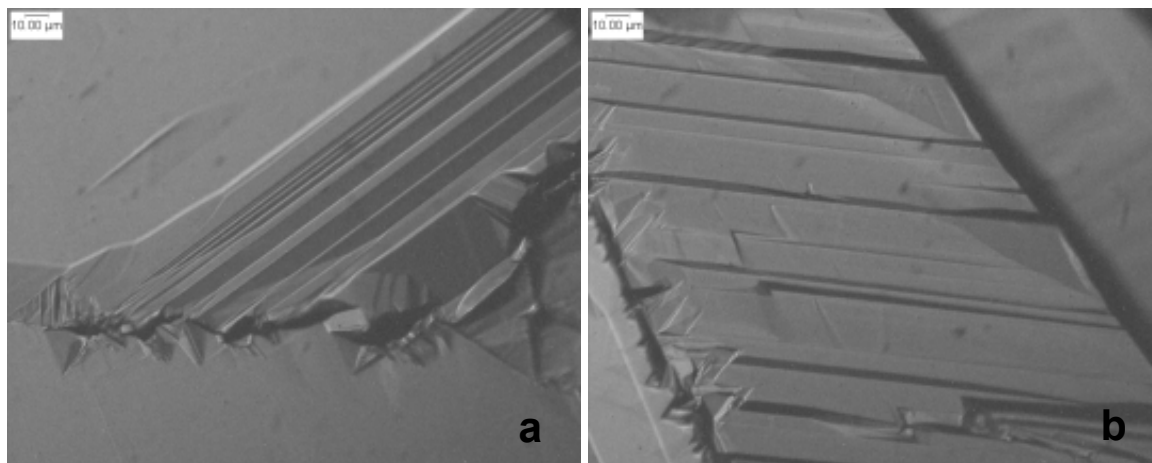


Fig. 2. Nomarski photomicrograph showing surface morphology of trichlorosilane APCVD epitaxial silicon films grown at 1150°C on a ZMR seed layer.

Orientation-dependent growth rate

Examining an entire surface after APIVT epitaxy on a 2.5-cm x 2.5-cm substrate, we observed that some grains grew at nearly twice the rate as some neighboring grains. This was also evident in a trichlorosilane APCVD film in Fig. 2b. In some APIVT films grown at faster than 1 $\mu\text{m}/\text{min}$, polycrystalline deposition occurred on one single grain, while the next grain showed epitaxy at a faster rate, as shown in Fig. 3. The photomicrograph to the left in Fig. 3 is focused on the epitaxially grown grain, whereas the one to the right is focused to the polycrystalline growth on the neighboring substrate grain. The epitaxy grain is 45 μm thick, as compared to a 30- μm average thickness for the polycrystalline part, after 25-min growth. This implies that because of the lower temperature of 900°C that we used, some grains of special orientations cannot grow at a fast enough rate to keep up with the incoming silicon atoms. Reducing the overall growth rate to ~1 $\mu\text{m}/\text{min}$ eliminated any polycrystalline deposition. Therefore, we may define 1

$\mu\text{m}/\text{min}$ as approximately the maximum epitaxial growth rate for all grains at 900°C . This maximum rate is obviously higher with a higher growth temperature.

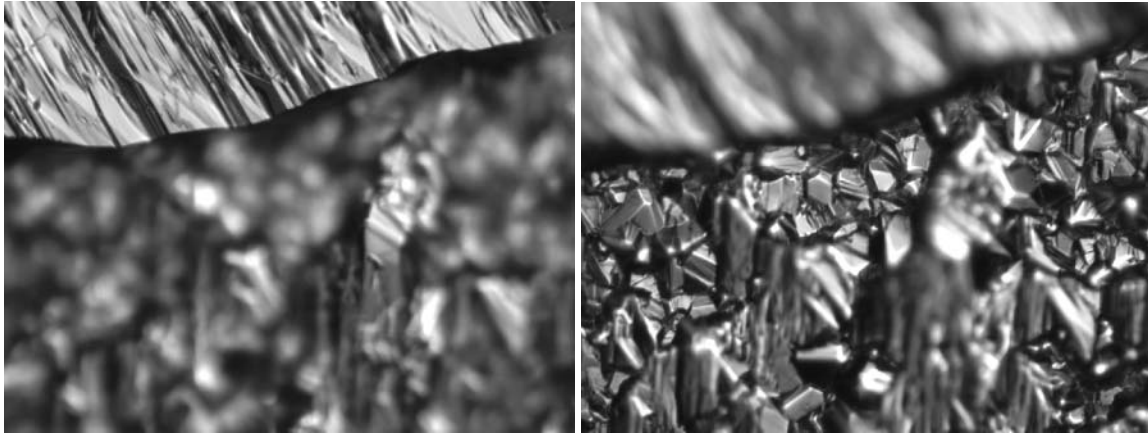


Fig.3. Photomicrograph of aerial view in the same area, showing two adjacent substrate grains that resulted in epitaxy and polycrystalline growth with focal points at the respective surfaces. Picture width = $350 \mu\text{m}$.

Summary

We report successful epitaxial silicon film growth on ZMR silicon seed layers by the inexpensive and fast epitaxy process of atmospheric-pressure iodine vapor transport at a lower temperature of $\sim 900^\circ\text{C}$ than the previous growth at 1150°C by trichlorosilane APCVD. Maintaining a clean interface is critical to obtaining epitaxial growth by any method, and it is particularly important for the APIVT technique because there are no in-situ cleaning gas agents available. In the current experimental system, this clean condition is accomplished by heating the substrate to the source temperature before actual growth starts.

Surface morphology depends strongly on the orientations of individual grains and the growth temperature. The APIVT films generally have rougher surfaces than the trichlorosilane APCVD films due to the lower temperature used and the near-equilibrium growth nature of APIVT. A maximum deposition rate to ensure epitaxial growth on all grains is determined to be about $1 \mu\text{m}/\text{min}$ for a growth temperature of 900°C .

This work was supported by the U.S. DOE through NREL under Contract# DE-AC36-99-GO10337.

References

- [1] T.H. Wang, T.F. Ciszek, M.R. Page, R.E. Bauer, Q. Wang, and M.D. Landry, *Proceedings of the 29th IEEE PVSC*, New Orleans, 2000, 94.
- [2] P. Sims, A. Ingram, D. Ford, R. Jonczyk, J. Yaskoff, E. DelleDonne, J. Rand, and A. Barnett, To be published in *Proceedings of the 3rd World Conference on Photovoltaic Energy Conversion*, Osaka, 2003.
- [3] T.H. Wang, T.F. Ciszek, and M.R. Page, *J. Crystal Growth*, 253 (2003) 183-189.

Solid-Source Doping of Float-Zoned Silicon with B, N, O, and C

T. F. Ciszek*

National Renewable Energy Laboratory, Golden, CO 80401 USA

(*address after 9/1/03: www.siliconconsultant.com, P.O. Box 1453, Evergreen, CO 80437 USA)

Abstract

We report on a solid-source method to introduce dopants or controlled impurities directly into the melt zone during float-zone growth of single- or multicrystalline ingots. Unlike the Czochralski (CZ) growth situation, float zoning allows control over the levels of some impurities (O, C) that cannot be avoided in CZ growth or ingot casting. But aside from impurity studies, the method turns out to be very practical for routine p-type doping in semicontinuous growth processes such as float-zoning, electromagnetic casting, or melt-replenished ribbon growth. Equations governing dopant incorporation, dopant withdrawal, and N co-doping are presented and experimentally verified. Doping uniformity, and doping initiation and withdrawal time constants are also reported. The method uses nontoxic source materials and is flexible with quick turnaround times for changing doping levels. Boron p-type doping with nitrogen codoping is particularly attractive for silicon lattice strengthening against process-induced dislocation motion and also allows greater freedom from incorporation of Si self-interstitial cluster or A and B swirl-type defects and “D”-type microdefects than nitrogen-free p-type material.

Introduction

Float-zoned (FZ) silicon crystals (or other continuous, melt-replenished Si materials such as electromagnetically cast ingots, melt-replenished ribbons, or rapidly solidified continuous ribbons on a substrate) are doped by different methods depending on the dopant's segregation coefficient. If $k \ll 1$ (e.g., Ga dopant or N impurity in Si), it is best to place all dopant at the starting end of the feed rod or growth process. If $k \approx 1$ (e.g., B dopant or O impurity in Si), it is best to add the impurity uniformly and continuously as growth progresses. The choices for continuous dopant addition have traditionally been to either predope the feedstock uniformly (this sometimes involves long scheduling times and is somewhat inflexible) or to dope from the gas phase (e.g., with diborane during growth). Diborane is exceptionally toxic and requires stringent safety measures. Figure 1 summarizes doping strategies and introduces our solid-source method. Its applicability to high k (~ 1 , e.g., B, O), low k ($\sim 10^{-4}$, e.g., N), and intermediate k ($\sim 10^{-2}$, e.g., C) materials is discussed and characterized in the subsequent sections.

Experimental Procedure

For single crystals, a <100> seed orientation was used and the initial growth was necked to produce dislocation-free crystals. The feedstock was undoped polycrystalline silicon rods with resistivity $> 5,000 \Omega\text{-cm}$. The growth experiments were carried out in argon. The zone melting was done with an induction coil operating at 2 MHz. A usual growth rate was $0.33 \text{ cm}\cdot\text{min}^{-1}$, with a rotation rate of 10-15 rpm.

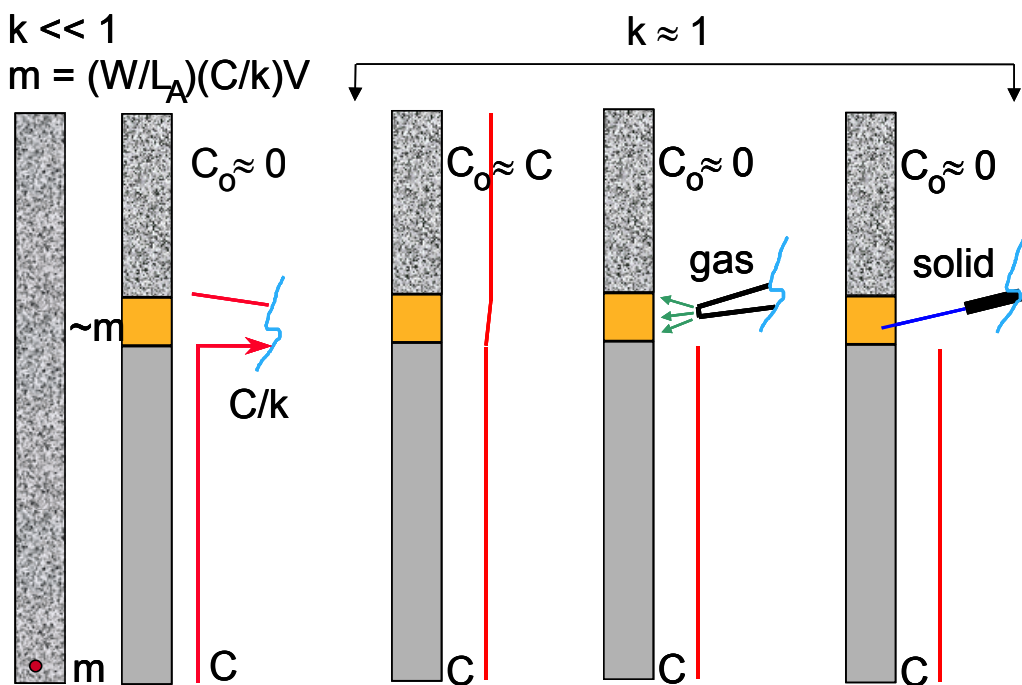


Fig. 1. Schematic representation of FZ doping strategies for $k \ll 1$ (pill doping with mass m at origin: W = atomic weight, L_A = Avogadro's No., C = desired concentration, k = effective segregation coefficient, V = melt volume); and for $k \approx 1$ (predoped feed, gas doping, and the solid-source method discussed in more detail in this manuscript).

Thin, long slivers of high-purity pyrolytic boron nitride were cut, cleaned in a mixed acid etch ($3\text{CH}_3\text{COOH}$: 1HF : 2HNO_3), and mounted on a translatable rod, which allowed the sliver tip to be inserted into the molten zone. This was the solid source for boron and nitrogen doping. High-purity fused quartz rods were used for O doping, and vitreous carbon slivers were used for C doping. The immersion was done manually with the sliver or rod attached to a metal rod passing through an "O"-ring-sealed connector in the chamber wall. The source was inserted radially, beneath the RF coil. Figure 2 is a photograph showing the doping arrangement for the particular case of O, N, and B co-doping a $<100>$ dislocation-free FZ silicon crystal. Here, a $0.8 \Omega\text{-cm}$ B-doped crystal containing $N_B \approx 2 \times 10^{16} \text{ atoms}\cdot\text{cm}^{-3}$ and $N_O \approx 8 \times 10^{16} \text{ atoms}\cdot\text{cm}^{-3}$ was produced with a

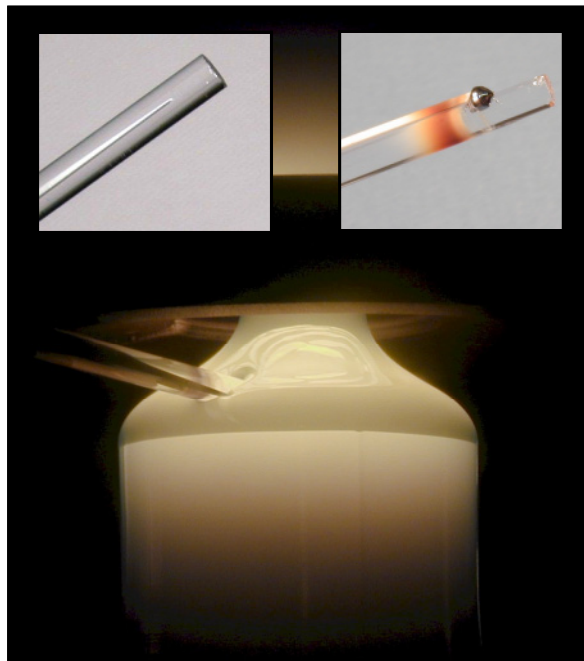


Fig. 2. B, N, and O co-doping a FZ crystal. The insets show the BN and SiO_2 solid sources before growth (left) and after growth (right).

gradually changing mid- 10^{15} atoms·cm⁻³ level for N_N (N is concentration and the subscript refers to the species). A 0.3-cm-diameter high-purity fused quartz rod was immersed 0.6 cm into the melt zone in conjunction with a thin BN sliver immersed 0.2 cm.

Our dopant incorporation model equation is

$$C_o = 4AD/\pi d^2v, \quad (1)$$

where C_o is the uniform dopant concentration entering the melt zone (atoms·cm⁻³), A is the surface area (cm²) of the immersed solid source, D is the dissolution rate (atoms·cm⁻²·min⁻¹) of the source's doping component in molten silicon, d is the crystal diameter (cm), and v is the crystal growth rate (cm·min⁻¹). A one-time determination of D with the other parameters known allows eq. (1) to be used to calculate the A required for a desired N.

Results

Table I gives the D values that we have determined for the solid sources mentioned earlier, in units atoms·cm⁻²·min⁻¹. They depend on specific experimental conditions and are subject to error from imprecise knowledge of A. The estimated accuracy of the D values is about 10% for 3.4-cm-diameter float-zoned crystal growth. It is best to determine the values within the set of experimental conditions that will be used in a particular growth configuration.

Table I. D Values for B, N, O, and C

Dopant	B	N	O	C
D	3.7×10^{19}	3.7×10^{19}	2.3×10^{17}	9.7×10^{18}

Some of the main features of solid-source B doping from a pyrolytic BN source can be deduced from Fig. 3. A 3.4-cm-diameter, dislocation-free, <100> FZ crystal was grown at 0.32 cm·min⁻¹ from a 3.4-cm-diameter feed rod that had a resistivity of 5,000 Ω-cm or greater. After 7.5 cm of undoped growth, a 0.01-cm x 0.015-cm cross-section pyrolytic BN sliver was inserted about 0.15 cm into the melt zone. After 4.3 cm of additional growth, the immersion depth was increased to about 0.4 cm for another 4 cm of growth. Then the doping sliver was withdrawn. The resultant longitudinal resistivity profile of the crystal (as measured by a linear 4-point probe on a flat surface ground along the length of the crystal) is shown. The time constant for reaching uniform ($0.22 \Omega\text{-cm}$ or 9×10^{16} atoms·cm⁻³) B doping, starting from undoped growth, is about 3.2 min. The time constant for changing from one uniform B doping level ($0.22 \Omega\text{-cm}$) to another ($0.12 \Omega\text{-cm}$ or 2.1×10^{17} atoms·cm⁻³) is about 2.4 min. The resistivity uniformity is about $\pm 9\%$ in each segment. The profile after withdrawal of the BN (at 16.9 cm) fits an equation of the type

$$\rho = \rho_o e^{(k_B/L)z}, \quad (2)$$

as expected, with a fit standard error of 0.05 (and a coefficient of determination, r², of 0.9995) for k_B/L = 0.795. Here ρ is resistivity, ρ_o is the resistivity at the point of dopant withdrawal, L is the effective zone length (cm), and z is the position after withdrawal (cm). The fitted value of k_B/L is consistent with k_B = 0.9 and L = 1.13 cm. L is the length the zone would be if all of the melt was in a right circular cylinder of diameter d. Radial resistivity profiles for a 5.2-cm-diameter, dislocation-free, <100> crystal doped to 1.3 Ω-cm are shown in Fig. 3 for positions 2 and 8 cm after dopant insertion. At 8 cm, the doping uniformity is $\pm 0.03 \Omega\text{-cm}$ or 2%.

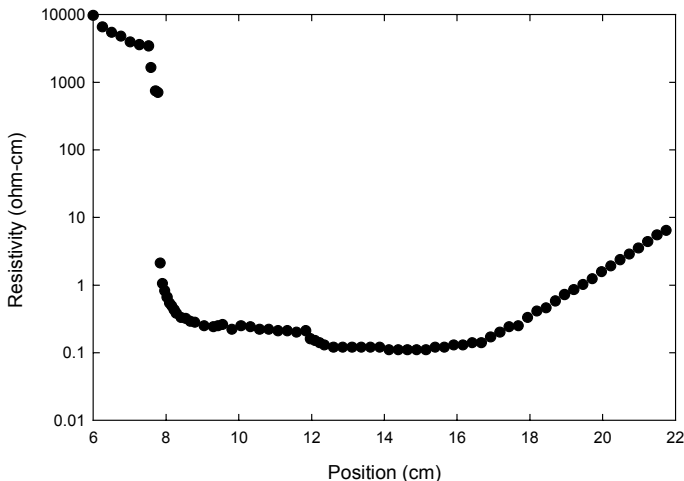


Fig. 3. Doping profile for insertion, change of immersed depth, and withdrawal of BN source.

Pfann's zoning equation:

$$N_N(z) = C_o[1-(1-k_N)e^{-k_N z/L}] = N_B[1-(1-k_N)e^{-k_N z/L}] = (4AD/\pi d^2 v)[1-(1-k_N)e^{-k_N z/L}]. \quad (3)$$

One-meter-long crystals can be grown with $\rho \geq 0.3 \Omega\text{-cm}$ without exceeding the N solubility limit of $4.5 \times 10^{15} \text{ atoms}\cdot\text{cm}^{-3}$. N is essentially electrically inactive as an n-type dopant. Nitrogen below the solubility limit is beneficial. It provides mechanical strengthening analogous to the way O does for CZ crystals, but at 100x lower concentration levels. It also allows swirl-defect-free growth at a larger range of growth rates than is the case for N-free crystals.

C doping is also governed by an equation analogous to eq. (3). Figure 5 shows that a nearly linear $N_C(z)$ distribution can be obtained by solid-source doping with a vitreous C sliver.

Summary and Discussion

A solid-source doping method for boron doping from a pyrolytic BN source has been described. It is applicable for B doping concentrations $\leq 6 \times 10^{16} \text{ atoms}\cdot\text{cm}^{-3}$, corresponding to $\rho \geq 0.3 \Omega\text{-cm}$ in meter-long crystals. Nitrogen incorporation below the solubility limit is desirable in FZ crystals for mechanical strengthening and point-defect control. This doping method has the benefit of nitrogen incorporation and allows B doping from a nontoxic source compared to diborane gas that is usually used for doping. Solid-source O and C doping were also described. Co-doping with B, N, and O was demonstrated. Equations for dopant intake into the melt, dopant withdrawal, and dopant distribution along the crystal were developed and experimentally verified.

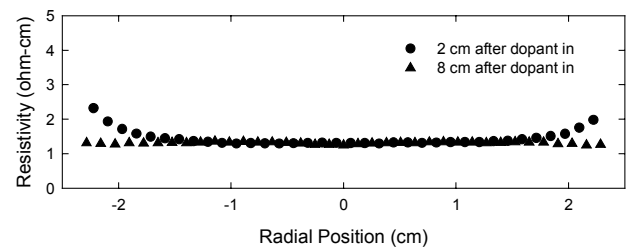


Fig. 4. Radial resistivity profiles for two locations along a 5.2-cm-dia. BN-doped crystal.

Of course, both nitrogen and boron enter the growing crystal during solid-source BN doping. Although k_B is about 0.9, a much lower value of $k_N = 7 \times 10^{-4}$ is characteristic of N in liquid silicon. The distribution of nitrogen along a BN-doped crystal, $N_N(z)$, can be obtained from

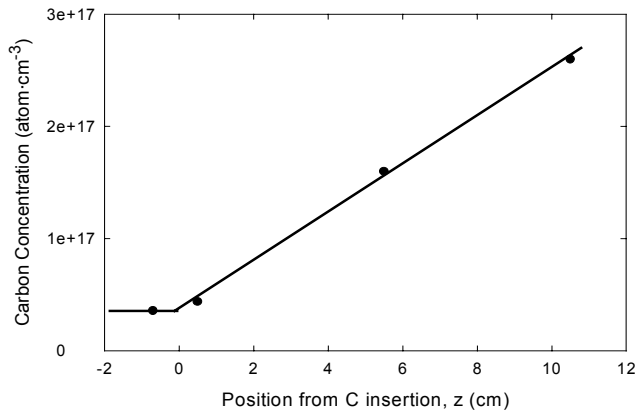


Fig. 5. Solid-source C doping

Ion Beam Mixing of Silicon-Germanium for Solar Cell Applications

Sufian Abedrabbo¹, Shadi Salem^{1*}, D. Arafah¹
Anthony Fiory², Bhushan Sopori³ and N.M. Ravindra²

¹Department of Physics, University of Jordan, Amman, Jordan 11942

² Department of Physics, New Jersey Institute of Technology, Newark, NJ 07102

³ National Renewable Energy Laboratory, Golden, CO 80401

Abstract

An overview of silicon-germanium alloys for solar cell applications is presented here. The overview considers factors such as methods of formation and device performance. In particular, results of preliminary experiments of ion-beam mixing of silicon germanium multi-layers deposited by physical vapor deposition and subsequently ion-implanted with varying doses of argon are described. Rutherford backscattering spectrometry (RBS) has been utilized to characterize the nature of the mixing of as-deposited films.

Introduction

Silicon - germanium (Si-Ge) alloys are becoming a major player in high frequency applications such as cellular phones and are competing with direct band gap compound semiconductors such as GaAs [1]. The alloys are also used in the formation of high-mobility strained silicon layers for high-performance applications in silicon microelectronics. Our interest in this alloy system is the ability to perform band-gap engineering to obtain efficient and inexpensive photovoltaic cells [2].

To put the role of Si-Ge in perspective, the market for compound semiconductors is estimated to be ~\$7.2 billion with Si-Ge comprising 38% of the total [3]. Si-Ge offers several advantages over the III-V compound semiconductor materials with the largest single advantage being the complete compatibility with conventional silicon CMOS processes. In addition, Si-Ge creates the ability to merge low-power, high-density digital circuitry of CMOS with the high speed of Si-Ge heterojunction bipolar transistor (HBT), making advanced Bi-CMOS processes ideally suited for highly integrated mixed signal circuits for applications in communications [4].

Si-Ge For Photovoltaic Applications

Thin film solar cells have largely been recognized to be potentially important for energy conversion and production of large area photovoltaic cells [5,6]. Current state of the art small-scale cells deliver conversion efficiencies near 16% while larger size modules yield efficiencies around 10%, [7,8]. Significant efforts are

* Visiting PhD candidate

being made in solar cell research to either increase the efficiency or reduce the cost of silicon solar cells for commercial production [9].

Previous investigations include data on deep and shallow defect states in Si-Ge and reveal that the efficiency is markedly influenced by many factors. These include the method of preparation, processing conditions, and structural alterations within the film components and incorporation of light impurities followed by the formation of an interfacial layer possibly by interdiffusion processes [10-12]. More specifically, the efficiency of silicon solar cells can be enhanced if a lower band gap material is introduced into the device. $\text{Si}_{1-x}\text{Ge}_x$ alloys are miscible for most values of Ge concentration, x . The increased lattice constant of the alloys relative to silicon is accommodated by lattice strain in thin layers or by misfit dislocations, such as in graded multiple layers. The commensuration of the interfaces depends upon the film thickness, x , growth method and thermal treatment.

These alloys have a lower band gap than silicon and act to extend the infrared response of the cell and increase the photo-generation and consequently current generation (or collection). Earlier investigations reveal that band gaps of alloys could be tailored from 1.12eV to 0.66eV [7,13 -16]. In particular, for solar cells, the publications in the area of $\text{Si}_{1-x}\text{Ge}_x$ alloys has been numerous and a relatively few favorable conclusions for the use of $\text{Si}_{1-x}\text{Ge}_x$ alloys have been established [5,6,13-17].

Methods of Preparation

Two major preparation techniques have been deployed for Si-Ge alloys [1]. These include Molecular Beam Epitaxy (MBE) [1,18,19], and Chemical Vapor Deposition (CVD), especially, Plasma Enhanced CVD (PECVD) [20-22]. Metal Organic CVD (MOCVD) [23], and laser assisted Physical Vapor Deposition techniques have also been utilized for processing multi-layers of the films [24].

In addition to the above methods, the novel technique of ion beam mixing (IM) by which non-equilibrium or meta-stable alloys and inter-metallic compounds on surfaces can be formed is of value. The rapid development in materials science and technology based on the surface and near surface properties of materials and their modifications under ion beam irradiation [25-27] has gained much attention in a wide variety of scientific and industrial fields; see for example, references in [26]. Important applications can be cited and include the adhesion between two (or multi-) layers, the preparation of junctions and electrical contacts, and low cost layer deposition by IM to give requisite interface bond strengths. Ballistic collisions, defect production and migration (whether chemically guided or chemically not guided), and other phenomena are, however, initiated when thin films are bombarded by energetic heavy ions [25-30]. Subsequently, changes in the spatial distribution of the elemental species accompanied by the formation of defects take place as a result of collisional

cascades intersecting the interface and produce intimate mixing between the layers. Limitations in the maximum energy of the bombarding ions will limit the thickness of the active device. While ion-implantation of Ge into Si can yield the desired composition and thickness, PVD of Ge followed by ion beam mixing utilizing Argon implantation offers an attractive alternative method.

Experimental Details

Germanium and silicon thin films were deposited in a chamber at a pressure of 10^{-4} Pa, on silicon substrates to form a multi-layer configuration of Si (substrate)/Ge (1200 Å)/ Si (800 Å)/ Ge (1200 Å)/ Si (830 Å). The substrate and the deposited germanium and silicon multi-layer structure are all p-type doped with the doping concentrations of 10^{15} , 10^{12} and 10^{13} cm $^{-3}$, respectively. Next, structural defects are introduced into the matrix by utilizing a beam of mono-energetic Ar $^+$ ions provided by the University of Jordan Van de Graaff accelerator (JOVAC). The incident energy of the ions is 300 keV while the fluence is varied from 3.5×10^{16} to 2.4×10^{17} ions/cm 2 .

The thickness of the multi-layer films was chosen to suit the energy of the bombarding ions as calculated from TRIM-2003 while keeping the substrate clean. In order to have a perfect mix of silicon and germanium films, the thickness of the films ought to be equal to the projected range R_p plus that of the straggling ΔR_p . Structural information of the multi-layer of silicon and germanium is probed using the Rutherford Backscattering (RBS) technique, using 2 MeV He $^+$ beam. Subsequently, after every irradiation at different dose levels, RBS was utilized to probe changes in the structures.

Results and Discussion

The RBS spectra plots represent counts (yield) versus channel number that can be easily converted to the equivalent yield versus energy using a simple calibration procedure [31]. The calibration was made using a silicon substrate that has the following multi-layer film structure: Au/Ag/Mn/Si substrate. Each of the metal films was 50 Å thick. The calibration was made using 2 MeV He $^+$ ions. A typical RBS spectrum of the calibration sample is shown in Fig.1. One step-edge signal due to Si, and three peaks due to scattering from Mn, Ag and Au are observed in the spectra. The calibration curve can then be constructed by plotting the channel number (corresponding to the half height edge of the step edge signal of Si and the maximum height of each isolated peak of Mn, Ag and Au) against the corresponding surface scattering energy for these elements (i.e., $K_{M2}E_0$), as in Fig.2, where K_{M2} is the kinematics factor of the target.

The following linear relationship between channel number (N) and scattered energy (E) was obtained: $E = [3N - 220]$ (keV). Slope of the line is (3.00 ± 0.06) keV representing the energy scale of multi-channel analyzer, and a standard deviation of 7.2%. Fig. 2 illustrates the ideal method of analyzing RBS spectra.

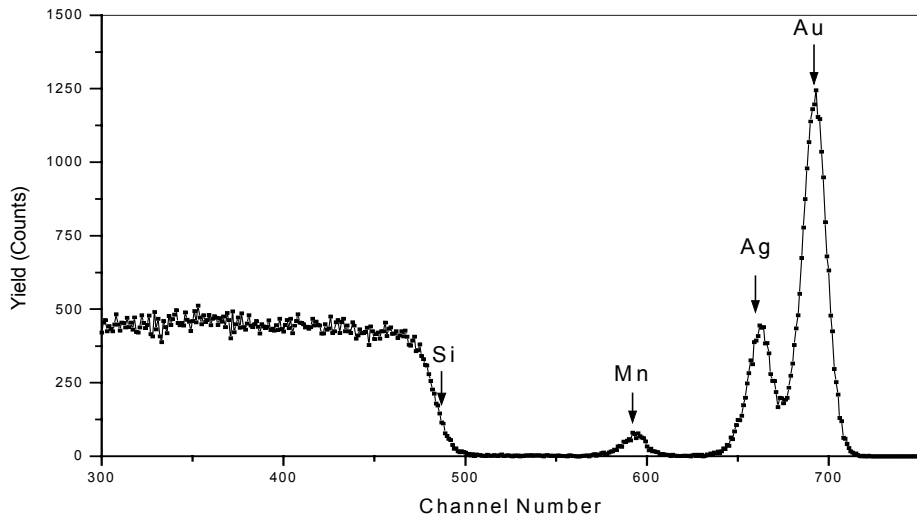


Fig. 1. RBS spectrum of the calibration sample.

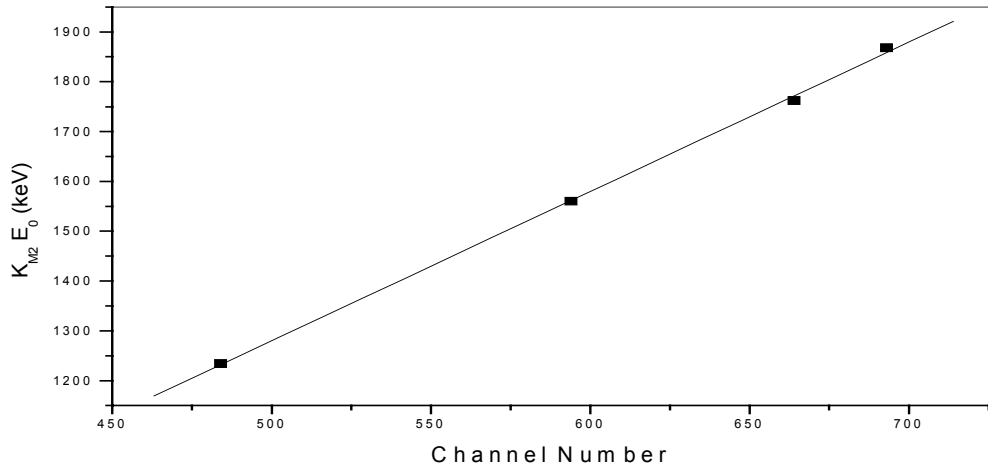


Fig. 2. The energy calibration curve of the RBS detection system.

Fig. 3 shows the RBS spectra illustrating structural changes in the multi-layers observed before and after the 300 keV Ar^+ beam irradiation. As seen from the figure, the first two peaks towards the higher channel numbers represent He^+ scattering due to germanium. The valley in between is shrinking and the peaks are spreading out indicating the mixing effect of argon. As the dose of argon is increased, the diffusion of Si top layer into the subsequent Ge layer and the Ge layer into the next Si layer until reaching the last Ge layer is clear. Ideally, in a perfect mix, the Ge layer channel should appear as one hump indicating a single

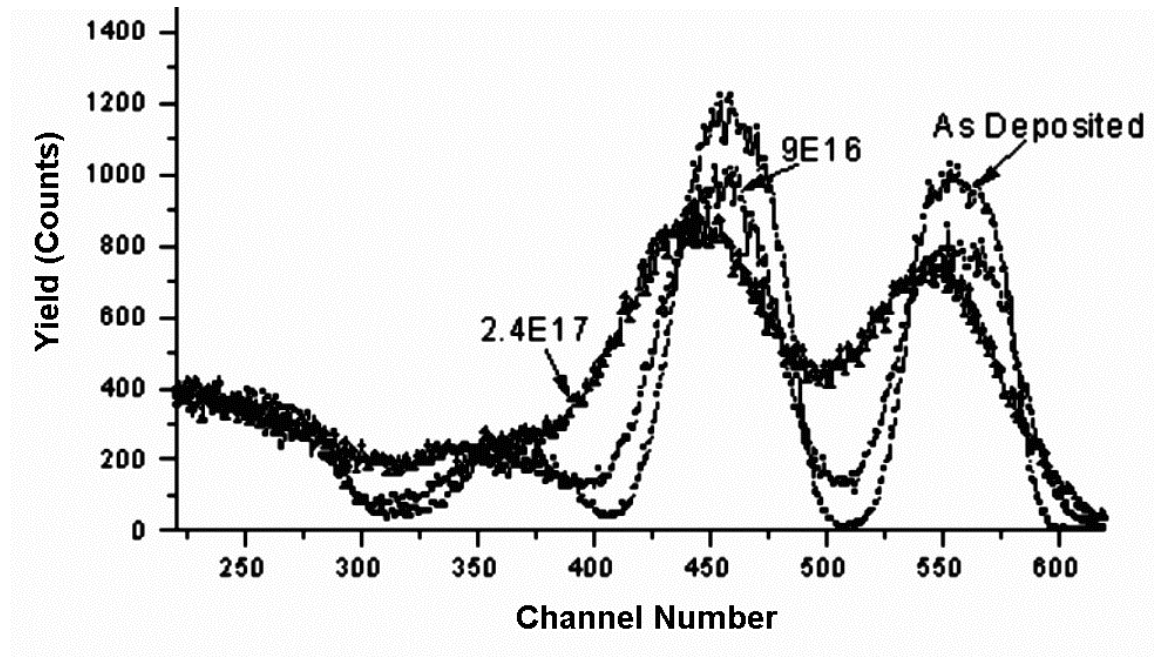


Fig. 3. RBS spectra of Ge-Si sample, as-deposited and after Ar irradiations at indicated fluences.

layer. This was not seen even at the maximum dose of Ar^+ ions used, suggesting that larger fluences are needed for uniform mixture of multi-layer film structure. Indeed, multi-layer structure has served as an indicator of the diffusion process taking place and helped to isolate the intended active area from the substrate, retaining its crystalline structure.

To analyze the data in Fig. 3, the signals of each element ought to be first separated from the others. This may prove to be a great challenge due to the fact that the top layer is not the heavier element and that all the layers are reasonably thick. This will lead to the signals of buried yet heavier element layers to coincide with each other and with the top layer signal.

This leads us to utilize a simpler and more reasonable method that depends on taking the ratio of the yields obtained at different doses of irradiation at a certain channel number to the signal of the as-deposited multi-layer structure. In this case, the choice falls on the channel number corresponding to the first Ge layer (from top), # 553. The division is performed at the three doses shown in Fig. 3 and the other doses not shown as well. The result of this analysis is shown in Fig. 4. In this figure, it is clear from the shape of the curve that the Ge percentage at this channel number and the corresponding depth is changing from 100% to 55% indicating that silicon from the cap layer has diffused into Ge and fraction of the Ge layer has diffused into the subsequent Si layer. Fig. 3 also conveys that as the top layer of Si is disappearing and diffusing, the apparent depth of the Ge layer appears to be shrinking. Obviously, at the highest dose used, this translates into a structure of $\text{Si}_{45}\text{Ge}_{55}$ for the top layer.

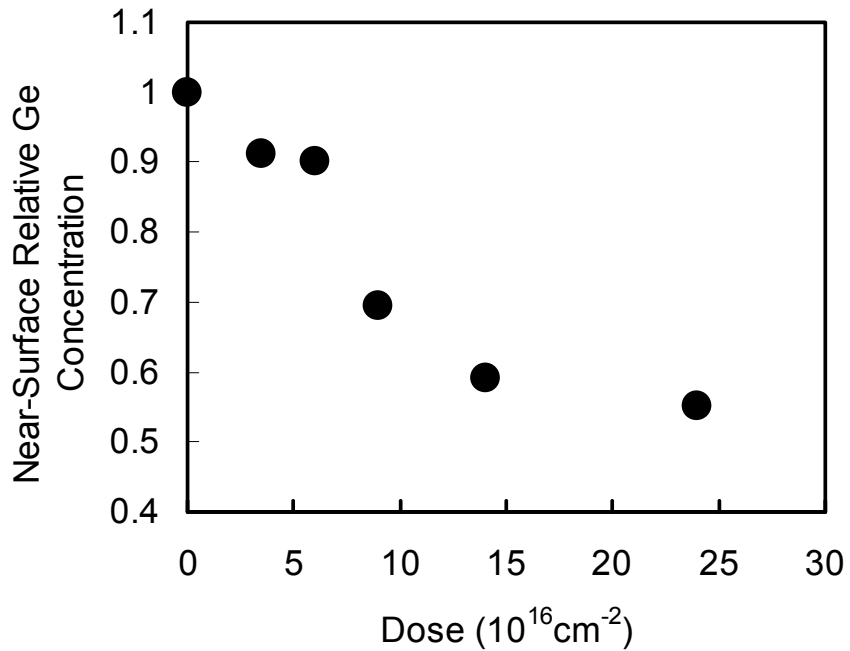


Fig. 4. Near-surface Ge concentration as function of Ar dose.

Applying the SRIM-2003 model, the ratio of 1.258 for the lateral penetration of argon ions into silicon to that in germanium at 300keV, for the given thickness of the layers of the as-deposited films as explained above, it was estimated that argon will not diffuse into $\sim 640 \text{ \AA}$ of the first layer of germanium, making the over all ratio of silicon 48% to germanium 52% in the newly formed alloy, if fully mixed. Considering a 5% error in the measurements, this result agrees with the analysis of Fig. 4 for the top layer of the Ge (2nd deposited Ge layer).

Argon bombardment has proven to be an efficient method for IM. However, structures are amorphous. Hence, the samples have to be annealed in order to obtain microcrystalline structures.

Conclusions

Numerous publications have reported silicon-germanium thin film structures as potential candidates for solar cell applications. Methods of preparation vary but are limited to CVD and MBE. In this work, for the first time in the literature, the novel technique of IM is utilized to fabricate a reasonably thick, yet easily processed Si-Ge thin film starting as multi-layer structure (two of each). The second layer of the film is the process monitoring indicator. Structural analysis of the mixed multi-layers of Si-Ge has been performed utilizing RBS. Structures containing more than 50% of Ge have been processed, with the possibility of

annealing without worrying about lattice mismatch problems at the interfaces due to the method of preparation.

Acknowledgment

The authors would like to thank the University of Jordan Van de Graaff accelerator crew for their support in making the sample especially Abu Husam and Mr. Adel Amro. The authors are also grateful to Dr. John .C. Hensel of NJIT for providing the wafers.

References

- [1] Gerhard Abstreiter, in Heterostructures in Semiconductors, Physica Scripta T68 (1968) pp 68-71.
- [2] L. M. Koschier, S. R. Wenham, M. A. Green, IEEE Trans. Electron. Devices 46 (1999) pp. 2111-2115.
- [3] *Demand for Advanced Communication Devices Drives the Compound Semi Market*, in Solid State Technology, p.52, July (2002).
- [4] *Compound Semis Poised for Dramatic Growth*, Electronic News, (www.e-insite.net/electronicnews, February 6, (2003).
- [5] S.A. Edmiston, A.B. Sproul M.A. Green and S.R. Wenham, Progress in Photovoltaics, 3 (1995) p. 333.
- [6] S R. Wenham, Progress in Photovoltaics, 2 (1994) p.181.
- [7] S.A. Healy, M.A. Green, Solar Energy Material and Solar Cells, 28 (1992) p. 273.
- [8] T.L. Chu, S. S. Chu, J. Britt, C. Ferekides, C. Wang, C. Q. Wu, and H. S. Ullal, *IEEE Electron Device Lett.* 13 (1992) p. 303.
- [9] E. Borne, J.P. Boyeaux and A. Laugier, First World Conference and Exhibition on Photovoltaic Solar Energy Conversion, December (1994), Hawaii, pp1637-1639
- [10] J.M. Ruiz and J. Casado, 13th European Photovoltaic Solar Energy Conference, October 1995, France, pp.1315-1318
- [11] D.-E. Arafa and R. Ahmad-Bitar, *Semiconductor Science and Technology*, 13 (1998) p. 322.
- [12] R. Ahmad-Bitar and D.-E. Arafa, Solar Energy Mater. and Solar Cells 51 (1998) p. 83.
- [13] D.-E. Arafa, 1999. Solar Energy Mater. and Solar Cells, submitted.
- [14] R. People, Physical Review B, 32(2) (1985) p.1405.
- [15] J. Xu, S. Miyazaki and M. Hirose, Jour. Of Non-Crystalline Solids, 208, (1996) pp. 277-281
- [16] X. Deng, X. Liao, S. Han, H. Povolny and P. Agarwal, Solar Energy Materials and Solar Cells 62 (2000) pp. 89-95.

- [17] J. Casado, J.M. Ruiz, 13th European Photovoltaic Solar Energy Conference, October 1995, France, pp.1311-1314
- [18] J. Konle, H. Presting, H. Kibbel and R. Sauer, Solid-State Electronics 45(2001), pp.1921-1925.
- [19] J. Konle, H. Presting, H. Kibbel, Physica E. 16(2003), pp. 596-601
- [20] M.E. Gueunier, J.P. Kleider, P. Chatterjee, P. R. Cabarrocas and Y. Poissant, Thin Solid Films 427 (2003), pp. 247-251.
- [21] J.K. Rath, F.D. Tichelaar, R.E.I. Schropp, Solar Energy Materials and Solar Cells 74(2002) pp. 553-560.
- [22] S. Hazra, A.R. Middya and S. Ray, Jour. Of Non-Crystalline Solids, 211(1997) pp. 22-29.
- [23] J. Zahler, C.G. Ahn, S. Zaghi, H. Atwater, C.Chu, Thin Solid Films 403-404 (2002) pp. 558-562.
- [24] C. Eisele, M.Berger, M. Nerding, H.P. Strunk, C.E. Nebel, and M. Stutzmann, Thin Solid Films 427 (2003), pp. 176-180.
- [25] R.J. MacDonald, E.C. Taglauer and K.R. Wandelt (Eds.): *Surface Science: Principles and Current Applications*, Springer Verlag Berlin, (1996).
- [26] O. Aucillo, R. Kelly (Eds.): *Ion Bombardment and Modification of Surfaces* Elsevier: Amsterdam, (1984).
- [27] N.M. Masoud, and D.-E. Arafah, *Phys. Stat. Sol. (a)* 172 (1999) p.155.
- [28] N.M. Masoud and D.-E. Arafah, *Phys. Stat. Sol. (a)*, submitted.
- [29] A. Miotello and R. Kelly, *Surface Science* 314 (1994) pp.275-288, and references therein.
- [30] N.M. Ravindra, D. Fathy, O.W. Holland and J. Narayan, in *The Physics and Technology of Amorphous SiO₂*, R.A.B. Devine, Editor, Plenum Press, NY, (1987), p. 279.
- [31] W.K. Chu, J. W, Mayer and M.A. Nicolet, *Backscattering Spectrometry*, Academic Press, NY (1978).

STABLE RECORD EFFICIENCIES FOR EFG AND STRING RIBBON SOLAR CELLS

Giso Hahn and Patric Geiger

University of Konstanz, Department of Physics, P.O.Box X916, 78457 Konstanz, Germany

[email: giso.hahn@uni-konstanz.de](mailto:giso.hahn@uni-konstanz.de)

ABSTRACT: Crystalline silicon ribbon materials have a high potential to significantly reduce wafer costs in PV due to their good use of the silicon feedstock without any losses related to block casting and subsequent sawing steps. This could lead to a significant reduction in Watt-peak (W_p) costs, if efficiencies are comparable to the ones obtained with standard cast multicrystalline wafers. Gettering and hydrogenation steps are necessary to improve the inhomogeneous as-grown material quality of the ribbon silicon materials due to the higher defect densities present. In this study we present results from three different solar cell processes for EFG and String Ribbon solar cells. Special attention is paid on the Al-gettering step with two different procedures tested (evaporation with subsequent alloying as well as screen-printing of Al-paste followed by a firing step). Efficiencies of the best cells benefit from the better back-surface-field (BSF) resulting from the screen-printed Al, and stable record efficiencies of 16.7% for EFG and 17.7% for String Ribbon could be achieved on 4 cm² solar cells. The latter represents the highest value stable under illumination for ribbon silicon material.

1. SILICON RIBBONS

Ribbon silicon has a high potential to bring down W_p costs in photovoltaics (PV) because of its good use of the silicon feedstock. As no sawing steps have to be carried out and no time and energy consuming block casting is involved, modules made out of ribbon silicon solar cells should have a substantial cost advantage. But this is only true if efficiencies are in the same range as for standard ingot cast multicrystalline silicon, which has the highest share in PV module production (58%) [1]. To increase the inhomogeneous (and locally quite poor) as-grown material quality, gettering and hydrogenation steps have to be applied to the defected ribbon materials. Recent studies [2-5] revealed that P- as well as Al-gettering steps can significantly enhance lifetimes of minority carriers in RWE Schott Solar's EFG (Edge-defined Film-fed Growth) and Evergreen Solar's SR (String Ribbon) material. Even more dramatic is the effect of hydrogenation, with a synergetic effect observed for a gettering step preceding the hydrogenation. Both, hydrogenation via a hydrogen-rich PECVD (Plasma-Enhanced Chemical Vapour Deposition) SiN_x with a subsequent firing step to release the hydrogen into the silicon bulk [2,3], as well as in-diffusion of hydrogen by a remote plasma [4,5] show large improvements in minority carrier lifetime. Spatially resolved measurements revealed that gettering is more effective in better areas of the as-grown wafer, whereas hydrogenation improves all areas significantly [4,5]. Lifetimes above 300 μ s could be detected locally in wafers that underwent a gettering as well as a hydrogenation step. But locally in the wafer, areas have been identified which could not be improved by gettering and/or hydrogenation at all [4,5]. This inhomogeneity within typical wafer dimensions of 10x10 cm² is still a problem to be addressed, and there is some research activity going on at the moment to clarify the nature of these defected regions which cannot be improved substantially within the solar cell process.

2. CELL PROCESSES

In the present study we were interested in the efficiency potential of EFG and SR material. Therefore we have chosen a solar cell process including evaporation of contacts to minimise grid shadowing losses and obtain a good blue response. In Fig. 1 the three applied processes are shown schematically. We used standard material quality with a base resistivity of 2-4 Ω cm. Wafers of 5x5 cm² size have been acidic etched prior to processing. In process A (standard process) an open-tube POCl₃ diffusion (80-100 Ω /sq.) is followed by a dry thermal oxidation (10-17 nm thick oxide) and the evaporation of 2 μ m of Al at the back side. The Al is alloyed at 800 °C for 30 min and during this Al-gettering step a back-surface-field (BSF) is formed resulting in a back surface recombination velocity S_b of about 1500 cm/s. The front contact (evaporation of Ti/Pd/Ag) is defined by photolithography and the back contact is formed by evaporation of 2 μ m Al. An Ag electroplating step was applied to reduce the series resistance. Cells of 2x2 cm² size

are separated by dicing and the solar cells are characterized by IV measurements. Afterwards, the incorporation of hydrogen is carried out on the processed cells by microwave-induced remote hydrogen plasma passivation (MIRHP) and cells are characterized again.

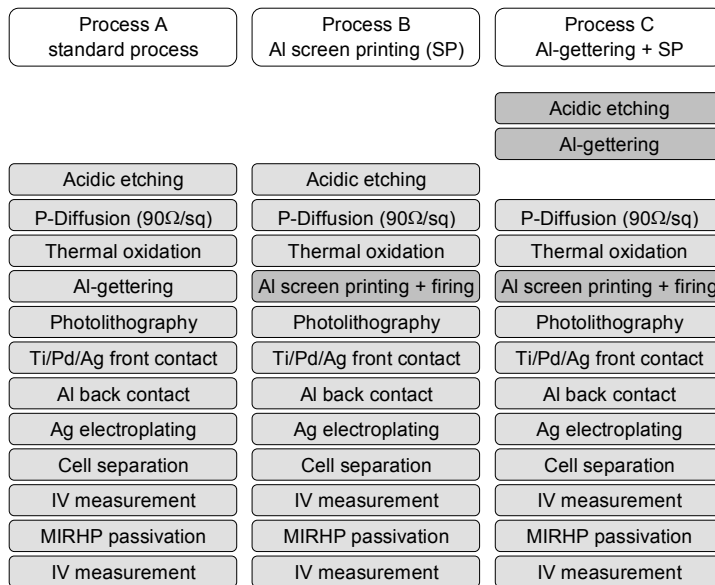


Fig. 1: Overview of the three processes used in this study for fabrication of 4 cm² EFG and SR solar cells.

For process B the formation of the BSF is carried out by screen printing of Al paste on the cell's back side followed by a firing step in a belt furnace. This results in S_b of about 200 cm/s (BSF thickness 8-10 µm). The lower S_b as compared to process A should lead to higher internal quantum efficiencies (IQEs) in the areas of high minority carrier lifetime. On the other hand, the short firing step and the use of Al-paste instead of pure Al in process B might result in a reduced Al-gettering effect. Therefore, in process C we applied the same Al-gettering step used in process A as an Al-pregettering step prior to POCl₃ diffusion. After evaporation of 2 µm Al and subsequent gettering at 800 °C for 30 min we etched off the eutectic layer as well as the formed BSF. Afterwards, cells are processed in parallel to process B.

3. RESULTS

Parts of the results have already been published elsewhere [6,7]. Illuminated IV results of the best cells before and after hydrogenation for each process shown in Fig. 1 are listed in Table 1. It can be seen that all parameters of all cells can be significantly improved by hydrogenation. This effect is even more dramatic for cells with lower efficiencies. Furthermore, the best cells fabricated according to process B show significantly higher short-circuit current densities J_{sc} and open-circuit voltages V_{oc} as compared to the standard process A. Comparing the results for processes B and C in Table 1 reveals the material inhomogeneity of the silicon ribbons. While no increase in efficiency could be observed for the best EFG cells, the Al-pregettering step led to a further increase in efficiency for the best SR cell.

To assess the effect of the different Al-gettering steps in processes A, B, and C a large statistic would therefore be necessary. As solar cell production capacity was limited (about 25 cells for each material and process have been fabricated) we have chosen another way to compare the effectiveness of the different gettering steps. Pairs of adjacent wafers with comparable grain structure have been processed according to the processes shown in Fig. 1. Results from pairs of such wafers are presented in the following and the effect of the different gettering steps can be observed on the same crystal grains of the different wafers.

In Fig. 2 the IQEs at 980 nm for pairs of adjacent wafers are shown. The lower S_b of process B leads to a significantly higher IQE as compared to process A in regions of high τ , despite of the shorter Al-gettering step in combination with Al screen-printing and firing. The Al-pregettering can further increase IQEs

*Table 1: Cell parameters for the best EFG and SR cells processed according to processes A, B, and C respectively (no antireflective coating). Shown are the values before and after hydrogenation (MIRHP). * Parameters for the best cells after ZnS/MgF₂ DARC have been independently measured at JRC Ispra.*

Process	EFG				SR			
	J _{sc} [mA/cm ²]	V _{oc} [mV]	FF [%]	η [%]	J _{sc} [mA/cm ²]	V _{oc} [mV]	FF [%]	η [%]
A before MIRHP, no ARC	21.4	560	77.0	9.2	22.5	557	78.4	9.8
A after MIRHP, no ARC	22.8	577	80.2	10.5	23.1	568	79.8	10.5
B before MIRHP, no ARC	20.0	547	77.0	8.4	24.4	590	76.9	11.1
B after MIRHP, no ARC	23.3	590	79.6	10.9	24.7	600	77.9	11.5
C before MIRHP, no ARC	21.4	551	75.3	8.9	24.6	601	76.8	11.4
C after MIRHP, no ARC	23.7	587	78.1	10.9	25.1	609	77.9	11.9
Best cell after DARC*	35.1	601	79.0	16.7	37.0	615	77.7	17.7

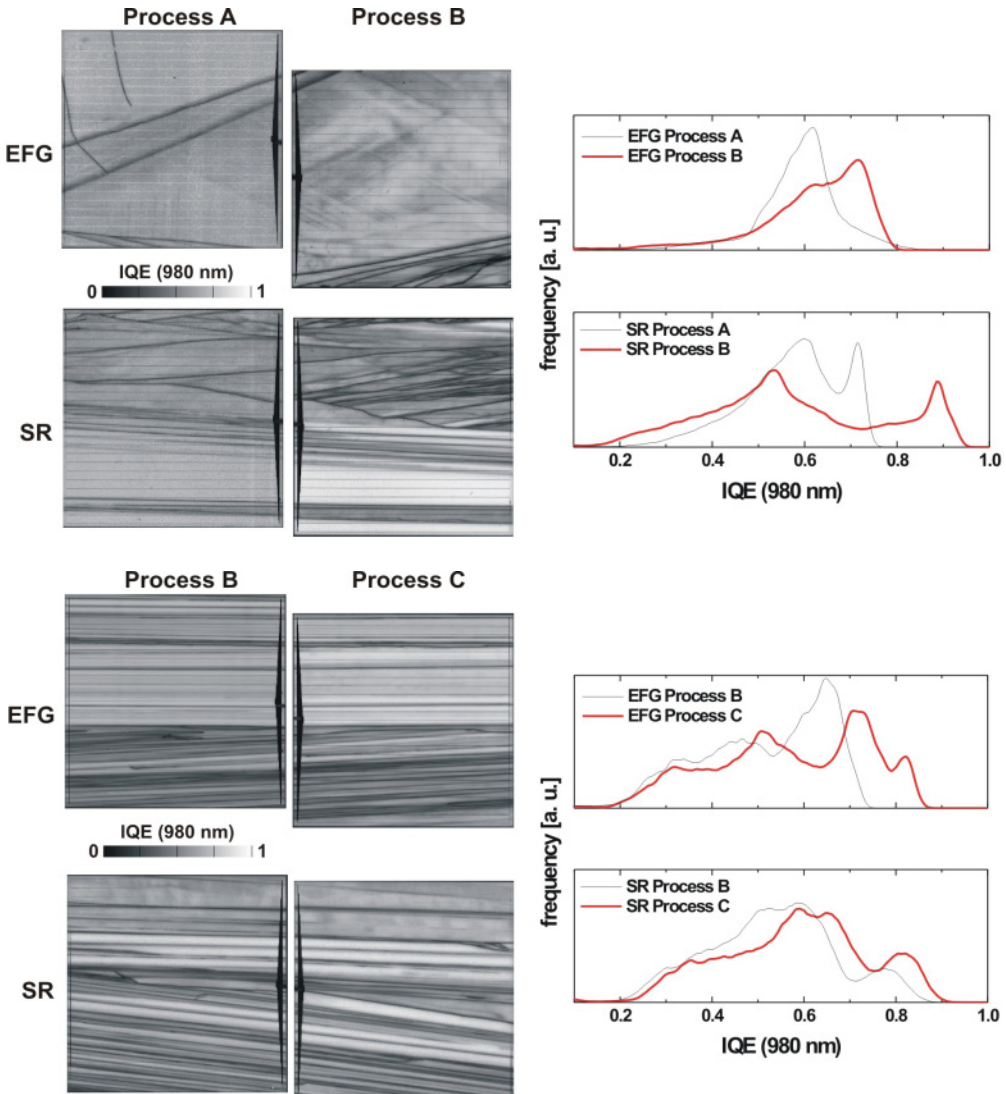


Fig. 2: IQEs at 980 nm for adjacent EFG and SR solar cells processed according to the sequences shown in Fig. 1 after hydrogenation. The lower S_b of the screen-printed BSF for process B results in higher IQEs as compared to process A (top) in areas of high bulk lifetime. Some areas of mainly good quality benefit from the Al-pregettering step of process C as compared to process B (bottom).

especially in good quality areas of the wafer due to the more effective gettering as can be visualized by comparing the pairs of wafers processed according to processes B and C respectively.

Interestingly, IQE values before hydrogenation for cells processed according to process B can be lower as compared to the adjacent cells processed with process A (Fig. 3). This could be due to the better Al-gettering effect of process A. Without hydrogenation lifetimes are not high enough to get the full benefit of the lower S_b for the screen-printed BSF. The situation changes when lifetimes are increased after hydrogenation and the lower S_b for process B can be used. Now the IQE especially in the long wavelength part of the spectrum is higher for process B. Additionally, the hydrogenation step might passivate defects introduced during the screen-printing step.

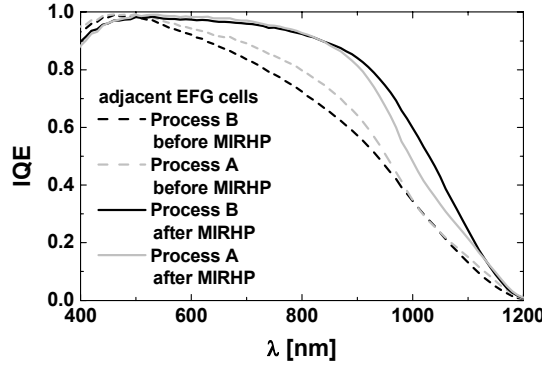


Fig. 3: IQEs of two adjacent EFG cells before and after hydrogenation (MIRHP). After hydrogenation the lower S_b for process B increases the IQE for long wavelengths, whereas without hydrogenation the lower Al-gettering efficiency results in lower IQE values (same two cells as already shown in Fig. 2, top).

To investigate the Al-gettering effect further, we stripped off the metal contacts, the BSF, and the emitter for the four EFG cells shown in Fig. 2. After a surface passivation using iodine/ethanol solution we measured the spatially resolved bulk lifetime τ using microwave-detected photoconductance decay as described in [4]. Results can be seen in Fig. 4 and the following conclusions can be drawn.

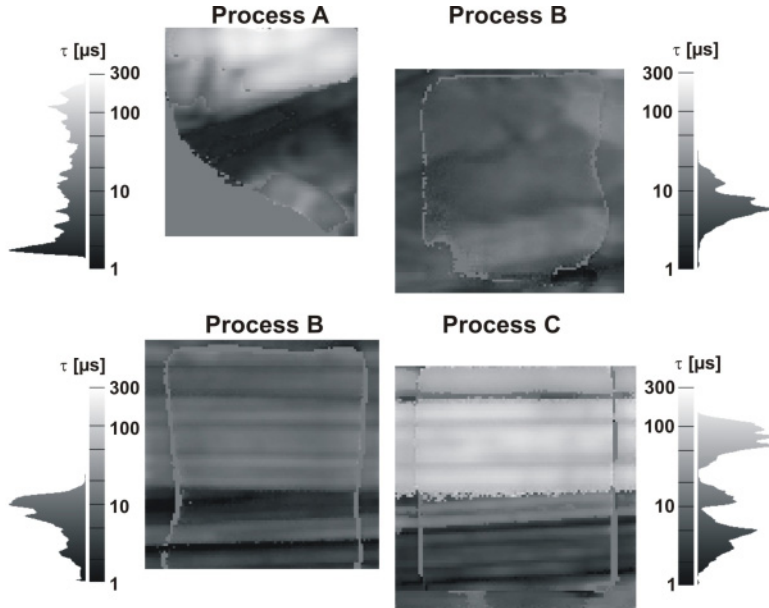


Fig. 4: Bulk lifetimes of the four EFG cells already presented in Fig. 2. The influence of the different Al-gettering steps can be seen by comparing adjacent wafers with the same grain structure.

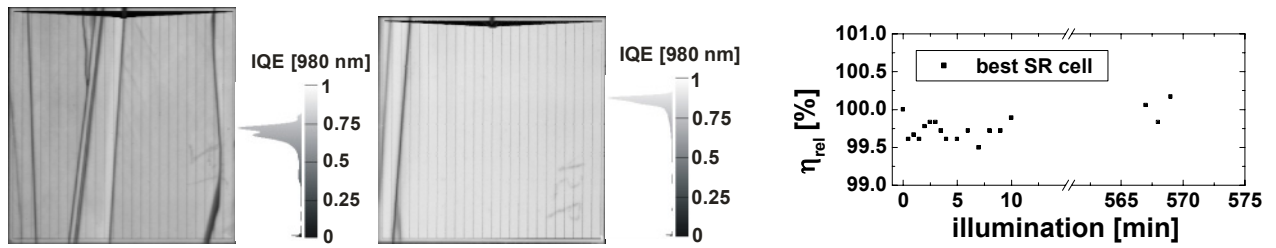
Comparing process A and B in Fig. 2 and 4: for process A (sample partly broken) no use of the high τ in the top part of the cell can be made due to the higher S_b . A higher IQE can be reached for process B despite of only average τ because of the lower S_b as compared to process A.

Comparing process B and C: a higher τ can be reached in the good quality region due to Al-pregettering, which can be used (higher IQE) due to the lower S_b for the Al screen-printing process.

4. BEST CELLS

IQE mappings at 980 nm for the two best cells can be seen in Fig. 5. Several electrically active grain boundaries are visible, whereas some grain boundaries present in the SR cell (invisible in Fig. 5) show no recombination activity at all.

The stability under an illumination of 1 sun was tested and results for the best SR cell are presented in Fig. 5 (right). The cell was measured immediately after a hotplate anneal (200°C , 30 min). Within measurement uncertainty the cell seems to be totally stable under illumination. This is in contrast to other results published recently [8,9]. These cells had a PECVD SiN/MgF₂ double layer ARC and it was found that the initial efficiency for cells with $\eta > 16\%$ after annealing decreases 0.5-1% absolute within a short time. An explanation for this decrease could be a less effective gettering under the rapid thermal firing conditions used in [8] with some Fe remaining in the wafer. Or the observed unstable efficiency in [8,9] may be related to the used SiN, too, and could be caused by a change of the fixed charge within the SiN as in our process a thermal oxide for surface passivation and a ZnS/MgF₂ double layer ARC is used.



REFERENCES

- [1] P. D. Maycock, *PV News*

PREDICTING MULTI-CRYSTALLINE SOLAR CELL EFFICIENCY FROM LIFETIME MEASURED IN SILICON BLOCKS

Ronald A. Sinton and Tanaya Mankad*

Sinton Consulting, Inc.

1132 Green Circle, Boulder, CO 80305 USA

*Consultant

ABSTRACT

Recent work has made great strides in identifying key features in multicrystalline blocks that can be used to predict the resulting cell efficiency as a function of position in the original block. Many of these studies use Quasi-Steady-State PhotoConductance performed on wafers cut from the blocks. Work is in progress to develop a QSSPC tool capable of spatially-resolved measurements on the as-grown-and-cut blocks. This would enable direct application of the new physical understanding to process control and optimization of the crystal growth. Additionally, the data could be used to determine the region of the block to be processed into solar cells. Progress on this instrument will be reported.

INTRODUCTION

There have been significant recent advances in the studies of multicrystalline blocks with respect to identifying the physical features of blocks that can be used to predict the resulting solar cell efficiency (1,2,3,4). Three of the key factors determining eventual cell performance are oxygen concentration, metallic impurities, and crystalline defects. Increasingly, each of these can be correlated to their unique combination of 4 factors: position in the ingot, its measured lifetime, measured trapping, and the Fe concentration as determined by lifetime measurements before and after light soaking to toggle the Fe:B pairs between states. In fact, lifetime measurements after light soaking have been shown to be very predictive for final efficiency. The light soaking temporarily “passivates” the Fe:B pairs. These Fe:B pairs may be limiting the lifetime in the as-grown material, but the same regions that are passivated by light soaking will be gettered by the processing of the wafers(1).

DESCRIPTION OF THE INSTRUMENT

Much of the data described above has been obtained using the QSSPC method(5) on wafers that have been cut from the block. Each wafer is tracked through processing steps or carefully controlled experiments in order to be able to identify the wafer's spatial origin in the block. In order to measure lifetime as a function of position in the block, the wafers need to be surface passivated, usually by means of light phosphorus diffusion or nitride deposition.

Recently, a tool has been introduced that can measure the QSSPC lifetime on as-grown, as-cut blocks of sili-

con(6). This instrument is similar to the standard QSSPC tool, except that it uses IR light to penetrate deeply into the silicon away from the unpassivated surface of the block. This allows a measurement that is quite sensitive to the bulk lifetime in the silicon despite the unpassivated surface.

Two views of the instrument are shown in Fig. 1.

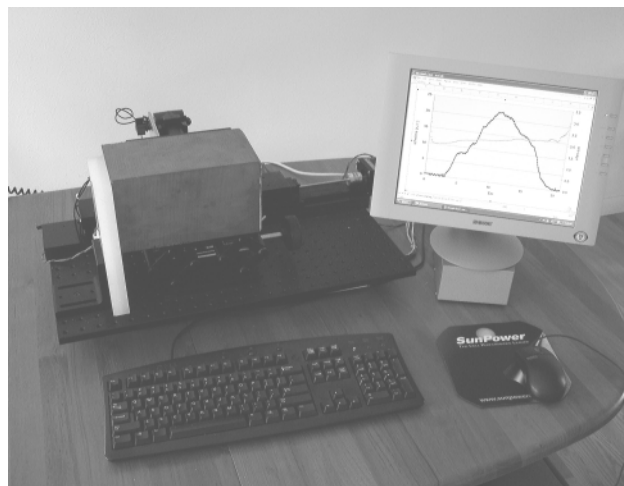


Fig. 1. A QSSPC block scanner (top). The sense head is shown below. The line pattern is scanned in the growth direction in order to give high resolution in that axis. This is useful to decide where to saw wafers. For the 2-D plots in this paper, only 1 of the 3mm light sources was used, (instead of the line formed by 10) giving a 2-3 mm resolution for 2-D data.

Lifetime data for an HEM block is shown in Fig. 2. This data was taken with a 2 mm step size in the growth direction (0 to 21 cm top to bottom), and a 3 mm step size in the cross section of the block. The absolute calibration of the measured lifetime is tentative at this time.

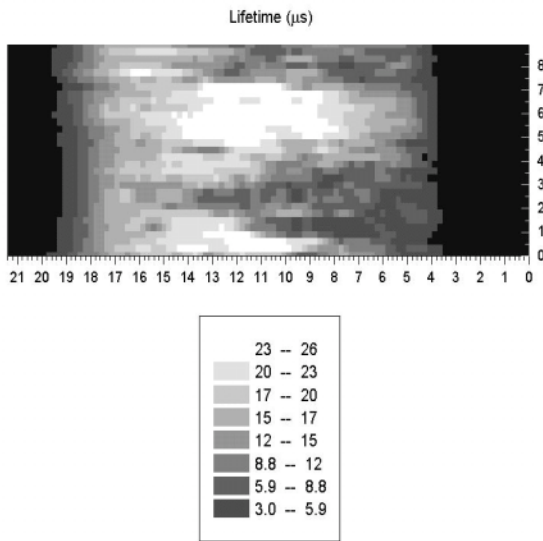


Fig. 2. A 2-D scan of QSSPC lifetime of an HEM block. (sample courtesy of Keith Matthei, GT Solar). The 0 point on the x-axis is the top of the 21-cm-long block.

A recent paper proposed that a better presentation of this data may be as $1/L$ where L is the diffusion length(7). It is well known that in cases of non-homogeneous lifetime, the area-average of lifetime gives an optimistic prediction of cell efficiency(8,9,10,11). The cell voltage depends on J_{ob} , which in the case of low lifetime depends on $1/L$. A plot of the data in the form of $1/L$ is shown in Fig. 3. This plot has the advantage of putting the high resolution into the low-lifetime regions that determine cell performance, rather than the high-lifetime regions that do not.

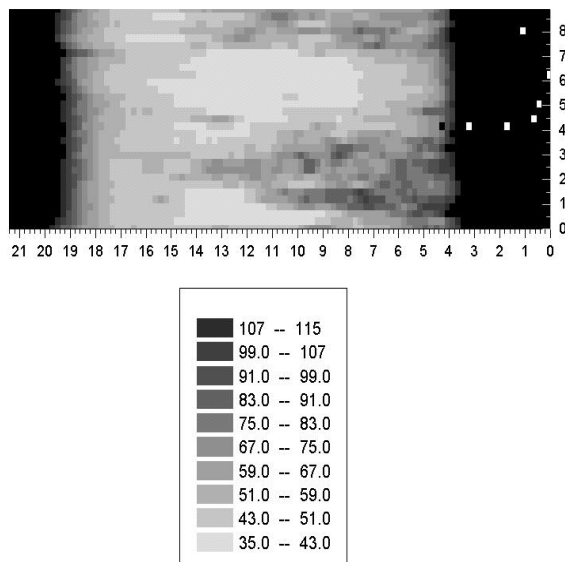


Fig. 3. The same data as in Fig. 2, but displayed in units of $1/L$, the recombination rate in the bulk of the silicon.

This data can be analyzed to predict the performance of wafers that might be sown from the block. Taking the data in cross section, each 2 mm column of pixels might represent the lifetime profile for 4 wafers that would be cut from that region. Then the parameter of interest would be the average in $1/L$ over this entire column. This data, as a function of position from the top to the bottom of the block, is shown for the “good” region of the block shown in Fig. 2.

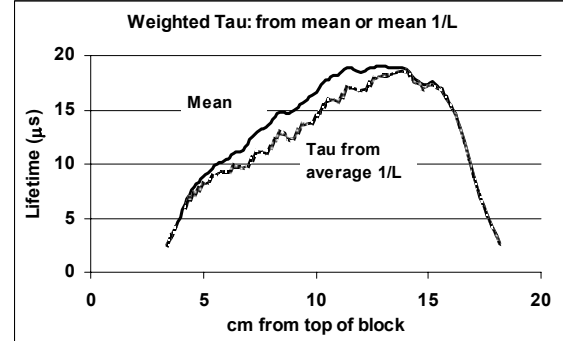


Fig. 4. The average lifetime of each column of pixels in Fig. 2 (top), compared to the average ($1/L$) of each column in Fig. 3. The $1/L$ average was converted back in lifetime for comparison. The difference is about 20% for much of this block, with the average lifetime value being 20% optimistic.

A comparison of the effective “wafer” lifetime obtained by averaging over lifetime or $1/L$ indicates that where there is large variation in lifetime across the block, the average lifetime is up to about 20% more optimistic than the effective lifetime as determined by the average $1/L$. In contrast, near the edges of the “good” region of the block, the lifetime becomes a rather homogeneous function of position at a given position on the top-to-bottom axis, and the two averaging methods give the same result.

A higher resolution measurement of the cross section is shown in Fig. 5. This measurement was done with a single 3 mm diameter light source, stepped in 1 mm increments. This might represent the region where 4-6 wafers would be sown.

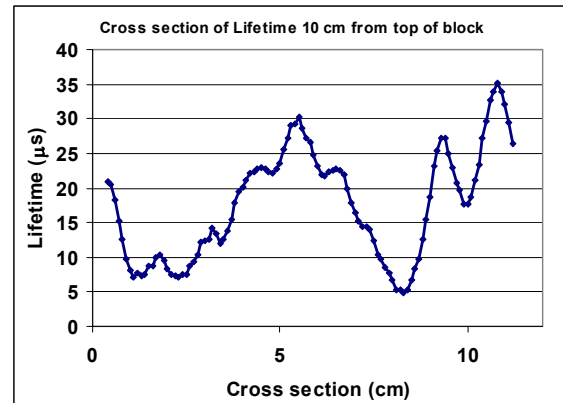


Fig. 5. The measured lifetime as a function of the position at a cross section at a point 10 mm from the top of the block. The average lifetime is $17.6 \mu\text{s}$. The lifetime as determined by averaging $1/L$ is $14.6 \mu\text{s}$.

Acknowledgements

This work was partially supported by U.S. D.O.E. contract ZDO-2-30628-08.

REFERENCES

- 1) L. J. Geerligs, "Mc-Si: Relation Between Ingot Quality and Cell Efficiency", Proc. 12th Workshop on Crystalline Silicon Solar Materials and Processes", NREL/BK-520-32717, August 2002.
- 2) D. Macdonald, A. Cuevas, and F. Ferrazza, " Response to Phosphorus Gettering of Different Regions of Cast Multicrystalline Silicon Ingots" Solid State Electronics, 43, 575-581, 1999.
- 3) D. Macdonald, A. Cuevas, M. Kerr, C. Samundsett, A. Sloan, A. Leo, M Mrcarica, S. Winderbaum, and S. Shea, "Characterization of a Commercial Silicon Solar Cell Process", Proc. 38th Annual Australian and New Zealand Solar Energy Society Conf., Brisbane, Australia, 2000.
- 4) D. Macdonald and A. Cuevas, "Cross Contamination as a Novel Technique for Studying Impurities in Multicrystalline Silicon" Proc. of the 8th Workshop on the Role of Impurities and Defects in Silicon Device Processing, Colorado, 1998.
- 5) Sinton, R.A. and Cuevas, A., Contactless determination of current-voltage characteristics and minority-carrier lifetimes in semiconductors from quasi-steady-state photoconductance data. Applied Physics Letters, 1996, 69(17), pp. 2510-2512.
- 6) Ronald A. Sinton, "Practical measurement of bulk lifetime and surface recombination by using wavelength dependence", To be published in Proc. PVSEC, Osaka, Japan, May 2003.
- 7) Ronald A. Sinton, "Predicting Multi-Crystalline Solar Cell Efficiency From Lifetime Measured During Cell Fabrication", To be published in Proc. PVSEC, Osaka, Japan, May 2003.
- 8) C. Ballif, S. Peters, D. Borchert, C. Hassler, J. Isenberg, R. Schindler, W. Warta, G. Willeke, "Lifetime Investigations of Degradation Effects in Processed Multicrystalline Silicon Wafers". Proc. 17th EPSEC, Munich, Oct. 2001 pg. 1818.
- 9) P. Geiger, G. Kragler, G. Hahn, P. Fath, E. Bucher, "Spatially Resolved Lifetime Investigations of Al- and P-Gettering in Combination with Remote Plasma Passivation in EFG Ribbon Silicon", Ibid. pg. 1715.
- 10) J. Isenberg, J. Dicker, W. Warta, "Analysis of the Effect of Diffusion Length Distributions on Global Solar Cell Parameters by Simplified 2D Modelling", Ibid, pg. 1571.
- 11) J. Isenberg, J. Dicker, S. Riepe, C. Ballif, S. Peters, H. Lautenschlager, R. Schindler, W. Warta, "Correlation of Spatially Resolved Lifetime Measurements with Overall Solar Cell Parameters", Proc. 29th IEEE Photovoltaic Specialist Conf., New Orleans, 2002.

Dependence of aluminium alloying on solar cell processing conditions

C.B. Honsberg, K.K. Anwar, H.R. Mehrvarz, J.E. Cotter, and S.R. Wenham

Centre for Photovoltaic Engineering
University of New South Wales
Sydney, Australia 2052
<mailto:c.honsberg@unsw.edu.au>

Abstract

The formation of a low surface recombination velocity rear surface using an aluminium alloyed back surface field (BSF) depends on the quality of the rear layer, particularly its uniformity and average thickness. The thickness and uniformity in turn depend on the processing conditions, including the presence of an interfacial SiO_2 layer between the silicon and aluminum, the wafer orientation in the furnace compared to the gas flows, and the unloading ramp rates. Variation of these parameters using n-type buried contact solar cells with rear collecting junctions show that the presence of an interfacial SiO_2 layer reduces the sensitivity to ramp-up temperature transients, and that parallel wafer orientation and low unloading temperature increase the open circuit voltages by 20 mV.

Introduction

The most common rear surface passivation in commercial solar cells is an aluminum alloyed back surface field (Al-BSF). The Al-BSF is formed by depositing an Al layer, by one of several techniques including screen printing and evaporation. After Al deposition, the wafer is heated by rapid thermal processing (RTP), in a belt furnace, or in a tube furnace to form an Si-Al alloy. Measurements of the Al-BSF by spectral response [1] and photoconductance decay [2] techniques show low surface recombination velocities, with $< 200 \text{ cm/sec}$ formed by either RTP [1] or by belt furnace [2]. Correcting the results for different substrate resistivities [3] gives an effective saturation current for the Al-BSF of $4 \times 10^{-13} \text{ A/cm}^2$.

A uniform, relatively thick Al-alloyed region is essential in achieving a high quality Al-BSF. For a uniform Al-alloyed region, the thickness of the Al-alloyed region is substantially determined by the thickness of the deposited Al and the temperature [4]. However, the uniformity of the rear layer depends on the details on the process, in particular the transient temperature conditions experienced by the wafers. Two approaches can be used to minimize the impacts of the transients.

The first approach involves using fast ramp rates [1] while also ensuring that the aluminium region is slightly hotter than the bulk silicon region [5]. The rapid heating and cooling minimizes the time spent under transient conditions. RTP processing uses this approach, and shows that fast ramp rates give improved performance [1]. The other approach to high quality Al-BSF layers involves controlling the transient temperature conditions experienced by the wafer by optimizing the furnace conditions for a given rear surface structure. This paper examines the effect of an interfacial SiO_2 layer, wafer orientation compared to gas flows, and unloading ramp rates on the electrical quality and uniformity of the rear Al-alloy layer.

Al-alloyed regions in buried contact solar cells

The Al-alloying step in buried contact (BC) solar cells is used not only to make the rear Al-BSF but also to make a deeper emitter and groove diffusion. The optimum Al-process for the BC process is one which improves the front as well as the rear surface. Therefore, the conventional BC solar cells involves an Al-alloy process with significantly different times and temperatures compared to the Al-alloy processes for screen printed solar cells using belt furnaces and RTP.

Despite the different optimization criteria and processing conditions for BC solar cells, the Al-alloyed regions have similar levels of surface passivation as those produced by the lower temperatures and shorter times of the Al-regions formed by RTP or belt furnaces. For the conventional BC solar cell, values of the rear Al-BSF range from 1,000 to 500 cm/sec on 1.0 Ω -cm to 3.0 Ω -cm material [6,7]. Converting these values to an effective saturation current [3] to account for differences in substrate resistivities gives saturation currents in the range of 8×10^{-13} A/cm², which is within a factor of two to the reported results from RTP and belt diffusion. BC solar cells using these Al-BSFs have achieved open circuit voltages of 660 mV [8].

While high quality Al-BSF layers have been achieved with the conventional BC solar cell, application of this Al-alloy process to other BC structures such as the simplified buried contact (SBC) solar cell [9] demonstrates the sensitivity of the Al-alloy process to details such as the presence of an interfacial SiO₂ layer between the Si and Al. In the SBC solar cell, the selective emitter of the conventional BC solar cell is replaced by a single-step emitter and groove diffusion. As a result, the rear surface does not have a thick SiO₂ layer between the silicon and the deposited Al. Applying the alloying process from the conventional BC structures results in a highly non-uniform rear Al-alloy layer, which often penetrates through the entire wafer and results in severe localized shunts. The non-uniformities in the rear surface arise from temperature gradients that occur during the loading and unloading process. This paper presents what mechanisms affect the transients and how to minimize their effects.

Experiment

To investigate the impacts of an interfacial SiO₂ layer, wafer orientation and cool-down ramp times on the rear Al-alloy quality, n-type rear-contact simplified BC structures are fabricated, with the Al-alloyed region acting as the emitter as shown in Figure 1. The structure is the same as the simplified BC structure, expect that the

wafers are n-type and the hence the p-type emitter is at the back of the solar cell and is formed by the Al-alloy layer. A rear junction n-type structure is used to examine quality of the Al-alloy region as this device structure is more sensitive to the Al-alloy quality than a conventional front junction solar cell.

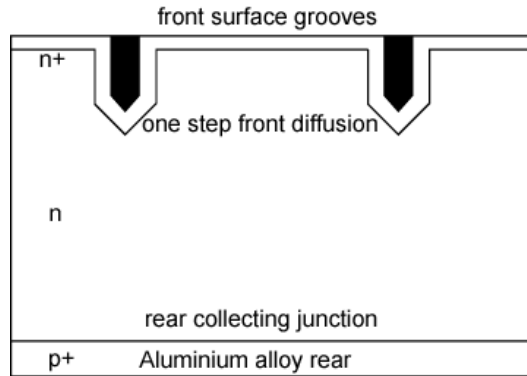


Figure 1: Schematic of the rear junction simplified BC solar cell used to examine the rear Al-alloy layer performance.

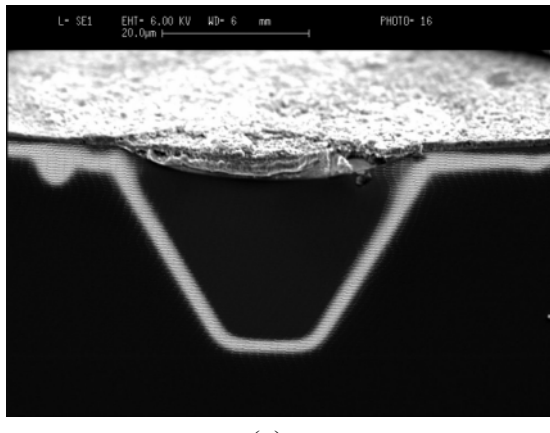
The rear junction SBC solar cells use untextured, 300 μm thick, 1.0 $\Omega\text{-cm}$ n-type FZ wafers, with emitter and groove diffusions of 50 Ω/\square . All the solar cells have an area of 9.0 cm². The SBC process is described in [10]. The focus of this paper is the rear Al-Si alloyed region, and three parameters affecting this alloying process are varied: (1) the presence or absence of an interfacial SiO₂ layer between the silicon and deposited Al; (2) the wafer orientation with respect to the gas flow in the furnace; and (3) the unloading temperature of the wafers, corresponding to varying the ramp rate. The varied parameters in the batches are shown in Table 1. In all cases, the thickness of the deposited Al is between 0.7 and 1.7 (nominally 1.5 μm), and process consists of a peak alloy temperature of 980 °C and a load/unload temperature of 800 °C. The wafers remain at 980 °C for 1 - 3 hours. The time of alloying process has a minor impact on the resulting thickness as the Al-region is formed via melt and regrowth and not via solid state diffusion, and is chosen for its impact on the front emitter and groove diffusion.

Table 1: Variation of parameters used in the fabrication of the rear junction SBC solar cells.

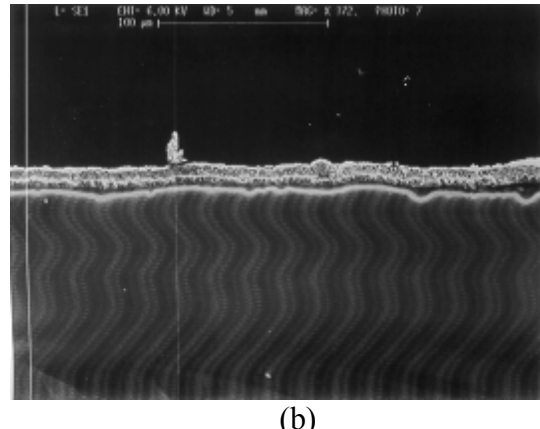
	Presence of SiO_2 on rear	Wafer orientation compared to gas flow	Unload Temp.
1	Yes	Perpendicular	800 °C
2	Yes	Parallel	800 °C
3	No	Perpendicular	800 °C
4	No	Parallel	800 °C
5	No	Parallel	400 °C

Interfacial SiO_2 layer

The key impact of the interfacial SiO_2 layer is that the resulting Al-alloy region is highly sensitive to the transient furnace conditions. Initial results on the n-type structures using non-optimized alloying conditions and without SiO_2 layers gave poor Al-alloyed back regions, characterized by highly variable Al-Si alloy layer as shown in Figure 2, giving low open circuit voltages (< 300 mV) and severe shunts. The SiO_2 layer retards the interaction of the Al and Si during temperature ramp-up, making devices without the interfacial SiO_2 layer sensitive to the temperature transients during loading. The reduced sensitivity to ramp-up transients explains why BC solar cells with a SiO_2 layer have similar saturation currents compared to RTP Al-alloy regions without interfacial oxides. The role of the interfacial oxide as chiefly affecting the ramp-up transients is further supported by the fact that for the remainder of the tests, the wafers with and without oxide performed identically.



(a)



(b)

Figure 2: SEM/EBIC micrograph of rear junction n-type SBC solar cells, with (a) non-uniformities from temperature transients, (b) more uniform Al-alloy regions.

Wafer orientation compared to gas flow

The orientation of the wafers in the furnace compared to the gas flow affects how uniformly the wafer is heated. Both with an oxide and without, the wafer orientation significantly affects the open circuit voltages of the test structures. The results shown in Table 2, demonstrate that loading of wafers parallel to the gas flows improves the Al-alloy quality, increasing the V_{oc} by approximately 10 mV compared to the case where the wafers are perpendicular to the gas flows. The reason for the improved V_{oc} with parallel gas flows is the improved temperature uniformity between wafers, which limit non-uniformities in the resulting Al-alloy region.

Table 2: Results for n-type simplified BC solar cells. Due to the similarity of the V_{oc} s (within 5 mV of each other), but larger variations in FF (due to non-optimum front surfaces), the results presented are the best efficiency result from the batch.

Wafer Orientation	Rear SiO_2	V_{oc} (V)	J_{sc} mA/cm ²	FF	η (%)
Perp.	Yes	0.587	22.56	0.74	9.75
Parallel	Yes	0.596	27.26	0.74	12.0
Perp.	No	0.584	30.12	0.64	11.2
Parallel	No	0.591	30.80	0.67	12.2

Furnace Unloading Temperature

In RTP processed Al-alloy layers, the ramp rates have a significant impact, with faster ramp rates giving improved performance [1]. However, if the temperature transients cannot be made very short, as is the case with tube furnaces, then the other extreme is better – longer cool down times minimize thermal gradients across the wafers and also promote regrowth that is closer to equilibrium and hence potentially higher quality. In this work, the unload rates were not controlled, but slow ramp rates are implemented by cooling the furnace to a temperature below the eutectic temperature (400 °C is used as the furnace set point temperature) with the wafers in the furnace. The wafers are oriented parallel to the gas flows during the Al-alloy process. The lower temperature unloading gives 10mV improvement in open circuit voltage compared to the case in which the unloading temperature is 800 °C, with measured results (unconfirmed) of $V_{oc} = 604.9$ mV, $J_{sc} = 29.34$ mA/cm², FF = 70.7 and $\eta = 12.56\%$.

Previous results on rear junction solar cells using RTP for the Al-alloy formation [11] give a V_{oc} of 606 mV, similar to the 605 mV measured from the rear junction SBC devices. In both of these structures, the base lifetime is at least 3 times the wafer thickness, and hence the front surface structure contributes to the measured V_{oc} . For the rear junction SBC solar cells used in this work, the front surfaces are unoptimized. The application of the developed Al-alloy process to simplified buried contact solar cells with an optimized front surface diffusions on p-type 1 Ω-cm untextured CZ wafers, gives open circuit voltages of 617 mV and efficiencies of 16.9% [10].

Conclusion

The minimization of transient temperature gradients during either loading or unloading in the formation of the Al-alloyed regions is a key component in formation of low effective surface recombination Al-BSFs. In conventional buried contact solar cells, the presence of the interfacial

SiO₂ layer makes the devices less sensitive to temperature gradients during loading. For both devices with and without interfacial oxide layers, placing the wafers parallel to the gas flows and reducing the ramp rates during cooling gives more uniform, higher quality Al-alloy regions. Rear junction, n-type SBC solar cells using the Al-alloy region have achieved 605 mV, and simplified BC solar cells using this Al-alloy process reached V_{oc} s of up to 617 mV and efficiencies of up to 17.1% on 1 Ω-cm p-type CZ wafers. Consequently, by understanding and controlling the temperature transients, a high quality Al-alloy region can be formed for a range of processes and furnaces.

References

- [1] S. Narasimha and A. Rohatgi, *IEEE Trans. Elec. Dev.*, Vol. 46, No. 7, 1363, 1999.
- [2] P. Lölgen, C. Leguijt, J.A. Eikelboom, R.A. Steernan, W.C. Sinke, L.A. Verhoef, P.F.A. Alkemade and E. Algra, *23rd IEEE Photovoltaics Specialists Conference*, 236-242, 1993.
- [3] S. Bowden, V. Yelundur and A. Rohatgi, *Proc. 29th IEEE Photovoltaics Specialists Conference*, 371-374, 2002.
- [4] J. del Alamo, J. Eguren and A. Luque, *Solid-State Elec.* 24 (1981) 415-420.
- [5] F.M. Robers and E.L.G. Wilkinson, *J. Mat. Sci.*, 3 (1968) 110-119.
- [6] S. Wenham, *Prog. Photov.*, 1, (1003) 3-10.
- [7] A.M. Slade, C.B. Honsberg, S.R. Wenham, *Solar Energy Materials & Solar Cells*, 66 (2001) 11-15.
- [8] C.B. Honsberg, and S.R. Wenham, *Prog. Photovol.* 3, (1995) 79-87.
- [9] C. Honsberg, S. Edmiston, A. Fung, M. Molitor, S. Wenham, *14th European PVSEC*, 1994, 146-149.
- [10] J.E. Cotter, H.R. Mehrvarz, K.R. McIntosh, C.B. Honsberg and S.R. Wenham, *16th European Photovoltaic Science and Energy Conference*, 2000.
- [11] D.L. Meier, H.P. Davis, R.A. Garcia, J. Salami, A. Rohatgi, A. Ebong, P. Doshi, *Solar Energy Materials & Solar Cells*, 65 (2001) 621-627.

Neutron activation analysis study of metal content of multicrystalline silicon for cost-efficient solar cells

**A.A. Istratov⁽¹⁾, T. Buonassisi⁽¹⁾, R.J. McDonald⁽²⁾,
A.R. Smith⁽²⁾, R. Schindler⁽³⁾, J.A. Rand⁽⁴⁾, J. Kalejs⁽⁵⁾, and E.R. Weber⁽⁶⁾**

University of California and Lawrence Berkeley National Laboratory, MS 62R0203, 1 Cyclotron Rd., Berkeley CA 94720, USA; e-mail: istratov@socrates.berkeley.edu

(2) Lawrence Berkeley National Laboratory, MS 72R0150, 1 Cyclotron Rd., Berkeley, CA 94720, USA

(3) Fraunhofer Institute for Solar Energy Systems, Heidenhofstrasse 2, D-79110 Freiburg, Germany

(4) Astropower, Solar Park, Newark, DE 19716-2000, USA

(5) RWE Schott Solar, Inc. 4 Suburban Park Drive Billerica, MA 01821-3980, USA

(6) University of California, Dept. of Materials Science and Engineering, 374 Hearst Mining Bld., Berkeley CA 94720, USA

It is well established that transition metals and their precipitates are one of the culprits of the efficiency degradation of solar cells. However, the actual metal concentrations in solar cells are often uncertain. There are very few published reports on the metal content of mc-Si (the study of Macdonald et al. [1] is the only recent publication known to us). Thus, a comparative study of transition metal concentrations in several types of mc-Si materials, as well as a comparative analysis of the areas with high and low minority carrier diffusion length within the same wafer could provide valuable information on the role of transition metals degradation of mc-Si solar cells efficiency.

In this article we present the results of instrumental neutron activation analysis (NAA) studies performed on three types of samples, Astropower silicon-film multicrystalline sheet material, Baysix cast material, and EFG ribbon-grown mc-Si. Since EFG wafers have large (typically 10-15 mm or greater) grains, samples from good ($LD > 80 \mu\text{m}$) and bad ($LD < 20 \mu\text{m}$) grains were cleaved using carrier diffusion length maps obtained by SPV. Since Baysix and Astropower samples had too small grain size to cleave samples of “good” and “bad” grains, Baysix samples were cleaved from wafers from the bottom of the ingot (relatively low diffusion length, $LD=25$ to $50 \mu\text{m}$, according to LBIC mapping performed at Fraunhofer ISE) and from the middle of the ingot (relatively high diffusion length, $LD=40$ to $200 \mu\text{m}$), whereas Astropower samples were cut from two wafers, which were fully processed solar cells with stripped off front and back contacts. One of the two cells had better electrical properties than the other one, with the average carrier lifetime approximately 50% higher in the cell with better electrical properties.

Details of the procedures used in NAA analyses can be found in Ref. [2]. A typical weight of the samples was 1 to 2 grams. Each sample was counted at least twice, and the obtained results were cross-checked for consistency.

The NAA results are presented in the Tables 1-4 below. The main metal impurities found in the samples were Fe, Ni, Co, Cr, and Mo (Table 1). All these metals were present in surprisingly high concentrations, consistent with the recent report of Macdonald et al. [1]. Since blank high purity CZ sample processed and measured in the same batch with mc-Si samples did not reveal any metal contaminants, we are confident that the metals detected in mc-Si were present within the samples. The primary contaminants in all three materials were Fe, Ni, and Cr, which may indicate stainless steel contamination of mc-Si. Since the experiments were not optimized for detection of isotopes with short lifetime such as copper (12.7 hours), the data for copper are

upper limits. One should keep in mind when analyzing the data in Table 1 that metal content of mc-Si may vary in a certain range depending on purity of feedstock or position of the wafer in the growth run. We did not accumulate enough database to reflect this range in our analyses. Additionally, Astropower samples used in this study were cleaved from fully processed solar cells after removal of the top and bottom contact layers, whereas Baysix and EFG were as-grown wafers which did not get processed.

Table 1. Average metal concentration found by neutron activation analysis of three types of multicrystalline silicon material: Astropower (sheet technology), BaySix (cast), and EFG (ribbon growth).

Element	ASTROPOWER (cm ⁻³)	BaySix (cm ⁻³)	EFG (cm ⁻³)
Fe	1.50E+16	4.00E+14	6.00E+14
Ni	1.80E+15	<i>less than DL (3e14)</i>	<i>less than DL (1.1e14)</i>
Co	9.70E+13	2.10E+13	1.70E+12
Cu	<i>less than DL (7.8e12)</i>	<2.4e14	<1.3e14
Cr	1.80E+15	1.00E+13	1.70E+12
Hf	<i>less than DL (1.8e12)</i>	7.80E+12	<i>less than DL (6.8e11)</i>
Mo	4.60E+13	1.50E+13	6.40E+12
W	2.00E+13	<i>less than DL (2.2e11)</i>	<i>less than DL (8e10)</i>
Au	4.80E+11	6.50E+10	2.00E+10
As	4.70E+13	3.40E+12	<i>less than DL (9.3e10)</i>
Sb	2.40E+14	1.70E+12	1.20E+11
Ga	2.50E+13	<i>less than DL</i>	9.00E+12

Analysis of samples cleaved from the areas with high and low minority carrier diffusion length (Tables 2-4) revealed that the difference in metal concentration in “good” and “bad” areas is small. Only gold was consistently found in the “bad” areas in 1.5 to 5 times higher concentrations than in the “good” areas of all three materials. The rest of the metals detected by NAA showed either no trend at all, or, in some cases, metals were even found in slightly higher concentration in the “good” areas.

Thus, two conclusions can be made. First, it is extremely likely that transition metals substantially contribute to, if not determine, the minority carrier diffusion length degradation in solar cells. In fact, it is surprising that material with such a high metal content (over 4×10^{14} cm⁻³ of iron and over 10^{12} cm⁻³ of Cr and Mo) may perform so well when processed into solar cells. Indeed, only approximately 2×10^{13} cm⁻³ of FeB pairs, or 2×10^{12} cm⁻³ of interstitial iron is sufficient to reduce the diffusion length to 50 microns; 2×10^{15} cm⁻³ of FeB or 2×10^{14} cm⁻³ of Fe_i would reduce the diffusion length to 5 microns [3]. The other transition metals found in the samples, particularly Cr and Mo, have recombination activity comparable with that of iron [4, 5] and can also substantially contribute to minority carrier diffusion length degradation. The relatively low recombination activity of these metals (as compared to that of interstitial/substitutional metals) can be tentatively explained by assuming that the metals are present chiefly in the form of precipitates or agglomerates with other structural defects of the crystal lattice, and possibly are inhomogeneously distributed in the wafers. Although metal precipitates are known to be recombination active, it is possible that at least in some chemical/structural states the recombination activity of a precipitate per metal atom is much lower than the recombination activity of homogeneously distributed in the bulk interstitial/substitutional metal atoms.

Table 2. Metal concentration in the areas of EFG samples with the higher than average ("good") and lower than average ("bad") minority carrier diffusion lengths. Due to different irradiation and counting conditions, the detection limits of this measurement run were lower than of the runs presented in Tables 1, 3, 4. Therefore, iron and some other metals were below the detection limits.

Element	"Good" areas (cm^{-3})	"Bad" areas (cm^{-3})
Cr	2.97E+12	5.94E+11
Mo	7.09E+13	6.00E+13
Sb	8.20E+10	9.00E+10
Au	5.00E+11	3.00E+12

Table 3. Metal concentration in BaySix wafers with relatively high (middle of the ingot) and relatively low (bottom of the ingot) minority carrier diffusion length

.Element	Sample A (middle of the ingot, better cell performance) (cm^{-3})	Sample B (bottom of the ingot, lower cell performance) (cm^{-3})
Ag	3e12	<i>less than DL (5e11)</i>
Cr	1.9e13	<i>less than DL (3e12)</i>
Fe	4.7e14	<i>less than DL (4.5e14)</i>
Ni	<i>less than DL (3e14)</i>	<i>less than DL (2.3e14)</i>
Co	8e12	2.80E+13
As	3.80E+12	2.90E+12
Sb	3.70E+11	3.20E+12
W	<i>less than DL (1e11)</i>	<i>less than DL (3.6e11)</i>
Au	1.50E+10	1.20E+11
Zr	3.3e14	3.5e14
Hf	1.40E+13	<i>less than DL (1.1e12)</i>
Cu	<1.6e14	<3.2e14
Se	2e13	4e12
Mo	1.50E+13	<i>less than DL (5.4e13)</i>

Table 4. Metal concentration in Astropower wafers with relatively high ("wafer A") and relatively low ("wafer B") minority carrier diffusion length areas.

Element	Wafer A (better cell performance) (cm^{-3})	Wafer B (lower cell performance) (cm^{-3})
Cr	3e+15	5e13
Fe	1.6e+16	8.7e15
Ni	2.8e+15	<i>less than DL (5e15)</i>
Co	1.3e+14	6.1e+13
Cu	<i>less than DL (5e12)</i>	<i>less than DL (1e13)</i>
Ga	2e+12	<i>less than DL(3e12)</i>
As	9e+13	3.5e+12
Zr	<i>less than DL (1.5e15)</i>	<i>less than DL (4e15)</i>
Hf	<i>less than DL (1.1e12)</i>	<i>less than DL (3e12)</i>
Mo	6e13	3e13
Sb	2e+13	5e+14
W	2e+13	2e+13
Au	3.5e+11	4e+11

The observation that there was no significant difference in metal concentration observed in “good” and “bad” areas of solar cells suggests that the recombination properties of metals may vary in a wide range depending on their chemical or structural state. A small variation in the chemical/structural state of metals which leads to a change in their recombination properties may account for the difference between “good” and “bad” grains in solar cells. Therefore, one does not necessarily have to remove the metals from the cells; it is sufficient to convert them to a less recombination efficient state to minimize their impact on the cell performance.

Our NAA results which indicate high metal contamination levels of mc-Si bear important consequences for the understanding of the limitations and problems with gettering of transition metals in solar cells. It is known that standard gettering techniques are not very efficient in removing metals from solar cells. There are two possible explanations for this. The first one is that at least some of the metals form gettering-resistant clusters, which cannot be dissolved at the gettering temperatures due to high binding energy of the metals in these compounds. The possibility of this mechanism was suggested by McHugo et al. [6], who detected clusters with the chemical state of iron similar to iron oxide or iron silicate in processed solar cell, and observed copper clusters which might have a higher stability than expected for copper silicide [7, 8].

The second possible mechanism of low efficiency of gettering in solar cells is kinetically limited precipitate dissolution. This mechanism was suggested by Plekhanov et al. [9]. They argued that gettering at temperatures at which equilibrium metal solubility is much lower than the total metal concentration in the sample would lead to extremely long (on the order of 10 hours) gettering times necessary to achieve an improvement in minority carrier diffusion length because only a very small fraction of metals can be dissolved at a given time even if there is no additional barrier for dissolution of metal precipitates.

This work was funded by NREL subcontract AAT-2-31605-03 and the AG-Solar project of the government of Northrhein-Westfalia (NRW), funded through the Fraunhofer Institute for Solar Energy Systems (ISE) (Germany). The operations of the Advanced Light Source at Lawrence Berkeley National Laboratory are supported by the Director, Office of Science, Office of Basic Energy Sciences, Materials Sciences Division, of the U.S. Department of Energy under Contract No. DE-AC03-76SF00098.

References

1. D. Macdonald, A. Cuevas, A. Kinomura, and Y. Nakano, in *29th Photovoltaic Specialists Conference*, p. 285, IEEE, New Orleans, LA (2002).
2. A. R. Smith, R. J. McDonald, H. Manini, D. L. Hurley, E. B. Norman, M. C. Vella, and R. W. Odom, *J. Electrochem. Soc.* **143**, 339 (1996).
3. A. A. Istratov, H. Hieslmair, and E. R. Weber, *Appl. Phys. A* **70**, 489 (2000).
4. J. R. Davis, A. Rohatgi, R. H. Hopkins, P. D. Blais, P. Rai-Choudhury, J. R. McCormic, and H. C. Mollenkopf, *IEEE Trans. Electron. Dev.* **ED-27**, 677 (1980).
5. R. H. Hopkins and A. Rohatgi, *J. Cryst. Growth* **75**, 67 (1985).
6. S. A. McHugo, A. C. Thompson, G. Lamble, C. Flink, and E. R. Weber, *Physica B* **273-274**, 371 (1999).
7. S. A. McHugo and C. Flink, *Appl. Phys. Lett.* **77**, 3598 (2000).
8. S. A. McHugo, A. Mohammed, A. C. Thompson, B. Lai, and Z. Cai, *J. Appl. Phys.* **91**, 6396 (2002).
9. P. S. Plekhanov, R. Gafiteanu, U. M. Gosele, and T. Y. Tan, *J. Appl. Phys.* **86**, 2453 (1999).

CHARACTERIZATION OF SILVER/GLASS/SILICON FRONT CONTACT INTERFACE IN A SILICON SOLAR CELL

Srinivasan Sridharan^{1*}, Chandra Khadilkar¹, Tung Pham², and Aziz Shaikh²

1. Ferro Corporation, Technical Center,
7500 East Pleasant Valley Road, Independence, OH 44131, U.S.A.

2. Ferro Corporation, Electronic Materials System,
1395 Aspen Way, Vista, CA 92083, U.S.A.

*corresponding author email: sridharan@ferro.com

ABSTRACT

The front contact/silicon interface plays a key role in determining the series resistance (R_s) and the shunt resistance (R_{sh}), the two most important parameters that affect the performance of a silicon (Si) solar cell. Therefore understanding the structure of this interface might help to optimize front contact inks to minimize R_s and maximize R_{sh} . This paper details the microstructural characterization of a silver (Ag) front contact/Si interface using back scattered Scanning Electron Microscopy (SEM) imaging of a polished cross section of the interface, Auger Electron Spectroscopy (AES) line scanning across the interface, and depth profiling for impurity diffusion into Si using Secondary Ion Mass Spectrometry (SIMS) technique. The results showed that the glass in the silver front contact ink plays a dominant role in controlling R_s through its thickness in between Ag and Si, and R_{sh} through its resistance to impurity diffusion into Si from Ag front contact.

INTRODUCTION

Typical front contact ink contains Ag metal powders and flakes, glass powder and other inorganic additives suspended in an organic medium of resin and solvent. Typical polycrystalline solar cell contains SiN_x or TiO_2 anti reflective coating. Therefore, the front contact ink/silicon interface can be denoted as Ag/ SiN_x or TiO_2/Si interface. Since the electrons have to make the transition from semi conductive Si to metallic Ag through the interface, the microstructural features in between Ag and Si might determine the resistance these electrons experience in making the jump from Si to Ag. Similarly most of the impurities that diffuse to the p/n junction lower R_{sh} by shunting across the junction. Again the microstructural features in between Ag and Si might determine the rate of migration of these detrimental impurities into Si. Therefore, microstructural characterization of Ag/ SiN_x or TiO_2/Si interface is a key in designing a front contact that gives low R_s and high R_{sh} . This paper details the microstructural characterization of an Ag/ SiN_x/Si interface.

EXPERIMENTAL

Si solar cells with differing R_s and R_{sh} were obtained as follows. Front contact Ag inks each having a different glass powder, while keeping Ag metal, dopants and organic vehicle the same were prepared. Commercially available Ag-Al or Al pastes were used for back contacts. The front and back contact pastes were screen printed on SiN_x coated polycrystalline 12.5 cm x 12.5 cm Si solar cells and fired in air in a 3-zone IR heating belt furnace to form contacts. The most optimum furnace zone settings for the zone lengths of 7", 16" and 7" were 780°C, 810°C and 930°C at a belt speed of 120"/minute.

The electrical performance (η , FF, R_s , R_{sh}) of the solar cell was measured with a solar tester (Oriel Instruments Model: 91193-1000) under AM1.5 sun conditions. The structure of the Ag/Si interface was characterized by back scattered SEM imaging of the polished cross section of the interface samples mounted at about 30° angle. The angled cross section helped to bring out thin features in between Ag and Si which otherwise would not be visible in a normal cross section. The polished sections were ultrasonically cleaned in methanol and dried. To aid in conductivity, about 3 nm of platinum/palladium was sputter coated onto the surfaces. SEM imaging was done on an Amray 3300FE field-emission scanning electron microscope using an accelerating voltage of 15 KV. The images were made using the secondary electron detector. Microbeam analyses were made on an Oxford ISIS 300 energy-dispersive spectrometer attached to SEM.

At selected locations, where Ag and Si appeared to be in contact even under 30° angled cross section, Auger Electron Spectroscopy (AES) line scans across Ag/Si interface were done using Physical Electronics 680 Scanning Auger Nanoprobe (Electron beam conditions: 10 keV, 25nA, 30° from sample normal; Ion Beam conditions: 3 keV, Ar^+ , 2.0 μA , 2mm x 2mm raster; Sputter rate: 200Å/minute for SiO_2 standard) to detect the presence of oxide (or glass) layer in between Ag and Si and to measure its thickness.

Impurity diffusion into Si was characterized by depth profiling using dynamic Secondary Ion Mass Spectrometry (SIMS) technique using a PHI Quadrupole SIMS instrument with primary ion species, Cs^+ for the elements P, B, As, C, and O, and O_2^+ for the rest of the elements analyzed. Angle of incidence for the primary ion beam is 60°. The secondary ions' polarities corresponding to the primary ions O_2^+ and Cs^+ were respectively +ve and -ve. The instrument conditions for these analyses were optimized for maximum sensitivity. No charge neutralization or surface conductive coatings were employed. The resulting ion yields were converted to atoms/cc concentration by comparing the observed ion yield rates to the ion yield rates of calibrated standards.

RESULTS AND DISCUSSION

Fig. 1 shows the high magnification view of the front contact (Ag)/silicon interface for two different inks that gave high (Fig. 1a) and low (Fig. 1b) R_s . In both cases a glass layer exists in between Ag and Si, and it appears that the front contact/silicon interface is actually Ag/glass/Si interface. Since the glassy phase is very resistive the observed difference in R_s

between figs. 1a & 1b could be qualitatively explained in terms of thick glass layer offering more resistance to electron transfer from Si to Ag compared to that by thin glass layer. The

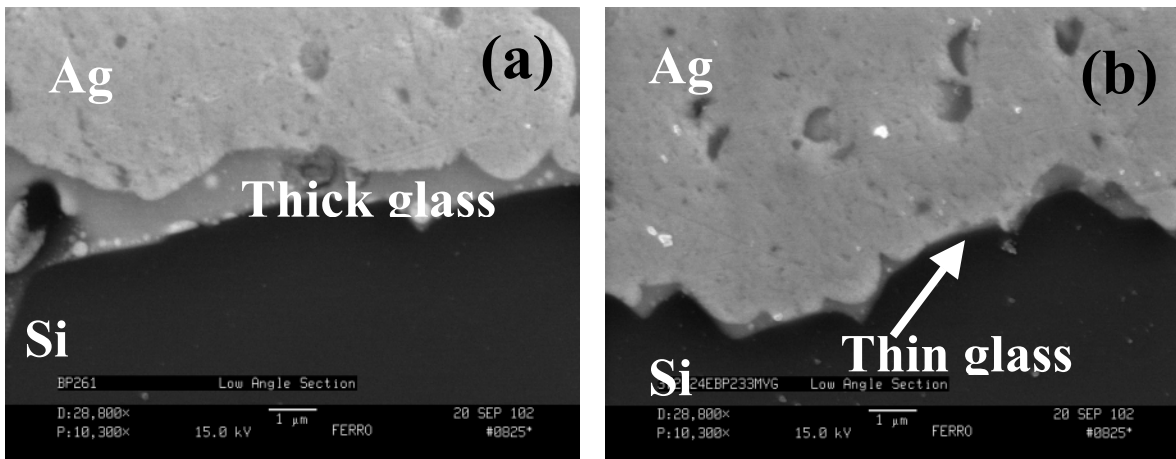


Fig. 1: SEM cross sections (angled) of two inks that gave (a) high R_s ($21.65 \text{ m}\Omega$) – thick glass interlayer and (b) low R_s ($8.5 \text{ m}\Omega$) – thin glass interlayer

spherical features observed at the glass/Si interface as well as in the glass layer itself in Fig. 1a, are mostly lead as well as silver metal particles. In the samples investigated thus far, it was observed that the presence or absence of these spherical particles, especially reduced lead, did not significantly affect R_s . It seems that the average thickness of the glass layer in between Ag and Si plays a key role in determining R_s ; thicker the glass layer more the series resistance is.

As shown in Fig. 2 in some of the samples with low R_s the glass seems to wet and spread but not corrode Si. This is evidenced by excellent retention of the surface texture of poly crystalline Si while forming the Ag/glass/Si interface in Fig. 2.

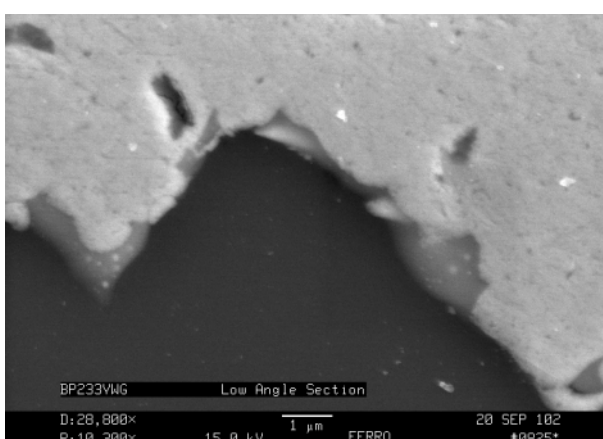


Fig. 2: SEM cross section of Ag/glass/Si interface where surface texture of Si is retained during front contact formation

Fig. 3 shows the results of a typical AES line scan obtained across Ag/Si interface which clearly shows the presence of oxygen rich thin layer in between Ag and Si, which is most likely due to the presence of glassy layer in between Ag and Si.

Fig. 4 is a SIMS depth profile comparing the diffusion of Ag and other impurities in solar cells with low (Fig. 4a) and high (Fig. 4b) R_{sh} . This clearly shows that the interfacial glass can act to slow down the diffusion of impurities to the junction.

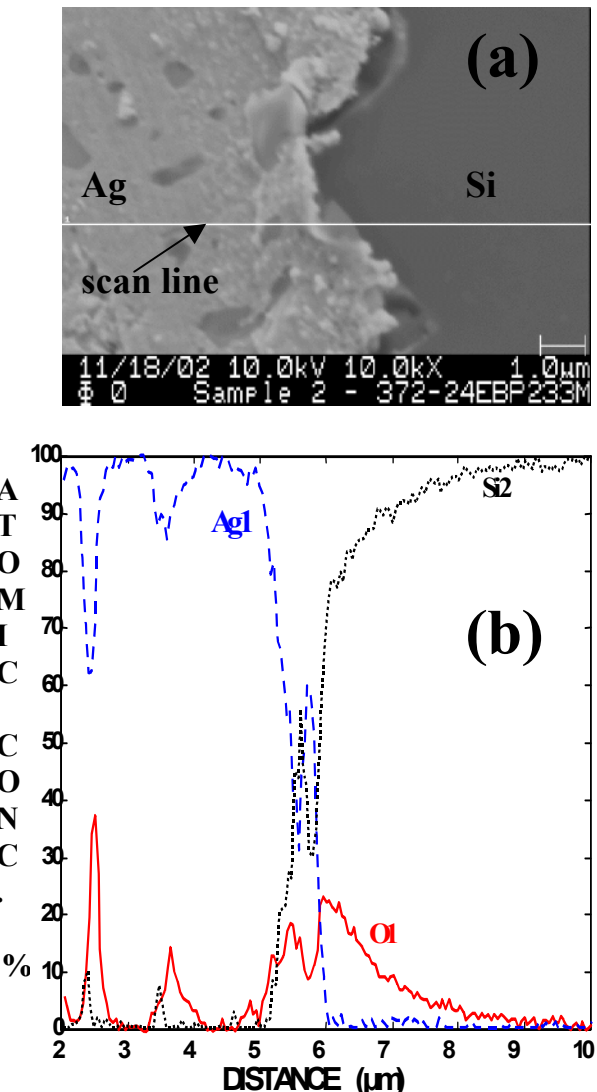


Fig. 3: (a) AES line scan across Ag/Si interface from left to right; (b) observed ionic species as a function of scan distance.

CONCLUSIONS

Microstructural characterization of the interface shows that the front contact interface is most likely Ag/glass/Si interface. Glass in the front contact ink plays a critical role in the formation of front contact/silicon interface and in determining its properties. Interfacial glass thickness controls the resistance to the flow of electrons from silicon to silver, and certain glasses in the silver paste slow down detrimental impurities diffusion into the junction.

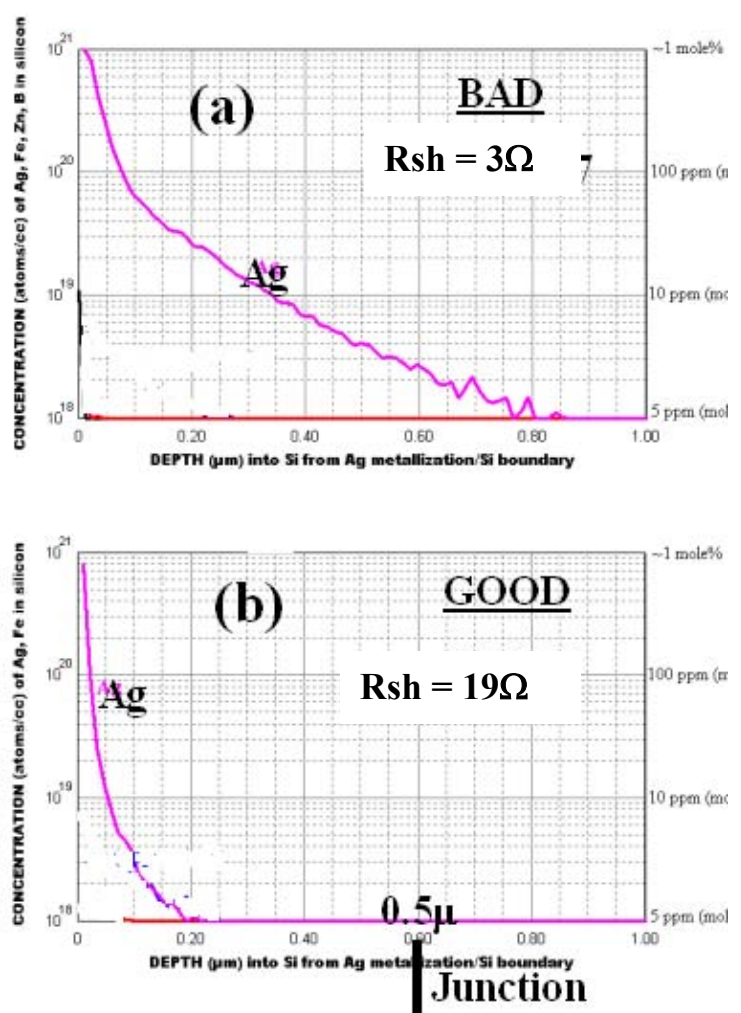


Fig 4: Concentration (atoms/cc) of Ag and other elements from the front contact as a function of depth (μm) into silicon from the front contact/silicon interface for two inks that gave (a) lower R_{sh} – BAD and (b) higher R_{sh} – GOOD, obtained by SIMS depth profiling technique

METALLIC PRECIPITATE CONTRIBUTION TO GENERATION AND RECOMBINATION CURRENTS IN ELECTRONIC DEVICES DUE TO THE SCHOTTKY EFFECT

T.Y. Tan and M. D. Negoita

Department of Mechanical Engineering and Materials Science
Duke University
Durham, NC 27708-0300

Abstract

The contribution of metallic precipitates to recombination and to generation currents in electronic devices fabricated using Si has been modeled for two types of structures: that of p-n junctions and that of MOS capacitors, with the precipitate located in the charge depletion region of the appropriate structure. The physical mechanism responsible for the electrical activity of the metallic precipitate is attributed to the Schottky junction property between the precipitate and the Si matrix material. Based on the physical model, numerical simulation results showed that the precipitate electrical behavior resembles that of *giant* Shockley-Read-Hall (SRH) recombination/generation centers. In the last part, the electrical activity of complex precipitate systems is accounted for using a generalization of the proposed model and experimental leakage currents in Co contaminated shallow junctions are fitted by simulations.

I. Metallic precipitate contribution to generation and recombination currents in p-n junction devices

Modeling of the electrical activity of metal silicide precipitates in a p-n junction device has been carried out by considering the role of a spherical precipitate located in the depletion region of a cylindrical 3D thin-layer p-n junction device, with the p-n junction under either a forward or a reverse bias voltage. After formulation, solutions to the problem are obtained with the p-n junction device operating under steady state conditions.

The problem has been solved by choosing a section containing the cylindrical axis and passing through the center of the precipitate. On this section or slice, the problem is reduced to that of a 2D case, since the field distribution, current flow, etc. are identical to that of a section obtained from a cylindrical precipitate extending indefinitely in the direction perpendicular to the section. The overall currents flowing through the device are simply calculated by integrating the section currents over the total precipitate area generated by rotating the slice around the axis of symmetry.

The steady-state two-dimensional model of the p-n junction has been used to accommodate the precipitate section geometry, and the Schottky effect model¹ has been used for the precipitate electrical activity. The two-dimensional structure under consideration is shown in Fig. 1 where the small circle represents the precipitate section. The complete solution to the problem has been presented in detail elsewhere.² Figure 2 show respectively the recombination current in a forward biased p-n junction (a) and in a reversed biased p-n junction (b), for two different precipitate concentrations.

The electric activity of metallic precipitates located in the depletion region of a p-n junction is dependent upon the device operation conditions. The precipitate dynamically

changes from a generation center when the p-n junction is reverse biased to a recombination center when the junction is forward biased. Also, calculations show that the current through the junction is proportional to the precipitate concentration. In conclusion a metallic precipitate acts as a giant SRH generation/recombination center. For the forward bias p-n junction (Fig. 2(a)) there are models explaining the $n = 2$ current regions using interface states or distributed generation-recombination centers in the space-charge region, which involve concepts arrived at on an empirical basis. In contrast, the metallic precipitate generation/recombination and the related $n = 2$ currents derived in our work is attributed to Schottky effect via thermionic emission at the metal-semiconductor interface, which is a fundamental physical phenomenon.

II. Metallic Precipitate Contribution to Carrier Generation in MOS Capacitors

The electrical activity of metallic precipitates within the variable depletion region of the MOS capacitor has been modeled by considering a spherical precipitate placed inside the depletion region of a cylindrical 3-dimensional MOS capacitor built on a p-type Si substrate. The problem has been solved for a longitudinal section passing through the center of the precipitate as in the case of the p-n junction. The two-dimensional structure used in simulation is shown in Fig. 3 where the small circle represents the precipitate.

The time-dependent two-dimensional semiconductor transport equations have been used as the governing equations to accommodate the precipitate section geometry, and the Schottky effect model¹ has been used to account for the precipitate electrical activity. The time-dependent solution and different steady-state solutions to the problem have been presented in detail elsewhere.³ In Fig. 4 the steady-states correspond respectively to flatband condition or the initial state in the time-dependent problem and strong inversion or final state in the time-dependent problem are presented for different positions of the precipitate inside the MOS capacitor depletion region. In Fig. 4 (a), the flatband state, the majority and minority carrier concentrations of the capacitor without the precipitate are equal to their values in the bulk region. There is no depletion region formed for the classic device. On the other hand, when a metallic precipitate is present, the majority carrier is depleted even with no applied gate voltage. Figure 4(b) shows the complicated dependence of the MOS capacitor states on the precipitate location under inversion conditions. In general, the presence of metallic precipitates in MOS capacitors shifts the threshold voltage (downward or upward) depending on the position of the precipitates in the device.

The precipitate serves as a highly effective carrier generation center when the capacitor is switched from the accumulation mode to the deep depletion mode. Also, the presence of precipitates inside the device depletion region shifts the threshold voltage.

III. Comparison to experimental data

A set of data on junction leakage currents generated by CoSi₂ formation has become available.⁴ An attempt is now being made to fit these data by our model. Following the experimental conditions, a simulation model consisting of a shallow p-n junction and a CoSi₂ precipitate system formed by 10 dispersed CoSi₂ precipitates (1 nm in radius and evenly distributed with $d = 8$ nm) have been used. From the experimental Co SIMS profiles, an average CoSi₂ precipitate density of $1.88 \times 10^{15} \text{ cm}^{-3}$ was estimated to be present on the n-side of p-n junction (the part of the device were precipitate system forms

when the Co diffuse in). Then, by adjusting the device volume (via device radius) the precipitate concentration in the model was set to the average experimental value, corresponding to a device radius of 13 nm. The leakage current density due to CoSi_2 precipitate formation obtained from simulation from experiments are presented in Fig. 5.

References

- [1] P.S. Plekhanov and T.Y. Tan, Schottky effect model of electrical activity of metallic precipitates in silicon, *Appl. Phys. Lett.*, vol. **76**, pp. 3777-3779, 2000.
- [2] M. D. Negoita, T. Y. Tan, Metallic Precipitate Contribution to Generation and Recombination Currents in p-n Junction Devices due the Schottky Effect (submitted to *J. Appl. Phys.*).
- [3] M. D. Negoita, T. Y. Tan, Metallic Precipitate Contribution to Carrier Generation in MOS capacitors due the Schottky Effect (submitted to *J. Appl. Phys.*).
- [4] M. Tsuchiaki, C. Hongo, A. Takashima, K. Ohuchi, *Jpn. J. Appl. Phys.*, **41**, 2437 (2002).

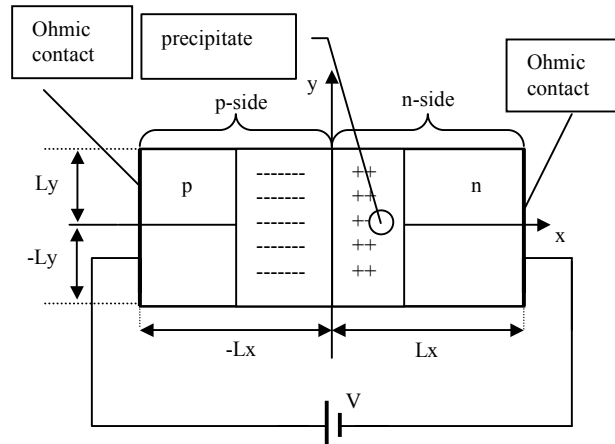


Figure 1. Schematic diagram of the p-n junction used in simulation.

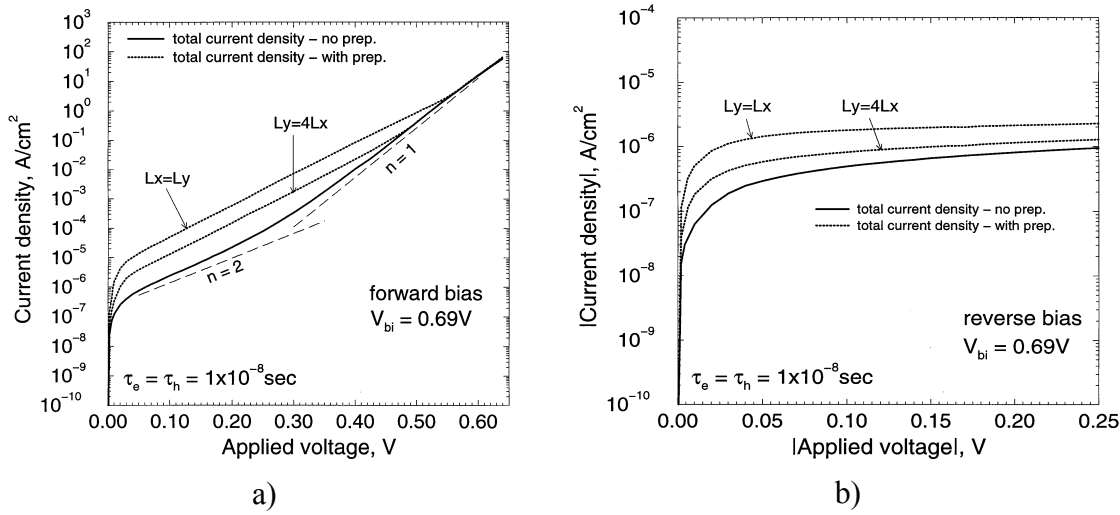


Figure 2. Current density in the biased p-n junction. a) forward biased; b) reverse biased.

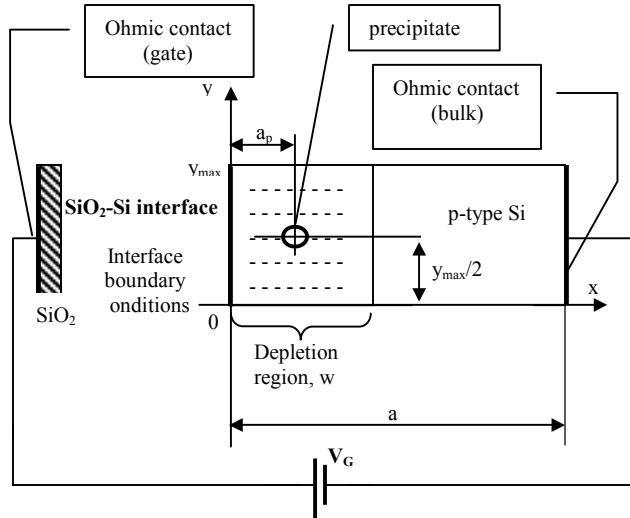


Figure 3. The schematic diagram of a longitudinal section through the center of the precipitate located at the rotation axis of the model cylindrical MOS capacitor.

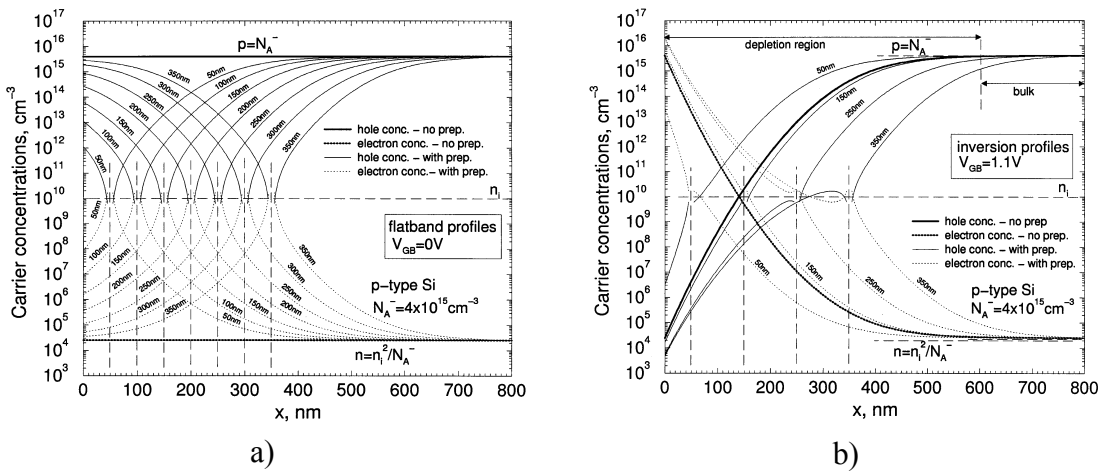


Figure 4 Carrier profiles along a line parallel to the depletion region electric field lines and passing through the center of the precipitate for different positions of the precipitate inside the space-charge region of a biased MOS capacitor. a) under flatband conditions; b) under strong inversion conditions.

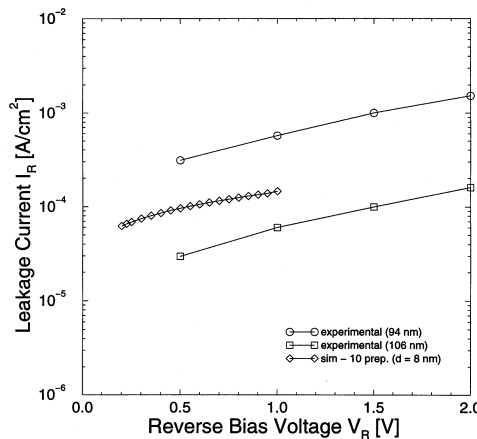


Figure 5. Comparison of the calculated leakage current due to the precipitate system formed by evenly distributed spherical CoSi_2 precipitates with a radius of 1 nm with the available experimental data.

Empirical Modeling of Ingot and Post Oxidation Level QSS Lifetime Measures in a Production Environment

John L. Coleman

E-mail: cole5820@blue.unco.edu

University of Northern Colorado, Greeley CO

Jeff Nickerson

E-mail: jeff.nickerson@shell.com

Shell Solar Incorporated, Camarillo CA

Ronald A. Sinton

E-mail: ron@sintonconsulting.com

Sinton Consulting, Boulder CO

Abstract: The advent of lifetime measurement systems suitable for high volume production environments has facilitated the development of empirical models of lifetime measures into ultimate cell performance. The construction of simple predictive lifetime models as a precursor to effective lifetime based process control on single crystal silicon manufacturing processes is discussed. Emphasis is given to appropriate measures of model adequacy, measurement system precision and agreement with theoretical models, essential elements to valid and reliable prediction. The evaluation of precision, adequacy and validity serves as a necessary prerequisite to predictions of final cell electrical performance based on post oxidation lifetime, as-grown lifetime and resistivity measures. Empirical models of sufficient precision, simplicity and theoretical validity to be useful in production environment decisions are presented.

Key Concepts: Lifetime, Measurement Systems Analysis, Prediction Intervals

Photovoltaic Process Control: The Prospect of Reduced Cost

The quasi-steady state photoconductance technique provides a fast contactless measurement of the minority-carrier lifetime in silicon wafers. Previously, this technique had been applied to an industrial process to show that measurements on wafers near the end of the process are very predictive of the final solar cell efficiency¹. These measurements are taken after phosphorus diffusion, the highest temperature step.

Recently, this same measurement technique has been adapted for use on as-grown blocks and ingots. This study evaluates the significance of the measurements on as-grown ingots, as well as the significance of measurements on phosphorus-diffused and oxidized wafers. A model is then developed to indicate the relationship between measurements on the as-grown material and the diffused/oxidized wafers. Further extensions indicate the predictive value of these measurements to the final solar cell efficiency. If measurements on as-grown material were shown to be predictive, then this could provide an excellent process control monitor for the material growth.

In addition, since major costs are incurred in wafering and cell fabrication, if poor material were identified directly after growth, then significant cost savings could be realized due to the improved yields that would result if only good material were fabricated into solar cells.

The study is comprised of approximately 400 measurements on multiple ingots across a range of lifetime and resistivity values. Wafers are followed through the process and corresponding lifetime measurements are made post-oxidation. Appropriate experimental error control strategies were employed to ensure validity. The analysis will now proceed via an examination of measurement system precision.

Lifetime Measurement Precision

Insight into the ability of the lifetime measurement system to correctly sort product based on uncorrected lifetime measurements is vital to drawing valid conclusions from the data. In this case, one measure of valuable insight into the precision of the measurement system may be gained via the following relation².

$$\hat{\sigma}^2_{Total} = \hat{\sigma}^2_{sample} + \hat{\sigma}^2_{measurement-system}$$

Total variance observed in the sample may be decomposed into sample-to-sample variation and within sample variation, the latter being the product of approximately four repeat measurements per sample. This repeatability variation, considered to be measurement error, will now be parsed out and compared to the sample-to-sample variability by the analysis of variance method of component estimation³. N=444 lifetime measurements were made on as-grown ingots for purposes of this analysis. Using Minitab v13 statistical software, the following analysis of variance table is obtained.

Source	DF	SS	MS	F	P
Sample	106	157449.2	1485.4	1551.82	0.00
Error	337	322.6	1.0		
Total	443	157771.7			

Table 1- MSA ANOVA

Selecting the MS_{sample} and MS_{error} from the ANOVA table and estimating the variance component for the sample variation via the following formula:

$$\hat{\sigma}^2_{sample} = (MS_{sample} - MS_{error}) / n$$

Where n = the approximate number of repeat measurements per sample and MS_{error} is considered an estimate of the measurement system variability. The actual calculation of the variance component follows.

$$(1485.4 - 1) / 4.175 = 357.9$$

Considering the additive nature of variance components the following relative comparison of measurement system precision can be made

$$\begin{aligned} \hat{\sigma}^2_{sample} / \hat{\sigma}^2_{total} * 100 \\ = 357.9 / 358.9 * 100 \\ = 99.7\% \end{aligned}$$

$$\begin{aligned} \hat{\sigma}^2_{measurement-system} / \hat{\sigma}^2_{total} * 100 \\ = 1.0 / 358.9 * 100 \\ = .3\% \end{aligned}$$

Thus, only .3 % of the total variation observed in the sample data of as-grown ingot lifetime, can reasonably be considered measurement system variation, 99.7% of the variability found in these data was due to differences in the samples. The suggestion based on these data is that the measurement system is more than precise enough to discriminate different samples of production ingot based on the lifetime measurements. Additional measurement systems assessments following similar methodology will now buttress this conclusion.

Ingots were followed through the processing sequence to post-oxidation and wafers selected from locations on the ingot in close proximity to the original measurements. The result was a new set of Post-Oxidation Lifetime (POLT) measurements. Following similar techniques for estimation of the variance components yielded the following estimates.

97.4% sample to sample variation
2.6% measurement system variation

Once again, this relative comparison suggests that the lifetime measurement system offers precise measurements for the wafer level POLT.

Examining the precision of the system in different regimes of lifetime offers a final illustration of the measurements systems suitability for production use.

“Low” lifetime ingot precision (.3-7 μ s)
99.9% sample to sample variation
.1% measurement system variation

“High” lifetime ingot precision (42-120 μ s)
98.9% sample to sample variation
1.1% measurement system variation

In both cases, the measurement system variability is small relative to total variability, thus the sample-to-sample variability dominates. This result offers further evidence that the measurement system is precise in the range of variability encountered in solar cell production.

In summary, while additional aspects of the measurement system precision, bias and stability are not evaluated and/or replicated here, the evidence offered supports the conclusion that the lifetime measurement system is a useful tool in discriminating the distribution of lifetime measurements encountered in solar cell production. In light of this result, predictive analyses utilizing data from this system will now be presented.

Prediction Equation of As-Grown Lifetime and Resistivity into POLT

Empirical modeling is now presented utilizing data derived from the lifetime measurement device. Surface effects are not corrected for, thus the measurements are the product of a combination of surface and bulk recombination. This lifetime measure is shown in practice to be a good predictor of the ultimate electrical performance of the cell.

The original as grown lifetime distribution appears in figure 1. The bulk of the data is around 2-25 μs with values extending up to about 75 μs .

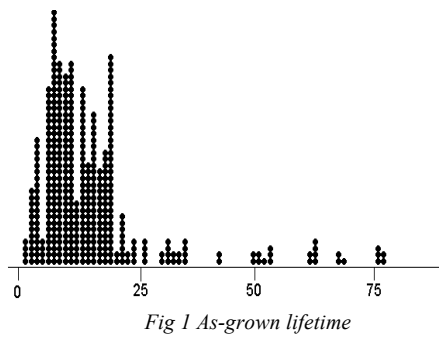


Fig 1 As-grown lifetime

Figure 2, the post oxidation lifetime distribution is somewhat more condensed with most values from 10-25 μs .

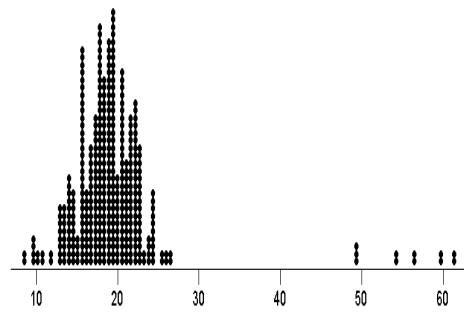


Fig. 2 post-oxidation lifetime

Only a few wafers remain grouped around 50-60 μs and estimation to follow offers cautionary advice about predictions in that regime.

Utilizing standard least squares regression techniques via Minitab v13 statistical software, an empirical model can be developed which approximates the relationship between the dependent variable, post-oxidation lifetime (POLT), and the independent variables, as-grown lifetime (AGLT) and resistivity (Res). The regression analysis follows.

The regression equation is:

$$\text{POLT} = 5.52 + 0.162 \text{ AGLT} + 10.1 \text{ Res}$$

Predictor	Coeff	SE Coef	T	P	VIF
Constant	5.5184	0.3110	17.74	0.000	
AGLT	0.16198	0.01963	8.25	0.000	3.1
Res	10.0521	0.4002	25.12	0.000	3.1

S = 2.286 R-Sq = 89.2% R-Sq(adj) = 89.1%

Analysis of Variance

Source	DF	Seq SS	Adj SS	Adj MS	F	P
AGLT	1	13453.0	356.0	356.0	68.12	0.000
Res	1	3297.1	3297.1	3297.1	630.86	0.000
Error	390	2038.2	2038.2	5.2		
Total	392	18788.3				

N=393 Table 2 - Regression and ANOVA model

The high R-square and R-square adjusted bolstered by the ANOVA with significant F-test demonstrate the model developed does fit the sample data well. Individual coefficient tests are offered by means of the T-statistics and corresponding P-values. The variance inflation factor (VIF) suggests small variance in the coefficient estimates and minimal collinearity concerns⁴. The established resistivity relationship is complemented in this model by the significant AGLT term. The two predictors combine to yield the equation of a plane.

For accuracy sake, one must consider that the possible values of resistivity and AGLT are subject to certain physical constraints.

Utilizing reasonable constraints on selection of potential resistivity values will ensure useful predicted values of POLT for a given AGLT as computed from the equation of best fit. A 3-D model of the prediction equation is presented in figure 3.

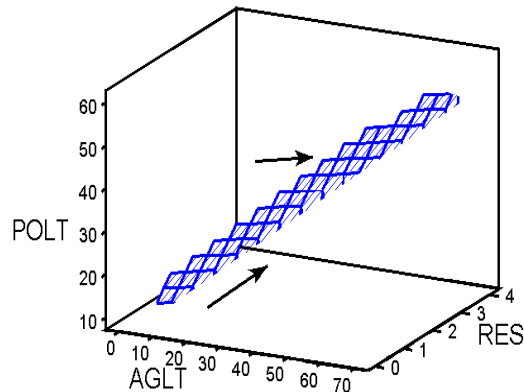


Fig. 3 3-D plot of model with constraints

The relationship between the empirical model derived from production level observations and a model provided by physics is now discussed.

Complementary Methods: Theoretically Based vs. Purely Empirical

The use of empirical modeling methods in process engineering contexts has gained widespread acceptance in many industries. The benefits of easily constructed approximations from which timely and precise manufacturing decisions can be made have been well established. The models are often easily complemented with a variety of prediction and confidence intervals, aiding the use of these models in decision making processes.

However, all too often, the benefits of empirical modeling methods are limited by the lack of a theoretical basis for such models⁵. Further, empirical modeling has been incorrectly couched in some quarters as an alternative to theoretically based models. The following discussion will juxtapose the equation developed previous and a theoretically based model in an effort to illustrate the complementary and sequential roles of theoretical and empirical models.

Consider the following model provided by physics.

$$\frac{1}{\tau_{POLT}} = \frac{K}{\tau_{Bulk}} + \frac{2 * Jo * Na}{q * n_i^2 * W}$$

After fitting K and Jo based on the data, the newly developed physics based model is compared to the equation of a plane produced via least squares regression, in figure 4.

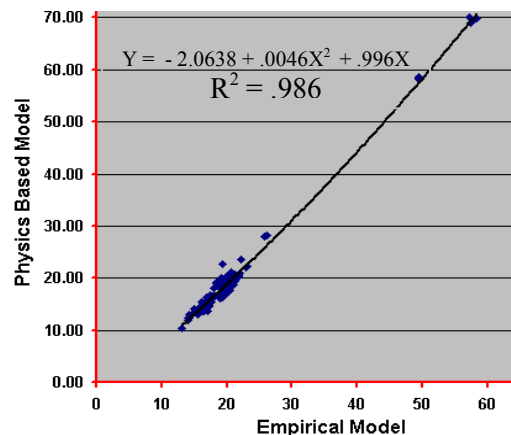


Fig 4 Regression plot of model agreement

Within the region of interest to the manufacturing operation, the relationship between AGLT, POLT and resistivity modeled previously, shows good agreement with the theoretically based models predictions in the $10-30 \mu s$ range, where most of the production cells reside.

Thus, an understandable and easily produced approximation, without benefit of measurement corrections or detailed theoretical basis, appears to be sufficiently precise as to allow useful predictions of product lifetime characteristics in the process space being encountered in production. Empirical models of this form may allow for timely estimation of local phenomenon over short time frames with significant precision, as well as facilitating additional insightful analyses. The purely empirical model will now be used in the development of prediction and confidence intervals of cell performance.

Predicted Values for New Observations

Utilizing the prediction equation with various combinations of AGLT and resistivity, produces estimates of the mean response for each combination (Predicted), and the standard error of this prediction (SE). 95% confidence and prediction intervals for the mean prediction and individual values respectively are also presented. The 95% prediction interval represents the best estimate, based on these data, of the distribution of POLT based on the input AGLT and Resistivity. The output follows.

AGLT/Res	Predict	SE	95.0% CI	95.0% PI
10/1	17.2	0.124	(16.9, 17.4)	(12.7, 21.7)
20/1.5	23.8	0.138	(23.6, 24.1)	(19.3, 28.3)
30/2	30.5	0.225	(30.0, 30.9)	(26.0, 35.0)
40/2.5	37.1	0.332	(36.5, 37.8)	(32.6, 41.7)
50/3	43.8	0.445	(42.9, 44.7)	(39.2, 48.4) X
60/3.5	50.4	0.560	(49.3, 51.5)	(45.8, 55.1) XX

Table 3 95% Confidence and Prediction Intervals

X –denotes a value that is away from the bulk of the data
XX- denotes a value that is extremely far from the bulk of the data

NOTE: The estimates and intervals presented for these values should be viewed with caution.

In summary, with the accuracy depending on the range of lifetime being estimated, the post oxidation lifetime can be predicted with some certainty. Note that following the production sequence, the measured lifetime can be expected to decrease from the as-grown measurement for values above about $30 \mu\text{s}$ and Res >2 . Further insurance as to the reliability of predictions will now be gained via residual analysis.

Empirical Model Diagnostics

Assessing the adequacy of the model is the necessary final step to ensure accuracy of the predictions. Via the following relation that examination will now be accomplished:

$$y_i - \hat{y} = e_i$$

Where e_i is the difference between the actual data point and the predicted value.

The residuals are then standardized for ease of interpretation. The residuals vs. fitted values (predicted) plot to follow is of concern, as it reveals the lack of POLT values between 30 and 60 μs .

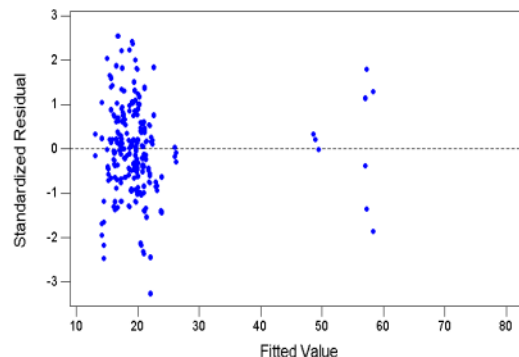


Fig. 5 Standardized residuals vs. fitted values

Care should be exercised with interpolation within this range. And extrapolation beyond this range is of course not advised.

The residuals vs. order plot (not shown) indicates a well balanced random pattern of standardized residuals, with only modest concern warranted about a few residuals >2 . Modest departures from normality are revealed in the probability plot of the residuals (not shown) but the departure is very much in-line with those encountered commonly in industrial experimentation and is not considered a serious departure.

An additional model of POLT into cell performance constructed with similar concern for measurement precision, model integrity and validity is now presented.

Empirical Model of Post Oxidation Lifetime into Electrical Performance

Following similar methodology, the model shown in figure 6 offers a mapping of post-oxidation lifetime (uncorrected for surface effects) into electrical performance (Isc). A reciprocal transformation is used on the predictor POLT and the response, Isc.

Confidence and prediction intervals are superimposed. Suitable R-squares and S values along with acceptable diagnostic plots (not shown) suggest the model fit is adequate.

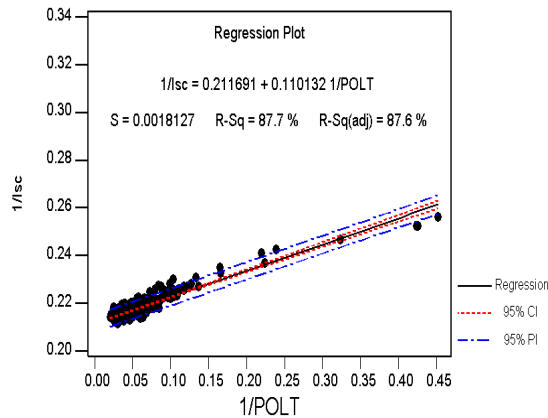


Fig. 6 Isc vs. POLT

The model is a useful and easily produced approximation of the true relationship. When considered in conjunction with the previous models presented it becomes clear that the possibility of utilizing lifetime in a production situation for process control is within the realm of possibility, even as far upstream as the as-grown ingot. A prediction interval is presented below using POLT estimates obtained from the empirical model of AGLT and resistivity into POLT.

AGLT/Res	POLT 95% PI	ISC 95% PI
20/1.5	(19.3, 28.3)	(4.5, 4.7)

Table 4 - 95% Confidence and Prediction Intervals

For a given AGLT/Res (20/1.5) one could reasonably expect a POLT value between 19.5 and 28.3 μs . Given this range of POLT, one could reasonably expect a final Isc of between 4.5 and 4.7.

In summary, approximations of electrical performance are shown to be possible based on AGLT/Res values. Further refinement of the model is needed to realize improvements in the precision of the estimates. Additionally, one must observe that the myriad of “events” that occur in production situations are inherently unpredictable.

Hence, all estimates presented presume a stable process.

The Evolution of Photovoltaic Process Control

The data presented here illustrates that even with a complex multi-step processing sequence, the effect of as-grown lifetime on post-oxidation lifetime, a strong predictor of cell performance, can be estimated with some precision. Ultimate cell electrical performance can also be predicted with the inferences becoming more tenuous but still useful when used in conjunction with other models of key process parameters⁶.

The entire regime of modeling presented suggest an iterative course of action for engineers, scientists and technicians in need of expeditious development of models of sufficient precision and simplicity as to allow cost effective decisions in production situations. The ultimate intent being development of real-time lifetime based control schemes. Further research will undoubtedly refine the approaches needed to realize that goal.

More generally, the implementation of production lifetime measurement devices has enabled further exploration of the photovoltaic processing space via readily available empirical modeling and estimation methods. The experience from the IC and other industries suggests that this evolution of methodology will offer significant process engineering enhancements with commensurate cost to benefit improvements in photovoltaic manufacturing.

References

- [1] Colleti G., De Iullis S., et. al.,
“Experimental Results of a Method for
Industrial Characterization of Crystalline
Silicon Wafers”, Proceedings of the
International Conference, PV in Europe
from PV Technology to Energy Solution,
pg. 71-74, October 2002
- [2] Montgomery D., *Introduction to
Statistical Quality Control, Fourth Edition*,
2001. John Wiley and Sons
- [3] Montgomery D., *Design and Analysis of
Experiments, Fourth Edition*, 1997.
John Wiley and Sons
- [4] Neter J., Wasserman W., Kutner M.,
Applied Linear Statistical Models, 1990.
Richard D. Irwin Inc.
- [5] Box G., Hunter W., Hunter J.S.,
Statistics For Experimenters, 1978.
John Wiley and Sons
- [6] Coleman J., "Process Optimization and
Control of a Photovoltaic Manufacturing
Process", Extended Abstracts and Papers
9th Workshop on Crystalline Silicon Solar
Cell Materials and Processes, pg. 171-174
August 1999.

Improvement of electronic quality in mc-Si wafers with SiN_x:H layer after rapid thermal processing accessed by scanning photoluminescence

I. Tarasov¹, M. Dybiec¹, S. Ostapenko¹, A. Rohatgi², V. Yelundur², A.M.Gabor³

¹University of South Florida, 4202 E. Fowler Ave, Tampa, FL 33620, USA

²Georgia Institute of Technology, 777 Atlanta Dr., Atlanta, GA 30332, USA

³Evergreen Solar, 259 Cedar Hill St., Malboro, MA 01752, USA

Abstract. We report on spectroscopic photoluminescence (PL) mapping performed at room temperature in commercially grade mc-Si ribbon wafers for solar cells. Besides, band-to-band luminescence of silicon with the maximum at 1.09eV and “defect” PL band at 0.8eV, we observe under UV excitation a broad visible emission from the SiN_x:H layer. The samples covered with SiN_x:H layer were subjected to rapid thermal processing at different temperatures, and PL maps were measured before and after treatment. Scanning PL technique was applied consecutively to all three bands. We observed that after RTP treatment the intensity of all PL bands were significantly increased, which indicates further reduction of non-radiative defects. This increase shows different amplitude and depends on RTP temperature.

Introduction

Thin amorphous silicon nitride (SiN_x:H) PECVD films are routinely used in multi-crystalline silicon (mc-Si) solar cell production. A principal function of the films is to provide anti-reflecting layer to enhance solar light penetration into silicon. It is also recognized that SiN_x:H deposition followed by annealing also stimulates hydrogen incorporation into silicon, which benefits electronic quality of the material by increasing the minority carrier lifetime [1]. There is a current need for diagnostics and control of the SiN_x:H film quality to achieve high-efficiency mc-Si solar cells. We report here on room temperature scanning photoluminescence (PL) study performed on Si₃N₄ coated mc-Si ribbon wafers.

Samples and experiments

The samples were parts of commercially grade ribbon mc-Si wafers with sizes 80mm x 70mm with an n⁺-p-p⁺ structure. Phosphorous diffusion to form the n⁺-emitter was performed in a conveyor belt furnace to achieve a sheet resistance 45-50 Ω/sq. A silicon nitride (SiN_x) antireflection coating was deposited on top of the n⁺ emitter in commercial low-frequency PECVD reactor. SiH₄ and NH₃ gases were used to deposit the SiN_x coating with an average refractive index of 2.1 and the thickness of 775Å. A commercial Al paste (Ferro FX-53-038) was printed on the entire backside of all wafers and annealed in a single wafer RTP system at temperatures in the range of 600-800°C (see Table 1). This simultaneous anneal of Al and SiN_x involves fast ramp-up and cooling rates to promote an enhanced PECVD SiN_x-induced hydrogen passivation of defects Si. For the PL mapping study, the 55mW HeCd laser (λ_{ex} =325nm) or pulsed AlGaAs laser diode (λ_{ex} = 804nm) were used as excitation sources. Usage of the HeCd laser provides favorable conditions for excitation of the SiN_x:H layer, while the AlGaAs laser light is absorbed exclusively in the silicon bulk. The details of the experimental setup were described elsewhere [2]. PL spectra were corrected to the spectral response of the optical system. The PL mapping technique was applied twice to each sample: (1) directly after SiN_x:H

deposition prior RTP, and (2) after RTP. A reference Cz-Si wafer was being held on the stage to assure a constant laser power and optical system gain intermitted by RTP.

Results and Discussion

(a) PL in mc-Si

The PL spectrum of mc-Si wafers at room temperature, under AlGaAs laser excitation, is generally composed of two broad bands, as shown in Figure 1 (curve 2). Band-to-band emission (I_{bb}) shows the maximum at 1.09eV and a defect band PL (I_{def}) observed at ~0.8eV. PL maximum shifts across the wafer between 0.76 abd 0.81eV. In areas with low recombination activity of defects (high lifetime regions) only band-to-band luminescence is observed, while in low lifetime regions both PL bands can be found. The defect band was previously studied and identified as luminescence of dislocations with low level of impurity contamination [3].

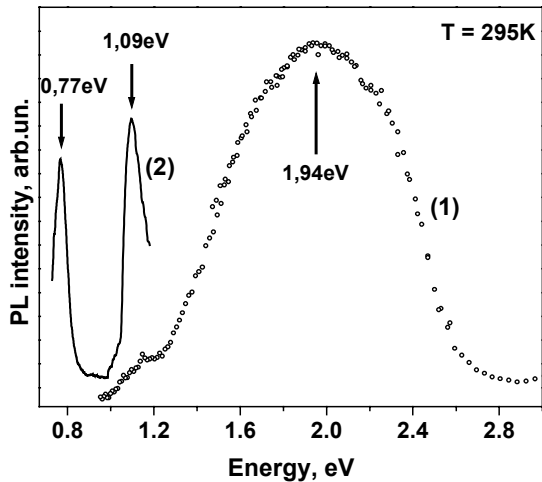


Figure 1. Room temperature PL spectra in ribbon mc-Si wafer covered with PECVD Si_3N_4 layer measured using two different excitation lasers: (1) 325nm HeCd laser, and (2) 804nm AlGaAs laser diode.

String Ribbon solar cells annealed in RTP at 740°C [5].

To quantify the RTP effect, we employed a point-by-point ratio of two PL intensities, $R = I_{def}/I_{bb}$, which is proportional to the concentration of electrically active dislocations [2]. In Table 1, the variation of “defect” concentration after RTP is expressed through the change of R-parameter. Figure 2 (e, f) shows the maps of R-parameter for the sample #C2 before and after RTP. It is observed that averaged across the maps R-parameter is reduced after RTP treatment.

We performed PL mapping of the I_{bb} and I_{def} intensities on a set of samples cut from the same ribbon wafers to analyze PL distributions across the whole wafer before and after RTP. The PL intensity of both bands is increased after RTP in all samples. In Figure 2, we show the PL maps of I_{bb} (a, b) and I_{def} (c, d) measured on the wafer #C2. Such increasing of the PL intensity after solar cell processing was previously observed and correlated with lifetime upgrading [4]. Therefore, we suggest that similar positive effect is revealed in this RTP study. Notice that lifetime upgrading (I_{bb} increase) has a maximum ratio for the wafers annealed at 740°C, while the smallest occurs at 800C RTP (Table 1). This maximum is consistent with the maximum V_{oc} enhancement found in

Table 1. Ratio of PL intensities measured at different spectral bands averaged across the mc-Si wafers subjected to RTP at different temperature.

Wafer ID (RTP temperature)	A1 (640°C)	A2 (640°C)	B1 (700°C)	B2 (740°C)	C2 (740°C)	D1 (740°C)	D2 (800°C)
$\frac{BB(RTP)}{BB(Initial)}$	2.97	2.77	3.42	3.54	3.50	2.68	2.17
$\frac{Def(RTP)}{Def(Initial)}$	1.28	1.16	1.57	1.90	1.15	1.26	1.03
$\frac{R(RTP)}{R(Initial)}$	0.43	0.59	0.39	0.33	0.42	0.44	0.67
$\frac{SiN(RTP)}{SiN(Initial)}$	1.15	1.01	1.08	1.43	1.71	1.33	1.14

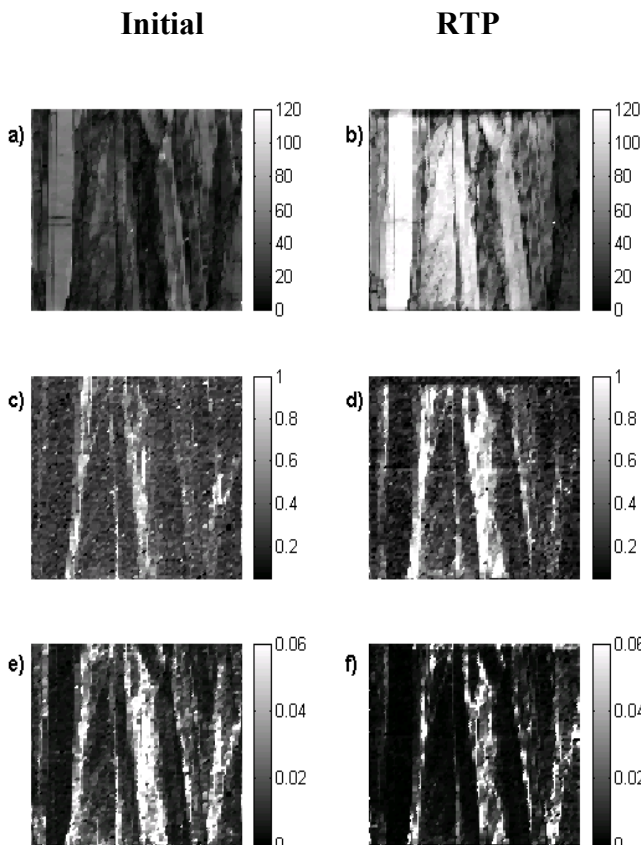


Figure 2. Room temperature PL mapping of (a,b) band-to-band intensity; (c,d) “defect” PL intensity, and (e,f) R-parameter measured before and after RTP in sample #C2.

In Figure 3, we show a dependence of the R-parameter versus inverse I_{bb} intensity, which is proportional to the concentration of non-radiative defects. A linear dependence of both values is straightforward, especially in the RTP samples. This indicates that after RTP electrically active dislocations are the major recombination centers, which control lifetime in mc-Si. We conclude that a reduction of the electrically active dislocation defects in bulk Si is a major positive effect of the RTP in terms of lifetime upgrading.

(b) PL in $\text{SiN}_x:\text{H}$ films

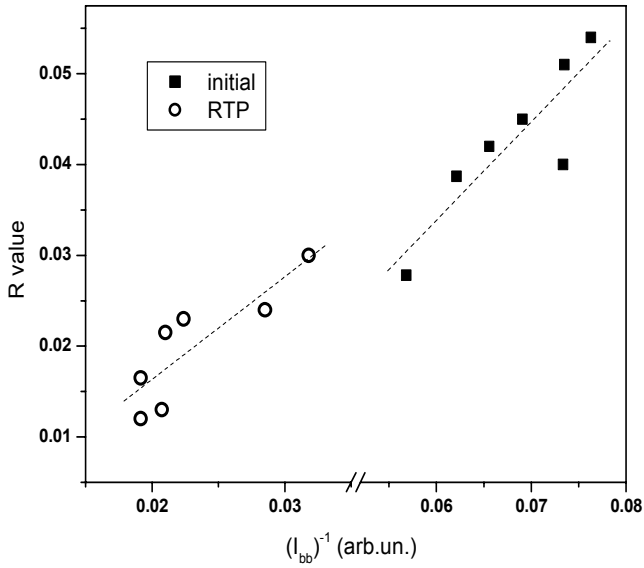


Figure 3. Dependence of active dislocation concentrations versus inverse band-to-band PL intensity in ribbon mc-Si samples before and after RTP treatment.

silicon nitride to the band-tail recombination in amorphous $\text{SiN}_x:\text{H}$ matrix [7]. However, we have not seen in our wafers characteristic properties of the band-tail luminescence, such as blue shifts with increasing the excitation intensity and decreasing temperature. It is conceivable to assign the “yellow” band to non-identified defects in $\text{SiN}_x:\text{H}$ layer.

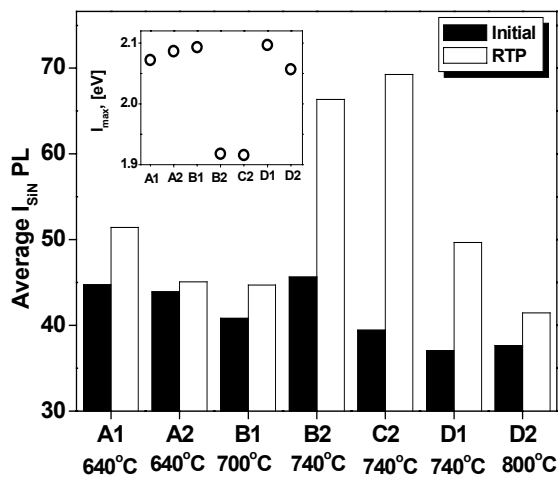


Figure 4. Average values of PL intensities from $\text{SiN}_x:\text{H}$ layer measures for seven ribbon mc-Si wafers before and after RTP treatment. The position of I_{SiN} PL maximum after RTP treatment is shown on the insert.

Broad “yellow” luminescence with the maximum at 1.94eV, I_{SiN} , is observed at room temperature on Si_3N_4 coated wafers excited by He-Cd laser as shown in Figure 1 (curve 1). The position of PL maximum may vary in the range from 1.86eV to 2.10eV depending on film deposition and annealing parameters. We also observe a noticeable variation of the visible PL intensity across the whole wafer [6]. No visible PL is found in wafers without $\text{SiN}_x:\text{H}$ layer. This proves that this luminescence originates from the $\text{SiN}_x:\text{H}$ layer itself. Prior results attributed similar PL band in silicon nitride to the band-tail recombination in amorphous $\text{SiN}_x:\text{H}$ matrix [7]. However, we have not seen in our wafers characteristic properties of the band-tail luminescence, such as blue shifts with increasing the excitation intensity and decreasing temperature. It is conceivable to assign the “yellow” band to non-identified defects in $\text{SiN}_x:\text{H}$ layer.

We performed PL mapping of the I_{SiN} intensity in all wafers before and after RTP. These results are presented in Fig.4. The $\text{SiN}_x:\text{H}$ PL intensity shows a maximum increase at 740°C RTP (samples B2, C2, and D1), which is specified in Table 1 as a ratio of average PL intensity across entire wafers before and after RTP. Increasing in I_{SiN} intensity can be interpreted as passivation of non-radiative defects in $\text{SiN}_x:\text{H}$ films with atomic hydrogen [8], which is released from the reservoir at the interface between $\text{SiN}_x:\text{H}$ film and silicon substrate and from the $\text{SiN}_x:\text{H}$ film itself. Summarizing, we conclude that starting at 640°C the atomic hydrogen passivates defects (active dislocations) in Si substrate increasing lifetime and PL intensity. Concurrently, there are no

hydrogen processes in the Si₃N₄ film (# A1, A2, B1). At 740C the hydrogen is also released into SiN_x:H film, which is evident from PL increase (#B2, C2, D1). Finally, above 740°C the out-diffusion of hydrogen occurs which is seen by reduction of the passivation effect in #D2 sample. Additional experiments are in progress to confirm the mechanism and optimize RTP processing.

Acknowledgements. The work was supported by NREL subcontracts ACQ-9-29639-03 and AAT-2-31605-02. We are thankful to Evergreen Solar, Inc. for supplying samples used in this study.

References.

- [1] V.Yelundur, A.Rohatgi, A.Ebong, A.M.Gabor, J.Hanoka, R.L.Wallace, *J.Electronic Materials*, **30** (2001), p.526.
- [2] S.Ostapenko, I.Tarasov, J.P.Kalejs, C.Haessler, E.U.Reisner, *Semicond.Sci.andTechnol.*, **269** (2000) p.588
- [3] M. Kittler, W. Seifert, T. Arguirov, I. Tarasov and S. Ostapenko, *Solar Energy Materials and Solar Cells*, **72** (2002) p.465
- [4] J.Bailey, J.P.Kalejs, C.Keaveny, *1st World Conf. on Photovoltaic Energy Conversion (New York: IEEE)* (1995), p.1356
- [5] A.Rohatgi, V.Yelundur, J-W. Jeong, D.S.Kim, A.M.Gabor, to be published in *Proc. WC-PEC-3*, 2003
- [6] I. Tarasov, S. Ostapenko, V. Yelundur, and A. Rohatgi, to be published
- [7] F.Giorgis, P.Mandracci, L.Dal Negro, C.Mazzoleni, L.Pavesi, *J.Non-Cryst.Solids*, **266-269** (2000) p.588
- [8] F.Duerinckx, J.Szlufcik, *Solar Energy Mater.&Cells*, **72** (2002) p.231

Light-Induced Lifetime Degradation in Multicrystalline Silicon

D. H. Macdonald¹, L. J. Geerligs¹ and S. Riepe²

¹ECN Solar Energy, PO Box 1, NL-1755 ZG Petten, The Netherlands

²Fraunhofer ISE, Heidenhofstr. 2, 79110 Freiburg, Germany

Abstract: The correlation between interstitial oxygen content and light-induced lifetime degradation in cast multicrystalline silicon is complex. On a wafer-averaged scale, there is a strong positive correlation, which has been parameterized in this paper to model the impact of this degradation on cell voltage for a typical industrial process. However, on a local, grain to grain scale within a given wafer, the degradation can vary by an order of magnitude, while the interstitial oxygen content remains almost unchanged. This supports recent suggestions that O_i is not directly involved in the chemical composition of the defect.

Light-induced degradation is a well-known phenomenon in boron-doped Czochralski (Cz) silicon [1], reducing the carrier lifetime and hence the cell efficiency. It has been linked to the presence of both boron and interstitial oxygen O_i, the latter being relatively abundant in standard Cz material. Degradation occurring under illumination of around 1 sun intensity takes approximately 24 hours to reach saturation. Since carriers injected through biasing also cause this degradation, the effect has become more properly known as “carrier-induced degradation” (CID) [2], as it is referred to in this paper from this point on. The initial non-degraded state can be recovered by annealing the sample above 200°C.

The extent of CID is characterized by the relative recombination center density N_t^{*}, which is defined as the difference of the inverse lifetimes before (τ_b) and after (τ_a) degradation [1]:

$$N_t^* = \frac{1}{\tau_a} - \frac{1}{\tau_b}$$

In Cz-Si, this parameter has a clear linear dependence on the boron concentration N_A, implicating the presence of B atoms in the defect composition. It also shows a dependence on the value of [O_i], but usually with much more scatter. This indicates that O_i itself may not to be directly involved in the defect, but occurs in association with it. Recently, the oxygen dimer [3] and intrinsic point defects [4] have been suggested as possible alternatives.

Similar degradation has been reported in cast multicrystalline silicon (mc-Si) [5,6]. The effect in mc-Si has been shown to be reversible upon annealing, as it is with Cz-Si, and the rate at which the degradation occurs is similar in both materials. These facts suggest that the defect is indeed the same. In this paper, we examine the relationship between the degradation in mc-Si and the interstitial oxygen content, on both a macroscopic level (averaged across a wafer), and from grain to grain. The results allow some insights into the possible composition of the defects. The determined dependence of the average degradation on [O_i] also allows cell performance to be modeled, and criteria for acceptable [O_i] levels in ingots to be established.

Fig 1 shows the interstitial oxygen profiles measured by Fourier-Transform Infrared spectroscopy (FTIR) for 3 mc-Si ingots from different manufacturers. The concentration at the bottom of ingot 3 is high even by Cz-Si standards. Fig 2 shows the effect of illumination on the effective lifetime for wafers from these ingots, as well as a Cz wafer ([O_i]=10ppma) and a Float-zone (FZ) wafer ([O_i]<1ppma). The lifetimes represent area-averaged values of several grains, measured with the QSSPC technique at an excess carrier density of 3×10¹⁵ cm⁻³. The FZ wafer showed no degradation, due to its low interstitial oxygen content, and confirms that the drop in lifetime observed in the other samples is not caused by changes in the surface passivating film (PECVD SiN), or by sample heating during illumination.

After 150 minutes illumination the samples were annealed at 250°C for 15 minutes, which caused the lifetimes to recover. Note also that the rate of lifetime decay is similar for the mc-Si and Cz samples, confirming that the defects are most likely the same. The two mc-Si wafers with the lowest lifetimes were sister wafers from the same ingot. One was measured without processing (other than etching, cleaning and surface passivating PECVD SiN deposition), and the other after emitter diffusion and hydrogenation

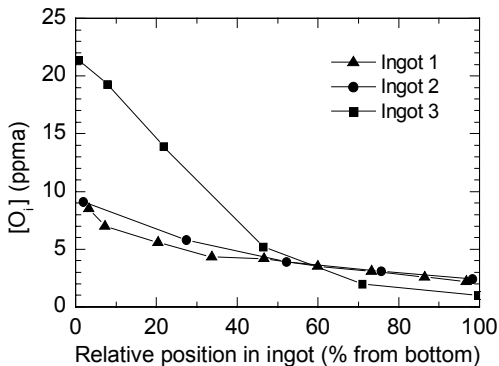


Fig 1. Interstitial oxygen content of mc-Si ingots from different manufacturers.

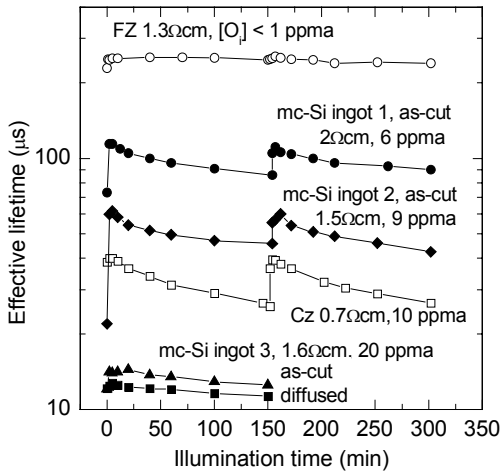


Fig 2. Carrier-induced degradation in various mc-Si, Cz and FZ wafers.

by spike firing a SiN film, in similar fashion to industrial processing. The extent of CID is almost identical in these two wafers, suggesting that neither gettering nor bulk hydrogenation significantly reduce CID in this material.

A further point of interest in Fig 2 is the sudden increase in lifetime of the mc-Si wafers within the first few minutes. This effect is almost completely absent in the FZ and Cz wafers. By analyzing the decay behavior of this initial change we have confirmed that it is caused by the splitting of FeB pairs [7]. At the injection level measured, FeB pairs are more strongly recombining than interstitial Fe, and so the lifetime increases after breaking the FeB pairs. After degradation for 150 minutes, the sample was allowed to relax in the dark for 24 hours, long enough for the pairs to re-form, as shown in Fig 3. The lifetime could then be recovered again after 5 minutes further illumination. Fortunately, the very different time constants of the FeB splitting and CID allow them to be studied independently.

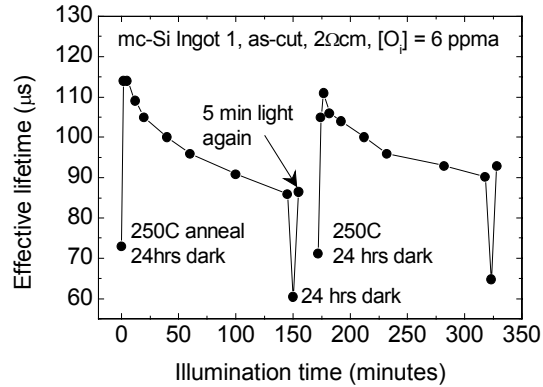


Fig 3. Details of lifetime changes due to FeB splitting and carrier-induced degradation.

By the use of lifetime mapping techniques, such as Carrier Density Imaging (CDI) [8] and Modulated Free-Carrier Absorption (MFCA), it is possible to study the degradation on a *local* scale, as shown in Fig 4. The first two maps show CDI images of the carrier lifetime before and after degradation for 16 hours. The third map shows the local N_t^* calculated using the expression above. The CDI images took approximately 3 min to capture, meaning that the FeB pairs were fully dissociated for almost the entire measurement time (dissociation is complete within tens of seconds in most cases).

In contrast to the QSSPC technique, both CDI and MFCA operate under fixed generation (equivalent to 1 sun in these measurements). This means that wafers or grains with higher lifetimes will be in higher injection, which will produce a greater apparent value for N_t^* , as has been shown by Rein *et al.* [9]. We estimate that these effects will produce an overestimation of N_t^* in the high lifetime regions of up to 50% for the conditions in this study. The overestimation would be less for lower lifetime grains and wafers. Unfortunately, this distortion is difficult to avoid when using mapping techniques.

The image clearly shows a large variation in N_t^* from grain to grain. Some high lifetime grains remained almost unchanged, while others degraded strongly. This is indicated on the left of Fig 5, which reveals little correlation between N_t^* and the initial lifetime. After degradation (right of Fig 5), all points lie below the limit imposed by the CID in parallel with a lifetime cap of $100\mu s$ due to surface recombination. Many points lie well away from this curve, meaning other bulk recombination centers, such as Fe, are also important in these regions.

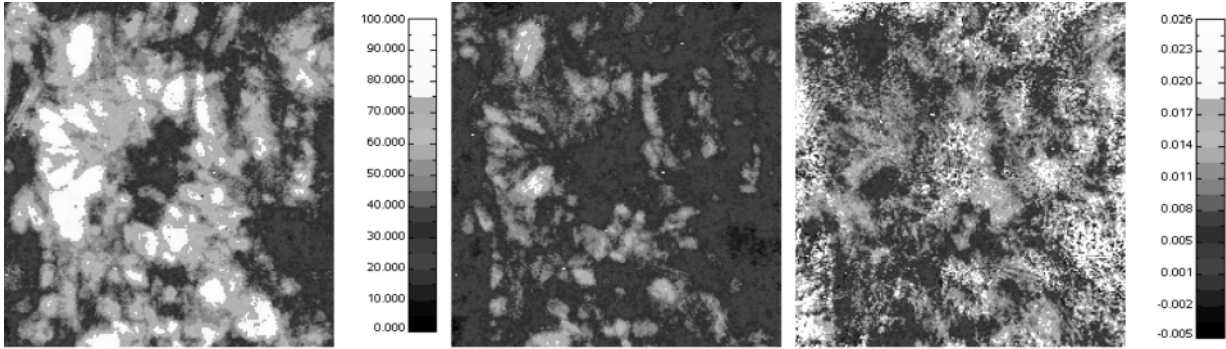


Fig 4. CDI images of a wafer from the top of ingot 3. The images on the left are lifetime maps before and after degradation (μs). The image on the right is the relative defect concentration N_t^* .

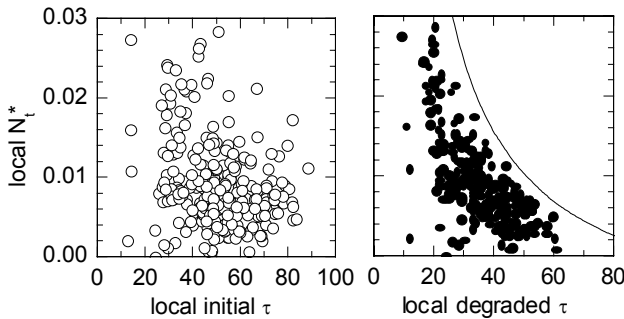


Fig 5. Scatter plot of local initial and degraded lifetimes (μs) versus local N_t^* , taken from a line scan through Fig 4.

It is instructive to match local N_t^* data from lifetime maps with $[\text{O}_i]$ measurements made within a 5mm region of individual grains, as shown in Fig 6 (note that 1ppma $[\text{O}_i] = 5 \times 10^{16} \text{ cm}^{-3}$). The corresponding N_t^* data were averaged over the same intra-grain regions. Several wafers from a single ingot are shown, as well as a Cz wafer. The mc-Si wafers were emitter diffused, stripped, and hydrogenated, and so should be representative of final cell substrates. In this figure, the parameter N_t^*/N_A has been plotted to remove the influence of the boron concentration [4]. The data sets with error bars were measured with CDI, while the others are based on MFCA maps. The uncertainties are similar in both cases. The wafer from the top of the ingot was measured with both techniques, as shown on the plot, resulting in good agreement for local N_t^* values.

The trend of increasing average degradation with increasing average $[\text{O}_i]$ is clearly evident. In the high $[\text{O}_i]$ region, the data agrees reasonably with fits for Cz-Si derived by Rein *et al* [4] and Bothe *et al*. [3]. The latter defined two fits, one for low $[\text{O}_i]$ which is almost linear, and another for high $[\text{O}_i]$ which is almost quadratic and aligns with Rein's fit. This shifting from a linear to a

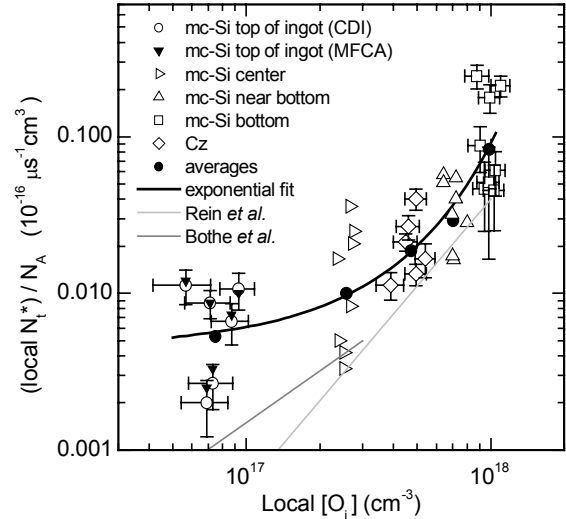


Fig 6. Correlation between local $[\text{O}_i]$ and N_t^*/N_A as measured with the CDI and MFCA techniques. All mc-Si wafers are from ingot 3. The black line is an exponential fit to the averages. The gray lines are fits to Cz data by Rein *et al.* and Bothe *et al.*

quadratic dependence is in accord with a proposed relationship between $[\text{O}_i]$ and the oxygen dimer concentration [3]. Such a shift is also reflected in our data for mc-Si. The apparent systematic overestimation in N_t^* in our data is partly due to the effect of using constant generation described above. However, this effect is not likely to explain the entire difference. The remaining difference could be caused by a different relationship between $[\text{O}_i]$ and CID in mc-Si compared to Cz-Si. At lower values of $[\text{O}_i]$, the magnitude of the lifetime is generally higher, meaning the constant-generation overestimation is greater. This could partly explain the apparent sub-linearity of our data in the low $[\text{O}_i]$ region.

Within any single wafer, the value of $[\text{O}_i]$ did not vary nearly as strongly as N_t^* . In fact, for each of

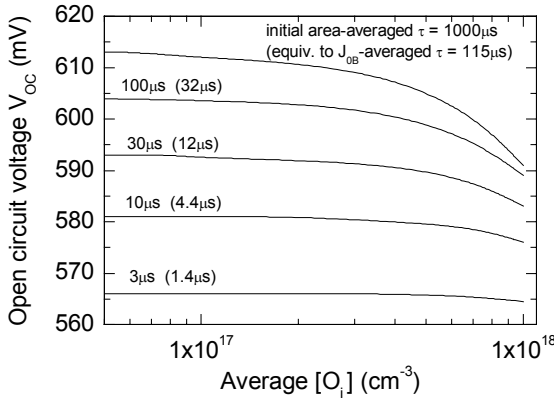


Fig 7. Modelled V_{OC} as a function of $[O_i]$ for standard SiN coated industrial mc-Si cells with modified-Gaussian lifetime distributions.

the individual sets of data in Fig 6, there appears to be no significant correlation at all between local $[O_i]$ and local N_t^*/N_A . This supports the suggestion that O_i is not involved in the defect.

To model the impact of CID on industrial mc-Si solar cells, it is useful to determine an empirical relation between N_t^*/N_A and $[O_i]$. A convenient way to characterize a dependence which changes from near linear to near quadratic is through an exponential fit, as shown on Fig 6, of the form:

$$\frac{N_t^*}{N_A} = 0.0045 \exp(3 \times 10^{-18} \times [O_i])$$

Fig 7 shows the impact of CID on cell V_{OC} , with several curves for different values of the area-averaged, non-degraded lifetime. In these PC1D simulations, typical optical and electronic parameters for SiN fired-through metallisation cells have been assumed. To allow a realistic simulation, we have assumed a modified Gaussian lifetime distribution before and after degradation [10,11]. The impact of these lateral variations on cell performance is accounted for by determining the area-averaged J_{0bulk} values [12], as calculated via PC1D, rather than using area-averaged lifetime values. The reduced lifetimes corresponding to these averaged J_{0bulk} values are shown on the plot.

Due to the constant generation artifact, the expression above will somewhat overestimate the degradation for a given $[O_i]$ value. For higher $[O_i]$ values, this error is only slight, and for lower $[O_i]$ values the impact of the degradation on cell voltage is negligible anyway. Therefore it should not significantly affect Fig 7.

The V_{OC} for the highest lifetime case shown is limited at low $[O_i]$ content to around 613mV by emitter and BSF recombination. Typical mc-Si material has initial area-averaged bulk lifetimes in the 30-100μs range. For the 30μs case, CID would reduce the V_{OC} from 593 to 588mV when $[O_i] = 7 \times 10^{17} \text{ cm}^{-3}$ (14ppma). A similar 5mV drop for 100μs material (from 605 to 600mV) would occur at $4 \times 10^{17} \text{ cm}^{-3}$ (8ppma). These restrictions would become greater in more homogeneous material, since the modified Gaussian distribution assumed here tends to obscure the effect due to low lifetime regions which dominate the voltage. A further point to consider is if the interstitial oxygen content is very high, there is likely to be an observable link between the starting lifetime itself and $[O_i]$. For low and moderate values of $[O_i]$, this link is obscured by the presence of other defects.

In summary, the wafer-averaged carrier-induced degradation in mc-Si exhibits a super-linear dependence on $[O_i]$, becoming approximately quadratic at higher $[O_i]$ values. From grain to grain however, there is great variation in the extent of degradation, suggesting $[O_i]$ is not directly involved in the defect. As a rule of thumb, it seems that if the $[O_i]$ content is kept below 10ppma, typical industrial mc-Si cells will not be adversely affected. However, as cell designs improve and material becomes more uniform, $[O_i]$ may need to be kept below 5ppma.

This work has been supported by NOVEM under contract 2020.01.13.11.2002. The authors are grateful to ECN staff for wafer processing and to S. W. Glunz for helpful suggestions.

- [1] J. Schmidt *et al*, 26th IEEE PVSC, Anaheim (1997).
- [2] S. W. Glunz *et al*, 3rd World Conf. On Photovoltaic Energy Conversion, Osaka, 2003.
- [3] K. Bothe *et al*, 3rd World Conf. On Photovoltaic Energy Conversion, Osaka, 2003.
- [4] S. Rein *et al*, 3rd World Conf. On Photovoltaic Energy Conversion, Osaka, 2003.
- [5] H. Nagel *et al*, 14th EC-PVSEC, 762-765 (1997).
- [6] M. Dhamrin *et al*, 29th IEEE PVSC, New Orleans, 2002.
- [7] D. Macdonald *et al*, submit. to J. Appl. Phys.
- [8] J. Isenberg *et al*, J. Appl. Phys, **93**, 4268 (2003).
- [9] S. Rein *et al*, 17th EC-PVSEC, Munich (2001).
- [10] P. E. Mijnarends, *et al*, Sol. Energy Mat. and Solar Cells **33**, 345-360 (1994).
- [11] J. Isenberg *et al*, 17th EC-PVSEC, Munich (2001).
- [12] R.A Sinton, 3rd World Conf. On Photovoltaic Energy Conversion, Osaka, 2003.

LASER DOPING FOR CRYSTALLINE SILICON SOLAR CELL EMITTERS

Ainhoa Esturo-Bretón, Thomas A. Wagner, Jürgen R. Köhler, and Jürgen H. Werner
Institut für Physikalische Elektronik, Universität Stuttgart, Pfaffenwaldring 47,
70569 Stuttgart, Germany

ABSTRACT

We investigate a new doping technique for solar cells based on silicon wafer. Spin coating of a phosphorous containing liquid results in a thin doping precursor on the surface of a p-type doped wafer. The optical focus of a frequency doubled pulsed Nd:YVO₄ laser (wavelength $\lambda = 532$ nm) melts a thin layer of silicon. As a result phosphorous atoms mix with the molten silicon. Subsequently to the laser pulse, rapid cooling of the molten silicon leads to an epitaxial recrystallization of a thin highly doped n-type emitter layer. We use this doping process for the production of 4 cm² sized solar cells with conversion efficiencies up to $\eta = 15.6\%$.

INTRODUCTION

Crystalline silicon, the leading technology in PV production, suffers mainly from the high wafer cost, which is in the range of 60 % of the total cell cost. The remaining 40 % processing cost is dominated by emitter processing steps, consisting of phosphorus diffusion, phosphorus glass etch and edge isolation.¹

Existing laser doping techniques²⁻⁶ use vacuum or a protecting atmosphere during irradiation of the samples. Our development of a laser doping process for crystalline silicon solar cell emitters aims at replacing costly high-temperature and vacuum processing steps by low temperature processing in air. This process offers the potential of a cost effective production of high efficient solar cells with high throughput.

WAFER PREPARATION

The cells consist of boron-doped p-type <100> oriented float zone wafers with a thickness $w = 375 \pm 25$ μm and a resistivity $\rho = 0.35$ Ωcm . Spin coating of a phosphorous containing doping liquid and subsequent drying on a hot-plate at a temperature of 300 °C results in a solid doping precursor

of thickness $d_p = 400$ nm or $d_p = 600$ nm depending on the rotation speed of the spin coater.

LASER DOPING PROCESS

A lens system consisting of cylindrical and spherical lenses focuses the Nd:YVO₄ laser beam onto the surface of the wafers. An autofocus system controls the size $s_F = 5 \mu\text{m} \times 200 \mu\text{m}$ of line beam focus and keeps the pulse energy density at a constant value during wafer processing. An xy-stage table fixes and moves the wafers during the laser processing. Figure 1 shows a sketch of the processing setup.

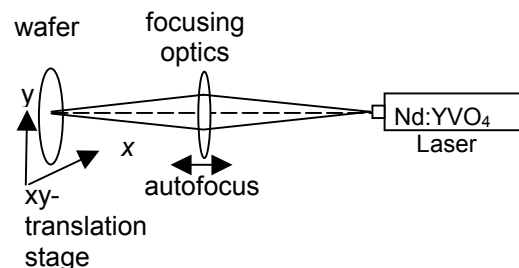


Fig. 1: The focusing optics transforms the 25 ns pulsed beam of a frequency doubled Nd:YVO₄-laser to a line beam of size $s_F = 200 \mu\text{m} \times 5 \mu\text{m}$ on the surface of the wafer. The size of the focus is controlled by an autofocus system. An xy-translation stage fixes the wafer and enables scanning in x- and y-direction.

We prepare different samples while varying pulse energy density E_p and overlap O between the pulses. An overlap of $O = 95\%$ means that the 95 % of the focused area will be illuminated again by the next laser pulse. Each pulse melts a few hundreds nanometers thick silicon layer. The molten area cools rapidly again down because of the short pulse duration (25 ns) and recrystallizes without defects as shown by transmission electron microscopy.⁷

After the laser process, a 30 s long dip in 5% HF solution removes the residuals of the doping precursor.

EMITTER CHARACTERIZATION

We use the four-point probe method⁸ to evaluate the sheet resistance ρ_s of the laser processed n-type emitters. Figure 2 shows the measured sheet resistance ρ_s several samples processed with different pulse energy density E_p , overlap O and thickness d_p of the doping precursor.

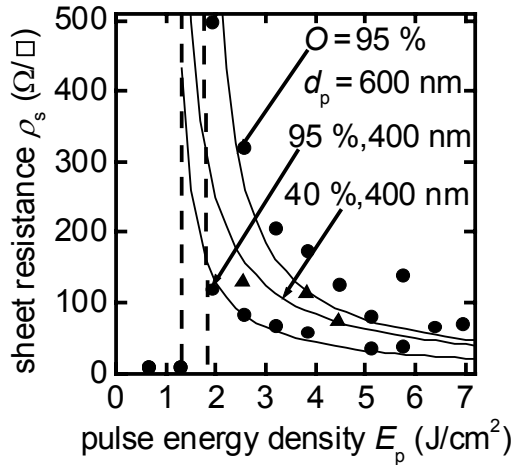


Fig. 2: Dotted lines indicate threshold energy $E_{th} = 1.3 \text{ J/cm}^2$ for precursor thickness $d_p = 400 \text{ nm}$, and $E_{th} = 1.7 \text{ J/cm}^2$ for $d_p = 600 \text{ nm}$. For energy densities $E_p > E_{th}$, the sheet resistance ρ_s reduces while increasing E_p . The solid curves are fitted to the data points according to $\rho_s \sim (E_p - E_{th})^{-1}$.

Energy densities $E_p < 1.3 \text{ J/cm}^2$ result in a sheet resistance of $10 \Omega/\square$, which corresponds to the sheet resistance of the non-processed wafer. Obviously, there exists a threshold energy density E_{th} for the laser doping process. We observe that increasing the thickness d_p of the doping precursor results in a higher sheet resistance ρ_s . A thicker doping precursor results in a higher laser energy absorption, consequently a thinner silicon layer d_{Si} is doped, resulting in a higher sheet resistance ρ_s . As a consequence the threshold energy density E_{th} for the samples with overlap $O = 95\%$ and thickness $d_p = 600 \text{ nm}$ of the doping precursor should be higher than for those with the same overlap O and $d_p = 400 \text{ nm}$. For samples with $d_p = 400 \text{ nm}$ we find $E_{th} = 1.3 \text{ J/cm}^2$ and for those with $d_p = 600 \text{ nm}$ then $E_{th} = 1.7 \text{ J/cm}^2$. The existence of a threshold pulse energy density E_{th} is consistent with

our model that the laser radiation first melts the surface of the silicon wafer, before phosphorous atoms penetrate into the molten silicon and dope the layer. For pulse energy densities $E_p > E_{th}$ the sheet resistance ρ_s decreases with increasing pulse energy density E_p . For $E_p > E_{th}$ we assume, that the thickness of the doped silicon layer d_{Si} linearly increases with the pulse energy density E_p according to

$$d_{Si} \propto E_p - E_{th}. \quad (1)$$

If we further assume, as a first approximation, a rectangular concentration profile and, if the concentration of phosphorous atoms in the doped layer is independent of the pulse energy, then the sheet resistance ρ_s depends only on the thickness d_{Si} of the doped silicon layer according to

$$\rho_s \propto 1/d_{Si}. \quad (2)$$

Equation (1) and (2) result in

$$\rho_s \propto (E_p - E_{th})^{-1}. \quad (3)$$

The solid lines in Fig. 2 are fits of Eq. (3) to the measured sheet resistance values.

The assumption that the thickness d_{Si} of the n-type doped layer increases linearly with the pulse energy is supported by Secondary Ion Mass Spectroscopy⁹ (SIMS) measurements. Figure 3 depicts the depth profiles of the phosphorous concentration of three samples with different pulse energy densities E_p , overlap O and thickness d_p of the precursor layer. We calculate the sheet resistance $\rho_{s,\text{model}}$ from the SIMS' concentration profiles assuming that every phosphorous atom in the layer is electrically active. For a thickness $d_p = 600 \text{ nm}$ of the precursor layer, the corresponding values of $\rho_{s,\text{model}} = 192 \Omega/\square$ for $E_p = 3.2 \text{ J/cm}^2$ and $\rho_{s,\text{model}} = 83 \Omega/\square$ for $E_p = 6.4 \text{ J/cm}^2$ are in good agreement with the measured sheet resistance $\rho_s = 206 \Omega/\square$ and $\rho_s = 67 \Omega/\square$ respectively. However, the phosphorous concentration profile of Figure 3 for the sample with pulse energy density $E_p = 3.2 \text{ J/cm}^2$, overlap $O = 40\%$ and thickness $d_p = 400 \text{ nm}$ of the doping precursor does not predict the measured sheet resistance ρ_s . Comparison of the calculated sheet resistance $\rho_{s,\text{model}}$ with the measured ρ_s leads to the conclusion, that only approximately 55 % of the phosphorous atoms are electrically active. An overlap $O = 95\%$ means that each area element

is hit by 20 subsequent laser pulses, whereas 40 % overlap corresponds to only 2.5 laser pulses per surface element. Our explanation for the above discrepancy between the measured sheet resistance ρ_s and the calculated $\rho_{s,\text{model}}$ from the depth profile is that the first few laser pulses are responsible for the penetration of phosphorous atoms into the silicon. The following laser pulses simply anneal the silicon and activate most of the incorporated phosphorous atoms. From the depth profiles in Fig. 3, we also conclude that multiple laser shots per area element decrease the phosphorous concentration. We explain this decrease by out-diffusion of phosphorous atoms during laser processing, when the doping precursor is depleted of phosphorous atoms after a few laser pulses. The decrease of phosphorous concentration towards the surface for overlap $O = 95\%$ and the increase with maximum phosphorous concentration close to the surface for overlap $O = 40\%$ supports our explanation.

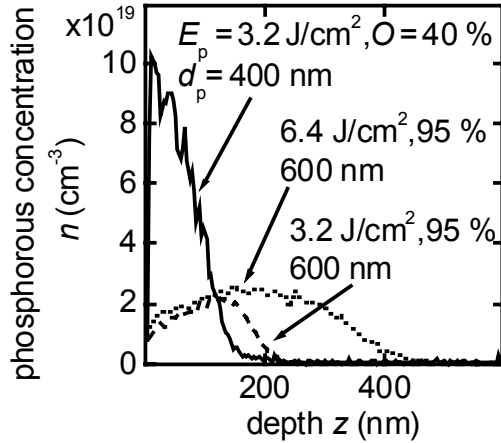


Fig. 3: Decreasing the overlap O leads to a higher phosphorous concentration n on the surface of the sample. For a constant overlap O and thickness d_p of the doping precursor, a higher pulse energy density E_p increases the emitter thickness d_{Si} .

SOLAR CELLS

For further characterization of the layers we process 4 cm^2 sized solar cells on the samples with doping precursor thickness $d_p = 400 \text{ nm}$ by evaporating front and back contacts. The front contact consists of a

$2 \mu\text{m}$ thick Ti/Pd/Ag grid on the n-type emitter and the back contact of a $1 \mu\text{m}$ thick Al layer on the p-type base. A 75 nm thick SiN_x anti-reflection coating of refractive index $n = 1.9$ optimizes light absorption.

Table I shows the cell parameters under 100 mW/cm^2 illumination. We address the reduced fill factor $FF = 74.5\%$ for the cell with $O = 95\%$ to $FF = 66\%$ compared to the cell with $O = 40\%$ to the increased sheet resistance of the emitter of $\rho_s = 130 \Omega/\square$ compared to $\rho_s = 80 \Omega/\square$. For overlap $O = 40\%$, the grid spacing of the front contact fingers is too large and results in a higher series resistance.

Table I: Solar cell parameters for two cells processed with pulse energy density E_p and overlap O .

E_p (J/cm^2)	O (%)	J_{sc} (mA/cm^2)	V_{oc} (V)	FF (%)	η (%)
3.2	40	34.5	0.620	66.0	14.5
2.5	95	33.9	0.619	74.5	15.6

Figure 4 shows the spectral response of a cell processed with $E_p = 3.2 \text{ J/cm}^2$ and overlap of 40 % and a cell with $E_p = 2.5 \text{ J/cm}^2$ and $O = 95\%$.

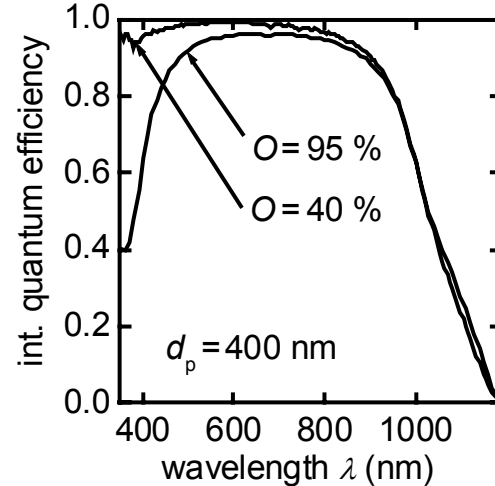


Fig. 4: Higher overlap O results in higher emitter degradation, as we deduce from the low quantum efficiency observed in the low wavelength regime.

For the cell with $O = 40\%$ we observe a high internal quantum efficiency in the regime of short wavelengths, in contrast to the cell processed with $O = 95\%$. We address the low blue response of the sample with O

= 95 % to impurity incorporation during the laser firing process.

Figure 5 shows the emitter degradation of cells processed with an overlap $O = 95 \%$ while increasing the pulse energy density from $E_p = 2 \text{ J/cm}^2$ to $E_p = 6.4 \text{ J/cm}^2$. In contrast, we do not find any emitter degradation in the cells with overlap $O = 40 \%$ while increasing the pulse energy density from $E_p = 2.5 \text{ J/cm}^2$ to $E_p = 4.4 \text{ J/cm}^2$.

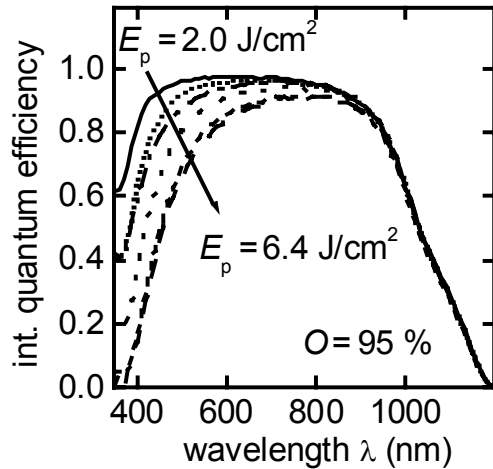


Fig. 5: For the cells with overlap $O = 95 \%$ there is a degradation of the emitter quality while increasing the pulse energy density E_p .

CONCLUSIONS

First investigations of our laser-doping process lead to the following results.

- Only pulse energy densities E_p over the threshold pulse energy density E_{th} lead to a n-type doped emitter.
- For constant overlap O and thickness d_p of the doping precursor, the emitter thickness increases linearly with the pulse energy density E_p .
- Complete activation of phosphor atoms requires frequent melting and recrystallization with overlap $O > 40 \%$.
- High overlap, $O = 95 \%$, together with high pulse energy density result in severe emitter degradation of the processed solar cells.

Optimally processed emitters show an internal quantum efficiency close to unity in the blue wavelength regime. From this finding we conclude that minority carrier re-

combination in the emitter is low. Consequently the diffusion length in the highly doped n-type layer exceeds the thickness of the emitter. This finding makes us confident, that the laser doping process is suitable for the production of high efficiency solar cells.

REFERENCES

- [1] R. Preu, R. Lüdemann, G. Emanuel W. Wetting, W. Eversheim, G. Güthenke, D. Untied, G. Schweitzer, in *Proceedings of the International Conference held in Glasgow, United Kingdom 1 – 5 May 2000*, edited by H. Scheer, B. McNelis, W. Palz, H. A. Ossenbrink and P. Helm (James & James (Science Publishers) Ltd., London), p. 1451.
- [2] A. Pokmurska, O. Bonchik, S. Kiyak, G. Savinski, A. Glikovsky, *Appl. Surf. Sci.* **154-155**, 712 (2000).
- [3] E. Fogarassy, R. Stuck, J. J. Grob, and P. Siffert, *J. Appl. Phys.* **52**, 1076 (1981).
- [4] T. Samemshima, S. Usuzi, M. Sekiya, *J. Appl. Phys.* **62**, 711 (1987).
- [5] T. F. Deutsch, J. C. C. Fan, G. W. Turner, R. L. Chapman, D. J. Ehrlich, and R. M. Osgood, Jr., *Appl. Phys. Lett.* **38**, 144 (1981).
- [6] P. G. Carey, T. W. Sigmon, R. L. Press, and T. S. Fahlen, *IEEE Electron Device Lett.* **6**, 291 (1985).
- [7] Unpublished results, private communication with M. Nerding, Institut für Werkstoffwissenschaften, Universität Erlangen, Germany.
- [8] S. M. Sze, *Physics of Semiconductor Devices*, 2nd Edition, (John Wiley & Sons, New York, 1981), p.31.
- [9] D. K. Schroder, *Semiconductor Materials and Device Characterization*, 2nd Edition, (John Wiley & Sons, New York, 1998), p.683.

Double Sided Buried Contact Solar Cells on Czochralski Wafers

Peter J Cousins, Christiana B. Honsberg and Jeffery E. Cotter

Centre of Excellence for Advanced Silicon Photovoltaic and Photonics
The University of New South Wales, Sydney, 2052, AUSTRALIA
E-mail: peter.cousins@student.unsw.edu.au

1 ABSTRACT

This paper reports initial results of double sided buried contact solar cells manufactured on industrial grade boron-doped Czochralski wafers. The importance of the thermal cycle to creating and maintaining high bulk lifetime in Czochralski material is considered and changes in apparent lifetime monitored throughout the manufacturing sequence using photoconductance decay. An improvement from the pre-process lifetime of $\sim 85 \mu\text{s}$ to $\sim 120 \mu\text{s}$ in the final device was observed, and an open-circuit voltage above 650 mV was recorded on $1 \Omega\text{cm}$ material. PC1D modelling of the final device estimates the rear surface recombination velocity at 200 cm/s – a value sufficiently low to achieve an efficiency of over 20%.

2 INTRODUCTION

Czochralski (CZ) grown mono-crystalline silicon is currently used in the large scale manufacture of solar cells. Although the electrical quality of boron-doped CZ material is significantly lower than laboratory materials (i.e. float-zoned, FZ), surface recombination and not bulk lifetime is still the largest limitation on the performance of production solar cells. For example, FZ material provides no performance advantage over CZ material in the Laser Groove Buried Contact (LGBC) solar cell, as the efficiency is limited by the high rear surface recombination.

Honsberg et. al.¹ suggested a device structure called the Double Sided Buried Contact (DSBC) solar cell (fig. 1) to address the surface recombination limitation of the LGBC. It utilises a localised rear contact scheme to enable a large percentage of the rear surface to be passivated with a Floating Junction (FJ), a technique known to provide very low recombination velocities². The DSBC solar cell manufactured on float-zoned wafers has provided superior performance to the LGBC solar cell³.

The improved rear surface recombination of the DSBC solar cell enables a performance improvement for increased bulk lifetimes. The lifetime of CZ wafers has been reported interstitial oxygen incorporated during ingot growth. Several authors have studied the effect of the thermal cycle on the bulk

lifetime. An initial high-temperature anneal has been shown to dissociate defects present in the pre-processed wafers^{4,5}, providing a large improvement in the bulk lifetime. Similarly, carefully chosen ramping rates and processing temperatures that avoid long periods at known defect nucleation temperatures⁶ have been effective in maintaining high bulk lifetimes.

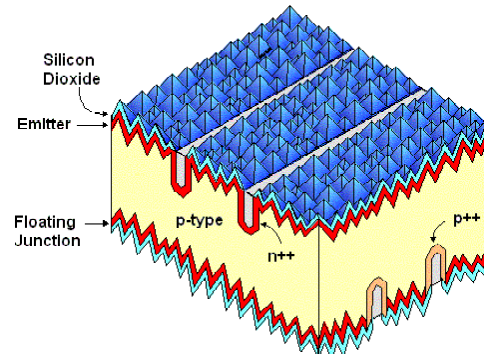


Fig. 1: Diagram of a double sided buried contact solar cell

This paper reports and models the manufacture of DSBC solar cells on industrial grade CZ wafers. Changes to the apparent lifetime were monitored throughout the manufacturing sequence using photoconductance decay technique. A defect model was used to investigate the formation and dissociation of oxygen related defects after each thermal cycle. Finally, the performance limitations of the resulting DSBC solar cell were determined using a PC1D model.

3 EXPERIMENT

Chemically etched 235 μm thick, 0.97 $\Omega\cdot\text{cm}$ boron-doped CZ silicon wafer were chemically passivated using 0.08 molar iodine in ethanol solution⁷. The apparent bulk lifetime was measured using the generalised method^{8,9} on a Sinton Consulting WCT-100 photo-conductance station. The pre-processing interstitial oxygen concentration was measured on an adjacent wafer using Fourier Transform Infra-Red spectroscopy (FTIR).

A DSBC solar cell (fig. 1) was manufactured on the CZ wafer – a process requiring three high temperature cycles:

- *Emitter Diffusion and Oxidation* – 15 minute phosphorus solid-source deposition and 180 minute TCA/wet/TCA oxidation. This thermal cycle diffuses the front emitter and rear FJ as well as growing a high quality silicon dioxide.
- *Phosphorus Groove Diffusion* – 90 minute phosphorus solid-source deposition, 90 minute drive-in and 50 minute TCA oxidation. This cycle diffuses the heavy n-type regions under the front contacts.
- *Boron Groove Diffusion* – 45 minute liquid source deposition and 270 minute drive-in. This cycle diffuses the heavy p-type regions under the rear contacts.

The formation and dissociation of oxygen related defects was monitored after each of these high temperature cycles using photoconductance decay lifetime measurements.

The device parameters were evaluated using a 1-sun solar simulator. The front and rear illuminated internal quantum efficiencies were also measured. Finally, the device was modelled using PC1D to determine the performance limitations of this DSBC solar cell manufactured on boron-doped CZ grown wafers.

4 RESULTS AND DISCUSSION

Initial Wafer

An interstitial oxygen concentration of $5.9 \times 10^{17} \text{ atom.cm}^{-3}$ (11.8 ppm) was measured using FTIR. The apparent bulk lifetime versus minority carrier density (Δn) before

any high temperature steps is shown in figure 3.

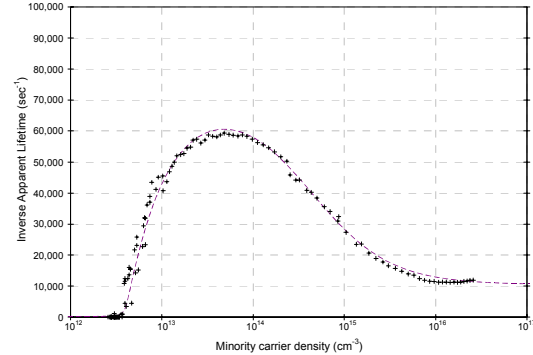


Fig. 2: Apparent lifetime versus Δn of a typical CZ wafer prior to high temperature processing. The defect model is shown as a dashed-line.

The pre-processed wafers have an apparent lifetime of 84 μs at 1 sun. This lifetime drops to $\sim 16 \mu\text{s}$ at lower minority carrier densities – a value more consistent with other reports^{5,10,11}. The variation in apparent lifetime with carrier density indicates the presence of both shallow and deep defects. These are not evident in measurements of boron-doped float-zoned wafers (very low oxygen concentrations) suggesting they are related to the presence of oxygen.

The dashed-line in fig. 2 illustrates the fit for a simple defect model containing both shallow and deep defects. The shallow defect model developed by Macdonald and Cuevas et. al.^{12,13} (Eq. 1) was used to calculate the apparent lifetime (τ_a) resulting from the inclusion of a single defect with a given density (N_{1t}) and trap/detrap time constant ratio (τ_t/τ_d).

$$\tau_a = \tau_r \left[1 + \frac{N_{1t}}{\left(\Delta n + N_{1t} \frac{\tau_t}{\tau_d} \right)} + \frac{\mu_p}{\mu_n + \mu_p} \right] \quad (1)$$

$$\text{and } \Delta n_a = \frac{\tau_a}{\tau_r} \Delta n,$$

where τ_r is the recombination lifetime, Δn is the excess minority-carrier concentration, Δn_a is the apparent excess minority-carrier concentration, and μ_n and μ_p are the electron and hole mobilities. Similarly the deep defect model developed by Shockley, Read and Hall^{14,15} (Eq. 2) was used to calculate the recombination lifetime (τ_r) resulting from the electron capture cross-sections (σ_n/σ_p).

$$\tau_r = \tau_p \frac{n_0 + n_1 + \Delta n}{n_0 + p_0 + \Delta n} + \tau_n \frac{p_0 + p_1 + \Delta n}{n_0 + p_0 + \Delta n} \quad (2)$$

where

$$n_1 = n_i \exp\left(\frac{E_t - E_i}{kT}\right), \quad p_1 = p_i \exp\left(\frac{E_i - E_t}{kT}\right),$$

$$n_1 p_1 = n_i^2, \quad \tau_p = \frac{1}{\sigma_p v_{th} N_{2t}}, \quad \tau_n = \frac{1}{\sigma_n v_{th} N_{2t}}$$

and n_o/p_o are the equilibrium electron/hole concentrations, n_i and p_i are the intrinsic electron/hole concentrations, E_i is the intrinsic Fermi energy, v_{th} is the thermal velocity and τ_p/τ_n are the hole/electron lifetimes.

The defect energy of the minority carrier trap could not be determined accurately – due to the noise – but was approximately 0.53 eV. This energy level, the defect density of $1.5 \times 10^{13} \text{ cm}^{-3}$ and the trap/detrap ratio of 5×10^{-4} are consistent with measurements by Schmidt et. al. on similarly doped (B_xO_y) CZ wafers.¹⁶ The deep defect parameters were $\tau_n = 14.9 \mu\text{s}$ and $\tau_p = 167 \mu\text{s}$.

Emitter Diffusion and Oxidation

The apparent lifetime versus Δn after the emitter diffusion and oxidation cycle is shown in fig. 3.

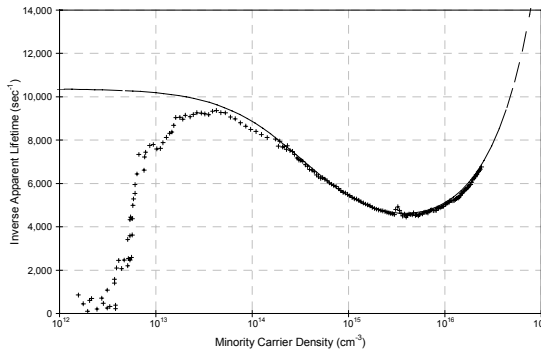


Fig. 3: Apparent bulk lifetime versus Δn after the emitter diffusion and oxidation cycle. The defect model is shown as a dashed-line.

The emitter diffusion and oxidation cycle increased the bulk lifetime to over $200 \mu\text{s}$ from $84 \mu\text{s}$ – a three-fold increase. Similar improvements in lifetime after high-temperature annealing have been reported by Glunz et. al.⁵ The change in the defect parameters was determined by fitting the apparent lifetime versus Δn curve using the deep defect model (Eq. 2). The effect of emitter recombination associated with the emitter and FJ regions was also included¹⁷. Changes to the shallow defects, seen in the wafers before processing (fig. 3) could not be

monitored, as the effect of Depletion-region Modulation¹⁸ associated with the pn -junction dominated the apparent lifetime at low Δn .

There was no significant change in the deep defect's capture and release cross-sections (σ_n, σ_p) – 11.2 in the pre-processed wafer compared with 12.9 after the emitter diffusion and oxidation cycle. Hence the thermal cycle did not alter the defect's electrical behaviour. However, the defect density (N_{2t}) was reduced by a factor of 11. It can be concluded the emitter diffusion and oxidation thermal cycle has annihilation a large number of the defects present in the pre-processed wafer.

Boron and Phosphorus Groove Diffusion

Processing at high temperatures, like those used for the two groove diffusion cycles, has been reported to suppress nucleation of oxygen related defect^{4,6}. Photoconductance decay lifetime measurements after both the phosphorus and boron groove diffusion cycles indicated no significant variations in the deep defect parameters.

Device Results

The final device parameters measured on a 1-sun solar simulator are tabulated in table 1. The front and rear internal quantum efficiencies are shown in fig. 4.

Table 1: Light $I-V$ parameters measured under standard test conditions at 1 sun.

Cell	V_{OC} (mV)	J_{SC} (mA/cm ²)	FF (%)	η (%)
CZ_1	650.3	31.3	76.7	15.6
PC1D Model	650.3	31.3	76.7	15.6

The high open-circuit voltage indicates a low rear surface recombination velocity and a high bulk lifetime – for CZ wafers. This voltage compares favourably to other non-photolithographic device structure¹⁹ (i.e. LGBC), and is also comparable to photolithographic devices¹⁰. The non-ideal front optics – a silicon dioxide anti-reflection (AR) coating and no front-surface texture – limit the short circuit current. Finally, the fill-factor has been limited by a combination of high series resistance, a result of a non-optimal front grid pattern, and junction

recombination, a result of cleaving small-area devices³.

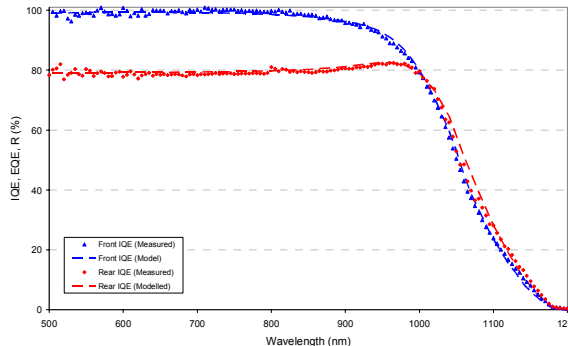


Fig. 4: Front and rear illuminated internal quantum efficiencies for the DSBC solar cell on a CZ wafer. The PC1D modelled quantum efficiencies are shown as a dashed-line.

The rear surface recombination velocity and bulk lifetime extracted using PC1D (table 4) are quite good. The main performance limitations are front optical and electrode designs. The same PC1D predicts addressing the front surface reflection and series resistance losses will lead to solar cells with efficiencies above 20%.

Table 4: PC1d Modelling parameters

Parameter	Value
Front AR coating	$t = 120 \text{ nm}$, $n = 1.46$ Broadband = 3%
Rear AR coating	$t = 120 \text{ nm}$, $n = 1.46$ Broadband = 8%
Internal reflection	Front and Rear = 50%
Wafer	1 $\Omega \cdot \text{cm}$, p-type, 235 μm
Emitter	Peak = $1.124 \times 10^{19} \text{ cm}^{-2}$
Lifetime	Depth Factor = 0.3889 122 μs
Surface Recombination	Front = 3000 cm/s Rear Eff. = 200 cm/s
Series resistance	1.3 $\Omega \cdot \text{cm}^{-2}$
Junction recombination	$9 \times 10^{-9} \text{ A} \cdot \text{cm}^{-2}$

5 CONCLUSION

This paper has reported DSBC solar cells on industry grade CZ boron-doped wafers. The apparent lifetime increased by a factor of three to over 200 μs , as a result of an 11 fold decrease in the deep defect density, after the emitter diffusion and oxidation cycle. An open-circuit voltage of over 650 mV was measured on the final device. PC1D modelling estimated a high bulk lifetime of 120 μs , and a low rear surface recombination velocity of 200 cm/s in the final device. Once front surface reflection and series resistance, limiting these results, have been addressed

the PC1D predicts the DSBC solar cell will achieve above 20% on industrial CZ wafers.

6 ACKNOWLEDGEMENTS

This work has been jointly funded by the Australian Research Council and the BP Solar European Technology Centre. The authors would like to acknowledge the contributions of Nigel Mason, Steve Roberts and Keith Heasman in supporting this work.

7 REFERENCES

- ¹ C. Honsberg, F. Yun, A. Ebong, M. Taouk, S. Wenham, and M. Green, Tokyo, Japan, 1993, p. 89-90.
- ² J. Zhao, A. Wang, A. Aberle, S. Wenham, and G. M, Applied Physics Letters **64**, 199-201 (1994).
- ³ K. McIntosh, PhD Thesis, University of New South Wales, 2001.
- ⁴ D. Yang, D. Li, L. Wang, X. ma, and D. Que, Solar Energy Materials & Solar Cells **72**, 133-38 (2002).
- ⁵ S. W. Glunz, S. Rein, W. Warta, J. Knobloch, and W. Wetting, Solar Energy Materials & Solar Cells **65**, 219-229 (2001).
- ⁶ B. Hergholz, in *Oxygen in Silicon*; Vol. 42, edited by F. Shimura (Academic Press, 1994), p. 513-76.
- ⁷ A. W. Stephens and M. A. Green, Solar Energy Materials and Solar Cells **45**, 255-65 (1997).
- ⁸ R. A. Sinton and A. Cuevas, Applied Physics Letters **69**, 2510-12 (1996).
- ⁹ H. Nagel, C. Berge, and A. Aberle, Journal of Applied Physics **86**, 6218-21 (1999).
- ¹⁰ S. W. Glunz, S. Rein, J. Knobloch, W. Wetting, and T. Abe, Progress in Photovoltaics **7**, 463-469 (1999).
- ¹¹ B. Damiani, A. Ristow, A. Ebong, and A. Rohatgi, Progress in Photovoltaics **10**, 185-193 (2002).
- ¹² A. Cuevas, M. Stocks, D. Macdonald, M. Kerr, and C. Samundsett, IEEE Transactions on Electron Devices **46**, 2026-34 (1999).
- ¹³ D. Macdonald and A. Cuevas, Applied Physics Letters **74**, 1710-12 (1999).
- ¹⁴ W. Shockley and W. Read, Physical Review **87**, 835-42 (1952).
- ¹⁵ R. Hall, Physical Review **87**, 387 (1952).
- ¹⁶ J. Schmidt, K. Bothe, and R. Hezel, Applied Physics Letters **80**, 4395-97 (2002).
- ¹⁷ A. Cuevas, Solar Energy Materials and Solar Cells **57**, 277-290 (1999).
- ¹⁸ P. Cousins, D. Neuhaus, and J. Cotter, Journal Applied Physics, Submitted (2003).
- ¹⁹ T. Bruton, N. Mason, S. Roberts, O. N. Hartley, S. Gledhill, J. Fernandez, R. Russell, W. Warta, S. Glunz, O. Schultz, M. Hermle, and G. Willeke, Osaka, 2003.

Silicon Surface and Heterojunction Interface Passivation Studies by Lifetime Measurement

M.R. Page, Qi Wang, T.H. Wang, Y. Yan, Steven W. Johnston, T.F. Ciszek
National Renewable Energy Laboratory, Golden, CO 80401

ABSTRACT

We report two investigations conducted by using photoconductivity decay lifetime measurement. The first is crystalline silicon (c-Si) surface passivation using quinhydrone/methanol (QM) for bulk minority-carrier lifetime measurement. QM shows great promise as a substitute for iodine-based solutions because of its superior stability and minimized surface recombination velocity in silicon. The second is interface passivation in an amorphous silicon (a-Si)/c-Si heterojunction structure as a parallel effort to develop and optimize heterojunction c-Si solar cells by hot-wire chemical vapor deposition (HWCVD). A thin buffer layer inserted between the a-Si and the c-Si substrate has been found to be much more effective than a directly deposited a-Si/c-Si interface in reducing the interface recombination velocity.

INTRODUCTION

In photoconductivity decay measurements, surface passivation is essential to obtain an effective lifetime that is close to the bulk minority-carrier lifetime in a silicon wafer, so that the true photovoltaic performance potential may be assessed. Various methods have been developed over the years to passivate silicon surfaces for this purpose. The most convenient and commonly practiced technique is iodine in methanol/ethanol solutions. However, quinhydrone/methanol seems to be even more stable and effective [1]. We report our experiments here confirming these claims and, hence, QM is used in our lifetime measurement procedure for wafer screening and other experiments.

When making a heterojunction with an intrinsic thin layer (HIT[®]) solar cell [2], a well-passivated c-Si/a-Si interface is very crucial for minimizing junction recombination and, therefore, to achieving a high-performance photovoltaic device. A real heterojunction is also very important for attaining a high open-circuit voltage [3]. That means a truly amorphous silicon layer must be deposited immediately on a c-Si surface. A buffer layer is therefore needed to help passivate the interface as well as to facilitate amorphous silicon deposition. Lifetime measurement offers a quick and accurate evaluation of the effectiveness of the buffer layers in passivation before completion of device-fabrication steps. This study attempts to quantify the passivation effects of a single-sided buffer layer deposited in a wedge form of materials ranging from no film to thick films.

EXPERIMENTAL

To carry out this study, we cut 6.35-cm x 6.35-cm squares or 1-cm x 2-cm

rectangles from 100-mm CZ-Si wafers with (100), p-type (B-doped), $11 \Omega\cdot\text{cm}$, single-side polished, and damage-removal etched back surface. These samples are then subjected to a stringent cleaning procedure. They are degreased with trichloroethylene, acetone, isopropyl alcohol, and methanol and dried with nitrogen. This is followed by an immediate 10-min soak in boiling de-ionized (DI) water ($90 \text{ M}\Omega\cdot\text{cm}$), 1-min DI water cascade rinse, 1% by volume hydrofluoric acid (HF) dip for 1-min or until hydrophobic, 1-min DI water cascade rinse, and drying with nitrogen.

The cleaned samples are either immersed in a nearly saturated quinhydrone/methanol solution for lifetime measurements, or undergo a buffer layer/a-Si deposition process on the polished face of the wafers and are measured for lifetime. Buffer layer and a-Si depositions are all done in a HWCVD system.

Lifetime measurements were performed with a system and method developed at NREL [4] that uses the radio frequency photoconductivity decay (RF-PCD) technique operating in the ultrahigh frequency (UHF) range of 700 MHz. Our minority-carrier injection source was an attenuated 1064-nm YAG laser with a spot size of approximately 5 mm. This allowed us to make lifetime profiles across the graded a-Si and buffer layer wedges. Injection levels were not measured, but great care was taken to keep conditions consistent and injection levels as low as possible.

QUINHYDRONE/METHANOL SURFACE PASSIVATION

From the findings of H. Takato et. al. [1], a mixture of 0.01 to $0.05 \text{ mol}/\text{dm}^3$ of QM yields a solution capable of surface passivation superior to iodine and methanol (IM) or ethanol solutions. The principle benefits of the QM solution are a stable surface passivation that is reached after a development period dependent upon quinhydrone dilution anywhere from 10-min to several hours. Surface recombination velocities as low as 4.2 cm/s for $150\text{-}\Omega\cdot\text{cm}$, p-type, (100), FZ-Si and stabilities that are measured on an hour timescale were reported [1]. The IM solutions achieve similar surface recombination velocities but have very poor stability with failing effectiveness immediately after submersion. Our own experiments with nearly saturated solutions of quinhydrone in methanol showed similar effects as in [1], with solution response after an initial 10-min development time. Fig. 1 illustrates the lifetime for three different surface conditions for $1\text{-cm} \times 2\text{-cm}$ samples cut from the same 100-mm wafer: an as-received wafer without any surface passivation or cleaning steps, as-cleaned samples with 1% HF dip hydrogen-terminated surface, and QM-solution-passivated samples measured over time up to 60-min. The as-received surface is very poorly passivated with an effective lifetime of about $6 \mu\text{s}$. After the cleaning procedure, the lifetime more than doubled owing to a hydrogen-terminated surface with variations from sample to sample of between 15.7 to $21.6 \mu\text{s}$. For QM-solution passivation, lifetime increased by more than an order of magnitude after development time of 10-min from an initial value of $16.7 \mu\text{s}$ to a final value of around $90 \mu\text{s}$. The nearly saturated QM solution we used stabilized much quicker than the 1 hour reported by Takato et. al. for $0.05 \text{ mol}/\text{dm}^3$ and appears to exhibit similar stability.

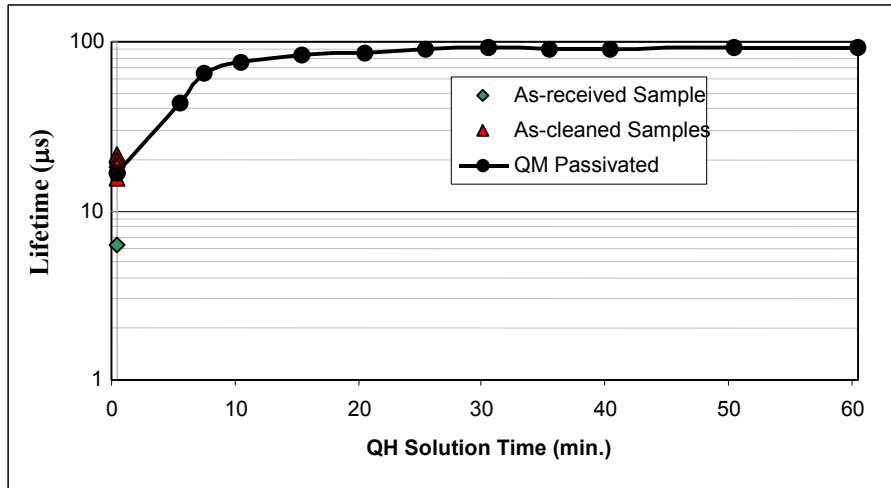


Fig. 1. Plot of as measured lifetime using RF-PCD technique for as-received, as-cleaned, and quinhydron/methanol-solution-passivated samples.

HETEROJUNCTION INTERFACE PASSIVATION

We have deposited thin films of intrinsic a-Si on crystalline silicon substrates with different buffer layers using our own in-house HWCVD systems capable of depositing 5-cm x 5-cm combinatorial films on 6.35-cm x 6.35-cm substrates [3]. The advantages of this technique are no plasma damage to the surface, no plasma instability, high deposition rate, in-situ atomic hydrogen treatment, and a simplified deposition system. Because of system limitations, films and surface treatments were performed on a single side of the c-Si substrate. This poses a problem for accurate minority-carrier lifetime measurement because there is still a significant amount of surface recombination at the back surface. On a relative scale, the results of lifetime measurements on single-side passivated silicon substrates are still valid, nevertheless.

From the results of Fig. 2, buffer layer A (BL-A) by itself contributes very little to surface passivation based on the minimal change in measured lifetime. Minor lifetime improvement was observed for intrinsic amorphous silicon deposited on c-Si and for buffer layer B (BL-B) on c-Si. The a-Si was deposited at 200°C substrate temperature for 1-min with tungsten filament temperature of 2000°C. The largest improvement in surface passivation as indicated by the magnitude of rise in lifetime from 7 to 16 μs was the i-a-Si/BL-A layers deposited on c-Si. The sharp rise and fall in lifetime at the ends are an indication of the edge of the deposited film, and lifetimes at the edge correlate well with the other samples' endpoints. Fig. 3 shows lifetime values on a combinatorial deposition of graded i-a-Si from 0 to 60 nm in thickness vertically with an increasing thickness of BL-A horizontally. The thinnest layer depositions are in the upper left-hand corner and the edges with lifetimes of 6 μs, indicating the edge of the combinatorial mask and revealing some misalignment to the substrate and the scanning shutter. The measured lifetime as one moves down vertically near the left edge increases steadily in value. If one scans to the right from the upper left corner, the lifetime does not change appreciably

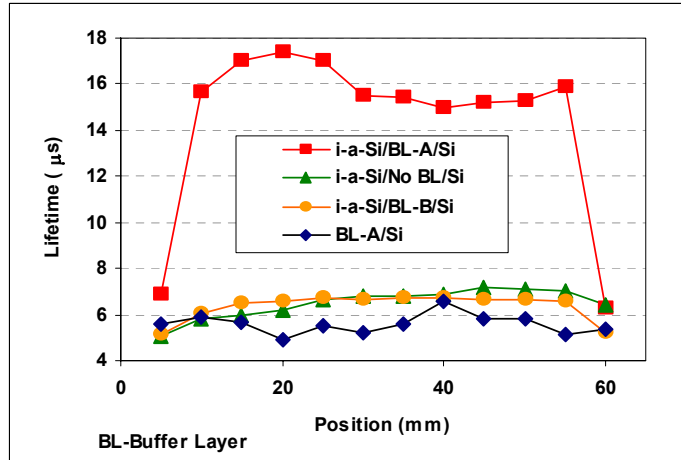


Fig. 2. Lifetime as a function of position (corresponding to increasing i-a-Si thickness if applicable) of different i-a-Si and buffer layer A/B combinations.

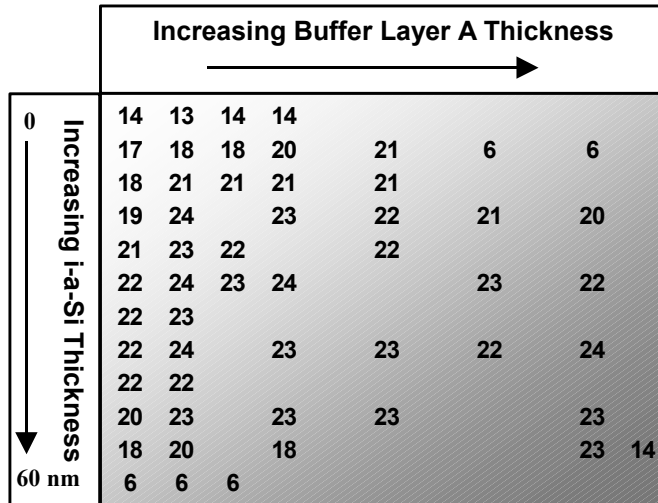


Fig. 3. Lifetime map in microseconds of combinatorial deposition of i-a-Si and BL-A layer wedges on a c-Si substrate.

for constant thin i-a-Si film, indicating that BL-A deposition alone is not adequate to passivate the interface, which correlates well with Fig. 2. However, at one-third of BL-A's maximum thickness, only about 10 nm of i-a-Si is sufficient to passivate the interface well, compared to nearly 30 nm of i-a-Si when BL-A is almost absent. BL-A's significance in assisting i-a-Si for effective interface passivation leads us to speculate that it immediately forces the deposition of a-Si rather than the usually poor epitaxial silicon, as confirmed by high-resolution TEM studies. Fig. 4 shows the lifetime variations on the same piece of sample along the i-a-Si thickness wedge deposited over BL-A and buffer layer C (BL-C) where BL-C is a co-deposition of BL-A and BL-B. The co-deposition material reveals further enhancement in lifetime, which may be attributed only to improved interface passivation because other variables are exactly the same between BL-A and BL-C. The behavior of the lifetime with i-a-Si thickness in Fig. 4 is similar to Fig. 3, except that the bulk lifetime of this particular sample was not as high, which resulted in lower measured lifetime. Again, we see that 10 nm of i-a-Si is enough for effective passivation when a good buffer layer is inserted.

CONCLUSIONS

The results of this study confirm that quinhydrone/methanol chemical solution is very effective and practical for silicon surface passivation for accurate bulk minority-carrier lifetime measurements. Compared to prior reports, the nearly saturated quinhydrone/methanol solution showed a shorter development time of only about 10-min to reach maximum surface passivation and demonstrated excellent stability.

Heterojunction interfaces of intrinsic amorphous silicon on c-Si showed significantly improved passivation with the use of a buffer layer. In particular, our BL-C buffer layer was the most effective in enhancing intrinsic amorphous silicon thin layer passivation of the crystalline silicon interface, potentially leading us toward high-performance heterojunction crystalline silicon solar cells.

This work was performed under DOE Contract #DE-AC36-99GO10337.

REFERENCES

- [1] Hidetaka Takato, Isao Sakata, Ryuichi Shimokawa, To be published in *Proceedings of the 3rd World Conference on Photovoltaic Energy Conversion*, Osaka, Japan, 2003.
- [2] Y. Kuwano, S. Nakano, M. Tanaka, T. Takahama, T. Matsuyama, M. Isomura, N. Nakamura, H. Haku, M. Nishikuni, H. Nishiwaki and S. Tsuda, *Mat. Res. Soc. Symp. Proc.* Vol. 258 (1992) 857-868.
- [3] Qi Wang, M.R. Page, Eugene Iwaniczko, Evan Williams, YanFa Yan, T.H. Wang, and T.F. Ciszek, To be published in *Proceedings of the 3rd World Conference on Photovoltaic Energy Conversion*, Osaka, Japan, 2003.
- [4] R.K. Ahrenkiel, Steven Johnston, *Solar Energy Materials and Solar Cells* 55 (1998) 59-73.

HYDROGEN PASSIVATION OF IRON IN MULTICRYSTALLINE SILICON

L. J. Geerligs, A. Azzizi, D. H. Macdonald, and P. Manshanden.
ECN Solar Energy, PO Box 1, NL-1755 Petten, the Netherlands

ABSTRACT

Concentrations of interstitially dissolved Fe can be measured by lifetime measurements before and after dissociation of FeB pairs. It allows the measurement of iron concentrations as low as $5 \times 10^{10} \text{ cm}^{-3}$. The technique is applied to determine the change in Fe concentration after different solar cell process steps. In particular, hydrogen passivation of iron in multicrystalline silicon wafers is investigated. The results indicate that the passivation can be accurately followed with this technique.

1. INTRODUCTION

Impurities and defects determine the quality of crystalline silicon. Iron (Fe) is one of the most dominant metallic impurities in multicrystalline silicon (mc-Si) materials [1]. High Fe contamination leads to a dramatic decrease in the minority carrier lifetime. The contamination of ingots with Fe depends on several factors such as contamination of feedstock, the smelting environment, and growing methods.

A number of techniques are capable of detecting and measuring the concentration of Fe in silicon materials. Secondary ion mass spectroscopy (SIMS) and Rutherford backscattering can be used, however the detection limits of those techniques is higher than $5 \times 10^{13} \text{ cm}^{-3}$ [2]. Other techniques such as deep level transient spectroscopy (DLTS) or electron paramagnetic resonance (EPR) permit to detect Fe at lower concentrations (10^{11} cm^{-3}), but with a long measurement time. However, the technique based on measurement of the lifetime before and after illumination of the wafer, causing Fe-B pairs to dissociate, is very effective in determining very low Fe concentrations (as low as $5 \times 10^{10} \text{ cm}^{-3}$). It has the advantages of being fast, non-contact, non-destructive and possible at room temperature.

In this paper we describe the application of this technique at high injection levels to multicrystalline silicon. A more elaborate discussion of the measurement technique will be published elsewhere [3].

The gettering of Fe has been studied with the FeB pair dissociation technique in some detail [4,5,6]. However, whether *hydrogen diffusion and passivation in mc-Si* can also be monitored with this technique has not been examined in literature before.

In this paper we present results which give a positive answer to this question. The incorporation of hydrogen into multicrystalline silicon materials is a very important industrial process step. It leads to a deactivation of certain impurities and defects and to a passivation of grain boundaries. However, it is challenging to monitor quantitatively the process. For example, SIMS measurements of deuterium have insufficient sensitivity [7] and FTIR measurements of PtH complexes require samples in which Pt is artificially in-diffused [8]. In contrast, virtually all multicrystalline materials contain already FeB in measurable concentrations. Therefore, FeB, if it is amenable to hydrogen-passivation and if this passivation can be measured conveniently, would be an ideal probe to study hydrogen passivation.

Kouketsu et al. [9] have reported the hydrogen passivation of Fe-B pairs and of iron-related hole traps in p-type silicon by DLTS and recombination lifetime measurements. In their study hydrogen ion implantation was used. In this paper hydrogen passivation of Fe in mc-Si material by hydrogen from remote PECVD SiNx coating layers is investigated [10].

2. Fe CONCENTRATION CALCULATIONS

Low-injection diffusion length measurements, made with the Surface PhotoVoltage (SPV) technique, have been used for many years for determining Fe concentrations in silicon. Zoth and Bergholz [11] showed that the Fe concentration is related to the diffusion lengths measured before and after dissociating the FeB pairs via:

$$[Fe] = A \times \left(\frac{1}{L_1^2} - \frac{1}{L_0^2} \right) = C \times \left(\frac{1}{\tau_1} - \frac{1}{\tau_0} \right)$$

Where L_0 and L_1 are the diffusion length and τ_0 and τ_1 the minority carrier lifetime respectively before and after illumination. This expression can also be written in terms of carrier lifetimes, as shown on the right. The critical point is knowledge of the pre-factors A or C (which are related through $A=D_n C$, with D_n the minority carrier diffusion coefficient).

Zoth and Bergholz empirically determined A for the very low injection conditions achieved with SPV, and for the resistivity range 5-15 Ωcm . However, photovoltaic silicon is usually outside this range. It is also desirable to use faster lifetime measurement

techniques that do not require special sample preparation other than surface passivation (such as QSSPC, microwave-PCD, MFCA etc). These techniques must operate at moderate to high injection to overcome minority carrier trapping effects, an artefact that does not affect SPV measurements. At these injection levels the value of A or C is very different.

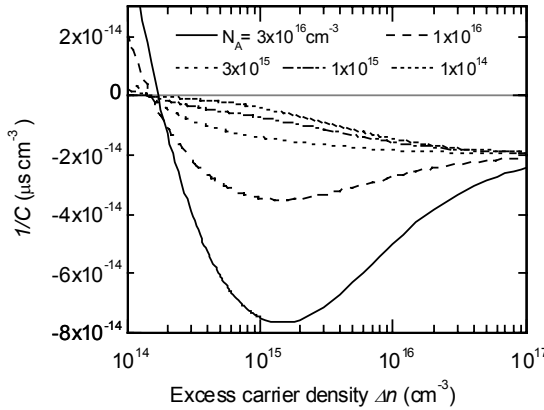


Fig. 1. Values of C for various doping levels

Fortunately, it is straightforward to calculate the factor C for any doping and injection level using the Shockley-Read-Hall model, provided that the recombination parameters are known for both interstitial Fe and FeB pairs. These parameters, specifically the energy level and capture cross sections for electrons and holes, may be found in the literature [12,13]. Fig 1 shows such calculated values for various doping levels.

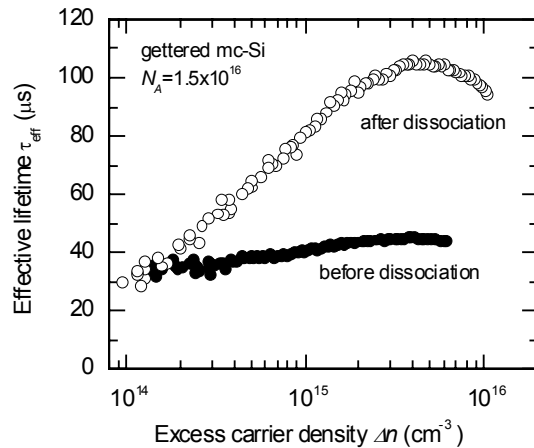


Fig.2. QSSPC lifetime curves before and after FeB dissociation by light soaking.

Fig 2 plots a typical pair of QSSPC lifetime measurements in multicrystalline silicon before and after FeB pair dissociation by light soaking for 5 minutes. Normally, a single value of Δn would be

chosen in order to calculate [FeB] with the corresponding value of C . Fig 3 however shows the resulting values of [FeB] calculated for *each* of the available values of Δn . The fact that the [FeB] values are independent of the choice of Δn gives confidence in the technique.

The uncertainty in [FeB], which is determined by the *difference* of inverse lifetimes, is less for higher values of Δn ($>10^{15} \text{ cm}^{-3}$) where the lifetime curves are further apart. The error bars in Fig. 3, are based on an uncertainty in each lifetime measurement of 10%. From Figs. 2 and 3 it is clear that the statistical error (noise in the equipment) is much smaller than 10% for all but the lowest injection levels. However, there could be hidden systematic errors. For example, there is a trend visible in Fig. 3 of an increase of the calculated FeB concentration with injection level. These uncertainties are roughly represented by assuming a conservative 10% uncertainty in lifetime.

A more detailed description of this method, including justifications for assumptions regarding the extent of dissociation, will be published elsewhere [3].

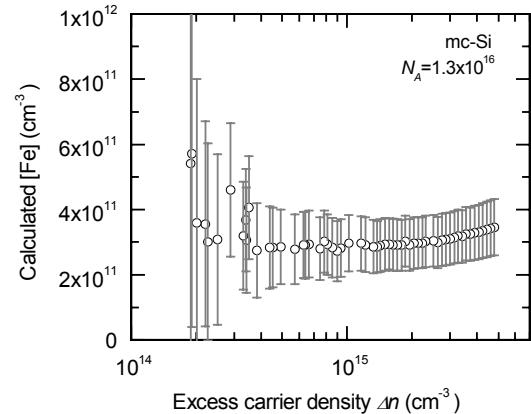


Fig.3. FeB concentration calculated from curves in Fig. 2.

3. HYDROGEN PASSIVATION OF FE

3.a Experiment

Samples were chosen from different positions from bottom to top in the central columns of p-type mc-Si ingots. The concentration of Fe is quite different for those positions due to segregation and solid-state diffusion from the crucible. Four different process schemes A-D (Fig. 4) were used to investigate the effectiveness of hydrogen passivation of FeB. Process A served to

measure the as-cut minority carrier lifetime and the starting FeB concentration in the material. After saw damage removal, a phosphorus emitter was diffused in a belt furnace at 890°C on groups **B** through **D**, resulting in a 45Ω sheet resistance. SiNx layers were deposited by PECVD on the front side of groups **C** and **D**. Wafers in group **D** were also coated with Al at the rear surface. Subsequently, the SiNx coated wafers of groups **C** and **D** were fired with standard metallisation firing-through conditions at ECN. Finally, nitrides, emitters and Al BSF were removed and new surface passivating nitrides deposited on both sides of the wafers. This allowed measurement of the bulk minority carrier lifetime. The measurement of the interstitial FeB concentration was based on the measurement of the minority carrier lifetime as presented in part 2.

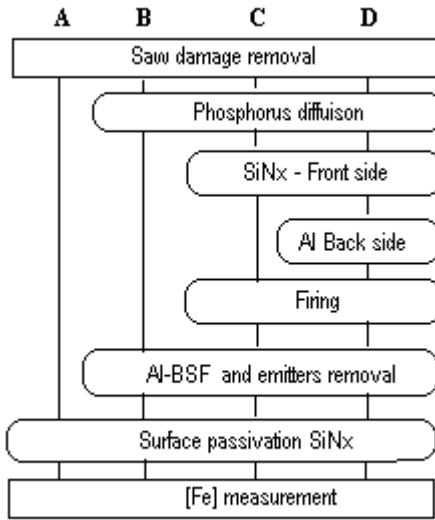


Fig. 4. Schematic of the processing groups

3.b Results

Fig. 5 shows for three different ingots the FeB concentrations in the wafers of group **B** and **C**. The effect of phosphorus gettering (group **B**) is to reduce excessive Fe contamination in top and bottom of ingot (as described previously in [6]). By subsequently firing a SiNx coating (group **C**), the measured FeB concentration is significantly reduced, compared to the concentration after phosphorus gettering. It is unlikely that the rapid firing (only a few seconds above 800°C) has actually strongly changed the FeB concentration. It is more likely that the in-diffused hydrogen has passivated a large fraction of the FeB pairs. Remarkably, the top and bottom wafers of the ingots do not show a clear reduction due to SiNx firing.

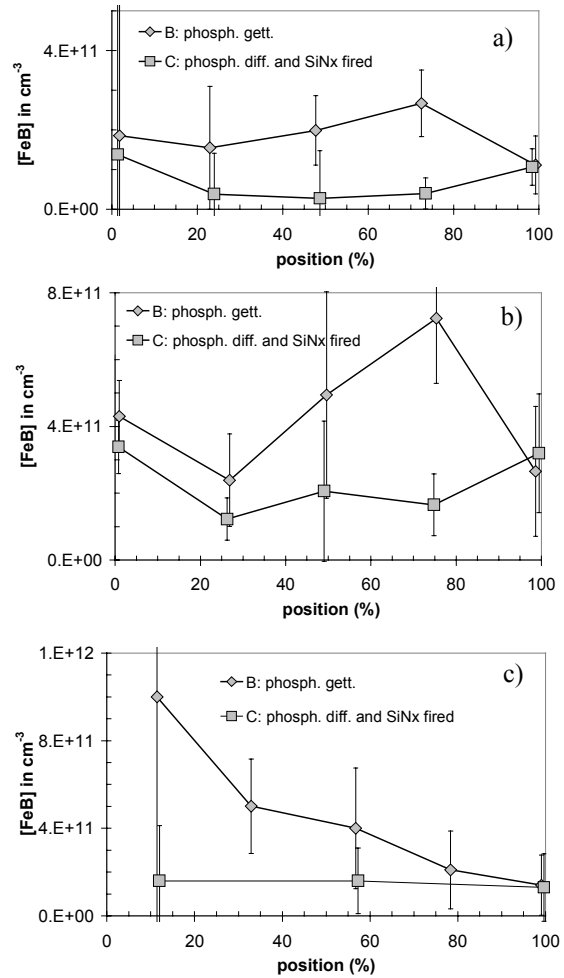


Fig. 5. Reduction of FeB concentration by SiNx firing. Shown are FeB concentrations measured on wafers from three ingots after phosphorus gettering (group **B**) and after phosphorus gettering followed by SiNx coating and firing (group **C**). The ingots are from two different manufacturers. Lines are guides to the eye.

Fig. 6 shows that the reduction of measured FeB concentration is not due to an Al rear side metallisation: The reduction of FeB concentration is not significantly different, whether the Al rear side metallisation is present (**D**) or not (**C**).

In the results of Figs. 5a-b and 6a-b, the emitter diffusion for group **B** was not performed in the same process batch as for groups **C** and **D**. Therefore a varying effectiveness of phosphorus gettering would be an alternative explanation for the difference of [FeB] between **B** and **C/D**. However, in Figs. 5c and 6c all wafers were phosphorus gettered in the same batch. Those results confirm the results of Figs. 5a-b and 6a-b.

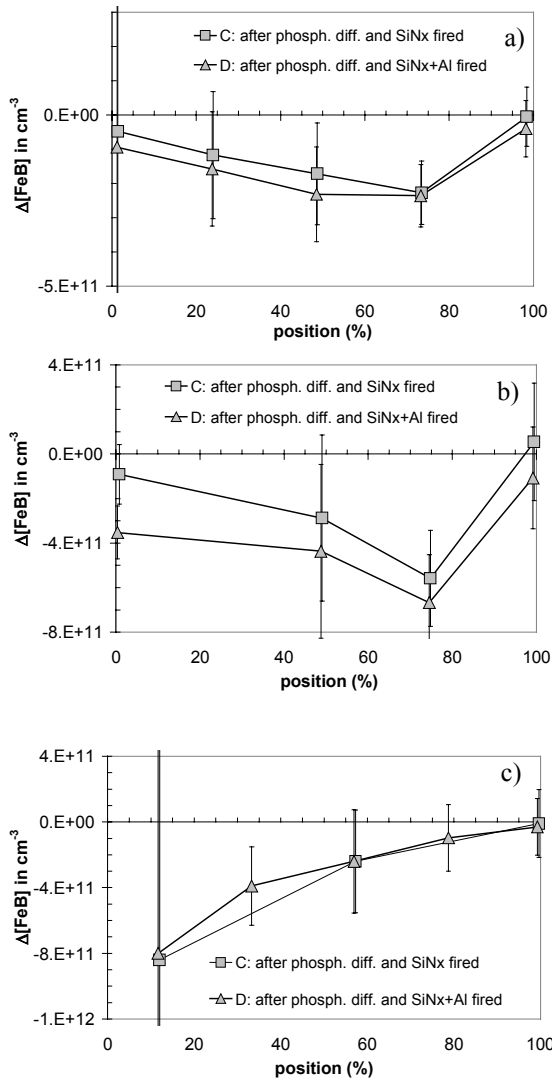


Fig. 6. Effect of Al rear side coating. Shown are changes in concentrations of FeB after firing of SiNx coating, without (C) and with (D) Al rear side metallisation, relative to concentration after phosphorus gettering only. a), b), c) correspond to Fig. 5. Lines are guides to the eye.

Further experiments are in progress to clearly confirm these results, and to apply them to the study of hydrogen passivation.

5. CONCLUSIONS

In conclusion, we have described how lifetime measurements can be applied to the determination of FeB pair concentrations in multicrystalline silicon.

As one application of this technique, we have presented preliminary results which show that FeB can be used as a probe of hydrogen passivation. This opens the way to a new sensitive technique to study

hydrogen diffusion in common multicrystalline materials.

ACKNOWLEDGMENTS

This work has been carried out with financial support of NOVEM (The Netherlands Agency for Energy and the Environment) under contract numbers 146.110-020.1 and 2020.01.13.11.2002. We acknowledge the manufacturers of mc-Si wafers who supplied test material. We acknowledge valuable discussions and assistance from the group members of ECN-solar.

REFERENCES

- [1] L.Jastrzebski, *Electrochim.Soc.*, 614-627 (1990).
- [2] B.O.Kolbesen, D.Palmer, *Fresenius' Journal of Analytical Chemistry* **333** (1989) 561.
- [3] D.Macdonald, L.J.Geerligs, A.Azzizi, subm. to *J. Appl. Phys.* (2003).
- [4] B. Sopori, *J. Electron. Mater.* **31**, 972 (2002).
- [5] C. Ballif, 17th EC-PVSEC, 1818 (2001).
- [6] L.J. Geerligs, 12th NREL workshop on crystalline silicon solar cell materials and processes, 288 (2002).
- [7] H. Dekkers et al., 3rd World Conference on Photovoltaic Solar Energy Conversion, Osaka (2003).
- [8] M. Stavola et al., 3rd World Conference on Photovoltaic Solar Energy Conversion, Osaka (2003).
- [9] M.Kouketsu, S.Isomae, *J. Appl. Phys.* **80** (3), 1485 (1996).
- [10] C.Schetter, H.Lautenschlager, F.Lutz, 13th EC-PVSEC, 407 (1995).
- [11] G.Zoth, E.Bergholz, *J. Appl. Phys.* **67**, 6764 (1990).
- [12] A.A.Istratov, H.Hieslmair, E.R.Weber, *Appl. Phys. A Mat. Sci. Process.* **69** (1999) 143.
- [13] D.Macdonald, A.Cuevas, J.Wong-Leung, *J. Appl. Phys.* **89** (2001) 7932.

Superprism reflector for thin crystalline silicon solar cells

T.M. Montalbo, K. Wada*, L.C. Kimerling

Massachusetts Institute of Technology

Cambridge, MA 02139

Utilization of a superprism reflector to increase crystalline silicon solar cell efficiency to 30% is explored. The superprism structure is based on a cubic lattice of voids in silicon and can be fabricated using interference lithography and anodic oxidation. Progress of a two-dimensional via-hole array formation is described.

The decreasing supplies and increasing consumption of oil, natural gas, and other standard energy resources, coupled with the need to reduce pollution, have led to research on alternative energy sources such as fuel cells, exotic-material batteries, nuclear power, and solar power. One benefit of solar power is that it is a renewable resource and with the advancement of silicon fabrication technology, silicon solar cells gained potential as an option to fossil fuels. Starting with their development at Bell Labs in 1954 and through today, these devices have been the subject of much research and improvement to make the technology marketable.

Typically silicon solar cells are manufactured in three forms: bulk crystalline, thin crystalline, and polycrystalline. Amorphous solar cells are still produced, but they are far less efficient. Conversion efficiencies for the three primary types vary from 16.6 to 24.7% in the lab and from 15 to 18% in the consumer market. [1-3] Since the price of the silicon wafer constitutes around 20-40% of the overall cost of the solar cell, [3] thin crystalline silicon solar cells have an advantage in that they use less material than their counterparts; however, because their active layer averages 20- μm thick, they are also less efficient. To improve this efficiency—and that of solar cells in general—several

modifications to the basic solar cell design (i.e. a *p-i-n* diode) have been proposed, including tandem structures, concentrators, photon quantum confinement, and introduction of impurity states in the bandgap. With these changes, conversion efficiency can potentially reach 74.4% in the case of tandem cells although only 32% has been achieved thus far for a GaInP/GaAs/Ge structure, and up to 26% has been reported for a cell with a concentrator; [1,4] the latter two design proposals among others are currently being researched at the University of New South Wales.

We propose adding a superprism to the back-side of a thin crystalline silicon solar cell as another route to increasing conversion efficiency. Like conventional prisms, superprisms exhibit both dispersion and refraction, but their effects on an incident light beam are far more pronounced. For example, when a light ray directed at a conventional prism is shifted from normal incidence to 7° off-normal, the ray will refract by 4.6°; for a superprism, the ray can bend by as much as 70°. [5] Thus with a superprism, we can redirect light within a solar cell so that it will travel nearly parallel to the plane of the cell instead of reflecting numerous times off the top and bottom surfaces before ultimately escaping without being absorbed.

* Corresponding author: kwada@mit.edu

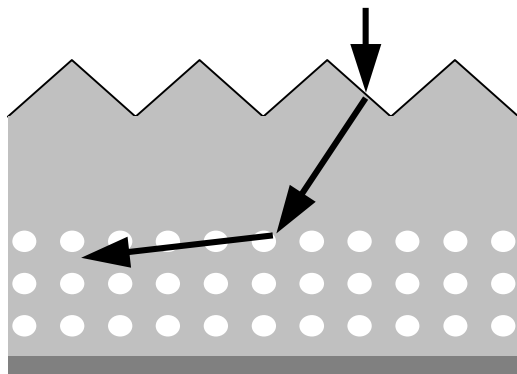


Figure 1 Schematic of solar cell with superprism backside reflector and backside metal contact. Arrows indicate one possible path light entering the cell can travel.

Photonic crystals represent one class of materials that possesses superprism properties. Consequently our design will encompass a thin silicon solar cell with a silicon-air photonic crystal on the backside as the superprism reflector. Light entering the cell will initially be refracted by a Lambertian top surface and, if not absorbed before reaching the cell's back surface, will be refracted even

more by the photonic crystal. (Figure 1) According to the photonic crystal's band structure, some wavelengths will bend more sharply than others; however, by choosing the appropriate unit cell dimensions of the fabricated device, we can tailor the design so that a desired wavelength will experience the greatest amount of refraction to the plane of the solar cell. In our case, we want to refract 1.2- μm light. At this wavelength, which is just below the indirect bandgap of silicon, silicon has an absorption coefficient of 0.074 cm^{-1} meaning that light needs to travel, on average, 13.5 cm before it is absorbed. This path length is on the same order as the size of a standard solar cell so if light travels nearly parallel to the solar cell plane, it will reflect fewer times off the top and bottom cell surfaces and have a better chance of being absorbed than without the superprism backside.

Typically, silicon solar cells are able to absorb wavelengths shorter than 1000 μm . If

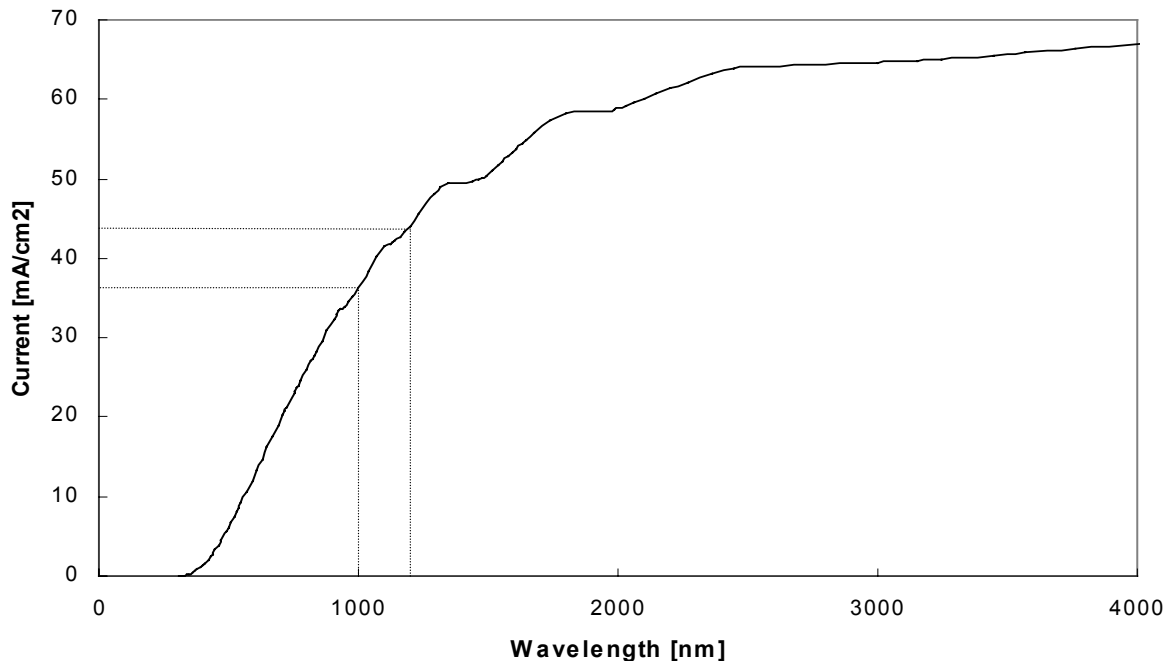


Figure 2 Current generated by a bulk crystalline silicon solar cell exposed to radiation from the AM1.5G solar spectrum. If the maximum wavelength absorbed increases to 1.2 μm , the current generated likewise increases.

each photon absorbed is converted into an electron-hole pair, then the ideal solar cell would be able to produce 36 mA/cm^2 , as illustrated in Figure 2; this corresponds to a conversion efficiency around 25%. On the other hand if a superprism is added to the backside of the solar cell, then the cell would theoretically be able to absorb light up to $1.2 \mu\text{m}$. Again assuming one electron-hole pair is generated per absorbed photon, the current produced would increase to 44 mA/cm^2 and the efficiency to 30%.

To fabricate of the superprism backside for proof of concept, we chose to make a 3D photonic crystal using porous silicon. For growing evenly-spaced pores, we used interference lithography for patterning a mask on n-type silicon and KOH to etch inverse pyramids that served as initiation sites for the pores. Anodic oxidation was used to form the cylindrical pores by illuminating the wafer backside to generate holes which, due to electric field concentration, collected at inverse pyramid tips and allowed oxidation to occur at those specific points. Many other papers describe the anodic oxidation process and the fabrication and characterization of 2D photonic crystals via this process more thoroughly. [6-9]. 3D photonic crystals are fabricated via methods similar to those for 2D crystals and can involve either modulation of the pore diameter by varying illumination intensity or annealing the pores in a hydrogen ambient to form voids. [10-12]

Thus far, our work has focused on fabricating the 2D photonic crystal. The primary challenge in obtaining a good quality structure is the small scale we are working with—specifically, a 390 nm lattice constant. Typi-

cally, the structures described in literature have a minimum period of 500 nm , the spacing needed for a hexagonal lattice to have complete bandgap around $1.3 \mu\text{m}$. [9] In our first few trials, pores were seen to initiate at inverse pyramid tips but due to weak illumination, only appeared randomly across the anodic oxidized region. (Figure 3) Following a model for pore growth in silicon developed by Lehmann [7] has produced promising results, but work still remains to refine of the 2D photonic crystal. Once this is completed, the structure will have to be characterized and its use as a superprism reflector for a solar cell evaluated before the fabrication process for the 3D photonic crystal begins.

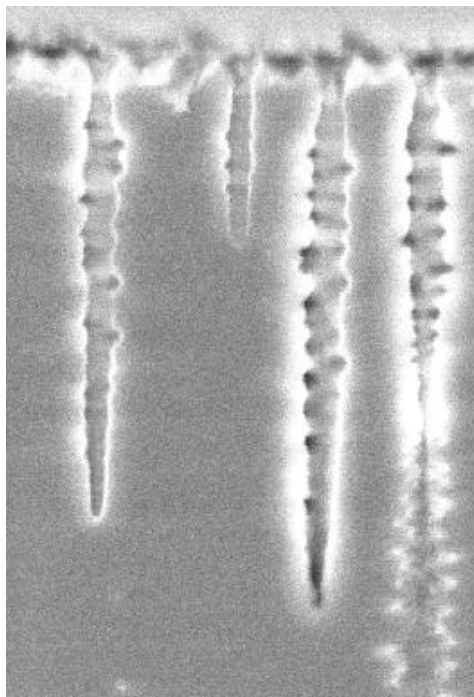


Figure 3 SEM micrograph of a wafer cross-section after porous silicon formation. Inverse pyramids can be seen near the top; many are without pores.

References

- [1] M.A. Green *et al.* (2003) Solar cell efficiency tables (version 22). *Prog. Photovolt: Res. Appl.* **11**, 347.
- [2] National Renewable Energy Laboratory, (2003). *Introduction to photovoltaic systems*. From http://www.nrel.gov/clean_energy/photovoltaic.html
- [3] University of New South Wales (2003). *Thin film solar cells*. From <http://www.pv.unsw.edu.au/info/thininfo.html>
- [4] University of New South Wales, (2001) *Third Generation Photovoltaics Annual Report*.
- [5] H. Kosaka *et al.* (1998) Superprism phenomena in photonic crystals. *Physical Review B*, **58**(16), R10,096.
- [6] V. Lehmann and H. Föll (1990) Formation mechanism and properties of electrochemically etched trenches in n-type silicon. *J. Electrochem. Soc.* **137**(2), 653.
- [7] V. Lehmann (1993) The physics of macropore formation in low doped n-type silicon. *J. Electrochem. Soc.* **140**(10), 2836.
- [8] U. Grüning *et al.* (1995) Two-dimensional infrared photonic band gap structure based on porous silicon. *Appl. Phys. Lett.* **66**(24), 3254.
- [9] S. Rowson *et al.* (1999) Two-dimensional photonic crystals in macroporous silicon: From mid-infrared (10 μm) to telecommunication wavelengths (1.3 – 1.5 μm). *J. Lightwave Tech.* **17**(11), 1989.
- [10] J. Schilling *et al.* (2001) Three-dimensional photonic crystals based on macroporous silicon with modulate pore diameter. *Appl. Phys. Lett.* **78**(9), 1180.
- [11] S.W. Leonard (2002) Complete three-dimensional band gap in macroporous silicon photonic crystals. *Appl. Phys. Lett.* **81**(16), 2917.
- [12] T. Sato *et al.* (2000) Micro-structure transformation of silicon. *Jpn. J. Appl. Phys. pt. 1*, **39**(9A), 5033.

A MONTE CARLO APPROACH FOR ASSESSING THE IMPACT OF MATERIAL AND PROCESS VARIABLES ON SOLAR CELL PERFORMANCE AND MANUFACTURING COST

Alan Ristow and Ajeet Rohatgi

University Center of Excellence for Photovoltaics Research and Education

School of Electrical and Computer Engineering

Georgia Institute of Technology

Atlanta, Georgia 30332-0250

Abstract

In the commercial production of silicon solar cells, variations in material and process parameters lead to variations in the output parameters of the finished cells. This paper presents the initial findings of a statistical model-based study aimed at realistic modeling of the effects on commercial PV module efficiencies that might result from these variations. In this study a Monte Carlo simulation approach is used in conjunction with the commercially available device-modelling program PC1D. It first examines how variations in input parameters collectively affect solar cell output for two different cell designs. A cost analysis model is then used to estimate the manufacturing cost of PV modules produced from each design. Finally, power loss resulting from mismatch between series-connected solar cells is estimated, along with its effect on module manufacturing cost.

1. Introduction

A number of factors affect the efficiency of solar cells produced from multicrystalline silicon (mc-Si) ingots. Variations in bulk lifetime and resistivity as a function of position within the ingot ensure that no two mc-Si wafers are exactly alike. Impurity and defect distributions affect gettering and bulk passivation efficiency, introducing variation in process-induced lifetime enhancement. The grown-in variation in bulk resistivity or surface doping concentration can alter the back surface recombination velocity (S_B) of a cell passivated with a back surface field (BSF) or rear dielectric. Variation in the emitter doping profile and surface quality due to process and material nonuniformities leads to variation in front surface recombination velocity (S_F). Likewise, variation during screen-printing and subsequent firing of front and back contacts can lead to variation in junction leakage, series and shunt characteristics, and S_B .

Typically, modeling with PC1D uses a single set of input parameters to produce a single output data point. This approach is useful in laboratory work, but it fails to account for the input variation observed in commercial settings. This work employs a statistical model, in conjunction with PC1D, to explore the effects of this variation on solar cell efficiency. Manufacturing cost is estimated in selected cases using a cost analysis spreadsheet developed by GT Solar Technologies, Inc. to illustrate the relationship between efficiency and manufacturing cost. It is hoped that this model can be further developed to assess the sensitivity of module manufacturing cost to solar cell input parameters.

2. Methodology

Two mc-Si solar cell designs were considered in this study. The first was a thick cell on a 300- μm substrate with an ohmic back contact. The second was a thin cell on a 175- μm substrate with dielectric back passivation and a screen-printed back surface reflector. All major input parameters were allowed to vary about their mean values in order to estimate the distribution of the solar cell output parameters caused by material and process-induced variations.

In order to achieve this, thirteen inputs were varied in a series of PC1D simulations. The inputs were selected based upon the perceived likelihood that they would vary in a commercial production setting. The inputs selected, along with the mean values assumed and their ranges, are shown in Table 1. For this preliminary study, input values were selected based upon limited knowledge of those that might be observed in a commercial production line. However, they are meant only to demonstrate the methodology presented here, and not to reflect an actual commercial product design. All inputs were uniformly distributed. Strong correlations are known to exist between back surface recombination velocity, S_B , and bulk resistivity, ρ , as well as between bulk lifetime, τ , and ρ ; the correlation coefficients for these pairs were set to -0.9 and $+0.9$, respectively, indicating that S_B decreases rapidly with increasing ρ while τ increases rapidly with increasing ρ . Other correlation coefficients used in this study were -0.9 between front surface recombination velocity, S_F , and sheet resistivity, ρ_S , and $+0.2$ between series resistance, R_S , and ρ_S , indicating a rapid decrease in S_F and slow increase in R_S with increasing ρ_S . As with the input values, the values selected for the correlation coefficients are based on limited knowledge of the true input values.

In order to simulate these variations, the Monte Carlo method was used to select sets of input values. Using simple sampling techniques, initial runs of this model with a small subset of inputs containing no more than four parameters required tens of thousands of samples to fully estimate

Table 1: Input parameter values and their ranges.

Parameter	Value
Series resistance, R_S ($\Omega \cdot \text{cm}^2$)	1.1 ± 0.2
Shunt resistance, R_{SH} ($\Omega \cdot \text{cm}^2$)	750 ± 400
Junction leakage current, J_{02} (nA/cm^2)	5.5 ± 4.5
Substrate thickness, W (μm)	175 ± 5^1
Bulk resistivity, ρ ($\Omega \cdot \text{cm}$)	300 ± 10^2
Bulk lifetime, τ (μs)	1.5 ± 1.0
Front surface recombination velocity, S_F (cm/s)	40 ± 35
Back surface recombination velocity, S_B (cm/s)	$125,000 \pm 25,000$
Emitter sheet resistivity, ρ_S (Ω/sq)	800 ± 600^1
Junction depth, x_j (μm)	$1,000,000^2$
Antireflection coating thickness (nm)	50 ± 5
Broadband reflectance (%)	0.30 ± 0.05
Wafer size (cm)	65 ± 5
	9 ± 2
	12.5 ± 0.5

¹Pertains to thin solar cells.

²Pertains to thick solar cells.

the distributions of the output parameters. This required computation times spanning several days using PC1D, and would have been prohibitively time-consuming using a more complex multidimensional device simulator such as DESSIS. Consequently, a variance-reduction technique called Latin hypercube sampling (LHS) was employed to drastically reduce the number of samples required for complete design characterization [1]. Using LHS, the initial four-parameter results were repeated reliably with as few as 50 samples per design. The results presented in this study are based on 200 samples per design.

While space limitations preclude a complete discussion of LHS, it may be described briefly as a probability-weighted orthogonal sampling method. It partitions each input parameter in such a way as to ensure each sampled value is equally probable. This guarantees the samples are clustered around the most probable value (i.e., the mean, for a normally distributed variable) while simultaneously ensuring extreme values are also sampled. In this way, the entire design space can be explored in a small number of simulations without giving undue weight to improbable parameter values. Several techniques exist for LHS of correlated variables; the one used in this study is described in [2].

The results of the device simulations were used to estimate the manufacturing cost of each design with the aid of a cost analysis spreadsheet based on one provided by GT Solar Technologies, Inc. The cost analysis was based on a plant incorporating 12 HEM multicrystalline silicon ingot-casting furnaces, and nominally rated at 25 MWp/year for solar cell efficiencies of 14%. Costs of equipment and materials were held constant for both cell designs, the only differences being device thickness and efficiency. Module manufacturing costs were estimated using the average efficiency calculated for each design, accounting for the variation in all thirteen variables specified in Table 1. Mismatch losses were estimated using a method due to Bucciarelli [3].

3. Model Results and Analysis

Monte Carlo simulations using LHS naturally produce output in the form of a cumulative density function (cdf), which are shown for each design in Figure 1 along with approximate probability density function (pdf) curves. From these, it is seen that the thin 175- μm design has a substantially higher efficiency than the thick 300- μm design. However, the variance, or spread, in efficiency is greater for the thin design than for the thick one. Table 2 summarizes the efficiency, module manufacturing cost, and factory output for each design. From this, it is seen that the improved back surface passivation and reduced silicon consumption of the thin solar cell design increase average efficiency from 14.0% to 14.8%, an improvement of 0.8% absolute, and reduce module manufacturing cost from \$1.82/Wp to \$1.56/Wp, a cost savings of \$0.26/Wp.

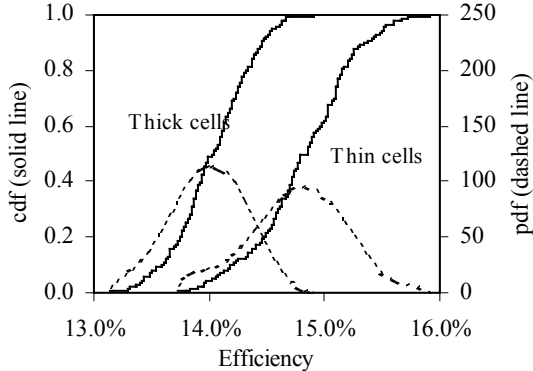


Figure 1: Efficiency distribution curves resulting from Monte Carlo simulation for thick and thin solar cell designs. The pdf curves are approximations.

Table 2: Efficiency, manufacturing cost, and plant volume for two solar cell designs.

	Thick Cells	Thin Cells
Mean efficiency	14.0%	14.8%
Standard deviation	0.3%	0.4%
Manufacturing cost (\$/Wp)	1.82	1.56
Factory output (MWp/yr)	25.4	35.4
Mismatch loss	1.0%	1.2%
Cost with mismatch (\$/Wp)	1.84	1.58

Mismatch losses were estimated at 1.0% for the thick cell design and 1.2% for the thin one, increasing manufacturing cost by \$0.02/Wp for each design. The distribution of output currents calculated in this preliminary study is not as broad as would be expected in a commercial setting; as a result, these mismatch losses are lower than might be observed on an industrial production line.

Device modeling using the Monte Carlo procedure described in this study allows the modeler to estimate minimum and maximum efficiency for a given cell design, as well as the mean efficiency. Furthermore, it allows an estimate of mismatch losses incurred by connecting cells in series during module production. A single run of PC1D on each design using the mean input parameter values produces efficiencies of 14.1% and 14.9% for the thick and thin cell designs, respectively. Comparison with Table 2 reveals that these are slightly higher than the mean values computed from the distributed output data. Information on output distribution and mismatch losses is not available from these two data points.

4. Improving the Model

There is considerable room for improvement in the model presented here. Statistical data from a commercial manufacturing environment would help establish more realistic means, variances, and statistical distributions than those used in this study. This would allow more realistic modeling of the manufacturing process, and would allow the modeler to more readily identify bottlenecks to performance improvement. In addition, further development of this model could aid solar cell designers in gauging the economic impact of specific design changes.

It is clear that this model could be used most effectively in conjunction with an efficient optimization procedure to find the lowest-cost solar cell design for a given set of inputs and constraints. Georgia Tech has such a procedure in the early stages of development, pending improvement and validation of the model presented here.

5. Conclusions

A Monte Carlo model has been developed to investigate the effects of input parameter variations on solar cell output parameters and PV module manufacturing costs. Preliminary results indicate that the model is able to produce probability density functions describing cell output parameters from which module manufacturing costs may be estimated. Validation of the method will depend on obtaining a statistically significant sample of input and output data for real solar cells. Once validated, this technique may be useful in estimating the economic impact of design changes.

Acknowledgements

The authors wish to thank Keith Matthei of GT Solar Technologies, Inc. for providing the cost analysis model and helpful discussions.

References

- [1] M. D. McKay, R. J. Beckman, and W. J. Conover, "A comparison of three methods for selecting values of input variables in the analysis of output from a computer code," *Technometrics*, vol. 21, pp. 239–245, May 1979.
- [2] M. Stein, "Large sample properties of simulations using Latin hypercube sampling," *Technometrics*, vol. 29, pp. 143–151, May 1987.
- [3] L. L. Bucciarelli, Jr., "Power loss in photovoltaic arrays due to mismatch in cell characteristics," *Solar Energy*, vol. 23, pp. 277–288, 1979.

Advances in Screen-Printed High-Sheet-Resistance Emitter Cells

Mohamed Hilali¹, Vichai Meemongkolkiat¹, and Ajeet Rohatgi¹

¹University Center of Excellence for Photovoltaics Research and Education, School of Electrical and Computer Engineering, Georgia Institute of Technology, Atlanta, GA 30332-0250

Abstract

A combination of paste and firing conditions have been developed to achieve good ohmic contacts to $100 \Omega/\text{sq}$. emitters using screen-printing technology. Different dielectric front-surface passivating layers were investigated to take full advantage of the lightly-doped emitter for screen-printed cells. Using an optimum passivation layer and a simple co-firing process in a belt-furnace an absolute efficiency of 17.48% was achieved on untextured $0.6 \Omega\text{-cm}$ FZ Si with an open-circuit voltage (V_{oc}) of 648 mV. The PV168 Ag paste in conjunction with optimum co-firing cycle resulted in a low series resistance of $0.85 \Omega\text{-cm}^2$ and a high fill factor of 0.782 on a $100 \Omega/\text{sq}$. emitter. Higher temperature firing to ensure Ag-Si alloying also reduced the shading losses by shrinking the gridline by ~27%.

Introduction

We have shown elsewhere that appropriate firing of a fritted Ag paste (Dupont PV168) through PECVD (Plasma Enhanced Chemical Vapor Deposition) silicon nitride (SiN_x) on a $100 \Omega/\text{sq}$. emitter can produce good series resistance, blue response, and back-surface field (BSF) [1]. The SiN_x layer serves as an antireflection (AR) coating and surface passivating layer. The front-surface passivation becomes particularly important in the case of high sheet-resistance emitters due to the light doping, which makes the emitter transparent and enhances the impact of the front-surface recombination velocity (FSRV). This paper demonstrates good ohmic contact to $100 \Omega/\text{sq}$. emitter using screen-printing technology and maximizes its benefit by introducing good surface passivation by PECVD SiN_x . The process is simple and manufacturable because screen-printing is used in conjunction with belt co-firing.

Experimental

Silicon solar cells were fabricated on p-type $0.6 \Omega\text{-cm}$ FZ Si in order to enhance the influence of the emitter on V_{oc} . Samples were cleaned and then diffused in a POCl_3 tube furnace to form $100 \Omega/\text{sq}$. emitters with a junction depth of ~0.28 μm . In order to achieve good surface passivation, the samples were coated with different dielectrics including (i) high-frequency (HF) PECVD SiN_x , (ii) low-frequency (LF) PECVD SiN_x , (iii) oxide/HF-PECVD SiN_x stack, and (iv) oxide/LF-PECVD SiN_x stack. In the case of stack passivation, ~80 Å rapid-thermal oxide (RTO) was grown prior to SiN_x deposition. Al was screen-printed on the back and dried at 200°C. The Ag metal grid was screen-printed on SiN_x using PV168 paste from Dupont. All the cells were then co-fired in a lamp-heated belt furnace at a set temperature $\geq 900^\circ\text{C}$. The cells were then isolated using a dicing saw followed by 400°C forming-gas-anneal (FGA) for ~15 min. Solar cells were characterized by IV measurements and spectral response. In addition, Photoconductance Decay (PCD) technique was used to obtain J_{oe} values for the $100 \Omega/\text{sq}$. emitter with different dielectrics after firing in order to decouple the impact of base and emitter region on V_{oc} and cell performance.

Results and Discussion

A. Surface Passivation of $100 \Omega/\text{sq}$. Emitter Due to Different Dielectrics

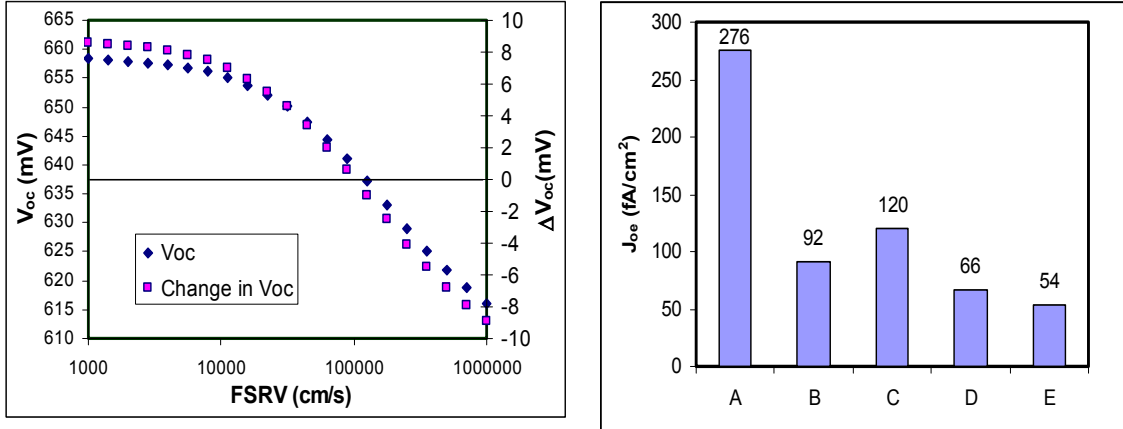


Figure 1. V_{oc} as a function of FSRV on 100 Ω/sq . emitter (left axis). Change in V_{oc} (ΔV_{oc}) for 100 Ω/sq . emitter as compared to a 45 Ω/sq . emitter cell as a function of FSRV (right axis).

Table 1: Notation for different passivating dielectrics used in this study.

Label	Description of Passivating Dielectric
A	HF PECVD SiN _x
B	Stack HF PECVD SiN _x /RTO
C	LF PECVD SiN _x with no NH ₃ clean
D	LF PECVD SiN _x with NH ₃ clean
E	Stack LF SiN _x with NH ₃ clean/RTO

Figure 1 shows the effect of FSRV on V_{oc} of 100 Ω/sq . emitter screen-printed cells. These results were obtained by model calculations using PC1D. Model calculations in Fig. 1 reveal that an FSRV above 25,000 cm/s, V_{oc} starts to decrease rapidly. The improvement in V_{oc} due to the high-sheet-resistance emitter is also shown as a function of FSRV. Notice that the V_{oc} can become worse for the 100 Ω/sq . emitter compared to the 45 Ω/sq . emitter if the front-surface passivation is really bad ($>100,000$ cm/s). Hence, it is crucial to investigate different passivation dielectrics on high-sheet-resistance emitters to achieve better cell performance. Table 1 shows the notation for different dielectrics used in this investigation. Figure 2 shows the J_{oe} values obtained by the PCD measurements [2] for the 100 Ω/sq . emitter passivated with these five dielectrics. J_{oe} is highest for HF-SiN_x (A) and lowest for the LF-SiN_x and stack passivation (D and E, respectively). It is important to note that these J_{oe} measurements reveal the passivation quality of the dielectric without the metal contact.

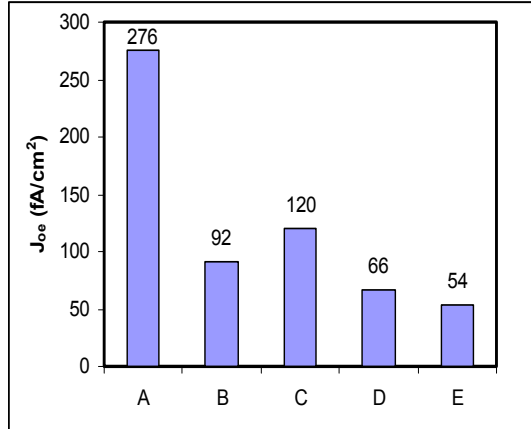


Figure 2. Measured J_{oe} using PCD technique on different passivating dielectrics.

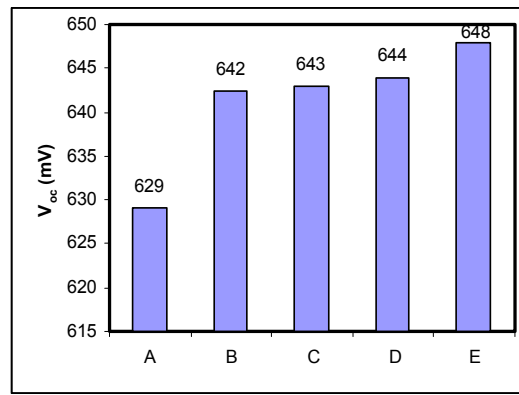


Figure 3. Measured V_{oc} of solar cells with different passivating dielectrics.

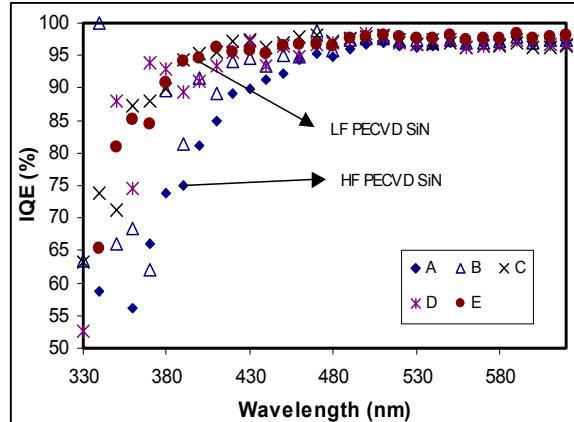


Figure 4. Short-wavelength IQE response of solar cells with different passivating dielectrics.

In order to compare the effect of each passivating dielectric on the cell performance, IV and IQE measurements were performed. Figure 3 shows the V_{oc} of the cells with different passivating

layers. As expected from the J_{oe} measurements, the highest V_{oc} (648 mV) was obtained for the LF-SiN_x/RTO stack and the lowest V_{oc} (629 mV) for the HF-SiN_x. Recall that low resistivity FZ was used to lower the J_{ob} value and make V_{oc} more sensitive to J_{oe} [3]. The measured bulk lifetime of the 0.6 $\Omega\text{-cm}$ FZ Si cells was 250 μs , indicating that high bulk lifetime is maintained during the belt-line processing. IQE measurements showed that the long-wavelength response of the cells was independent of dielectric passivation, however, figure 4 shows that the short-wavelength response was quite sensitive to the dielectric passivation. The best blue response was obtained for passivation layers E and D (LF-SiN_x and stack). The HF-SiN_x passivation exhibited the poorest blue response.

B. Reduction in Shading and Metal Resistivity Compared to Conventional Paste and Firing

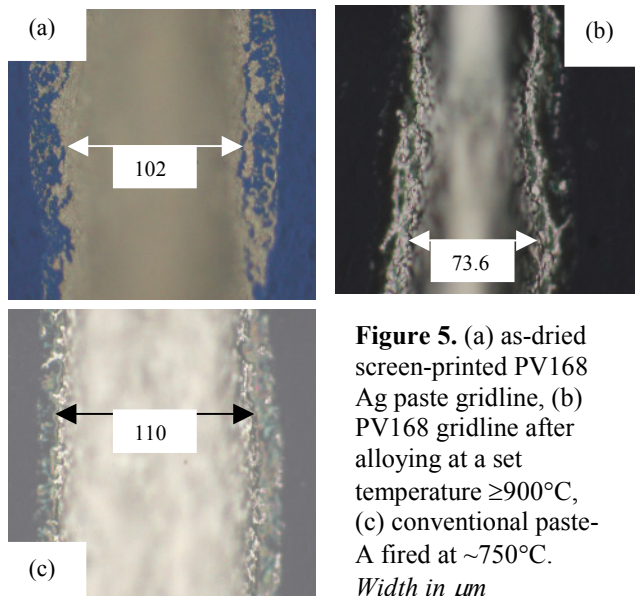


Figure 5. (a) as-dried screen-printed PV168 Ag paste gridline, (b) PV168 gridline after alloying at a set temperature $\geq 900^\circ\text{C}$, (c) conventional paste-A fired at $\sim 750^\circ\text{C}$.
Width in μm

The gridline width was $\sim 110 \mu\text{m}$ for paste A after the conventional firing between 700-800°C.

Figure 5 shows magnified images of (a) as-dried screen-printed PV168 Ag gridline, (b) alloyed PV168 gridline, and (c) conventional paste-A gridline fired at $\sim 750^\circ\text{C}$, which is below the Ag-Si eutectic temperature. The PV168 paste was alloyed using fast firing in the belt-line furnace at a set temperature $\geq 900^\circ\text{C}$. It was found that the metal resistivity of paste-A Ag grid was $\sim 2.8 \mu\Omega\text{-cm}$ while the resistivity of the alloyed PV168 Ag grid was $\sim 1.9 \mu\Omega\text{-cm}$, which is quite close to the resistivity of pure Ag ($1.7 \mu\Omega\text{-cm}$). The alloyed PV168 Ag grid shrank from $\sim 102 \mu\text{m}$ to $\sim 74 \mu\text{m}$ after firing which amounts to a 27% reduction in gridline width. This is consistent with the more compact structure and lower metal resistivity of the PV168 grid. The

C. High Efficiency Screen-Printed Cells on 100 Ω/sq . Emitter with Optimized Front-Surface Passivation and Grid Design

In addition to the optimization of the surface passivation, grid design was also optimized for the 100 Ω/sq . emitter. Table 2 shows the improvement in cell performance due to better front-surface passivation along with the improvement due to optimal grid design. On the 100 Ω/sq . emitter, a high FF of 0.782 was achieved for the LF-SiN_x passivating layer and 0.777 for the stack passivation. The LF-SiN_x passivated cell had a V_{oc} of 643 mV, which is significantly higher than the HF-SiN_x passivated cell with a V_{oc} of 629 mV. This enhancement in V_{oc} is in good agreement with the J_{oe} measurements. In the case of the bad passivation using HF-SiN_x, the V_{oc} for the 45 Ω/sq . emitter was 635.8 mV, which is greater than that for the 100 Ω/sq -emitter cell (629.3 mV). These results agree with the model calculations in figure 1, which show that the V_{oc} of a low sheet-resistance-emitter cell can be higher than that of a high-sheet-resistance emitter cell in the case of bad passivation. Moreover, by optimizing the gridline spacing (0.2 cm instead of 0.24 cm) for the 100 Ω/sq . emitter, the series resistance dropped to 0.85 $\Omega\text{-cm}^2$ as compared to 1.06 $\Omega\text{-cm}^2$ and the FF increased from 0.771 to 0.782. Notice that in this study, very high fill factors of 0.793 were achieved on the conventional 45 Ω/sq .-emitter cell. By considering LF- SiN_x only,

Table 2 shows that the short-circuit current (J_{sc}) was highest for the stack passivation (34.69 mA/cm^2) followed by the SiN_x passivation only (34.48 mA/cm^2). The J_{sc} was lowest for the $45 \Omega/\text{sq}$. (34.07 mA/cm^2). The V_{oc} showed the same trend. Consequently, the well-passivated high-sheet-resistance emitter gave 0.2% improvement in the absolute efficiency over the conventional $45 \Omega/\text{sq}$. emitter, in spite of the slightly lower FF. Figure 6 shows that the short-wavelength IQE of the $100 \Omega/\text{sq}$ -emitter cell is superior to that of the $45 \Omega/\text{sq}$ -emitter cell. At 410 nm, the IQE was 82.38% for $45 \Omega/\text{sq}$. emitter compared to 92.137% for the LF- SiN_x passivated $100 \Omega/\text{sq}$. emitter. All these improvements resulted in 17.5% efficient screen-printed planar cells on FZ Si with $100 \Omega/\text{sq}$. emitters.

Table 2: Cell IV data for the 45 and $100 \Omega/\text{sq}$. emitters showing performance improvement due to passivation and grid design. PV168 Ag paste is used in all the cases.

Front Passivation	Grid Design	Emitter	V_{oc} (mV)	J_{sc} (mA/cm^2)	FF	Eff (%)	n factor	R_s ($\Omega\cdot\text{cm}^2$)	R_{sh} ($\Omega\cdot\text{cm}^2$)
HF PECVD SiN	Optimized	45	635.8	33.32	0.788	16.70	1.01	0.762	8572
LF PECVD SiN	Optimized	45	637.5	34.07	0.793	17.22	1.07	0.696	38,453
HF PECVD SiN	Unoptimized	100	629.3	34.2	0.774	16.67	0.99	1.08	10,875
LF PECVD SiN	Unoptimized	100	643.0	34.49	0.771	17.10	1.03	1.065	496,500
LF PECVD SiN	Optimized	100	646.1	34.48	0.782	17.42	1.08	0.854	131,404
Stack (LF SiN/RTO)	Optimized	100	648.4	34.69	0.777	17.48	1.08	0.919	75,306

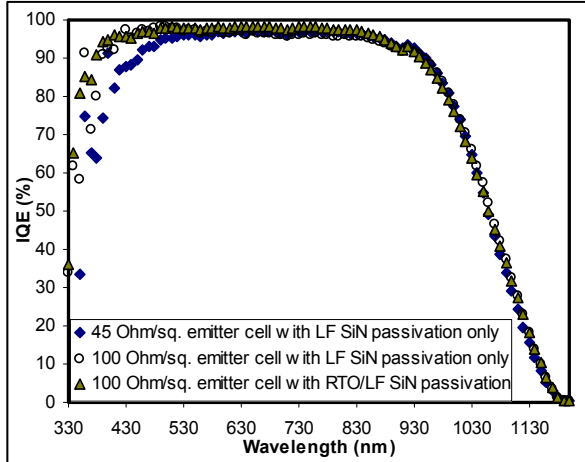


Figure 6: IQE response for the $45 \Omega/\text{sq}$. and $100 \Omega/\text{sq}$. emitter solar cells with LF- SiN_x and stack RTO/LF- SiN_x passivation.

appreciable improvement in the blue-response over the conventional $45 \Omega/\text{sq}$. emitter, resulting in 0.2% improvement in absolute efficiency in spite of slightly lower FF. Somewhat lower emitter sheet resistance ($80-100 \Omega/\text{sq}$) are now being investigated to recover the FF loss without sacrificing the blue response.

Conclusion

In this paper, high quality screen-printed contacts were achieved on $100 \Omega/\text{sq}$. emitters using PV168 Ag paste and rapid co-firing in the belt furnace. Different emitter passivating dielectrics were investigated. Low-frequency SiN_x and the stack passivation with RTO/ SiN_x were found to be very effective, resulting in a V_{oc} of 648 mV . Using this simple and fast contact co-firing scheme using the PV168 paste, FFs of 0.793 were achieved on $45 \Omega/\text{sq}$. emitters and 0.782 on $100 \Omega/\text{sq}$ emitters. In addition, the alloyed PV168 paste showed ~27% shrinkage after firing, resulting in gridline width of $74 \mu\text{m}$. The $100 \Omega/\text{sq}$. emitter also showed an

References

- [1] M. Hilali, J.-W. Jeong, A. Rohatgi, D. L. Meier, and A. F. Carroll, "Optimization of Self-Doping Ag Paste Firing to Achieve High Fill Factors on Screen-Printed Silicon Solar Cells with a $100 \Omega/\text{sq}$. Emitter," *Proc. of the 29th IEEE PVSC*, New Orleans, May 2002, pp.356-359.
- [2] D. MacDonald, A. Cuevas, "Trapping of Minority Carriers in Multicrystalline Silicon," *Appl. Phys. Lett.*, **vol. 74**, no. 12, 1999, pp. 1710-1712.
- [3] A. Rohatgi, M. Hilali, D. L. Meier, A. Ebong, C. Honsberg, A. F. Carroll, and P. Hacke, "Self-Aligned Self-Doping Selective Emitter for Screen-Printed Silicon Solar Cells," *Proc. of the 17th European Solar Energy Conference*, Munich, 2001, pp. 1307-1310.

RECORD HIGH EFFICIENCY SCREEN-PRINTED BELT CO-FIRED CELLS ON EFG Si RIBBON (16.1%) AND HEM mc-Si (16.9%)

A. Upadhyaya¹, K. Nakayashiki¹, M. Hilali¹, A. Rohatgi¹, J. Kalejs², B. Bathey², K. Matthei³

¹University Center of Excellence for Photovoltaic Research and Education, School of Electrical and Computer Engineering, Georgia Institute of Technology, Atlanta, GA 30332

²RWE Schott Solar, Inc. 4 Suburban Park Dr. Billerica, MA 01821

³GT Solar, 243 Daniel Webster Hwy, Merrimack, NH 03054

ABSTRACT

Record high efficiency screen-printed solar cells have been fabricated on EFG Si ribbon as well as on HEM mc-Si. These cells were fabricated using a simple manufacturable process involving POCl_3 diffusion for emitter and rapid co-firing of Ag grid and Al-BSF in a belt furnace. This resulted in very effective defect passivation and good contacts with low series resistance and junction leakage. Average bulk lifetimes in the range of 80 – 100 μs were achieved after cell processing along with Fill Factors of ~0.78. The EFG Si cells were fabricated on a $95 \pm 5 \Omega/\text{sq}$. emitter while the HEM mc-Si cells were fabricated on $45 \pm 5 \Omega/\text{sq}$. emitter. A combination of good ohmic contacts, effective back surface field and high bulk lifetimes resulted in record high 16.1% efficient screen-printed cells on EFG Si and 16.9% on HEM mc-Si.

High Efficiency Screen-printed Selective Emitter Cells on EFG Silicon

EFG Si ribbon is a promising material for low-cost and high-efficiency solar cells because it eliminates the need for mechanical sawing and damage etching. As a result, there is no kerf loss. However, like most low-cost mc-Si materials, the EFG material also has high impurity concentrations and crystalline defect density. The as-grown minority-carrier lifetime in EFG is quite low, normally less than 3 μs , which is not sufficient for high efficiency cells. It is essential to enhance the bulk minority-carrier lifetime of EFG during cell fabrication in order to obtain high efficiency cells (>15%). This paper reports on the implementation of a fast co-firing process for front and back contacts which significantly enhances the bulk lifetime in EFG and simultaneously produces high quality screen-printed contacts on high-sheet-resistance ($95 \pm 5 \Omega/\text{sq}$) emitter. The process is very simple, manufacturable, and capable of producing high efficiency screen-printed cells.

Figure 1 shows the progress of screen-printed or pad-printed silicon ribbon solar cells. Previous record of 15.9% involved a two-step firing in an RTP system using $45 \pm 5 \Omega/\text{sq}$. emitter.¹ In this paper, 16.1% efficient 4 cm^2 cells were achieved by a co-firing process on a $95 \pm 5 \Omega/\text{sq}$. emitter using screen-printing technology and a belt line furnace. A simple $n^+ - p - p^+$ cell design was used in conjunction with 2-3 $\Omega\text{-cm}$, 300 μm thick EFG Si grown at RWE Schott Solar, Inc. Cell fabrication involved phosphorus diffusion in a POCl_3 furnace to form $\sim 100 \Omega/\text{sq}$. emitter. A SiN_x AR coating with an average refractive index of ~ 2.04 and thickness of $\sim 760 \text{ \AA}$ was deposited on top of the n^+ emitter in a commercial low-frequency plasma enhanced chemical vapor deposition (PECVD) reactor. A commercial Al paste was printed on the entire backside and dried at 200°C. The front-metal grid was then screen-printed on top of the SiN_x AR coating using PV168

Ag paste from DuPont Corporation. The sample was then co-fired rapidly in a three-zone lamp-heated belt-furnace at set temperature $\geq 875^{\circ}\text{C}$ and belt speed $>80\text{ipm}$ to form the Al back-surface field (BSF) and front grid metallization, simultaneously. The firing process is similar to the one reported in [2] involving fast ramp-up and cooling rates to promote and enhance PECVD SiN_x-induced hydrogen passivation of defects in EFG Si.^{3,4} Finally, cells were annealed in forming gas at 400°C for 15 min.

Fig.2 shows the lighted I-V data for the 16.1% efficient EFG Si cell (verified by National Renewable Energy Laboratory). This cell had an open-circuit voltage (V_{oc}) of 601.5 mV, short-circuit current (J_{sc}) of $\sim 35.0 \text{ mA/cm}^2$, and a fill factor (FF) of 0.764. Moreover, the average cell efficiency was 15.73% with a standard deviation of 0.28%. This firing scheme achieved a low contact resistance value of $0.77 \Omega\text{-cm}^2$ on $95 \Omega/\text{sq}$. emitter while reducing the junction shunting resulting in a FF of ~ 0.764 . The fast contact co-firing in the belt-furnace helped in achieving very effective defect hydrogenation. This is supported by very high average lifetime of $\sim 103 \mu\text{s}$ in EFG Si with standard deviation of $43 \mu\text{s}$. In addition, Figure 3 shows the improvement in the short wavelength response due to the lightly doped emitter compared to the conventional $45 \Omega/\text{sq}$. emitter cell. All these improvements contributed to the record high efficiency (16.1%) EFG Si cell.

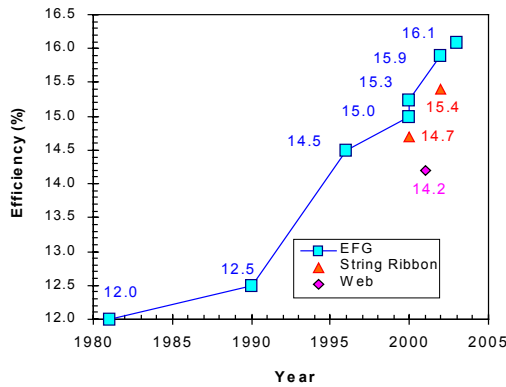


FIG. 1. Efficiency progress of silicon ribbon solar cells

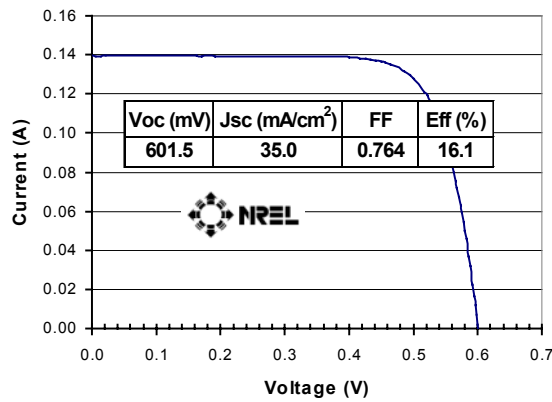


FIG. 2. I-V data for the record high 16.1% efficient screen-printed EFG solar cell, verified by NREL

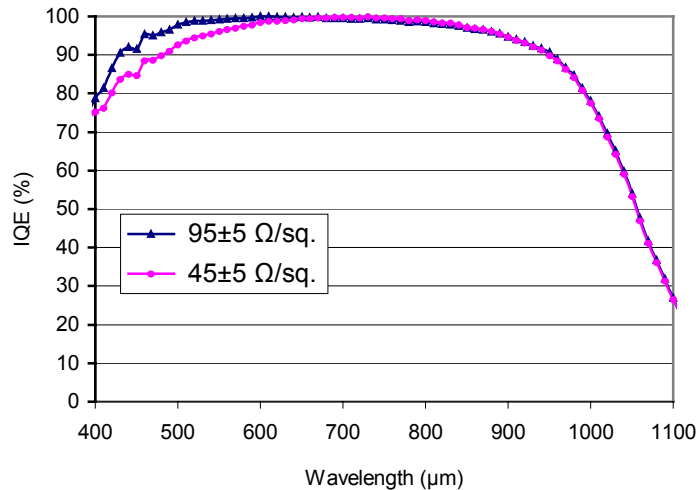


FIG. 3. IQE analysis of EFG solar cell with $95 \Omega/\text{sq.}$ and $45 \Omega/\text{sq.}$ emitters

High Efficiency Screen-printed Cells on HEM mc-Si

Like EFG Si ribbon, HEM mc-Si grown by a cast technique is also a promising low-cost material for cost effective PV. HEM is widely used in industry with commercial cell efficiency in the range of 13.5 – 15.0%. Efficiencies as high as 16.6% have been reported on 156cm^2 cast mc-Si material using screen-printing, single layer SiN_x AR coating, isotropic texturing and selective emitter.⁵ In this paper, we report on 4 cm^2 16.9% screen-printed, belt co-fired cells with single layer SiN_x AR coating. These cells do not have any texturing, double layer AR coating, or selective emitter. Process is simple and manufacturable involving POCl_3 diffusion to form $45 \Omega/\text{sq.}$ emitter, followed by SiN_x AR coating on the front, Ag grid printing on the front using commercial paste from DuPont Corp., Al screen-printing on the back, and a rapid firing in the belt furnace. Finally, cells are annealed at $400^\circ\text{C}/15$ min in forming gas.

Figure 4 shows the cell data for the 16.9% efficient HEM cell, tested and verified by NREL. This cell had an open circuit voltage of 627mV, short circuit current of 34.7mA/cm^2 , and fill factor of 0.777. Nine 4 cm^2 cells on a large area wafer had an average efficiency of 16.5%.

Hydrogenation from low frequency PECDV SiN_x played an important role in efficiency enhancement. This is reflected in the long wavelength IQE response of the HEM cells with high frequency (13.6MHz) and low frequency (50kHz) PECVD SiN_x . Low frequency SiN_x significantly improves the long wavelength response of the cells. This is attributed to the effective hydrogenation of defects due to rapid firing in conjunction with the use of low frequency SiN_x . PCD lifetime measurements showed that the $20 - 40 \mu\text{s}$ as-grown lifetime in the HEM mc-Si increased to $\sim 100 \mu\text{s}$ after the cell processing.

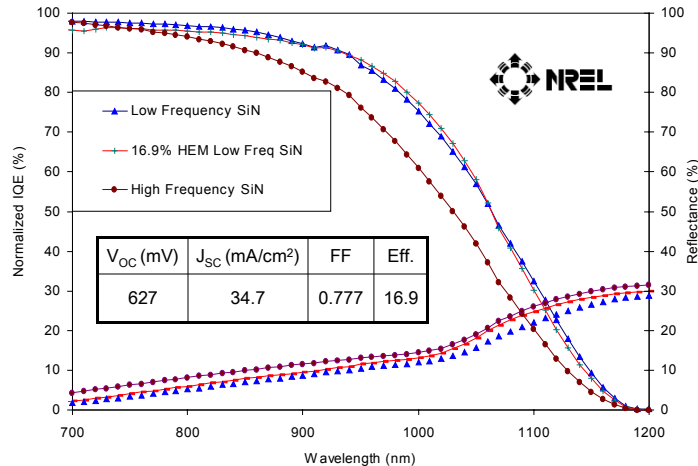


FIG. 4. Cell data of record high efficiency (16.9%) screen-printed HEM mc-Si cell, verified by NREL, and a comparison of IQE of HEM cells with low- and high-frequency SiN_x

Conclusions

Record high efficiency screen-printed solar cells have been achieved on EFG Si (16.1%) and HEM mc-Si (16.9%). This is the result of appropriate rapid co-firing of Ag grid, Al-BSF, and SiN_x AR coating which results in very effective defect hydrogenation, good back surface field, and high quality screen-printed contacts. Bulk lifetimes approaching 100 μ s were achieved with fill factors of ~0.78.

References

- ¹Ajeet Rohatgi and Ji-Weon Joeng, *J. Appl. Phys.*, 82, 224 (2003)
- ²M. Hilali, J. W. Jeong, A. Rohatgi, D. L. Meier, and A. F. Carroll, *Proceedings of 29th IEEE Photovoltaic Specialists Conference*, New Orleans, LA, 2002, (IEEE, New York, 2002), p.356
- ³A. Rohatgi, V. Yelundur, J. Jeong, A. Ebong, M. D. Rosenblum, and J. I. Hanoka, *12th International Photovoltaic Science and Engineering Conference*, Jeju, S. Korea, 2001, 23-1 (invited paper)
- ⁴J. Jeong, Y. H. Cho, A. Rohatgi, M. D. Rosenblum, B. R. Bathey, and J. P. Kalejs, *Proceedings of 29th IEEE Photovoltaic Specialists Conference*, New Orleans, LA, 2002, (IEEE, New York, 2002), p.250
- ⁵J. Szlufcik, F. Duerinckx, E. V. Kerschaver, J. Nijs, *Proceedings of 17th European Photovoltaic Solar Energy Conference*, Munich, Germany, 2001, pp. 1271-1276

Record High Efficiency Solar Cells on EFG(18.2 %) and String Ribbon(17.8 %) Silicon by rapid thermal processing

D.S.Kim, K.Nakayashiki, V.Yelundur, B.Rounsville, A.Rohatgi, *A.M.Gabor,

**B.R.Bathey, **J.P.Kalejs

University Center for Excellence in Photovoltaic Research and Education; School of Electrical and Computer Engineering, Georgia Institute of Technology, Atlanta, GA 30332 USA

*Evergreen Solar Inc., 259 Cedar Hill St., Marlboro, MA 01752 USA

**ASE Americas, Inc. 4 Suburban Park Dr., Billerica, MA 01821 USA

Abstract

Record high silicon ribbon solar cell efficiencies of 18.2 % and 17.8 % were achieved on EFG and String Ribbon silicon, respectively. These cells were fabricated with photolithography front contacts and double layer antireflection coating. Improved understanding and hydrogenation of defects in these promising low-cost ribbon materials contributed to the significant increase in bulk lifetime from 1-5 μ s to as high as 90-100 μ s during cell processing. It was found that SiN_x-induced defect hydrogenation in these ribbon materials takes place within one second at peak temperatures of 740-750 °C. In fact, bulk lifetime decreases with the increase in annealing temperature above 750 °C or annealing time in excess of one second due to the enhanced dissociation of the hydrogenated defects coupled with the decrease in hydrogen supply from the SiN_x film.

Introduction

Silicon ribbons such as String Ribbon and Edge-defined Film-fed grown (EFG) ribbon reduce both feedstock consumption and wafering cost since they are grown directly in the form of ribbon from a silicon melt^{1,2}. Ribbon wafers generally contain more point defects and higher dislocation density (10^5 - 10^6 /cm²) due to larger temperature gradient during the growth compared to the widely used ingot materials (HEM, CZ)³. This results in much lower as-grown bulk lifetimes in the range of 1-6 μ s in ribbon materials, which are not sufficient for high efficiency cells. Therefore, quality enhancement during cell processing is necessary to compete with other materials.

In spite of low as-grown lifetime, efficiencies of ribbon solar cells are approaching 13-15 % in production and 15-16 % in the laboratory due to bulk lifetime enhancement during cell processing⁴. In the past, high efficiency screen-printed silicon ribbon solar cells have been fabricated by optimizing rapid thermal processing (RTP) cycles to improve SiN_x-induced hydrogenation of bulk defects and quality of back surface field^{5,6}. These cells were fabricated by a two step process where the first step is used to form an effective Al BSF and provide Al-enhanced defect hydrogenation. The second firing step is performed at lower temperature (< 800°C) to form screen-printed Ag grid on the front. However, the latter step could degrade hydrogen passivation achieved in step one due to evolution of hydrogen from the defects. While hydrogen is found to be introduced into silicon⁷ due to the annealing of SiN_x AR coating, it is not clear how much and how fast the hydrogen diffuses into the underlying defective as-grown wafer because the diffusion mechanism can be influenced by temperature, defect type and concentration, doping concentration and conductivity type^{8,9,10,11}.

Recently, record high efficiency EFG(16.7%) and String Ribbon(17.7%) cells were reported by Hahn et. al. using photolithography contacts, thermal oxidation for front surface passivation, Al gettering for 30 min, ZnS/MgF₂ for double layer anti-reflection (DLAR) coating, and 60 min

microwave-induced remote hydrogen plasma (MIRHP) for defect passivation¹². This paper reports on further enhancement in these cell efficiencies using rapid gettering and hydrogenation, endorsing the potential of these materials for photovoltaic applications. We used industrial type SiN_x for surface and bulk defect passivation in addition to the first layer of the SiNx/MgF₂ double layer AR coating. Furthermore, defect hydrogenation and Al BSF formation were achieved simultaneously in one second by rapid thermal annealing at ~750 °C. Front contacts were formed by evaporation and photolithography which involve no additional heat treatment to prevent any subsequent dehydrogenation of defects. Record high efficiencies achieved in this study on ribbon materials are attributed to improved understanding and effective hydrogenation of defects by minimizing their dehydrogenation.

In this study, an RTP system was used for annealing the SiN_x coated samples with screen printed Al paste on the back because it can control (a) temperature ramp-up rate, (b) annealing time and temperature, and (c) cool-down rate, independently and accurately. It is shown that these features are important because hydrogenation is a very rapid process and shorter the hydrogenation cycle at ~750°C more effective it gets.

Experimental

String Ribbon and EFG samples used in this study had an average thickness of 300 μm and resistivity of 3 Ωcm. P-type EFG ribbon was grown at ASE Americas while String Ribbon was grown at Evergreen Solar, respectively. The phosphorus diffusion was performed using a liquid POCl₃ source in a tube furnace to obtain an 85 Ω/□ n⁺-emitter. SiN_x film with a thickness of 78 nm and index of 2.0 was deposited in a commercial low-frequency PECVD reactor on the phosphorus-diffused emitter. Aluminum paste (Ferro FX 53-038) was screen-printed on the back surface of the wafers. The SiN_x on the front and the Al on the rear were fired simultaneously in an RTP chamber to enhance hydrogen passivation. The ramp-up and cooling rates were set to greater than 50 °C/sec to achieve a uniform Al-BSF layer and provide good hydrogenation. The firing temperatures were varied from 700 to 800 °C^{13,14} and firing time from 1 to 60 seconds to understand and optimize the hydrogenation of defects and quality of BSF simultaneously. The front metal grid was defined by a photolithography process involving etching of the SiN_x film in BOE (buffered oxide etchant). Front contacts were then formed by evaporating 60 nm Ti, 40 nm Pd and 60 nm Ag followed by a lift-off process. Additional Ag was plated to increase the grid thickness to ~8 μm and reduce the series resistance to ~ 0.5 Ω·cm². Nine 4 cm² cells were fabricated on each wafer and isolated using a dicing saw followed by a 30 min forming gas anneal at 400 °C. In order to minimize the reflectance, the SiN_x thickness was adjusted to 67.8 nm and capped with 99.5 nm magnesium fluoride film by vacuum evaporation to form a DLAR, which reduced the integrated front surface reflectance to ~ 6.19 %.

Results and Discussion

Fig.1 shows the progress in efficiency of ribbon solar cells with photolithography contacts. Data for Dendritic Web and EFG cells with photolithography (PL) contacts is limited. Cell efficiencies of ~ 17 % have been reported on Dendritic Web Si in the past whereas relatively steady progress has been made on String Ribbon cells with PL contacts with maximum efficiency of 16.2 % in 2001. This paper reports on record high efficiencies of 18.2 % on EFG and 17.8 % on String Ribbon. These 4 cm² cells were tested and verified by NREL, demonstrating the potential of these ribbon materials.

Fig. 2 shows the process-induced lifetime enhancement in these materials. The as-grown bulk lifetime was in the range of 2-5 μs, which increased to 4-15 μs range after the 85 Ω/□

phosphorus emitter diffusion. The bulk lifetime improved significantly after the SiN_x/Al co-firing in the RTP chamber without the need for any additional or extra gettering step. In this study, lifetime enhancement was found to be very sensitive to the co-firing time and temperature. Average bulk lifetime increased from 4.5 μs to 73.7 μs in String Ribbon and from 3 μs to 95 μs in EFG with only one second RTP firing at ~ 750 °C. One second firing maintained bulk lifetime over 50 μs even at 800 °C whereas bulk lifetime dropped rapidly to 33 μs at 750 °C for 60 second firing. This indicates that hydrogen diffusion into silicon and bulk defect passivation by the hydrogen take place in a very short time. Optimum co-firing condition was found to ~750°C/1s. Fig.2 clearly shows that defect passivation or bulk lifetime enhancement degrades at higher co-firing temperature (>750 °C) or longer time (>1 second). The low starting lifetime in String Ribbon and EFG Si is the result of high dislocation density and metal impurities¹⁵. It has been reported that hydrogenated metal defects dissociate during high temperature annealing with activation energies in the range of 2.2~2.5 eV¹⁶. This can give rise to deep levels. The dissociation energy for the hydrogenated dislocation related Si-H bonds reported to be 2.6~3.5 eV¹⁷. Therefore, if hydrogen diffusion or supply into the silicon stops, the fraction of reactivated defects (N/N₀) can be described by the equation¹⁸

$$\frac{N}{N_0} = 1 - \exp[-t\nu \exp(-E_d / kT)] \quad (1)$$

where t is the annealing time, ν is attempt frequency($10^{13}\sim10^{14}$ /s), E_d is the activation energy for the reactivation process and T is the temperature. Calculations reveal that 63 % of passivated metal defects can re-activated in just 0.055 second at 740 °C assuming ν = 5×10^{13} /s and E_d = 2.5 eV. In contrast, it should take 53 second to re-activate 63 % of the hydrogenated dislocations, using an activation energy of ~3.1 eV and ν = 5×10^{13} /s. In order to maximize the bulk lifetime, the dehydrogenation process should be quenched after the defects are saturated with hydrogen. It has been shown that the Si-H concentration in the SiN_x film decreases rapidly within 20 seconds down to the detection limit at temperatures above 700 °C¹⁹ while the N-H concentration decreases rapidly followed by a slower decrease. This suggests that the supply of hydrogen from the SiN_x film or the hydrogen flux into the silicon decreases rapidly within the first 20 seconds and then decrease slowly. However, the activation of defect continues with time and it's rate increases with temperature (equation 1). This explains the observed decrease in bulk lifetime with the increase in firing time or temperature (Fig.2). In order to support the rapid activation rate, we removed the SiN_x film after the hydrogenation at 740°C/1s to stop the hydrogen supply and then re-annealed the sample at 740 °C. We found that in the absence of hydrogen supply it only took 2 seconds to activate the defects and the lifetime dropped from 74 μs to 9 μs.

Based on the above understanding and experimental data, optimum hydrogenation conditions (~750 °C/1s) were used (Fig.2) to fabricate ribbon cells. Fig.3 shows the light I-V characteristics of the record high efficiency cells achieved on EFG and String Ribbon silicon. The 18.2 % cell on EFG and 17.8 % cell on String Ribbon were tested and verified by NREL. The cells had Voc of ~620 mV and FF of 0.78. The J_{sc} for EFG and String Ribbon were of ~ 37 mA/cm² and 36.8 mA/cm², respectively. These results are consistent with very high bulk lifetimes approaching 100 μs and double layer AR coating.

In conclusion, ribbon silicon solar cells with efficiency of 18.2 % on EFG and 17.8 % on String Ribbon were achieved, supporting the potential of ribbon materials. It was found that effective defect hydrogenation in ribbon materials takes place within 1 second at 740~750 °C. Bulk lifetimes approaching 100 μs were achieved. The bulk lifetime was found to decrease with the increase in annealing temperature above 750 °C and annealing time over 1second due to the decrease in hydrogen supply from the SiN_x film and continued dissociation of the hydrogenated defects. These cell results with photolithography contacts and double layer AR coating suggest

that 16-17 % efficient manufacturable ribbon cells can be realized with screen printed Ag contacts and single layer SiN_x AR coating.

Acknowledgements

The author would like to thank T.Moriarty of NREL for the cell characterizations

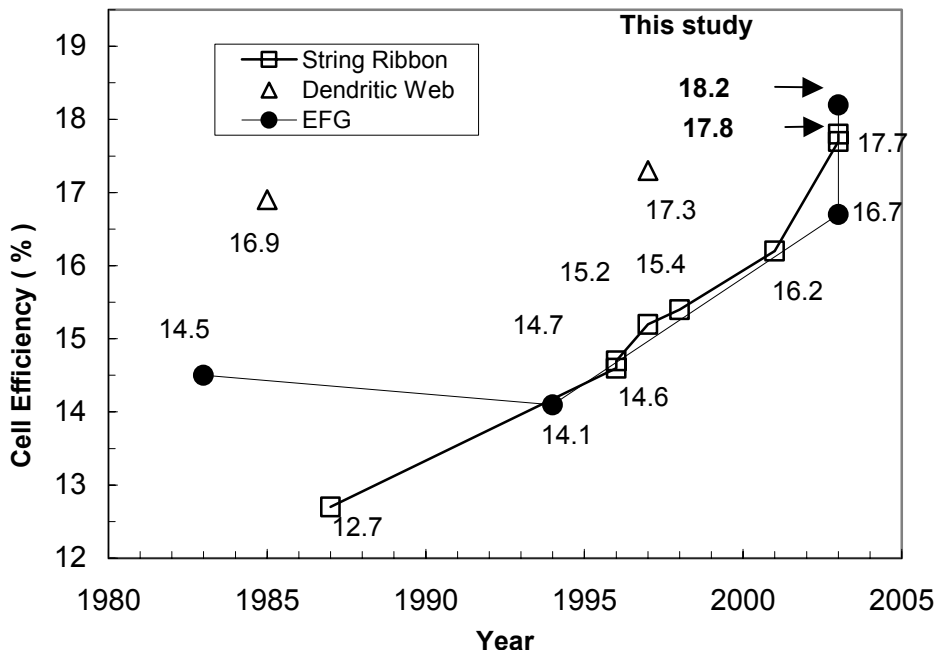


Fig. 1 Progress in efficiency of laboratory scale ribbon solar cells with photolithography contacts.

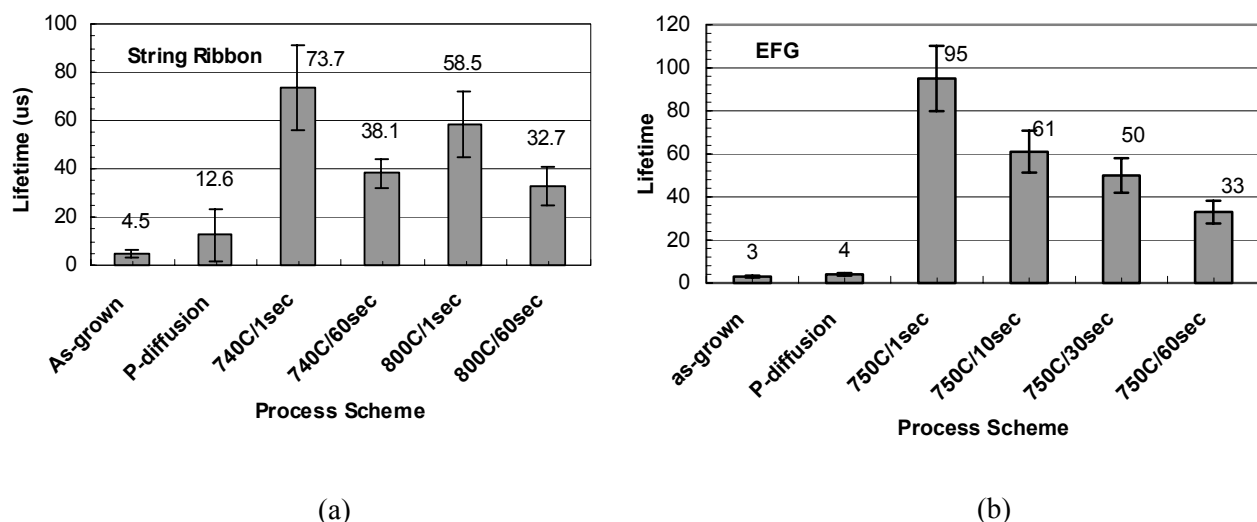


Fig. 2 Process induced lifetime enhancement in String Ribbon (a) and EFG Si (b). Lifetime is shown as a function of P-diffusion and SiN_x/Al co-firing at different condition.

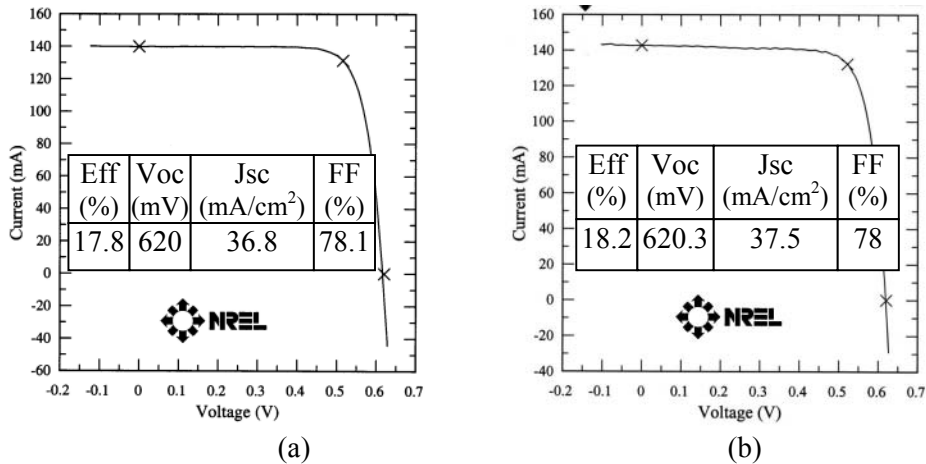


Fig. 3 Light I-V characteristics of ribbon silicon solar cells on String Ribbon(a) and EFG(b) measured by NREL.

References

- ¹ J.I.Hanoka, *Proceedings of 29th IEEE Photovoltaic Specialists Conference*, New Orleans, LA,, 19-24 May 2002, p.66.
- ² J.Kalejs, B.Mackintosh, W.Schmidt, and B.Woesten, *Proceedings of 29th IEEE Photovoltaic Specialists Conference*, New Orleans, LA,, 19-24 May 2002, p.74.
- ³ J.Kalejs, *Sol. Energy Mater. & Sol. Cells*, **72**, 139(2002).
- ⁴ G.Hahn, A.Hauser, A.M.Gabor, M.C.Cretella, *Proceedings of 29th IEEE Photovoltaic Specialists Conference*, New Orleans, LA, 19-24 May 2002, p.182.
- ⁵ Ajeet Rohatgi and Ji-Weon Jeong, *Appl. Phys. Lett.*, **82**, 224(2003).
- ⁶ V.Yelundur, A.Rohatgi, J-W.Jeong, J.I.Hanoka, *IEEE Tran. on Elect. Dev.*, **49**, 1405(2002).
- ⁷ F.Jiang, M.Stavola, A.Rohatgi, D.S.Kim, J.Holt, H.Atwater, J.Kalejs, *The Third World Conference on Photovoltaic Energy Conversion*, Osaka, Japan, 2003, in press
- ⁸ S.Fabian, S.Kalbitzer, Ch.Klatt, M.Behar, Ch.Langpape, *Phys. Rev. B*, **58**, 16144(1998).
- ⁹ N.H.Nickel and I.E.Beckers, *Phys. Rev. B*, **66**, 75211(2002).
- ¹⁰ B.L.Sopori, X.Deng, J.P.Benner, A.Rohatgi, P.Sana, S.K.Estreicher, Y.K.Park, M.A.Roberson, *Sol. Energy Mater. & Sol. Cells*, **41/42**, 159(1996).
- ¹¹ J.Pearson, W.Corbett and M.Stavola, *Hydrogen in crystalline semiconductors* (Springer-Verlag Heidelberg New York), 1991.
- ¹² G.Hahn and P.Geiger, *Prog. Photovolt:Res. Appl.*, **11**, 341(2003).
- ¹³ A.Rohatgi, V.Yelundur, J-W.Jeong, D.S.Kim, A.M.Gabor, *The Third World Conference on Photovoltaic Energy Conversion*, Osaka, Japan, 2003, in press.
- ¹⁴ J-W.Jeong, M.D.Rosenblum and J.P.Kalejs, A.Rohatgi, *J. Appl. Phys.*, **87**, 7551(2000).
- ¹⁵ R.O.Bell and J.P.Kalejs, *J. Mater. Res.*, **13**, 2732(1998).
- ¹⁶ S.J.Pearson, J.W.Corbett, and T.S.Shi, *Appl. Phys. A*, **43**, 153(1987).
- ¹⁷ C.K-Kemmerich, W.Beyer, *J. Appl. Phys.*, **66**, 552(1989).
- ¹⁸ W.L.Hansen, E.E.Haller and P.N.Luke, *IEEE Tran. on Nucl. Sci.*, **NS-29**, 738(1982).
- ¹⁹ G.V.Gadiyak, V.G.Gadiyak, M.L.Kosinova, E.G.Salman, *Thin Solid Films*, **335**, 19(1998).

Hydrogen enhanced clusterization of impurities atoms in crystalline silicon

B.N. Mukashev, Yu.V. Gorelkinskii, and Kh.A. Abdullin

Institute of Physics and Technology, Kazakhstan Ministry of Education and Science
480082 Almaty, Kazakhstan

The properties of hydrogen in crystalline silicon are extremely varied. For a long time hydrogen has been known to saturate dangling bonds at surface and grain boundaries, to passivate shallow impurities (such as boron, phosphorus and etc.), deep-level impurities and defects. In this report we demonstrate that, in addition to other effects, interaction of H atoms with impurities initiates the decomposition of the supersaturated solid solution of impurities and leads to the formation of impurity clusters, which are not observed in the absence of H.

Impurity clusters are formed in the hydrogenated Al-doped Si due to H-enhanced migration of Al atoms. A new ESR Si-AA15 spectrum was observed subsequent to the low-temperature (80 K) implantation of H into the FZ-Si:Al samples. The hyperfine structure of the AA15 spectrum is unambiguously indicative of the presence of the defects including two almost equivalent atoms with the nuclear spin $I=5/2$. The ^{27}Al nuclei are the only ones which can be such nuclei in FZ-Si:Al samples. The pairs can be formed only by means of the low-temperature migration of Al atoms. The necessity of the presence of H for the formation of the Al-Al pairs (AA15 center) indicates that Al atoms can migrate in the form of the (Al-H)_i complex.

The concentration of Al-Al pairs (ESR centers AA15) increases with an increase in the implantation dose of H in the range from 1×10^{15} to $5\times 10^{15} \text{ cm}^{-2}$. However, for higher H implantation doses, $\sim 1\times 10^{16} \text{ cm}^{-2}$, which corresponds to the bulk concentration of $\sim 1\times 10^{18} \text{ cm}^{-3}$, or for repetitive implantation of the samples containing the AA15 defects, the intensity of the AA15 spectrum considerably decreases or the spectrum is not formed at all. After the low-temperature implantation at 80 K and subsequent heating of the samples to 195 K, the complex ESR spectrum is formed. Further annealing leads to the emergence of a new complex center. The spectrum undergoes continuous modification up to the annealing temperature of $\sim 200^\circ\text{C}$, at which it vanishes. The properties of defects, which determine the emergence of complex ESR spectra for H-implanted FZ-Si:Al, make it possible to assume that these defects are clusters which contain more than two Al atoms.

The influence of hydrogen impurities on the formation of carbon nanoclusters in carbon-enriched ($>10^{17} \text{ cm}^{-3}$) float-zone silicon has been studied by means of EPR along with uniaxial-stress experiments. Hydrogen was incorporated by proton implantation at room temperature. As object of researches, an EPR spectrum not identified earlier (denoted as PK4) with $S=1/2$ and C_2 symmetry was used. We have found that hydrogen implantation in FZ silicon with elevated content of carbon upon subsequent annealing above $\sim 250^\circ\text{C}$ generates most prominent EPR signal of the PK4 defect. We have revealed reliably three sets of hyperfine (hf) satellites: 1) one equivalent Si atom with strong localization (~42%) of the resonant wave function of tetragonal symmetry; 2) four equivalent Si atoms with ~16% of the resonant wave function; 3) weak hfi which can be caused by an isotope of ^{13}C from four equivalent carbon atoms. Uniaxial stress experiments reveal very large value (~2.8 eV) of the activation energy for atomic reorientation that along with data of piezospectroscopic tensor are in good agreement with the cluster nature of the defect. We suggest that the presence of hydrogen leads to a strongly coordinated formation of nanocluster, which includes carbon and self-interstitial atoms. It is suggested that the electronic structure of this defect corresponds to the double donor in a positive charge state.

A Rapid, Non-contact Method for Measurement of Si Wafer Thickness: Principles and Preliminary Results

Bhushan Sopori, Chris Auriemma, Chuan Li, and Jamal Madjdpor

National Renewable Energy Laboratory

1617 Cole Blvd.

Golden, CO 80401

INTRODUCTION

The thickness of a semiconductor wafer can critically influence mechanical and/or electronic yield of the device(s) fabricated on it. For most microelectronic (surface) devices, the thickness of a wafer is important primarily for mechanical reasons—to provide control and stability of devices by minimizing stresses resulting from various device-fabrication processes. However, for minority-carrier devices, such as solar cells, the entire thickness of the wafer participates in the optical and electronic performance of the device. In either case, control of wafer thickness through careful measurement is a fundamental requirement in the commercial fabrication of electronic devices.

In the microelectronics industry, the thickness of a wafer is controlled through various steps involving wafering, etching, and polishing, which typically produce flat wafers with parallel surfaces. The thickness of such a wafer is well defined, and its measurement is somewhat straightforward. A variety of methods have been used in the semiconductor industry for wafer-thickness measurement. Two of the most common are:

- Dial gauge — a manual, mechanical measurement, generally used in the laboratory for a small number of wafers.
- Impedance method — which measures capacitance or eddy current loss in an rf bridge configuration.

The microelectronics industry uses almost exclusively non-contact, impedance methods for wafer-thickness measurements. These techniques take a few seconds for each wafer, but require knowledge of the resistivity of the wafers. However, they are not well suited for mapping the thickness variations.

The solar industry imposes very severe demands on a technique for wafer-thickness measurement because of the following reasons:

- Large throughput —Even a small commercial production facility deals with a large number of wafers (e.g., a typical manufacturing facility may use 50,000 wafers/day). Of these, a reasonable fraction must be measured for meaningful QA purposes. Concomitantly, measurement technique must be very rapid.
- Wafers are not typically flat —in particular, Si ribbons deviate strongly from non-parallel surfaces and have surfaces that exhibit strong variations in the surface morphology. Here, one must measure some kind of “average” thickness and/or determine a thickness profile.

- Wafers can be single-crystalline as well as multi(or poly)-crystalline—the impedance method can produce inaccuracies for multi- or polycrystalline wafers because of the extraneous impedance associated with grain boundaries and defects.
- Wafers have rough surfaces—Solar cells require rough or textured surfaces to lower surface reflectance and maximize optical absorption. This leads to inaccuracies in most measurement methods. Surface roughness is particularly detrimental for optical techniques. Another form of surface roughness can occur because of morphological problems arising from improper sawing.

The demands of solar industry are difficult to meet. The difficulties are further intensified by a need for minimizing the equipment and the measurement costs. The solar cell industry typically uses wafer weighing as a method for monitoring wafer thickness. Some companies (that use single-crystal wafers) employ impedance-based methods to measure thickness of a very small number of total wafers. Thus, solar industry needs a method for measurement of wafer thickness that can yield meaningful results for wafers that may have rough and/or non-parallel surfaces. Such a method should be rapid, accurate, and low cost.

We describe a new method for measuring wafer thickness. This is a non-contact, optical method that can determine an average value of the thickness of the entire wafer in a very short time (< 100 ms). It is applicable to wafers of all surface morphologies (polished, rough, textured) and lends itself readily for making maps of the wafer thickness.

PRINCIPLES OF THE NEW METHOD

In this method, the measurement parameter is the total reflectance spectrum of the test wafer. The measured reflectance (or preselected segments of it) is compared with a database of spectra generated by calculation or through measurements made on calibrated samples. This database includes reflectance spectra for wafers of different thickness and surface characteristics. The calculations are performed using *PV Optics* [1, 2]. Because the surface properties of the test wafer are known, the comparison yields the thickness of the wafer.

The total reflectance spectrum of the test wafer is measured by Sopori reflectometer (licensed to GTi, which offers this instrument for sale as GT-Fabscan). The measured reflectance spectrum carries information pertaining to thickness of the wafer as well as properties of its surfaces. It should be pointed out that surface properties of the test wafer are generally known before the desired measurement proceeds. The approach described here is applicable to any wafer (of any surface quality and thickness variation), but we will consider specific cases only—cases that are of interest to the solar or semiconductor industry.

To understand the principle of the proposed technique, we first consider reflectance of a double-sided, parallel polished Si wafer (see Figure 1). Consider a wafer of thickness (t), illuminated by a beam of light. The total reflectance (R_T) and total transmittance (T_T) can be written as:

$$R_T = R \left\{ 1 + \left[\frac{(1-R)^2 e^{-2at}}{1 - R^2 e^{-2at}} \right] \right\} \quad T_T = \frac{(1-R)^2 \cdot e^{-at}}{1 - R^2 e^{-at}}$$

where

$$R = \frac{(n-1)^2 + k^2}{(n+1)^2 + k^2}$$

and

$$T_r = \exp(-\alpha t) = \exp(-4\pi kt / \lambda)$$

Here, n, k, and α are the refractive index, extinction coefficient, and absorption coefficient, respectively.

Incident light

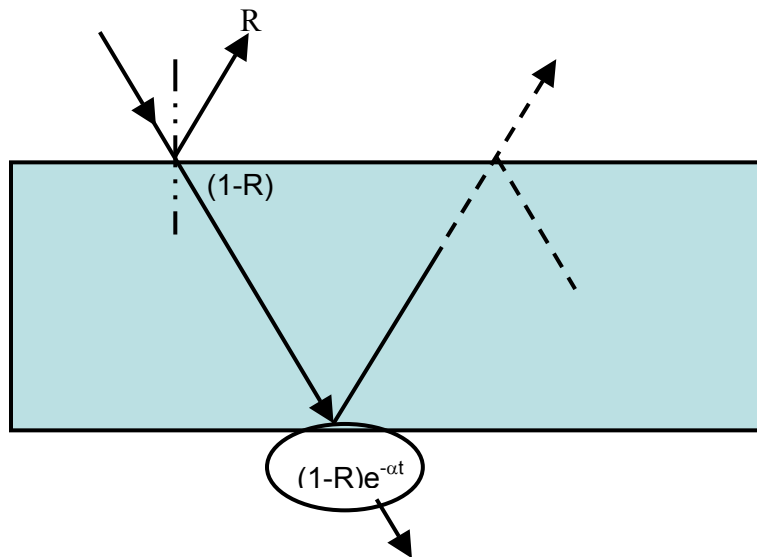


Figure 1. Illustration of total reflectance and transmittance of a semiconductor wafer.

Figure 2 is a plot of R_T for two samples, 50 μm and 300 μm in thickness. The R_T Vs λ can be divided into three regions. Region I corresponds to the high-absorption region; here the reflectance is simply from the front side of the wafer. In Region II, the absorption coefficient is moderate and the reflectance has contributions from the front as well as the back side (including multiplerereflections from within the wafer itself). In this region, the thicker wafer has lower reflectance for a selected value of λ . Region III is weakly absorbing. Concomitantly, reflectance is almost independent of the wafer thickness. Thus, region II is of primary interest for the measurement of wafer thickness.

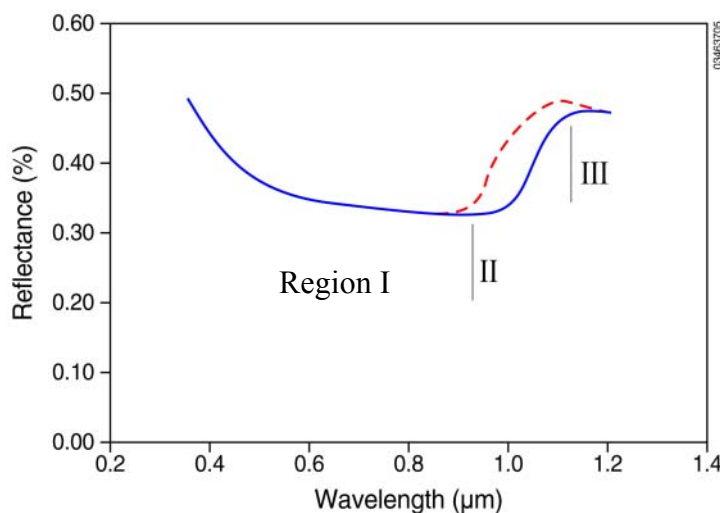


Figure 2. Calculated reflectance spectra of 50- μm (dotted) and 300- μm thick Si wafers.

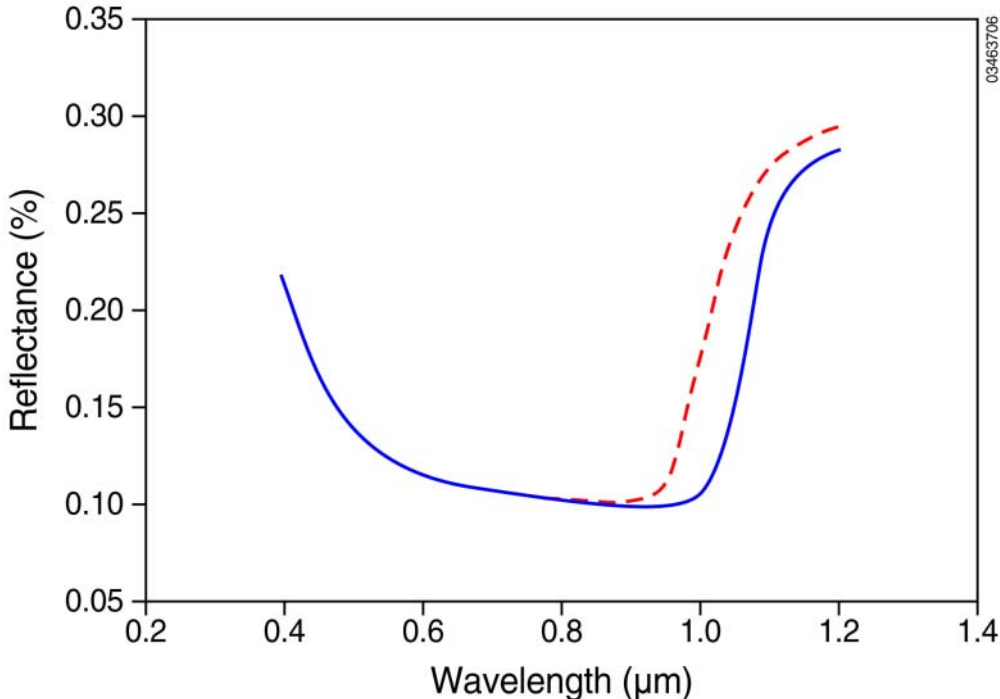


Figure 3. Calculated reflectance spectra of double-side-textured wafers that are 50 μm thick (dotted) and 300 μm thick (solid).

A similar R_T Vs λ can also be determined for unpolished wafers. Figure 3 shows calculated reflectance spectra of two double-side-textured wafers, one 50 μm thick and the other 300 μm thick. The reflectance spectra exhibit characteristics similar to those of Figure 2, with the following variations:

1. The reflectance in Region I is much lower (about 10%).
2. The reflectance in the Region III is also lower than in the corresponding region of Fig. 2.
3. We see in both cases (Figs. 2 and 3) that there is a large separation between the curves of thin and thick wafers in Region II. There are several approaches of using this region for measuring wafer thickness.

APPROACHES TO DECONVOLVE R_T VS λ CURVE

Because the reflectance spectrum of a wafer carries information that relates to the surfaces as well as the wafer thickness, it is important to develop a systematic approach to deconvolve the spectrum. As indicated, the reflectance of a Si wafer in the highly absorbing region is characteristic mainly of the surface morphology. Hence, Region I of the spectrum can be used to identify the nature of the front surface. A polished wafer exhibits the highest reflectance. A rough surface has lower reflectance, and periodic roughness can further lower the reflectance. If the surface characteristics and the thickness of a wafer are known, the entire reflectance spectrum can be calculated using *PV Optics*. Conversely, if the reflectance spectrum of a wafer

is known, we can judiciously use the results from *PV Optics* to infer the wafer thickness through curve fitting. Such a best fit can yield a set of surface parameters and the wafer thickness. However, in practice, surface characteristics of the wafer are known, which simplifies the measurement process and obviates the need for curve fitting. The measurement can be made using only a preselected segment of wavelength.

There are two such approaches to relate the reflectance to thickness of the wafer. One method is to preselect a suitable R-value within Region II, and then use the wavelength that yields this R-value as a parameter to relate to the wafer thickness. For example, in Figure 4, if we select $R=0.3$, we can get corresponding λ -values as $\lambda = 1.02 \mu\text{m}$ for the thinner wafer and $\lambda = 1.06 \mu\text{m}$ for the thicker wafer. It may be noted that for some wafers R Vs λ may have a shape such that the selected R-value can occur at more than one wavelength. Again, using Fig. 4 as an example, if we select $R=0.15$, there are two values of wavelength that yield this value of R . For the thicker wafer, these values are: $\lambda_1 = 0.45 \mu\text{m}$ and $\lambda_2 = 1.04 \mu\text{m}$. Hence, one can either make the choice of R to give an unambiguous value of λ or ignore wavelength value in Region I. In the second approach, one can pre-select a wavelength in the range of $0.9 \mu\text{m}$ and $1.15 \mu\text{m}$, and use the reflectance corresponding to this wavelength for determining the thickness of the wafer. This approach is somewhat easier to implement in practice—one only has to interpose a suitable narrow-band filter in the signal path before the detector. The amplitude of the signal transmitted through this filter is inversely related to the wafer thickness.

Because we are using reflectance (instead of transmittance), one can change the back reflectance by placing the wafer on a support of suitable reflectance. For example, a reflecting wafer support can be beneficial in increasing the sensitivity. This can be seen from Figure 4, which shows calculated reflectance of double-side-textured Si wafer on a reflecting support (Fig. 4 shows the R_T Vs λ for textured wafers of Figure 3 placed on a reflective mirror). This placement results in reflectance values in Region II, which can be unambiguous λ -values.

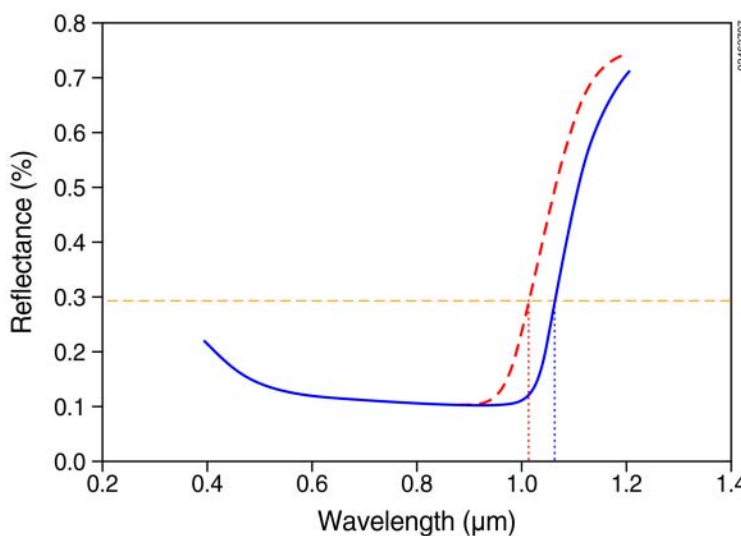


Figure 4. Reflectance spectra of double-side-textured, 50- μm (dotted) and 300- μm (solid) thick Si wafers, on reflecting support.

AVERAGE THICKNESS

The proposed technique relies on the changes in the optical absorption due to change in the wafer thickness. Hence, the measured thickness is “averaged” over the area of illumination. If the entire wafer is illuminated, this technique inherently averages the thickness of the wafer because it measures the reflectance of the entire wafer. This feature of the proposed method is very valuable for solar industry. The solar industry uses a variety of different types of wafers, and some of these include ribbons. The ribbons are not flat wafers but they taper away from the middle of the wafer. In these cases, the thickness monitoring requires an average thickness of the wafer.

METHOD AND SOME RESULTS

This method consists of measuring R_T Vs λ of the entire wafer in a GT-FabScan [3,4]. This instrument rapidly measures the wavelength dependence of reflectance of the entire wafer (or cell), up to 6-in x 6-in in size. These data are analyzed to derive parameters related to surface roughness and texture, antireflection coatings, front-metallization properties (area fraction and thickness), and the back-contact properties of a solar cell. The GT-FabScan operates according to the concept of “reciprocal optics”—in which the sample is illuminated through a very wide angle of incidence and the normal component of the reflected light is measured. We point out that one approach for implementing this concept is to use an integrating sphere to randomize the direction of the light before it impinges on the test sample. However, the integrating-sphere approach is not suitable for large-area measurements.

The approach used in the GT-FabScan is unique—it uses multiple, wide-angle, light sources to illuminate the large-area sample, and the light scattered normal to the sample is collected for analysis. This new approach makes the system quite simple, low cost, and rapid, and it permits use of high-power sources to enable measurement of “optically averaged” parameter values for large-area solar cells and wafers. However, because only the light reflected in a direction normal to the sample must be collected, this approach demands that all the extraneous light must be excluded. Such extraneous light includes non-normal components of the light reflected from the test wafer, as well as the scattered light from parts of the instrument such as the wafer holder and mounting brackets. To accomplish this, the GT-FabScan uses highly absorbing surfaces and a system of light-trapping baffles, resulting in an extremely high S/N ratio (of about 200). This allows the entire measurement and analysis to be made in less than 10 s, which can be further reduced to less than 1 s.

Here we present some results showing the repeatability of measuring the reflectance spectra and the sensitivity of the spectra to wafer thickness. These results are given in Figures 5-8. Excellent repeatability and thickness sensitivity of better than 20 μm can be observed.

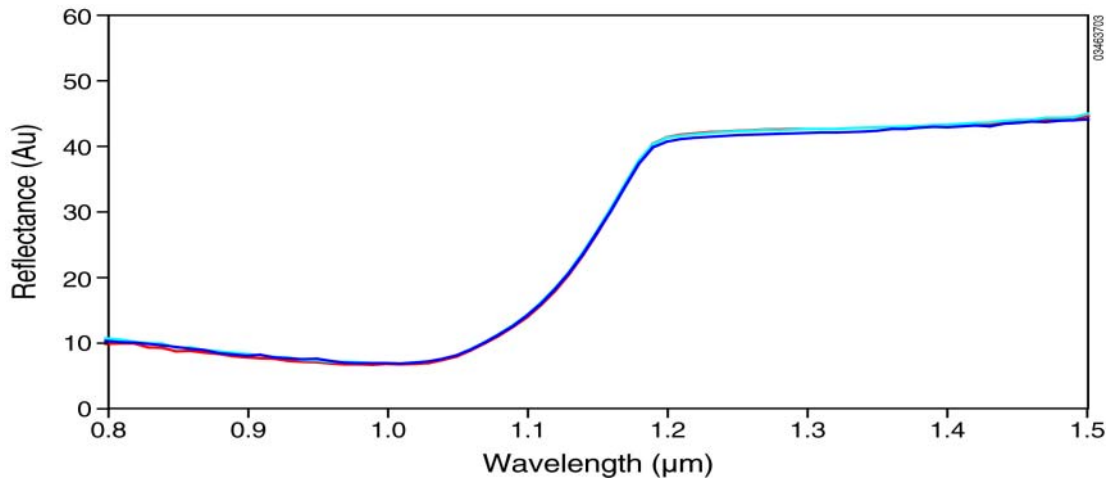


Figure 5: Illustration of repeatability. Three repeated measurements of reflectance spectra of the same wafer: single-crystal, double-side-textured. Thickness values are: Dial gauge : 233 μm , capacitance method: 221 μm , weighing: 219 μm .

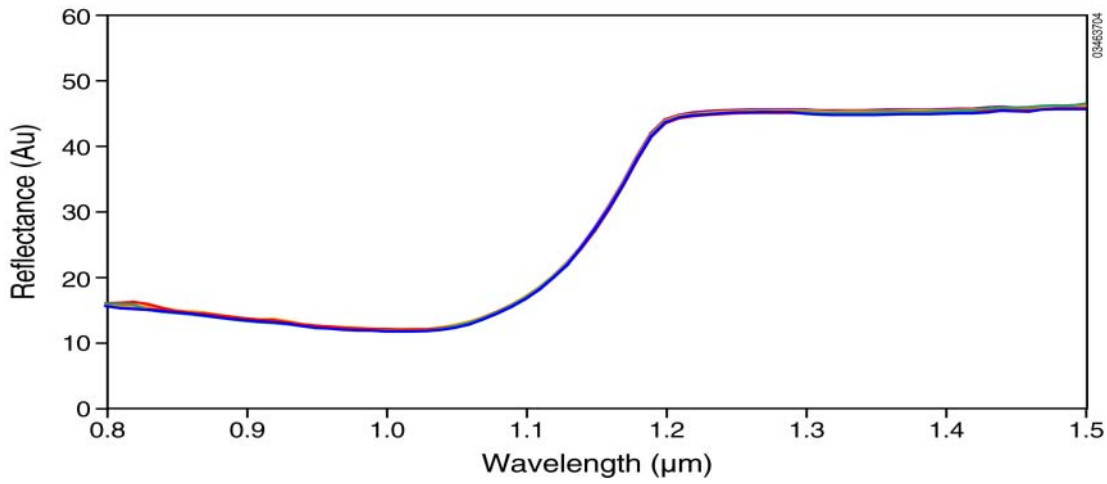


Figure 6. Reflectance spectra of five commercial 4-in x 4-in single-crystalline, double-sided textured, Si wafers of the same thickness. Thickness values are:
Dial gauge: 230 – 236 μm , capacitance method: 218 – 221 μm , weighing: 216 – 219 μm .

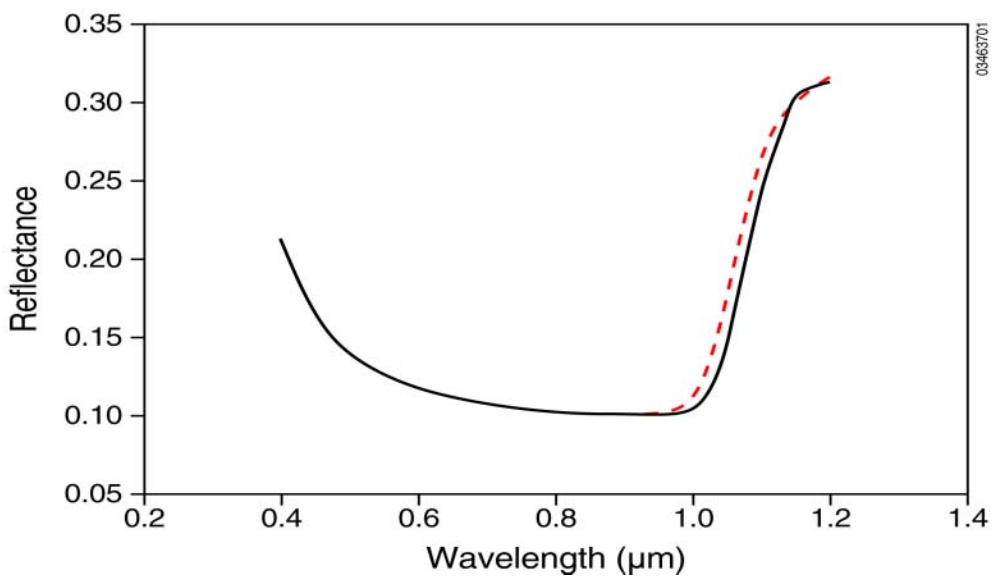


Figure 7a. Calculated reflectance spectra of two mc-Si wafers 150- μm (dotted) and 260- μm (solid) thick.

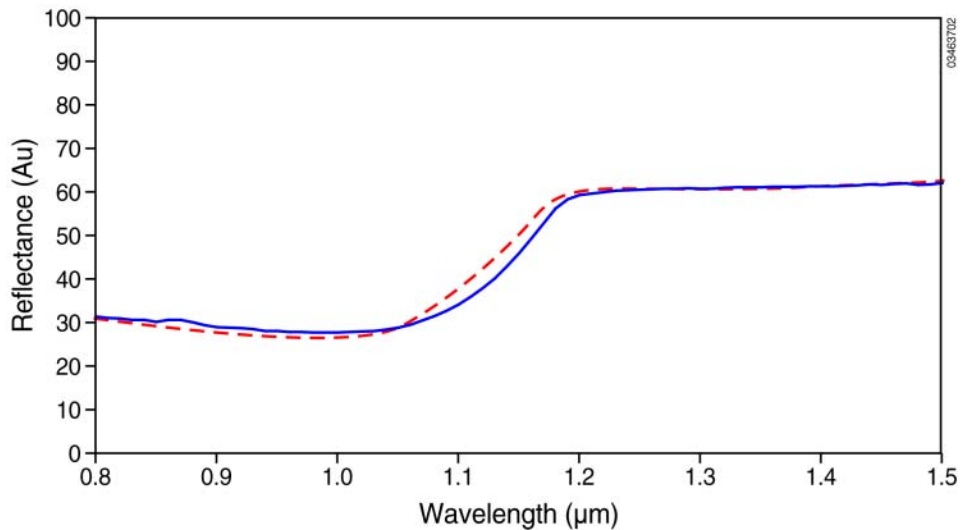


Figure 7b. Measured reflectance spectra of two mc-Si wafers 150- μm (dotted) and 260- μm (solid) thick.

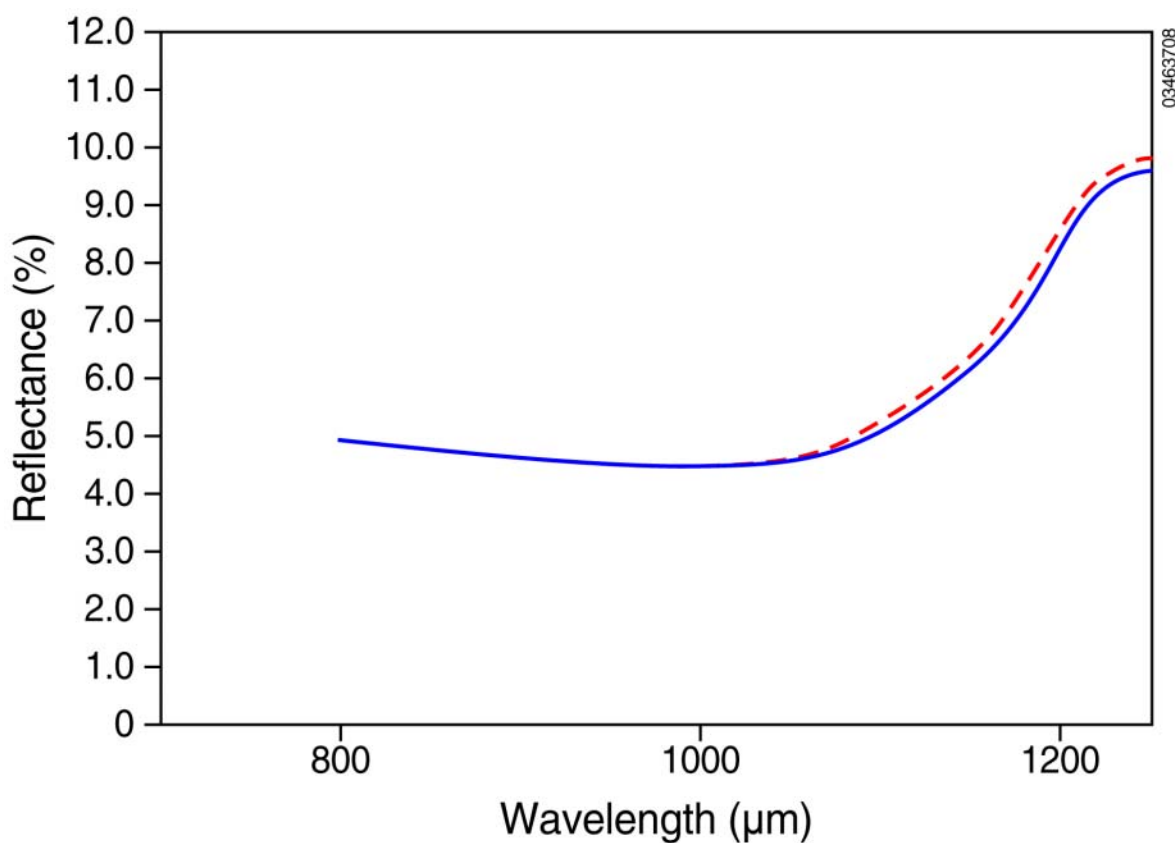


Figure 8. Measured reflectance spectra of a 125-mm x 125-mm, mc-Si wafer before (solid line) and after thinning (dotted line). The wafer was front textured and back polished and had about 50 μm bow. The original wafer-thickness \sim 300 μm . Difference in thickness is about 20 μm .

CONCLUSION

We have described a new technique for measurement of wafer thickness, which uses total reflectance of the wafer at a wavelength within the absorption edge of Si to determine its thickness. Because the total reflectance of a wafer depends on its thickness as well as its surface properties, one typically needs a broadband reflectance spectrum to separate surface effects on the thickness measurement. However, if the surface properties of the wafer are known, a single wavelength measurement can work well. This technique is compatible with the GT-FabScan, which allows large-area measurements to be made in a very short time, typically less than 1 s. This method of measurement is well suited for the solar industry.

This proposed method has another advantage — it can be easily adapted to make spatial maps of the thickness (imaging mode). To accomplish this, the reflectance is measured at a selected wavelength (or a narrow band) from the total signal of the reflectometer using an appropriate narrowband filter. The amplitude of the signal transmitted through this filter is related to the wafer thickness.

In other measurements, we have made some preliminary comparisons between the thickness measured by this technique and other techniques consisting of dial gauge, wafer weighing, and capacitance method. These results show an excellent agreement.

ACKNOWLEDGEMENT

This work was supported by the US Department of Energy under contract #DE-AC36-99G010337

REFERENCES

- [1]. B. L. Sopori, *Laser Focus*, **34**, 159 (Feb. 1998).
- [2]. B. L. Sopori and T. Marshall, *Proc. 23rd IEEE Photovoltaic Specialists Conference*, 1993 (New York: IEEE).
- [3] B. L. Sopori, "Principle of a new reflectometer for measuring dielectric film thickness on substrates of arbitrary characteristics," *Rev. Sci. Instrum.* **59(5)**, 725, 1988.
- [4] Proc. 9th Workshop on Crystalline Silicon Solar Cell Materials and Processing, pp 74-80, August 9-11, 1999, Breckenridge, CO.

DETAILED STUDY OF DEFECTS IN SILICON SOLAR CELLS BY CATHODOLUMINESCENCE SPECTRUM IMAGING

M. J. Romero¹, S. Ostapenko², M. M. Al-Jassim¹, I. Tarasov², and P. Sheldon¹

¹National Renewable Energy Laboratory, 1617 Cole Boulevard, Golden, CO 80401-3393

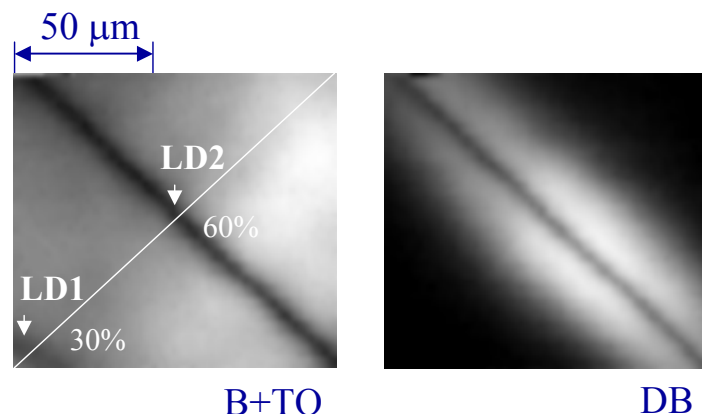
²University of South Florida, 4202 E. Fowler Avenue, Tampa, FL 33620

We have recently developed a spectrum imaging system for cathodoluminescence (CLsi) at NREL, which has been successfully applied to different semiconductors. The advanced multi-channel detection required for CLsi consists of an ultrafast spectrum acquisition triggered by the electron beam during scanning. Spectra are acquired either with a Roper Scientific silicon EEV-1340×400 cryogenic CCD or an InGaAs 512×1 cryogenic PDA, depending on the range of spectral emission. Acquisition times by pixel are typically of 10 to 20 ms (180 seconds for a 100×100 pixel image). The output of spectrum imaging measurements is thus represented by a series of emission spectra. CCDIMAG, the software developed for CLsi, processes this spectrum series to reconstruct monochromatic images or extract the spectrum from any area on the image. This system is operated on the JEOL-5800 scanning electron microscope (SEM). CLsi measurements can be performed at temperatures between 15 K and 300 K. A low-vibration ARS Displex DE-202 closed-circuit cryostat provides cryogenic operation. The interface for vibration isolation has been developed to be compatible with SEM observation.

Because of the technological importance of silicon for photovoltaics, a collaboration between NREL and USF has been established to study defects in multi-crystalline silicon solar cells (mc-Si) combining scanning photoluminescence and CLsi. From photoluminescence mappings, defective areas of the solar cells are selected to perform cathodoluminescence measurements with higher resolution.

The figure shows images of a selected area with a strong defect-band emission near 0.8 eV, as confirmed previously by scanning photoluminescence. At low temperatures, band-to-band emission is substituted with the TO phonon replica of the boron-bound exciton at 1.093eV (B+TO). Defect-band recombination is associated with linear defects highly effective as non-radiative recombination centers: DB recombination is observed for a linear defect with a contrast of 60%, but not for linear defects with contrast below 40%.

Based on a detailed analysis of the cathodoluminescence results, a model for these defects will be further discussed.



Cathodoluminescence images of linear defects identified in mc-Si solar cells for the (a) B+TO, and (b) defect-band transitions. The linear defect LD1, with a contrast of 30% does not show DB recombination. $E_b = 20 \text{ keV}$, $I_b = 2 \text{ nA}$, $T = 19.8 \text{ K}$.

REPORT DOCUMENTATION PAGE

Form Approved
OMB NO. 0704-0188

Public reporting burden for this collection of information is estimated to average 1 hour per response, including the time for reviewing instructions, searching existing data sources, gathering and maintaining the data needed, and completing and reviewing the collection of information. Send comments regarding this burden estimate or any other aspect of this collection of information, including suggestions for reducing this burden, to Washington Headquarters Services, Directorate for Information Operations and Reports, 1215 Jefferson Davis Highway, Suite 1204, Arlington, VA 22202-4302, and to the Office of Management and Budget, Paperwork Reduction Project (0704-0188), Washington, DC 20503.

1. AGENCY USE ONLY (Leave blank)	2. REPORT DATE August 2003	3. REPORT TYPE AND DATES COVERED Conference Proceedings August 10–13, 2003
4. TITLE AND SUBTITLE 13th Workshop on Crystalline Silicon Solar Cell Materials and Processes, Extended Abstracts and Papers		5. FUNDING NUMBERS WO97C100
6. AUTHOR(S) B.L. Sopori, Workshop Chairman/Editor		
7. PERFORMING ORGANIZATION NAME(S) AND ADDRESS(ES) National Renewable Energy Laboratory 1617 Cole Blvd. Golden, CO 80401-3393		8. PERFORMING ORGANIZATION REPORT NUMBER
9. SPONSORING/MONITORING AGENCY NAME(S) AND ADDRESS(ES) National Renewable Energy Laboratory 1617 Cole Blvd. Golden, CO 80401-3393		10. SPONSORING/MONITORING AGENCY REPORT NUMBER NREL/BK-520-34443
11. SUPPLEMENTARY NOTES		
12a. DISTRIBUTION/AVAILABILITY STATEMENT National Technical Information Service U.S. Department of Commerce 5285 Port Royal Road Springfield, VA 22161		12b. DISTRIBUTION CODE
13. ABSTRACT (<i>Maximum 200 words</i>): The 13 th Workshop will provide a forum for an informal exchange of technical and scientific information between international researchers in the photovoltaic and relevant non-photovoltaic fields. It will offer an excellent opportunity for researchers in private industry and at universities to prioritize mutual needs for future collaborative research. The workshop is intended to address the fundamental aspects of impurities and defects in silicon: their properties, the dynamics during device processing, and their application for developing low-cost processes for manufacturing high-efficiency silicon solar cells. A combination of oral, poster, and discussion sessions will review recent advances in crystal growth, new cell structures, new processes and process characterization techniques, and cell fabrication approaches suitable for future manufacturing demands.		
14. SUBJECT TERMS: photovoltaics; solar cells; crystalline silicon; materials and processes; impurities; device process; low cost; manufacturing; microelectronics;		15. NUMBER OF PAGES
		16. PRICE CODE
17. SECURITY CLASSIFICATION OF REPORT Unclassified	18. SECURITY CLASSIFICATION OF THIS PAGE Unclassified	19. SECURITY CLASSIFICATION OF ABSTRACT Unclassified
		20. LIMITATION OF ABSTRACT UL